



اوتام
UNIVERSITI
TEKNOLOGI
MARA



jmeche

Journal of mechanical engineering

Regular Issue Sept 2023
Volume No.20(3)

ISSN : 1823 - 5514

e-ISSN : 2550 - 164x

jmeche.uitm.edu.my



JOURNAL OF MECHANICAL ENGINEERING

EDITOR-IN-CHIEF:

Professor Jamaluddin Mahmud – Universiti Teknologi MARA, Malaysia

EDITORIAL BOARD:

Professor Wahyu Kuntjoro – Universiti Teknologi MARA, Malaysia

Professor Hoffmann – Elektrische Meßtechnik, Prozeß- und Analysenmeßtechnik

Professor Martin Bednarz – Technische Hochschule Ingolstadt, Germany

Professor Naveed Ramzan -University of Engineering & Technology, Lahore Pakistan

Professor Abdelmagid Salem Hamouda – Qatar University, Qatar

Professor Abdul Rahman Omar – Universiti Teknologi MARA, Malaysia

Professor Bernd Schwarze – University of Applied Science, Osnabrueck, Germany

Professor Bodo Heimann – Leibniz University of Hannover Germany

Professor Darius Gnanaraj Solomon – Karunya University, India

Professor Essam E. Khalil – University of Cairo, Egypt

Professor Hazizan Md. Akil – Universiti Sains Malaysia, Malaysia

Professor Ichsan S. Putra – Bandung Institute of Technology, Indonesia

Professor Masahiro Ohka – Nagoya University, Japan

Professor Mirosław L. Wyszynski – University of Birmingham, UK

Professor Mohd. Zulkifly Abdullah – Universiti Sains Malaysia, Malaysia

Professor Muhammad Azmi Ayub – Universiti Teknologi MARA, Malaysia

Professor Roslan Abd. Rahman – Universiti Teknologi Malaysia, Malaysia

Professor Salmiah Kasolang – Universiti Teknologi MARA, Malaysia

Professor Shahrir Abdullah – Universiti Kebangsaan Malaysia

Professor Shahrum Abdullah – Universiti Kebangsaan Malaysia

Professor Wirachman Wisnoe – Universiti Teknologi MARA, Malaysia

Professor Xinkai Chen – Shibaura Institute of Technology, Japan

Professor Yongtae Do – Daegu University, Korea

Dr. Yongki Go Tiauw Hiong – Raytheon Company, USA

Dr. Mohd. Afian Omar – SIRIM Malaysia Advanced Materials Research Center

Dr. Valliyappan David Natarajan – Universiti Teknologi MARA, Malaysia

MANAGING EDITORS:

Dr. Mohd Hanif Mohd Ramli

Dr. Siti Mariam Abdul Rahman

SECTION EDITORS:

Assoc. Prof. Ir. Ts. Dr. Baljit Singh Bathal Singh

Ir. Ts. Dr. Kausalyah Venkatasen

Dr. Abdul Malek Abdul Wahab

Dr. Nurul Hayati Abdul Halim

ASSISTANT MANAGING EDITORS:

Dr. Izdihar Tharazi

Dr. Mohd Afzan Mohd Anuar

Dr. Natasha Ahmad Nawawi

Mr. Muhamad Fauzi Othman

Mrs. Nurul Syuhada Khusaini

Mrs. Rosnadiyah Bahsan

Copyright © 2022 by the College of Engineering, Universiti Teknologi, MARA, 40450 Shah Alam, Selangor, Malaysia.

All published articles in this journal are open accessed. This allows anybody to freely download, print, copy, distribute or read them, as well as to reused and quoted with proper credit to the original published version. By submitting an article to JMechE, the authors grant full right to the journal to publish the article online once it has been accepted. However, the authors held ownership of their article.

Journal of Mechanical Engineering (ISSN 1823-5514, e-ISSN 2550-164X) is published by Penerbit UiTM (UiTM Press), Universiti Teknologi MARA, 40450 Shah Alam, Selangor, Malaysia.

The views, opinions, and technical recommendations expressed herein are those of individual researchers and authors and do not necessarily reflect the views of the university.

JOURNAL OF MECHANICAL ENGINEERING

An International Journal

Vol 20 (3)	15 September 2023	ISSN 1823-5514	eISSN 2550-164X
------------	-------------------	----------------	-----------------

1	GUI-Based Data Visualisation Tool for Option C IPMVP Using Jupyter Notebook <i>Ezmin Abdullah*</i> , <i>Nabil M. Hidayat</i> , <i>Nik Muhammad Akram</i> , <i>Ahmad Haziq Ahmad Hisham</i> , and <i>Nurain Izzati Shuhaimi</i> *https://orcid.org/0000-0002-1501-3889	1
2	Optimization of Machining Parameters in Turning for Different Hardness using Multi-Objective Genetic Algorithm <i>Mimi Muzlina Mukri</i> , <i>Nor Atiqah Zolpakar*</i> , and <i>Sunil Pathak</i> *https://orcid.org/0000-0002-5155-5132	25
3	Design of Two-Stage Force Amplification Frame for Piezoelectric Energy Harvester <i>Choe-Yung Teoh*</i> , <i>Joon Kit Wong</i> , <i>Ying Hao Ko</i> , <i>Muhammad Najib Abdul Hamid</i> , <i>Lu Ean Ooi</i> , and <i>Wei Hong Tan</i> *https://orcid.org/0000-0001-5847-6528	49
4	Development of an Order Processing System using Google Sheets and Appsheets for a Malaysian Automotive SME Factory Warehouse <i>Mohamad Khairi Hassan</i> , <i>Mohd Hazri Mohd Rusli*</i> , and <i>Noor Azlina Mohd Salleh</i> *https://orcid.org/0009-0003-0530-8506	63
5	Dynamic Behaviour of Flow Through Three Circular Cylinders in Staggered Arrangement with Three Disturbance Bodies Around the Upstream Cylinder <i>Banta Cut</i> , <i>Sutardi*</i> , <i>Wawan Aries Widodo</i> *https://orcid.org/0000-0002-2630-5385	83
6	Bending and Buckling Analysis of Functionally Graded Plates using a New Shear Strain Function with Reduced Unknowns <i>Ali Meftah*</i> *https://orcid.org/0000-0003-3664-3780	105

7	<p>Applied Machine Learning to Estimate Length of Separation and Reattachment Flows as Parameter Active Flow Control in Backward Facing Step <i>Ahmad Fakhri Giyats, Mohamad Yamin*, Cokorda Prapti Mahandari</i></p> <p>*https://orcid.org/0000-0002-9694-8263</p>	131
8	<p>Evaluating the Nonlinear Dynamic Stiffness of Rail Pad using Finite Element Method <i>Mohamad Hazman Halim, Abdul Malek Abdul Wahab*, Muhamad Sukri Hadi, Azmi Ibrahim, and Noraishah Mohamad Noor</i></p> <p>*https://orcid.org/0000-0003-0605-4117</p>	155
9	<p>Optimization and Mathematical Modelling of Surface Roughness Criteria and Material Removal Rate when Milling C45 Steel using RSM and Desirability Approach <i>Fnides Mohamed*, Fnides Brahim, Bensana Toufik, and Yaltese Mohamed Athmane</i></p> <p>*https://orcid.org/0000-0001-7982-9214</p>	173
10	<p>Accuracy of CFD Simulations on Indoor Air Ventilation: Application of Grid Convergence Index on Underfloor Air Distribution (UFAD) System Design <i>Nor Azira Mohd Zainuddin, Fauziah Jerai*, Azli Abd Razak, and Mohd Faizal Mohamad</i></p> <p>*https://orcid.org/0000-0002-6454-159X</p>	199
11	<p>Reducing The Risk of Agglomeration and Shrinkage Ceramic Body from Al₂O₃-ZrO₂ Composition <i>Norfauzi Tamin *, Ng Chuan Huat, Abdul Hamid, and Umar Al Amani Azlan</i></p> <p>*https://orcid.org/0000-0002-0387-8332</p>	223
12	<p>The Effects of Titanium Dioxide (TiO₂) Content on the Dry Sliding Behaviour of AA2024 Aluminium Composite <i>Hamid M. Mahan, S.V. Konovalov, Irina Panchenko, and Mudhar A. Al-Obaidi*</i></p> <p>*https://orcid.org/0000-0002-1713-4860</p>	239
13	<p>Comparison of Different Surface Pre-Treatment on Mild Steel for Cobalt-Nickel-Iron Electroplating <i>Koay Mei Hyie*, Nor Azirah Mohd Fohimi, Salina Budin, Normariah Che Maideen, and Md Zin Abu</i></p> <p>*https://orcid.org/0000-0002-0458-9786</p>	263
14	<p>The Characterization of the Sandwich Composite Consisted of Coconut Fibre-Polyester Resin and its Variations of Wood Core <i>Sumarji*, Wazirotus Sakinah, R. Puranggo Ganjar Widityo, and Mochamad Asrofi</i></p>	279

15	<p>Synthesisation of Zinc Oxide Nanowires Via Hybrid Microwave-Assisted Sonochemical Technique at Various Microwave Power</p> <p><i>Maryam Mohammad, Mohd Firdaus Malek*, Muhammad Faizal Abd Halim, Nurul Zulaikha Mohammad Zamri, Mohamad Dzulfiqar Bakri, Zuraida Khusaimi, Mohamad Hafiz Mamat, Mohamad Rusop Mahmood, and Tetsuo Soga</i></p> <p>*https://orcid.org/0000-0002-0714-4117</p>	293
16	<p>Influence of Nano Additives on Performance, Combustion, and Emission Characteristics of Diesel Engine using Tamarind Oil Methyl Ester-Diesel Fuel Blends</p> <p><i>Bikkavolu Joga Rao*, Pullagura Gandhi, Vadapalli Srinivas, Chebattina Kodanda Ramarao, and Pathem Uma Chaithanya</i></p> <p>*https://orcid.org/0000-0001-6971-865X</p>	313
17	<p>Performance of Hybrid Al₂O₃:SiO₂ W:EG in PEM Fuel Cell Distributor Plate</p> <p><i>Muhammad Syafiq Idris, Irnie Azlin Zakaria*, Putri Nur Afiqah Nazari, Wan Ahmad Najmi Wan Mohamed, and Wan Azmi Wan Hamzah</i></p> <p>*https://orcid.org/0000-0002-7822-5715</p>	335
18	<p>Influences of Main Machining Process Parameters and Tool Wear on The Machining Damage Generated During Edge Milling CFRP Composites</p> <p><i>Nguyen Thi-Hue, and Nguyen Dinh-Ngoc*</i></p> <p>*https://orcid.org/0000-0002-0631-0961</p>	355
19	<p>Influence of Operating Factors on Accurate Digging Depth Control of the Remote-Controlled Explosive Disposal Machine</p> <p><i>Dat Duy Nguyen, Dat Van Chu, and Sy Le Van*</i></p> <p>*https://orcid.org/0000-0003-1590-0039</p>	371
20	<p>The Influence of Repeated Heat Treatments on The Propagation of Fatigue Cracking of Medium Carburized Steel</p> <p><i>Majid Khaleel Najem, Jamal Nayief Sultan, Emad Toma Karash*, Adel M. Ali, and Hssein A. Ibrhim</i></p> <p>*https://orcid.org/0000-0001-8202-4038</p>	387

GUI-Based Data Visualisation Tool for Option C IPMVP using Jupyter Notebook

Ezmin Abdullah*, Nabil M. Hidayat, Nik Muhammad Akram,
Ahmad Haziq Ahmad Hisham, Nurain Izzati Shuhaimi
School of Electrical Engineering, College of Engineering,
Universiti Teknologi MARA, 40450, Shah Alam, MALAYSIA
*ezmin@uitm.edu.my

ABSTRACT

IPMVP is an acronym for International Performance Measurement and Verification Protocol, used for calculating energy savings by taking some external factors into account to give an equal base for a linear comparison between two periods. However, determining the significant independent variable for routine adjustment causes inconvenient repeated action of regression analysis modeling, which leads to the exhaustive calculation and human error risk. These exasperating actions led to the creation of this project, which aims to provide a user-friendly, insightful, and accurate energy-saving calculation program tool. Thus, the main objective of this project is to develop an energy-saving computational tool for option C IPMVP using web-based data analytic tools to improve efficiency and accuracy in each project. This paper used a web-based mathematical computation, Jupyter Notebook, to determine the significant independent variable for routine adjustment of the adjusted baseline. The program tool was validated using V-model software verification and validation methodology based on IEEE 1012 standards. The study can be concluded that the exhaustive calculation to determine the energy saving based on IPMVP standards can be significantly reduced with precision values at 50%, 80%, 90%, and 95% confidence levels using the proposed program which is equipped with insightful graphs and a user-friendly interface.

Keywords: IPMVP; Energy Saving; Energy Avoidance; GUI; Jupyter Notebook

Introduction

Measurement and Verification (M&V) of energy savings are important when new equipment investments or new operation management was made to adopt an energy efficiency operating plan [1]. It is the process of planning, measuring, collecting, and analysing data to verify and report the facility's energy savings resulting from the adoption of energy conservation measures (ECMs). The International Performance Measurement and Verification Protocol (IPMVP) was developed to measure and verify efficiency investment in energy efficiency engagement [2]. This protocol is owned by Efficiency Valuation Organization (EVO) as a result of a consensus approach. The IPMVP provides a complete framework to verify energy saving after making suitable adjustments for changes in condition [3]. With this proper framework, the process of M&V becomes more detailed and reliable.

However, the exhaustive calculations have made the process of M&V become intricate which leads to human error as well as time-consuming [4]. The main disadvantage of the process is that no proper calculation tool was provided for easy application. There are several studies that suggest application tools using Graphic User Interfaces (GUI). For instance, the GUI-based using Microsoft Visual Basic were introduced in [5]-[7] to calculate energy saving/avoidance for option A, B, and, C, respectively. The program successfully displayed the numerical results of energy saving. However, the selection of significant Independent Variables (IV) for routine adjustments was selected manually by modelling linear regression of IV separately. This program was not fully automatic and require improvement if more samples of independent variables were available to be tested.

There were also papers that developed a software tool for regression analysis but not based on IPMVP. This paper created software tools called "FuReA" for linear regression analysis problem-solving algorithms. This software executed a variety of tasks, including optimal solution search with the required level of dependability, graphic depiction of modelling, etc. [8]. The article proposed the ERA software to resolve issues by providing a user-friendly tool for computer-assisted regression analysis of kinetic experiments [9]. However, this software required subscription fees for a programmer to use.

It is now well established from a variety of studies that the Jupyter Notebook becomes a powerful programming platform for data analysis and visualisation [10]. It supports a variety of tools such as graphics, algorithms, and proofs, and has become the tool of choice for data scientists [11].

Software testing and validation account for a significant portion of development costs. Validation determines if the proposed program tool fits the criteria, whereas verification determines the system's compatibility with the user's needs and expectations as recommended by the IEEE 1012 standard [12]. Klebar et al. [13] approved that V-model is one of the comprehensive testing tools in their development. The model validated their automotive OEM

embedded system. Software sequence verification activities allow reducing time for development since all unpredictable things can be detected in advance. A thorough process in verification flow helped in developing effective validation flow [14] especially to a visual analytic which involves a lot of data to be processed [15].

Therefore, this project aims to minimize the burden of exhaustive calculation of energy saving/avoidance that led to human error and time-consuming. This paper proposed to develop an energy-saving/avoidance program tool for option C that comply with the IPMVP standard methodology using web-based data analytic tools within four independent variables in each project producing four linear regression models and statistical precision analysis. The proposed tool provides insightful data visualisation and accurate data analysis using linear regression models and statistical precision analysis. The remaining of the article is organized as follows. Section 2 presents a theoretical background of the IPVMP framework. Next, Section 3 describes the methodology for the proposed GUI-based and data analysis while Section 4 presents the results and discussion. Finally, implications, contributions, and future recommendations are presented in the conclusion.

Theoretical Background

IPMVP framework

IPMVP offers four types of options to determine energy-saving or energy avoidance namely options A, B, C, and D. Each option represents each type of situation, and it is impossible to generalise on the best IPMVP option. To measure overall energy saving in a facility, option C is the best option compared to options A and B which only measure retrofit isolation. Option C qualifies energy saving for the whole facility to determine saving usually after multiple ECM has been done to the building. Energy data and independent variables (IV) data must be recorded continuously throughout the length of the twelve-month baseline period and reporting period. Based on the IPMVP framework, there are three components that need to be prepared to calculate savings. The components are, adjusted baseline energy, reporting period energy, and non-routine adjustment (if any) which relies upon the following expression:

$$\begin{aligned} \text{Saving} & & (1) \\ &= (\text{Adjusted Baseline Energy} - \text{Reporting Period Energy}) \\ &\pm \text{Non routine Adjustment of Baseline Energy} \end{aligned}$$

where, reporting period energy is data from the data collection after retrofit and adjusted baseline energy is data calculated by first developing a

mathematical model of linear regression which correlates the actual baseline energy data, Y with suitable independent data, x .

Thus, in this case, multiple numbers of IV data must undergo linear regression analysis one by one to find the best correlation variables through the value of r -squared which equals or more than 0.75 [16]. Perhaps the most serious disadvantage of this step is the repetition of work which is prone to human error. Through this mathematical model, the value of conception, m and intercept, C are used to form the adjusted baseline energy, Y_{adj} by inserting the value of each reporting period IV, x' into the model [17]. The mathematical expression for baseline energy, Y and adjusted baseline energy, Y_{adj} are shown in Equations (2) and (3), respectively.

$$\text{Actual Baseline energy, } Y = mx + C \quad (2)$$

$$\text{Adjusted Baseline energy, } Y_{adj} = mx' + C \quad (3)$$

Next, since there is always uncertainty in any measurement, precision, and confidence level are used to quantify how true the value is within that margin [18]. The true value that falls within the range at a given confidence level is established as follows:

$$\text{Range} = \text{saving} \pm \text{absolute or relative precision} \quad (4)$$

Absolute precision is calculated by multiplying standard error, SE with the t from the t -table, and relative precision is divided by the saving estimation in percentage.

$$\text{Absolute precision} = t \times SE \quad (5)$$

$$\text{Relative precision} = \frac{t \times SE}{\text{Savings}} \times 100\% \quad (6)$$

where, SE is calculated using, n sample size, p number of regression variables in case it is multiple regression analysis, modelled baseline energy, Y_i and, actual baseline energy, Y . The SE equation can be expressed as follows:

$$SE = \sqrt{\frac{\sum(Y_i - Y)^2}{n - p - 1}} \quad (7)$$

The modelled baseline energy is calculated for each of the IV samples.

$$\text{Modelled Baseline energy, } Y_i = mx + C \quad (8)$$

In this project, we developed the GUI-based data visualisation for option C as a pilot project to determine energy saving in a very efficient way.

Methodology

The development of this project was carried out based on a software verification and validation process as shown in Figure 1. In the verification process, requirement specification, overall design, detail design, program specification, and coding were carried out to produce an interactive energy-saving calculation and data visualisation tool. Next, there are some processes were carried out in the validation process such as unit testing, integration testing, system testing, and user acceptance.

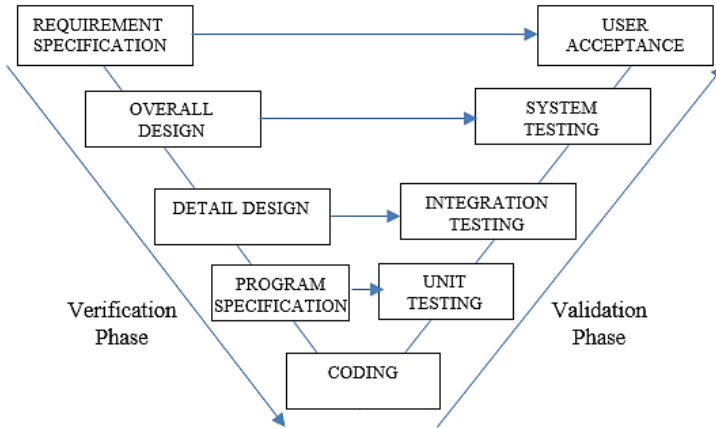


Figure 1: Software verification and validation methodology using V-Model [13]

Verification phase: developing energy-saving calculation and data visualisation tool

In this project, the main contribution relies upon the simplest steps for the users to use the tool. As the IPMVP framework shows exhausting calculations and steps, therefore, an efficient, and accurate tool is much needed. Therefore, we developed a Graphic User Interface (GUI) for users to calculate and visualise all the data only with a few clicks. Figure 2 shows the flow chart for the requirement specifications and overall design. Based on the requirement specification, the overall design flow was designed to suit the requirement. The overall design shows every function for the next step to detail the program specification.

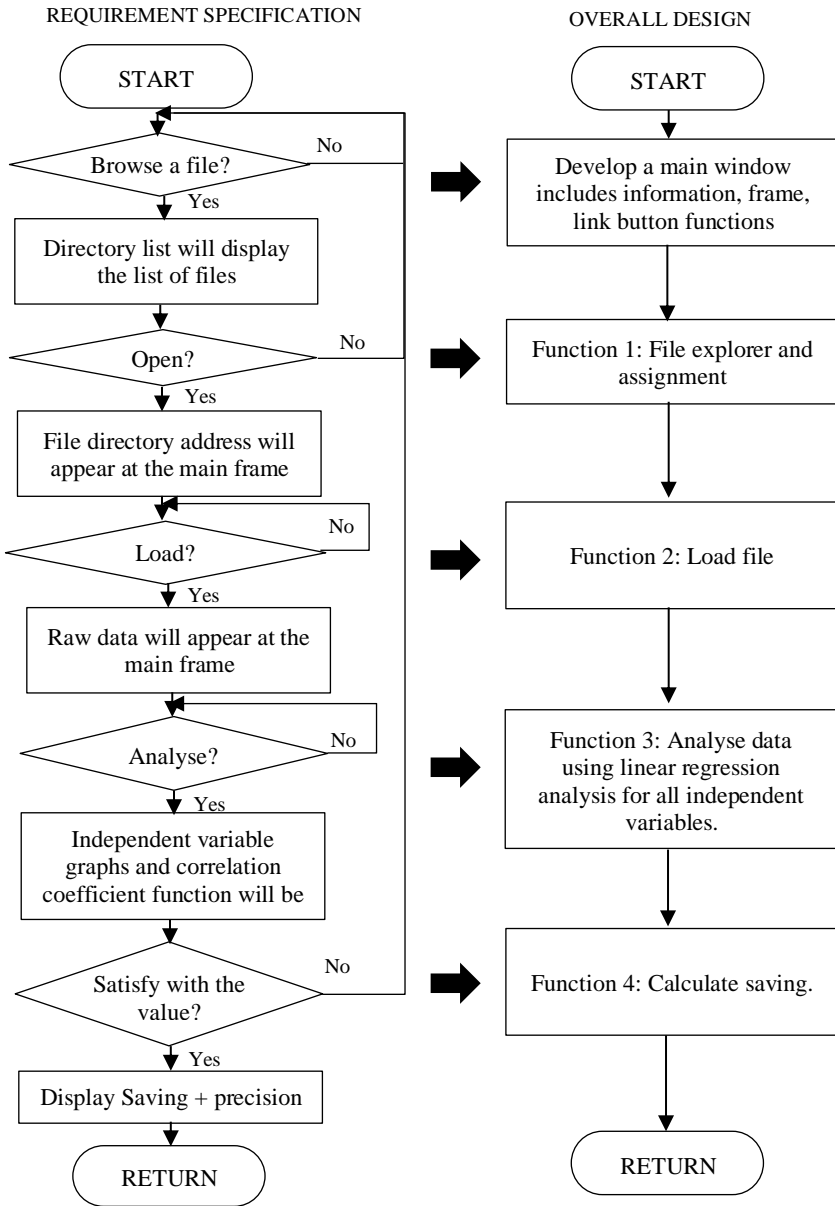


Figure 2: Flow chart of requirement specification and overall design

Table 1 shows the detailed design and program specification to list down all the necessary components to develop a full code. Components such

as package tools, window interface, analysis items, and visualisation items are listed in the detailed design, followed by code construction specifications which are defined in the program specifications. Lastly, the development of the program codes can be referred to as the pseudocodes in Table 2.

Table 1: Detail design and program specification

Detail design	Program specifications
Package Tools	Import <ul style="list-style-type: none"> • Pandas • Matplotlib • Seaborn • NumPy • Scikit-learn • Tkinter
Interface:	
1. Main Window 2. File explorer window 3. Load File window 4. Linear Regression window 5. Adjusted Baseline window 6. Energy Avoidance window	<ul style="list-style-type: none"> • Initialize Tkinter GUI • Setup link buttons for call functions
Load data	<ul style="list-style-type: none"> • Setup Dataset_path
Analysis:	
1. Linear regression for 4 independent variables 2. R-squared 3. Adjusted baseline Precision and confidence level	<ul style="list-style-type: none"> • Construct scatter plot • Compute the coefficient(m), intercept(c), R-squared, standard error (SE) reading. • Compute the precision based on confidence level
Visualisation:	
1. Display the respective data 2. Linear Regression plots 3. Comparison between adjusted baseline with actual baseline 4. Energy Avoidance result	<ul style="list-style-type: none"> • Setup tree view widget for information display • Plot the linear regression • Plot the adjusted baseline • Print Linear regression line equation • Print Energy Avoidance

Table 2: Pseudocodes for the program codes development

1	Program start
2	Initialize Tkinter GUI:
3	Frame for data display
4	Buttons for link functions:
5	Button 1: Call Function1 - new window
6	Button 2: Call Function 2 - new window
7	Button 3: Call Function 3 - new window
8	Tree view widgets for information display
9	Initialize Functions:
10	Function 1: File explorer and assign the chosen
11	file to label file Assign file location
12	Function 2: Load file
13	Read data from csv file
14	Print the data in the frame
15	Function 3: Analyze File
16	Construct Scatter plots (independent
17	variable1, 2, 3, 4)
18	Analyze the plots -- Linear Regression
19	Find out coefficient(m),
20	intercept(c), R squared, standard
21	error (SE))
22	Repeat for all independent variables
23	Determine which m and c has highest R ² .
23	Highest R ² = min (1 - R ²),
24	Print scatter plots
25	Print all Linear regression equation
26	and the highest R ²
27	Initialize button 1: call Function 4 -
28	new window
29	Initialize button 2: close
30	
31	Function 4: Determine energy saving
32	Extract independent
33	variable data that has
34	high correlation to the
35	dependent data referring
36	to Function 3, R ² value.
37	Calculate Adjusted
38	baseline, $y' = mx + c$,

```

39          Calculate Energy saving =
40          (Adjusted baseline -
41          Reporting baseline)
42          Calculate Absolute
43          precision (kWh)
44          Calculate Relative
45          precision (%)
46          Plot adjusted baseline and
47          reporting baseline
48          Print Adjusted baseline
49          and reporting baseline
50          graphs
51          Print Energy saving and
52          multiple precisions
53          based on multiple
54          confidence level (95%,
55          90%, 80%, 50%)
56  Program end

```

Validation phase: testing with sample data

In the validation phase, a set of datasets was prepared for program simulation to test the validity of the program tool.

Sample dataset

Prior to option C IPMVP, the usual baseline period is 12 months. Thus, the sample data for the Dependent Variable (DV) and IV can be considered as a full operating cycle before and after a retrofit. Table 3 shows the summarization of the type of data used for the validation of this project.

Table 3: Variable names and types

No.	Variable	Name of variable	Comment
1.	Dependent variable	Baseline energy	Energy data before a retrofit
2.	Dependent variable	Reporting period energy	Energy data after a retrofit
3.	Independent variables	Can be from multiple types of samples (eg: operating hours, number of working days, occupancy, weather, etc)	Data before a retrofit. To be used for routine adjustment.
4.	Independent variables	Can be from multiple types of samples (eg: operating hours, number of working days, occupancy, weather, etc)	Data after a retrofit. The data types must be the same as before the retrofit.

Data pre-processing

Once the sample data were collected, it was necessary to arrange the data in a specific format to allow the data to be saved in a table-structured format. In this project, CSV file type (*.csv) was used for an easier import to another storage database regardless of the specific software.

The first row of the table content was allocated for the labels. The columns are filled with months, dependent variables (DV) of the actual baseline and reporting baseline, and independent variables (IV) before and after retrofitting. Next, it is important to make sure the sample size of each variable must be 12 by following the one-year period of one cycle trend. In this example, the data was uploaded from January to December for each variable as shown in Figure 3.

	A	B	D	E	F	G	H	J	K	L	M
1	Month	Dependent	Independent1	Independent2	Independent3	Independent4	Dependent0	Independent01	Independent02	Independent03	Independent04
2	January	4850022	5271	21	100002	94731	3966405	3095	21	100800	97705
3	February	3838044	5775	15	71430	65655	5967247	3690	18	86400	82710
4	March	5578406	4990	22	104764	99774	6108354	2846	22	105600	102754
5	April	5959856	4670	20	95240	90570	5434476	2789	22	105600	102811
6	May	5021398	5038	20	95240	90202	4620803	2789	21	100800	98011
7	June	4444060	6654	20	95240	88586	5139372	3882	19	91200	87318
8	July	4863940	4665	22	104764	100099	4399953	1737	22	105600	103863
9	August	4395962	6129	21	100002	93873	3966405	3095	21	100800	97705
10	Septembe	4964390	3647	19	90478	86831	5967247	3690	18	86400	82710
11	October	6013058	4164	23	109526	105362	6108354	2846	22	105600	102754
12	Novembe	5231026	5649	20	95240	89591	5434476	2789	22	105600	102811
13	December	5212102	6060	20	95240	89180	4620803	2789	19	91200	88411

Figure 3: Data on energy consumption and four independent variables format in a CSV file

Significant independent variable

All Independent Variables (IV) were simulated using linear regression analysis to determine which IV has the best correlation to the DV. The correlation can be determined through the value of the *r*-squared generated for each IV. The *r*-squared indicates the level of the variance proportion to the DV and the acceptable benchmark defined by statistical terms is equal to or above 0.75. Then, the best-correlated IV was selected for the next step to calculate savings.

Routine adjustment

Using information extracted from the regression line of the best-correlated IV such as conception, *m*, and intercept, *C*, a routine adjustment can be made to account for differences between the baseline period and reporting period's condition. The routine adjustment is generated using Equation (3) and then was named adjusted baseline energy.

Energy saving precision

Four confidence levels (95%, 90%, 80%, and 50%) were set to quantify how true the value is within that margin. The precision for each confidence level stated above was generated using Equations (5), (6), (7), and (8).

Program tool validation

The program tool validation process was carried out based on the verification and validation using V-model [13]. The components such as window interface, analysis, and visualisation must follow and fulfill the verification design as referred to in Figure 1. Furthermore, all numerical results in this program must be corrected. The checklist for validation is summarized in Table 4.

Table 4: Validation checklist

Item	Unit testing	Integration testing	System testing	User testing
Interface:				
Main Window				
File Explorer window	Every window must show all related features such as frames, buttons, and text	The content displayed in the window interface must be true and same with calculations and plots		
Load file window			The flow of process must follow the overall design flow	
Linear regression window				
Adjusted baseline window				
Load data				
CSV file		Call for CSV file must be fulfilled		
Analysis				
Scatter Plot				
R-squared	Every calculation is correct. Must compare with manual calculation.			All components reflect the IPMVP standard
Adjusted baseline				
Visualisation				
Data display				
Graph comparison	Every plot, graphs and display are correct. Compare with manual calculation			
Energy avoidance				

Results and Discussion

The data visualisation using this proposed tool is displayed using only 4 click functions. For user experience, first, we will discuss the GUI-based data visualisation and followed by data analysis in the next sub-section.

GUI based data visualisation

An interface of the GUI is displayed as shown in Figure 4. Three buttons are located on the main window and the flow of instructions is written for users to apply. Firstly, the user will upload their CSV file by clicking the “Browse A File” button and a “Select A File” window will appear as shown in Figure 5. As this GUI is running with a data analytic application, it is convenient to use CSV files for exchanging data between different applications [19]. Thus, in the “Select A File” window, only CSV files are shown in the user directory list. Users can select a CSV file to be analysed by highlighting the intended file and then clicking open.

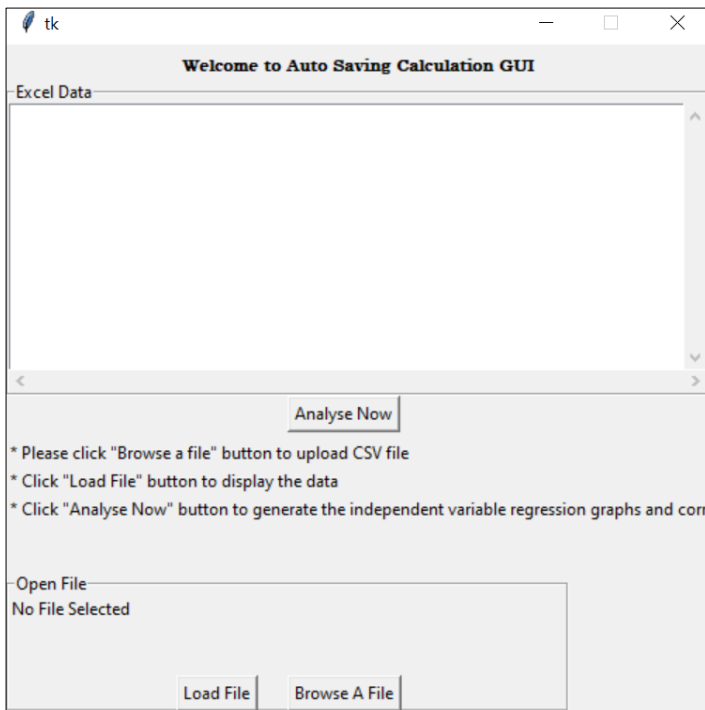


Figure 4: Main window of the GUI

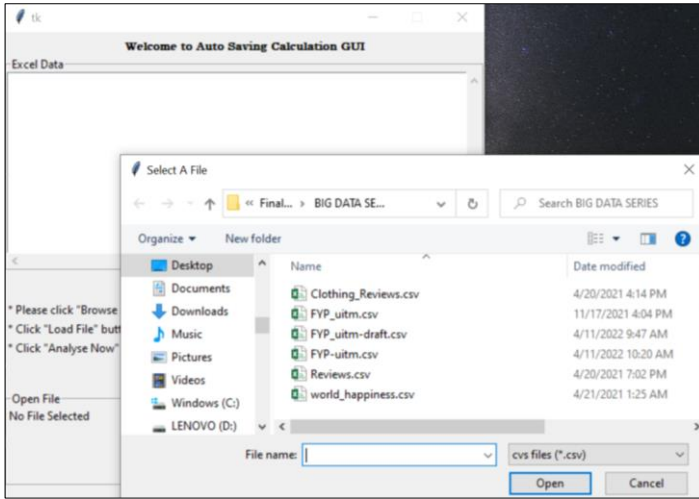


Figure 5: Window to browse and upload file

To make sure the selected file is properly uploaded to the program; the location of the file is displayed in the “Open File” frame at the bottom part of the GUI as shown in Figure 6. Next, the data can be observed by clicking the “Load File” button and the whole data from the CSV file will appear in the “Excel Data” frame. Users can scroll right or left to see other columns. In this project, the data that has been used to simulate this program was a sample from Universiti Teknologi MARA for two consecutive years.

The data on energy consumption were collected from the year 2018 and year 2019 and there were 4 IV were included in the data. Due to confidentiality reasons, all of these IVs were named independent 1, 2, 3, and 4, respectively. The dependent variable (DV) for this analysis was the Energy consumption data for 2018 (baseline energy consumption) and 2019 (reporting energy consumption). In the next sub-section, the data analysis of the data will be discussed in detail.

Data analysis

In this sub-section, data-driven energy analysis can be visualised using our proposed program. The correlation between multiple IVs can be obtained simultaneously with only one click on the “Analyse Now” button. This process reduces the risk of human error analysis and exhausting calculation steps. Information about the regression lines is depicted in the form of equations and r -squared for four IVs as shown in Figure 7. Furthermore, there are four graphs of linear regression lines are also shown in Figure 8 can be used as a fast method of visually depicting the relationship between the IV, x and the DV, Y .

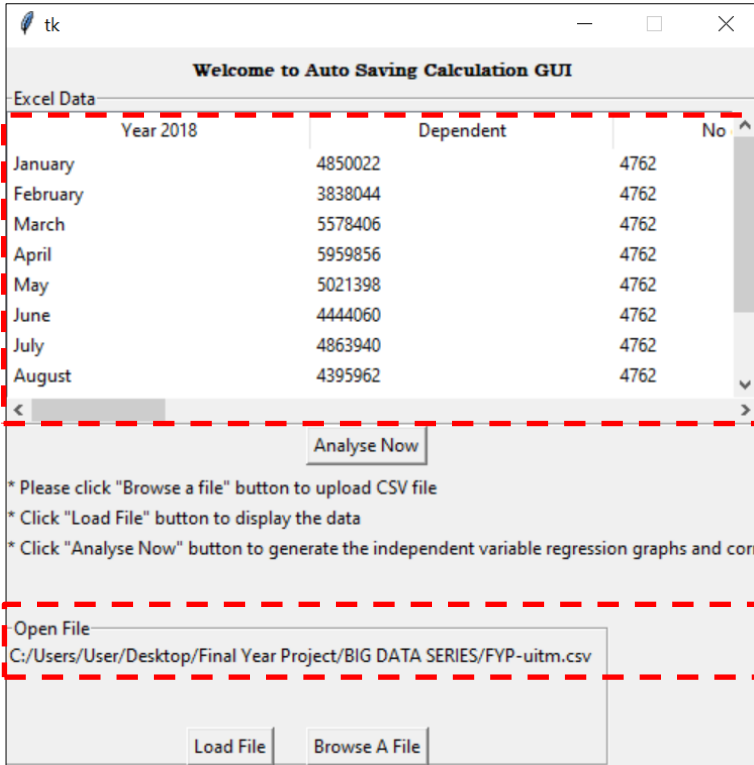


Figure 6: The data displayed on the main window

The information displayed in Figure 7 is not only important for the calculation of saving later on but also can be used to give some insights for proper actions for future energy saving measures (ESM) [20]. For instance, IV 1 shows the lowest correlation with the r -squared=0.2982 which can be interpreted as a very low correlation and has no significant effect on future ESM [21]. On the other hand, the best correlation shown in this simulation was the IV 4 with the r -squared=0.4466. With this information, users can choose whether they want to proceed with the calculation of energy saving or to close the program as the best correlation was not satisfied as it should be, which is, r -squared must be equal to or above 0.75. In some cases, the limitation of data collection makes the energy practitioners use the best data that they have [22]. Therefore, in this simulation, we proceeded to generate the value of energy-saving using IV 4 for validation purposes even though the sample data is inadequate.

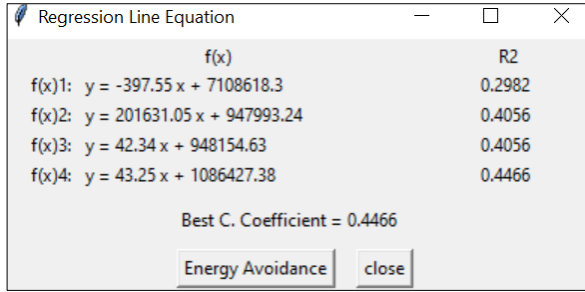


Figure 7: The display of regression lines equations and r -squared of the graphs

To obtain the energy avoidance/saving calculation, users can click the “energy avoidance” button and two windows will appear for the adjusted baseline graphs and energy-saving value with the relative precision according to the range of confidence levels as shown in Figure 9 and Figure 10, respectively. Referring to the graph in Figure 9, we can observe the trend of the one-year consumption for future actions as well as identify abnormal energy consumption [23]. The fluctuation of the lines was related to some events conducted within that year [24]. For instance, semester breaks were reported to be from the end of December to January 2019 and from the end of July to August for the reporting period. Hence, the low consumption during that time of the year. This graph can give some insights to the management for further investigation and evaluation of management and planning.

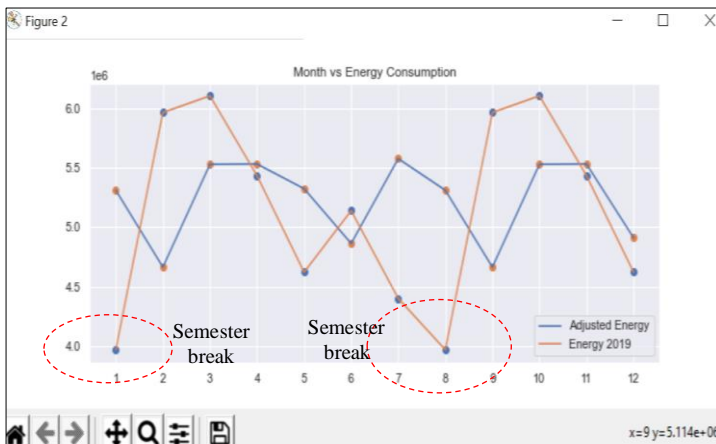


Figure 9: The comparison between the adjusted energy and actual energy consumption in 2019

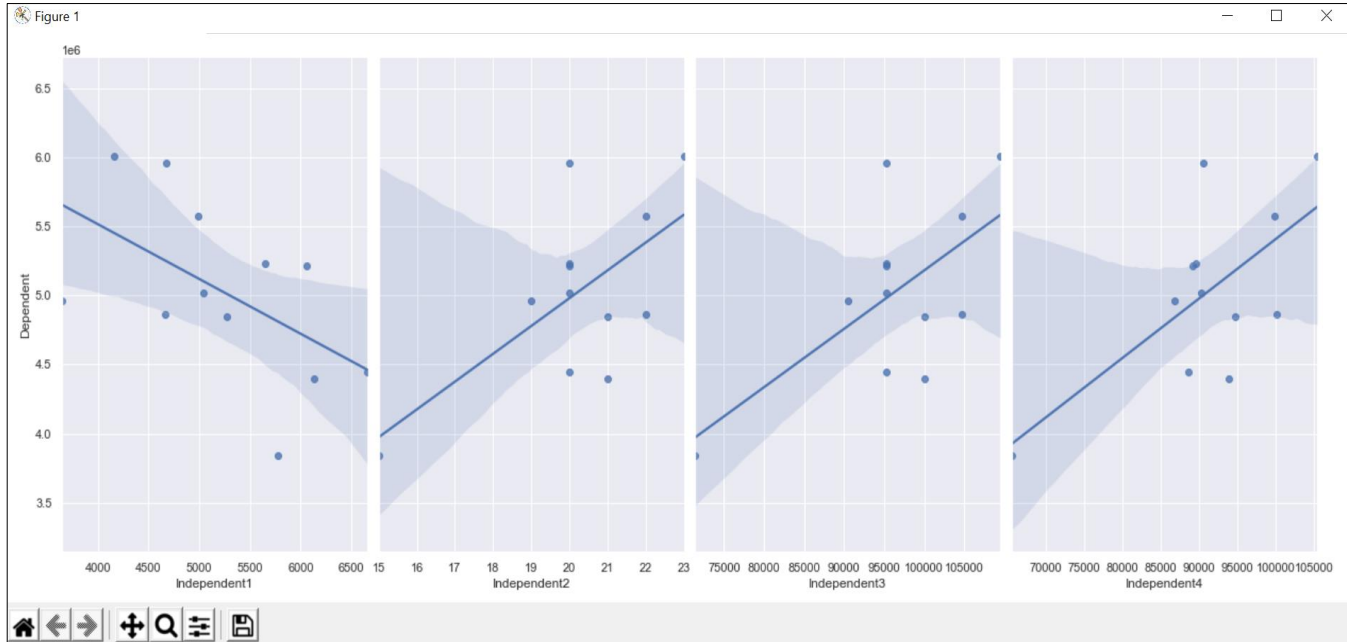


Figure 8: The graph of linear regression generated from the four independent variables

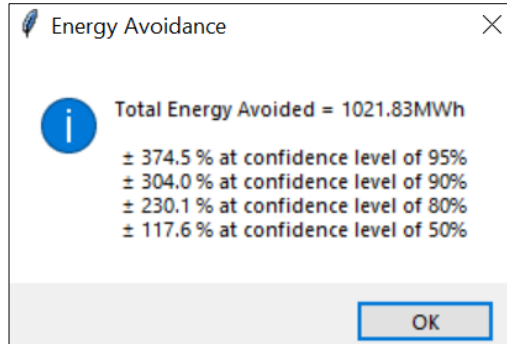


Figure 10: The total of energy avoided with precision value

Manual calculation

The numerical results in this program such as adjusted baseline, total energy avoidance, and precision analysis were compared with manual calculation as shown in Table 5, Table 6, and Equations (13), (15), (17), and (19). Lastly, the validation check of this program tool is summarized in Table 7. All items listed in Table 7 are successfully fulfilled.

Table 5: Manual calculation of adjusted baseline and energy avoided

Actual energy data		Adjusted baseline data			Energy savings	
2019	Energy 2019	Actual staff presence 2019	Factors		Adjusted energy baseline (kWh)	Energy saving avoidance (kWh)
			Sensitivity	Constant		
			43.2451x	1086878.45		
Jan	3966405	97705	4225262.496	1086878.45	5312.136475	1345.731
Feb	5967247	82710	3576802.221	1086878.45	4663.676887	-1303.570
Mar	6108354	102754	4443607.005	1086878.45	5530.480754	-577.873
Apr	5434476	102811	4446071.976	1086878.45	5532.945722	98.470
May	4620803	98011	4238495.496	1086878.45	5325.369462	704.566
Jun	5139372	87318	3776075.642	1086878.45	4862.950097	-276.422
Jul	4399953	103863	4491565.821	1086878.45	5578.439519	1178.487
Aug	3966405	97705	4225262.496	1086878.45	5312.136475	1345.731
Sep	5967247	82710	3576802.221	1086878.45	4663.676887	-1303.570
Oct	6108354	102754	4443607.005	1086878.45	5530.480754	-577.873
Nov	5434476	102811	4446071.976	1086878.45	5532.945722	98.470
Dec	4620803	88411	3823342.536	1086878.45	4910.216941	289.414
Total						1021.56

Table 6: Manual calculation of standard error

Month	Independent variable	Consumption, Y	Modelled, Y_i	$(Y_i - Y)^2$
Jan	94731	4850022	5183543	111236344156
Feb	65655	3838044	3926006	7737336314
Mar	99774	5578406	5401653	31241665430
Apr	90570	5959856	5003580	914464017682
May	90202	5021398	4987664	1137990852
Jun	88586	4444060	4917772	224402945253
Jul	100099	4863940	5415709	304449172821
Aug	93873	4395962	5146435	563209168379
Sept	86831	4964390	4841868	15011608628
Oct	105362	6013058	5643334	136695924910
Nov	89591	5231026	4961238	72785494799
Dec	89180	5212102	4943462	72167245434
Total				2454538914659

$$SE_{(\text{monthly})} = \sqrt{\frac{\sum(Y_i - Y)^2}{n - p - 1}} = \sqrt{\frac{2454538914659}{12 - 1 - 1}} \quad (9)$$

$$= 495433$$

$$SE_{(\text{annually})} = \sqrt{12} \times 495433 = 1716230 \quad (10)$$

$$\text{Absolute precision} = t \times SE_{(\text{annually})} \quad (11)$$

For confidence level 95%, DF=10, t=2.23,

$$\text{Absolute precision} = 2.23 \times SE_{(\text{annually})} \quad (12)$$

$$= 3827194$$

$$\text{Relative precision} = \frac{3827194}{1021.56 \times 10^3} \times 100\% \quad (13)$$

$$= 374.5\%$$

For confidence level 90%, DF=10, t=1.81,

$$\text{Absolute precision} = 1.81 \times SE_{(\text{annually})} \quad (14)$$

$$= 3106376.3$$

$$\begin{aligned} \text{Relative precision} &= \frac{3106376.3}{1021.56 \times 10^3} \times 100\% & (15) \\ &= 304.0\% \end{aligned}$$

For confidence level 80%, DF=10, t=1.37,

$$\begin{aligned} \text{Absolute precision} &= 1.37 \times SE_{(annually)} & (16) \\ &= 2351236 \end{aligned}$$

$$\begin{aligned} \text{Relative precision} &= \frac{2351236}{1021.56 \times 10^3} \times 100\% & (17) \\ &= 230.1\% \end{aligned}$$

For confidence level 50%, DF=10, t=0.7,

$$\begin{aligned} \text{Absolute precision} &= 0.7 \times SE_{(annually)} & (18) \\ &= 1201361 \end{aligned}$$

$$\begin{aligned} \text{Relative precision} &= \frac{1201361}{1021.56 \times 10^3} \times 100\% & (19) \\ &= 117.6\% \end{aligned}$$

Table 7: Validation checklist

Item	Unit testing	Integration testing	System testing	User testing
Interface:				
Main Window	√	√	√	√
File Explorer window	√	√	√	√
Load file window	√	√	√	√
Linear regression window	√	√	√	√
Adjusted baseline window	√	√	√	√
Load data				
CSV file	√	√	√	√
Analysis				
Scatter Plot	√	√	√	√
R-squared	√	√	√	√
Adjusted baseline	√	√	√	√
Visualisation				
Data display	√	√	√	√
Graph comparison	√	√	√	√
Energy avoidance	√	√	√	√

Conclusion

This project was undertaken to design a program of GUI-based data visualisation in determining the significant independent variables (IV) and energy-saving calculation that is compliant with option C IPMVP. This work contributes to existing knowledge of option C IPMVP by providing an efficient program tool for the energy practitioner to obtain insightful data visualisation and accurate results using web-based mathematical computation. This program also helps to avoid human error risk and is very easy to operate. The program was validated based on software verification and validation methodology using the V-model of IEEE 1012 standard.

Contributions of Authors

The authors confirm the equal contribution in each part of this work. All authors reviewed and approved the final version of this work.

Funding

This work received no specific grant from any funding agency.

Conflict of Interests

All authors declare that they have no conflicts of interest.

Acknowledgement

We would like to express our gratitude to Universiti Teknologi MARA Facility for providing the necessary materials that enabled us to conduct this research effectively. The access to their dataset was crucial in conducting analysis and validation of the software.

References

- [1] Y. Lai, S. Papadopoulos, F. Fuerst, G. Pivo, J. Sagi, and C. E. Kontokosta, "Building retrofit hurdle rates and risk aversion in energy efficiency investments", *Applied Energy*, vol. 306, pp. 1-28, 2022. doi: 10.1016/j.apenergy.2021.118048.

- [2] Efficiency Valuation Organization (EVO), “International Performance Measurement & Verification Protocol: Concepts and Options for Determining Energy and Water Savings”, *EVO 10000-1:2012*, vol. 1, pp. 1-86, 2012.
- [3] X. Xia and J. Zhang, “Mathematical description for the measurement and verification of energy efficiency improvement”, *Applied Energy*, vol. 111, pp. 247–256, 2013. doi: 10.1016/j.apenergy.2013.04.063.
- [4] Efficiency Valuation Organization (EVO), “M&V Issues and Examples Five-Year Statutory Protocol Review”, *DOE/EE -1287 -0286*, vol. 4.0, pp. 1-53, 2015.
- [5] M. David and N. Y. Dahlan, “Development of visual basic based GUI for option a energy savings of IPMVP”, *Proceedings of the 2014 IEEE 4th International Conference on System Engineering and Technology, ICSET 2014*, pp. 1–6, 2014. doi: 10.1109/ICSEngT.2014.7111788.
- [6] I. Ismail, N. H. Ahmad, N. Y. Dahlan, and H. Mohamad, “Development of GUI system using web application tool of microsoft visual studio for option b energy saving IPMVP”, *International Journal of Simulation: Systems, Science and Technology*, vol. 17, no. 41, pp. 46.1-46.4, 2017. doi: 10.5013/IJSSST.a.17.41.46.
- [7] C. A. Cosmas and N. Y. Dahlan, “Development of Visual Basic GUI for Option C energy saving of IPMVP”, in *IET Seminar Digest*, vol. 2014, no. CP659, pp. 1–6, 2014. doi: 10.1049/cp.2014.1508.
- [8] B. Izyumov and E. Kalinina, “Software tools for regression analysis of fuzzy data,” *Proceedings of 9th Zittau Fuzzy Colloquium*, pp. 221-229, 2001.
- [9] P. Zamostny and Z. Belohlav, “A software for regression analysis of kinetic data”, *Computers & Chemistry*, vol. 23, no. 5, pp. 479–485, 1999. doi: 10.1016/S0097-8485(99)00024-8.
- [10] L. Quaranta, F. Calefato, and F. Lanubile, “Eliciting Best Practices for Collaboration with Computational Notebooks”, *Proceedings of the ACM on Human-Computer Interaction*, vol. 6, no. CSCW1, pp. 1–41, 2022. doi: 10.1145/3512934.
- [11] B. Guo, J. Nagy, and E. Sekerinski, “Universal Design of Interactive Mathematical Notebooks on Programming”, *Proceedings of the 53rd ACM Technical Symposium on Computer Science Education V. 2 (SIGCSE 2022), March 3â•fi5, Providence, RI, USA, 2022*, vol. 1, no. 1, pp. 1132–1132, 2022. doi: 10.1145/3478432.3499102.
- [12] IEEE, “IEEE Standard for System, Software, and Hardware Verification and Validation”, *IEEE Std 1012-2016 (Revision of IEEE Std 1012-2012/ Incorporates IEEE Std 1012-2016/Cor1-2017)*, pp.1-260, 2017. doi: 10.1109/IEEESTD.2017.8055462.
- [13] K. N. Hodel, J. Reinaldo Da Silva, L. R. Yoshioka, J. F. Justo, and M. M. D. Santos, “FAT-AES: Systematic Methodology of Functional Testing

- for Automotive Embedded Software”, *IEEE Access*, vol. 10, pp. 74259–74279, 2022. doi: 10.1109/ACCESS.2021.3128431.
- [14] S. Naumenko et al., “Formal Methods of FPGA Project Verification Flow,” in *Proceedings of the 11th IEEE International Conference on Intelligent Data Acquisition and Advanced Computing Systems: Technology and Applications, IDAACS 2021*, vol. 2, pp. 1141–1146, 2021. doi: 10.1109/IDAACS53288.2021.9660906.
- [15] E. Auer, W. Luther, and B. Weyers, “Reliable visual analytics, a prerequisite for outcome assessment of engineering systems”, *Acta Cybernetica*, vol. 24, no. 3, pp. 287–314, 2020. doi: 10.14232/ACTACYB.24.3.2020.3.
- [16] S. Touzani, J. Granderson, D. Jump, and D. Rebello, “Evaluation of methods to assess the uncertainty in estimated energy savings”, *Energy and Buildings*, vol. 193, pp. 216–225, 2019. doi: 10.1016/j.enbuild.2019.03.041.
- [17] P. Therkelsen, P. Rao, D. Sholes, B. Meffert, R. Green, S. Nimbalkar, and A. Mckane, “The value of regression models in determining industrial energy savings”, *ECEEE Industrial Summer Study Proceedings Industrial Efficiency, Berlin, Germany*, pp. 389–399, 2016.
- [18] L. A. Damiano, “Reduction of errors in ventilation rate determinations”, *ASHRAE Transactions*, vol. 116, no. PART 2, pp. 54–69, 2010.
- [19] E. Oanta, A. Raicu, and B. Menabil, “Applications of the numerical methods in mechanical engineering experimental studies”, *IOP Conference Series: Materials Science and Engineering*, vol. 916, no. 1, pp. 1–9, 2020. doi: 10.1088/1757-899X/916/1/012074.
- [20] H. K. Khozani, E. Esmaeili, M. N. Bisheh, S. A. Ayatollahi, and M. Gilanifar, “Using Regression Analysis to Predict the Demand Function of Electricity: A Case Study”, *American Journal of Engineering and Applied Sciences*, vol. 13, no. 4, pp. 759–767, 2020. doi: 10.3844/ajeassp.2020.759.767.
- [21] S. Zhang, P. Sun, and E. P. Sun, “Research on energy saving of small public building envelope system”, in *Energy Reports*, vol. 8, pp. 559–565, 2022. doi: 10.1016/j.egy.2022.03.146.
- [22] A. Piccinini, M. Hajdukiewicz, and M. M. Keane, “A novel reduced order model technology framework to support the estimation of the energy savings in building retrofits”, *Energy and Buildings*, vol. 244, p. 110896, 2021. doi: 10.1016/j.enbuild.2021.110896.
- [23] M. Gaur, S. Makonin, I. V. Bajic, and A. Majumdar, “Performance Evaluation of Techniques for Identifying Abnormal Energy Consumption in Buildings”, *IEEE Access*, vol. 7, pp. 62721–62733, 2019. doi: 10.1109/ACCESS.2019.2915641.
- [24] Z. Miao, Y. Zhang, S. Liu, X. Chen, and T. Baležentis, “Heterogeneous strategy and performance decomposition: Energy-economy-environment nexus in the light of natural & managerial disposability”, *Environmental*

Impact Assessment Review, vol. 95, p. 106777, 2022. doi: 10.1016/j.eiar.2022.106777.

Appendices

Table A1: t-table (IPMVP, vol. 1, 2012) [2]

DF	Confidence Level				DF	Confidence Level			
	95%	90%	80%	50%		95%	90%	80%	50%
1	12.71	6.31	3.08	1.00	16	2.12	1.75	1.34	0.69
2	4.30	2.92	1.89	0.82	17	2.11	1.74	1.33	0.69
3	3.18	2.35	1.64	0.76	18	2.10	1.73	1.33	0.69
4	2.78	2.13	1.53	0.74	19	2.09	1.73	1.33	0.69
5	2.57	2.02	1.48	0.73	21	2.08	1.72	1.32	0.69
6	2.45	1.94	1.44	0.72	23	2.07	1.71	1.32	0.69
7	2.36	1.89	1.41	0.71	25	2.06	1.71	1.32	0.68
8	2.31	1.86	1.40	0.71	27	2.05	1.70	1.31	0.68
9	2.26	1.83	1.38	0.70	31	2.04	1.70	1.31	0.68
10	2.23	1.81	1.37	0.70	35	2.03	1.69	1.31	0.68
11	2.20	1.80	1.36	0.70	41	2.02	1.68	1.30	0.68
12	2.18	1.78	1.36	0.70	49	2.01	1.68	1.30	0.68
13	2.16	1.77	1.35	0.69	60	2.00	1.67	1.30	0.68
14	2.14	1.76	1.35	0.69	120	1.98	1.66	1.29	0.68
15	2.13	1.75	1.34	0.69	∞	1.96	1.64	1.28	0.67

Optimization of Machining Parameters in Turning for Different Hardness using Multi-Objective Genetic Algorithm

Mimi Muzlina Mukri, Nor Atiqah Zolpakar*

Faculty of Mechanical and Automotive Engineering Technology,
Universiti Malaysia Pahang, 25200 Pekan, Pahang, MALAYSIA
*noratiqahz@ump.edu.my

Sunil Pathak

HiLASE Center, Institute of Physics, Czech Academy of Sciences,
Za Radnici 828, 25241 Dolni Brezany, CZECH REPUBLIC

ABSTRACT

Surface finish and temperature rise are the crucial machining outcomes since it determines the quality of the machining and the tool life. During machining operations, choosing optimal machining parameters is critical since it affects the machining outcome. In this work, Multi-Objective Genetic Algorithm (MOGA) optimization is used to find the combination of machining parameters at different levels of hardness of 20, 36, and 43 to obtain minimum surface roughness and minimum cutting temperature in turning operation. Cutting depth, cutting speed, and feed rate are the machining variables that are used in the process of optimization. From the results, it shows that the minimum temperature rise is 243.333 °C with a surface roughness of 1.975 μm during machining of 20 hardness. It also observed that the hardness of the material significantly affects the surface roughness and temperature rise. The outcome shows that as the hardness of the material is increasing the temperature is increasing while the surface roughness is decreasing. This research also revealed that using a MOGA to optimize multi-objective replies produces positive outcomes.

Keywords: Optimization; Machining Parameters; Genetic Algorithm; Turning

Introduction

Turning is the process of eliminating metal from the external diameter of a revolving cylindrical workpiece by lowering the workpiece's diameter to a predetermined size while achieving a smooth metal surface [1]. This machining method is one of the most critical in creating components for a wide range of applications, including prototypes like custom-designed shafts and fasteners that are utilised in small quantities [2]. It is critical to choose cutting parameters for turning operations in order to obtain excellent cutting performance [3]. During machining, the cutting zone temperature is extremely high, and the chip absorbs the majority of the heat generated by the cutting operation. Tool wear, tool life, and surface quality all suffer as a result of high temperatures [4]-[5]. This statement is supported by Pimenov et al. [6] recent study is focused on cutting tool wear, cutting force determination, surface roughness fluctuations, and other machining reactions. Variations in these machining reactions cause significant changes in dimensional accuracy and productivity [7]. For every machining operation, high cutting temperatures and their associated detrimental consequences are a major problem. This must be controlled in order to enhance machined product quality, reduce machining costs, and increase production rates [8]. According to Halim et al. [9], excessive heat would develop in the cutting zone, raising the cutting temperature. As a result of this circumstance, cutting force and tool wear rates increased rapidly, and the surface quality deteriorated [9]. So, the optimization of this process is required to improve the efficiency of the process.

As stated by Bhuiyan et al. [10], many academics have been focused on optimizing process parameters in machining by devising an analytical technique for determining the ideal cutting speed in a single stage turning process since 1950. Generally, optimization methods can be classified into two which are conventional methods and non-conventional methods. Traditional approaches such as ANOVA, the Taguchi method, and others start with an estimation and converge towards the optimal solution with each iteration. This convergence is determined by the starting approximation used. Although traditional approaches are claimed to be effective in addressing one type of machining optimization issue, they may not be effective in tackling another [11]. There are still a few researchers using this technique in their studies. The Taguchi method was used by Akkus and Yakka [12] to determine the best value of surface roughness and the most effective parameters that contribute to surface roughness. According to the findings, among the three factors involved, cutting speed, feed rate, and cutting depth, the feed rate is the most important element that leads to surface roughness [12]. Using the Taguchi and ANOVA methodologies, Krishna et al. [13] and Palaniappan et al. [14] conducted research that highlighted the optimisation of turning process parameters to achieve excellent surface

quality. According to the findings, both researchers agree, the feed rate is the significant parameter that will affect surface roughness.

In recent years, engineering optimization problems have seen an increase in popularity for non-traditional optimization techniques including Genetic Algorithms (GA), Simulated Annealing (SA), Artificial Neural Networks (ANN), and many more approaches. These algorithms have been discovered to be promising search and optimization techniques for complicated optimization issues. The same approach hired by Shah et al. [15], Manav and Chinchankar [16], Durga et al. [17], and Narayan et al. [18] which is a multi-objective genetic algorithm (MOGA), to optimize machining settings such as that response variables including cutting force, temperature, material removal rate and surface roughness were optimized to their ideal range. The factors that affect each response variable are cutting speed, feed rate, and depth of cut.

To observe the effectiveness of conventional with non-conventional optimization, a lot of researchers mixed conventional and non-conventional methods in their study to optimize the machining parameters in turning operations. Kumar et al. [19] and Butola et al. [20] used the same Taguchi, ANOVA, and GA methodologies to optimize machining settings in order to get the finest Material Removal Rate (MRR), surface roughness, and temperature values. Taguchi and ANOVA are utilized to discover key values. ANOVA and GA are used to optimize process parameters and are agreed upon by both researchers. Mia and Dhar [21] provide work on the development of mathematical by using Response Surface Methodology (RSM), fuzzy inference system (FIS) to formulate the predictive model and simulated annealing (SA) in order to formulate the optimization model for the average surface roughness parameter in turning. The model is solved using GA, and the ideal start time for non-critical processes as well as the ideal duration for each process are determined [22]. Chabbi et al. [23] investigated the influence of cutting parameters on surface roughness, cutting force, cutting power, and productivity during turning using three optimisation techniques: RSM, Artificial Neural Network (ANN), and Desirability Function (DC). Bolivar et al. [24] employed an ANN and a GA to create a system that optimizes cutting insert selection and cutting parameters throughout the turning process (GA). This previous research showed that GA has a good reputation in searching optimize solutions not just single objective but multi-objective problems [7].

According to the background literature, a substantial study has been done on the relationship between the turning process and surface roughness. However, there have only been a few attempts to optimise the temperature rise during the turning process, despite the fact that this is one of the crucial factors that can affect both the surface roughness and tool life. The purpose of this study is to determine how cutting speed, feed rate, and depth of cut affect temperature increase and surface roughness when the material

hardness has been changed, given the relevance of temperature rise and surface roughness in the turning process.

Optimization using Multi-Objective Genetic Algorithm (MOGA)

For parametric optimization, the genetic algorithm has proved to be one of the most common multi-objective optimization strategies. Given that it works with a population of potential solutions, a genetic algorithm can be used to solve multi-objective optimisation problems and find many solutions simultaneously [25]. This function was used as the objective function in the MOGA Toolbox of MATLAB 2018b. For the optimization of surface roughness and the minimizing of temperature rise in turning, the objective function values are determined accordingly.

In this study, the optimization was conducted to obtain minimum temperature rise and also smaller surface roughness during the turning process. To generate minimum surface roughness, the machining setup needs to be set to high speed, and this will cause a temperature rise at the tool and also the workpiece. Because these two goals are incompatible, MOGA optimization is utilized to discover the feed rate, depth of cut, and cutting speed combination that creates the best surface roughness and temperature rise throughout the machining process. The objective functions for this work can be represented as follow:

$$f_1 = \text{Min } T(f, d, v)$$

$$f_2 = \text{Min } Ra(f, d, v)$$

The objective function used to represent temperature rise and surface roughness for the turning process is based on work by Tanikic [26] using RSM modelling. Equations (1) and (2) represent the objective function for temperature rise and surface roughness that has been used in this optimization [26].

$$T = -96.769 + 6.665.HRC + 1.659.V + 247.165.f + 113.067.a \quad (1)$$

$$Ra = 4.365 - 0.0501.HRC - 0.0156.V + 9.007.f + 0.225.a \quad (2)$$

While HRC is the hardness of materials, V is cutting speed, f is feed rate and a is depth of cut.

The algorithm is initiated by generating a randomly initial population. The initial population is made up of several factors that must be optimized, such as depth of cut, cutting speed, and feed rate in this example. The random number was chosen based on the lower and upper limits for each variable. The workpiece material was steel, AISI designation 4140, with dimensions 45 x 250 m. The cutting tool used and assembled of two parts is adopted: cutting tool holder PCLNR 32 25 P12, cutting tool insert CNMG 12 04 08 (grade 235). The lower and upper bounds for the variable parameters are listed below:

$$\begin{aligned} 80 &\leq \text{cutting speed, } v \leq 140 \\ 0.071 &\leq \text{feed rate, } f \leq 0.321 \\ 0.5 &\leq \text{depth of cut, } a \leq 2.0 \end{aligned}$$

These values were chosen based on the common setup used in the turning operation as reported by [25]. After a randomly initial population was created, then the real numbers of parameters transform into a sequence of a number of binary codes that know as a string. The string consists of chromosomes that indicate possible solutions. The independent variables are coded by a set of genes on the chromosome. The number of bits in the string equals the length of the chromosome, L . Each answer is offered by the L -bit binary code of chromosome, C . There are $2^L - 1$ viable solutions for choosing. The optimization process began with the creation of a chromosome containing the parameters that needed to be tweaked. The following is a generic representation:

$$C_k = [X_{k1}, X_{k2} \dots X_{kn}]$$

$$C_k = \left[\begin{array}{c} \left[\begin{array}{c} |110 \dots 00| |101 \dots 1| |001 \dots 11| \\ \longleftarrow X_1 \qquad \qquad \qquad \longleftarrow X_2 \qquad \qquad \qquad \longleftarrow X_3 \end{array} \end{array} \right] \end{array}$$

where X_1 , X_2 , and X_3 are the depth of cut, cutting speed, and feed rate respectively. The first generation of the population is then formed, complete with fitness function values. The next stage is to assess each chromosome in the population to see how it will be used in the second generation. There are numerous techniques for selecting chromosomes to be passed down to the next generation, but the operator utilized in this work is a tournament.

The tournament selection technique is carried out by putting selection pressure on the participants by holding a tournament with s contestants. In a tournament, for example, there are $s=6$ competitors. Six solutions will compete in a tournament, with the winner advancing to the mating pool. As demonstrated in Figure 1, each solution managed to participate in precisely two tournaments since the event was run in a methodical manner. The number of populations in the selection operator remains the same, but the new population has two better copies. The tournament winner, who has

greater average fitness than the general population, is included in the mating pool.

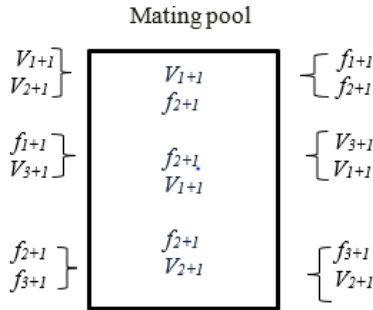


Figure 1: Tournament selection process with 6 contestants

The chromosome will go through a crossover phase after the selection operator. Since the reproduction phase would either replicate a good solution or eradicate the poor solution, no new solution is formed in the population during this phase. The crossover and mutation operators are used to generate a new solution. To create a new solution or offspring, the crossover operator selects two solutions (parents) from the mating pool and switches certain string segments between the two solutions at random positions on the string.

One drawback of the crossover operator is that not all of the newly produced children are better than their parents. Regardless of whether the new offspring is better or worse, other cross-sites or two other strings are picked for the crossing. While the offspring product of the crossover may not create better results than either parent solution, it is apparent that the probability of creating better solutions is higher than with random selection. This is due to reproduction, the operator before the crossing, being active. The representations of the string are probably going to have some advantageous bit combinations if the solution makes it through the tournament reproduction phase. Despite the fact that the crossover produces a poor solution, the bad solutions are removed during the subsequent reproduction step, leading to the conclusion that bad solutions have a brief life cycle. There is a chance you will receive a horrible solution, but there is also a chance you will get a good one. Because the offspring outperforms their parents, more reproductions are predicted in successive reproduction operations, and these solutions are more likely to survive until the following generation's crossover operator. As a result, as the number of iterations increases, so does the number of solutions in the population with comparable chromosomes.

The algorithm will next go on to the mutation operator, which alters a string locally in order to build a better string. For each bit, the bit-wise

mutation process needs the creation of a random integer. The solution in the population is then evaluated to decide whether to stop the algorithm or generate a new generation. This procedure is continual until the termination condition is reached. The flowchart of MOGA can be summarized in Figure 2. The operator setup that is used in the MOGA is listed in Table 1.

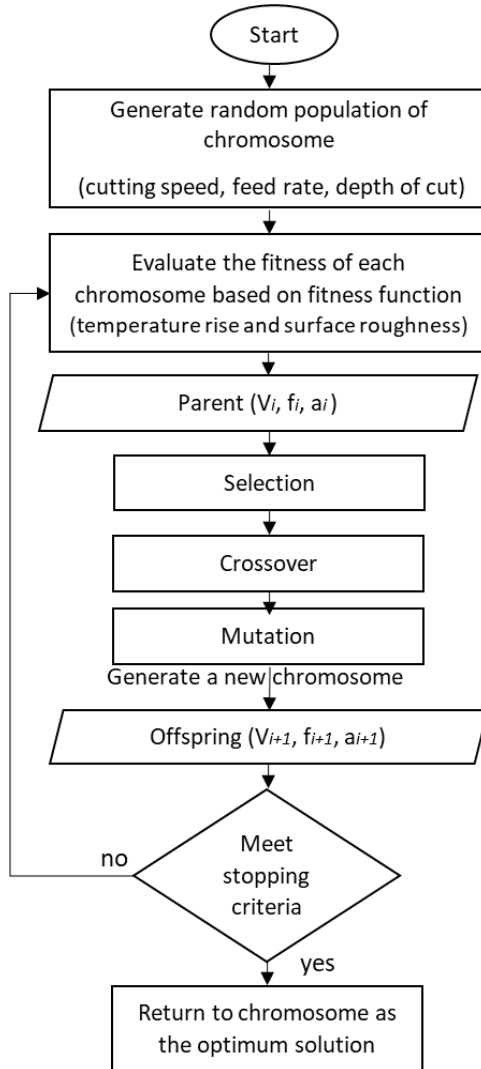


Figure 2: A flowchart of working principle of genetic algorithm

Table 1: Operators for MOGA

Parameters	Setting values
Population size, N	50
Generation	300
Selection function	Tournament
Crossover probability, P_c	0.8
Crossover function	Intermediate
Mutation function	Constraint dependent

Results and Discussion

Figures 3, 4, and 5 show the Pareto-optimal solutions for various hardness. The Pareto front for temperature increase and surface roughness for hardness 20 HRC is shown in Figure 3. Based on Figure 3, the Pareto front consists of 18 pareto-optimal solutions, and the algorithm converged at 140 generations. When the cutting parameters are 80 m/min, 0.071 mm/rev, and 0.5 mm for cutting speed, feed rate, and depth of cut, the lowest temperature rise achievable in this method is 243.333 °C. Meanwhile, the smallest surface roughness observed is 1.975 μm . The other solutions obtained in the Pareto front are listed in Table 2.

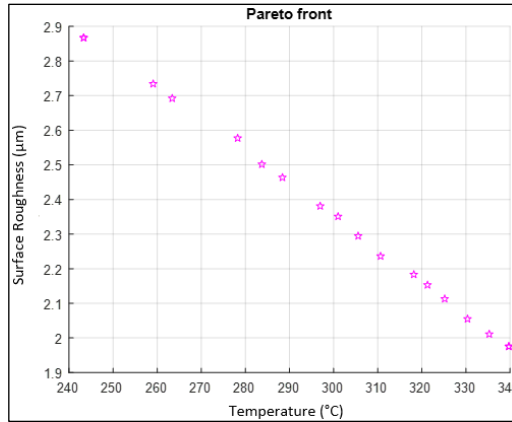


Figure 3: Pareto optimal front for hardness 20 HRC

Figure 4 shows the Pareto front for the temperature and surface roughness for the hardness 36 HRC. The Pareto front has 18 Pareto-optimal solutions, according to Figure 4, and the algorithm converged at generation 506. The lowest temperature rise achieved in this method is 363.071 °C when

the cutting parameters are 85.023 m/min, 0.084 mm/rev, and 0.504 mm for cutting speed, feed rate, and depth of cut, respectively. In the meanwhile, the least surface roughness found is 1.246 μm . Table 3 lists the alternative Pareto front solutions.

Table 2: Pareto optimal solutions for hardness 20 HRC

No	Cutting speed (m/min)	Feed rate (mm/rev)	Depth of cut (mm)	Temperature ($^{\circ}\text{C}$)	Surface roughness (μm)
1	80.000	0.071	0.500	243.333	2.867
2	137.579	0.072	0.506	339.731	1.975
3	135.026	0.071	0.506	335.284	2.011
4	137.579	0.072	0.506	339.731	1.975
5	132.284	0.071	0.502	330.356	2.055
6	99.853	0.073	0.513	278.244	2.577
7	128.646	0.071	0.509	325.175	2.113
8	80.000	0.071	0.500	243.333	2.867
9	114.039	0.072	0.507	301.002	2.351
10	106.522	0.072	0.507	288.388	2.463
11	126.224	0.072	0.510	321.286	2.153
12	124.417	0.072	0.509	318.181	2.183
13	120.469	0.071	0.502	310.647	2.236
14	103.947	0.072	0.504	283.728	2.501
15	117.226	0.072	0.502	305.565	2.294
16	91.631	0.072	0.505	263.391	2.692
17	111.625	0.072	0.509	296.957	2.381
18	89.028	0.072	0.505	259.079	2.734

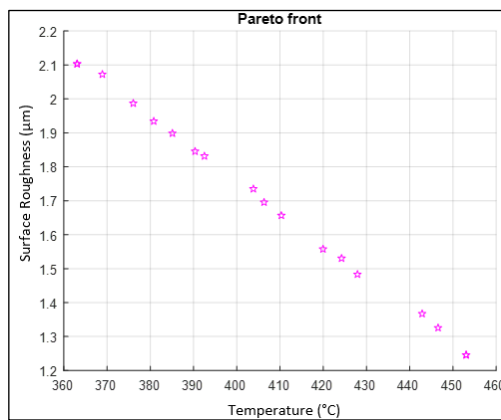


Figure 4: Pareto optimal front for hardness 36 HRC

Table 3: Pareto optimal solutions for hardness 36 HRC

No	Cutting speed (mm/min)	Feed rate (mm/rev)	Depth of cut (mm)	Temperature (°C)	Surface roughness (µm)
1	139.969	0.084	0.504	453.044	1.246
2	85.203	0.084	0.511	363.071	2.103
3	85.203	0.084	0.511	363.071	2.103
4	139.969	0.084	0.504	453.044	1.246
5	121.978	0.084	0.512	424.234	1.530
6	87.562	0.084	0.528	368.906	2.072
7	119.992	0.084	0.504	419.944	1.557
8	101.709	0.084	0.510	390.348	1.845
9	132.502	0.084	0.523	442.870	1.367
10	92.786	0.084	0.515	376.053	1.987
11	95.957	0.084	0.510	380.794	1.934
12	108.978	0.084	0.523	403.830	1.735
13	98.451	0.084	0.511	385.112	1.898
14	113.793	0.084	0.510	410.304	1.656
15	102.682	0.084	0.515	392.516	1.831
16	124.773	0.084	0.504	427.911	1.483
17	111.288	0.084	0.511	406.308	1.695
18	135.219	0.084	0.515	446.555	1.326

The Pareto front for temperature and surface roughness for hardness 43 HRC is shown in Figure 5. As shown in Figure 5, the Pareto front consists of 18 pareto-optimal solutions and converged at generation 332. When the cutting parameters are 80.133 m/min, 0.073 mm/rev, and 0.501 mm for cutting speed, feed rate, and depth of cut, the lowest temperature rise achievable using this method is 397.393 °C. Meanwhile, the least surface roughness determined is 0.781 µm, and Table 4 provides the Pareto front solutions.

Because the performance measurements are inherently contradictory, the surface quality degrades as the temperature rises, and the same pattern of performance measures can be seen in the solutions produced for all hardness, as illustrated in Figures 3, 4, and 5 [27]. It also observed that as the hardness of the workpiece is increasing, the temperature rise obtained is increasing but the surface roughness is decreasing. Because none of the Pareto optimum set's solutions is superior to the others, each of them is a viable option. The process engineer's requirements determine if one solution is better than the other. It should be highlighted that all of the solutions are equally good, and depending on the manufacturer's requirements, any set of input parameters can be used to get the matching response values.

The creation of the Pareto-optimal front, which comprises the final set of solutions, is seen in Figures 3, 4, and 5. The continuous nature of the optimization issue addressed determines the form of the Pareto optimum front. The findings in Tables 2, 3, and 4 indicate that the whole range of input parameters is mirrored in 18 Pareto-optimal solutions, with no bias towards the higher or lower side of the parameters. Because the performance measurements are inherently contradictory, the surface quality degrades as the temperature rises, and the same pattern of performance measures is found in the solutions derived for all hardness. As none of the Pareto optimum set's solutions is superior to the others, each of them is a feasible option. The process engineer needs to determine which solution to select. It should be emphasized that all of the solutions are equally effective, and depending on the manufacturer's criteria, any set of input parameters can be used to produce the associated response values.

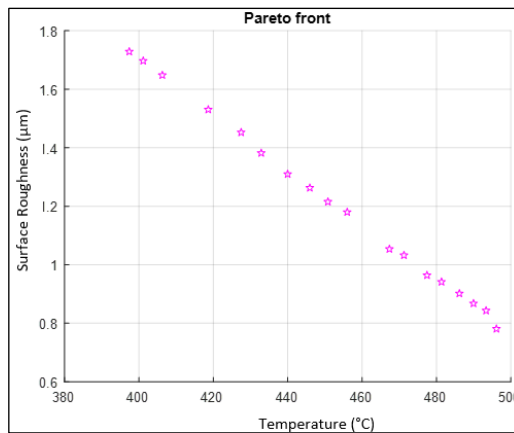


Figure 5: Pareto optimal front for hardness 43 HRC

Effect of cutting speed on the temperature rise and surface roughness

Figure 6 and Table 5 show the interaction effect between cutting speed (V) and temperature (T) for every hardness. Cutting speed has a considerable impact on temperature rise, as seen in Figure 6. In general, the temperature increase as the cutting speed increase. When the cutting speed is 80 mm/min, the temperature is 243.333 °C, and the temperature increase to 339.731 °C when the cutting speed is 137.579 m/min for hardness 20 HRC. For hardness 36 HRC, the lowest temperature is 363.071 °C for the cutting speed of 85.203 m/min while the highest temperature is 453.044 °C for the cutting speed of 139.969 mm/min. For hardness 43 HRC, the value of cutting speed is 80.133 m/min, the temperature is 397.393 °C. These results are tallying

with the theory of machining. All of the energy lost during the cutting process as a result of plastic deformation is converted to heat, raising the temperature in the cutting zone. Heat generation is inextricably tied to plastic deformation and friction. As the cutting speed rises, friction increases, resulting in a rise in cutting zone temperature [28].

Table 4: Pareto optimal solutions for hardness 43 HRC

No	Cutting speed (mm/min)	Feed rate (mm/rev)	Depth of cut (mm)	Temperature (°C)	Surface roughness (μm)
1	124.587	0.072	0.503	471.252	1.032
2	101.724	0.072	0.500	432.880	1.382
3	109.526	0.072	0.501	445.942	1.263
4	92.886	0.073	0.502	418.628	1.530
5	130.332	0.072	0.508	481.346	0.941
6	128.589	0.072	0.500	477.461	0.964
7	115.327	0.073	0.503	455.988	1.180
8	106.088	0.071	0.500	439.985	1.310
9	137.684	0.074	0.502	493.335	0.843
10	135.799	0.074	0.501	489.958	0.868
11	85.418	0.073	0.502	406.282	1.648
12	133.469	0.073	0.502	486.159	0.902
13	122.544	0.071	0.501	467.345	1.054
14	82.278	0.073	0.502	401.140	1.697
15	112.513	0.072	0.500	450.810	1.215
16	97.936	0.073	0.506	427.472	1.452
17	80.133	0.073	0.501	397.393	1.728
18	139.943	0.071	0.500	496.126	0.781

Table 5: Optimize process predicted by GA

Hardness 20 HRC		Hardness 36 HRC		Hardness 43 HRC	
V (m/min)	T (°C)	V (m/min)	T (°C)	V (m/min)	T (°C)
80.000	243.333	85.203	363.071	80.133	397.39
89.028	259.079	87.562	368.906	82.278	401.14
106.522	288.388	111.288	406.308	109.526	445.94
111.625	296.957	113.793	410.304	112.513	450.81
135.026	335.284	132.502	442.870	137.684	493.33
137.579	339.731	139.969	453.044	139.943	496.12

The results of the interaction between cutting speed (V) and surface roughness (SR) are shown in Figure 7 and Table 6. It is obvious that raising the cutting speed reduces surface roughness. This can be proven through

hardness 20 HRC, the surface roughness is 2.867 μm when the cutting speed is 80 m/min and the value of roughness decrease to 1.975 μm when the cutting speed value is 137.579 m/min. This phenomenon occurs for hardness 36 HRC, when the cutting speed value is 85.203 m/min, the surface roughness is 2.103 μm . However, when the value of cutting speed is 139.969 m/min, the value of surface roughness becomes 1.246 μm . The situation also happened for hardness 43 HRC, the value of cutting speed is 80.133 m/min, and the surface roughness value is 2.103 μm . Meanwhile, when the cutting speed value is 139.943 m/min, the value of surface roughness is 0.781 μm . This characteristic is related to the smaller built-up edge size at higher speeds when the built-up edge's impact becomes minimal. Furthermore, when the cutting speed increases, the cutting process becomes steadier, and vibration while cutting at the greatest speed is reduced. The result of the study is consistent with the study made by Anil et al. [29].

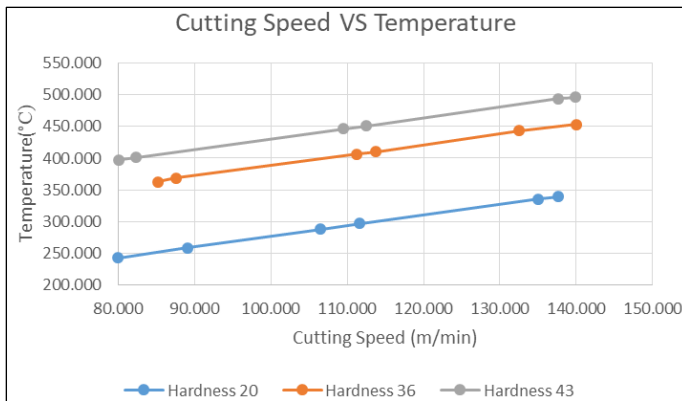


Figure 6: Interaction effect between cutting speed and temperature

Table 6: Optimize process by GA

Hardness 20		Hardness 36		Hardness 43	
V (m/min)	SR (μm)	V (m/min)	SR (μm)	V (m/min)	SR (μm)
80.000	2.867	85.203	2.103	80.133	1.728
89.028	2.734	87.562	2.072	82.278	1.697
106.522	2.463	111.288	1.695	109.526	1.263
111.625	2.381	113.793	1.656	112.513	1.215
135.026	2.011	132.502	1.367	137.684	0.843
137.579	1.975	139.969	1.246	139.943	0.781

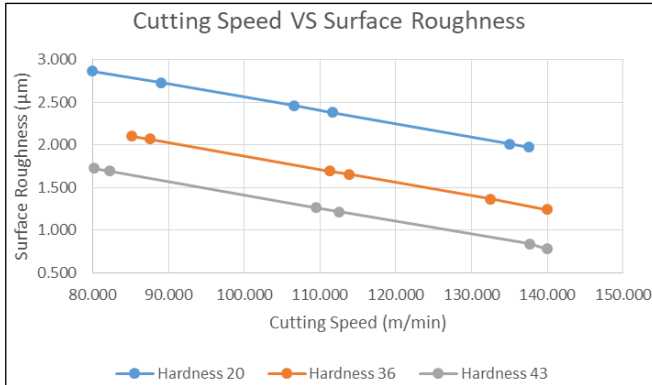


Figure 7: Interaction effect between cutting speed and surface roughness

Effect of feed rate on the temperature rise and surface roughness

Figure 8 depicts the interaction effect between feed rate and temperature for hardness 20 HRC, 36 HRC, and 43 HRC. According to Table 7, increasing the feed rate (f) will correspondingly raise the temperature (T) during machining. The lowest temperature is 243.333 °C when the feed rate is 0.071 mm/rev. After that, the maximum temperature is 339.731 °C, when the value of the feed rate is 0.072 mm/rev for the hardness 20 HRC. For hardness 36 HRC, the temperature is between 363.071 °C to 453.044 °C even though the feed rate is static at the value 0.084 mm/rev. When the hardness increases to 43 HRC, there are little variations in terms of the value of feed rate. The lowest temperature is 397.393 °C when the feed rate is 0.073 mm/rev and the maximum temperature is 493.335 °C when the feed rate is 0.074 mm/rev. The reason for this is because when the feed rate increases, the contact length between the tool and the workpiece likewise expands. When the feed rate goes up, the chip area rises, which increases the friction between the tool and chip interface, causing the temperature at the tool-chip interface to rise accordingly as well. The results have supported the study that was made by Sulaiman et al. [30], the heat is generated more in the shear zone when the feed rate increases due to the increment in the chip's segment which also contributes to the increase in friction.

The interaction impact between feed rate and surface roughness is depicted in Figure 9 and Table 8. It is seen that a decrease in the feed rate at any setting of cutting speed decreases the surface roughness significantly. This can be seen through the hardness 20 HRC when the feed rate is 0.073 mm/rev. The value of surface roughness is 2.577 µm. For hardness 43 HRC, the value of surface roughness becomes 1.728 µm when the value of the feed rate is 0.073 mm/rev, and the value of surface roughness decreases to 0.781

μm when the feed rate to 0.071 mm/rev. Decreasing feed results in flank wear which will deteriorate the surface of the workpiece.

Table 7: Optimize process by GA

Hardness 20 HRC		Hardness 36 HRC		Hardness 43 HRC	
f (mm/rev)	T ($^{\circ}\text{C}$)	f (mm/rev)	T ($^{\circ}\text{C}$)	f (mm/rev)	T ($^{\circ}\text{C}$)
0.071	243.33	0.084	363.07	0.073	397.39
0.072	259.07	0.084	368.90	0.073	401.14
0.072	288.38	0.084	406.30	0.072	445.94
0.072	296.95	0.084	410.30	0.072	450.81
0.071	335.28	0.084	442.87	0.072	477.46
0.072	339.73	0.084	453.04	0.074	493.33

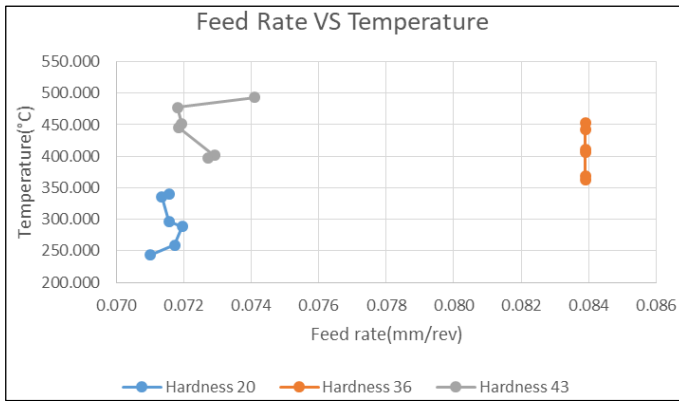


Figure 8: Interaction effect between feed rate and temperature

Table 8: Optimize process by GA

Hardness 20 HRC		Hardness 36 HRC		Hardness 43 HRC	
f (mm/rev)	SR (μm)	f (mm/rev)	SR (μm)	f (mm/rev)	SR (μm)
0.073	2.577	0.084	2.103	0.073	1.728
0.072	2.463	0.084	2.072	0.073	1.648
0.072	2.381	0.084	1.695	0.073	1.530
0.072	2.294	0.084	1.656	0.072	1.382
0.071	2.113	0.084	1.367	0.072	1.215
0.071	2.055	0.084	1.246	0.071	0.781

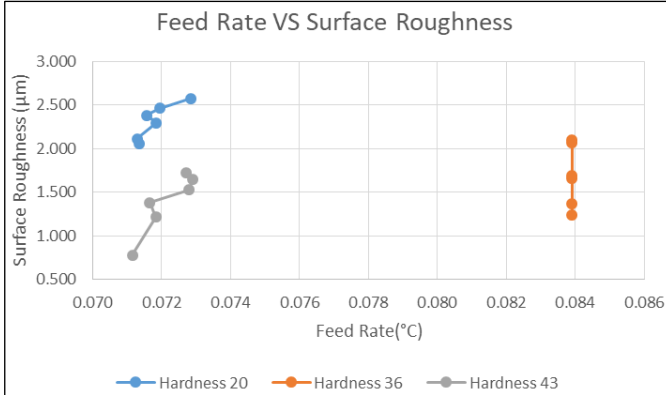


Figure 9: Interaction effect between feed rate and surface roughness

Effect of depth of cut on temperature and surface roughness

Table 9 and Figure 10 indicate the influence of cut depth on temperature. From Figure 10, it can easily find that increasing in the depth of cut (*doc*) will rise the temperature (*T*). It can be seen through the hardness 20 HRC when the temperature is 243.333 °C and the cut depth is 0.5 mm. When the depth of the cut is 0.509 mm, the temperature rises to 325.175 °C. The same thing happened to hardness 36 HRC when the temperature was 427.911 °C and the cut depth was 0.504 mm. However, the temperature rose to 368.906 °C when the depth of cut began to rise by 0.528 mm. The same thing occurred for hardness 43 HRC; at 0.501 mm of cut depth, the temperature was 397.393 °C, and at 0.508 mm of cut depth, the temperature was 481.346 °C. It is possible to argue that as cut depth increases the cutting insert experiences more cutting resistance, which raises temperature. Additionally, the total amount that the cutting tool took from the workpiece's radius during the cutting process was counted. High material hardness demands a deeper value of cut, increasing the strain on the tool and shortening tool life as a result of increased surface roughness.

Table 9: Optimize process by GA

Hardness 20 HRC		Hardness 36 HRC		Hardness 43 HRC	
<i>doc</i> (mm)	<i>T</i> (°C)	<i>doc</i> (mm)	<i>T</i> (°C)	<i>doc</i> (mm)	<i>T</i> (°C)
0.500	243.333	0.504	427.911	0.501	397.393
0.504	283.728	0.510	410.304	0.502	401.140
0.505	263.391	0.512	424.234	0.503	455.988
0.507	288.388	0.515	446.555	0.503	471.252
0.509	318.181	0.523	442.870	0.506	427.472
0.509	325.175	0.528	368.906	0.508	481.346

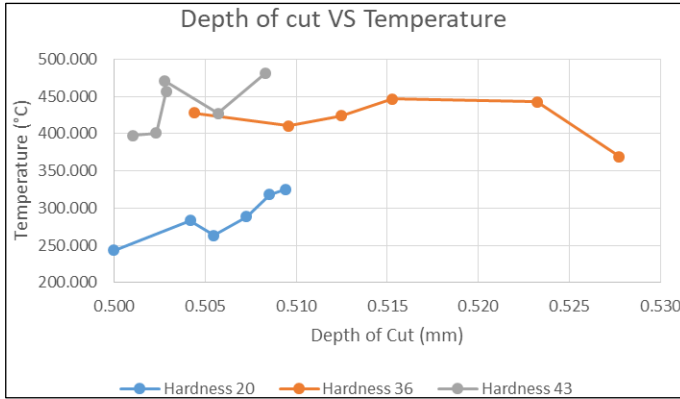


Figure 10: Interaction effect between depth cut and temperature

Table 10 and Figure 11 both display the interaction between surface roughness and depth of cut. It depicts how a deeper cut yields a lower-quality surface. According to Table 10, as the value of the depth of cut increases, so does the value of the surface roughness. With a hardness of 20 HRC, when the depth of cut is 0.502 mm, the surface roughness is 2.055 μm , and when the depth of cut is increased to 0.507 mm, the surface roughness increases to 2.463 μm . For a cut depth of 0.504 mm, the lowest value of surface roughness for hardness 36 HRC is 1.246 μm . The value of surface roughness increases to 2.072 μm when the depth of cut is increased to 0.528 mm. When the surface roughness value is 0.964 μm and the depth of cut value is 0.5 mm, this behaviour occurs for hardness 43. However, the measure of surface roughness increases to 0.941 μm when the depth of cut exceeds 0.508 mm. The cut depth is inversely related to the shear angle and heat-affected zone (HAZ). As the depth of the cut rises, the HAZ and shear angle increase, increasing the cutting force and friction, raising the temperature, and causing the removal of material to deposit on the tool's rake face [29]. As a result, as the depth of the cut rises, the surface roughness (SR) increases as well.

Table 10: Optimize process by GA

Hardness 20		Hardness 36		Hardness 43	
<i>doc</i> (mm)	<i>SR</i> (μm)	<i>doc</i> (mm)	<i>SR</i> (μm)	<i>doc</i> (mm)	<i>SR</i> (μm)
0.502	2.055	0.504	1.246	0.500	0.964
0.502	2.236	0.515	1.326	0.502	0.843
0.504	2.501	0.510	1.656	0.503	1.032
0.505	2.692	0.515	1.987	0.503	1.180
0.505	2.734	0.523	1.735	0.506	1.452
0.507	2.463	0.528	2.072	0.508	0.941

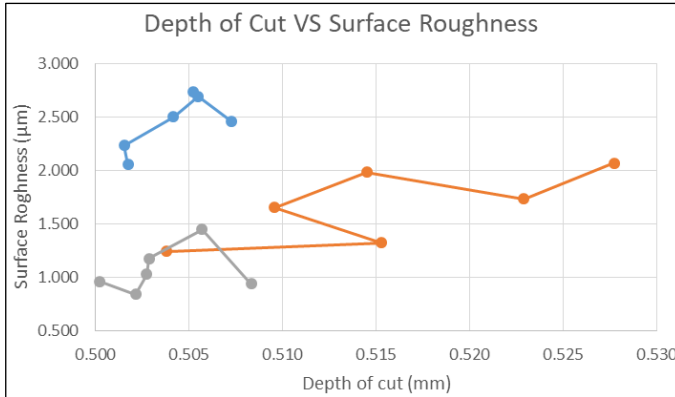


Figure 11: Interaction effect between depth of cut and surface roughness

Effect of the workpiece hardness on the temperature rise and surface roughness

In this study, the effects of workpiece hardness on temperature rise and surface roughness are examined. Changes in the workpiece's surface hardness and roughness measurements were measured throughout the turning process. The three types of workpiece hardness that were used in this study are 20 HRC, 36 HRC, and 43 HRC. It was discovered that surface roughness decreases with increasing hardness, but temperature increases as hardness increases. Table 11 demonstrates that rising temperatures are correlated with increasing levels of hardness. The temperature is between 243 °C and 339 °C, according to hardness 20. When the workpiece's hardness reaches 36, the temperature begins to rise between 363 °C and 453 °C. When the hardness is 43, the value begins to rise, which is between 397 °C and 496 °C. When the hardness is 20 HRC, the value for surface roughness ranges from 2.867 µm to 1.975 µm. When the hardness is 36 HRC, the range starts to widen from 2.103 µm to 1.246 µm. Surface roughness starts to decrease with a hardness of 43 HRC, going from 1.728 µm to 0.781 µm.

According to the table, surface roughness increases in value as material hardness increases. The range of 2.867 µm to 1.975 µm is the surface roughness value for hardness 20 HRC. Surface roughness drops from a value of 2.103 µm to 1.246 µm when hardness rises to 36 HRC. When the hardness is 43 HRC, the surface roughness measurement falls between 1.728 µm and 0.781 µm. Cutting speed significantly affects responses, as seen in Table 11. Lower cutting rates cause a rapid increase in surface roughness, whereas higher cutting speeds cause a quicker increase in hardness. The cutting parameter shows that the independent variable with the greatest influence on the response to the overall turning parameters was cutting

speed, followed by feed rate and depth of cut, which had negligible influence. This study coincides with the study conducted by Omat et al. [31]. As a result, machining has an obvious impact on the workpiece's surface layer's hardness and roughness, both of which are caused by the cutting parameters, particularly cutting speed. The turning process uses cutting force that causes the chips to rip as the tool moves forward, significantly deforming the plastic at the surface and in the layer's underneath. This deformation aftereffect will affect the metal ductility, hardness, and strength. Meanwhile, the underlying material fracture occurs as a result of the chip's severe deformation, resulting in poor surface roughness. The metal characteristics are also affected by the form, size, and depth of cut of the surface grooves.

The ability of a solid substance to endure persistent deformation without shattering is known as ductility in materials science. Ductility is also known as fracture strain or percent reduction in area. Increased surface hardness of the specimens resulted in a decrease in fracture strain. As a result of the plastic deformation created during machining, the material was projected to have been extended over a portion of its permitted plastic deformation, and hence the ductility of the hardened workpieces should have been reduced. Cutting speed had a significant impact on ductility, with high speeds resulting in a higher fracture strain value. This is because the surface roughness rises as the cutting speed lowers [32].

Table 11: Temperature range for every hardness

Hardness (HRC)	Cutting speed (m/min)	Feed rate (mm/rev)	Depth of cut (mm)	Temperature (°C)	Surface roughness (μm)
20	80 -	0.073 -	0.502 -	243 - 339	2.867 -
36	85.203 -	0.084	0.504 -	363 - 453	2.103 -
43	80.133 -	0.073 -	0.5 -	397 - 496	1.728 -

Conclusion

The study showed how to use MOGA to optimize the turning process. The findings suggest that MOGA can yield optimal process parameters and may be used to successfully optimize turning, demonstrating that MOGA is a beneficial optimization tool. The following conclusions may be taken from the optimization conducted on the turning machining process using MOGA:

- i. Due to the contradiction between surface roughness and temperature rise and the machining output, MOGA was able to determine a trade-off between these two objective functions by identifying a combination

- of feed rate, cutting speed, and depth of cut that satisfied both objective functions.
- ii. According to the results, the feed rate, cutting speed, and depth of cut are all significant causes of temperature rise and surface roughness.
 - iii. As the cutting speed increases, surface roughness decreases while the temperature rises.
 - iv. The temperature is improved by raising the feed rate, while surface roughness is greatly reduced when the feed rate is increased at any cutting speed.
 - v. The temperature is going to increase as the depth of the cut increases, and the surface roughness value will begin to rise as well.
 - vi. Although the surface roughness decreases as the hardness increases, the temperature rises as the hardness increases.
 - vii. When the cutting parameters are 80 m/min, 0.071 mm/rev, and 0.5 mm for cutting speed, feed rate, and depth of cut for hardness 20 HRC, the lowest temperature rise that can be achieved using this method is 243.333 °C. Accordingly, it was found that employing MOGA to optimize the machining settings for 20 HRC has improved the temperature rise by about 10.2% and surface roughness by about 20%.
 - viii. Meanwhile, when the cutting speed, feed rate, and depth of cut lowest surface roughness measured for hardness 36 HRC was 1.246 µm. The values are 85.023 m/min, 0.084 mm/rev, and 0.504 mm, respectively. 363.071 °C is the lowest temperature rise that can be produced using these combined parameters. Both temperature rise and surface roughness have increased by 34% as a result of the optimization for 36 HRC.
 - ix. The lowest temperature rise possible with this method is 397.393 °C when the cutting parameters are 80.133 m/min, 0.073 mm/rev, and 0.501 mm for cutting speed, feed rate, and depth of cut with hardness 43 HRC. The lowest surface roughness that has been identified is 0.781 µm. By optimizing the machining parameters for 43HRC, the temperature increase has improved by 34% and the surface roughness has improved by 4%.

Contributions of Authors

The authors confirm the equal contribution in each part of this work. All authors reviewed and approved the final version of this work.

Funding

This work was supported by the “UMP Fundamental Research Grant” [RDU1803144, Optimization of Machining Parameters on Temperature Rise In Cnc Turning of Al 6063 Using Genetic Algorithm, 2018].

Conflict of Interests

All authors declare that they have no conflicts of interest.

Acknowledgement

The authors acknowledge the UMP Fundamental Research Grant (RDU1803144) from Universiti Malaysia Pahang for providing financial support, and also for the use of the research facilities through the course of this research

References

- [1] A. F. Zubair and M. S. Abu Mansor, “Embedding firefly algorithm in optimization of CAPP turning machining parameters for cutting tool selections,” *Computer & Industrial Engineering*, vol. 135, pp. 317–325, 2019. doi: 10.1016/j.cie.2019.06.006.
- [2] B. N. K. P. P. Shirpurkar, S.R. Bobde, V.V.Patil, “Optimization of Turning Process Parameters by Using Tool Inserts- A Review,” *International Journal of Engineering and Innovative Technology (IJEIT)*, vol. 2, no. 6, pp. 216–223, 2012.
- [3] L. B. Abhang and M. Hameedullah, “Optimization of machining parameters in steel turning operation by Taguchi method,” *Procedia Engineering*, vol. 38, pp. 40–48, 2012. doi: 10.1016/j.proeng.2012.06.007.
- [4] M. Gopal, “Optimization of machining parameters on temperature rise in CNC turning process of aluminium 6061 using rsm and genetic algorithm,” *International Journal of Modern Manufacturing Technologies*, vol. 12, no. 1, pp. 36–43, 2020.
- [5] C. S. Akhil, M. H. Ananthavishnu, C. K. Akhil, P. M. Afeez, R. Akhilesh, and R. Rajan, “Measurement of Cutting Temperature during Machining,” *Journal of Mechanical and Civil Engineering*, vol. 13, no. 2, pp. 102–116, 2016. doi: 10.9790/1684-130201102116.

- [6] M. Kuntoğlu, A. Aslan, H. Sağlam, D. Y. Pimenov, K. Giasin, and T. Mikolajczyk, "Optimization and analysis of surface roughness, flank wear and 5 different sensorial data via tool condition monitoring system in turning of aisi 5140," *Sensors (Switzerland)*, vol. 20, no. 16, pp. 1–22, 2020. doi: 10.3390/s20164377.
- [7] D. Y. Pimenov, A. Bustillo, S. Wojciechowski, V. S. Sharma, M. K. Gupta, and M. Kuntoğlu, "Artificial intelligence systems for tool condition monitoring in machining: analysis and critical review," *Journal of Intelligent Manufacturing*, vol. 34, pp. 2079-2121, 2023, doi: 10.1007/s10845-022-01923-2.
- [8] N. Amulya, P. V. S. Subhashini, K. Chinmayi, and R. Naveen, "Parametric Optimization of Heat Generation during Turning Operation," *Journal of Mechanical Engineering and Automation*, vol. 6, no. 5A, pp. 117–120, 2016. doi: 10.5923/c.jmea.201601.22.
- [9] N. H. A. Halim, C. H. C. Haron, J. A. Ghani, and M. F. Azhar, "Prediction of cutting force for milling of Inconel 718 under cryogenic condition by response surface methodology," *Journal of Mechanical Engineering*, vol. 16, no. 1, pp. 1–16, 2019.
- [10] T. H. Bhuiyan and I. Ahmed, "Optimization of Cutting Parameters in Turning Process," *SAE International Journal of Materials and Manufacturing*, vol. 7, no. 1, pp. 233–239, 2014. doi: 10.4271/2014-01-9097.
- [11] A. Debroy and S. Chakraborty, "Non-conventional optimization techniques in optimizing non-traditional machining processes: A review," *Management Science Letters*, vol. 4, no. 1, pp. 23–38, 2013. doi: 10.5267/j.ms.l.2012.10.038.
- [12] H. Akkus and H. Yaka, "Optimization of Turning Process by Using Taguchi Method," *Sakarya University Journal of Science*, vol. 22, no. 5, pp. 1–1, 2018. doi: 10.16984/saufenbilder.409502.
- [13] S. Krishna Madhavi, D. Sreeramulu, and M. Venkatesh, "Evaluation of Optimum Turning Process of Process Parameters Using DOE and PCA Taguchi Method," *Materials Today Proceedings*, vol. 4, no. 2, pp. 1937–1946, 2017. doi: 10.1016/j.matpr.2017.02.039.
- [14] T. S. S.P. Palaniappan, K. Muthukumar, R.V. Sabariraj , S. Dinesh Kumar, "CNC turning process parameters optimization on Aluminium 6082 alloy by using Taguchi and ANOVA," *Materials Today Proceedings*, vol. 20, pp. 342–347, 2020. doi: 10.1016/j.matpr.2019.10.053.
- [15] D. R. Shah, N. Pancholi, H. Gajera, and B. Patel, "Investigation of cutting temperature, cutting force and surface roughness using multi-objective optimization for turning of Ti-6Al-4 V (ELI)," *Materials Today: Proceedings*, vol. 50 no. 5, pp. 1379-1388, 2021. doi: 10.1016/j.matpr.2021.08.285.

- [16] O. Manav and S. Chinchani, "Multi-Objective Optimization of Hard Turning: A Genetic Algorithm Approach," *Materials Today Proceedings*, vol. 5, no. 5, pp. 12240–12248, 2018. doi: 10.1016/j.matpr.2018.02.201.
- [17] V. Durga Prasad Rao, S. R. S. Mahaboob Ali, S. M. Z. M. Saqheed Ali, and V. Navya Geethika, "Multi-objective optimization of cutting parameters in CNC turning of stainless steel 304 with TiAlN nano coated tool," *Materials Today Proceedings*, vol. 5, no. 12, pp. 25789–25797, 2018. doi: 10.1016/j.matpr.2018.06.571.
- [18] N. Sathiya Narayanan, N. Baskar, and M. Ganesan, "Multi Objective Optimization of machining parameters for Hard Turning OHNS/AISI H13 material, Using Genetic Algorithm," *Materials Today: Proceedings*, vol. 5, no. 2, pp. 6897–6905, 2018. doi: 10.1016/j.matpr.2017.11.351.
- [19] A. Kumar, S. K. Pradhan, and V. Jain, "Experimental investigation and optimization using regression genetic algorithm of hard turning operation with wiper geometry inserts," *Materials Today: Proceedings*, vol. 27, pp. 2724–2730, 2019. doi: 10.1016/j.matpr.2019.12.191.
- [20] R. Butola, S. Kanwar, L. Tyagi, R. M. Singari, and M. Tyagi, "Optimizing the machining variables in CNC turning of aluminum based hybrid metal matrix composites," *SN Applied Sciences*, vol. 2, no. 8, pp. 1–9, 2020. doi: 10.1007/s42452-020-3155-8.
- [21] M. Mia and N. R. Dhar, "Modeling of Surface Roughness Using RSM, FL and SA in Dry Hard Turning," *Arabian Journal for Science and Engineering*, vol. 43, no. 3, pp. 1125–1136, 2018. doi: 10.1007/s13369-017-2754-1.
- [22] Y. Ren, S. Rubaiee, A. Ahmed, A. M. Othman, and S. K. Arora, "Multi - objective optimization design of steel structure building energy consumption simulation based on genetic algorithm," *Nonlinear Engineering*, vol. 11, no. 1, pp. 20–28, 2022. doi: 10.1515/nleng-2022-0012.
- [23] A. Chabbi, M. A. Yallese, M. Nouioua, I. Meddour, T. Mabrouki, and F. Girardin, "Modeling and optimization of turning process parameters during the cutting of polymer (POM C) based on RSM, ANN, and DF methods," *International Journal of Advanced Manufacturing Technology*, vol. 91, no. 5–8, pp. 2267–2290, 2017. doi: 10.1007/s00170-016-9858-8.
- [24] B. Solarte-Pardo, D. Hidalgo, and S. S. Yeh, "Cutting insert and parameter optimization for turning based on artificial neural networks and a genetic algorithm," *Applied Sciences (Switzerland)*, vol. 9, no. 3, 2019. doi: 10.3390/app9030479.
- [25] S. H. Yang and U. Natarajan, "Multi-objective optimization of cutting parameters in turning process using differential evolution and non-

- dominated sorting genetic algorithm-II approaches,” *International Journal of Advanced Manufacturing Technology*, vol. 49, no. 5–8, pp. 773–784, 2010. doi: 10.1007/s00170-009-2404-1.
- [26] D. Tanikić, “Computationally intelligent optimization of metal cutting regimes,” *Measurement*, vol. 152, p. 107358, 2020. doi: 10.1016/j.measurement.2019.107358.
- [27] E. G. Ng, D. K. Aspinwall, D. Brazil, and J. Monaghan, “Modelling of temperature and forces when orthogonally machining hardened steel,” *International Journal of Machine Tools and Manufacture*, vol. 39, no. 6, pp. 885–903, 1999. doi: 10.1016/S0890-6955(98)00077-7.
- [28] S. Sivarajan and R. Padmanabhan, “Green machining and forming by the use of surface coated tools,” *Procedia Engineering*, vol. 97, pp. 15–21, 2014. doi: 10.1016/j.proeng.2014.12.219.
- [29] K. C. Anil, M. G. Vikas, B. Shanmukha Teja, and K. V. Sreenivas Rao, “Effect of cutting parameters on surface finish and machinability of graphite reinforced Al-8011 matrix composite,” *IOP Conference Series: Materials Science and Engineering*, vol. 191, no. 1, pp. 1-5, 2017. doi: 10.1088/1757-899X/191/1/012025.
- [30] S. Sulaiman, A. Roshan, and S. Borazjani, “Effect of cutting parameters on cutting temperature of TiAL6V4 alloy,” *Applied Mechanics and Materials*, vol. 392, no. September, pp. 68–72, 2013. doi: 10.4028/www.scientific.net/AMM.392.68.
- [31] O. J. Zurita-Hurtado, V. C. Di Graci-Tiralongo, and M. C. Capace-Aguirre, “Effect of surface hardness and roughness produced by turning on the torsion mechanical properties of annealed AISI 1020 steel,” *Revista Facultad de Ingenieria*, vol. 2017, no. 84, pp. 55–59, 2017. doi: 10.17533/udea.redin.n84a07.
- [32] H. Sasahara, “The effect on fatigue life of residual stress and surface hardness resulting from different cutting conditions of 0.45%C steel,” *International Journal of Machine Tools and Manufacture*, vol. 45, no. 2, pp. 131–136, 2005. doi: 10.1016/j.ijmachtools.2004.08.002.

Design of Two-Stage Force Amplification Frame for Piezoelectric Energy Harvester

Choe-Yung Teoh*, Joon Kit Wong, Ying Hao Ko
Faculty of Engineering and Technology,
Tunku Abdul Rahman University of Management and Technology,
Kuala Lumpur, MALAYSIA
*teohcy@tarc.edu.my

Muhammad Najib Abdul Hamid
Engineering Section, Universiti Kuala Lumpur, Malaysian Spanish Institute,
Kedah, MALAYSIA

Lu Ean Ooi
School of Mechanical Engineering,
Universiti Sains Malaysia Engineering Campus, Pulau Pinang, MALAYSIA

Wei Hong Tan
Faculty of Mechanical Engineering & Technology,
Universiti Malaysia Perlis, Perlis, MALAYSIA

ABSTRACT

This paper describes the design of a two-stage force amplification frame for the piezoelectric energy harvester to capture mechanical energy from walking human footsteps. The frame design optimises the stress distribution to improve the force amplification ratio on the existing footstep energy harvesters. The magnification of the input force exerted on a piezoelectric stack increases the system's power output. A combination of single and compound two-stage frame design with additional linkage support was proposed, which maximise the conversion of tension to compression forces. The proposed frame also significantly reduces the maximum displacement of the frame to ensure walking comfort. The frame is tested with the input force of 85 N to 120 N based on the adult footstep during walking and running. The simulated results show that the proposed frame has a force amplification ratio of 25.3, an 11.85% improvement from the existing frames. The frame

also limits the maximum displacement to 1.02 mm, 22.14% compared to the existing frames.

Keywords: *Energy Harvester; Compound Two-Stage Frame; Piezoelectric; Force Amplification Mechanism; Force Amplification Ratio*

Introduction

Mechanical energy from various sorts of vibration, motion, or any other source is not being gathered. Therefore, this source of energy is wasted and thus dispersed to the surrounding. To effectively utilise these losses, wasted mechanical energy is absorbed by piezoelectric material and becomes valuable electrical energy [1]. Piezoelectric generation only depends on mechanical factors such as pressure, strain, or vibration. Piezoelectric material will convert these mechanical factors to electrical power [2]. Therefore, if the mechanical energy of human footsteps can be successfully converted into useful electrical energy, it will benefit energy conservation and reduce emissions [3]. Research on piezoelectric energy harvesting has been conducted extensively in various applications, including structural condition monitoring, implanted biomedical devices, rain energy harvesting, vibration-based harvesting, and other electronic devices [4]-[8].

The technology of piezoelectric on floor tiles to harvest energy is relatively new. By utilising human footsteps, useful energy can be harvested and generate electricity [9]. Energy production depends on humans' weight, deflection of piezoelectric material, type, and movement frequency. Piezoelectric floors were applied and tested at Tokyo stations by East Japan Railway Company in 2008, which have more than 400,000 people pass by per day [10]. It was installed around the ticket machines in the station instead of installing all over the station. The station installed 25 square meters of piezoelectric floors, producing approximately 1.4 kWh daily, enough to power the monitors and ticket machines. Besides that, PaveGen installed tiles on a public soccer field in Rio de Janeiro to store electricity for lighting after sunset [11].

Cantilever beams are the most common Piezoelectric Energy Harvester (PEH) as they generate an enormous average strain with external force than plates, diaphragms, and disks. Cantilever beams are well-functioned with input excitations and tip plucking by using a proof mass placed at the end to reduce the resonance frequency and improve the inertial force. However, the cantilever beam cannot work with high compressive force excitation as it has a smaller force-to-displacement ratio [12]. The conventional piezoelectric harvesting module combines a piezoelectric unimorph and a bimorph cantilever arrangement. One or two layers of piezoelectric element are laminated to a single flexible plate and function in

bending mode. Typically, typical cantilever-type energy harvesters generate a negligible amount of output power. It is easily broken and cracks near the clamping end under a small amount of pressure.

A variable-geometry cantilever beam was used to enhance the power harvesting process. However, it suffered from overstraining near the clamping area. Calio et al. [13] used a trapezoidal cantilever beam to avoid overstrain. The strain was distributed more evenly along with the beam structure, and it could sustain higher excitation loading, which led to an increase in the harvested energy density. Trapezoidal shape cantilever beam has a more evenly distributed strain throughout the beam than the rectangular beam, consisting of non-uniform strain distribution. Besides, a trapezoidal cantilever produced twice the energy compared to a cantilever beam in a rectangular shape for the same volume of PZT material.

A flex-compressive mode cymbal transducer was designed by Wang et al. to fully utilise the compressive stress in piezoelectric elements as the tensile strength of a piezoelectric material was always lower than the compressive strength [14]. The transducer improved the stiffness of the cymbal mechanism and enhanced the load capacity. The flex-compressive mode piezoelectric energy harvesting cell (F-C PEHC) was assembled from two PZT piezoelectric stacks and four types of steel elements. The cymbal top plate with short limbs was implemented to enhance the load capacity. The structures were mechanically assembled and had no bonding layer, and all the structural parts were replaceable.

A non-linear parametric model was developed by Chen et al. [15] to estimate the deformation of the frame accurately by considering the possible constraints of each frame part. The results of the non-linear parametric model showed an accuracy of at least 95%. The results showed that the force amplification ratio was improved by reducing the thickness of the linkage, and a longer linkage improved the bending deflection of the frame. However, a longer and thinner linkage produced more significant stress on the linkage and the blocks.

As the force amplification frame, various lever mechanisms may be utilised. The bridge-type amplification frame, which has a high amplification ratio and a small size, was one of them. However, the conventional bridge-type amplification frame is limited by its low load capacity, which cannot withstand high loading forces. The force amplification cannot be promised by force applied onto the frame because different humans have different weights when walking on the frame. Hence, Wen et al. [16] developed a compound two-stage (CTS) force amplification frame to increase the frame stability under high loading force conditions. When an input force was exerted vertically downward on the top of the outer frame, the frame produced a horizontal tension force along the x-axis, pulling the outer frame's output ends on both sides away from the centre. As the output ends of the outer frame were attached to the input ends of the inner frame, the outer frame

generated a tensile force that pulled the input ends of the inner frame away from the centre. Thus, the output ends of the inner frame generated compressive force along the z-axis, which was connected to both ends of the piezoelectric stack. Consequently, compared to the conventional bridge-type amplification frame, this frame has a greater force amplification ratio, a greater safety factor, and a smaller size.

The force amplification frame consisted of two shapes which were convex and concave frames. Convex and concave frames applied tensile and compressive force to the piezoelectric stack. Generally, the force amplification ratio for a convex frame was higher than the concave frame for a single amplification frame because the input end has a large deformation. High deformation caused a decrease in safety factors when the surface area of bending increased. According to the law of energy conservation, the increase in input force decreased the output displacement of the frame for the two-stage force amplification mechanism. The concave frame's inner frame could not generate a high force amplification ratio due to the outer frame's diminished output displacement. Mechanical deformation consumed the majority of the strain energy stored in the frame, thereby decreasing the total amplification ratio of the frame [16].

A standard bridge-type amplification frame has only single input and output ends, where external force was applied to a small contact area. The structure was not able to sustain tension stress. Besides that, each force amplifier can only support a limited load capacity, and it can damage the structure when the load exceeds the yield strength of the material. Hence, a protective structure was needed to improve the strength of the mechanism. A wedge structure can support a large force, but it has a relatively small safety factor and an enormous size. Wen and Xu [16] designed an integrated multi-stage (IMS) force amplifier that used both force amplifiers in the frame to improve output performance and sustain high input force.

The structural characteristic of the wedge mechanism allowed it to convert and amplify the vertically downward input force into horizontal force. The leverage structure improved the force amplification and reduced the physical size of the frame. However, the limitation of this structure was that the frictional force acting on the contact surface between the two wedges restricted the movement and caused a reduction in the force amplification ratio.

The existing bridge-type force amplification frames have a limited capacity for tolerating the loading force. When different human weights are exerted on the frame, the force amplification cannot be guaranteed by the loading forces exerted on the frame. Researchers have tried to optimise the force amplification frame by balancing the safety factor and force amplification ratio, but improving it is challenging [16]. Hence, factors such as force amplification ratio and force transmission efficiency are still insufficient in the current research. The conversion efficiency reduces with

the size of the piezoelectric modules because the coverage of footprints reduces when the module area increases [17]. Besides, a large area of mechanical strain may damage the material due to its brittleness. The output voltage generated from piezoelectric material is also significantly low compared to other energy sources [2]. The level of comfort experienced by humans when stepping on a frame is directly related to its displacement—generally, a smaller displacement results in greater comfort. However, the output energy of a piezoelectric energy harvester depends on the degree of compression of the piezoelectric stack. The amplification frame acts as a converter to maximise the output energy, converting the vertical load from the human step into a horizontal load that compresses the piezoelectric stack. The vertical displacement should be at a minimum, and the horizontal displacement to be at a maximum. Therefore, this paper aims to optimise the force amplification ratio of the piezoelectric energy harvester while minimising the frame displacement to ensure human comfort. This can be achieved by improving the effectiveness of force conversion through the design of the frame.

Mechanical Design

Mechanism description of the amplification frame

The proposed design of the energy harvester's amplification frame is shown in Figure 1. This design is composed of a combination of the single and compound two-stage frame. It consists of two-beam layers at the inner frame to ensure the stress is evenly distributed. The design is supported with a layered beam at the outer frame to avoid high-stress concentration. Besides, a linkage is added at the outer frame to assist in pushing the output end of the inner frame inward to compress the piezoelectric stack attached to the output ends of the inner frame. Figure 1(a) depicts the input force, F_i , acting vertically downward at point A onto the outer frame's input end. This force compresses the input ends A , pushing the BC ends outward and the DE ends inward, leading to the compression of the inner frame, as illustrated in Figure 1(b). The DE ends apply compression forces to the piezoelectric stack inside the inner frame. Furthermore, the tensile force on BC helps to further compress the DE ends. Figure 1(c) presents the system's overall design, where the applied force F_i causes the BC ends to extend outward and the DE ends to compress inward. The detail dimension of the amplification frame is shown in Figure 2.

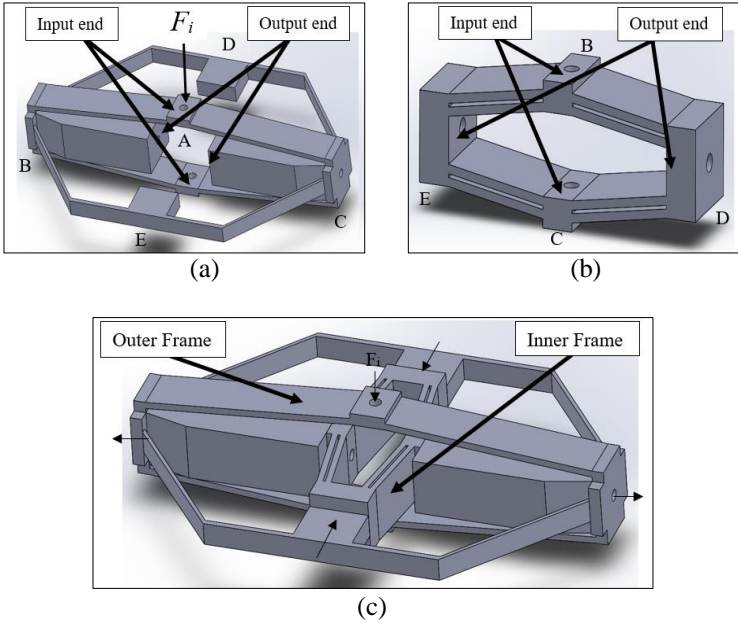


Figure 1: (a) Outer frame; (b) inner frame; and (c) assembly of the outer and inner frame

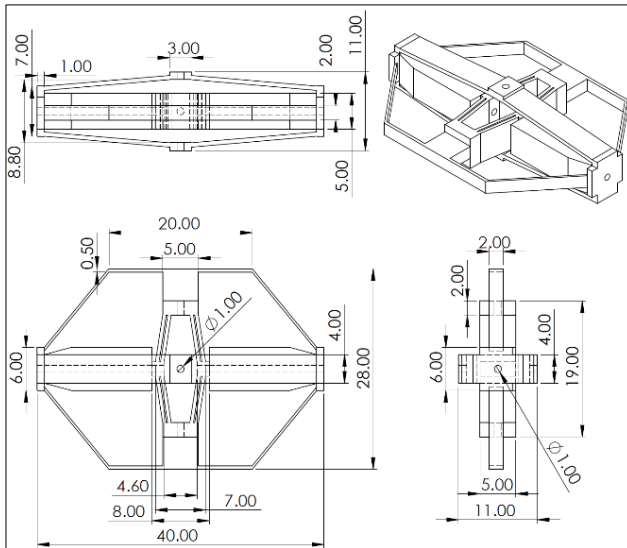


Figure 2: Detail dimension of the amplification frame

Design criteria and constraints

The design of the piezoelectric energy harvester's amplification frame was made with several considerations and constraints, including the selection of material, amplification mechanism, and frame features. Alloy steel 4150 was proposed as the frame material in this design because of its high tensile and yield strength and higher Young's modulus (E) to density, ρ ratio. A greater E - ρ ratio allows the frame to have more significant deformation. The material properties of alloy steel 4150 are shown in Table 1.

Table 1: Material properties of alloy steel 4150

Properties	Value
Density	$8.03 \times 10^3 \text{ kg/m}^3$
Poisson's ratio	0.27
Young's modulus	190 GPa

The proposed amplification frame is based on the frame designed by Wen et al. [18]. The force amplification frame design by Wen et al. [18] utilised the outer frame for pulling the inner frame and inducing compression on the output ends of the inner frame, thereby compressing the piezoelectric stack. The outer frame itself was pulling on the inner frame. Hence, the compression of the piezoelectric stack is entirely dependent on the outer frame's pulling force. This design lacked a sufficient force amplification ratio because the forces were only transmitted to the inner frame via the connection between the output ends of the outer frame and the input ends of the inner frame, which did not maximise force transmission. When an extra compressive force acts on the inner frame's output ends, the inner frame's output ends experience additional compressive force from the outer frame, which increases the force amplification ratio.

Hence, the proposed design in this paper used a combination of single and compound two-stage frames to maximise the force transmission. This design consists of two layers of the beam at the inner frame to ensure the stress was evenly distributed and to avoid high-stress concentrations occurring in the single-layer outer frame design. Besides that, an additional linkage was added to the outer frame to assist in pushing the output end of the inner frame inward to compress the piezoelectric stack attached to the output ends of the inner frame.

Finite element modelling and simulation

The finite element model was created to estimate the force amplification ratio of the force amplification frame. The numerical analysis of the proposed frame was done in ANSYS simulation software. The results of stress distribution, total deformation, reaction force, Factor of Safety (FOS) and amplification ratio for a range of input forces were analysed. The input force

of 100 N was applied vertically on the top and bottom ends of the outer frame, giving a compressive load of 100 N. The detailed location of the constraints and force inputs on the model are shown in Figure 3. Both output ends of the inner frame were fixed to determine the reaction force from the applied input force through the outer and inner force amplification frame. Mesh refinements were used on the beam's surface, and the outer frame's input ends to obtain accurate stress distribution and total deformation results along the beam. The mesh size of 1 mm was used in the simulation based on the result obtained from the mesh convergence test. The model validation was made by comparing the total deformation and maximum stress of the model published by Wen et al. [18] before modification was made to the Wen et al. [18] model.

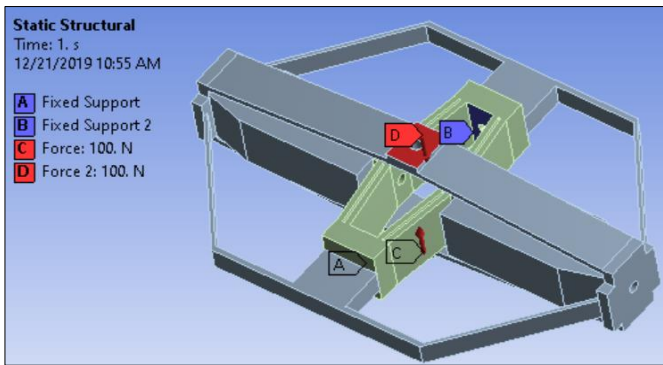


Figure 3: Location of the constraints and force inputs in the ANSYS simulation model

Results and Discussion

The effect of input force on the force amplification ratio

After validating the model with an input force of 100 N, the model was analysed with input forces ranging from 5 N to 160 N with a 5 N increment. Figure 4 displays the ratio of force amplification for input forces ranging from 5 N to 160 N. Based on clinical data from Keller et al., the range of input force from 85 N to 120 N was equivalent to the force input from average human footsteps [19]. However, the model was analysed from 5 N to show the full range of energy input, including the input force from children's steps. Furthermore, the input force is tested until the safety limit of the model, which is 160 N, to cover the extreme case.

The results with an input force of 100 N were compared with the existing literature models. Figure 4 shows that the force amplification ratio

fluctuated from 25.299 to 25.300 when the input force increased from 5 N to 50 N. The 0.004% fluctuation here is insignificant to explain the effect of input force on the amplification ratio. Still, it is due to the deviation from Discrete Element Modeling. With the input range from 55 N to 160 N, the amplification ratio increase gradually from 25.2982 to 25.2994 with the rise in the input force. The trend is comparable with peer results [20]. This design's amplification ratio was relatively higher than existing models, with an amplification ratio between 17.90 and 22.62. The improvement in the force amplification ratio will contribute to the larger power output.

Deriving from the result in Figure 4, the factor of safety of the proposed design is 1.35 to 1.85 with an input force of 85 N to 120 N. At the input force of 160 N, the factor of safety will reach unity, and this is the maximum allowable input force for this design. Based on the size of the proposed amplification frame, each floor tile can fit in 16 units of the frames. Thus, the maximum weight a floor tile can support is up to 260 kg, sufficient for typical human steps.

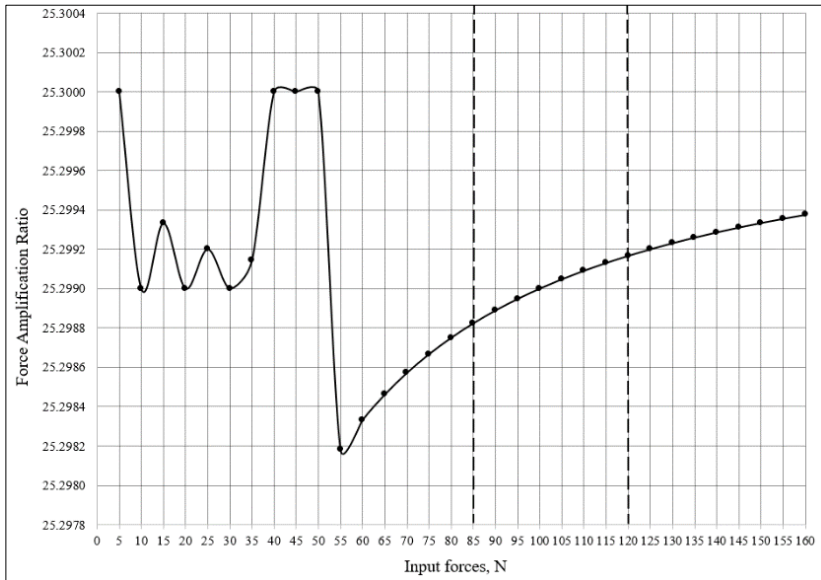


Figure 4: Graph of force amplification ratio against input forces, N

Stress distribution of the proposed frame when subjected to 100N input force.

Figure 5 showed the stress distribution of the model when a compressive force of 100 N was applied. The results showed that the maximum stress on the frame was 1075.90 MPa. The stress was concentrated on the outer frame,

where the maximum stress occurred near the outer frame's input end, as shown in Figure 6. Besides, there was also a high-stress concentration at both ends of the outer frame. The stress was evenly distributed on the inner frame along the compound beams, reducing the stress concentrated at a particular location.

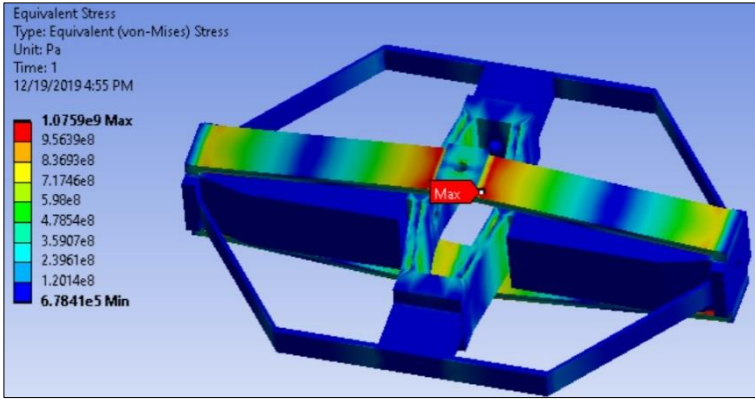


Figure 5: Maximum equivalent (Von-Mises) stress for input force of 100 N

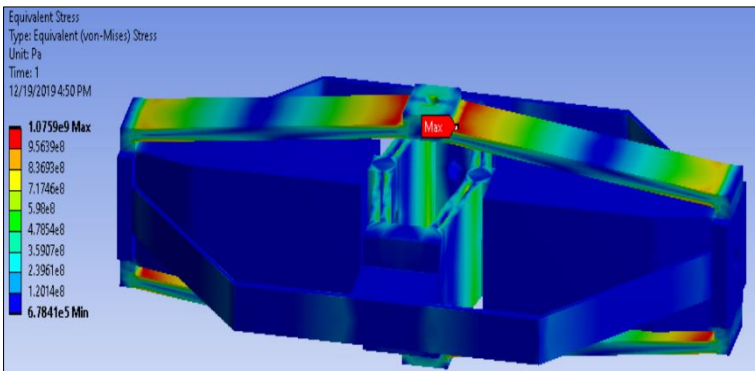


Figure 6: Location of maximum stress on the beam of the outer frame

Total deformation of the proposed frame based on input force of 100 N

Figure 7 showed the frame's total deformation and the maximum deformation location when 100 N compressive force was applied to the model. The results showed that the maximum deflection was 1.0186 mm, located at the outer frame's centre. The deflection was lower than the peers' models, which was

1.31 mm to 4.21 mm. The reduction in the frame's deflection ensures human comfort while stepping on it.

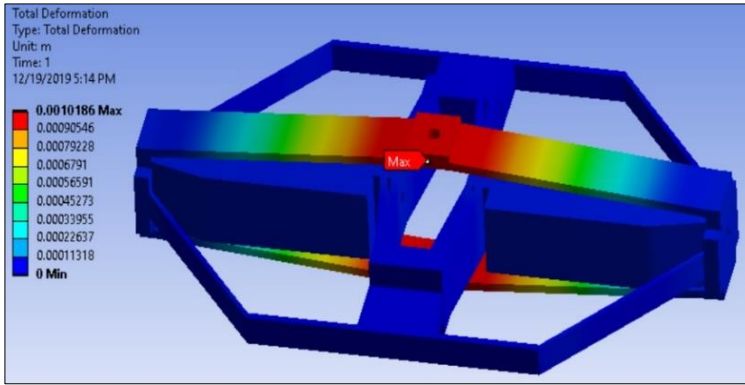


Figure 7: Total deformation when input force of 100 N was applied

Performance comparison with existing frames

The performance of this newly proposed frame showed improvement in most aspects compared to existing designs. The comparison table was constructed as shown in Table 2. The model had the highest force amplification ratio among other current designs. The force amplification ratio obtained for this proposed design was 25.30 compared to 22.62 on the existing designs, with an 11.85% improvement. Besides, the FOS of the proposed design was also higher than the single two-stage harvester design, which was 1.60 compared to 1.23 but lower than the compound two-stage harvester design and IMS harvester design. Moreover, the total deformation for the proposed design was the lowest among all existing designs. Lower deformation of the frame ensured human comfort while stepping on it.

Table 2: Performance comparison of various designs of the energy harvester's frames

Indicator	Proposed design	Single two-stage harvester [18]	Compound two-stage harvester [18]	IMS harvester [16]
Input force (N)	100	100	100	67.73
Maximum	1.02	4.21	1.31	3
Minimum factor	1.6	1.23	2.94	1.98
Force	25.3	22.62	17.9	18.83

Conclusion

This paper presents the design and modelling of a piezoelectric energy harvester's amplification frame based on a multi-stage force amplification mechanism. The main design variables of the models are optimised to achieve the best force amplification ratio with a more prominent safety factor. The proposed model has a force amplification ratio of 25.30, and 11.85% improvement compared to existing designs. A minimum Factor of Safety (FOS) of 1.6 was obtained for the proposed design, supporting the application. The model also showed a deformation of 1.02 mm, which is the lowest compared to existing designs. The reduction in the deformation improves human comfort while stepping on it.

Contributions of Authors

The authors confirm the equal contribution in each part of this work. All authors reviewed and approved the final version of this work.

Funding

This work received no specific grant from any funding agency.

Conflict of Interests

All authors declare that they have no conflicts of interest

Acknowledgment

This paper is done with the financial support from Tunku Abdul Rahman University of Management of Technology.

References

- [1] S. Ahmad, M. Abdul Mujeebu, and M. A. Farooqi, "Energy harvesting from pavements and roadways: A comprehensive review of technologies, materials, and challenges", *International Journal of Energy Research*, vol. 43, no. 6, pp. 1974-2015, 2019.

- [2] A. Majeed, "Piezoelectric Energy Harvesting for Powering Micro Electromechanical Systems (MEMS)", *Journal of Undergraduate Research*, vol. 5, no. 1, pp. 17-21, 2015.
- [3] F. Shu, T. Yang, and Y. Liu, "Enhancement of power output by a new stress-applied mode on circular piezoelectric energy harvester", *AIP Advances*, vol. 8, no. 4, p. 045102, 2018.
- [4] R. S. Roy, C. L. Lim, C. G. Lim, and N. M. Adam, "ANSYS water-wind flow simulation to study pressure generated under various conditions to generate electricity using piezoelectric cells", *Journal of Mechanical Engineering*, vol. 17, no. 3, pp. 1-11, 2020.
- [5] M. S. Mohd Resali and H. Salleh, "Wireless condition monitoring system for rotating machinery powered by a hybrid vibration based energy harvester", *Journal of Mechanical Engineering*, no. 2, pp. 249-267, 2017.
- [6] M. S. Mohd Resali and H. Salleh, "Effect of rubber compound treatment and PTFE extension beam on piezoelectric energy harvester power density", *Journal of Mechanical Engineering*, no. 2, pp. 199-214, 2017.
- [7] S. Ben Ayed, A. Abdelkefi, F. Najjar, and M. R. Hajj, "Design and performance of variable-shaped piezoelectric energy harvesters", *Journal of Intelligent Material Systems and Structures*, vol. 25, no. 2, pp. 174-186, 2014.
- [8] Z. Yang, S. Zhou, J. Zu, and D. Inman, "High-performance piezoelectric energy harvesters and their applications", *Joule*, vol. 2, no. 4, pp. 642-697, 2018.
- [9] A. M. M. Asry, F. Mustafa, M. Ishak, and A. Ahmad, "Power generation by using piezoelectric transducer with bending mechanism support", *International Journal of Power Electronics and Drive Systems*, vol. 10, no. 1, p. 562, 2019.
- [10] F. Laumann, M. M. Sørensen, R. F. J. Lindemann, T. M. Hansen, and T. Tambo, "Energy harvesting through piezoelectricity-technology foresight", *Energy Procedia*, vol. 142, pp. 3062-3068, 2017.
- [11] A. Z. Tejani, "Biomechanical energy harvesting in architectural design, using piezoelectric transducers in pedestrian flooring systems", *International Journal of Environmental Research and Development*, vol. 8, no. 1, pp. 15-24, 2018.
- [12] Y. Kuang, A. Daniels, and M. Zhu, "A sandwiched piezoelectric transducer with flex end-caps for energy harvesting in large force environments", *Journal of Physics D: Applied Physics*, vol. 50, no. 34, p. 345501, 2017.
- [13] R. Calì et al., "Piezoelectric energy harvesting solutions", *Sensors*, vol. 14, no. 3, pp. 4755-4790, 2014.
- [14] X. Wang, Z. Shi, J. Wang, and H. Xiang, "A stack-based flex-compressive piezoelectric energy harvesting cell for large quasi-static loads", *Smart Materials and Structures*, vol. 25, no. 5, p. 055005, 2016.

- [15] W. Chen, Y. Wang, and W. Deng, "Deformable force amplification frame promoting piezoelectric stack energy harvesting: Parametric model, experiments and energy analysis", *Journal of Intelligent Material Systems and Structures*, vol. 28, no. 7, pp. 827-836, 2017.
- [16] S. Wen and Q. Xu, "Design of a novel piezoelectric energy harvester based on integrated multistage force amplification frame", *IEEE/ASME Transactions on Mechatronics*, vol. 24, no. 3, pp. 1228-1237, 2019.
- [17] E. Bischur and N. Schwesinger, "Organic piezoelectric energy harvesters in floor", in *Advanced Materials Research*, 2012, vol. 433-440, pp. 5848-5853, 2012.
- [18] S. Wen, Q. Xu, and B. Zi, "Design of a new piezoelectric energy harvester based on compound two-stage force amplification frame", *IEEE Sensors Journal*, vol. 18, no. 10, pp. 3989-4000, 2018.
- [19] T. S. Keller, A. Weisberger, J. Ray, S. Hasan, R. Shiavi, and D. Spengler, "Relationship between vertical ground reaction force and speed during walking, slow jogging, and running," *Clinical biomechanics*, vol. 11, no. 5, pp. 253-259, 1996.
- [20] H. Y. Li, F. Guo, Y. Wang, Z. Wang, C. Li, M. X. Ling, G. B. Hao, "Design and modeling of a compact compliant stroke amplification mechanism with completely distributed compliance for ground-mounted actuators", *Mechanism and Machine Theory*, vol. 167, p. 104566, 2022.

Development of an Order Processing System using Google Sheets and Appsheet for a Malaysian Automotive SME Factory Warehouse

Mohamad Khairi Hassan

Sugihara Grand Industries Sdn Bhd, 42000 Port Klang, Selangor, MALAYSIA

Mohd Hazri Mohd Rusli*, Noor Azlina Mohd Salleh

Smart Manufacturing Research Institute (SMRI),

School of Mechanical Engineering, College of Engineering,

Universiti Teknologi MARA, 40450, Shah Alam, MALAYSIA

*hazrirusli@uitm.edu.my

ABSTRACT

The automotive industries in Malaysia have grown well and developed many suppliers in their supply chain including Small Medium Enterprise (SME). The order handling process at a supplier's factory has become one of the most critical areas in the supply chain. Adaptation to technology such as IoT enables the automotive supplier to better manage their customer orders and avoid mistakes that affect the supply chain. In order to improve the order processing activities, a study has focused on developing a mobile device application using Google Appsheet and Google Sheets as a cost-effective system for managing supply orders. A study was conducted in one of Malaysian SME automotive companies, which manages the orders manually by using a log book with a lot of recording and redundant work. By using Google Sheets, all the information and data involved in order processing activities is imported and digitized. Then, a mobile application is created using Appsheet so that the ordering activities and processing can be completed on a mobile device. All information gathered by the mobile app (Google Appsheet) is immediately saved in Google Sheets on an Excel-based database, allowing for further data analysis. The research conducted has managed to integrate these two applications into a system for Malaysia's SME factory to manage the ordering activities in the automotive supply chain. This system enables the user to shorten their order processing

time since data is captured in real time and mistakes due to manual error can be avoided.

Keywords: *Order Processing System; Mobile Apps; Google Sheet; Google Appsheet; Iot Warehouse*

Introduction

Massive growth in mobile device technology makes people dependent on it either in social life or for work. Mobile phones are now not just carrying out their original function as a device to make and receive a call or message as a priority, but are doing much more to fulfill people's needs in life, such as serving as a camera, scanner, recorder, and mini computer. People are carrying their mobile devices anywhere at any time and involving the device as much as possible in each of their life activities. This has also had a great impact on the work system in the world today since it has been proven to improve work effectiveness and be able to deliver quick and accurate results. Monitoring of a business operation is done by using a smartphone, which can help users get results in real-time as input for an action based on the result [1]. An appropriate mobile application is able to be developed in order to fit user requirements and improve process operation with the support of mobile devices [2].

The automotive industries in Malaysia have grown well and have created a component supply chain by involving vendors, which involve SME factories. Vendors that produce the components of automotive parts play a very important role in ensuring continuous part supply to the car assembler in the right quantity and on time. To maintain the chain of supply, the required parts or components are determined by the Automotive assembler based on their production plan, and ordering from the vendors is initiated. This order is initiated through either Delivery Instruction (DI) or Kanban.

The DI is referring to a document released by the automotive assembler describing what item is required for delivery along with information on quantity and when to deliver. While Kanban is described as a visual signal that is used by downstream processes to trigger upstream actions in the Just-In-Time (JIT) process [3], it is also used to provide information about the item's required quantity at the dedicated delivery time. Vendors that received the order information either from DI or Kanban will process the order procedures and prepare the required parts. Finally, the arrangement for delivery is made, and the order is completely filled. The flow of order processing for automotive parts is described in Figure 1.

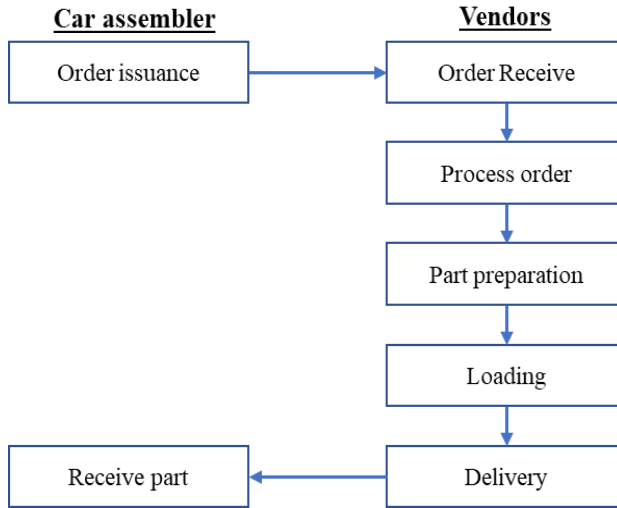


Figure 1: General process flow of ordering parts in the automotive supply chain

This research has been initiated to find and develop an alternative method of managing an order from a customer in the warehouse of an automotive SME factory. System development is focusing on Google applications, which are Appsheet for mobile device software customization and Google Sheet for data collection and analysis. This paper explains how to create a mobile application using an Appsheet for processing warehouse orders step by step. It serves as a reference for users creating applications using the Appsheet's fundamental features. This paper provides a clear understanding of developing a system for mobile devices by using Google Appsheet and Google Sheets for a systematic order processing activity applicable to automotive SME factory warehouses.

A case study has been conducted at one of the SME automotive factories, named PSB Sdn Bhd, that supplies interior parts to a few automotive suppliers as a second tier in the chain. Their warehouse is occupied with determining which item the customer needs for the day and delivering it in accordance with the quantity and time. Entering orders from their customers is referring to a task that takes place before actually filling the order, where the challenge is in establishing clear communication throughout the logistical or warehouse operation [5].

An order from the customer is received through email containing an order document that is Kanban in the early morning and the delivery has to be completed within a couple of hours. Due to this time limitation (from order receipt until delivery), a single step of order handling processing is critical, and

even small mistakes will lead to delivery failure and can affect the customer assembly line. Details on manual order processing activities conducted at the PSB can be described in Figure 2.

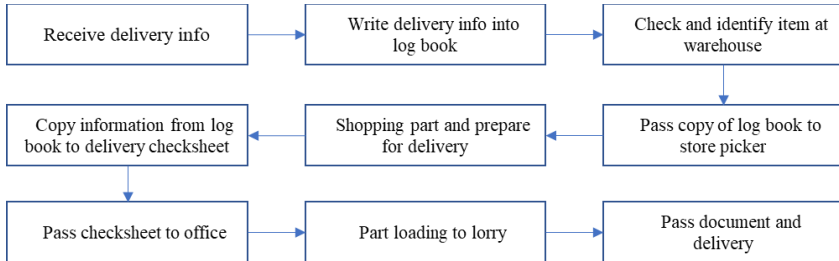


Figure 2: Flow chart of order processing activities at PSB Sdn. Bhd.

All the steps as stated in the above figure have not been fixed on their timing since the process will depend on the customer's order type as well as the order quantity. However, it is supposed to be conducted in order to set a standard and a key performance indicator (KPI) for future improvement [5].

In a single cycle of delivery activities, a lot of specific information must be recorded. Table 1 below describes the information needed for the item that is going to be delivered. Each of these pieces of information is important for both parties to ensure the item delivered meets the order requirement. Besides, the information will become more important if the item is found to not meet the standard requirement, such as having quality issues that require tracing the root cause of the issues for a countermeasure.

Table 1: Item information required for delivery

No.	Item	Purpose / Importance
1	Item name	Product identification
2	Item number	Product identification
3	Quantity	Informing how many actual items
4	Shipping batch order	Tracing for which receiving batch
5	Size	Informing actual item dimension
6	Lot number	Tracing for the production batch at the

This makes the order processing and part-picking activities costly and shall be considered in the total operation factors [6]. Processes that are conducted manually are identified as waste in a Value Stream Mapping (VSM) analysis and will just increase the logistical cost of the operation [7]. There is a risk of error due to a typo or mistake when the information is written manually

and then copied to another check sheet. Since this process is critical, only a competent person with a high focus is able to perform the task.

A process that is carried out manually with paper-based practices will lead to common issues that are normally faced by the logistics industry, such as inventory that is not visualized, shipment processing errors, space underutilization, a lot of paperwork, and observation of existing manual order processing activities, a risk factor was identified that can lead to a failure at the customer's place, as described in Figure 3.

Risk 1	Risk 2	Risk 3	Risk 4	Risk 5	Risk 6
Error copying info from kanban	Error in reading information from hand written log book info	Entering wrong data of picked item	Copying wrong info from log book to customer checksheet	Wrong calculation of total quantity delivery of item	Delay of delivery
Create mistake when copying order info (order number, item number and quantity)	Info written in log book not clear. Interpreted wrongly while copying info Lead to wrong pick item	Item details wrongly wrote in log book. Difficulties handling the log book and pen while assessing the parts in the warehouse	Data wrongly entered into checksheet. Impact of wrong billing and other documents	Wrong count for total quantity by using a manual calculator. Will give impact as per risk 4	Next process to wait until the previous process is completed before start. Total process time increased.

Figure 3: Risk of conducting a manual ordering process

Based on the risks observed, a systematic approach is proposed to address these issues, which is to digitize the whole ordering process as a solution. A digital solution will have an obvious impact on the warehouse operation through a Warehouse Management System (WMS), which improves the warehouse operation's effectiveness [9]. Efforts in waste reduction in a warehouse's operational activities will improve the overall warehouse performance, which will either directly or indirectly improve a company's business performance [10].

A cloud-based database system is introduced with a custom Graphical User Interface (GUI), which enables the user to interact with the data from their mobile device at any time and anywhere, as long as there is an active internet connection by using Google Appsheet. The data is then saved in Google Drive and made available for free use in Google Sheets for further data analysis.

Literature Review

A warehouse operation using a manual method is facing a problem with operation data that is not able to be updated in time. Although Enterprise Resource Planning (ERP) is used, it still isn't able to meet business and customer needs because of things like the person in charge's delayed updating of data, a lack of communication, and information about activities that aren't synchronized [11]. A mobile application was found to be widely used in assisting an operation in the supply chain, such as in order entry and processing (communication), stock ordering (inventory), order picking and assembly (unitization and packaging), and order delivery (transportation) [12].

Google Sheets is a cloud-based application that provides a similar function to Microsoft Excel but offers more benefits than just a spreadsheet. Google Sheets provides online document sharing, so multiple users can interact on the same page at any one time by using supporting devices such as a laptop, phone, or tablet. Users have no worries about their data every time they update since it is online, the data will automatically save to the drive as long as the internet is connected. Additionally, previous revisions can still be found by using the version history feature, allowing users to go back to a specific starting point whenever necessary. The file can also be accessed at any time with an internet connection by using an internet browser without requiring specific software installation [13].

Appsheet is an application that provides a no-code development platform for application software, that allows users without coding experience to create mobile, tablet, and web applications using data sources like Google Drive, DropBox, Office 365, and other cloud-based spreadsheet and database platforms [14].

A few studies have been conducted on a real business operation in which the mobile application was developed in order to smooth the operation and minimize risk. A pediatric clinic in Colombo South Teaching Hospital, Sri Lanka has successfully used an electronic database management system (E-DBMS) which was developed using Google AppSheet and Google Sheets [15]. This application (Google Sheets and Appsheets) has also been used by a lecturer at Politeknik Sultan Mizan Zainal Abidin to develop an application for their student coursework marking system. From the study, it was highlighted that developing the application for mobile devices by using Google Appsheets is easily understandable even though the system developer does not have a computer programming background and is able to produce effective outcomes that meet the objective [6]. In Sri Lanka, AppSheet is used to create a clinical database, and it has proven to be a cost-free, user-friendly solution to digitization [16].

One study conducted on application development for yoga activities also used the Appsheets for mobile user interaction, and it was proven successful [17]. Besides using a function of medium for input data, Appsheets has also been

applied for rendering information from Google Sheets documents that enable data to be visualized and referred to [18]-[19]. Various sectors have proven that Google Sheet, partnered with Google Appsheet, is able to manage data collection and storage, such as in the fields of education, hospitals, and health, as well as COVID-19 data [15]-[20].

Data that is captured by the mobile application (Google Appsheet) is saved in a Google Sheet, which is ready for further analysis and on the right platform to be visualized using visual management tools [21]. This will finally digitize a part of the warehouse operation that is able to add value to the company's business, which includes improving productivity, seamless electronic communication, a dashboard, and real-time inventory [22].

Successful implementation of a mobile application in various sectors as described above, shows that the combination of Google Sheets and Google Appsheet is able to deliver a good outcome to the user, which helps in improving work efficiency. It will help in transforming manual data operations into digital ones by having a database system that uses a mobile device as a medium for data collection.

Methodology

This section will discuss the method used in conducting this study, which is generally described in terms of process flow as per Figure 4.

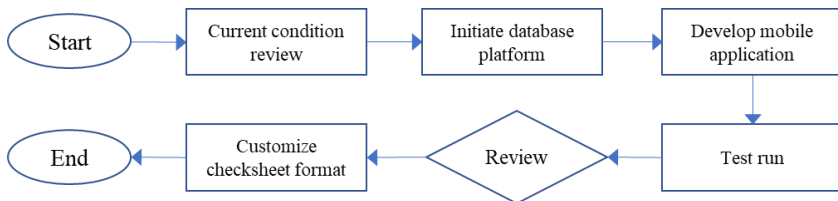


Figure 4: General process flow of conducting the study

The current practice of the PSB warehouse operation activities is reviewed to understand the flow, method, and documentation involved in managing order processing. This is basically to identify the type, source, and flow of the data for the ordering process from receiving information until delivery. Then, a database is created where all the manual data is digitized in a specific data format. A mobile application is then developed for a medium of data entry which requires a test run and fine-tuning to make it function. Finally, customization is made to the data format to initiate the customer checksheet and replace the manual format.

The development of the order processing system was divided into three phases, which are data preparation, developing mobile applications, and report customization as shown in Figure 5.

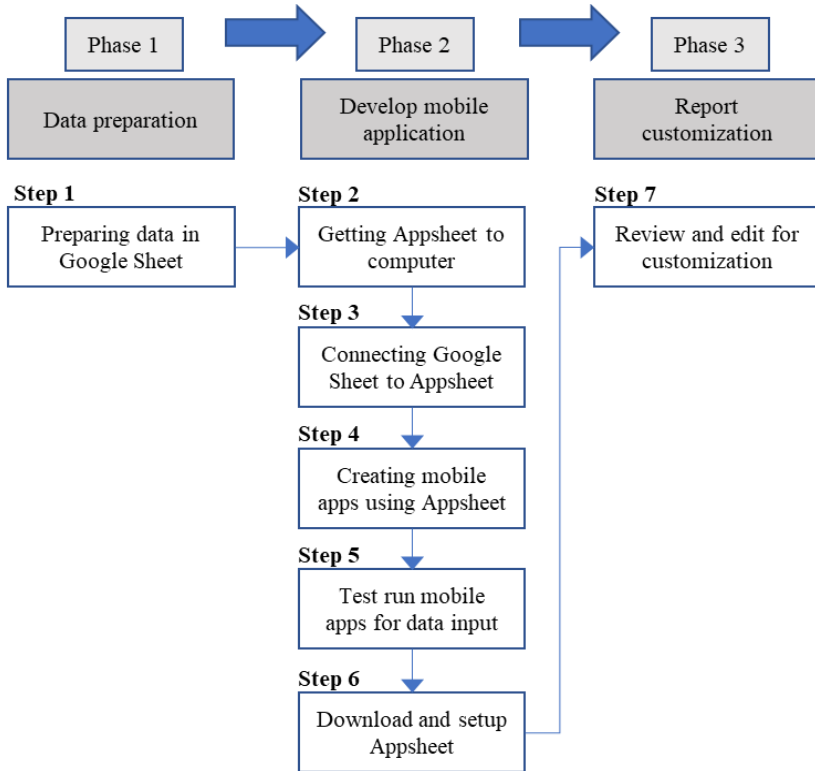


Figure 5: Development flow of order processing system

Phase 1 starts with the digitization of existing formats on manual paper into Google Sheets which requires format creation, utilizing the built-in formulation and file linkage. Phase 2 involves the development of a mobile application that will become the user interface to the database in Google Sheets. Finally, Phase 3 focuses on customization of the Google Sheets format and data reporting format which replace manual checksheets in the delivery operation activities.

Step 1: Preparing data table in Google Sheet

Google Sheets is used as a cloud database where all the data captured by the system is stored, analyzed, and integrated to produce outcome results. Besides, it also became a platform to develop a mobile application in Step 2. Storing data

into a file in Google Sheets is secure since the accessibility can be set by a specific user account with the access function of viewer, commenter, or editor. Even with editor accessibility, the file owner can still protect a certain cell or area of the Google Sheet from any data editing or manipulation.

Step 2: Getting Appsheet to computer

Google Appsheet is used to create mobile applications while working on a computer. It can be started directly from the Appsheet website without having to download or install anything. The software is launched by signing into the Appsheet account via <https://about.appsheet.com/home> from a supporting browser.

Step 3: Connecting data from Google Sheets to AppSheet

Appsheet is generating an application from the Google Sheet source, so it is required to be connected. To do this, the Google Sheet that was initiated in step 1 was selected as a file to be connected with the Appsheet by clicking the “create” menu and selecting “start with existing data”. The selected file is then used by the Appsheet to generate the application.

Step 4: Customizing the Appsheet to create mobile apps

The actual mobile interface is displayed in the right-hand section of the Appsheet page, and this can be altered to suit the needs of the user. When creating mobile apps, some basic customization can be used, such as file renaming, which will eventually become the name of the application, choosing items to appear, designing the application view, and fixing a logo. The Appsheet edit page's menu on the left side can be used to start customizing, which enables users to design the application interface in a way that best suits their needs. Users can choose how data is displayed by sorting the viewed item, grouping, and header sequence in a deck, table, dashboard, or card.

Step 5: Test run input Appsheet to Google Sheet table

In order to ensure input data using the Appsheet from a mobile phone or tablet is workable and applicable for the user, a test run has been conducted using the Appsheet from a computer. Data is added using the “+” icon so the input interface appears for data entry. To confirm data capture from the Appsheet, actual data sources in the Google Sheet were checked by opening the file that is used for Appsheet reference.

Step 6: Download and setup AppSheet

The Google Appsheet is compatible with the operating systems of mobile phones and tablets, which can be downloaded from the Google Play Store for Android and the App Store for Apple devices. It is free to download and requires setting up after installation. Users have to sign in with the same account with

which they logged in previously in Step 2, and then, to start the application, the saved Appsheet file needs to be selected from the menu option. The same interface that was initiated during setup on the computer will appear on mobile phones or tablets after and this will make the installed application ready to be used.

Step 7: Review and edit for customization

The steps in Step 5 above were repeated by using the Appsheet application on the mobile device to ensure data captured from the devices was able to sync with the Google Sheet file. Some customization can be applied in order to make the mobile application more user-friendly, such as fixing the selection input, using barcode or QR code scanning, and determining a pre-set value.

Fix selection input from the list

Entering fixed data input can be done by selecting from a list that can be set in the Appsheet. The list of items to be selected can be set in the Google Sheet file by inserting a row before the data and placing a list of fixed items for selection. Then, the editing needs to be done in the Appsheet from a computer wherein the column tab, the desired item can be selected by changing the type from pre-set value to “Enum” as shown in Figure 6. After completing and saving the changes, this function can be tested by running the application from the installed mobile device.

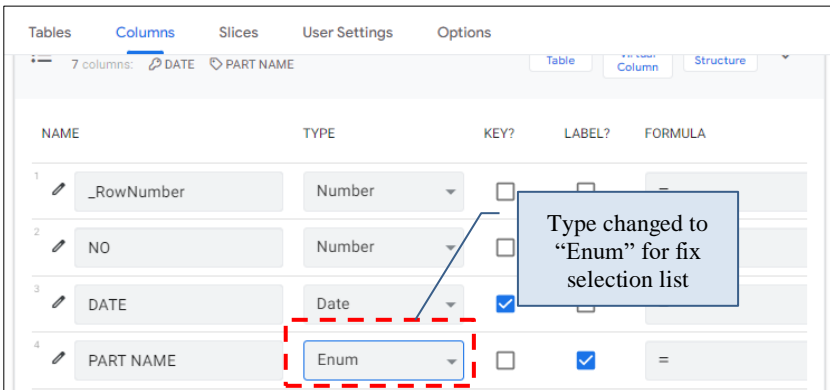


Figure 6: Assigning type to select from the list

Applying the function of scan barcode using the device camera

Input that is provided with a barcode or QR code can be scanned for data by Appsheet using the device camera. This is done by activating the “scan?” function in the desired item name as shown in Figure 7.

DISPLAY NAME	DESCRIPTION	SEARCH?	SCAN?
<input type="text"/>	<input type="text"/>	<input type="checkbox"/>	<input checked="" type="checkbox"/>

Figure 7: Selection to activate the scanning function for the item

This function activates when the QR code icon is pressed, which triggers the device camera to be used for QR code or barcode scanning. Information from the scanned code will be automatically filled in the column, which will help to ease the data entry.

Pre-set value of input

Input values that are fixed and can be set by default are able to be set themselves by the Appsheet function. In this application's development, input for the date has been set to the current date by changing the type to "DateTime" in the row for date input.

Results and Discussions

A complete system of order processing has been successfully developed for PSB and managed to fulfill the PSB management expectation of running the order processing activities at the warehouse digitally. Compared with the current method of operating the order processing system, this system has totally eliminated the manual practice by using a log book as a record and replacing it with a digital sheet. Orders received from customers are captured directly using mobile devices through the application developed as shown in Figure 8.

Data about ordering items and actual delivery that are captured from mobile devices is stored in a Google Sheets database. By using the built-in function in Google Sheets, data has been arranged to create a specific format that meets the customer's request for a delivery checksheet. The activity of copying data from a log book into a blank check sheet that was previously conducted prior to delivery is now eliminated. Figure 9 shows a manual recording checksheet that was prepared by copying information from the log book. The total quantity of the delivery item was calculated and summarized manually and this exposed it to the risk of wrong data.

The data is retrieved directly from the database (Google Sheets), which reduces the risk of error while establishing the delivery record for the customer by doing away with manual calculation and data copying. This will cut down on some of the processing time in the ordering operations, which helps reduce operating time since records won't need to be filled out manually. Figure 10

PYROCELL SDN BHD				TO APM					
OUTGOING DELIVERY CHECK SHEET				CUSTOMER : APM					
DATE 22-May-2023									
PO NUMBER	P20008469			P20009830			P20009830		
PART NUMBER	D93L-TR510BL02 (STD BOL)			D51A, TR136BL01 (4% WAX), W=1.55M			D51A, TR136BL01 (4% WAX), W=1.55M		
ITEM CODE	MT1857BK157F			MT1888BK194F			MT1888BK194F		
TOTAL ORDER	50			500			500		
SHIP NO	Ss#1			Ss#04			Ss#04		
ROLL #	Roll No	Batch No	Length (m)	Roll No	Batch No	Length (m)	Roll No	Batch No	Length (m)
1)	124	371062-0	59.80	63	373502-0	38.00	85	374115-0	35.60
2)				12	373436-0	37.60	7	373435-0	38.00
3)				27	373437-0	36.00	86	374115-0	36.00
4)				146	374174-0	30.00	81	374114-0	36.00
5)				66	373502-0	36.00	87	374115-0	38.60
6)				153	374175-0	38.00	80	374114-0	39.00

Figure 10: Delivery format from the mobile apps input

The system that allows data to be transferred and stored in real-time has reduced the total lead time for order processing. Users are able to work concurrently without being required to wait until the previous part is complete to start on the next part. The flow of ordering process activities, which is depicted in Figure 2 is used to benchmark the manual method (before condition) versus the implementation of the order processing system (after condition). Table 2 shows the comparison of time spent conducting an order processing. Compared with the previous manual method, there were six steps eliminated, which are Steps 3, 4, and 6. When the person who received the order entered the information in Step 2, the picker at the warehouse also received the order information from the second device and immediately started shopping for the item at the warehouse, which is what Step 5 is about.

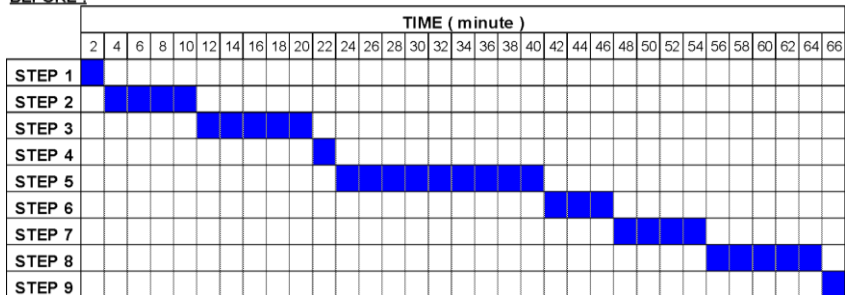
The use of the internet for real-time data transfers has eliminated the two previous steps (Steps 3 and 4). The data that is updated in Google Sheets in real time is able to be seen by the office staff for item part confirmation and printed as a check sheet, which eliminates Step 6. Step 7 starts concurrently with Step 5, so the completion time has improved. A comparison of the time taken for conducting the order processing using the manual method and the digital method is shown in Figure 11.

Referring to Figure 11, the completion time with the manual method was recorded at 66 minutes, while with the order processing system, it was reduced to 36 minutes, for a total reduction of 45% in processing time. Besides the processing time that has been reduced with the help of a new method (the order processing system), the activities that run concurrently also contributed to this reduction as per Steps 5 and 7 in Table 2.

Table 2: Comparison of operation time before and after conditions

Step	Details	Before (min)	After (min)	Description
Step 1	Receive delivery info	2	2	
Step 2	Write info to into log book	7	4	Manual write to digital
Step 3	Checking and identify items at warehouse	10	0	Combine with Step 5
Step 4	Pass copy of log book to store picker	3	0	Combine with Step 5
Step 5	Shopping part and prepare for delivery	18	16	Concurrent with Step 2
Step 6	Copy information from log book to delivery checksheet	6	0	Print from digital data
Step 7	Pass checksheet to office	8	2	Concurrent with Step 5
Step 8	Part loading to lorry	10	10	
Step 9	Pass document and delivery	2	2	
Total		66	36	

BEFORE :



AFTER :

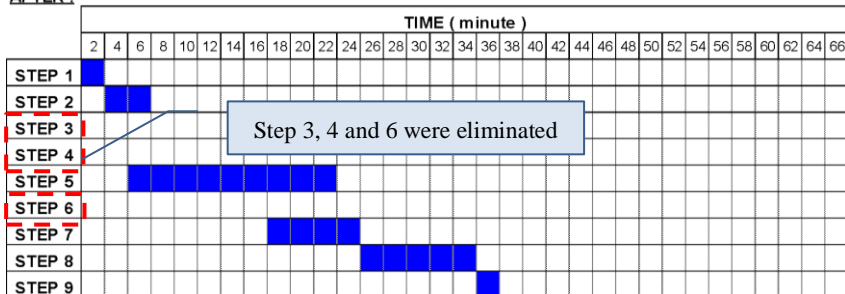


Figure 11: Comparison before and after of handling order processing

With the simple interface of the mobile device by Appsheet, users were able to key in the info into a specified box with some input data that can be captured by the function of camera scanning. This will help in avoiding the error of copying information from Kanban as per risk 1. Besides, the pre-set date value that has been set during customization of mobile application development helps in determining the actual date of the activities conducted.

The same information will be viewed by the picker, which is responsible for selecting the right part by referring to the Appsheet summary. With clear information written digitally, the risk of error in reading the order information can be avoided. Dealing with the device is also much more convenient compared with bringing a pen and book to the site to write information. As a result, the risk of making a mistake with the item is reduced.

The delivery information that has been captured from the mobile device through the AppSheet was able to be seen in the summary view. Figure 12 shows a view of the application on mobile devices, where it was grouped by the order date with a total quantity for the particular date. Each of the ordered items is listed with the quantity and it can be scrolled down to see the whole list.

Date	Total
7/26/2022	2,105.00
TR089 GY01 1.3T 3020...	48.41
TRIP 2	
TR089 3T BLK 3020-38...	48.54
TRIP 2	
TE020 BL02 5T 3020-3...	48.86
TRIP 2	
TE020 BL02 5T 3020-3...	50.78
TRIP 2	
PINK FOAM 5T+40D 30...	
TRIP 2	

Figure 12: Example of Appsheet view after grouping

The selection of the Google application in this system development was found suitable for capturing data, using it as a database platform, and as a mobile application. The Google account that was created for free has sufficient drive space for data storage. A database that uses Google Sheets has come out and offers sufficient features for free. It was easy to use even for newcomers. The use of AppSheet in developing the mobile application was found to be applicable to meeting the purpose of having a medium for data entry with the function of reviewing and editing the data. With no cost for prototype application development and a reasonable subscription price for application

deployment, Appsheet is the best choice for the SME warehouse factory to get into the system and expose itself to the IoT.

Conclusion

A simple, self-developed, and effective system for managing a customer order in an automotive supply chain was successfully established by using Google Sheets and Google Appsheet. Users have gained a significant benefit from the implementation of this system. Redundant manual recording of delivery data, which is exposed to a risk of error has been totally eliminated with the use of mobile applications. Real-time data updates into the Google Sheets have allowed multi-users to work on the same page of data, and this makes a flow of tasks that can be performed concurrently possible. Thus, the total lead time for ordering process activities can be reduced significantly. Exposure to digitization has given the associates of PSB Sdn. Bhd. the opportunity to gain knowledge, especially in the IoT, and this will enhance the adaptation of the IoT towards achieving the National Fourth Industrial Revolution (4IR) Policy.

Contributions of Authors

The authors confirm that each part of this work has been equally distributed, and the final version of this paper has been reviewed and agreed upon by all the authors.

Funding

This work received no specific grant from any funding agency.

Conflict of Interests

All authors declare that they have no conflicts of interest

Acknowledgement

The author would like to thank the management and associates of PSB Sdn Bhd for the resource, facilities, and support during the study is carried out.

References

- [1] M. H. Widiyanto, B. Sanjaya, V. Aurellia, and S. A. Chrysanthia, "Implementation Mobile Smart Farming Monitoring System With Low-Cost Platform Using Blynk", *Journal of Theoretical and Applied Information Technology*, vol 100, no. 9, pp. 2723-2745, 2022. <http://www.jatit.org/volumes/Vol100No9/4Vol100No9.pdf>
- [2] V. Rajan, N. V. Sobhana and R. Jayakrishnan, "Machine Fault Diagnostics and Condition Monitoring Using Augmented Reality and IoT", *Second International Conference on Intelligent Computing and Control Systems (ICICCS)*, pp. 910-914, 2018. <https://doi.org/10.1109/ICCONS.2018.8663135>.
- [3] M. Almani, O. Oleghe, M. Afy-Shararah, and K. Salonitis, "Implementing Pull Manufacturing in Make-To-Order Environments", *Advances in Transdisciplinary Engineering*, pp. 334-341, 2022. <https://doi.org/10.3233/atde220613>.
- [4] D. Aurino, S. Tri, and A. Novita, "Process Analysis on Order Processing Function to Reduce Order Processing Time", *Indonesian Context. International Journal of Research in Management & Technology*. vol 6, no. 3, pp. 1-13, 2016. <https://www.researchgate.net/publication/305617866>
- [5] S. Ksenija, A. Milan, and P. Vukašin, "Warehousing Process Optimization In Elite Anywhere Corp. Using Lean Philosophy", *Proceedings of The First International Conference Good practice in Road Traffic and Transport At: Belgrade*, pp. 90-97, May 2022. <https://www.researchgate.net/publication/360588542>
- [6] M. Dina, R. Widya, S. Bhumyamka, and D. Bambang. "Warehouse Management System for Smart Digital Order Picking Systems", *International Journal of New Media Technology*, vol 6, pp. 74-80, 2020. <https://doi.org/10.31937/ijnmt.v6i2.1215>.
- [7] Milan Andrejić, "Value Stream Mapping In Ordering Process -A Case Of Retail Chain", *International Journal for Traffic and Transport Engineering*, vol. 11, no. 4, pp. 488-506, 2021. [https://doi.org/10.7708/ijtte2021.11\(4\).01](https://doi.org/10.7708/ijtte2021.11(4).01)
- [8] Natesan Andiyappillai, "Digital Transformation in Warehouse Management Systems (WMS) Implementations", *International Journal of Computer Applications*, vol. 177, no. 45, pp. 0975 – 8887, 2020. <https://doi.org/10.5120/ijca2020919957>
- [9] B. Suleiman, and W. Santosh, "Implementation of Digital Approach in Warehouse Management in Oman Oil Companies", *The First International Conference on Environmental Sciences and Engineering for Sustainable Development*, 2022. [Online]. Available: <https://www.researchgate.net/publication/359669061>

- [10] Abushaikha, Ismail, Salhieh, Loay and Towers, "Improving distribution and business performance through lean warehousing", *International Journal of Retail and Distribution Management*, vol. 46, no. 8, pp. 780-800, 2018. <https://doi.org/10.1108/IJRDM-03-2018-0059>
- [11] A. Wongjak and S. Chansamorn, "Mobile Warehouse Management and Transportation Planning System for Wheat Flour", *2021 Research, Invention, and Innovation Congress: Innovation Electricals and Electronics*, pp. 293-297, 2021. <https://doi.org/10.1109/RI2C51727.2021.9559747>.
- [12] Mkansi, M., de Leeuw, S. and Amosun, O, "Mobile application supported urban-township e-grocery distribution", *International Journal of Physical Distribution & Logistics Management*, vol. 50, no. 1, pp. 26-53, 2020. <https://doi-org.ezaccess.library.uitm.edu.my/10.1108/IJPDLM-10-2018-0358>
- [13] F. Mohd and A. B. Mohd Khairulazman, "Penggunaan Google Sheet Dan Appsheets Dalam Proses Membangunkan App Pengiraan Markah Penilaian Kerja Kursus", *e-Proceedings of the Green Technology & Engineering 2020*, pp. 88-97, 2020. [Online]. Available: <https://www.researchgate.net/publication/346017168>
- [14] "Google AppSheet | Build apps with no code", AppSheet. [Online]. Available: <https://about.appsheet.com/home/> (Accessed Nov 2, 2022).
- [15] Wijesekara, D.S., Peiris, P.L.S., Fernando, D.S., Palliyaguru, T.D.N. and Fonseka, W.A.D.N., "Developing an electronic record keeping system at a paediatric clinic in Colombo South Teaching Hospital, Sri Lanka", *Sri Lanka Journal of Child Health*, vol. 49, no. 2, pp. 116–124, 2020. <http://doi.org/10.4038/sljch.v49i2.8958>
- [16] J. Malaka, N. Malith, de Silva, G P U P, and P. Aloka, "Creation of a multiaccess database for hepatopancreaticobiliary surgery using open-source technology in a country that lacks electronic clinical database management systems", *Annals of Hepato-Biliary-Pancreatic Surgery*. vol. 25, no. 1, pp. S403-S403, 2021. <https://doi.org/10.14701/ahbps.EP-206>.
- [17] R. Maša, N. Valentina, and P. Nenad, "Adopting AR and Deep Learning for Gamified Fitness Mobile Apps: Yoga Trainer Case Study", *11th International Conference on Applied Information and Internet Technologies*, pp. 167-171, 2021. [Online]. Available: <https://www.researchgate.net/publication/355297698>
- [18] N. Petrovic, V. Roblek, M. Khokhobaia, and I. Gagnidze, "AR-Enabled Mobile Apps to Support Post COVID-19 Tourism", *2021 15th International Conference on Advanced Technologies, Systems and Services in Telecommunications*, 2021, <https://doi.org/10.1109/telsiks52058.2021.9606335>.

- [19] Nenad N. Petrović, “Data-Driven Solutions in Smart Cities: The case of Covid-19”, *Companion Proceedings of the Web Conference*, pp. 648–656, 2021. <https://doi.org/10.1145/3442442.3453469>
- [20] J. Banusing, C. Jason, and P. John, “Arijo: Location-Specific Data Crowdsourcing Web Application as a Curriculum Supplement”, *International Journal of Advanced Computer Science and Applications*, vol. 9, no. 2, pp. 133-141, 2018. <https://doi.org/10.14569/ijacsa.2018.090219>.
- [21] L. P. Steenkamp, D. Hagedorn-Hansen, and G. A. Oosthuizen, “Visual Management System to Manage Manufacturing Resources”, *Procedia Manufacturing*, vol. 8, pp. 455–462, 2017. <https://doi.org/10.1016/j.promfg.2017.02.058>.
- [22] N. Andiyappillai, “Digital Transformation in Warehouse Management Systems (WMS) Implementations”, *International Journal of Computer Applications*, vol. 177, no. 45, pp. 34–37, 2020, <https://doi.org/10.5120/ijca2020919957>.

Dynamic Behaviour of Flow Through Three Circular Cylinders in Staggered Arrangement with Three Disturbance Bodies Around the Upstream Cylinder

Banta Cut, Sutardi*, Wawan Aries Widodo
Department of Mechanical Engineering,
Faculty of Industrial Technology and Systems Engineering,
Institut Teknologi Sepuluh Nopember, Jl. Arief Rahman Hakim,
Sukolilo, Surabaya 60111, INDONESIA
*sutardi@me.its.ac.id

ABSTRACT

Studies on flow through cylinders have been widely carried out, both experimentally and numerically. The purpose of those studies is to obtain information about flow phenomena around the cylinder arrangement, such as aerodynamic forces, vortex shedding, and vortex-induced vibration. This study aims to evaluate the flow characteristics that pass through three circular cylinders arranged in a stagger and reduce the drag force (C_D) by adding 3 disturbance bodies (DB) around the upstream cylinder. The longitudinal distance L/D varies from 1.5 to 4.0, while the transversal distance T/D is kept constant. Next, the diameter ratio d/D is set to 0.16. The diameter of cylinder 1, $D=25$ mm, and the diameter of the DB, $d=4$ mm. The DB is placed around cylinder 1 at three angle locations with a gap, $\delta=4$ mm. The study is performed using Ansys fluent® 19.1 software in 2-D unsteady RANS with the transition $k\text{-}\kappa\text{-}\omega$ turbulence model. The flow Reynolds number based on D is 22×10^4 . The results showed that the L/D and the use of DB affect the cylinder drag coefficient (C_D). There is a C_D reduction for cylinder 1 up to 20% at $L/D=3.0$. For cylinders 2 and 3, the reduction in C_D occurred at $L/D=4.0$ up to approximately 13% and 17%, respectively.

Keywords: Cylinder Arrangement; Disturbance Body; Transition K-Kl-Omega; Drag Coefficient

Nomenclature

U	free stream velocity of the fluid (m/s)	
V_{max}	maximum velocity of fluid (m/s)	
D	diameter of the main cylinder (m)	
d	diameter of disturbance body (m)	
T/D	non-dimensional transversal distance	
L/D	non-dimensional longitudinal distance	
Re	Reynolds number	
P/D	pitch ratio	
G/D	non-dimensional distance of the gap between the main circular cylinder and the disturbance body	
DB	disturbance body	
θ	position angle of DB	
VIV	vortex-induced vibration	
ρ	the density of fluid (kg/m ³)	
IDB	inlet disturbance body	
FVM	finite volume method	
Nu	Nusselt number	
MRT	multiple relaxation time	
δ	distance between cylinder 1 and DB (m)	
WIV	wake-induced vibration	
LBM	lattice Boltzmann method	
μ	absolute viscosity of the fluid (Pa.s)	
u_i, v_j	velocity component in the i th or j th direction (m/s)	
t	time (s)	
p	pressure (Pa)	
C_D	drag coefficient	$C_D = \frac{F_D}{1/2 \rho V^2 A}$
$C_{D'}$	drag coefficient fluctuation	
C_L	lift coefficient	$C_L = \frac{F_L}{1/2 \rho V^2 A}$
$C_{L'}$	lift coefficient fluctuation	
t	time step (s)	
Ri	Richardson number	
St	Strouhal number	
f	frequency (Hz)	
PSD	power spectral density	

Introduction

The use of circular cylinders in engineering with various configurations such as in-line, tandem, side-by-side, staggered, and square arrays, has been widely used. This application creates an interaction between the fluid flow and the bluff body arrangement resulting in drag and lift forces on the bluff body. Modifications to various configurations of the bluff body arrangement or constructions are intended to reduce drag force, thus reducing the overall load, and the constructions will last longer. Efforts to reduce the drag have inspired the authors to conduct further research on the flow passes through three circular cylinders in a staggered arrangement with L/D variations and the use of a Disturbance Body (DB).

The research on flow through a single-cylinder [1] shows that the interaction between the fluid flow and the bluff body is strongly influenced by the free-stream velocity, the specimen's shape, and the surface roughness. These variables will determine the magnitude of the drag force. The effect of the Reynolds number on the flow through a circular cylinder concluded that the greater the Reynolds number, the more turbulent the flow that results in the separation point being delayed [2]. Another study explains that turbulent flow can overcome the adverse pressure gradient effect and reduce wake area and drag [3]. The addition of DB in front of a single cylinder has also been investigated experimentally [4] as well as numerically [5]. The last two studies showed that there is drag reduction on the circular cylinder and the system.

Similar research shows that there is more significant influence of Reynolds number (Re) compared to the influence of d/D and L/D on the decrease in pressure drag [6]-[7]. Circular cylinders in tandem arrangement situated in a narrow channel with variations of L/D and Re also greatly affect the decrease in pressure and drag [8]. The use of two cylindrical DB in front of the upstream cylinder [9]-[11], is very effective in reducing the drag that occurs in the main circular cylinder. The fluid flow through two circular cylinders in various arrangements with variations of Re and P/D indicates that the flow characteristics are very similar to that of the flow through a single cylinder [12].

Flow through two circular cylinders in tandem and staggered arrangement, both elastically or permanently installed has been studied [13]-[14]. It shows that the downstream cylinder is affected by the presence of Wave-Induced Vibration (WIV), and the effect is very sensitive to differences in the distance (L/D). The study of two cylinders in staggered arrangement placed in a planar shear flow has also been studied [14]. Two different distances were used in that study, namely $P/D=1.125$ and 1.250 , and were set at shear parameters K of 0.00 and 0.05 . At a condition of no shear flow which is referred to as uniform flow, the flow behaviour around the two cylinders behaves as a single cylinder. Similar research [15]-[16], indicates that the peak of the vortex shedding is weaker and more swirling near the base of the

cylinder. At short and medium distances, there has been a change in the Strouhal number followed by a change in the flow pattern. Other research with similar methods has also been carried out, namely numerical simulation using the LES method. The result shows that the inner lift force occurs at a distance $P/D=1.5 - 3.0$ and angle= 10° because the existence of the flow passes through the narrow gap between the cylinders [17]. The lift force on the outer side occurs at a distance of $P/D=3 - 4$ and angle= 20° , due to the interaction between the vortices that are released from the upstream cylinder and re-attaches to the downstream cylinder. Experimental test of flow passing through two circular cylinders arranged side by side, tandem, and staggered has also been studied [18]. The result shows that at low flow velocity $U^* < 7$, the vibration can be damped, while at higher flow velocity $U^* \geq 7$, the oscillation increases. In addition, in the tandem arrangement, the vibration is smaller [18].

The flow passes through three circular cylinders [19]-[20] in an equilateral triangle arrangement, showing that the drag reduction for the upstream cylinder is found at an angle, $\alpha=10^\circ$. For the upper downstream cylinder, it occurs at an angle of 25° , and for the lower downstream cylinder, it occurs at an angle of $\alpha=20^\circ$ [19]. The smallest drag coefficient occurs at distances $(N/d)=1.7$ and 2.2 [20]. The use of IDB in front of the upstream cylinder [21] with L/D variations can reduce the drag for the upstream cylinder and also significantly affects the distribution of C_p and the velocity profile behind three circular cylinders in a staggered arrangement. Similar studies have also been carried out using multiple relaxation time (MRT) based lattice Boltzmann method (LBM) [22]-[23]. The results of these studies show that the staggered arrangement has a significant effect on the wake structure, force fluctuations, and vortex shedding. Flow through three circular cylinders with varying turning angle $\beta=0^\circ, 30^\circ$, and 60° shows that the upstream cylinder greatly affects the downstream cylinder, and the drag coefficient decreases as the velocity decrease [24]. Yang et al. [25] showed that P/d and turning angle affect significantly the flow passes three equilateral circular cylinders arrangement. Simulation studies of the flow through three circular cylinders in tandem, side by side, and staggered arrangement using the Boltzmann boundary-lattice method indicate various flow patterns that influence the vortex shedding structures and flow properties [26]. The average shift position and hydrodynamic forces of two circular cylinders arranged side by side located behind a stationary upstream cylinder are significantly influenced by the upstream cylinder wake and the wake-vortex interaction of the upstream cylinder [27].

Numerical simulation using the 2-D finite volume method for three circular cylinders in a triangular arrangement has also been carried out [28]. The variations in L/D , the orientation angle (0° and 180°), and the flow Reynolds number ($Re=100$ and 200) were used in the study. At $Re=100$, the flow behind the downstream cylinder is monostable (similar to a single cylinder), while at $Re=200$, the bias flow phenomenon disappears. The study

shows that the combination effects of the flow Reynolds number and the distance L/D significantly influence the biased-flow pattern of the wake behind the cylinder arrangement. A study of flow through square cylinders in staggered arrangement [29] shows that the flow is periodic and organized and that there are flow disturbances over a large distance ratio. However, when the distance ratio decreases, the flow becomes more turbulent due to the influence of the larger flow disturbance. The same study with variations of Reynolds number and transversal distance (S_T/D) and longitudinal distance (S_L/D), shows that the ratio of distance and Re affect significantly the flow and wake formed behind the bluff body arrangement [30]-[31]. The effects of distance (S_T/D) and (S_L/D) on C_D and Nu change significantly with changes in the value of Ri [31].

Based on the previous studies, we performed a numerical simulation study of the flow through three circular cylinders in the staggered arrangement by adding three DB around the upstream cylinder. The staggered arrangement of the cylinders is set so that varying in longitudinal distance L/D and are constant in transversal distance T/D . This numerical simulation was performed using the k- κ - ω transition turbulence model and was analysed at $Re=2.2 \times 10^4$. The distribution of C_p , distribution of C_D , distribution of C_L , and Strouhal number are presented and analysed in this study.

Numerical Methods

Basic equations and numerical simulation domain

The basic equations, which include the continuity equation and the momentum equation, can be written as shown in Equation (1) and Equation (2), respectively:

$$\frac{\partial v_i}{\partial x_i} = 0 \quad (1)$$

$$\rho \frac{\partial v_i}{\partial t} + \rho v_j \frac{\partial v_i}{\partial x_j} + \frac{\partial P}{\partial x_i} - \mu \nabla^2 v_i = 0, \quad (2)$$

where v_i , ρ , t , μ , and P represent the components, namely velocity, density, time, absolute or dynamic fluid viscosity, and pressure, respectively. Figure 1 shows the numerical simulation domain for three circular cylinders arranged in a staggered configuration with three DB 's around cylinder 1.

The numerical simulation domain and the meshing model used are quadrilateral-submap, as shown in Figures 2(a) and (b). Several parameters in determining variation can be seen in Table 1.

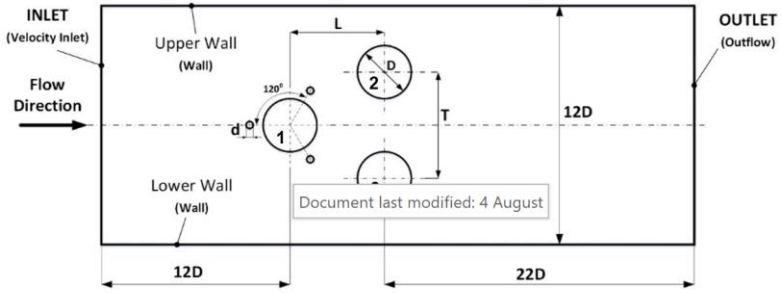


Figure 1: The numerical simulation domain and boundary conditions for three circular cylinders in a staggered arrangement with three DB's

Meshing solution and determination of boundary conditions

Meshing is made using Gambit 2.4.6 software. The type of meshing in this numerical simulation is a quadrilateral structured 2-D mesh, as shown in Figure 2. The boundary conditions in this study are shown in Table 2.

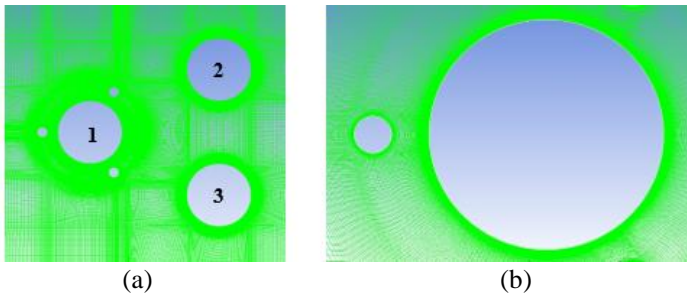


Figure 2: (a) Meshing of three circular cylinders in a staggered arrangement with three DB around cylinder 1, and (b) meshing cylinder 1 with DB (enlargement)

Table 1: Research parameters

Research parameters	
Reynolds number	2.2×10^4
The ratio of the distance between the centres of circular cylinders L/D and T/D	$L/D=1.5, 2.0, 3.0, \text{ and } 4.0$ $T/D=2.0$
Ratio of the diameter of disturbance body to the circular cylinder, d/D	0.16
The ratio of the gap between the DB and the circular cylinder to the circular cylinder diameter, δ/D	0.16

Processing

Physical phenomenon modelling

This numerical simulation was carried out using ANSYS Fluent® software version 19.1, with the modelling of physical phenomena including pressure-based solver, unsteady flow, and the transition $k\text{-}kl\text{-}\omega$ turbulence model [32]-[33]. This turbulence model was chosen for the flow with Re in the transition range [32]-[33]. The fluid is air at atmospheric pressure with an average temperature of 27 °C. The air density (ρ) and the absolute fluid viscosity (μ) are set to be 1.225 kg/m³ and 1,7894 x 10⁻⁵ kg/m.s, respectively.

Boundary conditions and solution method

In this study, the inlet velocity of the fluid is 14.1 m/s which corresponds with the flow with the Reynolds number of 2.2x10⁴. The inlet turbulence intensity and the hydraulic diameter are to be set at 0.04 and 300 mm, respectively. The solution method for the pressure-velocity coupling is set as SIMPLEC, while the spatial discretization for pressure, momentum, turbulent kinetic energy, and the specific dissipation rate is set to be the second order upwind to obtain good accuracy on the simulation results. The residual value is set on the order of 10⁻⁶, and the method used for initialization is the hybrid initialization method.

Table 2: Boundary conditions

Name	Type
Inlet	Velocity inlet
Outlet	Outflow
Upper wall	Wall
Lower wall	Wall
Circular cylinder	Wall
Disturbance body (DB)	Wall

To be able to capture the phenomenon of vortex shedding around and behind the bluff body arrangement, the iteration uses a small-time step size. The time step size value is based on the Strouhal number. For flow passes through a circular cylinder, the Strouhal number within a quite wide Reynolds number range is approximately 0.2 [34]. Then;

$$St = 0.2 = \frac{f x D}{U} . \quad (3)$$

Next, the time cycle and time step size are determined using Equation (4).

$$t = \frac{1}{f} \quad (4)$$

Post-processing

In the post-processing of the numerical simulation, a grid independence test is performed to evaluate the best meshing quality with the smallest error. The grid independence test is carried out using six types of meshing density, starting from a loose mesh (coarse), medium, fine, and very fine. The results of this test are then expressed in the form of Y^+ and drag coefficient (C_D) (Tables 3 and 4), and compared with the results of previous studies [20], [23]. This Y^+ result is very necessary to obtain the best meshing density with the smallest error, also to determine the shear stress near the wall more accurately, and thus the smallest errors C_D .

The results of numerical simulations for six types of meshing show that mesh D with a meshing density of 180,765, the average in Y^+ is 2.159 (see Table 3). This result is close to the results of mesh E and F, which are more tightly packed. Hence, for the need for running time efficiency, mesh D is used for the rest of this study. Evaluation of C_D (Table 4) shows that the smallest error of the six types of meshing is also for the mesh density of 180,765.

Table 3: Grid independence to Y^+

Number	Nodes	Y^+ Maximum	Y^+ Minimum	Y^+ Average
Mesh A	42,362	6.793	0.199	3.291
Mesh B	98,157	5.721	0.074	4.395
Mesh C	160,530	5.276	0.085	4.876
Mesh D	180,765	4.120	0.112	2.159
Mesh E	200,216	4.119	0.111	2.158
Mesh F	220,227	3.612	0.111	1.912

Table 4: Grid independence test of drag coefficient

Experiment [20]	Cyl. 1	Cyl. 2	Cyl. 3	Simulation [23]	Cyl. 1	Cyl. 2	Cyl. 3		
C_D	0.7	0.8	1.0	C_D	0.9	1.1	1.1		
Present study (Num)	C_D	Difference	C_D	Difference	C_D	Different			
Nodes	Cyl. 1	[20]	[23]	Cyl. 2	[20]	[23]	Cyl. 3	[20]	[23]
42,362	0.920	24%	2%	1.133	29%	3%	1.194	16%	8%
98,157	0.956	27%	6%	1.198	33%	8%	1.127	11%	2%
160,530	0.940	26%	4%	1.065	25%	-3%	1.152	13%	5%
180,765	0.919	24%	2%	1.089	27%	-1%	1.115	10%	1%
200,216	0.935	25%	4%	1.287	38%	15%	1.265	21%	13%
220,227	0.954	27%	6%	1.209	34%	9%	1.233	19%	11%

Results and Discussion

The results of the present study will be presented in the form of the distribution of C_p , C_D , and C_L . In addition, the velocity profiles and flow visualization results will also be presented and analysed. The C_D will be validated with experimental data [20] and numerical simulation results [23].

Distribution of C_p for three circular cylinders in a staggered arrangement with three disturbance bodies

The C_p distribution for the staggered arrangement of three circular cylinders with DB is shown in Figure 3. On cylinder 1 for all distances ($L/D=1.5, 2.0, 3.0,$ and 4.0), the average stagnation point occurs at $\theta=24^\circ$ (Table 5). Based on the present numerical results, the average location of the stagnation points, or more accurately the re-attachment points, of cylinder 1 do not change significantly with the presence of DB. Aside from the flow separation points from the cylinder shifted slightly backward resulting in a narrowing of the wake area. Up to this stage, however, we have not yet discussed the shift of the temporal stagnation and separation points. Furthermore, the flow interacts with the bluff body of cylinder 1 and experiences acceleration because the flow passes through a narrow space (Figure 4). This acceleration causes a decrease in C_p drastically to values of $-1.6, -0.75,$ and -1.65 for $L/D=1.5, 2.0,$ and 3.0 , respectively. For $L/D=4.0$, the C_p is minimum ($C_{p_{min}} = -1.67$). The values of $C_{p_{min}}$ for cylinder 1 for all distances (L/D) are almost the same (within $\sim 4\%$), except for $L/D=1.5$. At a distance of $L/D=1.5$, some researchers called it a close distance between the upstream cylinder and the downstream cylinder, which is known as the bistable effect (Figure 3(a)). The separated flow from cylinder 1 and its impingement on cylinders 2 and 3 will have a significant effect on the wake of cylinder 1. Hence, the presence of the disturbance body (DB) on the main cylinder along with the attendance of the downstream cylinders affects the asymmetrical flow at the upper and lower sides. (Figures 4(a) and 5(a))

For cylinder 2 and cylinder 3, the distribution of C_p is symmetric, where the distribution of C_p on the upper side of cylinder 2 is similar to the distribution of C_p on the lower side of cylinder 3, and vice versa. Next, the distribution of C_p on the lower side of cylinder 2 resembles the distribution of C_p on the upper side of cylinder 3. However, the distribution of C_p in cylinder 2 and cylinder 3 is very fluctuating, where the maximum C_p occurs at different angles. At $L/D=2$ the maximum C_p occurs at an angle $=4^\circ$ for cylinder 2 and an angle $=353^\circ$ for cylinder 3. For $L/D=1.5$ and 3.0 , the maximum C_p for cylinder 2 occurs at $\theta=4^\circ$, and for cylinder 3 is at $\theta=356^\circ$ with the maximum C_p being 1.0 . At $L/D=4$, however, the maximum C_p occurs at $\theta=12^\circ$ for cylinder 2 and at $\theta=348^\circ$ for cylinder 3. Figure 5 provides a detailed description of the flow velocity through a staggered arrangement of three circular cylinders with DB.

The phenomenon of bubble separation after the flow hits DB for all distances (L/D), can be seen in Figure 4. The flow that passes through the

narrow gap between DB at an angle of 0° with cylinder 1 and behind DB at $\theta = 120^\circ$ and 240° , causes the flow more turbulent and reattaches to the surface of cylinder 1 (Figure 5). The use of 3 DB at angles $=0^\circ, 120^\circ$, and 240° is intended to agitate the boundary layer development on the cylinder wall and delay the boundary layer separation from the cylinder wall. Figures 4 and 5 show a qualitative description of the location of the boundary separation due to the addition of interfering bodies. In addition, in Figure 5, the positions of stagnation and separation points have also been marked and have been included in Table 5. In Table 6, we show a comparison of the CD between this study and that of Yan et al. [23].

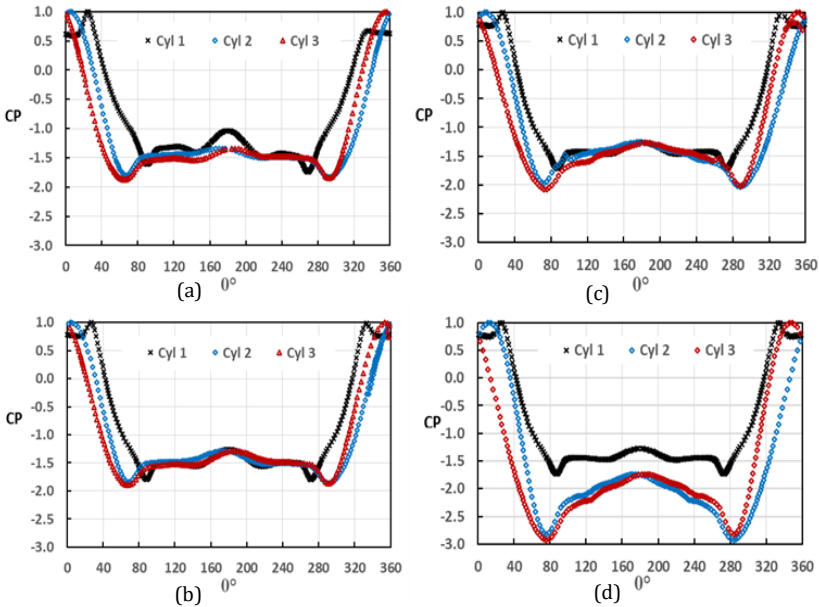


Figure 3: Distribution of C_p on three circular cylinders in staggered arrangement with three DB at angles of $0^\circ, 120^\circ$, and 240° , (a) $L/D=1.5$, (b) $L/D=2.0$, (c) $L/D=3.0$, and (d) $L/D=4.0$

Vortex shedding formation behind the cylinder arrangement is also strongly influenced by the flow disturbances separated from the DB. For example, for $L/D=2.0$ and 3.0 with a certain time step, the vortex on the upper side rotates clockwise, while the vortex on the lower side rotates counterclockwise. The vortex movement above cylinder 2 and below cylinder 3 has high turbulence intensity. This vortex interaction is conjectured to be responsible for the highly fluctuating lift (C_L) of the cylinder.

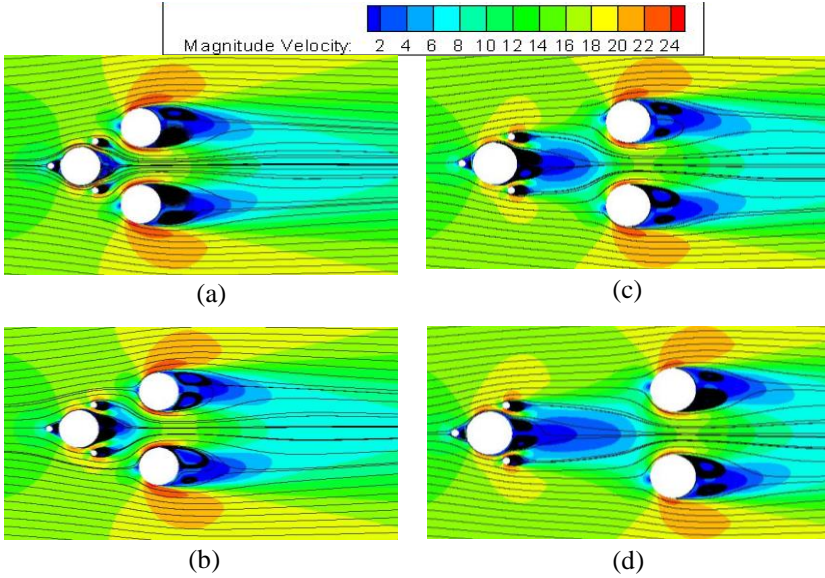


Figure 4: Visualization of velocity magnitude (m/s) on three circular cylinders in staggered arrangement with three DB at angles of 0°, 120°, and 240°; (a) $L/D=1.5$, (b) $L/D=2.0$, (c) $L/D=3.0$, and (d) $L/D=4.0$

Drag and lift coefficients

Figure 6 shows the distribution of C_D on all cylinders investigated in this study. The distribution of C_D of cylinder 1 for all values of L/D , is much smaller than the value of C_D of cylinders 2 and 3. This is because the use of DB around cylinder 1 has a significant effect on flow separation that occurs in cylinder 1. The separated flow from DB with high turbulence intensity interacts with the boundary layer on cylinder 1. The flow interaction results in the transition of the laminar boundary layer on cylinder 1 into the turbulent boundary layer. Therefore, this turbulent boundary layer can overcome the adverse pressure gradient effect on the cylinder surfaces and delay the boundary layer separation. This boundary layer separation delay causes the wake size behind the cylinder to become narrower resulting in C_D reduction on cylinder 1.

In general, the L/D has a significant effect on both C_D and C_L for all cylinders. As the distance increases, the character of C_D approaches as a single cylinder drags characteristics. On average, C_D on the cylinder 1 is lower than that of the C_D on cylinders 2 and 3. The low C_D on the first cylinder is probably due to the presence of the disturbance bodies. The C_D characteristics on cylinders 2 and 3 are almost similar since the positions of cylinders 2 and 3 relative to cylinder 1 are the same. The results of the present C_D compared with the previous experimental studies [20] are approximately within 6% and within approximately 6.5% with the numerical simulation results of [23].

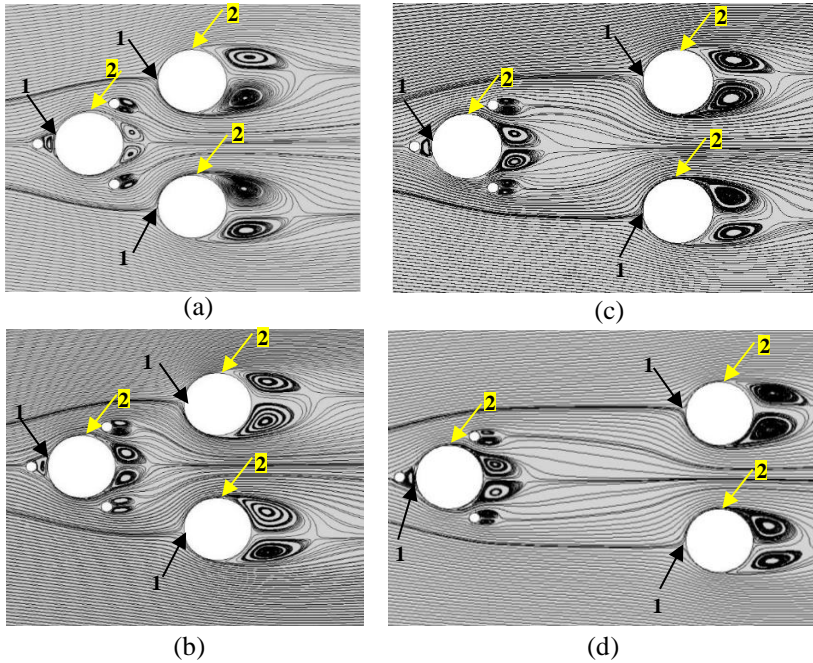


Figure 5: Velocity path line on three circular cylinders in staggered arrangement with 3 DB at angles of 0° , 120° , and 240° ; (a) $L/D=1.5$, (b) $L/D=2.0$, (c) $L/D=3.0$, and (d) $L/D=4.0$; 1=stagnation point; 2=separation point

Table 5: Stagnation and separation point

L/D	Position of stagnation and separation points (angle θ)					
	Cylinder 1		Cylinder 2		Cylinder 3	
	Stagnation	Separation: up, low	Stagnation	Separation: up; low	Stagnation	Separation: up; low
1.5	24	93; 262	5	85; 276	354	84; 264
2	27	96; 264	4	93; 275	353	89; 261
3	27	96; 265	7	92; 268	350	95; 265
4	341	133; 259	12	95; 262	348	92; 265

Lift characteristics for all three cylinders are also significantly affected by the distance L/D . As the distance increases up to $L/D=4.0$, this lift fluctuation is still clearly discerned. Next, the separated flow from cylinder 1 followed by the nozzle effect of the flow in the gap between cylinders 2 and 3 may have a significant effect on the cylinder lift characteristics. The high flow

velocity between cylinders 2 and 3 creates a low-pressure region resulting in the unsymmetrical lift characteristics of the two cylinders.

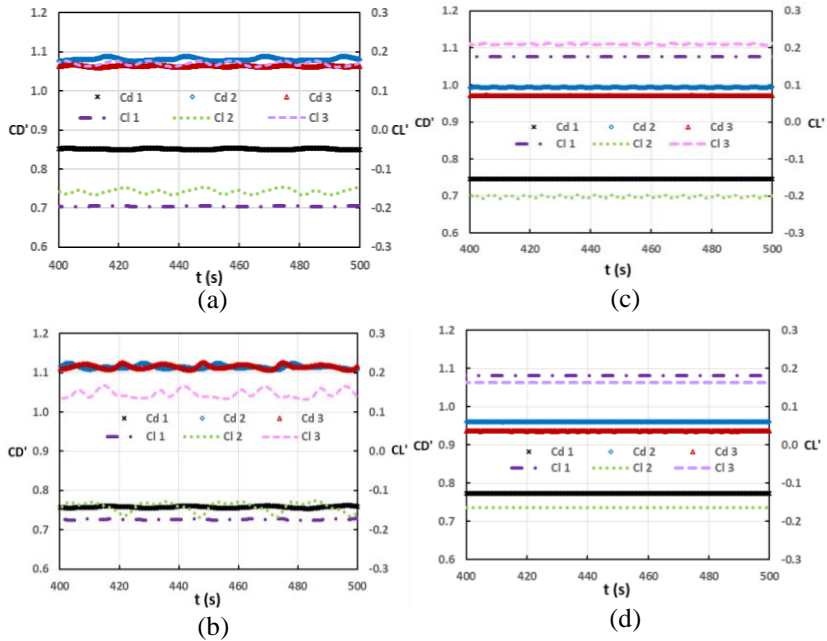


Figure 6: Coefficients of drag and lift on three circular cylinders in staggered arrangement with three DB at angles of 0° , 120° , and 240° ; (a) $L/D=1.5$, (b) $L/D=2.0$, (c) $L/D=3.0$, and (d) $L/D=4.0$

Vorticity contour analysis

Figure 7 shows the vorticity magnitude of the three-cylinder arrangement with three DB around cylinder 1. The results show that the shear layer that is released from cylinder 1 for all L/D still greatly affects cylinder 2 and cylinder 3 events for the larger L/D . The vorticity development around those cylinders is strongly affected by the interaction of the two shear layers from the upper and lower sides of the cylinder arrangement. The larger the shear layer that is released, the greater the vorticity magnitude formed. In the flow with high shear, the vorticity magnitude is large, and the flow structure is very fluctuating between the upper and lower sides of the cylinder. This difference in vorticity can be seen in the different colours in Figure 7. The red colour shows the higher vorticity magnitude, while the blue indicates the lower value of vorticity or shear layer. This difference in vorticity region results in the different fluctuating C_L for different cylinder configurations. This vorticity is also strongly influenced by the Strouhal number ($St=fD/U$) that also affected by the ratio L/D .

Figure 8 shows power spectral density (PSD) based on the fluctuating C_L and the effect of L/D on the cylinder vibration frequency that is expressed in terms of Strouhal number (fD/U), where D and U are cylinder diameter and freestream velocity, respectively. The frequency, f , is adapted from the fluctuating lift signals for each cylinder. In the present study, as the distance L/D increases from 1.5 to 4.0, the amplitude of the fluctuating lift also increases. In general, the peak of the amplitude of the fluctuating lift of cylinder 1 is lower than that of cylinders 2 and 3, while the amplitudes of the fluctuating lift of cylinders 2 and 3 are almost similar. The Strouhal numbers in the present study are between 0.14 and 1.80, where these values are in good agreement with many literatures for the same Reynolds number range ($Re=2.2 \times 10^4$) [35].

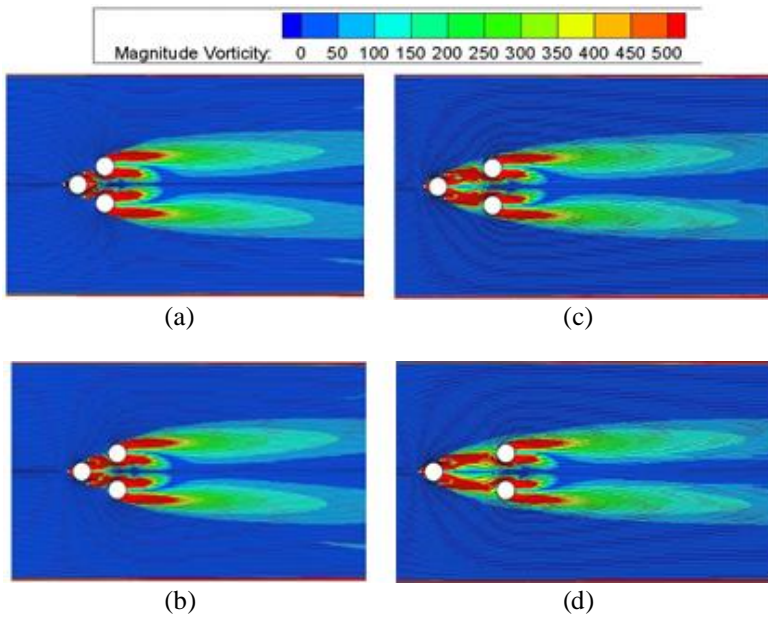


Figure 7: Contour of vorticity (s^{-1}) for three circular cylinders in staggered arrangement with three DB at angles 0° , 120° , and 240° ; (a) $L/D=1.5$, (b) $L/D=2.0$, (c) $L/D=3.0$, and (d) $L/D=4.0$

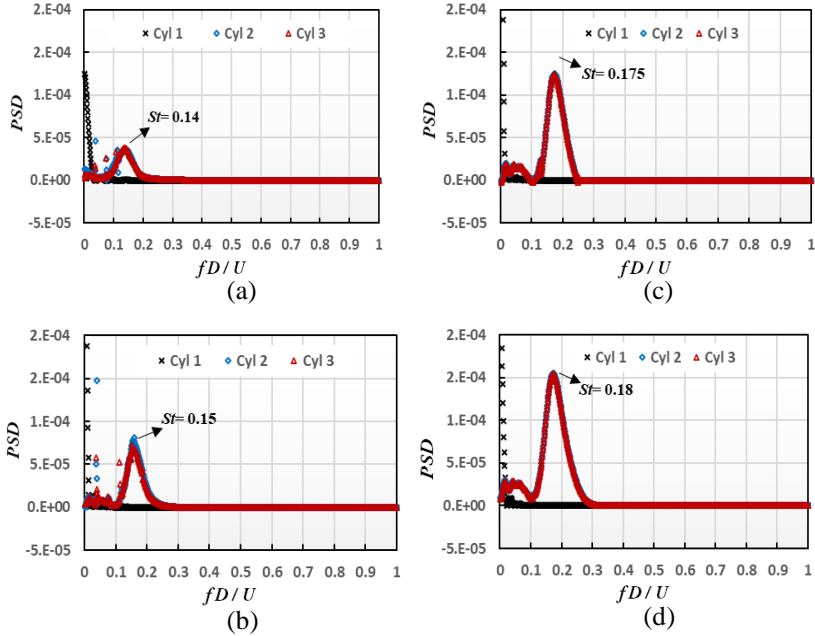


Figure 8: Strouhal number for three circular cylinders in staggered arrangement with three DB at angles 0° , 120° , and 240° ; (a) $L/D=1.5$, (b) $L/D=2.0$, (c) $L/D=3.0$, and (d) $L/D=4.0$

Discussion

The distribution of C_D and C_L for three circular cylinders in staggered arrangement differs from that occurs in a single-cylinder configuration. The values of C_D and C_L for cylinder 1, cylinder 2, and cylinder 3 obtained in this study are in good agreement with the results of previous studies. The comparison of the present results and the previous experimental results [20] as well as the numerical simulation [23], are shown in Table 6 and Figure 9. However, the fluctuations in the distribution of C_D and C_L that occur in the simulation results of Yan et al. [23] are much larger. This is due to the difference in Reynolds number and the difference in the cylinders and the DB configuration between the present study and the previous ones.

The existence of three DB around cylinder 1 at positions of 0° , 120° , and 240° can reduce C_D as a whole system when compared with the C_D of Yan et al. study [23] (Table 6). The drag of cylinder 1 is reduced up to 6%, 18%, 20%, and 16% for $L/D=1.5$, 2.0, 3.0, and 4.0, respectively. For cylinders 2 and 3, the drag reductions are up to 2% and 3% at $L/D=1.5$, 11% and 13% at $L/D=3$,

and 14% and 17% at $L/D=4$. This C_D reduction is most probably due to the presence of the disturbance body (DB) situated around cylinder 1. The existence of this DB can significantly modify the boundary layer structure around cylinder 1 resulting in narrowing the wake size behind cylinder 1. This wake reduction causes a reduction in C_D , not only for cylinder 1 but also for cylinders 2 and 3. On the contrary, for $L/D=2$, there was an increase in C_D by 1% for cylinders 2 and 3. Furthermore, in this three-cylinder arrangement, cylinder 2 exhibits the lowest value of C_L among the others (Figure 9). The cause of low C_L for cylinder 2 is caused by the higher flow velocity passing through the narrow gap between cylinder 2 and cylinder 3.

Table 6: Comparison of C_D between the present study and Yan et al. [23]

Yan et al. [23]	Cylinder 1		Cylinder 2		Cylinder 3	
C_D	0.9		1.1		1.1	
Present Study	C_D		C_D		C_D	
L/D	Cylinder 1	Difference	Cylinder 2	Difference	Cylinder 3	Difference
1.5	0.852	-6%	1.080	-2%	1.063	-3%
2.0	0.761	-18%	1.115	1%	1.116	1%
3.0	0.748	-20%	0.995	-11%	0.974	-13%
4.0	0.776	-16%	0.962	-14%	0.940	-17%

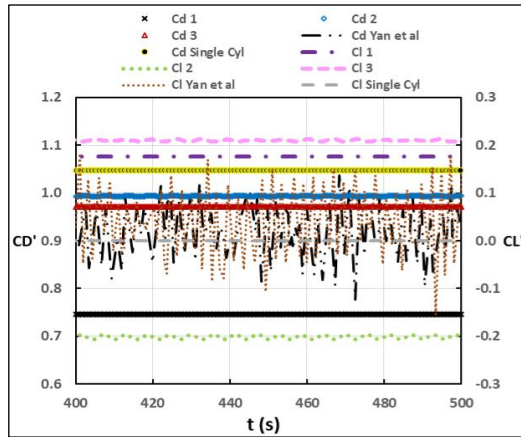


Figure 9: C_D and C_L for three circular cylinders in staggered arrangement with three DB at $\theta=0^\circ$, 120° , and 240° for $L/D=3$ compared with the previous studies [23]

Conclusion

Some conclusions that can be drawn from the results of the present study are as follows:

- i. The use of three DB at $\theta=0^\circ$, 120° , and 240° , can reduce C_D significantly on three circular cylinders arranged in stagger. The maximum reduction in C_D is up to approximately 20% compared to the simulation results of Yan et al. [23]. The reduction in C_D seems a function of the longitudinal distance between cylinders (L/D).
- ii. At $L/D=1.5$, C_D for the cylinder 2 is greater than that for cylinder 1, while at $L/D=2.0$ there was an increase in its C_D . With a further increase in L/D , the C_D for cylinder 2 tends to decrease.
- iii. At $L/D=1.5$, there is a small reduction in C_D for cylinder 3, up to approximately 3%. At $L/D=2.0$, on the other hand, there is an increase in its C_D up to 1%, although this value is probably within the uncertainty value. Similar to that of C_D on cylinder 2, further increase in L/D , up to about 4.0, the C_D for cylinder 3 tends to decrease.

Contributions of Authors

The authors confirm the equal contribution in each part of this work. All authors reviewed and approved the final version of this work.

Funding

This work was supported by Sepuluh Nopember Institute of Technology Grant through the Directorate of Research and Community Service.

Conflict of Interests

All authors declare that they have no conflicts of interest.

Acknowledgment

The support of the Directorate of Research and Community Service, Sepuluh Nopember Institute of Technology, Surabaya, Indonesia is gratefully acknowledged.

References

- [1] M. M. Zdravkovich, "Conceptual overview of laminar and turbulent flows past smooth and rough circular cylinders", *Journal of Wind Engineering and Industrial Aerodynamics*, vol. 33, no. 1–2, pp. 53–62, 1990. doi: 10.1016/0167-6105(90)90020-D.
- [2] M. M. Zdravkovich, "The effects of interference between circular cylinders in cross flow† An earlier version as originally presented as an invited paper, entitled 'Forces on pipe clusters', at the International Symposium on Separated Flow around Marine Structures, Norwegian", *Journal of Fluids and Structures*, vol. 1, no. 2, pp. 239–261, 1987. doi: 10.1016/S0889-9746(87)90355-0.
- [3] P. J. Pritchard and J. C. Leylegian, *Fox and McDonald's Introduction To Fluid Mechanics*, Eighth Edi. Manhattan: John Wiley & Sons, Inc, 2011.
- [4] W. A. Widodo and P. Hariyanto, "Studi eksperimen pengaruh penambahan disturbance body terhadap karakteristik aliran resusun secara tandem dalam saluran sempit", *Jurnal Teknik ITS*, vol. 1, no. 1, pp. 122–125, 2012.
- [5] P. F. Zhang, J. J. Wang, and L. X. Huang, "Numerical simulation of flow around cylinder with an upstream rod in tandem at low Reynolds numbers", *Applied Ocean Research*, vol. 28, no. 3, pp. 183–192, 2006. doi: 10.1016/j.apor.2006.08.003.
- [6] A. M. Makka and W. A. Widodo, "Studi Eksperimen Aliran Melintasi Silinder Sirkular Tunggal Dengan Bodi Pengganggu Berbentuk Silinder Yang Tersusun Tandem Dalam Saluran Sempit Berpenampang Bujur Sangkar", *Jurnal Teknik ITS*, vol. 1, no. 1, pp. F92–F96, 2012.
- [7] T. Tsutsui and T. Igarashi, "Drag reduction of a circular cylinder in an air-stream", *Journal of Wind Engineering and Industrial Aerodynamics*, vol. 90, no. 1, pp. 527–541, 2002. doi: 10.1007/s10494-005-9008-0.
- [8] A. Daloglu, "Pressure drop in a channel with cylinders in tandem arrangement", *International Communications in Heat and Mass Transfer*, vol. 35, no. 1, pp. 76–83, 2008. doi: 10.1016/j.icheatmasstransfer.2007.05.011.
- [9] W. A. Widodo and N. Hidayat, "Experimental study of drag reduction on circular cylinder and reduction of pressure drop in narrow channels by using a cylinder disturbance body", *Applied Mechanics and Materials*, vol. 493, no. 5, pp. 198–203, 2014. doi: 10.4028/www.scientific.net/AMM.493.198.
- [10] W. A. Widodo and R. P. Putra, "Reduction of drag force on a circular cylinder and pressure drop using a square cylinder as disturbance body in a narrow channel", *Applied Mechanics and Materials*, vol. 493, pp. 192–197, 2014. doi: 10.4028/www.scientific.net/AMM.493.192.
- [11] A. A. A. Daman and W. A. Widodo, "Pengaruh Penambahan Inlet Disturbance Body Terhadap Karakteristik Aliran Melintasi Silinder

- Sirkular Tersusun Tandem”, *Thermofluid VI, Seminar Nasional Thermofluid VI Yogyakarta, 2014*, pp. 79–84, 2014.
- [12] D. Sumner, “Two circular cylinders in cross-flow: A review”, *Journal of Fluids and Structures*, vol. 26, no. 6, pp. 849–899, 2010. doi: 10.1016/j.jfluidstructs.2010.07.001.
- [13] M. J. Janocha, M. C. Ong, P. R. Nystrøm, Z. Tu, G. Endal, and H. Stokholm, “Flow around two elastically-mounted cylinders with different diameters in tandem and staggered configurations in the subcritical Reynolds number regime”, *Marine Structures*, vol. 76, pp. 1–20, 2021. doi: 10.1016/j.marstruc.2020.102893.
- [14] H. Fukushima, T. Yagi, T. Shimoda, and K. Noguchi, “Wake-induced instabilities of parallel circular cylinders with tandem and staggered arrangements”, *Journal of Wind Engineering and Industrial Aerodynamics*, vol. 215, p. 104697, 2021. doi: 10.1016/j.jweia.2021.104697.
- [15] H. Li and D. Sumner, “Vortex shedding from two finite circular cylinders in a staggered configuration”, *Journal of Fluids and Structures*, vol. 25, no. 3, pp. 479–505, 2009. doi: 10.1016/j.jfluidstructs.2008.11.001.
- [16] W. Xu, H. Wu, K. Jia, and E. Wang, “Numerical investigation into the effect of spacing on the flow-induced vibrations of two tandem circular cylinders at subcritical Reynolds numbers”, *Ocean Engineering*, vol. 236, p. 109521, 2021. doi: 10.1016/j.oceaneng.2021.109521.
- [17] G. Wu, X. Du, and Y. Wang, “LES of flow around two staggered circular cylinders at a high subcritical Reynolds number of 1.4×10^5 ”, *Journal of Wind Engineering and Industrial Aerodynamics*, vol. 196, no. 4, pp. 104044, 2020. doi: 10.1016/j.jweia.2019.104044.
- [18] Q. Zou, L. Ding, R. Zou, H. Kong, H. Wang, and L. Zhang, “Two-degree-of-freedom flow-induced vibration of two circular cylinders with constraint for different arrangements”, *Ocean Engineering*, vol. 225, p. 108806, 2021. doi: 10.1016/j.oceaneng.2021.108806.
- [19] M. Tatsuno, H. Amamoto, and K. Ishi-i, “Effects of interference among three equidistantly arranged cylinders in a uniform flow”, *Fluid Dynamics Research*, vol. 22, no. 5, pp. 297–315, 1998. doi: 10.1016/S0169-5983(97)00040-3.
- [20] Z. Gu and T. Sun, “Classification of flow pattern on three circular cylinders in equilateral-triangular arrangements”, *Journal of Wind Engineering and Industrial Aerodynamics*, vol. 89, no. 6, pp. 553–568, 2001. doi: 10.1016/S0167-6105(00)00091-X.
- [21] B. Cut, R. Akram, Iskandar, A. Rahman, M. Zulfri, and Nazaruddin, “Experimental Review on Influence of Inlet Disturbance Body (IDB) at 30° Against Inhibitory Force Reduction on Three Circular Cylinders with Composed of Stagger (Variation $L/D(\text{constant}=2)$, $T/D = 1.5, 2, 3 \text{ \& } 4$)”, *IOP Conference Series: Materials Science and Engineering*, vol. 536, no. 1, pp. 1–9, 2019. doi: 10.1088/1757-899X/536/1/012017.

- [22] S. Yang, W. Yan, J. Wu, C. Tu, and D. Luo, "Numerical investigation of vortex suppression regions for three staggered circular cylinders", *European Journal Mechanics - B/Fluids*, vol. 55, pp. 207–214, 2016. doi: 10.1016/j.euromechflu.2015.10.004.
- [23] W. Yan, J. Wu, S. Yang, and Y. Wang, "Numerical investigation on characteristic flow regions for three staggered stationary circular cylinders," *European Journal of Mechanics - B/Fluids*, vol. 60, pp. 48–61, 2016. doi: 10.1016/j.euromechflu.2016.07.006.
- [24] Y. Ma, Y. Luan, and W. Xu, "Hydrodynamic features of three equally spaced, long flexible cylinders undergoing flow-induced vibration", *European Journal of Mechanical - B/Fluids*, vol. 79, pp. 386–400, 2020. doi: 10.1016/j.euromechflu.2019.09.021.
- [25] Z. Yang, X. Wang, J. H. Si, and Y. Li, "Flow around three circular cylinders in equilateral-triangular arrangement", *Ocean Engineering*, vol. 215, p. 107838, 2020. doi: 10.1016/j.oceaneng.2020.107838.
- [26] R. Wang, Y. He, L. Chen, Y. Zhu, and Y. Wei, "Numerical simulations of flow around three cylinders using momentum exchange-based immersed boundary-lattice Boltzmann method", *Ocean Engineering*, vol. 247, p. 110706, 2022. doi: 10.1016/j.oceaneng.2022.110706.
- [27] W. Chen, C. Ji, N. Srinil, Y. Yan, and Z. Zhang, "Effects of upstream wake on vortex-induced vibrations and wake patterns of side-by-side circular cylinders", *Marine Structures*, vol. 84, p. 103223, 2022. doi: 10.1016/j.marstruc.2022.103223.
- [28] S. Zheng, W. Zhang, and X. Lv, "Numerical simulation of cross-flow around three equal diameter cylinders in an equilateral-triangular configuration at low Reynolds numbers", *Computer & Fluids* vol. 130, pp. 94–108, 2016. doi: 10.1016/j.compfluid.2016.02.013.
- [29] D. Chatterjee and G. Biswas, "Dynamic behavior of flow around rows of square cylinders kept in staggered arrangement", *Journal of Wind Engineering and Industrial Aerodynamics*, vol. 136, pp. 1–11, 2015. doi: 10.1016/j.jweia.2014.10.019.
- [30] Y. Gao, X. Qu, M. Zhao, and L. Wang, "Three-dimensional numerical simulation on flow past three circular cylinders in an equilateral-triangular arrangement", *Ocean Engineering*, vol. 189, p. 106375, 2019. doi: 10.1016/j.oceaneng.2019.106375.
- [31] G. M. Barros, G. Lorenzini, L. A. Isoldi, L. A. O. Rocha, and E. D. dos Santos, "Influence of mixed convection laminar flows on the geometrical evaluation of a triangular arrangement of circular cylinders", *International Journal of Heat Mass Transfer*, vol. 114, pp. 1188–1200, 2017. doi: 10.1016/j.ijheatmasstransfer.2017.07.010.
- [32] F. R. Menter, R. Langtry, S. Völker, and P. G. Huang, "Transition Modelling for General Purpose CFD Codes", *Flow Turbulence Combust*, vol. 77, pp. 31–48, 2005. doi: 10.1016/B978-008044544-1/50003-0.
- [33] E. Salimpour, "A modification of the k-kL- ω turbulence model for

- simulation of short and long separation”, *Computers & Fluids*, vol. 181, pp. 67-76, 2019. doi: <https://doi.org/10.1016/j.compfluid.2019.01.003>.
- [34] T. Camp and R. Figliola, “Fluid mechanics”, in *Mechanobiology Handbook*, 2nd Ed., CRC Press, New York, pp. 23-44, 2011. doi: 10.2478/jtam-2013-0011.
- [35] M. Mahbub Alam and Y. Zhou, “Strouhal numbers, forces, and flow structures around two tandem cylinders of different diameters”, *Journal of Fluids and Structures*, vol. 24, no. 4, pp. 505-526, 2008. doi: 10.1016/j.jfluidstructs.2007.10.001.

Bending and Buckling Analysis of Functionally Graded Plates using a New Shear Strain Function with Reduced Unknowns

Ali Meftah*

University Center of Nour Bachir, Institute of Sciences,
Department of Technology, El Bayadh, 32000, ALGERIA
*genietech2013@yahoo.fr

ABSTRACT

In this article, functionally graded plates' buckling and bending analyses are investigated using a new shape function. The parabolic transverse shear stresses throughout the thickness are regarded by this function as meeting the shear stress-free surface conditions and enabling an accurate distribution of shear deformation according to the thickness of the plate without integrating shear correction factors. Compared to previous shear theories, this higher-order shear theory has the fewest unknowns. The equations for the functionally graded plates are produced by employing the Hamiltonian principle, and the solutions are obtained using Napier's technique. The outcomes of the current analysis are provided and contrasted with those found in the literature.

Keywords: *Hamilton's Principle; Shape Function; Buckling; Bending*

Introduction

Advanced composite material known as Functionally Graded Material (FGM) has compositions that change depending on the performance needed. The volume fractions of the elements are continuously graded and altered to create the FGM [1], which may be used for a variety of applications including thermal coatings for ceramic engines, gas turbines, nuclear fusion, optical thin layers, biomaterial electronics, and more.

The use of Functionally Graded (FG) plate designs in engineering over the past few years has led to the creation of numerous plate theories that

can accurately forecast the vibration, bending, and buckling, behaviours of FG plates [2]. The Classical Plate Theory (CPT) is supported by the concepts of Love Kirchhoff [3]. In which the effects of deformation in transverse shears are ignored and a line parallel to the mean plane of the plate remains perpendicular after deformation. To account for the transverse shear effect, the first-order transverse shear strain theory expands the traditional plate theory. In this case, the tangential stresses remain constant across the thickness of the plate, necessitating the employment of correction factors [4]. There are studies on First-Order Shear Deformation Theory (FSDT) that led to the Reissner - Mindlin plate model, as well as [5]-[9].

Higher Order Shear Deformation Theory (HSDT), a subclass of finer theories, is based on the growth of thickness displacement to an order of two or more. These theories are particularly well adapted to simulate the behaviour of thin, moderately thick, and thick plates, where transverse strain is important. While the higher-order theory is predicated on a nonlinear distribution of the fields in the thickness, the bulk of these models use a Taylor series expansion [10]. The consequences of transverse shear strain and/or transverse normal strain are therefore considered. For these models, correction adjustments are not necessary. These models are mentioned in [7], [11]-[13].

There has been extensive research on the behaviour of functionally graded plates and shells. Cheng and Batra [14] examined the deflections of a homogeneous Kirchhoff plate to those of a simply supported reinforced composite polygonal plate using calculations from first-order shear strain theory and third-shear deformation theory. Cheshmeh et al. [15] employed HSDT to carry out a numerical study on the thermal vibration and buckling analysis of CNTRC-composite plates in various forms. Kulkarni et al. [16] provided an analytical solution based on the inverse trigonometric shear deformation theory for the buckling and bending analysis of FGP. Rectangular FG plates exposed to non-linearly distributed plane edge stresses were examined for buckling [17]. They used a non-mesh technique for their analysis. Additionally, they arrived at a closed-form solution for a simply supported plate by investigating the buckling analysis of a rectangular FG plate utilizing FSDT [18].

The bending analysis of FG plates was provided by [19] using a two-variable improved plate theory. Bodaghi and Saidi [20] focused on the study of buckling caused by different mechanical and thermal loads on rectangular thick FG plates. The third-order shear deformation plate theory was used [21] to develop a new, better plaque theory for FGM plaques that only had four unknown functions. Becheri et al. [22] investigated the buckling and vibration of symmetrically laminated plates. They applied shear deformation theories of the first and third orders for the thermos-elastic deformation of simply supported, functionally graded plates with constrained dimensions, Pelletier and Vel [23] presented an accurate 3-D solution. For the bending

analysis of rectangular FG plates, Zenkour [24] displayed a 3-D elasticity solution, where Young's modulus of the plate is presumptively assumed to vary exponentially with thickness coordinate and Poisson's ratio constant.

The buckling and bending of FG plates are discussed in this article using a novel shape function that is used to develop an HSDT with only four unknowns. The defining differential equations are then reduced to a set of ordinary differential equations linked in the thickness direction and resolved using Navier's methods for simply supported rectangular plates. Numerical findings for the FG plate are shown. To make the results believable, displacements and stresses for different homogenization procedures and exponents in the power law that govern the variation across the thickness of the plate are supplied.

Some Shape Functions

A novel shape function for shear deformation is created and shown using several models, which are listed in Table 1.

Table 1: The shape functions of several HSDT

Models	Shear strain shape function $f(z)$	Derivative $f'(z)$
Reissner et al. [5]	$\frac{5}{2}z \left(1 - \frac{4z^2}{3h^2}\right)$	$\frac{5}{2} - \frac{10z^2}{h^2}$
Ambartsumyan [25]	$\frac{z}{2} \left(\frac{h^2}{4} - \frac{z^2}{3}\right)$	$\frac{h^2}{8} - \frac{z^2}{2}$
Soldatos [26]	$h \sinh\left(\frac{z}{h}\right) - z \cosh\left(\frac{1}{2}\right)$	$\cosh\left(\frac{z}{h}\right) - \cosh\left(\frac{1}{2}\right)$
Touratier [27] Zenkour [24]	$\frac{h}{\pi} \sin\left(\frac{z\pi}{h}\right)$	$\cos\left(\frac{z\pi}{h}\right)$
Karama et al. [28]	$ze^{-2\left(\frac{z}{h}\right)^2}$	$e^{-2\left(\frac{z}{h}\right)^2} - \frac{4e^{-\frac{2z^2}{h^2}}z^2}{h^2}$
Grover et al. [29] Benbakhti et al. [30] Meftah et al. [31]	$\sinh^{-1}\left(\frac{3z}{h}\right) - z \frac{6}{h\sqrt{13}}$	$\frac{3}{h\sqrt{\frac{9z^2}{h^2} + 1}} - \frac{6\sqrt{13}}{13h}$
Present model	$2^5h \left(\frac{z}{2^5h} - \frac{1}{3}\left(\frac{z}{2h}\right)^3\right)$	$1 - \left(\frac{2z}{h}\right)^2$

Theoretical Formulations

Take into account an FG plate with the dimensions of a , b , and h as illustrated in Figure 1. The material characteristics of the FG plate vary with plate thickness due to a power law of the elements' volume fractions. The FG plate is made up of ceramic and metal parts.

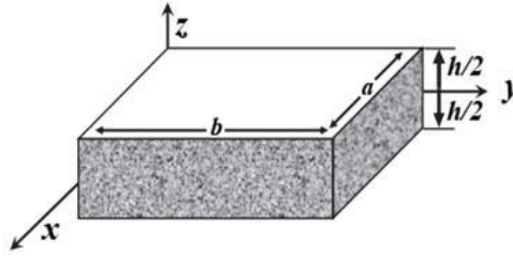


Figure 1: FG plate and coordinates

Properties of efficient materials of FG plates

Thai and Choi [32] denote the material qualities of FG plates.

$$p(z) = (p_c - p_m)v_c + p_m \quad (1)$$

P_c and P_m are the matching material qualities of the ceramic and metal placed on the plate's top and bottom surfaces, respectively. The volume proportion of the ceramic V_c material is as follows:

$$V_c(z) = \left(\frac{z}{h} + \frac{1}{2}\right)^p \quad (2)$$

Here p denotes the positive power-law index and $z \in \left[-\frac{h}{2}, \frac{h}{2}\right]$; zirconia distribution along plate thickness, Elastic modulus of the FG plate is provided by the exponential law [24]:

$$E(z) = E_0 e^{p\left(\frac{z}{h} + \frac{1}{2}\right)} \quad (3)$$

The homogenous Elastic modulus of materials is indicated by E_0 .

Higher-order shear deformation theories

At the plate's coordinates (x , y , and z), a material point has the following displacement field:

$$\begin{aligned}
 u(x, y, z) &= u_0(x, y) - z \frac{\partial w_0}{\partial x} - f(z) \frac{\partial \varphi}{\partial x} \\
 v(x, y, z) &= v_0(x, y) - z \frac{\partial w_0}{\partial y} - f(z) \frac{\partial \varphi}{\partial y} \\
 w(x, y, z) &= w_0(x, y)
 \end{aligned} \tag{4}$$

With, u , v , and w the directions are moved in x , y , z , and u_0 , v_0 , and w_0 are deviations from the median plane, φ owing to bending, the plane rotates. $f(z)$ represents the mode shapes determining the thickness-dependent stress and transverse deformation distributions, in this case, I created a new shape function in the form:

$$f(z) = 2^5 h \left[\frac{z}{2^5 h} - \frac{1}{3} \left(\frac{z}{2h} \right)^3 \right], \text{ and } g(z) = -\frac{df}{dz} \tag{5}$$

Kinematic and constitutive relations

$$\begin{Bmatrix} \varepsilon_{xx} \\ \varepsilon_{yy} \\ \gamma_{xy} \end{Bmatrix} = \begin{Bmatrix} \varepsilon_{xx}^0 \\ \varepsilon_{yy}^0 \\ \gamma_{xy}^0 \end{Bmatrix} + z \begin{Bmatrix} k_x^b \\ k_y^b \\ k_{xy}^b \end{Bmatrix} + f(z) \begin{Bmatrix} k_x^s \\ k_y^s \\ k_{xy}^s \end{Bmatrix}, \begin{Bmatrix} \gamma_{xz} \\ \gamma_{yz} \end{Bmatrix} = g(z) \begin{Bmatrix} \gamma_{xz}^0 \\ 0 \\ \gamma_{yz}^0 \end{Bmatrix} \tag{6a}$$

$$\begin{Bmatrix} \varepsilon_{xx}^0 \\ \varepsilon_{yy}^0 \\ \gamma_{xy}^0 \end{Bmatrix} = \begin{Bmatrix} \frac{\partial u_0}{\partial x} \\ \frac{\partial v_0}{\partial y} \\ \frac{\partial u_0}{\partial y} + \frac{\partial v_0}{\partial x} \end{Bmatrix}, \begin{Bmatrix} k_x^b \\ k_y^b \\ k_{xy}^b \end{Bmatrix} = \begin{Bmatrix} -\frac{\partial w_0}{\partial x} \\ -\frac{\partial w_0}{\partial y} \\ -2 \frac{\partial w_0}{\partial y \partial x} \end{Bmatrix}, \begin{Bmatrix} k_x^s \\ k_y^s \\ k_{xy}^s \end{Bmatrix} = \begin{Bmatrix} -\frac{\partial \varphi_0}{\partial x} \\ -\frac{\partial \varphi_0}{\partial y} \\ -2 \frac{\partial \varphi_0}{\partial y \partial x} \end{Bmatrix}, \begin{Bmatrix} \gamma_{xz}^0 \\ \gamma_{yz}^0 \end{Bmatrix} = \begin{Bmatrix} \frac{\partial \varphi}{\partial x} \\ \frac{\partial \varphi}{\partial y} \end{Bmatrix} \tag{6b}$$

For elastic FGMs, the constitutive relations can be written as follows:

$$\begin{Bmatrix} \sigma_{xx} \\ \sigma_{yy} \\ \tau_{yz} \\ \tau_{xz} \\ \tau_{xy} \end{Bmatrix} = \begin{bmatrix} C_{11} & C_{12} & 0 & 0 & 0 \\ C_{12} & C_{22} & 0 & 0 & 0 \\ 0 & 0 & C_{44} & 0 & 0 \\ 0 & 0 & 0 & C_{55} & 0 \\ 0 & 0 & 0 & 0 & C_{66} \end{bmatrix} \begin{Bmatrix} \varepsilon_{xx} \\ \varepsilon_{yy} \\ \gamma_{yz} \\ \gamma_{xz} \\ \gamma_{xy} \end{Bmatrix} \tag{7}$$

where:

$$C_{11}(z) = C_{22}(z) = \frac{E(z)}{1-(\nu(z))^2}, C_{12}(z) = \nu(z)C_{11}(z) \tag{8a}$$

$$C_{44}(z) = C_{55}(z) = C_{66}(z) = \frac{E(z)}{2(1+\nu(z))} \quad (8b)$$

Equations of motion

Here, the constitutive equations and the relevant motion equations for the displacement field are acquired using Hamilton's rule. The analytical formulation of the principle is as follows:

$$\int_0^t (\delta U + \delta V - \delta K) dt = 0 \quad (9)$$

δU : variation of the deformation energy; δV_e : work done; δK : variation of the kinetic energy of the FGM plate. The fluctuation of the plate's strain energy is determined by:

$$\begin{aligned} \delta U &= \int_A \int_{-\frac{h}{2}}^{+\frac{h}{2}} (\sigma_{xx} \delta \varepsilon_{xx} + \sigma_{yy} \delta \varepsilon_{yy} + \tau_{xy} \delta \gamma_{xy} + \tau_{xz} \delta \gamma_{xz} \\ &\quad + \tau_{yz} \delta \gamma_{yz}) dA dz \\ &= \int_A [N_{xx} \frac{\partial \delta u_0}{\partial x} - M_{xx}^b \frac{\partial^2 \delta w_0}{\partial x^2} - M_{xx}^s \frac{\partial^2 \delta \varphi}{\partial x^2} + N_{yy} \frac{\partial \delta v_0}{\partial y} \\ &\quad - M_{yy}^b \frac{\partial^2 \delta w_0}{\partial y^2} - M_{yy}^s \frac{\partial^2 \delta \varphi}{\partial y^2} + N_{xy} \left(\frac{\partial \delta u_0}{\partial y} + \frac{\partial \delta v_0}{\partial x} \right) - 2M_{xy}^b \frac{\partial^2 \delta w_0}{\partial x \partial y} \\ &\quad - 2M_{xy}^s \frac{\partial^2 \delta \varphi}{\partial x \partial y} + Q_x \frac{\partial \delta \varphi}{\partial x} + Q_y \frac{\partial \delta \varphi}{\partial y} - q \delta w_0] dA = 0 \end{aligned} \quad (10)$$

The definitions of solicitations with N, M, and Q are:

$$(N_{xx}, N_{yy}, N_{xy}) = \int_{-h/2}^{+h/2} (\sigma_{xx}, \sigma_{yy}, \tau_{xy}) dZ \quad (11a)$$

$$(M_{xx}^b, M_{yy}^b, M_{xy}^b) = \int_{-h/2}^{+h/2} z \cdot (\sigma_{xx}, \sigma_{yy}, \tau_{xy}) dZ \quad (11b)$$

$$(M_{xx}^s, M_{yy}^s, M_{xy}^s) = \int_{-h/2}^{+h/2} f \cdot (\sigma_{xx}, \sigma_{yy}, \tau_{xy}) dZ \quad (11c)$$

$$(Q_x, Q_y) = \int_{-h/2}^{+h/2} g \cdot (\tau_{xz}, \tau_{yz}) dZ \quad (11d)$$

The transverse loads and the fluctuation of the work done in the plane are given by:

$$\delta V = - \int_A \bar{N} \delta w_0 dA - \int_A q \delta w_0 dA \quad (12)$$

Such as:

$$\bar{N} = N_{xx}^0 \frac{\partial^2 w_0}{\partial x^2} + 2N_{xy}^0 \frac{\partial^2 w_0}{\partial x \partial y} + N_{yy}^0 \frac{\partial^2 w_0}{\partial y^2} \quad (13)$$

The following factors affect how kinetic energy fluctuates:

$$\begin{aligned} \delta K &= \int_{A-h/2}^{+h/2} (\dot{u} \delta \dot{u} + \dot{v} \delta \dot{v} + \dot{w} \delta \dot{w}) \rho(z) dA dz \\ &= \int_A \left\{ I_0 (\dot{u}_0 \delta \dot{u}_0 + \dot{v}_0 \delta \dot{v}_0 + \dot{w}_0 \delta \dot{w}_0) - I_1 \left(\dot{u}_0 \frac{\partial \delta \dot{w}_0}{\partial x} + \frac{\partial \dot{w}_0}{\partial x} \delta \dot{v}_0 + \dot{v}_0 \frac{\partial \delta \dot{w}_0}{\partial y} + \frac{\partial \dot{w}_0}{\partial y} \delta \dot{v}_0 \right) \right. \\ &\quad + I_2 \left(\frac{\partial \dot{w}_0}{\partial x} \frac{\partial \delta \dot{w}_0}{\partial x} + \frac{\partial \dot{w}_0}{\partial y} \frac{\partial \delta \dot{w}_0}{\partial y} \right) - J_1 \left(\dot{u}_0 \frac{\partial \delta \dot{\varphi}}{\partial x} + \frac{\partial \dot{\varphi}}{\partial x} \delta \dot{u}_0 + \dot{v}_0 \frac{\partial \delta \dot{\varphi}}{\partial y} + \frac{\partial \dot{\varphi}}{\partial y} \delta \dot{v}_0 \right) \\ &\quad \left. + K_2 \left(\frac{\partial \dot{\varphi}}{\partial x} \frac{\partial \delta \dot{\varphi}}{\partial x} + \frac{\partial \dot{\varphi}}{\partial y} \frac{\partial \delta \dot{\varphi}}{\partial y} \right) + J_2 \left(\frac{\partial \dot{w}_0}{\partial x} \frac{\partial \delta \dot{\varphi}}{\partial x} + \frac{\partial \dot{\varphi}}{\partial x} \frac{\partial \delta \dot{w}_0}{\partial x} + \frac{\partial \dot{w}_0}{\partial y} \frac{\partial \delta \dot{\varphi}}{\partial y} + \frac{\partial \dot{\varphi}}{\partial y} \frac{\partial \delta \dot{w}_0}{\partial y} \right) \right\} dA \end{aligned} \quad (14)$$

The mass density denoted by $\rho(\mathbf{z})$, the time variable t is differentiated using the dot-superscript convention, and (I_i, J_i, K_i) are mass inertias.

$$(I_0, I_1, I_2, J_1, J_2, K_2) = \int_{-h/2}^{+h/2} (1, z, z^2, f, zf, f^2) \rho(z) dz \quad (15)$$

Replacing Equation (10), Equation (12), and Equation (14) into Equation (9) and integrating the displacement gradients by parts and setting the coefficients of $\delta \mathbf{u}_0$, $\delta \mathbf{v}_0$, $\delta \mathbf{w}_0$ and $\delta \boldsymbol{\varphi}_0$ to zero separately. The resulting motion equations are as follows:

$$\delta u_0: \frac{\partial N_{xx}}{\partial x} + \frac{\partial N_{xy}}{\partial y} = I_0 \dot{u}_0 - I_1 \frac{\partial \dot{w}_0}{\partial x} - J_1 \frac{\partial \dot{\varphi}}{\partial x} \quad (16a)$$

$$\delta v_0: \frac{\partial N_{xy}}{\partial x} + \frac{\partial N_{yy}}{\partial y} = I_0 \dot{v}_0 - I_1 \frac{\partial \dot{w}_0}{\partial y} - J_1 \frac{\partial \dot{\varphi}}{\partial y} \quad (16b)$$

$$\begin{aligned} \delta w_0: \frac{\partial^2 M_{xx}^b}{\partial x^2} + 2 \frac{\partial^2 M_{xy}^b}{\partial x \partial y} + \frac{\partial^2 M_{yy}^b}{\partial y^2} + \bar{N} + q \\ = I_0 \ddot{w}_0 + I_1 \left(\frac{\partial \ddot{u}_0}{\partial x} + \frac{\partial \ddot{v}_0}{\partial y} \right) - I_2 \nabla^2 \ddot{w}_0 - J_2 \nabla^2 \ddot{\varphi} \end{aligned} \quad (16c)$$

$$\begin{aligned} \delta\varphi_0: \frac{\partial^2 M_{xx}^s}{\partial x^2} + 2 \frac{\partial^2 M_{xy}^s}{\partial x \partial y} + \frac{\partial^2 M_{yy}^s}{\partial y^2} + \frac{\partial Q_x}{\partial x} + \frac{\partial Q_y}{\partial y} \\ = J_1 \left(\frac{\partial \ddot{u}_0}{\partial x} + \frac{\partial \ddot{v}}{\partial y} \right) - J_2 \nabla^2 \dot{w}_0 - K_2 \nabla^2 \ddot{\varphi} \end{aligned} \quad (16d)$$

The stress resultants are given by replacing Equation (6a) with Equation (7) and the findings there form into Equations (11a), (11b), (11c), and (11d).

$$\begin{Bmatrix} N \\ M^b \\ M^s \end{Bmatrix} = \begin{bmatrix} A & B & B^s \\ B & D & D^s \\ B^s & D^s & H^s \end{bmatrix} \begin{Bmatrix} \varepsilon^0 \\ k^b \\ k^s \end{Bmatrix} \quad (17)$$

$$\begin{Bmatrix} Q_x \\ Q_y \end{Bmatrix} = \begin{bmatrix} A_{55}^s & 0 \\ 0 & A_{44}^s \end{bmatrix} \begin{Bmatrix} \gamma_{xz}^0 \\ \gamma_{yz}^0 \end{Bmatrix} \quad (18)$$

where $\mathbf{A}, \mathbf{A}^s, \mathbf{B}, \mathbf{D}, \mathbf{B}^s, \mathbf{D}^s, \mathbf{H}^s$ are the plate's stiffness defined by:

$$(A, B, D, B^s, D^s, H^s) = \int_{-h/2}^{+h/2} (1, z, z^2, f, fz, f^2) C(z) dZ \quad (19)$$

$$A_{44}^s = A_{55}^s = \int_{-h/2}^{+h/2} g^2(z) C_{44}(z) dZ = \int_{-h/2}^{+h/2} g^2(z) C_{55}(z) dZ \quad (20)$$

The motion equations can be expressed in the form of displacements. (u_0, v_0, w_0 et φ) by substituting Equations (17 and 18) into Equation (16) as follows:

$$\begin{aligned} A_{11} \frac{\partial^2 u_0}{\partial x^2} + A_{66} \frac{\partial^2 u_0}{\partial y^2} + (A_{12} + A_{66}) \frac{\partial^2 v_0}{\partial x \partial y} - B_{11} \frac{\partial^3 w_0}{\partial x^3} - (B_{12} + 2B_{66}) \frac{\partial^2 w_0}{\partial x \partial y^2} \\ - B_{11}^s \frac{\partial^3 \varphi}{\partial x^3} - (B_{12}^s + 2B_{66}^s) \frac{\partial^3 \varphi}{\partial x \partial y^2} \\ = I_0 \ddot{u}_0 - I_1 \frac{\partial \ddot{w}_0}{\partial x} - J_1 \frac{\partial \ddot{\varphi}}{\partial x} \end{aligned} \quad (21a)$$

$$\begin{aligned} A_{22} \frac{\partial^2 v_0}{\partial y^2} + A_{66} \frac{\partial^2 v_0}{\partial x^2} + (A_{12} + A_{66}) \frac{\partial^2 u_0}{\partial x \partial y} - B_{22} \frac{\partial^3 w_0}{\partial y^3} \\ - (B_{12} + 2B_{66}) \frac{\partial^2 w_0}{\partial x^2 \partial y} \\ - B_{22}^s \frac{\partial^3 \varphi}{\partial y^3} - (B_{12}^s + 2B_{66}^s) \frac{\partial^3 \varphi}{\partial x^2 \partial y} = I_0 \ddot{v}_0 - I_1 \frac{\partial \ddot{w}_0}{\partial y} - J_1 \frac{\partial \ddot{\varphi}}{\partial y} \end{aligned} \quad (21b)$$

$$\begin{aligned}
 & B_{11} \frac{\partial^3 u_0}{\partial x^3} + (B_{12} + 2B_{66}) \frac{\partial^3 u_0}{\partial x \partial y^2} + (B_{12} 2B_{66}) \frac{\partial^3 u_0}{\partial x \partial y^2} - D_{11}^s \frac{\partial^4 \varphi}{\partial x^4} - D_{22}^s \frac{\partial^4 \varphi}{\partial y^4} \\
 & - 2(D_{12}^s + 2D_{66}^s) \frac{\partial^4 \varphi}{\partial x^2 \partial y^2} + \bar{N}(w) + q \\
 & = I_0 \ddot{w}_0 + I_1 \left(\frac{\partial \ddot{u}_0}{\partial x} + \frac{\partial \ddot{v}}{\partial y} \right) - I_2 \nabla^2 \ddot{w}_0 - J_2 \nabla^2 \ddot{\varphi}
 \end{aligned} \tag{21c}$$

$$\begin{aligned}
 & B_{11}^s \frac{\partial^3 u_0}{\partial x^3} + (B_{12}^s + 2B_{66}^s) \frac{\partial^3 u_0}{\partial x \partial y^2} + (B_{12}^s + 2B_{66}^s) \frac{\partial^3 v_0}{\partial x^2 \partial y} + B_{66}^s \frac{\partial^3 v_0}{\partial y^3} \\
 & - D_{11}^s \frac{\partial^4 w_0}{\partial x^4} - D_{22}^s \frac{\partial^4 w_0}{\partial y^4} - 2(D_{12}^s + 2D_{66}^s) \frac{\partial^4 w_0}{\partial x^2 \partial y^2} + A_{55}^s \frac{\partial^2 \varphi}{\partial x^2} + A_{44}^s \frac{\partial^2 \varphi}{\partial y^2} \\
 & - D_{11}^s \frac{\partial^4 \varphi}{\partial x^4} - H_{11}^s \frac{\partial^4 \varphi}{\partial y^4} - 2(H_{12}^s + 2H_{66}^s) \frac{\partial^4 \varphi}{\partial x^2 \partial y^2} - H_{22}^s \frac{\partial^4 \varphi}{\partial y^4} \\
 & = J_1 \left(\frac{\partial \ddot{u}_0}{\partial x} + \frac{\partial \ddot{v}}{\partial y} \right) - J_2 \nabla^2 \ddot{w}_0 - K_2 \nabla^2 \ddot{\varphi}
 \end{aligned} \tag{21d}$$

Analytical Solutions for the FG Plate

The displacement variables are written as a combination of arbitrary parameters and well-known trigonometric functions to ensure that the motion formulas and boundary conditions are respected. The Navier solution method is used for this.

$$\begin{Bmatrix} u_0 \\ v_0 \\ w_0 \\ \varphi \end{Bmatrix} = \sum_{m=1}^{\infty} \sum_{n=1}^{\infty} \begin{Bmatrix} u_{mn}^0 \cos(\alpha x) \sin(\beta y) e^{i\omega t} \\ v_{mn}^0 \sin(\alpha x) \cos(\beta y) e^{i\omega t} \\ x_{mn}^0 \sin(\alpha x) \sin(\beta y) e^{i\omega t} \\ y_{mn}^0 \sin(\alpha x) \sin(\beta y) e^{i\omega t} \end{Bmatrix} \tag{22}$$

$$\alpha = m\pi/a, \quad \beta = n\pi/b \tag{23}$$

The double Fourier sinus series expands the transverse force \mathbf{q} as well:

$$\mathbf{q}(x, y) = \sum_{m=1}^{\infty} \sum_{n=1}^{\infty} \mathbf{q}_{mn} \sin(\alpha x) \sin(\beta y) e^{i\omega t} \tag{24}$$

α and β are natural numbers, a and b are the dimensions of the plate according to the x and y axes, correspondingly, $\mathbf{q}_{mn} = \mathbf{q}_0$ for a load with a

sinusoidal distribution. Taking into account that the plate is experiencing a compressive load in its plane:

$$N_{xx}^0 = -N_0, N_{yy}^0 = -\gamma N_0, N_{xy}^0 = 0,$$

γ is a non-dimensional load parameter. Substituting Equation (22) into Equation (21), it's discovered the problem:

$$\left(\begin{array}{cccc} [S_{11} & S_{12} & S_{13} & S_{14}] \\ [S_{12} & S_{22} & S_{23} & S_{24}] \\ [S_{13} & S_{23} & S_{33} + \lambda & S_{34}] \\ [S_{14} & S_{24} & S_{34} & S_{44}] \end{array} \right) - w^2 \left(\begin{array}{cccc} [m_{11} & 0 & m_{13} & m_{14}] \\ [0 & m_{22} & m_{23} & m_{24}] \\ [m_{13} & m_{23} & m_{33} & m_{34}] \\ [m_{14} & m_{24} & m_{34} & m_{44}] \end{array} \right) \begin{array}{l} \left\{ \begin{array}{l} u_{mn}^0 \\ v_{mn}^0 \\ x_{mn}^0 \\ y_{mn}^0 \end{array} \right\} \\ \left\{ \begin{array}{l} 0 \\ 0 \\ q_{mn} \\ 0 \end{array} \right\} \end{array} \quad (25)$$

where:

$$\begin{aligned} s_{11} &= A_{11}\alpha^2 + A_{66}\beta^2, s_{12} = (A_{11} + A_{66})\alpha\beta, s_{13} \\ &= -B_{11}\alpha^3 - (B_{12} + 2B_{66})\alpha\beta^2, \\ s_{14} &= -B_{11}^s\alpha^3 - (B_{12}^s + 2B_{66}^s)\alpha\beta^2, s_{22} = A_{66}\alpha^2 + A_{22}\beta^2, \\ s_{23} &= -B_{22}\beta^3 - (B_{12} + 2B_{66})\alpha^2\beta, s_{24} = -B_{22}^s\beta^3 - (B_{12}^s + 2B_{66}^s)\alpha^2\beta, \\ s_{33} &= D_{11}\alpha^4 + 2(D_{12} + 2D_{66})\alpha^2\beta^2 + D_{22}\beta^4, \\ s_{34} &= D_{11}^s\alpha^4 + 2(D_{12}^s + 2D_{66}^s)\alpha^2\beta^2 + D_{22}^s\beta^4, \quad (26) \\ s_{44} &= H_{11}^s\alpha^4 + 2(H_{12}^s + 2H_{66}^s)\alpha^2\beta^2 + H_{22}^s\beta^4 + A_{55}^s\alpha^2 + A_{44}^s\beta^2, \\ m_{11} &= m_{22} = I_0, m_{13} = -\alpha I_1, m_{14} = -\alpha J_1, m_{23} = -\beta I_1, m_{24} = -\beta J_1, \\ m_{33} &= I_0 + I_2(\alpha^2 + \beta^2), m_{34} = J_2(\alpha^2 + \beta^2), m_{44} = K_2(\alpha^2 + \beta^2) \\ \lambda &= -N_0(\alpha^2 + \gamma\beta^2). \end{aligned}$$

Numerical example

We study a rectangular, simply supported FG plate with dimensions a and b , located, respectively, in the x - and y -axes (see Figure 1). In Table 2, the material qualities are listed.

Table 2: Qualities of plate materials

Material	Young's modulus (GPa)	Mass density (kg/m ³)	Poisson's ratio
Aluminium (Al)	70	2.702	0.3
Alumina (Al ₂ O ₃)	380	3.800	0.3
Zirconia (ZrO ₂)	151	3.000	0.3
Silicon carbide (SiC)	420	3.210	0.3

The accuracy of the current analysis is examined in the section that follows, which also examines the effects of the geometric ratio and the power-law index on the deflections, stresses, and critical buckling loads of FG plates. The following dimensionless parameters are chosen because they are more practical:

$$\bar{u} = \frac{100E_c h^3}{q_0 a^4} u \left(0, \frac{b}{2}, z\right), \bar{w} = \frac{10E_c h^3}{q_0 a^4} w \left(\frac{a}{2}, \frac{b}{2}\right) \quad (27)$$

$$\bar{\sigma}_{xx}(z) = \frac{h}{q_0 a} \sigma_{xx} \left(\frac{a}{2}, \frac{b}{2}, z\right), \bar{\tau}_{xy}(z) = \frac{h}{q_0 a} \sigma_{xy}(0, 0, z), \quad (28)$$

$$\bar{\tau}_{xz}(z) = \frac{h}{q_0 a} \sigma_{xz} \left(0, \frac{b}{2}, z\right)$$

$$\hat{N}_{cr} = \frac{N_{cr} a^2}{D_{11} - (B_{11}^2 / A_{11})}, \bar{N}_{cr} = \frac{N_{cr} a^2}{E_m h^3} \quad (29)$$

Bending analysis

To check the accuracy of the proposed model in investigating the bending, Tables 3 (square plates, $h/a=0.1$) and 4 determine the central deflections, transverse shear stresses, and normal stresses of plates (Al/Al₂O₃) under sinusoidal loads. The outcomes of several shear deformation theories were compared, including quasi-3D, 3D, sinusoidal shear deformation theory (SSDT), third-order shear deformation theory (TSDT), and those that took into account both transverse shear and normal stresses. It can be seen from these results that the computations based on the present 2D (HSDT) theory present an excellent agreement with those predicted by the other theories of TSDT [33] and HSDT [34] and present a good correlation with those predicted by Quasi-3D [35], Quasi-3D [36], SSDT [37], and HSDT [38].

Table 3: Dimensionless ($\bar{u}, \bar{w}, \bar{\sigma}_{xx}, \bar{\tau}_{xy}, \bar{\tau}_{xz}$) of square plates (Al/Al₂O₃)

p	Theory	$\bar{u}(-h/4)$	\bar{w}	$\bar{\sigma}_{xx}(h/3)$	$\bar{\tau}_{xy}(-h/3)$	$\bar{\tau}_{xz}(h/6)$
1	Quasi-3D [35]	0.6436	0.5875	1.5062	0.6081	0.2510
	Quasi-3D [36]	0.6436	0.5876	1.5061	0.6112	0.2511
	SSDT [37]	0.6626	0.5889	1.4894	0.6110	0.2622
	HSDT [38]	0.6398	0.5880	1.4888	0.6109	0.2566
	TSDT [33]	0.6414	0.5890	1.4898	0.6111	0.2599
	HSDT [34]	0.6414	0.5891	1.4898	0.6111	0.2608
	HSDT [39]	0.6401	0.5883	1.4892	0.6110	0.2552
	Present	0.6414	0.5890	1.4898	0.6111	0.2608
2	Quasi-3D [35]	0.9012	0.7570	1.4147	0.5421	0.2496
	Quasi-3D [36]	0.9013	0.7571	1.4133	0.5436	0.2495
	SSDT [37]	0.9281	0.7573	1.3954	0.5441	0.2763
	HSDT [38]	0.8957	0.7564	1.3940	0.5438	0.2741
	TSDT [33]	0.8984	0.7573	1.3960	0.5442	0.2721
	HSDT [34]	0.8984	0.7573	1.3960	0.5442	0.2721
	HSDT [39]	0.8961	0.7567	1.3947	0.5439	0.2721
	Present	0.8984	0.7573	1.3960	0.5442	0.2737
4	Quasi-3D [35]	1.0541	0.8823	1.1985	0.5666	0.2362
	Quasi-3D [36]	1.0541	0.8823	1.1841	0.5671	0.2362
	SSDT [37]	1.0941	0.8819	1.1783	0.5667	0.2580
	HSDT [38]	1.0457	0.8814	1.1755	0.5662	0.2623
	TSDT [33]	1.0502	0.8815	1.1794	0.5669	0.2519
	HSDT [34]	1.0502	0.8815	1.1794	0.5669	0.2537
	HSDT [39]	1.0466	0.8818	1.1766	0.5664	0.2593
	Present	1.0502	0.8815	1.1794	0.5669	0.2537
8	Quasi-3D [35]	1.0830	0.9739	0.9687	0.5879	0.2262
	Quasi-3D [36]	1.0830	0.9739	0.9687	0.5879	0.2261
	SSDT [37]	1.1340	0.9750	0.9466	0.5856	0.2121
	HSDT [38]	1.0709	0.9737	0.9431	0.5850	0.2140
	TSDT [33]	1.0763	0.9747	0.9477	0.5858	0.2087
	HSDT [34]	1.0763	0.9746	0.9477	0.5858	0.2088
	HSDT [39]	1.0719	0.9744	0.9444	0.5852	0.2117
	Present	1.0763	0.9746	0.9477	0.5858	0.2088

The variations in-plane displacement, normal and tangential stresses across the thickness of the square plate (Al /Al₂O₃) are shown in Figure 2. It can be seen that the lower part of the plate is in tension and the upper part. In compression, the dimensionless displacement increased with the increase in the power index, and was equal to zero, for ($z/h=0$).

Table 4: Dimensionless deflection (\bar{W}) of plates (Al/Al₂O₃)

h/a	a/b	Theory	p					
			0.1	0.3	0.5	0.7	1	1.5
0.5	1	3D [24]	0.576	0.524	0.476	0.432	0.372	0.289
		Quasi-3D	0.573	0.518	0.467	0.422	0.361	0.277
		Quasi-3D	0.577	0.522	0.471	0.425	0.364	0.279
		HSDT [38]	0.636	0.575	0.519	0.468	0.401	0.307
		HSDT [34]	0.636	0.575	0.519	0.468	0.401	0.307
		HSDT [39]	0.621	0.561	0.507	0.457	0.392	0.301
	Present	0.619	0.575	0.519	0.468	0.399	0.305	
	0.5	3D [24]	1.194	1.085	0.986	0.895	0.772	0.601
		Quasi-3D	1.188	1.074	0.970	0.875	0.749	0.575
		Quasi-3D	1.193	1.079	0.974	0.879	0.753	0.578
		HSDT [38]	1.277	1.155	1.044	0.943	0.809	0.623
		HSDT [34]	1.277	1.155	1.044	0.943	0.808	0.623
		HSDT [39]	1.256	1.136	1.027	0.928	0.796	0.615
	Present	1.256	1.155	1.043	0.942	0.807	0.621	
	0.3	3D [24]	1.443	1.311	1.191	1.081	0.933	0.727
		Quasi-3D	1.435	1.297	1.172	1.058	0.905	0.696
		Quasi-3D	1.441	1.303	1.177	1.062	0.909	0.699
		HSDT [38]	1.534	1.387	1.254	1.132	0.972	0.750
HSDT [34]		1.534	1.387	1.254	1.132	0.971	0.750	
HSDT [39]		1.511	1.367	1.236	1.116	0.958	0.741	
Present	1.510	1.387	1.253	1.132	0.971	0.749		
0.2	1	3D [24]	0.349	0.316	0.287	0.260	0.225	0.180
		Quasi-3D	0.347	0.314	0.283	0.256	0.219	0.169
		Quasi-3D	0.348	0.315	0.284	0.257	0.220	0.169
		HSDT [38]	0.360	0.325	0.294	0.266	0.229	0.178
		HSDT [34]	0.360	0.325	0.294	0.266	0.229	0.178
		HSDT [39]	0.357	0.323	0.292	0.264	0.228	0.177
	Present	0.359	0.326	0.295	0.267	0.230	0.180	
	0.5	3D [24]	0.815	0.739	0.670	0.608	0.525	0.412
		Quasi-3D	0.812	0.734	0.663	0.599	0.513	0.396
		Quasi-3D	0.814	0.736	0.665	0.600	0.515	0.397
		HSDT [38]	0.832	0.753	0.681	0.617	0.531	0.415
		HSDT [34]	0.832	0.753	0.681	0.617	0.531	0.415
		HSDT [39]	0.828	0.749	0.678	0.614	0.529	0.413
	Present	0.831	0.753	0.681	0.617	0.531	0.413	
	0.3	3D [24]	1.013	0.919	0.833	0.756	0.653	0.512
		Quasi-3D	1.009	0.912	0.824	0.744	0.638	0.492
		Quasi-3D	1.012	0.915	0.827	0.747	0.640	0.494
		HSDT [38]	1.032	0.934	0.845	0.765	0.660	0.515
HSDT [34]		1.032	0.934	0.845	0.765	0.660	0.515	
HSDT [39]		1.028	0.930	0.842	0.762	0.657	0.513	
Present	1.031	0.934	0.845	0.765	0.659	0.514		

Concerning the greatest axial tension rises as the power index p whereas it appears minimal compressed stresses positioned at the lower part

of the plate intended certain values of p ($p=0, \bar{\sigma}_{xx} = -2$ and $p=0.5, \bar{\sigma}_{xx} = -0.65$) the axial stress is in tension in the upper part ($p=0, \bar{\sigma}_{xx} = 2$ and $p=40, \bar{\sigma}_{xx} = 8.07$).

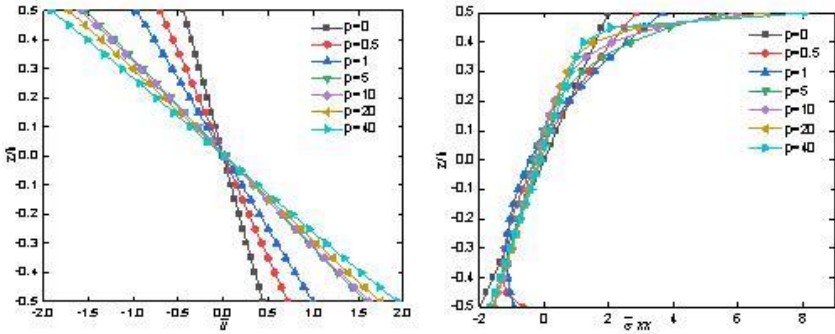


Figure 2: In-plane displacement (\bar{u}) and stress ($\bar{\sigma}_{xx}$) along the thickness of Al/Al₂O₃ square plates ($h/a=0.1$)

Figure 3 displays the change in tangential cross-thickness stresses on the FG plate, for homogeneous plates, the mid-plane is where the highest shear stress is located, and it tends to migrate slightly to the top surface, this is an asymmetric characteristic of the FGM through the thickness of the FG plate.

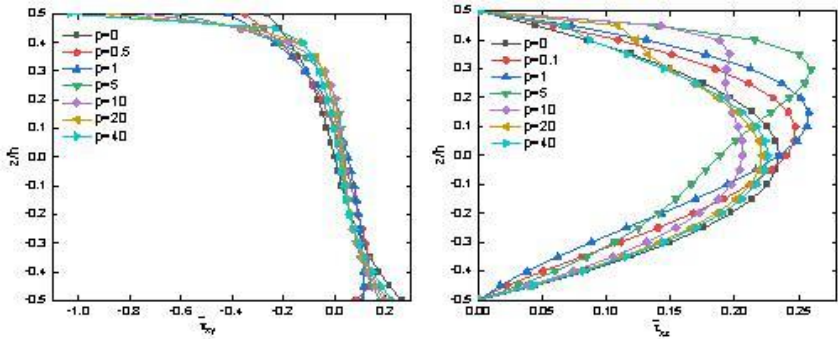


Figure 3: In-plane stress ($\bar{\tau}_{xy}$) and ($\bar{\tau}_{xz}$) along the thickness of Al/Al₂O₃ square plates ($h/a=0.5$)

Buckling analysis

Calculated critical buckling loads and compared them to those accessible in the literature to assess the efficacy of the current results in forecasting a

buckling response of FG plates. The following example investigates the buckling reactions of Al/Al₂O₃ and Al/SiC plates under three different types of in-plane loads: uniaxial compression, biaxial compressions, axial compression, and tension ($\gamma=0$), ($\gamma=1$), and ($\gamma=-1$), respectively. Because of differences in material characteristics over the thickness, stretching-bending coupling arises in FG plates.

Table 5: The critical buckling load (\bar{N}_{cr}) of Al/SiC square plates ($h/a=0.1$)

γ	Theory	p					
		0	0.5	1	2	5	10
0	HSDT [39]	37.4215	37.6650	37.7560	37.6327	36.8862	36.5934
	FSDT [42]	37.3708	-	37.7132	37.7089	-	-
	HSDT [20]	37.3714	-	37.7172	37.5765	-	-
	HSDT [43]	37.3721	-	37.7143	37.6042	-	-
	Present	37.3721	37.6302	37.7143	37.6042	36.9183	36.5615
1	HSDT [39]	18.7107	18.8325	18.8780	18.8163	18.4431	18.2967
	FSDT [42]	18.6854	-	18.8566	18.8545	-	-
	HSDT [20]	18.6860	-	18.8571	18.8020	-	-
	HSDT [43]	18.6861	-	18.8572	18.8021	-	-
	Present	18.6861	18.8151	18.8572	18.8021	18.4591	18.2807
-1	HSDT [39]	72.3281	73.4526	73.8426	73.2827	69.9876	68.7244
	FSDT [42]	72.0834	-	73.6307	73.6112	-	-
	HSDT [20]	72.2275	-	73.6645	73.1587	-	-
	HSDT [43]	72.0983	-	73.6437	73.1436	-	-
	Present	72.0983	73.5127	74.2938	74.2403	71.0104	69.0775

When the plate is subjected to in-plane compressive loads, this coupling induces deflection and bending moments.

The results of Table 5 present the critical buckling load of a simply supported square plate (Al/SiC) with a constant geometric ratio ($h/a=0.1$). The outcomes are contrasted with those of the HSDT [39], FSDT [42], HSDT [20], and HSDT [43]. The computed results have good accuracy for square plates.

To further illustrate the accuracy of the present theory for a wide range of thickness ratio (a/h), geometric ratio (b/a), different values of gradient index (p), and different cases of the dimensionless load parameter (γ), comparison of the variations of critical buckling load (\bar{N}_{cr}) of Al/Al₂O₃ plates computed by the present theory, HSDT [43] and HSDT [39] is presented in Table 6, as seen in the table, there is a good agreement between the computed results from the proposed theory and the computed results from other HSDT.

Table 6: The critical buckling load (\bar{N}_{cr}) of Al/Al₂O₃ plates

γ	b/a	h/a	Theory	ρ						
				0	0.5	1	2	5	10	
0	2	0.2	HSDT[43]	6.7203	4.4235	3.4164	2.6451	2.1484	1.9213	
			HSDT[39]	6.7417	4.4343	3.4257	2.6503	2.1459	1.9260	
			Present	6.7203	4.4235	3.4164	2.6451	2.1484	1.9213	
	0.1	HSDT[43]	7.4053	4.8206	3.7111	2.8897	2.4165	2.1896		
		HSDT[39]	7.4115	4.8225	3.7137	2.8911	2.4155	2.1911		
		Present	7.4053	4.8206	3.7111	2.8897	2.4165	2.1896		
	0.05	HSDT[43]	7.5993	4.9315	3.7930	2.9382	2.4944	2.2690		
		HSDT[39]	7.6009	4.9307	3.7937	2.9585	2.4942	2.2695		
		Present	7.5993	4.9315	3.7930	2.9582	2.4944	2.2690		
	1	0.2	HSDT[43]	16.0211	10.6254	8.2245	6.3432	5.0531	4.4807	
			HSDT[39]	16.1003	10.6670	8.2597	6.3631	5.0459	4.4981	
			Present	16.0211	10.4629	7.9086	5.94263	4.7928	4.355	
0.1		HSDT[43]	18.5785	12.1229	9.3391	7.2631	6.0353	5.4528		
		HSDT[39]	18.6030	12.1317	9.3496	7.2687	6.0316	5.4587		
		Present	18.5785	11.9128	8.9338	6.7404	5.6678	5.2707		
0.05		HSDT[43]	19.3528	12.5668	9.6675	7.5371	6.3448	5.7668		
		HSDT[39]	19.3593	1.25652	9.6702	7.5386	6.3437	5.7689		
		Present	19.3528	12.3413	9.2339	6.9752	5.9399	5.5643		
1		2	0.2	HSDT[43]	5.3762	3.5388	2.7331	2.1161	1.7187	1.5370
				HSDT[39]	5.3934	3.5475	2.7406	2.1202	1.7167	1.5408
				Present	5.3762	3.5388	2.7331	2.1161	1.7187	1.5370
	0.1	HSDT[43]	5.9243	3.8565	2.7689	2.3117	1.9332	1.7517		
		HSDT[39]	5.9292	3.8580	2.9710	2.3129	1.9324	1.7529		
		Present	5.9243	3.8565	2.9689	2.3117	1.9332	1.7517		
	0.05	HSDT[43]	6.0794	3.9452	3.0344	2.3665	1.9955	1.8152		
		HSDT[39]	6.0807	3.9445	3.0350	2.3668	1.9953	1.8156		
		Present	6.0794	3.9452	3.0344	2.3665	1.9955	1.8152		
	1	0.2	HSDT[43]	8.0105	5.3127	4.1122	3.1716	2.5265	2.2403	
			HSDT[39]	8.0501	5.3335	4.1299	3.1815	2.5230	2.2491	
			Present	8.0105	5.2314	3.9543	2.9713	2.3964	2.1775	
0.1		HSDT[43]	9.2893	6.0615	4.6696	3.6315	3.0177	2.7264		
		HSDT[39]	9.3015	6.0659	4.6748	3.6344	3.0158	2.7293		
		Present	9.2893	5.9564	4.4669	3.3702	2.8339	2.6354		
0.05		HSDT[43]	9.6764	6.2834	4.8337	3.7686	3.1724	2.8834		
		HSDT[39]	9.6796	6.2826	4.8351	3.7693	3.1718	2.8844		
		Present	9.6764	6.1706	4.6169	3.4876	2.9699	2.7821		
1		2	0.2	HSDT[43]	8.9604	5.8980	4.5551	3.5268	2.8646	2.5617
				HSDT[39]	8.9890	5.9124	4.5676	3.5337	2.8612	2.5679
				Present	8.9604	5.8980	4.5551	3.5268	2.8646	2.5617
	0.1	HSDT[43]	9.8738	6.4275	4.9481	3.8529	3.2219	2.9195		

		HSDT[39]	9.8820	6.4299	4.9516	3.8548	3.2206	2.9214
		Present	9.8738	6.4275	4.9481	3.8529	3.2219	2.9195
	0.05	HSDT[43]	10.1324	6.5753	5.0574	3.9442	3.3259	3.0253
		HSDT[39]	10.1345	6.5742	5.0583	3.9447	3.3255	3.0260
		Present	10.1324	6.5753	5.0574	3.9442	3.3259	3.0253
1	0.2	HSDT[43]	26.2058	17.7704	13.8486	10.5589	16.9590	6.8970
		HSDT[39]	24.4999	17.9424	13.9872	10.6421	7.9571	6.9626
		Present ^a	26.2058	17.7947	13.8958	10.6164	7.9927	6.9132
	0.1	HSDT[43]	35.8416	23.5920	18.2206	14.1073	11.4583	10.2468
		HSDT[39]	35.9559	23.6497	18.2704	14.1349	11.4447	10.2717
		Present ^a	35.8416	23.6343	18.3023	14.2113	11.5283	10.2812
	0.05	HSDT[43]	39.4951	25.7100	19.7925	15.4115	12.8878	11.6779
		HSDT[39]	39.5280	25.7197	19.8065	15.4190	12.8824	11.6857
		Present ^a	39.4951	25.7602	19.8890	15.5361	12.9764	11.7220

^a Critical buckling

In Figure 6(a), the buckling responses of the Al/Al₂O₃ plate, are studied for three types of loads in the plane considered: ($y=0$), ($y=-1$), and ($y=1$). For the three cases, for the power-law index ($P=0$) the essential buckling load, in terms of value ($\bar{N}cr$) is maximum, then with the increase in (p) will decrease the critical load ($\bar{N}cr$).

A variety of thickness to the ratio (a/h), varying gradient index values (p), and for ($y=1$), the value of the critical buckling load ($\bar{N}cr$) is maximum for ($p=0$), then after certain values of (a/h), the curves remain flat, as plotted in Figure 6(b).

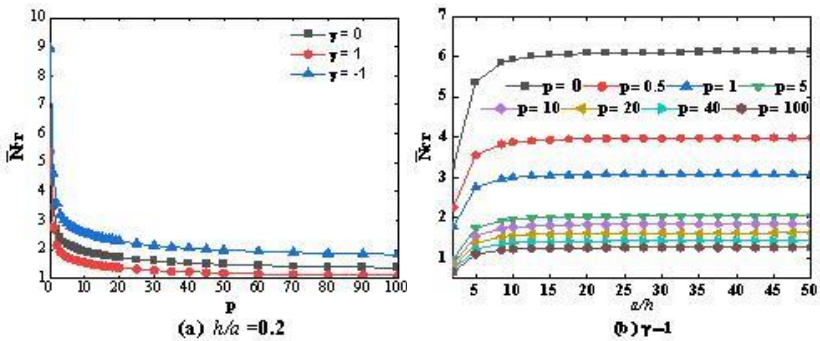


Figure 6: The critical buckling load ($\bar{N}cr$) of rectangular plates (Al/Al₂O₃) ($b/a=2$) is affected by the power-law index p and side-to-thickness ratio ($a=0.9h$)

Conclusion

The current study uses a novel 2D HSDT to analyse the buckling and bending of simply supported FG plates. By developing a new shear deformation shape function, the theory is constructed. Hamilton's rule is used to generate equations describing motion. Navier's technique is used to resolve these equations. The results were compared to those given by several plate theories for the novel shear deformation shape function employed in this work. As a consequence, when compared to the FSDT and other HSDTs with a greater number of unknowns, the created HSDT delivers findings with extremely good accuracy. As a result, the current model may be used as a benchmark to evaluate the effectiveness of approximative numerical methods.

Contributions of Authors

The author confirms that this work is individual. the author reviewed , and approved the final version of this work.

Funding

This work received no specific grant from any funding agency.

Conflict of Interests

The author declares that they have no conflicts of interest.

References

- [1] M. Koizumi, "FGM activities in Japan", *Composites. Part B Engineering*, vol. 28, no. 1–2, pp. 1–4, 1997.
- [2] D. K. Jha, T. Kant, and R. K. Singh, "Free vibration response of functionally graded thick plates with shear and normal deformations effects", *Composite Structures*, vol. 96, pp. 799–823, 2013. doi: 10.1016/j.compstruct.2012.09.034.
- [3] G. Kirchhoff, "Über das gleichgewicht und die bewegung einer elastischen scheibe", *Journal Für Die Reine Und Angewandte Mathematik (Crelles Journal)*, vol. 1850, no. 40, pp. 51–88, 1850.
- [4] J. Cugnoni, "Identification par decalage modal et fréquentiel en

- matériaux composites”, Ph.D dissertation, Faculty of Eng., Federal Ins. of Tech., Lausanne, 2005. [Online]. Available: <https://core.ac.uk/download/pdf/147900375.pdf>
- [5] E. Reissner, “The effect of transverse shear deformation on the bending of elastic plates”, *Journal of Applied Mechanics*, vol. 12, no. 2, pp. A69–A77, 1945. doi: 10.1115/1.4009435.
- [6] Q. Zhang, S. Li, A. Zhang, Y. Peng, and J. Yan, “A peridynamic Reissner-Mindlin shell theory”, *International Journal for Numerical Methods in Engineering*, vol. 122, no. 1, pp. 122–147, 2021. doi: 10.1002/nme.6527.
- [7] Z. Kolakowski and J. Jankowski, “Some inconsistencies in the nonlinear buckling plate theories—fsdt, s-fsdt, hsdt”, *Materials (Basel)*, vol. 14, no. 9, pp. 1–20, 2021. doi: 10.3390/ma14092154.
- [8] C.-U. Nguyen, J.-L. Batoz, and A. Ibrahimbegovic, “Notable highlights on locking-free techniques of Reissner-Mindlin plate finite elements in elastostatics”, *Coupled System Mechanics An International Journal*, vol. 10, no. 3, pp. 229–246, 2021. doi: <https://doi.org/10.12989/csm.2021.10.3.229>.
- [9] J. Videla, S. Natarajan, and S. P. A. Bordas, “A new locking-free polygonal plate element for thin and thick plates based on Reissner-Mindlin plate theory and assumed shear strain fields”, *Computers & Structures*, vol. 220, pp. 32–42, 2019. doi: 10.1016/j.compstruc.2019.04.009.
- [10] A. Bhar, S. S. Phoenix, and S. K. Satsangi, “Finite element analysis of laminated composite stiffened plates using FSDT and HSDT: A comparative perspective”, *Composite Structures*, vol. 92, no. 2, pp. 312–321, Jan. 2010. doi: 10.1016/j.compstruct.2009.08.002.
- [11] A. Tounsi, H. Ait Atmane, M. Khiloun, M. Sekkal, O. Taleb, and A. Anis Bousahla, “On buckling behaviour of thick advanced composite sandwich plates”, *Composite Materials and Engineering*, vol. 1, no. 1, pp. 1–19, 2019. <https://doi.org/10.12989/cme.2019.1.1.001>.
- [12] A. Bouhadra, A. Tounsi, A. A. Bousahla, S. Benyoucef, and S. R. Mahmoud, “Improved HSDT accounting for effect of thickness stretching in advanced composite plates”, *Structural Engineering and Mechanics*, vol. 66, no. 1, pp. 61–73, 2018. doi: <https://doi.org/10.12989/sem.2018.66.1.061>.
- [13] F. Tornabene, N. Fantuzzi, M. Baccocchi, and E. Viola, “Mechanical behaviour of damaged laminated composite plates and shells: Higher-order Shear Deformation Theories”, *Composite Structures*, vol. 189, pp. 304–329, Apr. 2018. doi: 10.1016/j.compstruct.2018.01.073.
- [14] Z. Q. Cheng and R. C. Batra, “Deflection relationships between the homogeneous Kirchhoff plate theory and different functionally graded plate theories”, *Archives of Mechanics*, vol. 52, no. 1, pp. 143–158, 2000.

- [15] E. Cheshmeh, M. Karbon, A. Eyvazian, D. won Jung, M. Habibi, and M. Safarpour, "Buckling and vibration analysis of FG-CNTRC plate subjected to thermo-mechanical load based on higher order shear deformation theory", *Mechanics Based Design Structures and Machines*, vol. 50, no. 4, pp. 1137–1160, 2022. doi: 10.1080/15397734.2020.1744005.
- [16] K. Kulkarni, B. N. Singh, and D. K. Maiti, "Analytical solution for bending and buckling analysis of functionally graded plates using inverse trigonometric shear deformation theory", *Composite Structures*, vol. 134, pp. 147–157, 2015. doi: 10.1016/j.compstruct.2015.08.060.
- [17] B. A. S. Shariat, R. Javaheri, and M. R. Eslami, "Buckling of imperfect functionally graded plates under in-plane compressive loading", *Thin-Walled Structures*, vol. 43, no. 7, pp. 1020–1036, 2005. doi: 10.1016/j.tws.2005.01.002.
- [18] S. Abrate, "Free vibration, buckling, and static deflections of functionally graded plates", *Composites Science and Technology*, vol. 66, no. 14, pp. 2383–2394, 2006. doi: 10.1016/j.compscitech.2006.02.032.
- [19] I. Mechab, H. A. Atmane, A. Tounsi, H. A. Belhadj, and E. A. A. Bedia, "A two variable refined plate theory for the bending analysis of functionally graded plates", *Acta Mechanica Sinica*, vol. 26, no. 6, pp. 941–949, Dec. 2010. doi: 10.1007/s10409-010-0372-1.
- [20] M. Bodaghi and A. R. Saidi, "Levy-type solution for buckling analysis of thick functionally graded rectangular plates based on the higher-order shear deformation plate theory", *Applied Mathematical Modelling*, vol. 34, no. 11, pp. 3659–3673, 2010. doi: 10.1016/j.apm.2010.03.016.
- [21] M. Bourada and E. A. Adda Bedia, "Analyse du flambement des structures hétérogènes sandwichs sous chargement thermique en utilisant les théories à ordre élevé", 2013.
- [22] T. Becheri, K. Amara, M. Bouazza, and N. Benseddiq, "Buckling of symmetrically laminated plates using nth-order shear deformation theory with curvature effects", *Steel and Composite Structures*, vol. 21, no. 6, pp. 1347–1368, 2016. doi: 10.12989/scs.2016.21.6.1347.
- [23] J. L. Pelletier and S. S. Vel, "An exact solution for the steady-state thermoelastic response of functionally graded orthotropic cylindrical shells", *International Journal of Solids and Structures*, vol. 43, no. 5, pp. 1131–1158, 2006. doi: 10.1016/j.ijsolstr.2005.03.079.
- [24] A. M. Zenkour, "Benchmark trigonometric and 3-D elasticity solutions for an exponentially graded thick rectangular plate", *Archive Applied Mechanics*, vol. 77, no. 4, pp. 197–214, Feb. 2007. doi: 10.1007/s00419-006-0084-y.
- [25] S. A. Ambartsumyan, "Theory of anisotropic plate", *Technomic Publication Company*, 1969.
- [26] K. Soldatos, "A transverse shear deformation theory for homogeneous

- monoclinic plates,” *Acta Mechanica*, vol. 94, no. 3, pp. 195–220, 1992.
- [27] M. Touratier, “An efficient standard plate theory”, *International Journal of Engineering Science*, vol. 29, no. 8, pp. 901–916, 1991. doi: 10.1016/0020-7225(91)90165-Y.
- [28] M. Karama, K. S. Afaq, and S. Mistou, “Mechanical behaviour of laminated composite beam by the new multi-layered laminated composite structures model with transverse shear stress continuity”, *International Journal Solids Structure*, vol. 40, no. 6, pp. 1525–1546, 2003. doi: 10.1016/S0020-7683(02)00647-9.
- [29] N. Grover, D. K. Maiti, and B. N. Singh, “A new inverse hyperbolic shear deformation theory for static and buckling analysis of laminated composite and sandwich plates”, *Composite Structures*, vol. 95, pp. 667–675, Jan. 2013. doi: 10.1016/j.compstruct.2012.08.012.
- [30] A. Benbakhti, M. B. Bouiadjra, N. Retiel, and A. Tounsi, “A new five unknown quasi-3D type HSDT for thermomechanical bending analysis of FGM sandwich plates”, *Steel and Composite Structures*, vol. 22, no. 5, pp. 975–999, Dec. 2016. doi: 10.12989/scs.2016.22.5.975.
- [31] A. Meftah, A. Bakora, F. Z. Zaoui, A. Tounsi, and E. A. A. Bedia, “A non-polynomial four variable refined plate theory for free vibration of functionally graded thick rectangular plates on elastic foundation”, *Steel and Composite Structures*, vol. 23, no. 3, pp. 317–330, 2017. doi: 10.12989/scs.2017.23.3.317.
- [32] J. N. Reddy, “Analysis of functionally graded plates”, *International Journal Numerical Methods in Engineering*, vol. 47, no. 1-3, pp. 663–684, 2000. doi: 10.1002/(SICI)1097-0207(20000110/30)47:1/3<663::AID-NME787>3.0.CO;2-8.
- [33] C.-P. P. Wu and H.-Y. Y. Li, “An RMVT-based third-order shear deformation theory of multilayered functionally graded material plates”, *Composite Structures*, vol. 92, no. 10, pp. 2591–2605, 2010. doi: 10.1016/j.compstruct.2010.01.022.
- [34] H.-T. Thai and D.-H. Choi, “A simple first-order shear deformation theory for the bending and free vibration analysis of functionally graded plates”, *Composite Structures*, vol. 101, pp. 332–340, 2013. doi: 10.1016/j.compstruct.2013.02.019.
- [35] E. Carrera, S. Brischetto, and A. Robaldo, “Variable Kinematic Model for the Analysis of Functionally Graded Material plates”, *AIAA Journal*, vol. 46, no. 1, pp. 194–203, Jan. 2008. doi: 10.2514/1.32490.
- [36] C.-P. Wu, K.-H. Chiu, and Y.-M. Wang, “RMVT-based meshless collocation and element-free Galerkin methods for the quasi-3D analysis of multilayered composite and FGM plates”, *Composite Structures*, vol. 93, no. 2, pp. 923–943, 2011. doi: 10.1016/j.compstruct.2010.07.001.
- [37] A. M. Zenkour, “Generalized shear deformation theory for bending analysis of functionally graded plates”, *Applied Mathematical*

- Modelling*, vol. 30, no. 1, pp. 67–84, 2006. doi: 10.1016/j.apm.2005.03.009.
- [38] J. L. L. Mantari, A. S. Oktem, C. Guedes Soares, and C. G. Soares, “Bending response of functionally graded plates by using a new higher order shear deformation theory”, *Composite Structures*, vol. 94, no. 2, pp. 714–723, 2012. doi: 10.1016/j.compstruct.2011.09.007.
- [39] T.-K. K. Nguyen, “A higher-order hyperbolic shear deformation plate model for analysis of functionally graded materials”, *International Journal Mechanics and Materials in Design*, vol. 11, no. 2, pp. 203–219, May 2015. doi: 10.1007/s10999-014-9260-3.
- [40] A. M. Zenkour, “A simple four-unknown refined theory for bending analysis of functionally graded plates”, *Applied Mathematical Modelling*, vol. 37, no. 20–21, pp. 9041–9051, 2013. doi: 10.1016/j.apm.2013.04.022.
- [41] J. L. Mantari and C. Guedes Soares, “Generalized hybrid quasi-3D shear deformation theory for the static analysis of advanced composite plates”, *Composite Structures*, vol. 94, no. 8, pp. 2561–2575, 2012. doi: 10.1016/j.compstruct.2012.02.019.
- [42] M. Mohammadi, A. R. Saidi, and E. Jomehzadeh, “A novel analytical approach for the buckling analysis of moderately thick functionally graded rectangular plates with two simply-supported opposite edges”, *Proceedings of the Institution of Mechanical Engineers, Part C: Journal Mechanical Engineering Science*, vol. 224, no. 9, pp. 1831–1841, 2010. doi: 10.1243/09544062JMES1804.
- [43] H.-T. Thai and D.-H. Choi, “An efficient and simple refined theory for buckling analysis of functionally graded plates”, *Applied Mathematical Modelling*, vol. 36, no. 3, pp. 1008–1022, Mar. 2012. doi: 10.1016/j.apm.2011.07.062.

Appendix

The program Maple calculates dimensionless deflection (\bar{W}) of plates (Al/Al_2O_3)

```
restart;
with(linalg);
pi:=evalf(Pi);
omega:=0;
t:=0;
h:=1;
m:=1;
n:=1;
a:=2*h;
Ec:=380;
```

```

Em:=70;
rhoc:=3800;
rhom:=2702;
p:=0.1;
b:=a;
qmn:=q0;
lambda:=m*pi/a;
beta:=n*pi/b;
nu:=0.3;
E(z):=Ec*exp(p*(z/h+0.5));rho(z):=rhoc*exp(p*(z/h+0.5));
C11:=E(z)/(1-nu^2);C22:=C11;C12:=nu*C11;C44:=E(z)/(2*(1+nu));
C55:=C44;C66:=C44;
f(z):=(2^5)*h*((z/((2^5)*h))-(1/3)*(z/(2*h))^3);g(z):=diff(f
(z),z);
II:=int(rho(z),z=-h/2..h/2);
I1:=evalf(int(rho(z)*z,z=-h/2..h/2));
I2:=evalf(int(rho(z)*z^2,z=-h/2..h/2));
J1:=evalf(int(rho(z)*f(z),z=-h/2..h/2));
J2:=evalf(int(rho(z)*z*f(z),z=-h/2..h/2));
K2:=evalf(int(rho(z)*(f(z))^2,z=-h/2..h/2));
A11:=int(C11,z=-h/2..h/2);
A22:=int(C22,z=-h/2..h/2);
A12:=int(C12,z=-h/2..h/2);
A66:=int(C66,z=-h/2..h/2);
B11:=int(C11*z,z=-h/2..h/2);
B22:=int(C22*z,z=-h/2..h/2);
B12:=int(C12*z,z=-h/2..h/2);
B66:=int(C66*z,z=-h/2..h/2);
D11:=int(C11*z^2,z=-h/2..h/2);
D22:=int(C22*z^2,z=-h/2..h/2);
D12:=int(C12*z^2,z=-h/2..h/2);
D66:=int(C66*z^2,z=-h/2..h/2);
Bs11:=evalf(int(C11*f(z),z=-h/2..h/2));
Bs22:=evalf(int(C22*f(z),z=-h/2..h/2));
Bs12:=evalf(int(C12*f(z),z=-h/2..h/2));
Bs66:=evalf(int(C66*f(z),z=-h/2..h/2));
Ds11:=evalf(int(C11*z*f(z),z=-h/2..h/2));
Ds22:=evalf(int(C22*z*f(z),z=-h/2..h/2));
Ds12:=evalf(int(C12*z*f(z),z=-h/2..h/2));
Ds66:=evalf(int(C66*z*f(z),z=-h/2..h/2));
Hs11:=evalf(int(C11*(f(z))^2,z=-h/2..h/2));
Hs22:=evalf(int(C22*(f(z))^2,z=-h/2..h/2));
Hs12:=evalf(int(C12*(f(z))^2,z=-h/2..h/2));
Hs66:=evalf(int(C66*(f(z))^2,z=-h/2..h/2));

```

```

As44:=evalf(int(C44*(g(z))^2,z=-h/2..h/2));
As55:=evalf(int(C55*(g(z))^2,z=-h/2..h/2));
lambda:=m*pi/a;
mu:=n*pi/b;
k11:=A11*(lambda)^2+A66*(mu)^2;
k12:=(A12+A66)*lambda*mu;
k13:=-B11*(lambda)^3-(B12+2*B66)*lambda*(mu)^2;
k14:=evalf(-Bs11*(lambda)^3-(Bs12+2*B66)*lambda*(mu)^2);
k22:=A66*(lambda)^2+A22*mu*(lambda)^2;
k23:=-B22*(mu)^3-(B12+2*B66)*mu*(lambda)^2;
k24:=evalf(-Bs22*(mu)^3-(Bs12+2*B66)*mu*(lambda)^2);
k33:=D11*(lambda)^4+2*(D12+2*D66)*(mu)^2*(lambda)^2+D22*(mu)^4;
k34:=evalf(Ds11*(lambda)^4+2*(Ds12+2*D66)*(mu)^2*(lambda)^2+
Ds22*(mu)^4);
k44:=Hs11*(lambda)^4+2*(Hs12+2*Hs66)*(mu)^2*(lambda)^2+Hs22*(
mu)^4+As55*(lambda)^2+As44*(mu)^2;
m11:=II;
m22:=m11;
m12:=0;
m13:=-lambda*I1;
m14:=-lambda*J1;
m23:=-mu*I1;
m24:=-mu*J1;
m33:=II+I2*((lambda)^2+(mu)^2);
m34:=J2*((lambda)^2+(mu)^2);
m44:=K2*((lambda)^2+(mu)^2);
R:=Matrix([[ k11 , k12 , k13 , k14 ],
[ k12 , k22 , k23 , k24 ],
[ k13 ,k23 ,k33 , k34 ],
[ k14 , k24 , k34 , k44 ]]);
M:=Matrix([[ m11 , m12 ,m13 , m14 ],
[ m12 , m22 , m23 ,m24 ],
[ m13 , m23 , m33 , m34 ],
[ m14 , m24 , m34 , m44 ]]);
X:=R-(omega)^2*M;
q:=Vector[column]([ 0 , 0 ,qmn , 0 ]);
sol:=linsolve(X,q);
umn:=sol[1];
vmn:=sol[2];
xmn:=sol[3];
ymn:=sol[4];
x:=a/2;y:=b/2;
u0:=umn*cos(lambda*x)*sin(mu*y)*exp(i*omega*t);
v0:=vmn*sin(lambda*x)*cos(mu*y)*exp(i*omega*t);

```

```
w0:=xmn*sin(lambda*x)*sin(mu*y)*exp(i*omega*t);  
phi0:=ymn*sin(lambda*x)*sin(mu*y)*exp(i*omega*t);  
w:=w0;  
W (bar):=(10*Ec*(h)^3*w)/((q0*(a)^4));
```

Applied Machine Learning to Estimate Length of Separation and Reattachment Flows as Parameter Active Flow Control in Backward Facing Step

Ahmad Fakhri Giyats, Mohamad Yamin*, Cokorda Prapti Mahandari
Department of Mechanical Engineering, Faculty of Industrial Technology,
Gunadarma University, Depok 16424, INDONESIA
*mohay@staff.gunadarma.ac.id

ABSTRACT

Recently, large amounts of data from experimental measurements and simulations with high fidelity have extensively accelerated fluid mechanics advancement. Machine learning (ML) offers a wealth of techniques to extract data that can be translated into knowledge about the underlying fluid mechanics. Backward-Facing Step (BFS) is well-known for its application to fluid mechanics, particularly flow turbulence. Typically, a numerical approach can be used to understand the flow phenomena on BFS. In some instances, numerical investigations have a computational time limitation. This paper examines the application of ML to predict reattachment length on BFS flow. The procedure begins with a simulated meshing sensitivity of 1.27 cm in step height. This numerical analysis was conducted in the turbulent zone with a Reynolds number between 35587 and 40422. OpenFOAM® was used to perform numerical simulations using the turbulence model of k-omega shear stress transport. ML employed information in the form of Velocity and Pressure at every node to represent the type of turbulence. Using Recurrent Neural Networks (RNNs) as the most effective model to predict reattachment length values, the reattachment length was predicted with a Root Mean Square Error of 0.013.

Keywords: Data-Driven; Machine-Learning; Fluids Mechanics; Backward-Facing Step

Introduction

In recent years, fluid mechanics has been a field full of data and complex problems. Many conventional research data, flow field observations, and extensive numerical simulations are accessible, accompanied by the development of high computing. The advantages of developing high computing-based programming architecture, current experimental capabilities, measurement methodologies, and "Big Data" have become indispensable to the advancement of fluid mechanics. In the meantime, a suitable and efficient method for processing enormous data quantities, such as the "cluster database," has been developed by Perlman et al. [1] and Giovanni [2] for data analysis and disclosure, which can be carried out.

The rapid development of data has spread across various disciplines, so obtaining potential information quickly and accurately is the focus of research in this decade. Considering some hardware architecture improvements, storage, more efficient data transmission, rapid algorithm development, and development of open source-based frameworks, as well as data-driven research methods, have received much attention from academics and commercial opportunities. Deep Learning (DL), one with a neural network technique, has distinct benefits when confronted with nonlinear high dimensional problems, which are rapidly integrated into fluid mechanic research.

Machine learning classes are supervised, semi-supervised, and unsupervised learning [3]. With many advantages, machine learning has been gradually applied to reduced-order models, prediction, reconstruction, closed turbulence models, and active flow control systems in fluid mechanics data analysis [3]-[4]. Rowley et al. [5] used Proper Orthogonal Decomposition (POD) to examine near-wall flow features at varying Reynolds numbers in a turbulent channel flow.

The integration of machine learning with fluid dynamics has a history. Teo et al. [6] developed a neural network (neural network) to create particles in the photo to measure the velocity. The same is done by adding how many neural layers (multi-layer). The development continues, and the application of neural networks for adaptive controllers is carried out to reduce turbulence barriers [7]. This study describes a simple control network that employs suction and blowing based on the shear stress of the wall in the span direction to reduce up to 20 percent less wall friction. At this period, neural network applications are still difficult to comprehend, and neural network development is still in its infancy.

The machine learning algorithm will simulate some fluid features, such as the lift profile given a specific airfoil geometry, and provide a proxy that can be optimized. Utilizing machine learning (ML) to tackle the fluid optimization problem directly is also possible by developing a machine learning model to influence the fluid's behaviour towards some engineering

aim via active control. Besides, many successful advances in using DL techniques to accelerate topology optimization [8].

In 2021, Usman et al. [9] were concerned with Fluid-Structure Interaction (FSI) in machine component design. Computational Fluid Dynamics (CFD) accuracy strongly comes from mesh size; hence, the computational cost is proportional to the resolution of tiny features. Multiple physics and scales exponentially increase the computing complexity, extending the process's duration. ML has demonstrated a highly promising ability to predict solutions for differential equations. It has provided excellent approximations in a fraction of the time required by standard simulation techniques [9].

In 2022, Vinuesa et al. [10] had a perspective on ML. They highlighted some areas of the highest potential impact, including accelerating direct numerical simulations, improving turbulence closure modelling, and developing enhanced reduced-order models.

Based on the literature study above, DL is still being developed to estimate reattachment lengths in flow separation [11] with instability in the separation flow [12]. Reattachment length refers to the distance the separated flow returns to the surface. The reattachment length can be calculated using numerical models such as Unsteady Reynolds-Averaged Navier-Stokes (URANS) or Large Eddy Simulation (LES). In fluid flow analysis, reattachment length is commonly employed to determine how the flow separates and returns to the surface [11].

Determining the reattachment length is difficult to estimate, so this research's estimation is intended to validate changes due to changing parameters (pressure, velocity, C_f). A robust system has been developed in this case to determine the reattachment length accurately. Where the reattachment length is one of the sequences to minimize bubble separation, if it is reduced, it can be avoided to a minimum (drag reduction for external flow, pressure drop for internal flow) with the aim that it can be applied to active flow control or fluid power systems.

The following is the structure of this paper: The section "Methodology" demonstrates our proposed technique and the experimental details. The following section provides the results and discussion. The last section summarizes our research.

Methodology

Selection turbulence models

Consider the flow of fluid across a thin plate from the horizontal direction. When a fluid constructed velocity to a plate's leading edge, the layer of laminar boundary form begins. The flow is highly anticipated in the locality. A small distance from the leading edge, the transition zone evolves into a fully-fledged

turbulent region, as depicted schematically in Figure 1(a) [13]. The Reynolds number characterizes the flow transition between the three regions over the flat plate. The velocity and pressure fields can be predicted using the Navier-Stokes equations in a steady-state laminar regime. The flow is assumed to be steady and uniform to predict the flow behaviour accurately. The Reynolds number remains constant in the laminar regime, so no averaging is required. Figure 1(b) depicts the fundamental physical and geometric models of the Backward-Facing Step (BFS) (under the 2-D scheme). The BFS methodology characterized a uniform velocity inflow, which may be either turbulent or laminar, originating from a channel of height (H). A step of height (h) is also present on the lower or upper sides. As depicted in Figure 1(b), The BFS flow field consists of several regions: the separated shear layer, the recirculation shear layer, the attached or recovery region, and the reattachment region.

Figure 1(c) depicts a fundamental model encompassing the three essential characteristics of a separated flow: reattachment length, vortex evolution, and free shear flow separation.

Solving the equations of Navier-Stokes is challenging because the Reynolds number fluctuates with time and space, leading to minor flow eddies and oscillations within an insufficiently short period. Under such conditions, the Reynolds Averaged Navier Stokes formulation is preferable.

The turbulent flow close to a flat wall can be divided into four categories: "buffer layer," "laminar or viscous sublayer," "free stream," and "transition zone." Eventually, the flow turns completely turbulent at the transition zone, and the mean fluid velocity is related to the distance from a flat plate or stationary wall. Consequently, this region is sometimes referred to as the log law region. The laminar sublayer is too thin in the turbulence model. Hence, it is beneficial to approximate this region.

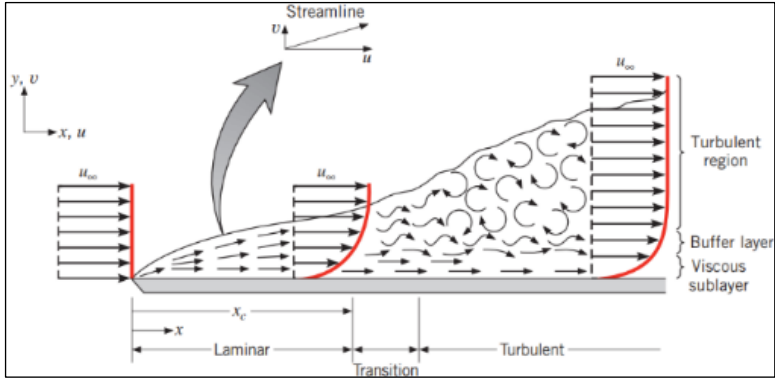
A more detailed review of problems and successes of turbulent computing flow and the appropriate sources of turbulence modelling was explained by Argyropoulos et al. [16].

RANS turbulence models

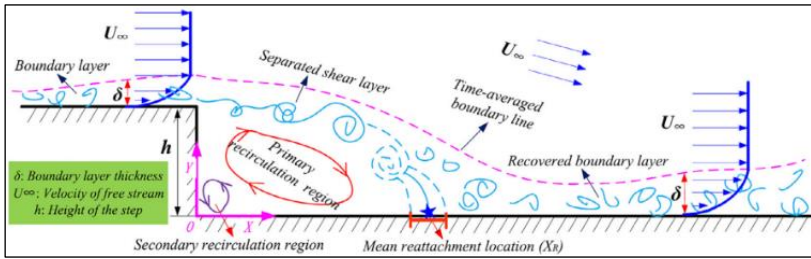
First, eddy viscosity with zero equations is the simplest turbulence model. The first model is zero-equation, embracing the mixing-length concept developed by Prandtl (the equivalent of a gas's mean free paths) hypothesis [17].

Zero-equation models are insufficient for simulating every flow type because they disregard diverse physical characteristics, such as non-local effects on turbulent eddy viscosity. In addition, flow history is not considered to overcome these deficiencies.

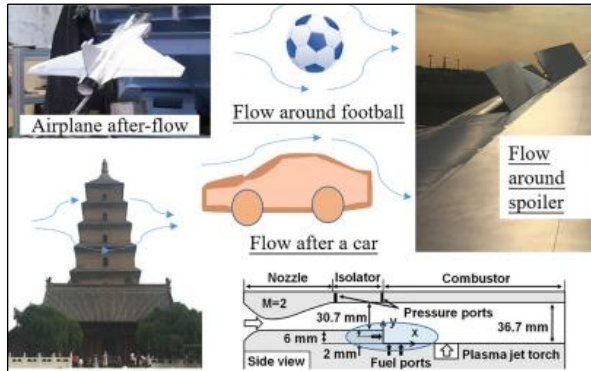
Second, similar to the turbulent model with zero-equation, a length scale must be specified for turbulence in this model. Results indicate that the One-equation eddy-viscosity model is unsuitable for indoor environments due to its inability to replicate turbulent flow at corners in the presence of flow barriers. This model demonstrates promising findings for zero flow separation.



(a)



(b)



(c)

Figure 1: Generalization theory of BFS and their applications; (a) fluid flow over thin horizontal plate [13], (b) schematic BFS flow evolutions [14], and (c) various BFS model applications [15]

Third, two equations of the eddy-viscosity answer the kinetic energy dissipation rate and kinetic energy from the Reynolds transport equation. This model includes a partial differential transport equation and the expression for turbulent kinetic energy k' k -epsilon model (k - ϵ). Launder and Spalding's [18] one of the well-known models for modelling indoor and outdoor airflow is the k - ϵ model [2], [18].

The RNG k -epsilon (RNG k - ϵ) employs statistical techniques to eliminate motion characteristics with low scales methodically. The RNG k -epsilon is obtained using a statistical technique. The fluid flow regulating equation is adjusted concerning significant motion elements. The RNG k -model cannot predict the effect of corners due to restrictions on using a coarse grid near walls and corners [19]-[20].

In the k -omega model (k - ω), Omega- ω is the ratio of (dissipation rate of energy from turbulent kinetic) over k (turbulent flow's kinetic energy). Omega- ω is the conversion rate of turbulent kinetic energy (k) to internal energy. Omega- ω represents the turbulence scale. Comparing the k - ϵ model to the k - ω model, The k - ω model is more accurate in predicting places with unfavourable pressure flow conditions [21]. Several k - ω models have been developed to address specific flow problems that the traditional model cannot adequately evaluate. These models include the shear stress transport (SST) k - ω models and customized k - ω models. The (SST) k - ω model is commonly used when accurate flow predictions near wall boundaries are required, owing to its high efficacy. The (SST) k - ω is similar to the k - ϵ model and yields virtually identical results for various flow circumstances.

Large Eddy Simulation (LES) and Detached Eddy Simulation (DES)

Higher computer capacity and user skills are required for LES. LES uses sub-grid scale eddies filtering to solve the numerical simulation equation for large eddies. Comparing LES, k - ω , and RNG k - ω for air circulation analysis in a room environment, the study conducted by Tian and colleagues provides evidence that utilizing all three turbulence models results in a precise prediction of the experimental configuration [14]. In addition, he concluded that LES provides more accurate results than RANS models and that the results are close to the actual conditions. The LES technique can validate the k - ϵ model, given its capacity to address complex flow phenomena and consider the wall function.

Some researchers use the DES model for complex enclosed airflow analysis, but it does not play a significant role in cold storage airflow analysis. RANS models are not good at predicting massive separation in free shear flows, whereas the DES model is suitable for very high flow instability.

The performance and cost of DES are situated between those of the LES and RANS models. In BFS analysis, achieving steady-state conditions within the chamber is crucial. Once the flow has been properly established, there are

minimal perturbations. Utilizing LES or DES for such needs is an expensive and time-consuming endeavour.

Recurrent Neural Networks (RNNs)

RNNs are neural network data sequences where each value depends on previous values. This RNN is a feed-forward network with feedback loops [22]. RNNs are superior at simulating temporal dynamic behaviour to traditional feed-forward neural networks because they bring the concept of time to them [23]. Some RNNs units maintain a previous time step's internal memory state, denoting a context window of indefinite size. Numerous RNNs applications have been proposed and researched [24]. Basic RNNs and long short-term memory are the two most common units described in the following section.

Basic recurrent neural networks

As shown in Figure 2(a), The term of input time series with T the model of the sample is $\{x_t\}_{t=1}^T$. And the term of the output of models containing T samples of the specified time series is $\{s_t\}_{t=1}^T$. At time t , the input of models (x_t) and it produces the result (prediction), S_t . The following equations define a fundamental RNNs unit:

$$S_t = \tanh(x_t u + S_{t-1} \omega + b) \quad (1)$$

The tangent function of hyperbolic, $\tanh(x) = \frac{e^x - e^{-x}}{e^x + e^{-x}}$. Moreover, the model's parameters u , ω , and b are given. In addition to the current input x_t , the model at time t also receives its output from the prior period (s_{t-1}). The hyperbolic tangent activation function's argument is the linear combination of $x_t u + S_{t-1} \omega + b$, which enables the unit to simulate nonlinear input-output relationships. Additional activation functions, such as logistic functions, rectified linear units (ReLU), or sigmoid functions, may be used in various implementations [25].

Long short-term memory networks

RNNs are known to exhibit the issue of limited "short-term memory": historical data is utilized to generate forecasts if a sequence is of adequate length. The inability to effectively transmit vital information from preceding eras to subsequent ones, such as significant patterns from the same month in previous years. LSTM is a neural network that addresses short-term memory problems by utilizing gates to preserve and combine significant long-term memory with the latest input [26]. LSTM paved the path for substantial advancements in various domains, including speech recognition and natural language processing [27].

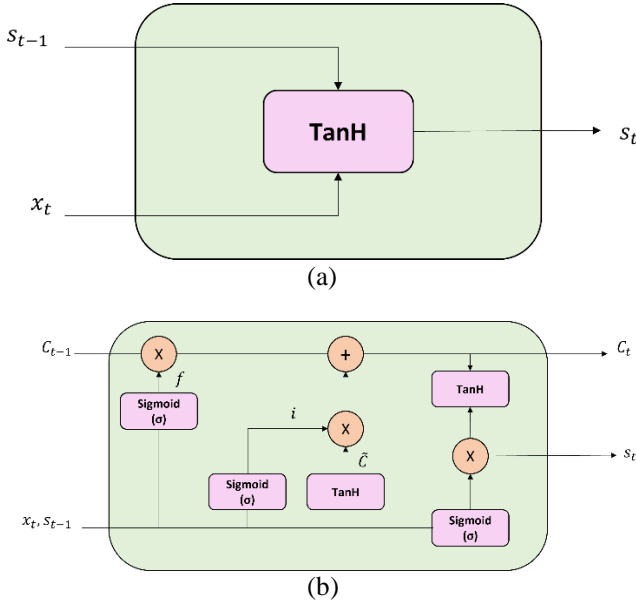


Figure 2: Illustration of recurrent neural networks; (a) illustration of the basic-RNNs unit, and (b) illustration of LSTM unit

Following Figure 2(b), it can be observed that each line facilitates the transmission of an entire vector value from the output of a given node to serve as the input for subsequent nodes. The circular symbols in orange signify pointwise operations, while the rectangular shapes in pink represent the layers of a trained neural network. When lines merge, they become one, whereas when lines fork, their material is copied and sent to separate locations.

The LSTM unit can selectively "remember" or "forget" information through the precise control of three gates, namely the input, forget, and output, which a specific memory cell state facilitates. The gates control the flow of data into and out of the state of memory cells. The following equations define an LSTM unit:

$$i = \sigma(x_t u^i + S_{t-1} \omega^i + b^i) \quad (2)$$

$$f = \sigma(x_t u^f + S_{t-1} \omega^f + b^f) \quad (3)$$

$$o = \sigma(x_t u^o + S_{t-1} \omega^o + b^o) \quad (4)$$

$$\tilde{c} = \tanh(x_t u^c + S_{t-1} \omega^c + b^c) \quad (5)$$

$$c_t = f \times c_{t-1} + i \times \tilde{c} \quad (6)$$

$$s_t = o \times \tanh(c_t) \quad (7)$$

The logistic activation function or sigmoid is $\sigma(x) = \frac{1}{1+e^{-x}}$. The parameters learned to regulate the input gate i are u^i , ω^i , and b^i . The parameters learned that govern the forget gate f are u^f , ω^f , and b^f . The parameters learned to control the output gate o are u^o , ω^o , and b^o , and c is the newly identified candidate activation for the condition of the cell u^c , ω^c , and b^c . The cell state c_t is utilizing a linear combination update $c_t = f \times c_{t-1} + i \times \tilde{c}$, where the previous cell state value is c_{t-1} . The input gate i identifies the aspects of the candidate c will be utilized to alter the status of a memory cell, while the forget gate f decides which elements of the previous memory are retrieved (c_{t-1}) will be deleted. The output gate o then determines which portions of the newly updated cell state (c_{t-1}) will be displayed in the output s_t .

Evaluation metrics

Under Aparicio et al. [28], we publish our findings on evaluation metrics with Root Mean Squared Error (RMSE). The RMSE is calculated using:

$$RMSE = \sqrt{\frac{1}{T} \sum_{t=1}^T (x_t - \hat{x}_t)^2} \quad (8)$$

where x_t is the Reynolds change rate for t , and \hat{x}_t is the corresponding prediction.

Model geometry

This study uses numerical simulation to develop and solve the model, meshing, numerical equation, and boundary condition setup. In addition, this work utilizes Python with the RNNs Method to support the neural networks. The main method in this study is divided into three major groups: training cases, machine learning models, and test cases. This study's flow methodology is explained in Figure 3.

In the training case, it is the stage for generating datasets that will be used in the ML model stage; at this stage, the resulting dataset is in the form of fluid characteristics at each coordinate spread over the slicing plane and image capture where each data is obtained at each speed interval. The ML model is the next stage of research, namely creating a model that can estimate the reattachment distance. In constructing this model, the LSTM architecture is used.

In the final stage, the Test case is used to prove and evaluate the model that has been made.

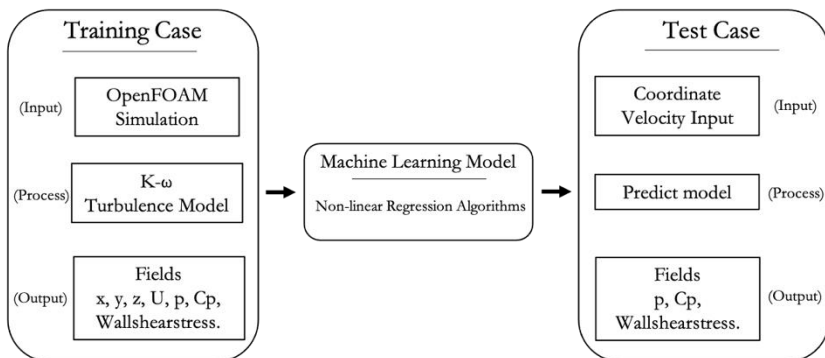


Figure 3: The current research framework

Before starting the numerical simulations with various configurations of multiple components and levels, the CFD simulation program must be validated as suitable software for subsequent step activities. The validation technique aims to validate that the computational fluid dynamics with several parameter settings accurately depict the actual conditions and are consistent with experimental findings. In addition, after completing the validation procedure, the following step is to simulate a model. The estimation procedure is concluded by utilizing RNNs and analysing the evaluation metrics.

BFS is one of the essential separation-flow models for theoretical and technical advancement. Airfoils at extreme attack angles, spoiler flows, inlet tunnel flow of an engine or inside a condenser/combustor, flow separation behind a vehicle, and flow around a boat or a complex building are examples of daily applications for backward-facing step flow [15].

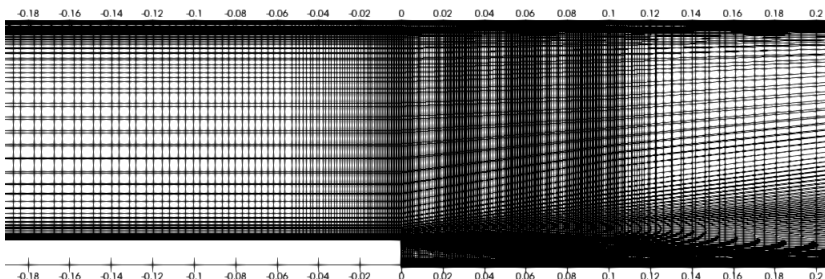


Figure 4: Cross-section of BFS fine mesh

BFS flows known as "backward flow," "sudden expansion flows," "back-step flow," "circular expanding flow," or "diverging channel" involve the fundamental characteristics of general separation flows. It is ideal for two-dimensional topics discussed under certain flow conditions or with simple step geometries and has a three-dimensional nature. It is essential for separation flows over a wide Reynolds number range [15].

From a flow dynamics perspective, the BFS flow is characterized by enormous separation vortices in the backward step zone and a few minor vortices at the corner. Occasionally, complex vortex series can occur under certain physical and geometric conditions. Many researchers have compared predictions with validated turbulent models against existing data. BFS in turbulent flow at boundary walls is a common occurrence. The investigation of flow structure in the BFS has been rigorously examined and investigated in the literature, shown in Table 1.

Table 1: Recent study representative numerical studies of BFS

Title	Re	Method	$\Delta x/h$	Comment
McQueen et al. [29]	5000 - 6700	OpenFOAM	5 – 6.7	Incompressible
Sazhin et al. [30]	10, 389, 648	Direct Monte Carlo	0.7-2	Flowrate
Talib et al. [31]	5000 - 20000	CFD (fluent)	2-3	Heat transfer
Loksupapaiboon et al. [32]	15500	OpenFOAM	2-5	Incompressible

A model of the BFS is created using blockMesh OpenFOAM. Figure 4 shows the cross-section of the BFS. Additionally, the air is used as a working fluid in this task due to its simplicity and ease of operation. The model adapts the 2D Backward-Facing Step research, Langley Research Centre Turbulence Modelling Resource [33].

A mesh independence check was performed to make the solution more independent. In order to achieve the convergence criteria, the residual error was set to $10E-4$, and the mesh must be refined globally to obtain more acceptable mesh cells [34]. The mesh must be refined until the error is reduced. At 767,500 cells, mesh independence is achieved, as shown in Table 2.

Table 2: Number of cells in each case and mesh-dependent analysis
 $Re=36000$

Case	Coarse	Medium	Fine	Rumsey [33]
Number of cells	22,165	363,090	767,500	Experimental
Reattachment length (mm)	0.0835	0.0797	0.0786	0.0790

Coarse, medium, and fine are the three types of two-dimensional meshing. As depicted, three two-dimensional scenarios were executed to undertake a grid independence analysis. The cell number in each scenario is displayed in Table 2.

Table 3: Number of cells in each case and mesh-dependent analysis
 $Re=36000$

Indicator	Value
Points	942312
Internal Points	599800
Faces	2473755
Internal faces	2131245
Cells	767500

The distance from the "Step" to the point at which the direction of the Wallshear value receives a change called the reattachment length. Table 3 show compares the experimental results and the recorded reattachment length values.

Numerical setup

It is intended to obtain flow characteristics at this stage as it passes the BFS. Numerical computing is performed with a custom-built open-source CFD package. OpenFOAM® "blockMesh" creates geometries along the x , y , and z axes. As shown in Figure 4, the model is given a unit width for the two-dimensional condition [34].

For the meshing arrangement, the geometry is divided into six blocks with edge names: inlet, outlet, front and back, top wall, and bottom wall. Meshing is performed with a greater concentration of cells in the centre and along the walls. This method captures the turbulent flow in this region more accurately. A grid independence test was carried out [34]. In Table 3, the number of cells was shown in each case. The mesh arrangement for numerical computation is carried out on an acceptable mesh type with a 767500-cell number in the two-dimensional case.

Based on the selection in the section "RANS Turbulence Models," it was considered that k-omega turbulence is a good model for understanding the flow separation process, where the turbulence model will be used in this study. The Reynolds Averaged Navier Stokes equation, represented by equation [35], determines the flow in the Backward-Facing Step.

$$\bar{u}_j \frac{\partial \bar{u}_i}{\partial x_j} - \frac{\partial}{\partial x_j} \left[\nu_{eff} \left(\frac{\partial \bar{u}_i}{\partial x_j} + \frac{\partial \bar{u}_j}{\partial x_i} \right) \right] = - \frac{\partial p}{\partial x_i} \quad (9)$$

In this numerical computation, several equations are used in iterations. $K-\omega$ is built from the two-equation model for the turbulence kinetic energy (k) and turbulence-specific dissipation rate (ω) base model. The equation for the turbulence-specific dissipation rate is [35]:

$$\frac{\partial \epsilon}{\partial t} + \bar{u}_j \frac{\partial \epsilon}{\partial x_j} - \frac{\partial}{\partial x_j} \left[\left(\nu + \frac{\nu_T}{\sigma \epsilon} \right) \frac{\partial \epsilon}{\partial x_j} \right] = C_1 \frac{\epsilon}{k} \nu_T \frac{\partial \bar{u}_i}{\partial x_j} \left(\frac{\partial \bar{u}_i}{\partial x_j} + \frac{\partial \bar{u}_j}{\partial x_i} \right) - C_2 \frac{\epsilon^2}{k} \quad (10)$$

And the kinetic energy of turbulence:

$$\frac{\partial k}{\partial t} + \bar{u}_j \frac{\partial k}{\partial x_j} - \frac{\partial}{\partial x_j} \left[\left(\nu_{eff} \right) \frac{\partial k}{\partial x_j} \right] = \nu_T \frac{\partial \bar{u}_i}{\partial x_j} \left(\frac{\partial \bar{u}_i}{\partial x_j} + \frac{\partial \bar{u}_j}{\partial x_i} \right) - \epsilon \quad (11)$$

By defining the specific dissipation $\omega = \frac{\epsilon}{k}$ as the second transported variable, we have the $k-\omega$ model. The equation used for k is the same implemented for the $k-\epsilon$ model, while the equation for ω becomes:

$$\frac{\partial \omega}{\partial t} + \bar{u}_j \frac{\partial \omega}{\partial x_j} - \frac{\partial}{\partial x_j} \left[\left(\nu + \alpha_\omega \nu_T \right) \frac{\partial \omega}{\partial x_j} \right] = \alpha \frac{\omega}{k} \nu_T \frac{\partial \bar{u}_i}{\partial x_j} \left(\frac{\partial \bar{u}_i}{\partial x_j} + \frac{\partial \bar{u}_j}{\partial x_i} \right) - \beta \omega^2 \quad (12)$$

The turbulence viscosity SST is obtained using [36]:

$$\nu_t = \frac{\alpha_1 k}{\max(\alpha_1 \omega, b_1 F_{23})} \quad (13)$$

In isotropic turbulence, the kinetic energy of turbulence can be approximated by [36]:

$$k = \frac{3}{2} (I |u_{ref}|)^2 \quad (14)$$

where I represents intensity, and u_{ref} reference velocity. The turbulence-specific dissipation rate (ω) can be determined as [36]:

$$\omega = \frac{k^{0.5}}{C_\mu^{0.25} L} \quad (15)$$

where C_μ is equal to 0.09 (constant) and L as the reference length scale, the algorithm used is Semi-Implicit Method for Pressure-Linked Problems (SIMPLE) to solve model equations in OpenFOAM®.

The boundary conditions given are "constant velocity profile" for inlet faces, "zero gradients" for outlet faces, and "wall (no slip)" for lower and upper wall faces in the 2D case. Only the front and rear faces are "empty" in 2D [36].

$$Re = \frac{uL}{\nu} \tag{16}$$

where ν : kinematic viscosity of a fluid ($\nu = \mu/\rho$); μ : dynamic viscosity of a fluid; ρ : fluid density; L : characteristic length; u : inlet velocity (m/s) in temperature of air 25 °C.

This numerical method is used as a dataset which is carried out on variations in the entry velocity at the entry velocity interval, $V=44.2 - 50$ m/s with a training frequency of 0.01 m/s so that the data set obtained has a total of 600 datasets *.csv in the form of data reattachment length along the x-axis from step.

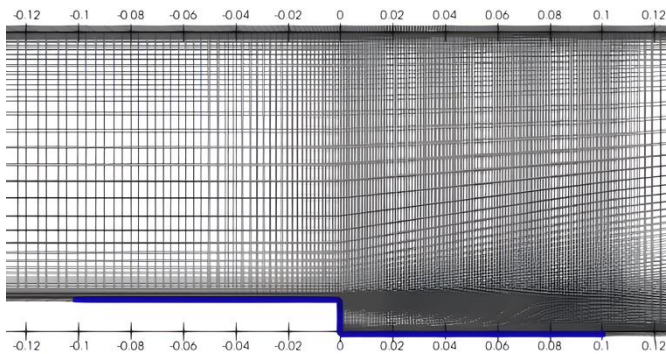


Figure 5: Sample area data of BFS (blue line)

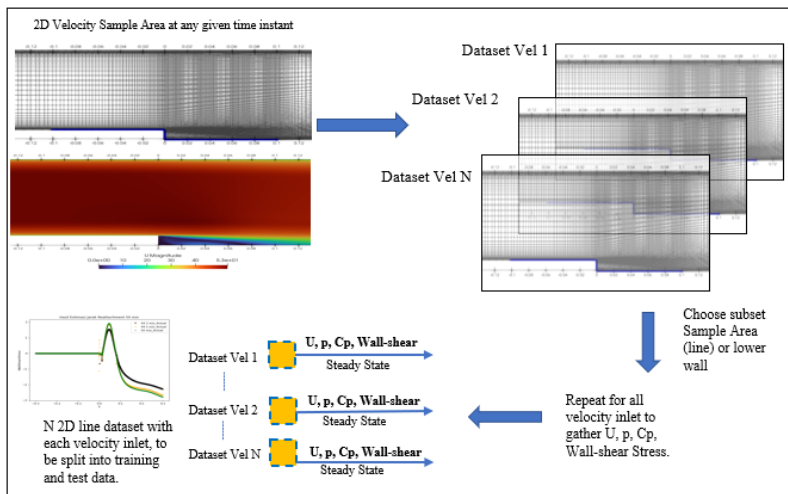


Figure 6: Extracting 2-D datasets process from a line of the flow field

Data from numerical simulations include the coefficient of pressure, pressure, wall shear, and velocity in the area of $1.0 < x > -1.0$ on the surface of the lower wall of the model, see Figure 5. The number of samples taken at each velocity is 3000 nodes.

Long short-term memory setup

The data obtained from the simulation results, namely the reattachment length (change in the value of the x-axis wall shear direction), is stored at each velocity increase in the simulation iteration process. Data is retrieved at 600 different velocities and extracted with a mechanism, as shown in Figure 6.

The data are combined in one *.csv document, which is then estimated by creating a model using the Neural Networks LSTM approach in subsection "long short-term memory networks." The estimation results are evaluated using Equation 8. This evaluation is a parameter of the model's feasibility to make estimates of the next Reynolds number.

Results and Discussion

Numerical simulation results

According to the specific model dimensions and operational conditions, the validation procedure is executed by evaluating the numerical simulation results with the actual research data from prior research [33]. The validation step must confirm that the CFD software depicts the actual state appropriately.

Based on the graph in Figure 7, the numerical data from prior research and numerical results from the initial setup for BFS with a modified Reynolds Number do not differ significantly. The disparity arises since the numerical simulation is conducted assuming the system conditions. Nonetheless, numerous numerical settings were challenging to manage. However, since both plots reflect the same trendline, there is no visible variation in value.

As shown in Figure 5, the sampling area for data from the coefficient of pressure (C_p), pressure (p), and wall shear (W_{ss_x}). From the simulation results, the data is processed to get the attachment length by measuring the step distance to the change in the direction of the wall shear value, which shows the reattachment point. Paraview is used for post-processing data to observe the structure as a contour graph.

Figure 8(a) is a flowing contour depicting a velocity contour plot for the case at 50 m/s as a mean velocity. From the results of numerical studies, each cell element is produced as coordinates with velocity, pressure, pressure coefficient, and shear stress (wall shear stress). The reattachment distance value is obtained from the selection of data on changes in the direction value of the wall shear stress in the lower wall (sample) area [34].

As shown in Figure 8(b), the reattachment point occurs between the distances 0.07-0.08 as a sign of the limit of changes in backward and forward

flow. Table 4 shows the reattachment distance with the inlet condition at 44.2 m/s, having a length of 0.07837 mm.

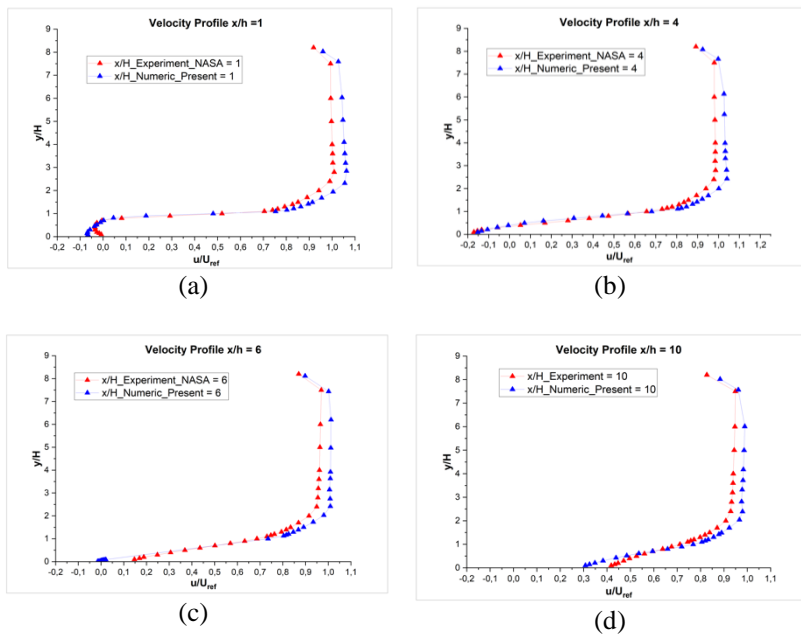


Figure 7: Comparison between the experimental [33] and the present numerical value with variation range "x" from step "h" based on the setup; (a) 1 x/h, (b) 4 x/h, (c) 6 x/h, and (d) 10 x/h

While in Tables 5 and 6 show the reattachment distance with inlet-velocity conditions of 48.2 m/s and 50.0 m/s. The result of reattachment length is 0.07747 mm and 0.774775 mm, respectively. This result has a slightly varied reattachment length value. Compared with the results of [33] with the same configuration, it also has a reattachment value of $6.26 \pm 0.1 x/h$ or 0.0790 mm. This difference is due to the instability phenomenon caused by a strong adverse pressure gradient. An adverse pressure gradient study has been carried out by Driver and Seigmeler [37].

From picking random data 44.2, 48.2, and 50.0 m/s. Observably, the distance of the reattachment points from the step decreases with continuing to increase velocity. Likewise, it can be seen in Figure 8(c), a wall shear graph from various velocities. From Figure 8(c), the green line is the wall shear line at 50 m/s as the mean velocity, which is relatively lower than the other two wall shears.

The results of each reattachment length from velocity variations are processed in a pre-processing stage. Processing is done by separating the overall data until there are only Reynolds number, velocity, and Wallshear_x values. The data changes as the velocity increases or the Reynolds number changes.

Figure 9(a) illustrates the results of separating the reattachment length data for each Reynolds number or velocity variation. Due to the small Reynolds range, the data was insufficient because of awake vorticities and different Reynold numbers.

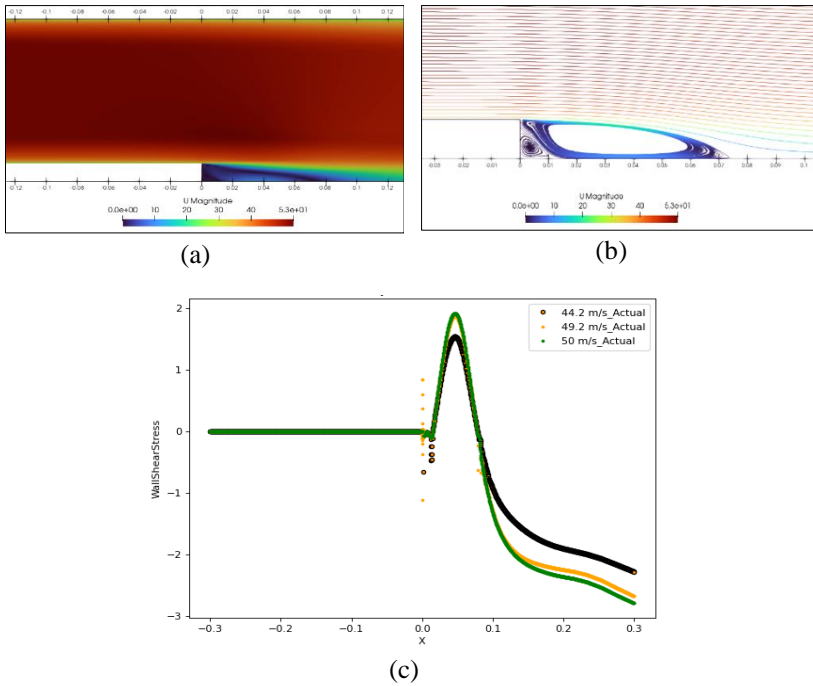


Figure 8: Numerical results of the current study; (a) freestream contour on Backward-Facing Step (50 m/s), (b) streamline contour on Backward-Facing Step (50 m/s), and (c) compared wall shear 44.2 m/s, 48.2 m/s, and 50 m/s

Table 4: Results of reattachment point simulation in velocity 44.2 m/s

Coor_x	C_p	p	Wss_x
0.0780781	-0.00306	-389.648	0.02241340
0.0783784	-0.00214	-209.273	0.00374021
0.0786787	-0.00124	-121.148	-0.0147147
0.0786787	-0.00036	-0.36035	-0.0328505

Table 5: Results of reattachment point simulation in velocity 48.2 m/s

Coor_x	Cp	p	Wss_x
0.0771772	-0.00208	-389.648	0.0423038
0.0774775	-0.00101	-209.273	0.0172398
0.0777778	-0.00009	-121.148	-0.0073336
0.0780782	0.00100	-0.36035	-0.0318490

Table 6: Results of reattachment point simulation in velocity 50.0 m/s

Coor_x	Cp	p	Wss_x
0.0771772	-0.00306	-389.648	0.02241340
0.0774775	-0.00214	-209.273	0.00374021
0.0777778	-0.00124	-121.148	-0.0147147
0.0780781	-0.00036	-0.36035	-0.0328505

Long Short-Term Memory (LSTM) result

The results of training simulations of numerical data have been sorted and tidied up based on variations in velocity. In this case, the data for training and testing is separated with a ratio of 80:20. As shown in Figure 9(b), the orange line represents the test data, while the line with blue colour represents the data used for testing.

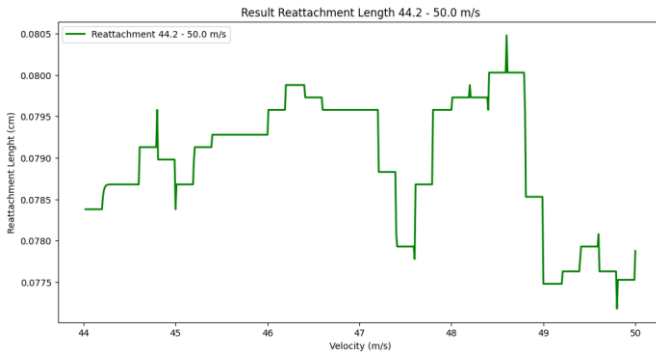
Data training is carried out from the model that has been created and modified. The "data loss" training process from every data was carried out. From Figure 10(a), it can be seen that the loss value continues to fall, at least when doing training. From the estimation results using the LSTM approach, the reattachment length value is obtained with a relatively more significant value (0.079745) than the numerical simulation results.

Figure 10(b) shows that the orange line is described as the prediction line, and the blue line is numerical data. Based on that figure, the nonlinear line was predicted from recent data, and the result was significantly close to the actual data value. The neural network employed is developing a base model in some previous studies with satisfactory results. After performing hypertuning to optimize parameters such as epoch, batch, iteration, and activation function, select the optimal model that can be used to estimate reattachment length. As evaluation metrics, the model's results are evaluated with Root Mean Square Error (RMSE) [28] metric: 0.013.

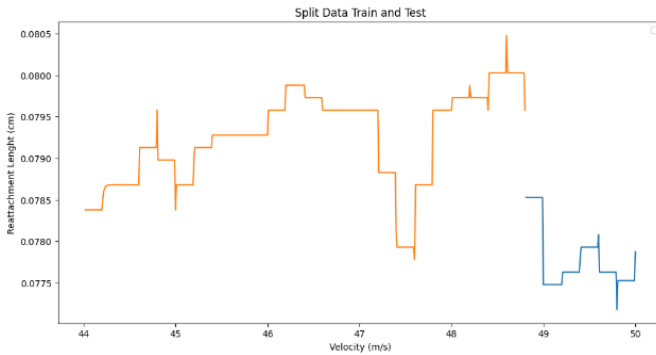
Conclusion

This study succeeded in carrying out a numerical study approach to describe the fluid structure and implement ML using the LSTM method. From the simulation process, the data change length of the reattachment based on the

velocity increase is used as a dataset to estimate and reduce the iteration time of the numerical simulation. The estimation results using the LSTM algorithm resulted in reasonably good training. Reattachment length can be estimated with parameter data in geometric configuration and suitable conditions in this study. This model can estimate the reattachment length. Using the machine learning model, it gets the predicted reattachment length from Re 35587 - 40422 variation with a step height of 1.27 cm. The numerical simulation process in modelling the flow structure is intended to optimize a system. Besides that, the simulation is used as data from the results of physical interactions. The machine learning methods can be applied by one of the trainings using a data processing approach to streamline time. The estimation process is expected to Velocity increase the process of consideration for optimizing the system.

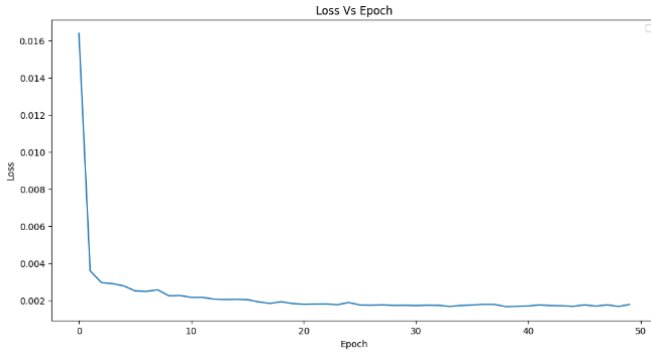


(a)

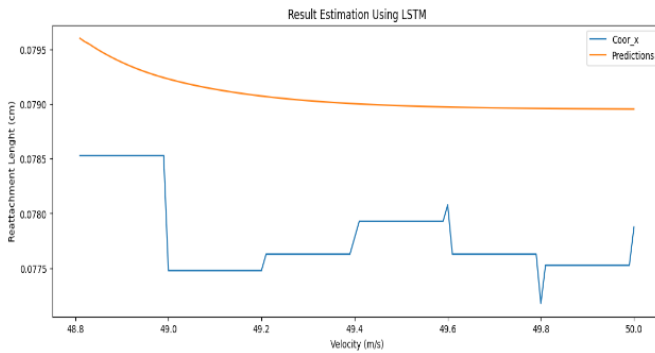


(b)

Figure 9: Results of the present numerical study and split data; (a) reattachment length vs. velocity, and (b) split data training and testing from the present setup



(a)



(b)

Figure 10: Results of long short-term memory; (a) Epoch vs. loss training process, and (b) result estimation prediction vs. simulation

Contributions of Authors

The authors confirm the equal contribution in each part of this work. All authors reviewed and approved the final version of this work.

Funding

This work was supported by the Ministry of Education and Culture, Research and Technology, Higher Education of the Republic of Indonesia [grant number 155/E5/PG.02.00.PT/2022].

Conflict of Interests

All authors declare that they have no conflicts of interest.

Acknowledgment

We thank the High Processing Computer Gunadarma University team for assistance in providing resource computation.

References

- [1] E. Perlman, R. Burns, Y. Li, and C. Meneveau, “Data exploration of turbulence simulations using a database cluster”, *Proceedings of the 2007 ACM/IEEE conference on Supercomputing - SC '07, Reno, Nevada: ACM Press*, p. 1, 2007. <https://doi.org/10.1145/1362622.1362654>
- [2] Giovanni Calzolari and W. Liu, “Deep learning to replace, improve, or aid CFD analysis in built environment applications: A review”, *Building and Environment*, vol. 206, p. 108315, 2021. <https://doi.org/10.1016/j.buildenv.2021.108315>
- [3] S. L. Brunton, B. R. Noack, and P. Koumoutsakos, “Machine Learning for Fluid Mechanics”, *Annual Review of Fluid Mechanics*, vol. 52, no. 1, pp. 477–508, 2020. <https://doi.org/10.1146/annurev-fluid-010719-060214>
- [4] B. Podvin, Y. Fraigneau, J. Jouanguy, and J.-P. Laval, “On Self-Similarity in the Inner Wall Layer of a Turbulent Channel Flow”, *Journal of Fluids Engineering*, vol. 132, no. 4, p. 041202, 2010. <https://doi.org/10.1115/1.4001385>
- [5] C. W. Rowley and S. T. M. Dawson, “Model Reduction for Flow Analysis and Control”, *Annual Review of Fluid Mechanics*, vol. 49, no. 1, pp. 387–417, 2017. <https://doi.org/10.1146/annurev-fluid-010816-060042>
- [6] C. L. Teo, K. B. Lim, G. S. Hong, and M. H. T. Yeo, “A neural net approach in analyzing photograph in PIV”, in *Conference Proceedings 1991 IEEE International Conference on Systems, Man, and Cybernetics, Charlottesville, VA, USA: IEEE*, pp. 1535–1538, 1991. <https://doi.org/10.1109/ICSMC.1991.169906>
- [7] C. Lee, J. Kim, D. Babcock, and R. Goodman, “Application of neural networks to turbulence control for drag reduction”, *Physics of Fluids*, vol. 9, no. 6, pp. 1740–1747, 1997. <https://doi.org/10.1063/1.869290>
- [8] J. Luo, Y. Li, W. Zhou, X. Chen, and W. Yao, “A Novel Method to Accelerate the Solution of Compliance Using Deep Learning for

- Topology Optimization”, *Advances in Mechanical Design*, vol. 111, pp. 1781–1792, 2022. https://doi.org/10.1007/978-981-16-7381-8_111
- [9] A. Usman, M. Rafiq, M. Saeed, A. Nauman, A. Almqvist, and M. Liwicki, “Machine Learning Computational Fluid Dynamics”, *2021 Swedish Artificial Intelligence Society Workshop (SAIS), Sweden: IEEE*, pp. 1–4, 2021. <https://doi.org/10.1109/SAIS53221.2021.9483997>
- [10] R. Vinuesa and S. L. Brunton, “Enhancing computational fluid dynamics with machine learning”, *Nature Computational Science*, vol. 2, no. 6, pp. 358–366, 2022. <https://doi.org/10.1038/s43588-022-00264-7>
- [11] D. Teso-Fz-Betoño, M. Juica, K. Portal-Porras, U. Fernandez-Gamiz, and E. Zulueta, “Estimating the Reattachment Length by Realizing a Comparison between URANS k-Omega SST and LES WALE Models on a Symmetric Geometry”, *Symmetry*, vol. 13, no. 9, p. 1555, 2021. <https://doi.org/10.3390/sym13091555>
- [12] H. Nowruzzi, S. S. Nourazar, and H. Ghassemi, “On the Instability of Two Dimensional Backward-Facing Step Flow using Energy Gradient Method”, *Journal of Applied Fluid Mechanics*, vol. 11, no. 1, pp. 241–256, 2018. <https://doi.org/10.29252/jafm.11.01.28235>
- [13] “1000+ COMSOL Multiphysics® Modeling Examples for Download”, 2022. [Online] <https://www.comsol.com/models> (Accessed Sep 05, 2022).
- [14] Z. F. Tian, J. Y. Tu, G. H. Yeoh, and R. K. K. Yuen, “On the numerical study of contaminant particle concentration in indoor airflow”, *Building and Environment*, vol. 41, no. 11, pp. 1504–1514, 2006. <https://doi.org/10.1016/j.buildenv.2005.06.006>
- [15] L. Chen, K. Asai, T. Nonomura, G. Xi, and T. Liu, “A review of Backward-Facing Step (BFS) flow mechanisms, heat transfer and control”, *Thermal Science and Engineering Progress*, vol. 6, pp. 194–216, 2018. <https://doi.org/10.1016/j.tsep.2018.04.004>.
- [16] C. D. Argyropoulos and N. C. Markatos, “Recent advances on the numerical modelling of turbulent flows”, *Applied Mathematical Modelling*, vol. 39, no. 2, pp. 693–732, 2015. <https://doi.org/10.1016/j.apm.2014.07.001>
- [17] W. Tollmien, H. Schlichting, and R. W. Riegels, “Über die ausgebildete Turbulenz,” in *Ludwig Prandtl Gesammelte Abhandlungen*, Springer, Berlin Heidelberg, pp. 736-751, 1961.
- [18] B. E. Launder and D. B. Spalding, “The numerical computation of turbulent flows”, *Computer Methods in Applied Mechanics and Engineering*, vol. 3, no. 2, pp. 269–289, 1974. [https://doi.org/10.1016/0045-7825\(74\)90029-2](https://doi.org/10.1016/0045-7825(74)90029-2)
- [19] V. Yakhot, S. A. Orszag, S. Thangam, T. B. Gatski, and C. G. Speziale, “Development of turbulence models for shear flows by a double expansion technique”, *Physics of Fluids A: Fluid Dynamics*, vol. 4, no. 7, pp. 1510–1520, 1992. <https://doi.org/10.1063/1.858424>

- [20] V. Yakhot and S. A. Orszag, “Renormalization group analysis of turbulence. I. Basic theory”, *Journal of Scientific Computing*, vol. 1, no. 1, pp. 3–51, 1986. <https://doi.org/10.1007/BF01061452>
- [21] P. G. Huang, P. Bradshaw, and T. J. Coakley, “Assessment of Closure Coefficients for Compressible-Flow Turbulence Models”, *NASA Technical Memorandum 103882*, p. 18, 1992.
- [22] D. P. Mandic and J. A. Chambers, “Recurrent Neural Networks for Prediction in Wiley Series”, in *Adaptive and Learning Systems for Signal Processing, Communications, and Control*. Chichester, UK, 2001. <https://doi.org/10.1002/047084535X>
- [23] J. Chung, C. Gulcehre, K. Cho, and Y. Bengio, “Empirical Evaluation of Gated Recurrent Neural Networks on Sequence Modeling”, *arXiv*, 2014. Accessed: Sep. 05, 2022. [Online]. Available: <http://arxiv.org/abs/1412.3555>
- [24] Z. C. Lipton, J. Berkowitz, and C. Elkan, “A Critical Review of Recurrent Neural Networks for Sequence Learning”, *arXiv*, 2015. <https://doi.org/10.48550/ARXIV.1506.00019>
- [25] P. Ramachandran, B. Zoph, and Q. V. Le, “Searching for Activation Functions,” *arXiv*, 2017. <https://doi.org/10.48550/ARXIV.1710.05941>.
- [26] S. Hochreiter and J. Schmidhuber, “Long Short-Term Memory”, *Neural Computation*, vol. 9, no. 8, pp. 1735–1780, 1997. <https://doi.org/10.1162/neco.1997.9.8.1735>
- [27] Y. Yu, X. Si, C. Hu, and J. Zhang, “A Review of Recurrent Neural Networks: LSTM Cells and Network Architectures”, *Neural Computation*, vol. 31, no. 7, pp. 1235–1270, 2019. https://doi.org/10.1162/neco_a_01199
- [28] D. Aparicio and M. I. Bertolotto, “Forecasting inflation with online prices”, *International Journal of Forecasting*, vol. 36, no. 2, pp. 232–247, 2020. <https://doi.org/10.1016/j.ijforecast.2019.04.018>
- [29] T. McQueen, D. Burton, J. Sheridan, and M. C. Thompson, “Active control of flow over a backward-facing step at high Reynolds numbers”, *International Journal of Heat and Fluid Flow*, vol. 93, p. 108891, 2022. <https://doi.org/10.1016/j.ijheatfluidflow.2021.108891>
- [30] O. Sazhin, “Gas outflow into vacuum over a forward- and backward-facing step in a wide range of rarefaction”, *International Journal of Heat and Mass Transfer*, vol. 179, p. 121666, 2021. <https://doi.org/10.1016/j.ijheatmasstransfer.2021.121666>
- [31] A. R. Abu Talib and A. K. Hilo, “Fluid flow and heat transfer over corrugated backward-facing step channel”, *Case Studies in Thermal Engineering*, vol. 24, p. 100862, 2021. <https://doi.org/10.1016/j.csite.2021.100862>
- [32] K. Loksupapaiboon and C. Suvanjumrat, “Numerical simulation of flow over a passive disturbance and backward-facing step”, *IOP Conference*

- Series: Materials Science and Engineering*, vol. 1137, no. 1, p. 012046, 2021. <https://doi.org/10.1088/1757-899X/1137/1/012046>.
- [33] C. Rumsey, “2DBFS: 2D Backward Facing Step”, Turbulence Modeling Resource, Langley Research Center, Nov 18, 2021. [Online]. Available https://turbmodels.larc.nasa.gov/backstep_val.html/ (Accessed Aug 7, 2023)
- [34] A. Satheesh Kumar, A. Singh, and K. B. Thiagarajan, “Simulation of backward facing step flow using OpenFOAM®”, *AIP Conference Proceedings*, vol. 1, p. 2204, 2020. <https://doi.org/10.1063/1.5141565>
- [35] D. Cappelli and N. N. Mansour, “Performance of Reynolds Averaged Navier-Stokes Models in Predicting Separated Flows: Study of the Hump Flow Model Problem”, *31st AIAA Applied Aerodynamics Conference*, 2013. <https://doi.org/10.2514/6.2013-3154>
- [36] F. R. Menter, M. Kuntz, and R. Langtry, “Ten years of industrial experience with the SST turbulence model. Begell”, *Turbulence, Heat and Mass Transfer*, pp. 625-632, 2003.
- [37] D. M. Driver and H. L. Seegmiller, “Features of a reattaching turbulent shear layer in divergent channel flow”, *AIAA Journal*, vol. 23, no. 2, pp. 163–171, 1985. <https://doi.org/10.2514/3.8890>

Evaluating the Nonlinear Dynamic Stiffness of Rail Pad using Finite Element Method

Mohamad Hazman Halim, Abdul Malek Abdul Wahab*,
Muhamad Sukri Hadi

School of Mechanical Engineering, College of Engineering,
Universiti Teknologi MARA, 40450 Shah Alam, Selangor, MALAYSIA
*abdmalek@uitm.edu.my

Azmi Ibrahim

School of Civil Engineering, College of Engineering,
Universiti Teknologi MARA, 40450 Shah Alam, Selangor, Malaysia

Noraishah Mohamad Noor

Rapid Rail Sdn. Bhd, Kuala Lumpur, MALAYSIA

ABSTRACT

Unwanted vibration and noise from railroads have a significant negative impact on the environment, causing damage to roads, buildings, and other structures. To mitigate this condition, rail pads have been installed as dampers to lessen the impact of vibration and shock on the railway track. The rail pad is made of a polymeric substance having nonlinear properties. This research examined the dynamic stiffness of rail pads made of thermoplastic elastomers (TPEs). ANSYS software was used to estimate the impact of temperature, toe load, and frequency under dynamic loading. The three-dimensional (3D) finite element model (FE) was created based on hyperelastic theory. The dynamic stiffness of the interlayer decreases with increasing temperature. For the effect of peak load and frequency, both parameters were directly proportional to dynamic stiffness. An increase in either parameter results in a stiffening of the interlayer. Frequency has the least effect on the dynamic stiffness of the track bed compared to temperature and peak load, with the average percentage difference between high and low being 28.31%, 55.57%, and 21.9%, respectively.

Keywords: *Rail Pad; Dynamic Load; Deformation; Temperature; Frequency*

Introduction

An important part of the railroads that keeps the operation running smoothly is the rail fastening system [1]. The rail pad, which is positioned below the rail, is one of the crucial parts of the fastening mechanism [2]–[4]. The rail pad's primary purpose is to provide sufficient vertical rigidity for ballasted and slab track [5]–[6]. Elastic rail pads are a practical way to lessen wheel/rail contact, slow down ballast pulverization, and minimize railroad maintenance expenses. The sleeper's protection is one of the rail pad's purposes [7]–[8]. Additionally, the rail pad enhances the ballast's protection from larger dynamic overloads [9]–[10].

The materials used to create the rail pads have significant nonlinear and dissipative mechanical properties that are greatly impacted by the loads and environmental conditions [11]. The excitation frequency [12]–[13], the amplitude of the load [14]–[15], the temperature [16], and the rail pad stiffness [13], [17] are all factors that have been documented in previous research.

The mechanical properties of rail pads in operation settings have been examined through several experimental investigations and numerical calculations. Fenander [12] investigated the reaction of the pads using experimental work and discovered that stiffness very slightly increases with frequency and dramatically rises with preload. To improve the accuracy of the forecast of the broadband vibration and noise produced by high-speed rail vehicles, experimental research was undertaken to acquire frequency-dependent dynamic performance of high-speed rail pads during the passage of rail cars [13]. The experimental work by Kaewunruen et al. [7] stated that the track surface (or vertical deviation) tends to deform at larger displacement amplitude and resonates at a lower wavelength of track roughness under dynamic conditions.

Wei et al. [14] modelled the rail pad numerically using the finite element method (FEM) and found that the vertical stiffness of TPE rail pads changed with load amplitude. Koroma et al. stated that it was important to consider the preload effect on predicting the dynamic stiffness of TPEs rail pads using FE analysis [18]. To explore the effects of the stimulation frequency and displacement amplitude, Zhu et al. [15] modelled the rail pad using 3D-CVST.

Analysing the rail pad geometry solutions in terms of deformation will consume a long time to complete the result by having the experimental approach in the laboratory. In earlier investigations, a variety of numerical calculation methods for estimating the dynamic stiffness of rail pads were investigated. Unfortunately, there needs to be more development

in analysing the rail pad hyperelastic material dynamic stiffness using finite element (FE) modelling. Therefore, this work predicted the behaviour of dynamic stiffness for a particular rail pad material, thermoplastic elastomers (TPEs), using FE analysis. The 3D model was established using ANSYS software. On dynamic stiffness, the effects of temperature, toe stress, and frequency were anticipated.

The laboratory and field investigation could have been more extensive in budget and time for design options. As a result, the FE method was created to analyse the impact of key factors quickly. The proposed model may be used to evaluate how rail pads' dynamic stiffness would behave under various parametric circumstances. FE analysis can be employed as a decision-support tool for maintenance practitioners to evaluate the dynamic stiffness of railpads. This enables them to make well-informed decisions about maintenance strategies. By using FE analysis, practitioners can identify areas that require improvement, predict the performance of various railpad configurations, and optimize maintenance interventions. These actions aim to enhance overall track performance and minimize long-term costs.

Material and Method

Rail pad

The material of the rail pad in this study is thermoplastic elastomers (TPEs). The rail pad is a rubber-like material that exhibits nonlinear behaviour. The hyperelastic model is used to show the nonlinear behaviour of the rail pad for rubber-like materials. Equation (1) shows the general principal stresses for the Ogden model. As shown in Equation (2), the Ogden formula was applied to model the dynamic stiffness characteristic of rail pads under uniaxial dynamic load [19]. The rail pad's dimensions are 150 mm long, 150 mm wide, and 8 mm thick ($l \times w \times t$).

The Ogden model is an all-encompassing hyperelasticity model with a Helmholtz free energy per reference volume stated in terms of the major stretches being used. There are numerous ways to express the Ogden model's Helmholtz free energy. The principal stresses σ_i , $i \in [1]-[3]$, for the Ogden model, are given by:

$$\sigma_i = \frac{2}{J} \sum_{k=1}^N \frac{\mu_k}{\alpha_k} ((\lambda^*_i)^{\alpha_k} - \frac{1}{3} [(\lambda^*_1)^{\alpha_k} + (\lambda^*_2)^{\alpha_k} + (\lambda^*_3)^{\alpha_k}]) + \sum_{k=1}^N \frac{2k}{D_k} (J - 1)^{2k-1} \quad (1)$$

where J is a Jacobian determinant, N is the number of chains per reference unit volume, α is the shear displacement, and μ is the shear modulus. The indices i and j take the values 1, 2, and 3. Then, the stresses from the incompressible Ogden model in uniaxial loading are given by;

$$\sigma_{uniax} = \frac{2}{J} \sum_{k=1}^N \frac{2\mu_k}{\alpha_k} \left[\lambda^{\alpha_k} - \left(\frac{1}{\sqrt{\lambda}} \right)^{\alpha_k} \right] \quad (2)$$

Rail and sleeper

To represent the rail and sleeper, a solid element with a nominal cross-sectional form was employed. Steel and concrete were used to make the rail and sleeper, respectively. In solid materials like steel and concrete, linear elasticity is a normal technique for modelling the mechanical behaviour of very small strains [20]-[21]. The rail constructions' characteristics and attenuation factors are stated in Othman et al. [22]. The figures were gathered from various scientific journals and the web's typical material attributes.

Simulation test campaign

CATIA V5 software was used to generate the models for the rail, rail pad, and sleeper. The International Union of Railways (UIC) design guidelines were followed when creating the steel rail. Figure 1 depicts in isometric detail the rail, rail pad, and sleeper in 3D.

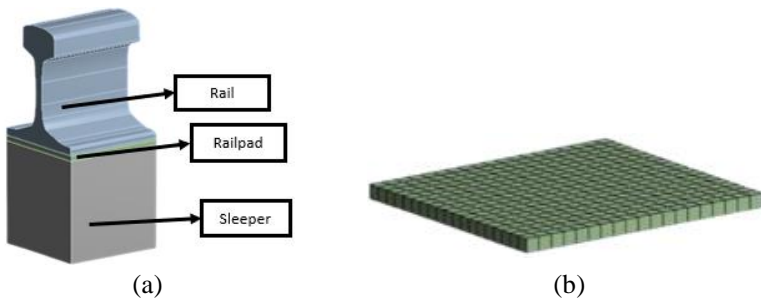


Figure 1: 3D Model of (a) simplified fastening system, and (b) rail pad [22]

The fastening system's 3D model was then imported into the ANSYS programme for analysis as well as simulation. It was projected that toe load, temperature, and frequency would have an impact on the TPE's dynamic stiffness. Standard toe load measurements are 18 kN. The toe load occurred in three instances. First, the scenario that reflected the 18 kN system's appropriate assembly. Then, 5 kN and 30 kN of under- or over-torque,

respectively, were studied. These were assessed to demonstrate the impact of excessive toe load tightness.

Starting at the typical room temperature of 20 °C, the simulation was run at various temperatures. Considering Malaysian conditions, a 52 °C maximum and a 0 °C minimum temperature were used for the test. The hottest temperature ever recorded in Malaysia was 40.1 °C. However, the rail pad's temperature might reach as high as 52 °C due to heating brought on by the wheels' repetitive motion over the railway. To use comparable temperature ranges, four distinct temperatures were included (0 °C, 20 °C, 35 °C, and 52 °C).

Boundary conditions and meshing

Figure 2 demonstrates the finite element method's applied toe load, load, and boundary conditions, incorporating frictionless and fixed support. The force produced as wheels pull on rails is known as the applied load. The load was time-based in cycles and for each steadily raised load applied, the deformation of the rail pad was recorded. An imposed boundary condition is used in this simulation. It was used at the base of the concrete sleeper as a fixed support. On the edges of the rail pad, frictionless support was used. While the simulation analysis is being performed, these boundary conditions give mediocre support and prohibit any component from moving freely.

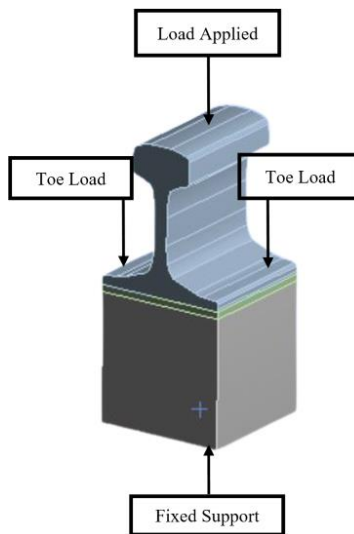


Figure 2: Boundary condition for fastening system railway track [22]

The contact between two surfaces also impacts the simulation results. The location of the interaction was therefore established. A friction

coefficient was used to identify the rail, sleeper, and rail pad as having frictional contact. In this work, the friction coefficient was set at 0.16 [23]. Two distinct geometries in this frictional contact can convey shear stresses. That kind of circumstance is referred to as “sticking”.

Mesh creation is necessary for any physical problem's finite element model. Nodes and elements are used to define it. The 3D element was used to model the fastening system. All components (rail, concrete, and rail pad) used the multi-zone method for meshing. This meshing technique was frequently employed due to speed and accuracy. The multi-zone approach is the best meshing technique since it discretized the model with the fewest number of elements while simultaneously having the highest element quality and least skewness [24]. One advantage of the multi-zone approach in this context is the ability to tailor the mesh resolution to different regions of the rail pad, ensuring higher accuracy where it is most needed. This adaptability is particularly beneficial in capturing the complex behaviour of rail pads, which experience nonlinear effects due to their material properties and the dynamic loads imposed on them. The element quality and skewness of the mesh were assessed to guarantee a high mesh grade.

Dynamic analysis

Elastic deformation, δ is required to determine the rail pad's dynamic stiffness. The following equations can be used to compute this:

$$\delta = \frac{\sigma \times L}{E} = \frac{F \times L}{A \times E} \quad (3)$$

where the normal stress σ , the elastic modulus E , the force F , the length L , and the area A are present, for computing the modulus of elasticity E , the equation is:

$$E = \frac{\sigma}{\varepsilon} \quad (4)$$

where ε represents the strain. This can be determining the average stress σ , using the formula below:

$$\sigma = \frac{P}{A} \quad (5)$$

where A is the area and P is the normal force.

Dynamic tests were used to assess the effects of different service conditions on the pad. Thus, in this work, the dynamic stiffness under the influence of different temperatures, toe loads, and frequency were estimated.

The dynamic testing utilised the three amplitudes described in standards EN 13481-2 and EN-13146-9 [25].

TPE rail pad material was used for the test in the dynamic simulation, and it was exposed to reference conditions such as the applied load, toe load, and boundary condition. For dynamic analysis, the finite element equations of motion were numerically time-integrated [25]. The rail pad in Figure 3 underwent a dynamic examination by having 100 sinusoidal cycles for each load applied. The deformation of the rail pad for each load was recorded.

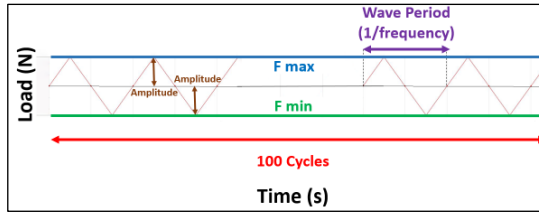


Figure 3: Dynamic cycle of load-deformation

Results and Discussion

Validation

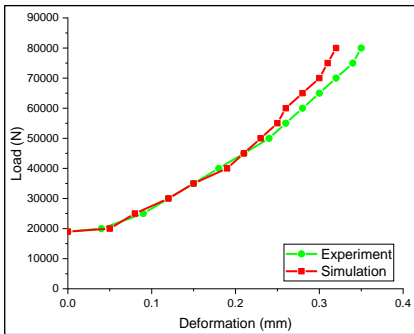
For validation of the simulation model, a mesh convergence test was performed. The parameters for the mesh setup considered in this investigation are shown in Table 1. The deformation of rail for load 80 kN starts stabilized at 10 mm size of elements. The simulations with sizes of elements 10 mm, 9 mm, and 8 mm produced readings comparable to those in the validation research study [25]. However, it took longer than the simulation to complete as the size of the element decreased. As the size of elements reduces, the number of nodes and elements increases. This contributes to the longer time taken for the simulation to complete. Therefore, 10 mm was used for further simulation in the current investigation, as the time taken for completion was less compared smaller size of elements.

Figures 4(a) and 4(b) demonstrate the outcomes for load displacement in dynamic analysis. The load was applied at 5 kHz for 100 cycles. The toe load was 18 kN and the temperature was at 20 °C, known as the reference condition. This numerical computation followed the experimental setting of the previous study [25]. For the results, the average value of 100 cycles of deformation was taken. The dynamic compressive force that nonlinearly boosted the rail pad's displacement is seen in Figure 4(a). Figure 4(b) shows displacement is high at the edge of the railpad at a maximum load of 80 kN. These dynamic loads can lead to stress redistribution within the railpad

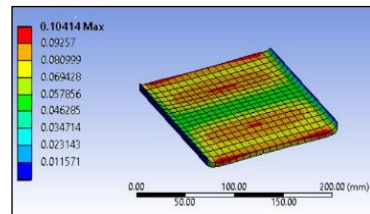
material, causing higher displacement at the edge where the load is concentrated. The simulation's results agree with those reported by Sainz-Aja et al.'s experimental test [25]. The average percentage error was 4.68%, as tabulated in Table 2. The rigid body displacement, which occurred at 20 kN, 30 kN, and 40 kN, was corrected for accurate results. This was a common problem for geometrically nonlinear small-strain conditions [26]. As a percentage error below 10%, it was concluded that the simulation model could be accepted.

Table 1: Mesh convergence analysis

Size of element (mm)	Nodes	Elements	Time consumption (min)	Average total deformation at 80 kN (mm)
19.4	28457	5624	24	0.40
16.0	32505	6555	27	0.39
12.0	37267	7650	30	0.38
10.0	39648	8197	30	0.33
9	40838	8470	32	0.33
8	42028	8743	33	0.33



(a)



(b)

Figure 4: (a) Evaluating the contrasts between simulation versus experiment results [25], and (b) TPE rail pad displacement

Dynamic stiffness assessment

The influence of temperature

Throughout the operation, the rail pad is exposed to a range of temperatures. Figure 5 demonstrates how temperature affects the TPE rail pad's dynamic stiffness. The temperature that has been analysed were 0 °C, 20 °C, 35 °C, and 52 °C. The load was applied at 5 kHz for 100 cycles. 18 kN was the toe

load for both sides and the applied load was up to 80,000 kN in the step of 5000 kN. The deformation of rail pad increase as temperature increase. This trend is in agreement with previous work [27]-[28]

Table 2: Comparing simulation and experimental results [25]

Load (N)	Deformation		Percentage error (%)
	Reference	Simulation	
19000	0.00	0.00	0.00
20000	0.04	0.05	11.43
25000	0.09	0.08	6.90
30000	0.12	0.12	1.47
35000	0.15	0.15	0.52
40000	0.18	0.19	3.03
45000	0.21	0.21	0.68
50000	0.24	0.23	4.97
55000	0.26	0.25	6.91
60000	0.28	0.26	6.23
65000	0.30	0.28	6.64
70000	0.32	0.30	5.83
75000	0.34	0.31	6.43
80000	0.35	0.33	5.71

Figure 6 illustrates the effect of temperature on the elongation of a railpad under a maximum load of 80 kN. The red colour area is the highest deformation while the blue colour area shows the lowest deformation occurs. At a temperature of 0 °C, the highest deformation value is 0.0821 mm at the near centre of railpad. As the temperature increases, the highest deformation moves towards the edge of railpad. For temperature 52 °C, the highest deformation is 0.1697 mm more than 51% increment. At the highest temperature, the areas experiencing significant elongation were predominantly located at the edges of the railpad, as compared to the lowest temperature in this study. The value of maximum deformation increases as the temperature increases.

Table 3 shows the percentage difference of deformation between the lowest and highest temperatures at 0 °C and 52 °C, respectively. The average percentage difference between 0 °C and 52 °C is 28.31% for the stated dynamic load applied. The deformation difference decreases as the dynamic load increases. At 2 kN load, the percentage difference of deformation is 63.98%. As the load reaches 80 kN, the percentage difference of deformation reduces to 11.91%. This demonstrates how the impact of temperature diminishes as dynamic load increases.

Reduced dynamic stiffness is a result of increased rail pad displacement. Thus, increasing temperature leads to a lessening in dynamic

stiffness [25]. The rail pads' elastic modulus will decrease as the temperature rises. As a result, the rail pads endure greater deformation the lower their modulus of elasticity. In general, the temperature has an inverse relationship with the rail pad's stiffness. As a result, the rail pad's rigidity declines as the temperature rises. Temperature increases molecular mobility, thereby allowing the rail pads to lengthen at a microscopic level. However, as the compression load increases, the molecular mobility is restricted, resulting in less deformation due to temperature. According to the underlying theory of materials science, the inverse relationship between temperature and rail pad stiffness can be explained by increased molecular mobility at higher temperatures, leading to greater microscopic lengthening of the rail pad, while increased compression load restricts molecular mobility, resulting in reduced deformation due to temperature.

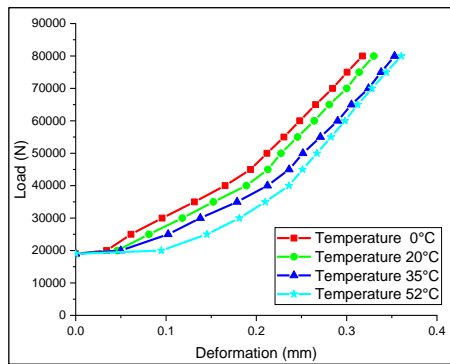


Figure 5: The rail pad deformation for different temperature

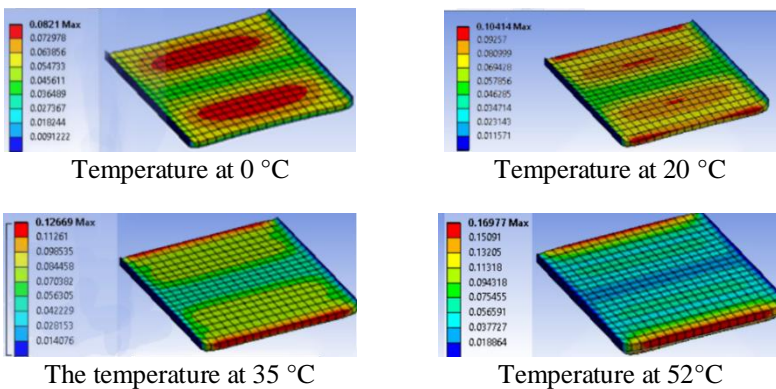


Figure 6: The effect of temperature on the elongation of rail pads at a maximum load of 80 kN

Table 3: Comparison of deformation differences between high and low temperatures for different loads.

Load (N)	Deformation		Differences (%)
	0 °C	52 °C	
19000	0.00	0.00	0
20000	0.03	0.09	63.98
25000	0.06	0.15	57.87
30000	0.10	0.18	47.20
35000	0.13	0.21	37.39
40000	0.17	0.24	29.94
45000	0.19	0.25	22.90
50000	0.21	0.27	20.73
55000	0.23	0.28	18.45
60000	0.25	0.30	16.80
65000	0.27	0.31	14.94
70000	0.28	0.33	13.30
75000	0.30	0.34	12.65
80000	0.32	0.36	11.91

Effect of toe load

Figure 7 shows the impact of various toe loads, 5 kN, 18 kN, and 30 kN, the TPE rail pad's dynamic stiffness under reference conditions (at a temperature 20 °C). Increasing the toe load results in an increase in the vertical dynamic stiffness. The highest railpad deformation occurred at toe load 30 kN rather than 5 kN and 18 kN. The significance of the gap difference also shows the difference between 5 kN and 30 kN compared to 18 kN and 30 kN in its deformation value. The results agreed with previous work carried out by Sainz-Aja et al. [25] and Oregui et al. [29]. Also, it is clear that when the toe stress increases, the rail pad's deformation decreases even under the same weight. On this effect, the toe load restricts the longitudinal and lateral deformation of the rail pad. The restriction rises as the toe load increases the compress. The rail pad will likely benefit from high preloads and become stiffer [30]. The information about toe load and its effect on restricting rail pad deformation is relevant in this study as it suggests that higher toe loads, resulting in increased compression, can lead to greater restriction and stiffness of the rail pad, which can influence its deformation behaviour under different frequencies and temperatures.

Effect of frequency

The results for dynamic stiffness under the effect of frequency are depicted in Figure 8. It has been observed that the stiffness of rail pads rises with frequency. This supports the findings provided by previous researchers [25]. Dynamic loads with a frequency of 20 Hz have the lowest deformation

compared to 2.5 Hz. In comparison between 2.5 Hz and 20 Hz, the different percentage of the deformation was 7.68%. The deformation is larger for a frequency of 2.5 Hz and it is notable that the deformation difference does not have much significance when the frequency is more than 5 Hz.

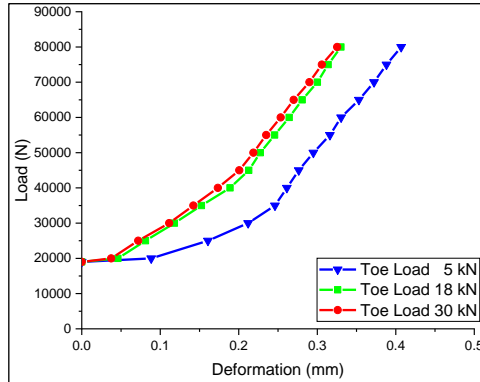


Figure 7: Toe load's impact on dynamic stiffness

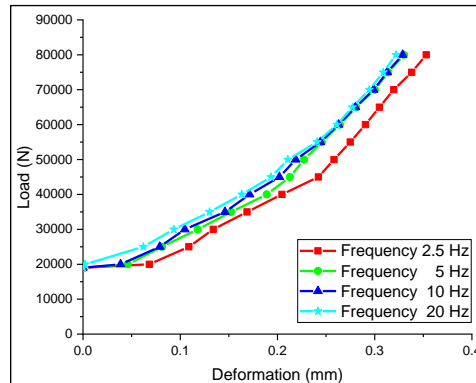


Figure 8. The effect of frequency load dependence on the dynamic stiffness

Figure 9 compares rail pad deformation for different frequencies and temperatures, providing insights from a mechanics and materials science perspective regarding the effect of heat. The reference case allows for comparison, revealing a significant disparity in deformation between high and low temperatures at the lowest frequency of 2.5 Hz. Conversely, at the highest frequency of 20 Hz, the difference in deformation is less pronounced. The average difference in deformation between high and low temperatures is measured at 16.87% for 2.5 Hz and 8.70% for 20 Hz. These results suggest

that, compared to lower frequencies, higher frequencies have a reduced impact on the dynamic stiffness of the TPE rail pad when subjected to temperature variations. These findings are consistent with Squicciarini et al.'s research [31], indicating that temperature decreases the rail pad's shear modulus while frequency increases it, thus influencing the dynamic stiffness of the elastomeric rail pad.

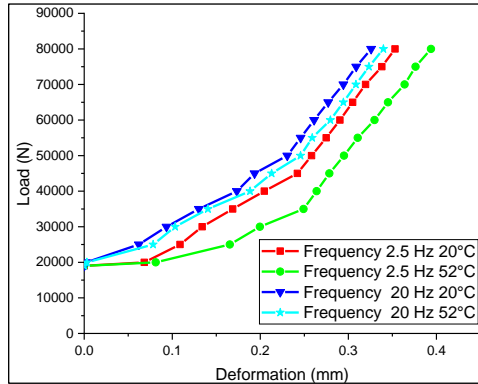


Figure 9: The dynamic stiffness of the rail pad at various temperatures and frequencies

Conclusion

The predicted trends of dynamic stiffness using the FE method were found to be in good agreement with previous work, indicating the accuracy of the FE analysis method. The TPE rail pad displays high nonlinearity and variability with the loading condition. Temperature, toe load, and frequencies were the sensible factors that were investigated. The results of the simulation allow for the following inferences:

- i. The TPE rail pad's dynamic stiffness reduced as temperature decreased. It was normal for this kind of behaviour in polymeric materials. As temperature varied in the range of 0-52 °C, changes in stiffness were seen by fixing the other variables to reference standard values. The results demonstrated the great thermal sensitivity of the rail pad.
- ii. Toe loading correlated with dynamic stiffness. When the toe stress rises, the rail pad becomes firmer.
- iii. The displacement of the rail pad changes because of the rise in frequency in the range of 2.5 Hz and 20 Hz, growing into a sizeable distortion. This demonstrates how frequency influences the pads' dynamic stiffness. At low frequencies, the frequency impact becomes

significantly different. Typically, the rail pads get stiffer as the frequency rises.

In this simulation, comparing temperature and toe load, the frequency has a low influence on affecting the rail pad's dynamic stiffness. FE analysis, utilizing advanced simulation techniques and software like ANSYS, offers a cost-effective alternative to traditional physical testing methods in the railway industry. By creating virtual models of TPE rail pads and conducting simulations, engineers can accurately predict their behaviour under different operating conditions, including temperature variations. This eliminates the need for costly and time-consuming physical prototypes and extensive testing, resulting in substantial cost savings in material procurement, manufacturing, and experimental procedures. By integrating this degradation model into the FEM simulations, engineers can gain valuable insights into the potential degradation mechanisms of TPE rail pads, such as fatigue, creep, or material aging due to environmental factors. This enables them to forecast the performance degradation of rail pads and make informed decisions regarding maintenance schedules, replacement intervals, and overall system reliability. As a result, it might aid in the creation of decision support systems to improve maintenance and optimise track performance, hence reducing costs and prolonging the usable life of the infrastructure.

Contributions of Authors

The authors confirm the equal contribution in each part of this work. All authors reviewed and approved the final version of this work.

Funding

This work was supported by the “Fundamental Research Grant Scheme for Research Acculturation of Early Career Researchers (RACER/1/2019/TK03/UITM//2)”

Conflict of Interests

All authors declare that they have no conflicts of interest

Acknowledgment

The Ministry of Higher Education Malaysia financially supported this research through the Fundamental Research Grant Scheme for Research

Acculturation of Early Career Researchers (RACER/1/2019/TK03/UITM//2). The authors acknowledge the support received from the Ministry of Higher Education Malaysia. We also gratefully acknowledge Universiti Teknologi MARA for the preparation, execution, writing, and publication of this article.

References

- [1] M. Sol-Sánchez, F. Moreno-Navarro, and M. C. Rubio-Gámez, “The use of elastic elements in railway tracks: A state of the art review”, *Construction and Building Materials*, vol. 75, pp. 293–305, 2015. doi: 10.1016/j.conbuildmat.2014.11.027.
- [2] M. Sol-Sánchez, F. Moreno-Navarro, and M. C. Rubio-Gámez, “The use of deconstructed tire rail pads in railroad tracks: Impact of pad thickness”, *Materials & Design*, vol. 58, pp. 198–203, 2014. doi: 10.1016/j.matdes.2014.01.062.
- [3] K. Knothe, M. Yu, and H. Ilias, “Measurement and Modelling of Resilient Rubber Rail-Pads,” *System Dynamics and Long-Term Behaviour of Railway Vehicles, Track and Subgrade*, vol. 6, pp. 265–274, 2003. doi: 10.1007/978-3-540-45476-2_16.
- [4] . Ge, L. Ling, X. Yuan, and K. Wang, “Effect of distributed support of rail pad on vertical vehicle-track interactions”, *Construction and Building Materials*, vol. 262, p. 120607, 2020. doi: 10.1016/j.conbuildmat.2020.120607.
- [5] J. Chen and Y. Zhou, “Dynamic vertical displacement for ballastless track-subgrade system under high-speed train moving loads”, *Soil Dynamics and Earthquake Engineering*, vol. 129, no. November, pp. 1–10, 2020. doi: 10.1016/j.soildyn.2019.105911.
- [6] Z. Zeng, A. Ahmed Shuaibu, F. Liu, M. Ye, and W. Wang, “Experimental study on the vibration reduction characteristics of the ballasted track with rubber composite sleepers,” *Construction and Building Materials*, vol. 262, p. 120766, 2020. doi: 10.1016/j.conbuildmat.2020.120766.
- [7] S. Kaewunruen, A. Aikawa, and A. M. Remennikov, “Vibration Attenuation at Rail Joints through under Sleeper Pads”, *Procedia Engineering*, vol. 189, no. May, pp. 193–198, 2017. doi: 10.1016/j.proeng.2017.05.031.
- [8] N. Karpuschenko, D. Velichko, and A. Sevostyanov, “Effectiveness of Intermediate Rail Fastenings on the Railway Sections of Siberia”, *Transportation Research Procedia*, vol. 54, no. 2020, pp. 173–181, 2021. doi: 10.1016/j.trpro.2021.02.062.
- [9] C. Ngamkhanong, Q. Y. Ming, T. Li, and S. Kaewunruen, “Dynamic train-track interactions over railway track stiffness transition zones

- using baseplate fastening systems”, *Engineering Failure Analysis*, vol. 118, no. May, p. 104866, 2020. doi: 10.1016/j.engfailanal.2020.104866.
- [10] M. Sol-Sánchez, F. Moreno-Navarro, and M. C. Rubio-Gámez, “The use of deconstructed tires as elastic elements in railway tracks”, *Materials (Basel)*, vol. 7, no. 8, pp. 5903–5919, 2014.
- [11] J. Sadeghi, M. Seyedkazemi, and A. Khajehdezfuly, “Nonlinear simulation of vertical behavior of railway fastening system”, *Engineering Structures*, vol. 209, no. February, p. 110340, 2020. doi: 10.1016/j.engstruct.2020.110340.
- [12] A. Fenander, “Frequency dependent stiffness and damping of railpads”, *Proceedings of the Institution of Mechanical Engineers, Part F: Journal of Rail and Rapid Transit Part F J. Rail Rapid Transit*, vol. 211, no. 1, pp. 51–62, 1997. doi: 10.1243/0954409971530897.
- [13] K. Wei, Q. Yang, Y. Dou, F. Wang, and P. Wang, “Experimental investigation into temperature- and frequency-dependent dynamic properties of high-speed rail pads,” *Construction and Building Materials*, vol. 151, no. October 2018, pp. 848–858, 2017. doi: 10.1016/j.conbuildmat.2017.06.044.
- [14] K. Wei, P. Zhang, P. Wang, J. Xiao, and Z. Luo, “The influence of amplitude- and frequency-dependent stiffness of rail pads on the random vibration of a vehicle-track coupled system”, *Shock and Vibration*, vol. 2016, pp. 1-10, 2016. doi: 10.1155/2016/7674124.
- [15] S. Y. Zhu, C. B. Cai, Z. Luo, and Z. Q. Liao, “A frequency and amplitude dependent model of rail pads for the dynamic analysis of train-track interaction,” *Science China Technological Sciences*, vol. 58, no. 2, pp. 191–201, 2015. doi: 10.1007/s11431-014-5686-y.
- [16] K. Wei, F. Wang, P. Wang, Z. X. Liu, and P. Zhang, “Effect of temperature- and frequency-dependent dynamic properties of rail pads on high-speed vehicle–track coupled vibrations”, *Vehicle System Dynamics*, vol. 55, no. 3, pp. 351–370, 2017. doi: 10.1080/00423114.2016.1267371.
- [17] A. K. Mazlan, A. Malek, A. Wahab, M. A. Anuar, and A. K. Makhtar, “Nonlinear Static Stiffness of Rail Pads for Different Materials and Thicknesses using Finite Element Method”, *Journal of Mechanical Engineering*, vol. 11, no. 1, pp. 49–64, 2022.
- [18] S. G. Koroma, M. F. M. Hussein, and J. S. Owen, “The effects of railpad nonlinearity on the dynamic behaviour of railway tracks,” *Conference: Institute of Acoustics spring conference*, vol. 35, no. 1, pp. 176–183, 2013.
- [19] J. S. Bergstrom, *Mechanics of Solid Polymers*. Elsevier, 2015.
- [20] E. Kabo, J. C. O. Nielsen, and A. Ekberg, “Prediction of dynamic train-track interaction and subsequent material deterioration in the presence of insulated rail joints”, *Vehicle System Dynamic*, vol. 44, no. SUPPL. 1, pp. 718–729, 2006. doi: 10.1080/00423110600885715.

- [21] N. K. Mandal, “On the low cycle fatigue failure of insulated rail joints (IRJs)”, *Engineering Failure Analysis*, vol. 40, pp. 58–74, 2014.
- [22] M. I. H. Othman, A. M. A. Wahab, M. S. Hadi, and N. M. Noor, “Assessing the nonlinear static stiffness of rail pad using finite element method”, *Journal of Vibroengineering*, vol. 24, no. 5, pp. 921–935, 2022. doi: 10.21595/jve.2022.22293.
- [23] E. Harea, R. Stoček, and M. Machovský, “Study of friction and wear of thermoplastic vulcanizates: The correlation with abraded surfaces topology”, *Journal of Physics: Conference Series*, vol. 843, no. 1, pp. 1–9, 2017. doi: 10.1088/1742-6596/843/1/012070.
- [24] C. J. Ren *et al.*, “Anti-vibration slab mat to suppress train track vibrations”, *Journal of Engineering Science and Technology*, vol. 13, no. Special Issue, pp. 1–12, 2018.
- [25] J. A. Sainz-Aja, I. A. Carrascal, D. Ferreño, J. Pombo, J. A. Casado, and S. Diego, “Influence of the operational conditions on static and dynamic stiffness of rail pads”, *Mechanics of Materials*, vol. 148, no. June, pp. 1–19, 2020. doi: 10.1016/j.mechmat.2020.103505.
- [26] F. Nishino, S. Malla, and T. Sakurai, “Solution of finite-displacement small-strain elasticity problems by removal of rigid body displacements,” *Doboku Gakkai Ronbunshu*, vol. 2000, no. 661, pp. 11–26, Oct. 2000. doi: 10.2208/jscej.2000.661_11.
- [27] K. Wei, Z. X. Liu, Y. C. Liang, and P. Wang, “An investigation into the effect of temperature-dependent stiffness of rail pads on vehicle-track coupled vibrations”, *Proceedings of the Institution of Mechanical Engineers Part F Journal of Rail and Rapid Transit*, vol. 231, no. 4, pp. 444–454, 2017. doi: 10.1177/0954409716631786.
- [28] R. A. Broadbent, D. J. Thompson, and C. J. C. Jones, “Evaluation of the effects of temperature on railpad properties, rail decay rates and noise radiation”, *16th Int. Congr. Sound Vib. 2009, ICSV 2009*, vol. 1, pp. 132–139, 2009.
- [29] M. Oregui, A. Núñez, R. Dollevoet, and Z. Li, “Sensitivity Analysis of Railpad Parameters on Vertical Railway Track Dynamics”, *Journal of Engineering Mechanics*, vol. 143, no. 5, p. 04017011, 2017. doi: 10.1061/(asce)em.1943-7889.0001207.
- [30] S. Kaewunruen and A. M. Remennikov, “An alternative rail pad tester for measuring dynamic properties of rail pads under large preloads”, *Experimental Mechanics*, vol. 48, no. 1, pp. 55–64, 2008. doi: 10.1007/s11340-007-9059-3.
- [31] G. Squicciarini, D. J. Thompson, M. G. R. Toward, and R. A. Cottrell, “The effect of temperature on railway rolling noise”, *Proceedings of the Institution of Mechanical Engineers, Part F: Journal of Rail and Rapid Transit*, vol. 230, no. 8, pp. 1777–1789, 2016. doi: 10.1177/0954409715614337.

Optimization and Mathematical Modelling of Surface Roughness Criteria and Material Removal Rate when Milling C45 Steel using RSM and Desirability Approach

Fnides Mohamed^{1,2}, Fnides Brahim³, Bensana Toufik²,
Yaltese Mohamed Athmane¹*

*¹Mechanics and Structures Research Laboratory (LMS),
May 8th, 1945, University, PO Box 401, Guelma 24000, ALGERIA*

²Higher School of Technological Education in Skikda, Azzaba, ALGERIA

³Dept CMP, FGM&GP, USTHB, Bab-Ezzouar, Algiers, ALGERIA

**fnides_mohamed@yahoo.fr*

ABSTRACT

This work consists of studying the workability of C45 steel in face milling by using coated carbides (GC4040). The objective is to investigate the evolution of surface roughness (R_a , R_y , and R_z) and Material Removal Rate (MRR) according to cutting speed, feed rate, and depth of cut. A full-factorial design (4^3) was adopted in order to analyse the obtained experimental results via both Analysis of Variance (ANOVA) and Response Surface Methodology (RSM) design. The levels of cutting speed were as follows: $V_{c1}=57$ m/min; $V_{c2}=111$ m/min; $V_{c3}=222$ m/min and $V_{c4}=440$ m/min. The ranges of feed rate were $f_{z1}=0.024$ mm/tooth; $f_{z2}=0.048$ mm/tooth; $f_{z3}=0.096$ mm/tooth and $f_{z4}=0.192$ mm/tooth. As for the depth of cut levels, they included $ap_1=0.2$ mm; $ap_2=0.4$ mm; $ap_3=0.6$ mm, and $ap_4=0.8$ mm. To determine mathematical models to make predictions, a statistical analysis of the results by using RSM was applied to obtain the main effects and interactions plot of the answer. Furthermore, a multi-objective optimization procedure for minimizing R_a and maximizing the metal removed rate using the desirability approach was also implemented. Therefore, the developed models can be effectively used to predict the surface roughness criteria and the material removal rate in machining C45 steel. The results indicated that feed rate is a significant factor affecting surface roughness (R_a : 52.37%, R_y : 80.97%, and R_z : 54.96%), followed by cutting speed (R_a : 37.88%, R_y : 12.90%, and R_z : 24.43%). Meanwhile, cutting speed

and feed rate are the most significant parameters on the MRR with a contribution of 29.5% followed by the depth of cut with 11.62%.

Keywords: *Milling; C45; Modelling; Optimization; Roughness; ANOVA*

Introduction

The manufacturing process, in particular machining, plays an important role in determining the levels of integrity on the surfaces to be produced. In manufacturing industries, different machining processes are used to remove material from the workpiece, and milling is one of the most widely used processes due to its ability to remove material quickly with a surface roughness quality [1]-[2]. In the machining process, modelling, and optimization [3]-[4] are important tasks, allowing the choice of the most convenient cutting conditions in order to obtain desired values in a certain variable, which usually has a direct economic impact such as the machine time or the total cost of operation. The response surface methodology is a general approach to obtaining the maximum value of a dependent (response) variable that depends on several independent (explanatory) variables. This technique combines the Design of Experiments (DOE) and multiple regressions.

Modelling is applied to look at the form of influence like linear, quadratic, or cubic and what mathematical equation it governs, with a given precision, the variation of the phenomenon according to the influential factors. The modelling of response is done by choosing experimental points whose number is at least equal to the sum of the effects, interactions, and quadratic effects. Thus, a matrix of n rows and k columns is defined. Rizvi and Ali [5] presented mathematical modelling and optimization of surface roughness (R_a) and Material Removal Rate (MRR) during the machining of AISI 1040 steel in which response optimization that represents the optimal combination of cutting process parameters are observed to be cutting speed of 400 rpm, feed rate of 0.3 mm/rev, and cutting depth of 2.1 mm. Cutting speed is the most significant parameter that affects R_a , R_z , and MRR. Good agreement was observed by Ghosh et al. [6] between the experimental with predicted R_a value for the RSM-PSO technique during modelling and the optimization of cutting parameters for keyway milling operation of C40 steel under wet conditions.

To study the influences of cutting parameters on the surface roughness criteria during face milling AISI 1045 steel, Trung et al. [7] suggested two models of surface roughness prediction, one of which is built on the basis of Johnson transformation and the other is developed according to Response Surface Method (RSM). Palanisamy et al. [8] optimized cutting parameters (V_c , f_z , and ap) and modelled results such as MMR, surface roughness, cutting force, and tool tip temperature using Taguchi-based Gray's Relational Analysis (GRA) and RSM, respectively when machining Incoloy 800H. Surface

roughness and MRR are important parameters in the machining process. Bouzid et al. [9] proposed modelling technique of the surface roughness and optimization of cutting parameters to determine the optimal cutting regime by minimizing roughness and maximizing MRR during the machining of AISI 1040 steel. Concerning the machinability of AISI 5140 steel, Kuntoğlu et al. [10] carried out a study to determine the optimal cutting conditions, analysis of vibrations, and surface roughness under different cutting parameters. Using the neural network method, Sureshkumar et al. [11] investigated the influence of cutting parameters (v_c , f_z , and ap) on surface roughness in milling operation. Modelling and optimization play important roles in choosing the optimum cutting regimes during machining to achieve the desired results [12].

To minimize the surface roughness and maximize the MRR when turning X20Cr13 stainless steel, Bouzid et al. [13] concluded that the optimal values should include a feed rate of 0.08 mm/rev, depth of cut of 0.15 mm and cutting speed of 120 m/min. The experimental study of Pandiyan et al. [14] involved machining AA6351 alloy steel by a CNC machining centre which was evaluated according to RSM with an objective function and optimization methods to find the values of process variables that produce desirable values of the response where mathematical models are developed from the responses obtained and validated. Ozdemir [15] studied the effect of cutting parameters on the machinability of X37CrMoV5-1 hot work tool steel. He found that the feed rate was 95.90% effective on the Ra value, whereas the cutting speed and the cutting depth factors were not effective. The Ra value increased as the feed rate increased. Factors and ratios affecting the MRR value were determined as 61.70% for feed rate, 27.42% for cutting depth, and 5.04% for cutting speed, respectively.

This paper presents the effect of the cutting regime (V_c , f_z , and ap) on surface roughness criteria (Ra , Ry , and Rz) and MRR in face milling of C45 steel using coated carbide (GC4040) inserts.

Materials and Methods

All the tools used to conduct the experiments are presented which consist of a presentation of various equipment that are used to monitor the evolution of the surface roughness during face milling. In addition, the different methods used for planning and the conditions for carrying out the experiments are cited. The experiments necessary for this study were carried out at the Laboratory of Mechanics and Structure (LMS), Department of Mechanical Engineering, University of May 8, 1945 - Guelma.

Machine tools, cutting tools, and tool holder

The machine tool used for these tests included a vertical milling machine from the National Society for the Production of Industrial Machine Tools (PMO),

model ALMO with a power of 5 KW (Figure 1) on C45 grade steel specimens machined (65 x 65 x 250 mm) (Figure 2) with three ($Z=3$) GC4040 coated carbide inserts (Figure 3) fixed on a 100 mm diameter milling cutter (Figure 4), where Z is the number of insets.

Spindle rotational speeds available on the milling machine (N ; *rev/min*) are 45; 63; 90; 125; 180; 250; 355; 500; 710; 1000; 1400; 2000. The different feed rates of this machine are in (V_f ; *mm/min*): 10; 16; 20; 25; 31.5; 50; 63; 80; 100; 125; 160; 200; 250; 314; 400; 500; 630; 800, with f_z calculated using the following Equation (1).

$$f_z = \frac{V_f}{N * Z} \tag{1}$$

where Z : number of inserts ($Z=3$ inserts).

In order to reduce uncertainties due to resumption operations, the roughness was directly measured on the workpiece without dismounting from the lathe using a 2D roughness meter *Sj- 201p* (Mitutoyo) which was selected to measure surface roughness criteria (Figure 5) in the machining direction. The measurements were repeated three times on the surface at three references.



Figure 1: Machine Tools (PMO), model ALMO

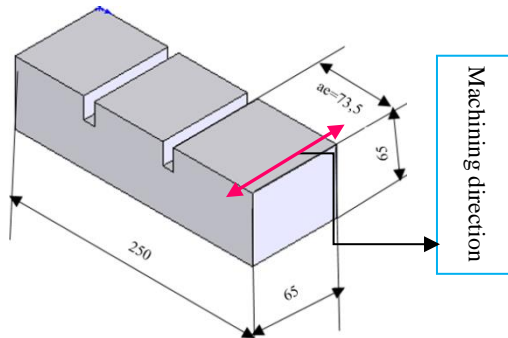


Figure 2: Specimens machined (65 x 65 x 250 mm)

Due to the medium-high carbon content, C45 steel can be welded with some precautions, and it has a low hardenability in water or oil. It is fit for surface hardening gives this steel grade a high hardness of the hardened shell and its chemical composition is shown in Table 1. Concerning the measurement of the roughness, a roughness meter *Sj-201p* was used.



Figure 3: Insert
GC4040



Figure 4: Coromill
245 milling cutter



Figure 5: Roughness meter
Sj-201p and roughness
measurement method

Table 1: Chemical composition % of C45 steel

$Cr + Mo + Ni = \max 0.63$							
C	Si	Mn	Ni	P	S	Cr	Mo
0.43 - 0.5	max	0.5 - 0.8	max	max	max	max	max

Planning of experiments

To calculate the constants and coefficients of the mathematical models, Minitab and Design-Expert (both software) were used and characterized by Analysis of Variance (ANOVA), multiple regressions, and the RSM. In the current study, the relation between the cutting conditions and the technological parameters is given in Equation (2).

$$Y = \phi(Vc, fz, ap) \quad (2)$$

where Vc : cutting speed, fz : feed rate, ap : depth of cut.

ϕ is the response function and the approximation of Y is proposed by using a non-linear (quadratic) mathematical model which is suitable for studying the interaction effects of process parameters on machinability characteristics. In the present work, the RSM-based second order mathematical model is given by Equation (3).

$$Y = b_0 + \sum_{i=1}^k b_i X_i + \sum_{ij} b_{ij} X_i X_j + \sum_{i=1}^k b_{ii} X_i^2 + \varepsilon_{ij} \quad (3)$$

$$(\varepsilon_{ij} = y_{ij} - \bar{y}_{ij})$$

where b_0 is the free term of the regression equation, the coefficients b_1, b_2, \dots, b_k and b_{11}, b_{22}, b_{kk} are the linear and the quadratic terms, respectively, while b_{12}, b_{13}, b_{k-1} are the interacting terms. X_i represents the input parameters (Vc, f , and ap) and ε_{ij} is the error of fit for the regression model. Output surface roughness and MRR are also called response factors.

Multi-factorial method 3 factors and 4 levels (Table 2) were chosen. Cutting parameters were selected based on the chemical composition, tool manufacturer guidelines, and cutting hardness of the workpiece material. Full-factorial design ($4^3=64$ runs) was selected for the design of experiments and the experimental results are given in Table 3.

Multiple response optimization is a procedure that enables the determination of the independent cutting speed parameters (Vc, f , and fz) that lead to optimal response results. The desirability function (DF) is expressed as Equation (4).

$$Df = \left(\prod_{i=1}^n d_i^{w_i} \right) \tag{4}$$

$$F(x) = -Df$$

where:

Df : desirability function,

d_i : specific desirability of each of the (n) target outputs. It is expressed as a function of the target for each target output.

W_i : the corresponding weighting function.

The MRR in milling operations is the volume of material that is removed per unit time in mm^3/min . The study of this parameter is important since the goal is to manufacture low-cost and high-quality products in a short time. The value of MRR is calculated using the following Equation (5).

$$MRR = ap \times ae \times fz \times Z \times \frac{Vc \times 1000}{\pi \times D} \tag{5}$$

where; ae (cutting width)=73.5 mm, $Z=3$ teeth, $D=100$ mm (milling cutter).

Table 2: Factors and levels used in the experiments (multi-factorial method)

Factors	Symbol	Levels			
		Level 1	Level 2	Level 3	Level 4
Cutting speed (m/min)	Vc	57	111	222	440
Feed rate (mm/ tooth)	fz	0.024	0.048	0.096	0.192
Depth of cut (mm)	ap	0.2	0.4	0.6	0.8

Results and Discussion

Statistical data treatments were carried out in two steps. In the first one, the ANOVA and the effect of each factor and its interactions were determined. To achieve this goal, the response surface plots were generated considering two parameters at a time while the third one was kept constant. The second step focused on the modelling aspects using RSM outputs.

Table 3: Experimental data for C45 steel

Runs	Factors			Responses			
	<i>Vc</i> ; m/min	<i>fz</i> ; mm/tooth	<i>ap</i> ; mm	<i>Ra</i> ; μm	<i>Ry</i> ; μm	<i>Rz</i> ; μm	<i>MRR</i> ; mm ³ /min
1	57	0.024	0.2	4.071	7.928	5.85	192.13
2	57	0.024	0.4	4.155	8.224	6.12	384.26
3	57	0.024	0.6	4.218	7.788	5.99	576.39
4	57	0.024	0.8	4.26	9.132	6.295	768.52
5	57	0.048	0.2	5.265	9.592	7.705	384.26
6	57	0.048	0.4	5.312	9.8	7.705	768.52
7	57	0.048	0.6	5.417	9.46	7.295	1152.78
8	57	0.048	0.8	5.68	9.216	7.09	1537.04
9	57	0.096	0.2	6.163	10.116	8.845	768.52
10	57	0.096	0.4	6.394	11.244	9.51	1537.04
11	57	0.096	0.6	6.541	9.252	9.795	2305.56
12	57	0.096	0.8	6.583	10.144	10.08	3074.08
13	57	0.192	0.2	7.234	11.956	9.03	1537.04
14	57	0.192	0.4	7.318	11.728	10.31	3074.08
15	57	0.192	0.6	7.465	12.18	9.075	4611.12
16	57	0.192	0.8	7.381	11.376	10.69	6148.16
17	111	0.024	0.2	3.365	6.864	4.895	374.15
18	111	0.024	0.4	3.365	5.64	5.205	748.3
19	111	0.024	0.6	3.386	5.736	5.01	1122.44
20	111	0.024	0.8	3.659	6	4.8	1496.59
21	111	0.048	0.2	3.785	7.152	5.225	748.3
22	111	0.048	0.4	3.848	7.248	5.32	1496.59
23	111	0.048	0.6	4.29	7.44	5.035	2244.89
24	111	0.048	0.8	4.079	6.588	4.655	2993.19
25	111	0.096	0.2	5.31	7.956	5.415	1496.59
26	111	0.096	0.4	5.415	7.968	5.605	2993.19
27	111	0.096	0.6	5.436	8.004	5.89	4489.78
28	111	0.096	0.8	5.562	8.976	6.175	5986.37
29	111	0.192	0.2	6.528	10.86	7.79	2993.19
30	111	0.192	0.4	6.612	11.076	7.98	5986.37
31	111	0.192	0.6	6.843	12.84	8.835	8979.56

32	111	0.192	0.8	6.885	12.756	9.025	11972.74
33	222	0.024	0.2	2.653	5.2	4.04	748.3
34	222	0.024	0.4	2.821	5.128	4.035	1496.59
35	222	0.024	0.6	3.184	4.84	4.32	2244.89
36	222	0.024	0.8	3.389	5.28	4.7	2993.19
37	222	0.048	0.2	4.31	7.224	5.32	1496.59
38	222	0.048	0.4	4.31	7.968	5.415	2993.19
39	222	0.048	0.6	4.31	8.34	5.7	4489.78
40	222	0.048	0.8	4.394	7.008	4.985	5986.37
41	222	0.096	0.2	5.478	10.656	6.555	2993.19
42	222	0.096	0.4	5.415	8.004	5.7	5986.37
43	222	0.096	0.6	5.562	8.868	6.175	8979.56
44	222	0.096	0.8	5.457	8.232	5.985	11972.74
45	222	0.192	0.2	6.99	12.48	8.455	5986.37
46	222	0.192	0.4	6.032	11.784	8.455	11972.74
47	222	0.192	0.6	6.053	12.984	9.12	17959.1
48	222	0.192	0.8	6.948	11.4	8.265	23945.4
49	440	0.024	0.2	1.092	4.716	2.945	1483.11
50	440	0.024	0.4	1.113	4.932	3.04	2966.22
51	440	0.024	0.6	1.197	5.808	3.23	4449.33
52	440	0.024	0.8	1.218	5.688	3.325	5932.44
53	440	0.048	0.2	2.596	4.28	3.515	2966.22
54	440	0.048	0.4	2.575	3.836	3.515	5932.44
55	440	0.048	0.6	2.68	4.312	3.99	8898.66
56	440	0.048	0.8	3.159	5.412	3.8	11864.8
57	440	0.096	0.2	3.352	7.98	6.08	5932.44
58	440	0.096	0.4	3.394	7.968	5.7	11864.8
59	440	0.096	0.6	3.373	8.436	5.795	17797.3
60	440	0.096	0.8	3.394	8.172	5.795	23729.7
61	440	0.192	0.2	4.549	10.656	7.505	11864.8
62	440	0.192	0.4	4.57	10.404	7.695	23729.7
63	440	0.192	0.6	4.612	10.992	7.885	35594.6
64	440	0.192	0.8	4.612	10.608	5.89	47459.5

Modelling using RSM technique

ANOVA analysis

ANOVA is useful for understanding the influence of given input parameters from a series of experimental results by the method of designing experiments for machining processes, and it also helps to provide an interpretation [16]. Essentially, it partitions the total variation in an experiment into components attributable to the factors controlled and the errors generated. The statistical significance of the fitted quadratic models is assessed by p -values and F -values from the ANOVA.

In ANOVA Tables 4, 5, and 6, the p -value is the probability (ranging from 0 to 1). If the p -value is greater than 0.05, the parameter is insignificant; if the p -value is less than 0.05, the parameter is significant. The squared sum (SS) is used to estimate the square of the deviation from the general mean (Equation 6).

$$SS_f = \frac{N}{N_{nf}} \sum_{i=1}^{N_{nf}} (\bar{y}_i - \bar{y})^2 \quad (6)$$

where:

\bar{y} : the average response,

\bar{y}_i : average of the measured responses for each level i of the F -factor,

N : the total number of trials,

N_{nf} : the number of levels of each f factor.

The squared mean (MS) is calculated by dividing the squared sum by the number of degrees of freedom (Equation 7).

$$MS_i = \frac{SS_i}{dl_i} \quad (7)$$

The F -Value is used to check the compatibility of the mathematical model on the grounds that the calculated F -Values must be greater than the tabulated F (F -Table) (Equation 8).

$$F_i = \frac{MS_i}{MS_e} \quad (8)$$

where MS_e is the mean squared sum of the errors.

Column (Cont%) of the ANOVA table shows the contribution of factors (in percent) to the total variance, indicating the degree of percent effect on response (Equation 9).

$$Cont. \% = \frac{SS_f}{SS_T} \times 100 \quad (9)$$

The coefficient of determination (R^2), defined as the ratio of explained variation to total variation, is a measure of the goodness of fit (Equation 10).

$$R^2 = \frac{\sum(y_i - \bar{y})^2}{\sum(\bar{y}_i - \bar{y})^2} \quad (10)$$

ANOVA results for response surface criteria (R_a , R_y , and R_z)

To determine the influence of any given input parameter from a series of experimental results by DOE for the machining process, the statistical method

of ANOVA was used to properly interpret the experimental data [4]. The coefficient of determination R^2 is an important criterion that is defined as the ratio of the explained variation to the total variation and is a measure of the degree of adjustment. R^2 (adj) is an average measure explained by the model, adjusted for the number of terms in the model, and the obtained results are analysed using Design Expert 12.

Tables 4 to 6 show the results of the analysis of variance for R_a , R_y , and R_z , respectively. This analysis was performed for p -values of less than 0.05 (95% reliability or better). Table 4 summarizes the results of the analysis of variance for the surface roughness criterion R_a , and it is noted that the most important factor affecting the criterion of surface roughness R_a is the feed rate (f_z) with a contribution of 52.37%. The increase in feed rate generates furrows which become deeper and wider with each increase in the feed rate. The cutting speed has a contribution of 37.88% and it is the second most influential factor. In the third position, it goes to the effect of product $f_z \times f_z$ with a contribution of 4.40%. The depth of cut (ap) effect is insignificant, but we do not take it into account because its reliability does not exceed 8%. We also neglect the interactions of $f_z \times ap$, $ap \times V_c$, and $V_c \times f_z$ as well as the effects of products V_c^2 , and ap^2 because they are not important.

Table 5 summarizes the results of the ANOVA analysis for the roughness criterion, R_y . It is noted that the feed rate contributes the greatest effect with 80.97%, then the cutting speed has a contribution of 12.90%, followed by the interaction of combined parameter $V_c \times f_z$ with a contribution of 1.55%. Regarding the depth of cut, interactions, and effects of products have a low contribution. Referring to Table 6, the feed rate and the cutting speed are the two most important factors contributing to the effect of the roughness R_z , with contributions of 42.01%, and 24.44%, respectively, followed by f_z^2 , and V_c^2 with contributions of 13.44%, and 3.56%, while the other factors are insignificant.

Main effects and interactions

Figures 6, 7, and 8 represent the main effects plot in which the differences between the average responses of one or more factor levels were examined. This is a major effect when different levels of a factor affect the response. The main effects plot shows a plot of the mean response for each factor level connected to a line. The main effects plot shows that feed rate is the most influential factor as it exhibits the greatest trend for roughness criteria (R_a , R_y , and R_z) as a function of feed rate, followed by cutting speed, and finally, the effect of depth of cut, which does not affect significantly with respect to cutting speed and feed rate as shown in the main effects diagram of R_a , R_y , and R_z .

Table 4: Analysis of variance for R_a

Source	<i>Df</i>	<i>SS</i>	<i>MS</i>	<i>F</i>	<i>P</i>	<i>Cont.%</i>	Remarks
Regression	9	163.255	18.1395	119.761	0.000000	95.22%	Significant
<i>Vc</i>	1	64.952	0.8116	5.358	0.024458	37.88%	Significant
<i>fz</i>	1	89.783	17.1105	112.967	0.000000	52.37%	Significant
<i>ap</i>	1	0.584	0.0014	0.009	0.924464	0.34%	Insignificant
<i>Vc</i> × <i>Vc</i>	1	0.235	0.2354	1.554	0.217919	0.13%	Insignificant
<i>fz</i> × <i>fz</i>	1	7.546	7.5464	49.823	0.000000	4.40%	Significant
<i>ap</i> × <i>ap</i>	1	0.075	0.0746	0.493	0.485825	0.04%	Insignificant
<i>Vc</i> × <i>fz</i>	1	0.001	0.0009	0.006	0.939487	0.000%	Insignificant
<i>Vc</i> × <i>ap</i>	1	0.020	0.0199	0.131	0.718424	0.01%	Insignificant
<i>fz</i> × <i>ap</i>	1	0.059	0.0591	0.390	0.534957	0.03%	Insignificant
Error	54	8.179	0.1515				
Total	63	171.435					

Table 5: Analysis of variance for R_y

Source	<i>Df</i>	<i>SS</i>	<i>MS</i>	<i>F</i>	<i>P</i>	<i>Cont.%</i>	Remarks
Regression	9	330.787	36.7541	36.5299	0.00001	85.89%	Significant
<i>Vc</i>	1	49.689	49.689	49.387	0.001298	12.90%	Significant
<i>fz</i>	1	271.373	271.373	269.72	0.00001	80.97%	Significant
<i>ap</i>	1	0.0761	0.0761	0.0757	0.78432	0.024%	Insignificant
<i>Vc</i> × <i>Vc</i>	1	1.806	1.806	1.7948	0.18595	0.46%	Insignificant
<i>fz</i> × <i>fz</i>	1	1.415	1.415	1.4065	0.24083	0.36%	Insignificant
<i>ap</i> × <i>ap</i>	1	0.029	0.029	0.0292	0.864882	0.007%	Insignificant
<i>Vc</i> × <i>fz</i>	1	6.003	6.003	5.9665	0.017883	1.55%	significant
<i>Vc</i> × <i>ap</i>	1	0.368	0.368	0.3653	0.548103	0.09%	Insignificant
<i>fz</i> × <i>ap</i>	1	0.011	0.011	0.0113	0.915879	0.002%	Insignificant
Error	54	54.331	1.0061				
Total	63	385.118					

Table 6: Analysis of variance for R_z

Source	<i>Df</i>	<i>SS</i>	<i>MS</i>	<i>F</i>	<i>P</i>	<i>Cont.%</i>	Remarks
Regression	9	210,334	23,370	31,877	0,000000	84.16	Significant
<i>Vc</i>	1	61,072	14,607	19,924	0,000041	24.44	Significant
<i>fz</i>	1	105,001	36,898	50,329	0,000000	42.01	Significant
<i>ap</i>	1	0,252	0,485	0,662	0,419384	0.1	Insignificant
<i>Vc</i> × <i>Vc</i>	1	8,895	8,895	12,133	0,000990	3.56	Significant
<i>fz</i> × <i>fz</i>	1	33,583	33,583	45,807	0,000000	13.44	Significant
<i>ap</i> × <i>ap</i>	1	0,217	0,216	0,295	0,588814	0.087	Insignificant
<i>Vc</i> × <i>fz</i>	1	0,638	0,638	0,870	0,354900	0.26	Insignificant
<i>Vc</i> × <i>ap</i>	1	0,633	0,632	0,863	0,356959	0.26	Insignificant
<i>fz</i> × <i>ap</i>	1	0,042	0,041	0,057	0,811982	0.017	Insignificant
Error	54	39,589	0,733				
Total	63	249,923					

DF: degree of freedom; *SS*: sum of squares; *MS*: adjusted mean squares.

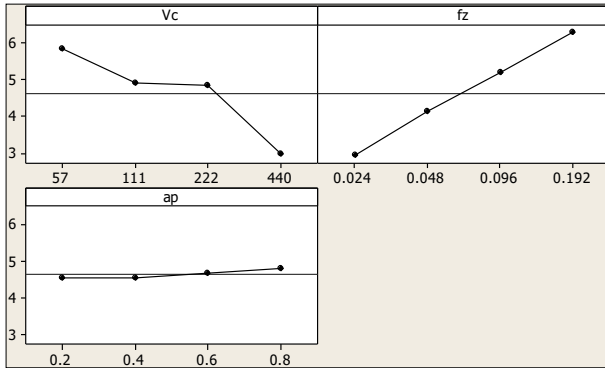


Figure 6: Main effects plot for R_a

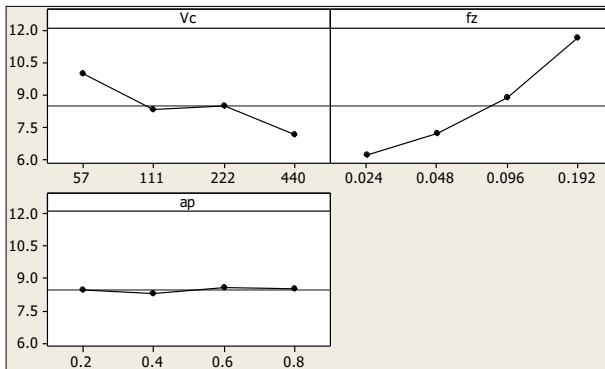


Figure 7: Main effects plot for R_y

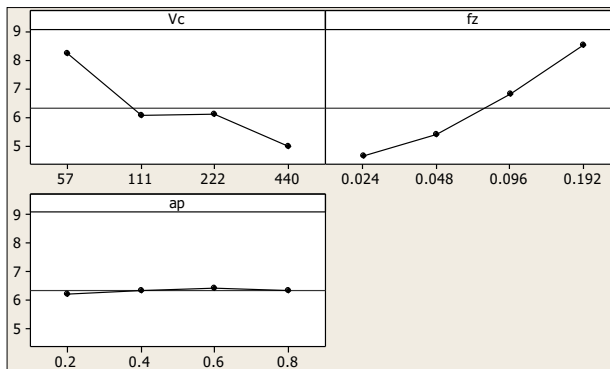


Figure 8: Main effects plot for R_z

Figures 9, 10, and 11 show the interaction diagram in which parallel lines indicate the absence of interaction between the two segments: the greater the difference in slope between the lines, the greater the degree of interaction. However, the interaction plot does not indicate whether the interaction is statistically significant. It appears from the interaction diagrams (R_a , R_y , and R_z) that the interaction of the cutting conditions does not have a significant impact on the surface roughness criteria (R_a , R_y , and R_z) except in the case of the interaction between the cutting speed and the feed rate in the two diagrams of R_y and R_z . We, therefore, notice a small convergence of the roughness values R_y when the feed rates are high. Moreover, the roughness values of R_z are approachable when the feed rate increases, especially when $f_z=0.096$ mm/tooth.

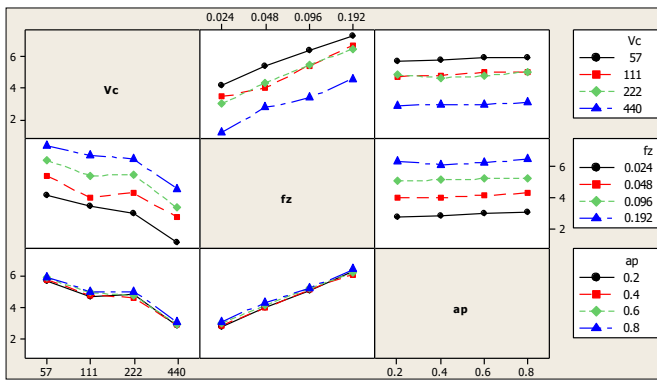


Figure 9: Interaction plot for R_a

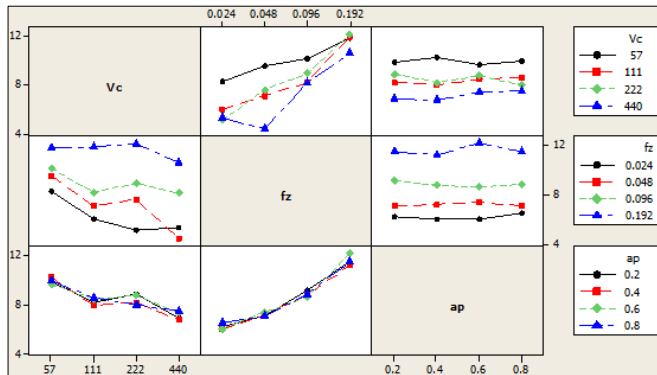


Figure 10: Interaction plot for R_y

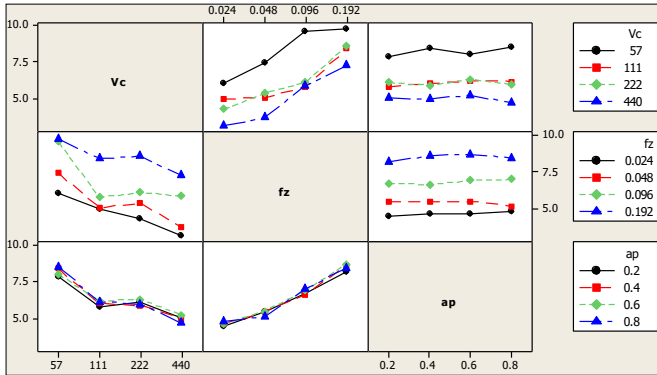


Figure 11: Interaction plot for R_z

Regression equations

The relationship between input parameters and performance measurements (outputs) is modelled by quadratic regression using Minitab 16 software. The regression equations are obtained together with determination coefficients (R^2). The arithmetic mean roughness (R_a) model and coefficients of determination are given in Equation (11).

$$\begin{aligned}
 R_a = & 3.0909 - 0.004458 Vc + 46.4462 fz - 0.124696 ap - \\
 & 4.109 \times 10^{-6} Vc^2 - 0.000392 Vc \times Fz - 0.000537084 Vc \times ap \\
 & - 121.033 fz^2 - 2.11146 fz \times ap + 0.853516 ap^2 \\
 R^2 = & 95.23\% \quad , \quad R^2(adj) = 94.43\%
 \end{aligned}
 \tag{11}$$

The maximum height of the profile (R_y) model is given below in Equation (12). Its coefficient of determination is $R^2=85.89\%$.

$$\begin{aligned}
 R_y = & 7.80398 - 0.0158878 Vc + 36.463 fz - 0.928013 ap \\
 & + 1.138 \times 10^{-5} Vc^2 + 0.032419 Vc \times fz + 0.002308 Vc \times ap \\
 & - 52.4124 Fz^2 + 0.924819 fz \times ap + 0.535938 ap^2 \\
 R^2 = & 85.89\%
 \end{aligned}
 \tag{12}$$

The mean of the third point height (R_z) model is given below in Equation (13). Its coefficient of determination is $R^2=84.95\%$.

$$\begin{aligned}
 R_z = & 5.66873 - 0.0190703 Vc + 36.5371 fz + 2.17619 ap \\
 & + 2.52746 \times 10^{-5} Vc^2 + 0.0113375 Vc \times fz - \\
 & 0.00303 Vc \times ap - 77.2339 fz^2 + 2.09941 fz \times ap - 1.455 ap^2 \\
 R^2 = & 84.16\%
 \end{aligned}
 \tag{13}$$

Models are reduced by eliminating terms with no significant effect on the responses, and they are given by Equation (14) and Equation (15).

$$\begin{aligned} Ra &= 3.46201 - 0.00686135 Vc + 45.309 fz - 121.033 fz^2 \\ R^2 &= 94.66\% \end{aligned} \quad (14)$$

$$\begin{aligned} Ry &= 7.4366 - 0.00891901 Vc + 25.2762 fz \\ &+ 0.0324191 fz \times Vc \text{ with } R^2 = 84.93\% \end{aligned} \quad (15)$$

$$\begin{aligned} Rz &= 6.10858 - 0.0195655 Vc + 39.9393 fz \\ &+ 2.52746 \times 10^{-5} Vc^2 - 77.2339 fz^2 \\ R^2 &= 84.19\% \end{aligned} \quad (16)$$

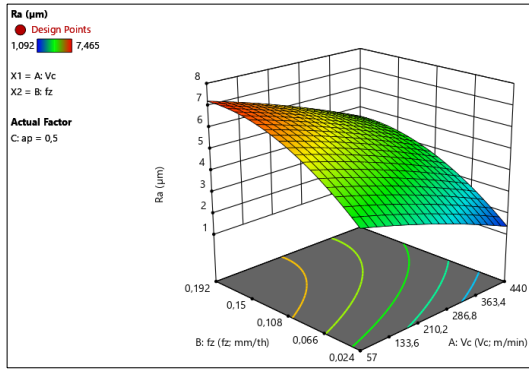
Response surface and contour plots of R_a , R_y , and R_z

Response surfaces (as shown in Figures 12, 13, and 14) show that the feed rate has the greatest effect and that each reduction in the feed rate reduces the surface roughness parameters significantly, followed by the cutting speed with a significant effect, while the depth of cut is minimally affected.

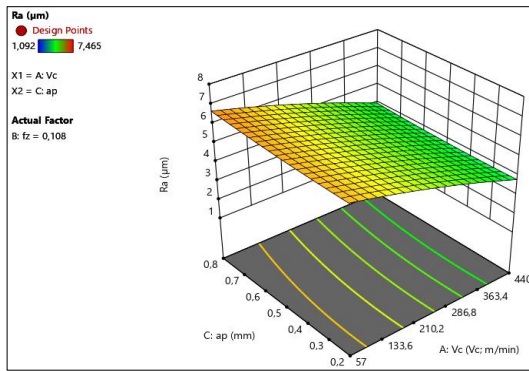
These graphs (Figures 12, 13, and 14) also show that high roughness criteria require a high feed rate (0.192 mm/tooth) and low cutting speed (57 m/min), while low roughness criteria require a low feed rate (0.024 mm/tooth) and high cutting speed (440 m/min). Therefore, the best roughness is achieved by applying a small feed rate and a high cutting speed.

Model verification was performed using residual analysis. The coloured dots indicate the surface roughness value. The curves of the normal probability of R_a , R_y , and R_z are presented in Figures 15 to 17. It is clear that the residuals are very close compared to the straight line of normality, which implies that the errors are normally distributed. Thus, the already obtained mathematical models can be used to predict surface roughness.

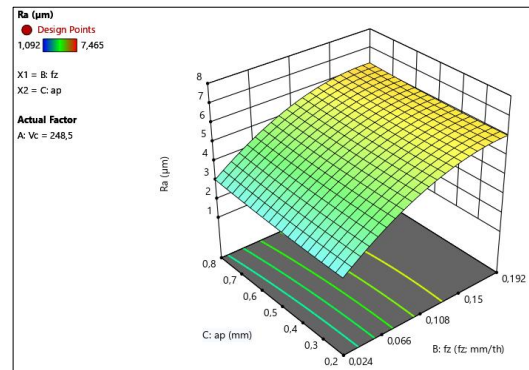
Table 7 shows the results of the ANOVA analysis for the MRR. It is noted that all factors (fz , Vc , and ap) and interactions ($fz \times ap$, $ap \times Vc$, and $Vc \times fz$) have no significant effect; thus, the feed rate and the cutting speed are the two important factors contributing to the effect of the MRR with contributions of 29.69% and 29.09%, respectively. The interaction ($Vc \times fz$) has a contribution of 14.87%, followed by the depth of cut with a contribution of 11.62% of the total effect, while the interactions ($fz \times ap$ and $ap \times Vc$) have low contributions (5.94% and 5.82%), respectively.



(a)

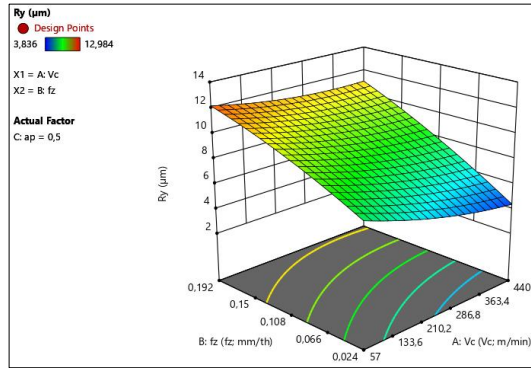


(b)

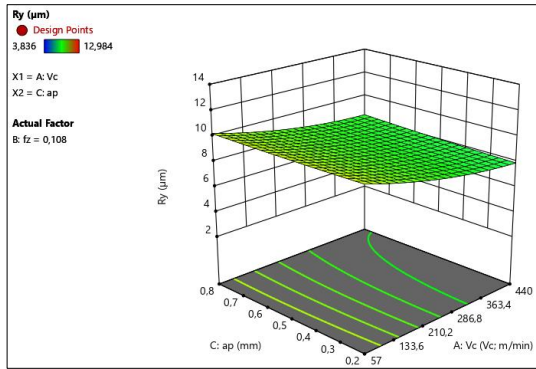


(c)

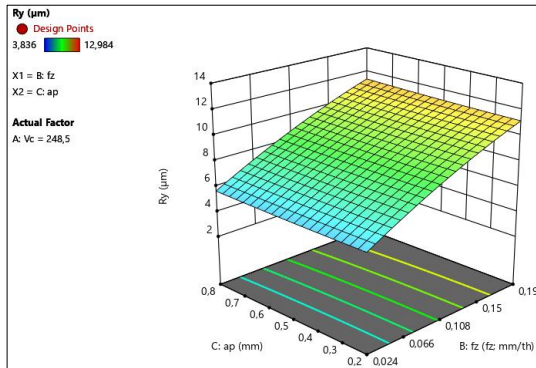
Figure 12: Response surface for Ra as a function of (a) Vc , fz , (b) Vc , ap , and (c) ap , fz



(a)

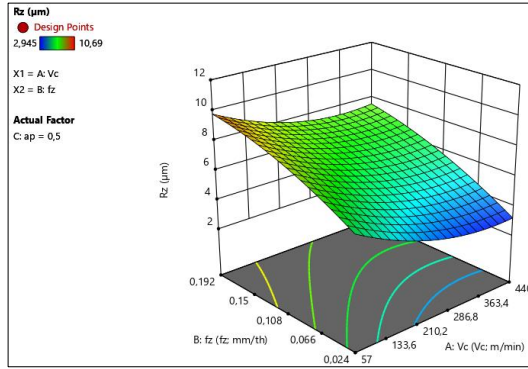


(b)

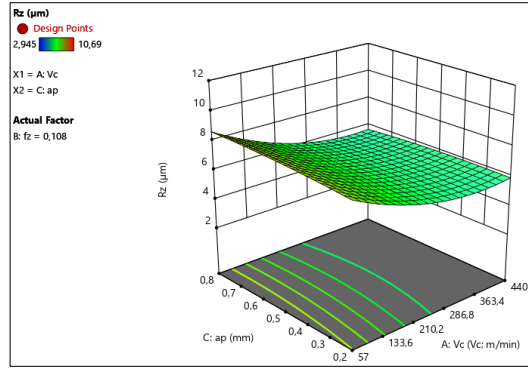


(c)

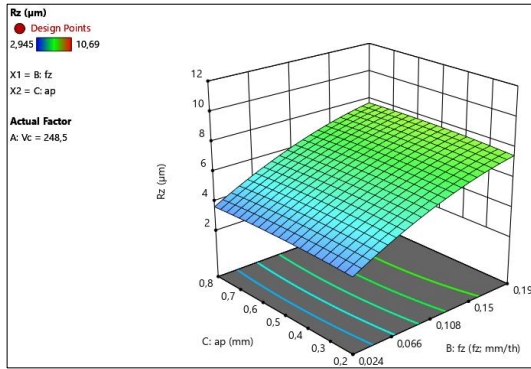
Figure 13: Response surface for R_y as a function of (a) V_c, f_z , (b) V_c, a_p , and (c) a_p, f_z



(a)



(b)



(c)

Figure 14: Response surface for R_z as a function of (a) V_c , f_z , (b) V_c , ap , and (c) ap , f_z

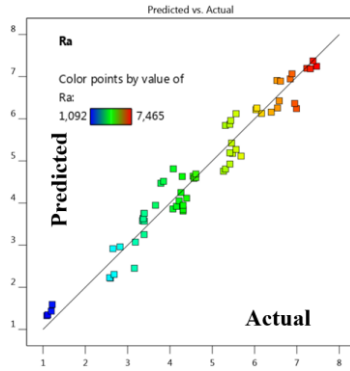


Figure 15: Normal probability of R_a

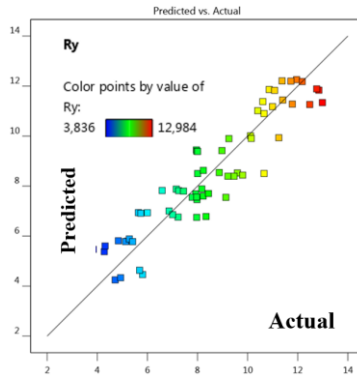


Figure 16: Normal probability of R_y

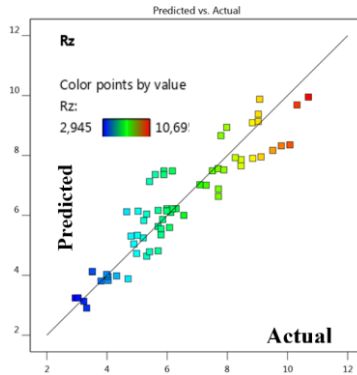


Figure 17: Normal probability of R_z

Table 7: Analysis of variance for *MRR*

Source	<i>DF</i>	<i>SS</i>	<i>MS</i>	<i>F</i>	<i>P</i>	<i>Cont.%</i>	Rem.
Regr.	9	4595454514	510606057	195,7	0,000	97.03%	Significant
<i>Vc</i>	1	1377709478	40774922	15,63	0,000	29.09%	Significant
<i>fz</i>	1	1406419728	42101246	16,14	0,000	29.69%	Significant
<i>ap</i>	1	550338006	15201146	5,829	0,020	11.62%	Significant
<i>Vc*fz</i>	1	704162218	704162218	70,00	0,999	14.87%	Insignificant
<i>Vc*ap</i>	1	275541693	275541693	105,6	0,809	5.82%	Insignificant
<i>fz*ap</i>	1	281283390	281283390	107,8	0,999	5.94%	Insignificant
Error	54	140831875	2607998				
Total	63	4736274157					

Main effects and interactions of *MRR*

For the main effects, the diagram in Figure 18 illustrates that the depth of cut has almost a constant effect between all levels, while the increase in feed rate and speed of cut produces a simple increase in the effect between their levels. Figure 19 indicates the interactions for *MMR*. From these diagrams, the interactions of the three cutting parameters ($fz \times ap$, $ap \times Vc$, and $Vc \times fz$) have no significant impact on the material removal rate. The mathematical model can be reduced as follows: $MRR = f(Vc, fz, \text{ and } ap)$.

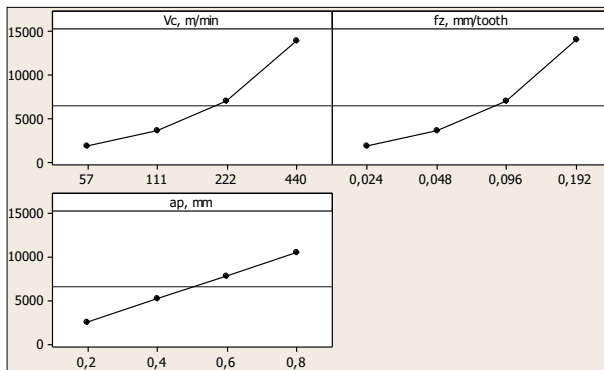


Figure 18: Main effects plot for *MMR*; mm^3/min

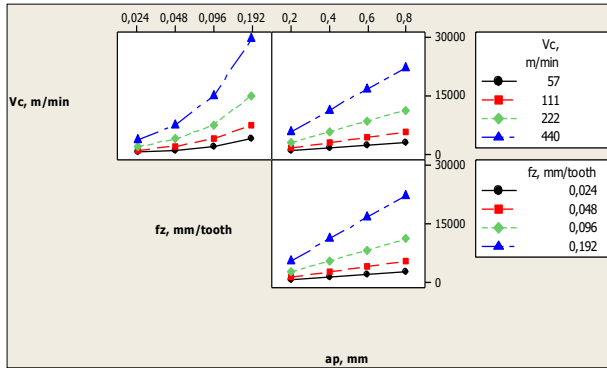


Figure 19: Interaction plot for MRR , mm^3/min

Regression equations

The material removal rate RMM model is given below in Equation (17).

$$\begin{aligned}
 MRR = & 6557,07 - 31,6003 Vc - 72856,3 fz - 13114,1 ap + \\
 & 351,115 Vc \times fz + 63,2007 Vc \times ap + 145713 fz \times ap \quad (17) \\
 R^2 = & 97,03 \quad , \quad \text{Adjusted } R^2 = 96,71\%
 \end{aligned}$$

Multi-response optimization Ra and MRR using desirability approach.

Optimization methods were used to obtain the optimum machining conditions for milling operations using surface roughness and MRR as responses.

In order to decrease the level of desirability, Figure 20 and Table 8 show the optimization results (minimize Ra and maximize MRR). Values of optimal cutting parameters were found to be as follows: $Vc=440$ m/min, $fz=0.096$ mm/tooth, and $ap=0.8$ mm. The optimum surface roughness and MRR were as follows: $Ra=3.756 \mu\text{m}$ and $MRR=23435.874 \text{ mm}^3/\text{min}$ with combined desirability=0.830035.

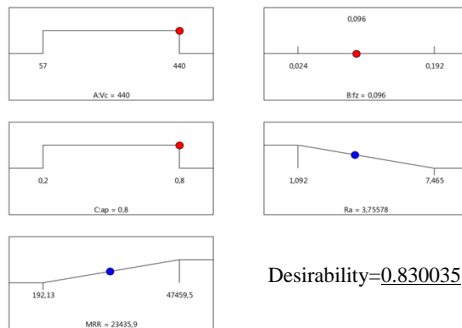


Figure 20: Ramp function graph for surface roughness and MRR

Table 8: Response optimization for surface roughness and MRR

Number	V_c	f_z	ap	R_a	MRR	Desirability
1	440.00	0.096	0.800	3.756	23435.874	0.830035
2	440.00	0.096	0.792	3.749	23206.315	0.828512
3	440.00	0.096	0.769	3.732	22543.256	0.825466
4	440.00	0.096	0.717	3.695	21067.795	0.814805
5	439.99	0.096	0.710	3.690	20845.963	0.813282
6	440.00	0.096	0.704	3.687	20686.579	0.811759
7	440.00	0.096	0.688	3.677	20220.899	0.808713
8	440.00	0.096	0.626	3.642	18445.980	0.79196
9	440.00	0.096	0.548	3.608	16194.432	0.767592

Conclusions

In this work, it studied the effects of these parameters such as feed rate, cutting speed, and depth of cut on roughness criteria (R_a , R_y , and R_z) with Material Removal Rate (MRR) while face milling C45 steel using a GC4040 cutting insert. Based on the experimental results, the following conclusions can be drawn:

- i. The ANOVA analysis of the surface roughness criteria reveals that the feed rate (f_z) has a significant effect on the different surface roughness criteria (R_a , R_y , and R_z) with contributions of 52.37%, 80.97 %, and 54.96%, followed by the cutting speed (V_c) with contributions of 37.88%, 12.90%, and 24.43% on each R_a , R_y , and R_z , respectively, while the effect of depth of cut is negligible.
- ii. The contour plots in this work enabled us to visualize the response surface in two dimensions, and these two methods make it possible to compare the influence of factors on the response.
- iii. The mathematical model of the MRR was the most representative model because its coefficient of determination R^2 was 97.03%, followed by the model of R_a , R_y , and R_z with 95.23%, 85.89%, and 84.95%, respectively. Producing very good ratios, it shows that the studied surface roughness criteria and MRR are mainly related to each response of the cutting parameters (V_c , f_z , and ap) which is close to 100%.
- iv. Values of optimal cutting parameters are found to be as follows: $V_c=440$ m/min, $f_z=0.096$ mm/tooth, and $ap=0.8$ mm. The optimum surface roughness and MRR are as follows: $R_a=3.756$ μ m and MRR=23435.874 mm³/min with a combined desirability=0.830035.

Contributions of Authors

The authors confirm the equal contribution in each part of this work. All authors reviewed and approved the final version of this work.

Funding

This work received no specific grant from any funding agency.

Conflict of Interests

All authors declare that they have no conflicts of interest

Acknowledgment

Special thanks to the staff and members of the Mechanics and Structures Research Laboratory (LMS) and Higher School of Technological Education in Skikda who always provide facilities that are needed in order to complete this work.

References

- [1] A. M. Ravi, S. M. Murigendrappa, and P. G. Mukunda, "Experimental investigation of influence of tool temperature on cutting forces in the thermally enhanced machining of high chrome white cast iron", *Procedia Materials Science*, vol. 5, pp. 2099-2104, 2014.
- [2] S. Chihaoui, M. A. Yallese, S. Belhadi, A. Belbah, K. Safi, & A. Haddad, "Coated CBN cutting tool performance in green turning of gray cast iron EN-GJL-250: modeling and optimization", *The International Journal of Advanced Manufacturing Technology*, vol. 113, no. 11, pp. 3643-3665, 2021.
- [3] B. Lakhdar, Y. M. Athmane, B. Salim, & A. Haddad, "Modelling and optimization of machining parameters during hardened steel AISID3 turning using RSM, ANN and DFA techniques: Comparative study", *Journal of Mechanical Engineering and Sciences*, vol. 14, no. 2, pp. 6835-6847, 2020.
- [4] M. Fnides, M. A. Yallese, R. Khattabi, T. Mabrouki, & F. Girardin, "Modeling and optimization of surface roughness and productivity through RSM in face milling of AISI 1040 steel using coated carbide

- inserts”, *International Journal of Industrial Engineering Computations*, vol. 8, no. 4, pp. 493-512, 2017.
- [5] S. A. Rizvi, & W. Ali, “Mathematical modelling and optimization of surface roughness and material removal rate during the machining of AISI 1040 steel”, *Academic Journal of Manufacturing Engineering*, vol. 19, no. 3, pp. 50-57, 2021.
- [6] G. Ghosh, P. Mandal, & S. C. Mondal, “Modeling and optimization of surface roughness in keyway milling using ANN, genetic algorithm, and particle swarm optimization”, *The International Journal of Advanced Manufacturing Technology*, vol. 100, no. 5, pp. 1223-1242, 2019.
- [7] D. D. Trung, “Influence of cutting parameters on surface roughness during milling AISI 1045 steel”, *Tribology in Industry*, vol. 42, no. 4, pp. 658–665, 2020.
- [8] A. Palanisamy, N. Jeyaprakash, V. Sivabharathi, & S. Sivasankaran, “Effects of dry turning parameters of Incoloy 800H superalloy using Taguchi-based Grey relational analysis and modeling by response surface methodology”, *Proceedings of the Institution of Mechanical Engineers, Part C: Journal of Mechanical Engineering Science*, vol. 236, no. 1, pp. 607-623, 2022.
- [9] L. Bouzid, M. A. Yallese, K. Chaoui, T. Mabrouki, & L. Boulanouar, “Mathematical modeling for turning on AISI 420 stainless steel using surface response methodology”, *Proceedings of the Institution of Mechanical Engineers, Part B: Journal of Engineering Manufacture*, vol. 229, no. 1, pp. 45-61, 2015.
- [10] M. Kuntoğlu, A. Aslan, D. Y. Pimenov, K. Giasin, T. Mikolajczyk, , & S. Sharma, “Modeling of cutting parameters and tool geometry for multi-criteria optimization of surface roughness and vibration via response surface methodology in turning of AISI 5140 steel”, *Materials*, vol. 13, no. 19, p. 4242, 2020.
- [11] B. Sureshkumar, V. Vijayan, S. Dinesh, & K. Rajaguru, “Neural network modeling for face milling operation”, *International Journal of Vehicle Structures and Systems*, vol. 11, pp. 214-219, 2019.
- [12] J. Mumtaz, Z. Li, M. Imran, L. Yue, M. Jahanzaib, S. Sarfraz, & K. Afzal, “Multi-objective optimisation for minimum quantity lubrication assisted milling process based on hybrid response surface methodology and multi-objective genetic algorithm”, *Advances in Mechanical Engineering*, vol. 11, no. 4, pp. 1-13, 2019.
- [13] L. Bouzid, S. Boutabba, M. A. Yallese, S. Belhadi, & F. Girardin, “Simultaneous optimization of surface roughness and material removal rate for turning of X20Cr13 stainless steel”, *The International Journal of Advanced Manufacturing Technology*, vol. 74, no. 5, pp. 879-891, 2014.
- [14] G. K. Pandiyan, & T. Prabakaran, “Optimization of machining parameters on AA6351 alloy steel using response surface methodology (RSM)”, *Materials Today: Proceedings*, vol. 33, pp. 2686-2689, 2020.

- [15] M. Ozdemir, "Effect of cutting parameters on the machinability of X37CrMoV5-1 hot work tool steel," *Materials Testing*, vol. 64, no. 3, pp. 412–429, 2022.
- [16] R. Suresh, S. Basavarajappa, G. L. Samuel, "Some studies on hard turning of AISI 4340 steel using multilayer coated carbide tool", *Measurement*, vol. 45, no. 7, pp. 1872-1884, 2012.

Accuracy of CFD Simulations on Indoor Air Ventilation: Application of Grid Convergence Index on Underfloor Air Distribution (UFAD) System Design

Nor Azira Mohd Zainuddin, Fauziah Jerai*, Azli Abd Razak,
Mohd Faizal Mohamad

School of Mechanical Engineering, College of Engineering,
Universiti Teknologi MARA, 40450, Shah Alam, Selangor, MALAYSIA
*fauziahjerai@uitm.edu.my

ABSTRACT

Underfloor air distribution system (UFAD) mesh flow velocity was simulated using Computational Fluid Dynamics (CFD). Three mesh sizes were used to explore the domain's core x-y plane velocity contour and profiles. Compared to medium and fine, the coarse mesh underestimated the velocity significantly. A slight discrepancy occurred where the shear flow was dominant. The symmetrical flow velocity for both sides of the room length was shown in the xy-plane at the centre of the inlet. The mean error for coarse and medium mesh was larger than for the medium and fine mesh. It shows that the difference between the medium mesh and the fine was accepted. The computational time for medium mesh was acceptable for simulation, and it will not vary substantially even if the grid is refined further. The normalised mean square error (NMSE), the factor of two observations (FAC2), the factor of 1.3 observations (FAC1.3), and the fractional bias (FB) are used to measure the performance of the models and the value of the outcomes was exceptional. As a result, the accuracy of the finding can be improved by conducting additional research with manikins and in a fully occupied room under real-world conditions. In addition, this study could analyse and anticipate the optimal scenario regarding ventilation performance, etc.

Keywords: *Computational Fluid Dynamics (CFD); Discretization Error; Grid Convergence Index (GCI); Mesh Refinements; Verification*

Introduction

An underfloor air distribution (UFAD) system is used in many modern commercial buildings, like open office buildings because it is considered an energy-efficient way to move air. To prevent cold draughts and UFAD short-circuits, it is important to control the supply air's temperature and velocity. This could reduce the efficiency of new commercial buildings to remove heat generated by a highly sensible cooling load [1]-[2]. The UFAD indoor air distribution system may improve thermal comfort, air quality, and HVAC energy usage [3].

Displacement ventilation (DV) operates like UFAD systems for cooling. In cooling mode, DV and UFAD systems draw cold air from the floor and exhaust it from the ceiling. Thermal plumes from overheated sources cause floor-to-ceiling air movement by entraining and lifting air. High heat loads are accommodated through buoyancy-driven airflow. Its thermal plume cools the room. DV and UFAD deliver space air differently. UFAD diffusers mix more than DV diffusers, which are low-velocity. This lets a reduced air volume supply meet room load. Air rising in the room uses heat gain's natural buoyancy in space to generate a vertical temperature differential. Due to differing fluid dynamics, UFAD can have a lower supply air temperature and higher flow rate than DV [4].

Indoor environments are frequently modelled using Computational Fluid Dynamics (CFD) [5]-[7]. CFD simulations require accurate computational mesh and flow problem physics. In CFD models, input models and numerical uncertainty might influence the numerical solutions. The accuracy is linked with the grid resolution. For example, spatial discretization error is the most challenging and demanding approximation. The discretization error can be decreased by refining the grid. Increasing discretization scheme order and mesh size or quality reduces numerical errors. When raising mesh resolution, it is necessary to consider all elements affecting mesh quality. Uniformity, aspect ratio, orthogonality, and skewness values are essential mesh qualities to examine. These mesh metrics will affect the solution method's accuracy, robustness, and efficiency; therefore, whether a mesh is good or bad depends on the numerical discretization. Getting a solution that does not rely on the mesh size can be very expensive and take a long time, significantly if the mesh size is reduced randomly. Finding the proper mesh density for a given problem has proven challenging while maintaining computational time and accuracy within acceptable limits. Making a well-distributed mesh from the start can save from using adaptive mesh techniques, and it is essential to set the correct values at the beginning.

Other than that, CFD modelling is difficult for ventilation when developing unstable turbulence models like Large Eddy Simulation (LES) and representing inlet boundary conditions. The challenge is predicting internal airflow and ventilation. Reynolds-averaged Navier–Stokes (RANS) or

Unsteady RANS (URANS) equations are extensively employed for ventilation simulation due to their inexpensive cost, but their accuracy is restricted by unresolved temporal turbulent fluctuations, an assumption of Reynolds stress isotropy, and low-Reynolds-number effects. RANS models were not designed to forecast flow regimes like boundary layer separation [8]. RANS models overestimate turbulent dissipation, which raises wall shear stress, delays the separation of the wall boundary layer, and misaligns the wall jet. These issues may make it difficult to anticipate air flow and turbulence, which is crucial for removing indoor pollutants. Building ventilation systems aren't optimised by RANS models. Owing to RANS's constraints, we need to improve the numerical equations and apply the right LES models for ventilation simulations while considering low-Reynolds-number effects [9].

Most indoor CFD models use hexahedral, tetrahedral, or hybrid meshes [10]-[11]. The hexahedral mesh can be structured or unstructured, but the other two are not structured. Several CFD studies have looked at how mesh types and cell shapes affect the mean flow profile. The grid independence test was utilised in various ways while examining the indoor environment. There is a structured and unstructured mesh. The structured mesh comprises two main types: regular topology and repeated primitive shapes in space. For structured meshes, flow-aligned hexahedral elements can improve solution accuracy with a small number of cells but making the mesh topology may take time. For unstructured, the connections between the vertices are not regular, and there is no any underlying shape repetition. These meshes are more flexible, easier to make and saves time. However, it may need more cells to be as accurate as structured meshes [12].

Researchers have modelled particle movement and settlement in indoor environments using Mixing Ventilation (MV), Displacement Ventilation (DV), and Underfloor Air Distribution (UFAD) systems. Semi-empirical deposition models explain how particles build up at solid boundaries. The size-dependent deposition characteristics are well figured out in these models, which are used to facilitate the rules [5]. A semi-empirical expression in the range of particle sizes from 0.01-10 μm is compared to an existing numerical model. The deposition and fate of particles are depicted, and a positive outcome is only possible if the near-wall grid is sufficiently small and the turbulent kinetic energy near the wall is adequately muted depending on its component normal to the wall [6].

Before creating our mesh, we must establish the optimal mesh type for our case. In addition, it substantially impacts the cost and accuracy of CFD simulations. Numerous CFD studies have done grid independence evaluations to assess their performance. A spatial discretization error may occur if the mesh is too large or small. Through mesh refinement, the numerical dissipation may be minimized. In addition, a large grid number could be damaging. If the round-off error is huge, it might quickly exceed the truncation error, resulting in decreased accuracy. There may be adverse outcomes if the number of cells

in a cell is too few or too many. Therefore, it is essential to determine the optimal grid number [13].

This study aims to figure out the Grid Convergence Index (GCI) for indoor airflow of an underfloor air distribution (UFAD) system with three different grid resolutions. It is the most common and accurate way to figure out how uncertain the result is. The goal is to determine how the mesh resolution affects the order of accuracy and numerical solution accuracy. It is based on the lower accuracy limit, which can lead to incorrect conclusions when the observed accuracy order differs from the formal order of accuracy [14]. Three kinds of uncertainty can affect the numerical solutions: uncertainty in the inputs, the model, and uncertainty in the math itself. These include spatial and temporal discretization, convergence, and rounding errors [15]. There are many different approximations, but one of the most important and hardest is the error that comes with a grid resolution or spatial discretization error. Grid refinement can be used to reduce the error that comes from discretization. Adjusting the mesh and discretization step size helps reduce numerical errors. All elements that degrade mesh quality when resolution is increased must be considered.

A study compared simulated airflow and temperature distributions in a first-class cabin with the variables (hexahedral, tetrahedral, and hybrid cells) was done in 2015. The study discovered that hexahedral meshes were the most precise, but also the most expensive to compute [16]. In addition, it looked at how mesh refinement and cell topology changed the indoor airflow profile by looking at a graph between the data and the results from computer simulations but not quantitatively.

Grid Convergence Index (GCI) was used [17]-[20] to look at how mesh resolution and cell geometry predict outdoor environments, like how pollutant gas spreads around buildings. The grid resolution affects the accuracy of numerical results by looking at how indoor air temperature changes over time and how old the air is [21]-[22]. Instead, some researchers looked at temperature and velocity profiles. When calculating the velocity flow profile, the hexahedral mesh outperforms the tetrahedral mesh but also took the most time to make. The hybrid meshes were the least accurate but took the least amount of time to calculate. By increasing the number of grids in the hybrid mesh to get the same level of accuracy as with hexahedral meshes, the same amount of time is spent on computing. From the study, the accuracy of simulations with hexahedral meshes with 12 million cells, hybrid meshes with 24 million cells, and tetrahedral meshes with about 15 million cells would be the same. Also, each of these simulations would take about 80–90 hours to run on the computer network [16].

By adding more grids to the hybrid mesh, accuracy can be increased. Hexahedral mesh matches experimental data faster than other mesh designs [21], [23]-[24]. The GCI method can figure out the order of convergence and the asymptotic answer in a solid way. Even though more study needs to be

done on blast situations and finite element (FE) calculations, this method seems to be a good estimate. Researchers can analyse the airflow, air quality, and thermal comfort by using a good simulation to predict the real airflow, air quality, and thermal comfort data. This study identifies the optimal mesh size that could rank the error based on how far off the key predicted and measured results were from each other. A study of air velocity distributions showed that different mesh types led to different simulation results due to truncation problems.

Methodology

Model development

Most buildings are ventilated either mechanically, naturally, or both. Airflow within rooms is often turbulent, and turbulence disperses particles more efficiently. Before figuring out how particles move, it is important to know how the air flows around them. The Eulerian method is used to simulate the air in this numerical analysis. A new drift-flux model is used to solve the turbulent airflow field utilising the Renormalization Group (RNG) k - ϵ turbulence model as validated by paper [10]. RNG k - ϵ models simulate three-dimensional (3D) turbulent airflow [25]. They are computationally efficient and stable compared to seven-equation Reynolds stress models. RNG and traditional k - ϵ models have different constant coefficients despite similar formulations. Compared to the standard k - ϵ model and other turbulence or laminar models [26], the RNG k - ϵ model is more suited for simulations of indoor airflow. The general version of the governing Equation (1) for an incompressible fluid is as follows:

$$\frac{\partial y}{\partial x}(\phi) + \nabla \cdot (u_\phi) = \nabla \cdot (\tau_\phi \nabla \phi) + S_\phi \quad (1)$$

u is the velocity vector, ϕ represents each of the three velocity components, u , v , and w . τ_ϕ is the effective diffusion coefficient ϕ . S_ϕ is the source term of the general Equation (2). When $S_\phi=1$, the Equation changes into the continuity equation.

Most airflows indoors are turbulent. So, turbulence modelling is essential for most CFD simulations [27]. Reynolds-Averaged Navier-Stokes (RANS) turbulence modelling has become a popular way to model how air moves in closed spaces. For indoors, the air phase flow is viscous, incompressible, isothermal, and has the same density. RNG k ϵ turbulence model has been used with the Reynolds-Averaged Navier-Stokes (RANS) equations as a guide. They can be written down in general terms:

$$\rho \bar{u}_j \frac{\partial \bar{u}_i}{\partial x_j} = \rho \bar{f}_i + \frac{\partial}{\partial x_j} \left[-\rho \delta_{ij} + \mu \left(\frac{\partial \bar{u}_i}{\partial x_j} + \frac{\partial \bar{u}_j}{\partial x_i} \right) - \rho \overline{u'_i u'_j} \right] \quad (2)$$

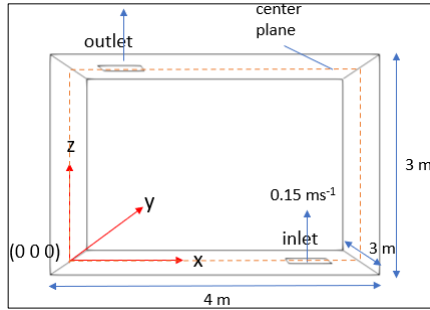


Figure 1: The sectional perspective of the room geometry used for the development of the indoor airflow profile model

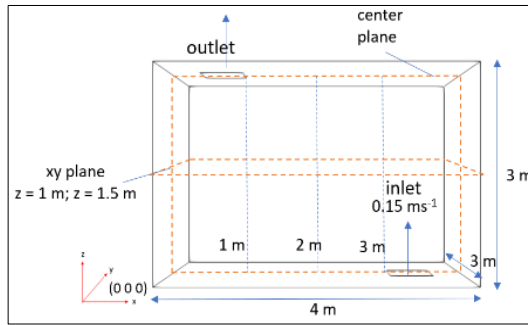


Figure 2: The centre plane of the model

Figure 1 shows the sectional perspective of the room geometry, where width (W) x height (H) x length (L) = 4 x 3 x 3 m. Figure 2 shows the centre of each xy -plane and the xz -plane for the domain. The inlet and outlet dimensions are 0.6 x 0.6 m (refer to JKR dwg. std) and are located on the floor and at the top.

Boundary condition

Boundary conditions specify the set of computational mesh faces that align with the physical domain's edges. There are two different kinds of boundary conditions: numerical and physical. Von Neumann and Dirichlet boundary conditions are the two forms of numerical boundary conditions. These boundary conditions affect the gradient along the border and the value on the

boundary (or a constant value) of the variable [28]. Below is the description of the physical boundary conditions for an incompressible flow:

- i. Inlet: the velocity value is determined, and a zeroGradient pressure condition is set.
- ii. Outlet: the outflow border is specified in the same manner as the total mass balance. The pressure distribution is specified, and the pressure and velocity boundary conditions are fixed to fixedValue and zeroGradient, respectively.
- iii. Non-slip wall: the flow velocity on the wall is the same as the wall's velocity. As there is no flow through the wall, the pressure gradient is set to zeroGradient.

Three different patches in the computational domain have been made for this study. A part of the top surface is an outlet, while a part of the bottom surface is an inlet. The side surface is sometimes known as a wall. At the inlet patch, a fixedValue boundary condition is established, whereas, at the wall patch, a zeroGradient is applied. Tables 1 and 2 provide further information on boundary conditions. The industry Code of Practice on Indoor Air Quality (DOSHS 2010) [29] has an acceptable range such as:

- i. Air Temperature: 23 – 26 °C
- ii. Relative Humidity: 40 – 70%
- iii. Air Movement: 0.15 – 0.5 ms⁻¹

The parameters input is referred to DOSHS to make it as actual conditions to get the ideal values.

Table 1: Boundary conditions

Flow of Properties	Type of Patches		
	Outlet	Inlet	Walls
U	zeroGradient	fixedValue	fixedValue
K	zeroGradient	zeroGradient	kqRWallFunction
P	fixedValue	zeroGradient	zeroGradient
nuT	zeroGradient	zeroGradient	nutkWallfunction
ϵ	zeroGradient	fixedValue	epsilonWallFunction

Table 2: Explanation of boundary conditions

Type	Description of boundary conditions
zeroGradient	Normal gradient of ϕ is zero
fixedValue	Value of ϕ is specified
nutkWallfunction	On corresponding patches in the turbulent fields k and nut
kqRWallFunction	On corresponding patches in the turbulent fields k , q , and R
epsilonWallFunction	On corresponding patches in the epsilon field

Grid Convergence Index (GCI)

A discretization error is made in the simulation when a finite time and space domain is used. So, a number answer can only be thought of as a close estimate of the real answer. Grid Convergence Index (GCI) uses the mesh size to figure out how big this error is. The GCI first released Roache in 1994 [30]. This distance between our computed value and the asymptotic value can be thought of as the relative error bound. Users can see how big of an error that might be making and where it might fall inside the error band. While low GCI values indicate that the computational solution is close to the asymptotic on the mesh size, this also demonstrates how much the solution will vary when the mesh size is refined [30], [31]-[32]. If the solution is already good enough, making the mesh smaller will not make it much different. Some authors have shown that it is not always true the results are better when the mesh is finer [33]-[34]. Based on that idea, generally, the results are better when the mesh is finer. Compared to other methods, this one has some significant advantages since it does not need an analytical solution, gives a confidence limit for the estimated error band, and can be used with as few as two mesh solutions.

In the past, the exact analytical solution was used to find the convergence error, and then a graph was used to show the range of convergence. However, most real-world problems do not have clear answers. Most traditional discretization methods presume an exact solution f_{exact} and its numerical approximation $f(h)$. The discretization error is calculated using Equation (3), $E(h)$, and ignores higher-order terms when the mesh is fine enough [30], [35]-[36]:

$$E(h) = f_{exact} - f(h) \approx Ah^p \tag{3}$$

where h is a measure of the mesh's discretization, A is a constant, and p is the convergence rate. So, three unknowns are left: the constant A , the convergence rate p , and the exact solution f_{exact} . The GCI method is based on figuring out these unknowns and estimating them. GCI was employed with three mesh refinements and a constant grid refinement ratio. The meshes used for this study (called A, B, and C) resulted in the following ratio, $r=h_A/h_B=h_B/h_C=2$.

Applying Equation (3) to mesh sizes A, B, and C estimates the order of convergence, where $h_A > h_B > h_C$. Then, the unknown constant A can be eliminated, and the unknown p can be obtained [37]:

$$p = \frac{\ln\left(\frac{f_A - f_B}{f_B - f_C}\right)}{\ln(r)} \tag{4}$$

The analytical conclusion can be approximated by utilising ABC's two best grids to get the asymptotic solution for h approaching zero since the order of convergence is known:

$$f_{h \rightarrow 0} \approx f_{exact} \approx f_A - \frac{f_B - f_C}{r_{CB}^p - 1} \quad (5)$$

Equation (5) calculates the relative error (ϵ) of finer meshes to mesh (r) and convergence (p) ratios [37]-[38]. The definition of the relative error is as follows:

$$\epsilon_{CB} = \frac{f_B - f_C}{f_C} \quad (6)$$

which should never be used since the formula does not incorporate r or p . Equation (7) gives the GCI error as a percentage.

$$GCI_{CB} = F_S \frac{\epsilon_{CB}}{r_{CB}^p - 1} \quad (7)$$

F_S calculates the safety factor by multiplying the relative error term from GCI scenarios. As the exact solution is unclear, this error estimates the finest mesh employed relative to the numerically converged solution [30]. This factor has a value of 3 when two meshes are analysed, and 1.25 when three or more meshes are analysed. The second value was utilised in this investigation. This safety factor indicates the degree of confidence that the calculated error bound is within 95%. Last but not least, the extrapolated (or computed) solution, denoted f_{CB}^* for the finer mesh combination, gives an approximation of the numerically asymptotic solution:

$$f_{CB}^* = \frac{r_{CB}^p \cdot f_A - f_B}{r_{CB}^p - 1} \quad (8)$$

This approach is only applicable when all grids fall inside the asymptotic range, at which point Equation (8) is asymptotically true (also the solution that can be extrapolated to other mesh combinations). By comparing two GCI values from three meshes, the asymptotic range of convergence can be determined. This is based on the assumption that the ratio between errors and mesh spacing must be constant for the asymptotic range of convergence to be fulfilled [38].

$$GCI_{BA} \approx r^p GCI_{CB} \quad (9)$$

Lastly, since the GCI only gives the error bound, Equation (10) shows how to get the range that the converged solution should be within a 95% certainty.

$$|f_c(1 - \frac{GCI_{CB}}{100\%}), f_c(1 + \frac{GCI_{CB}}{100\%})| \tag{10}$$

Results and Discussion

Validation with Chen et al. [10] simulation

The accuracy of this work is judged by comparing steady-state simulation to scale-modeling data for a basic model room conducted by Chen et al. [10]. The characteristics of the CFD model, including the computational grid, turbulence model, boundary conditions, and near-wall treatment, are used to establish a trustworthy CFD model for validation research. The geometry and condition of their experimental setup are the same as our CFD setup. To validate the precision of airflow estimates, the x-direction velocity is compared to the experimental data reported by Chen et al. [10]. The model geometry done by Chen et al. is shown in Figure 3 in length (x), width (y), and height (z); 0.8 m, 0.4 m, and 0.4 m. Its inlet and outlet are the exact sizes, 0.04 x 0.04 m.

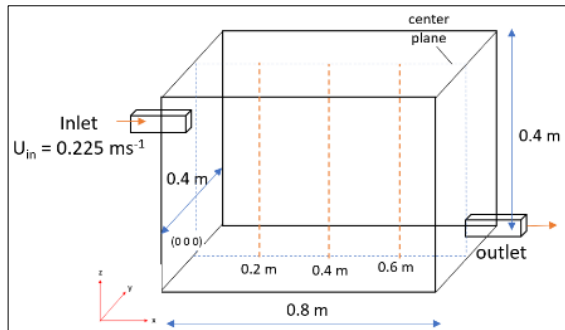


Figure 3: Ventilation chamber and experiment diagram by Chen et al. [10]

Two grid systems with 40 20 20 and 80 40 40 grids have been used with the grid-independent test. The comparison shows that the difference is not very big (less than 5%), and grid 40 20 20 is used. Velocity profiles at $x=0.2$ m, 0.4 m, and 0.6 m are compared with the experimental and simulation results. Inlet velocity is 0.225 ms^{-1} (corresponding to air change rates of 10 h⁻¹). Chen's simulation is performed on an SGI Onyx 3800, and the solver used is the SIMPLER algorithm to couple the pressure and velocity fields [10]. The present simulation is done in OpenFOAM, and the solver is SIMPLE, which gives suitable velocity corrections; however, the pressure correction is less accurate [23], [39].

Figure 4 shows the graph of Chen's experiment, Chen's simulation, and the present simulation which compares the calculated velocity field with

experimental records in the x-direction at $x=0.2$ m, $x=0.4$ m, and $x=0.6$ m of the centre plane [10].

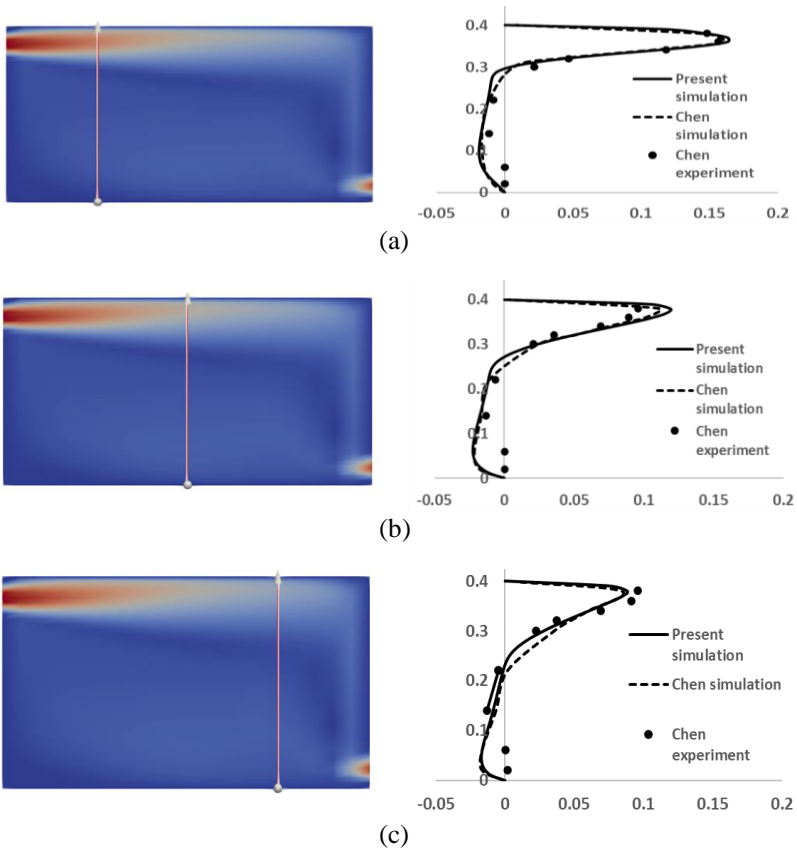


Figure 4: The contour of velocity (inlet velocity 0.225 ms^{-1}) and the comparison of measured and predicted x direction velocities at three different locations [10]; (a) $x=0.2$ m, (b) 0.4 m, and (c) 0.6 m

Validation metrics

The factor of two observations (FAC2), the factor of 1.3 observations (FAC1.3), the normalised mean square error (NMSE), and the fractional bias (FB) are four validation metrics used in this study to acquire a quantitative assessment of the performance of the chosen RANS turbulence models [12], [40]. In addition, every turbulence model's statistical performance is assessed in terms of streamwise velocity [21], [41]. These models include STD k

epsilon, RNG k epsilon, RLZ k epsilon, and SST k omega. Metrics are computed via Equations (11), (12), (13), and (14).

$$FAC2 = \frac{1}{N} \sum_{i=1}^N n_i \text{ with } n_i = \begin{cases} 1, \text{ for } 0.5 \leq \frac{P_i}{O_i} \leq 2 \\ 0, \text{ else} \end{cases} \quad (11)$$

$$FAC1.3 = \frac{1}{N} \sum_{i=1}^N n_i \text{ with } n_i = \begin{cases} 1, \text{ for } 0.77 \leq \frac{P_i}{O_i} \leq 1.3 \\ 0, \text{ else} \end{cases} \quad (12)$$

$$FB = \frac{[O] - [P]}{0.5 ([O] + [P])} \quad (13)$$

$$NMSE = \frac{(\overline{O_i - P_i})^2}{\overline{O_i} \overline{P_i}} \quad (14)$$

with P_i as the predicted value (Chen’s simulation [10]), O_i as the observed (present simulation/measured) value, and n as the number of measurement locations, equal to 32 for three different locations. The overbar denotes averaging over the whole dataset. Table 3 depicts the results for velocities along three vertical lines ($x=0.2, 0.4,$ and 0.6). The ideal values correspond to a perfect agreement between Chen’s simulation and the present simulation result in which $FAC2=1, FAC1.3=1, FB=0,$ and $NMSE=0$. FAC counts the fraction of data points where the predictions are within 2 or 1.3 of the observations based on the predicted and observed value ratio. FB is a linear measure of the mean bias and reveals systematic errors.

Table 3: Validation metrics for x-velocity for present simulation with Chen’s simulation

Present simulation vs.	FAC2	FAC1.3	FB	NMSE
Chen’s simulation [10]	0.7813	0.6875	-0.446	0.00358
Ideal values	1	1	0	0

FAC2 for all lines was 0.7813, and FAC1.3 was 0.6875, near the ideal value of 1. FB value showed an underestimate of the present simulation than the predicted value, which was -0.446 and near the ideal value of 0. Meanwhile, NMSE showed a value of 0.00358 which was slightly near the ideal value of 0. This indicates that the observed data agrees well with Chen’s simulation data. Figure 5 shows a scatter plot of measured versus modelled values for horizontal, along with three velocity components, U_x . Again, all data points (32) in the vertical profiles are included.

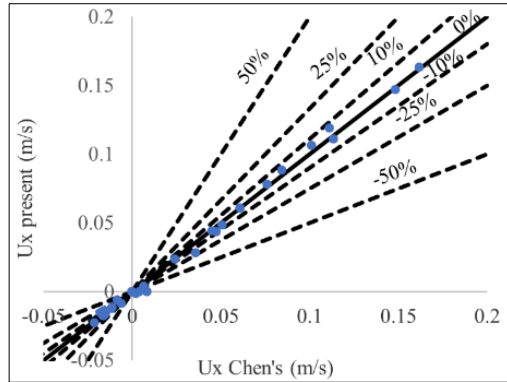


Figure 5: Compares the present and Chen’s [10] simulation results in three locations. As indicated, black dotted lines correspond to 10%, 25% , and 50% errors

Turbulence model verification

Four RANS models are used to simplify the calculations in this paper for the validation simulation. The 3D steady RANS (Reynolds-Average Navier Stokes) equation is solved using the combination of four turbulence models: two-equation eddy viscosity models such as renormalization group k epsilon model (RNG k - ϵ), standard k epsilon model (STD k - ϵ), realizable k epsilon model (RLZ k - ϵ), and shear stress transport k omega (SST k - ω). The statistical performance of every turbulence model is evaluated. However, RLZ k - ϵ and SST k - ω are not converged.

Figure 6 compares the graph of Chen’s [10] simulation and the present simulation of RNG k - ϵ and STD k - ϵ model. Table 4 shows the validation metrics for x -velocity for both turbulence models RNG and STD k - ϵ model. FAC2 for RNG k - ϵ and STD k - ϵ were 0.47 and 0.53, while the ideal value for FAC2 was 1.

Table 4: Validation metrics of x -velocity for RNG and STD k epsilon model simulation with Chen’s simulation

	FAC2	FAC1.3	NMSE
RNG k epsilon	0.47	0.4	0.00025
STD k epsilon	0.53	0.4	0.00017
Ideal values	1	1	0

Both turbulence model values for FAC1.3 were 0.4, where the ideal value is 1. NMSE values were 0.00025 and 0.00017 for RNG k - ϵ and STD k - ϵ , which is slightly near to the ideal value of 0. This indicates that the observed

data agrees better with STD $k-\epsilon$ simulation data. Figures 7 and 8 show the scatter plot of measured versus modelled values for horizontal, along with three velocity components, U_x for RNG $k-\epsilon$ and STD $k-\epsilon$ model, as compared with Chen's simulation [10].

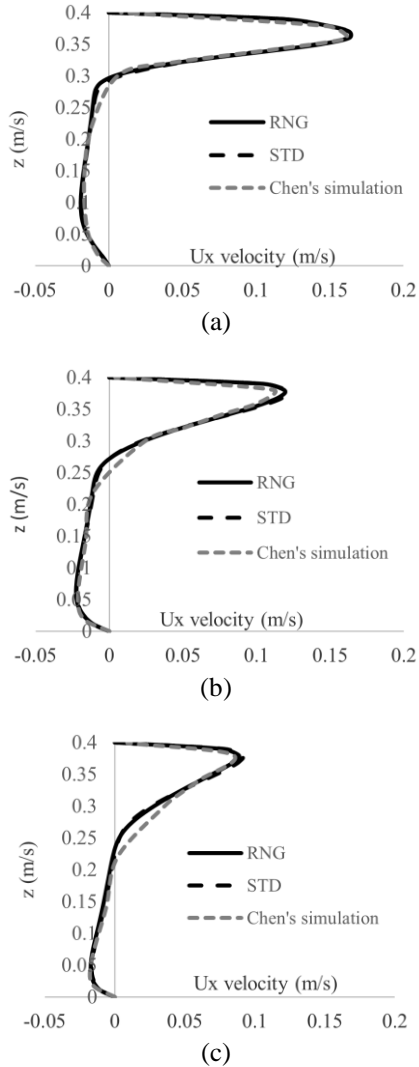


Figure 6: Compares the present and Chen's simulation [10] results in STD k epsilon turbulence model. As indicated, black dotted lines correspond to 10%, 25%, and 50% errors

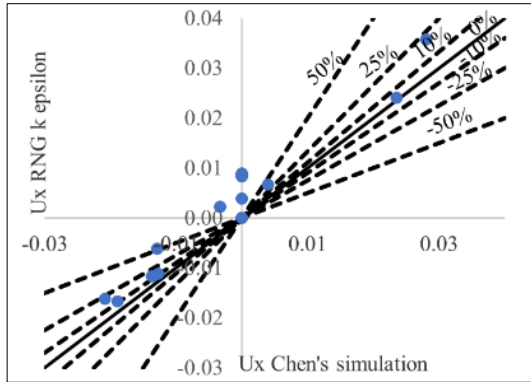


Figure 7: Compares the present and Chen's simulation [10] results in RNG k epsilon turbulence model. As indicated, black dotted lines correspond to 10%, 25%, and 50% errors

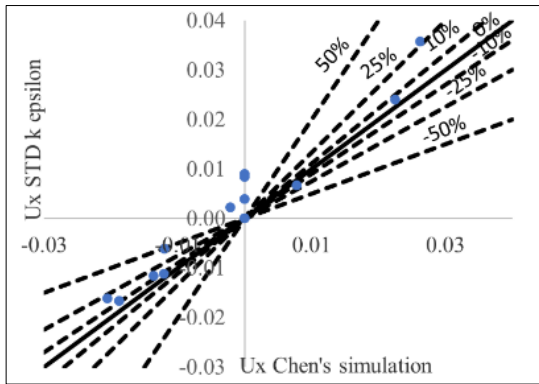


Figure 8: Compares the present and Chen's simulation [10] results in STD k epsilon turbulence model. As indicated, black dotted lines correspond to 10%, 25%, and 50% errors

Grid refinement

The research on grid refinement was performed on each of the three grid resolutions. The grid size in Example A is the largest, the resolution in Case B is medium, and the resolution in Case C is the finest [21]. Case A has the coarsest grid, Case B has the medium resolution, and Case C has the finest resolution. These cases are shown in Table 5 for their specification while Figure 10 depicts their visualization. By increasing the grid size the domain is discretized into coarse, medium, and fine grids. This results in a total grid

number of 1,414,933, 3,981,287, and 5,668,675, along with their respective computing times.

Table 5: Specification case for coarse, medium, and fine grid

Case	A (Coarse)	B (Medium)	C (Fine)
Number of cells	1 414 933	3 981 287	5 668 675
Computation time	03 h 36 m 06	24 h 50 m 21	48 h 18 m 02

Truncation error decreased with grid number. Mesh type had little effect on simulation outcomes at large grid numbers [14]. Figure 13 compares simulated and measured airflow distributions with coarse (1 million cells), medium (3 million cells), and fine (5 million cells) meshes at a room cross-section. Figure 11(a) shows the cross-section location.

Velocity contour and streamlines

Figure 9 shows the schematic of the room geometry for the xy -plane. Figure 10 shows the velocity contour for three different grid sizes measured at the xy -plane, where room height, $z=1$, and room width, $x=2$, are at the central location of the domain. It shows that the coarse grid is different from the medium and fine grids. It shows the medium and fine grids are slightly the same.

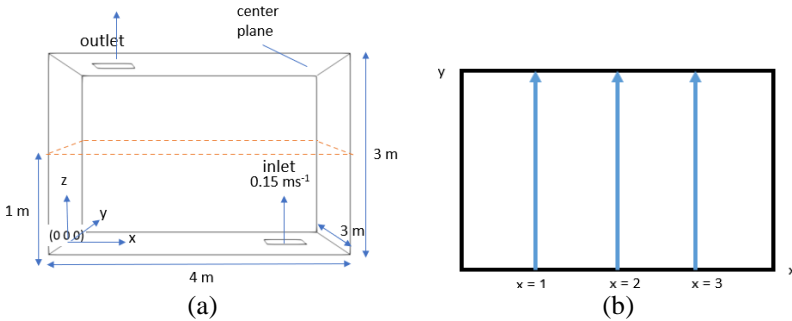


Figure 9: a) Schematic of the room geometry at xy -plane, and b) line at xy -plane

Figure 11 shows the velocity profile for the three cases. The horizontal axis represents the x velocity, U_x , while the vertical axis indicates the room length, y . It shows the symmetrical flow velocity for both sides of the room length at three-line positions $x=2$, $x=6$, and $x=8$. This result was taken at the room's height of $z=1$ m. It was considered for the sitting position. At lines $x=2$ and $x=4$, in the middle of the room, the flow velocity is the highest compared to both sides of the room. When $x=6$, the velocity profile shape is different and near zero velocity.

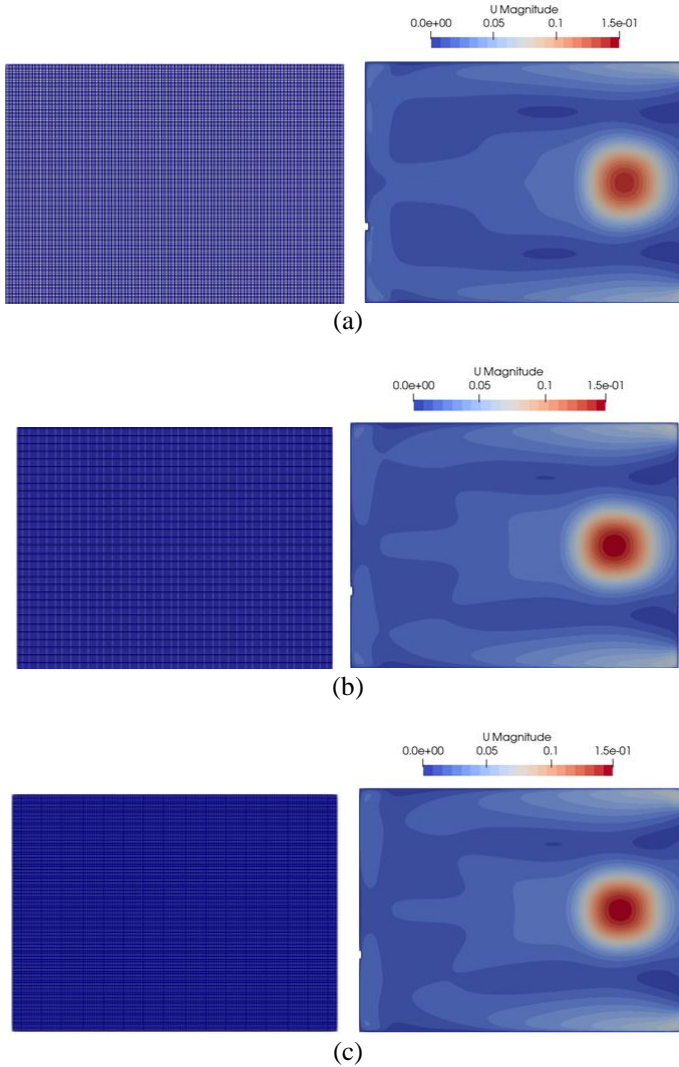


Figure 10: Block mesh and geometry structure with velocity contour for different cases: at the x - y plane, $z=1$, at the middle domain; (a) coarse, (b) medium, and (c) fine

The profile also shows that a significant difference can be observed for the coarse mesh (dashed line) compared to medium (solid line), while less significant for medium (solid line) and fine (dotted line) grids. Similar velocity profiles can be found using either a medium or fine grid. Due to the nearly

grid-independent nature of the medium grid's output, it is selected for further simulations [10], [42]-[43]. The GCI is a metric for determining the degree of grid convergence. Figure 11 also shows the mean error for medium and fine mesh, where line $x=2$ is 0.14% error, $x=4$ is 0.08% error, and $x=8$ is 0.09% error. The difference between medium mesh and fine, as shown, is accepted. Therefore, the computational time for medium mesh is acceptable for simulation. Overlooked will add a level of complexity, which makes the whole process of prototype or numerical modelling almost unsolvable.

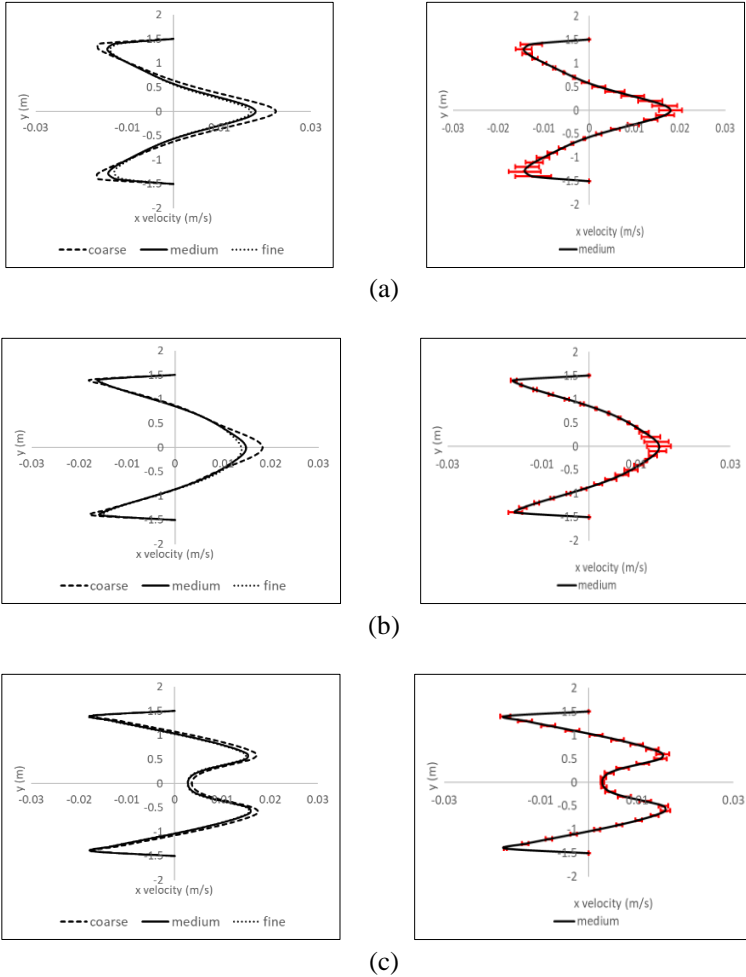


Figure 11: Velocity profile and graph with error bar to compare the medium and fine mesh at the x - y plane, (a) $x=2$, (b) $x=4$, and (c) $x=6$

Conclusion

Computational fluid dynamics (CFD) is an efficient tool for analysing airflow in a built-in environment. To sustain the quality of CFD simulations, the process of numerical modelling must be appropriately governed; this is becoming an essential supplementary to experimental and theoretical methods. CFD numerical data can explain airflow performance in terms of air quality, occupants' thermal comfort, and building energy savings. Consequently, this work presents turning CFD analyses of indoor airflow in the building environment. The performance of CFD modelling is investigated in terms of the efficiency of computational grids, convergence criteria, and validation techniques. More often, numerical models are used to show how natural processes work. Since we have improved numerical tools, it is possible to describe the behaviour of complex flow phenomena more precisely. Even though more complicated systems can be solved, there is still some assumption about how accurate the solutions are. Putting the results of experiments and simulations next to each other is not enough to prove how good the outcome is. CFD problems can be solved via a variety of mesh-independent solution approaches. The most well-known methods are Grid Resolution, General Richardson Extrapolation, and Grid Convergence Index techniques. The Grid Convergence Index (GCI) methodology provides a way to calculate and report discretization error estimates in CFD simulations. It lets us measure how much uncertainty there is in grid convergence. Solutions on three distinct grids are provided to study the effect of the numerical scheme, boundary conditions, and grid independence. Using a kind of Richardson extrapolation, the level of grid independence is determined, and the analysis reveals that the optimal grid solution has a Grid Convergence Index (GCI) of less than 5%. Due to a satisfactory correlation, the suggested method is successfully validated compared to experimental results in the scientific literature [10]. These results are verified with four validation metrics to gain a quantitative assessment of the performance of the chosen RANS turbulence models: FAC2, FAC1.3, NMSE, and FB. The result of FAC2, FAC1.3, FB, and NMSE is accepted. With an increasing number of mesh revisions, this method's implementation will yield better results. In addition, to successfully deliver a mesh-independent solution, the method avoids the difficulties and expenses associated with conducting experiments for extremely small meshes. The main goal of grid convergence studies is to find the best grid size so that the accuracy of the answer is not affected by the size of the computational grid. The number of cells and the amount of time it takes to do the calculations are both related. Increasing the grid density to get better results will increase the amount of time it takes to do the calculations. So, a grid convergence study is a test that needs to be done to reduce the amount of time it takes to solve a problem without sacrificing the accuracy of the answer. The results here let us choose the right

mesh for future or more complicated simulations involving airflow in buildings.

Contributions of Authors

The authors confirm the equal contribution in each part of this work. All authors reviewed and approved the final version of this work.

Funding

This research was financially supported by UiTM Lestari COVID Research Grant (600-RMC/LESTARI COVID/5/3 (010/2020)).

Conflict of Interests

All authors declare that they have no conflicts of interest

Acknowledgement

First and foremost, I would like to sincerely thank my main supervisor, Assoc. Prof. Ir. Ts. Dr. Azli Abd Razak, my co-supervisors, Dr. Fauziah Jerai, Ir. Dr. Mohamed Azly Abdul Aziz, and my lecturer Dr. Mohd Faizal Mohamad for their guidance and understanding. Most importantly, they provided positive encouragement and a warm spirit to do the study. This paper publication fee is supported by College of Engineering Universiti Teknologi MARA.

References

- [1] J. Gao, H. Wang, X. Wu, F. Wang, and Z. Tian, "Indoor air distribution in a room with underfloor air distribution and chilled ceiling: Effect of ceiling surface temperature and supply air velocity", *Indoor and Built Environment*, vol. 29, no. 2, pp. 151–162, 2020. doi: 10.1177/1420326X19853605.
- [2] M. P. Wan and C. Y. Chao, "Numerical and experimental study of velocity and temperature characteristics in a ventilated enclosure with underfloor ventilation systems", *Indoor Air*, vol. 15, no. 5, pp. 342–355, 2005. doi: 10.1111/j.1600-0668.2005.00378.x.
- [3] S. J. Cao and C. Ren, "Ventilation control strategy using low-dimensional

- linear ventilation models and artificial neural network”, *Building and Environment*, vol. 144, pp. 316–333, 2018. doi: 10.1016/j.buildenv.2018.08.032.
- [4] S. Schiavon, D. Rim, W. Pasut, and W. W. Nazaroff, “Sensation of draft at uncovered ankles for women exposed to displacement ventilation and underfloor air distribution systems”, *Building and Environment*, vol. 96, pp. 228–236, 2016. doi: 10.1016/j.buildenv.2015.11.009.
- [5] N. P. Gao and J. L. Niu, “Modeling particle dispersion and deposition in indoor environments”, *Atmospheric Environment*, vol. 41, no. 18, pp. 3862–3876, 2007. doi: 10.1016/j.atmosenv.2007.01.016.
- [6] A. C. K. Lai and F. Chen, “Modeling particle deposition and distribution in a chamber with a two-equation Reynolds-averaged Navier-Stokes model”, *Journal of Aerosol Science*, vol. 37, no. 12, pp. 1770–1780, 2006. doi: 10.1016/j.jaerosci.2006.06.008.
- [7] L. K. Moey, N. M. Adam, and K. A. Ahmad, “Effect of venturi-shaped roof angle on air change rate of a stairwell in tropical climate”, *Journal of Mechanical Engineering.*, vol. SI 4, no. 4, pp. 135–150, 2017.
- [8] A. Murga, S. J. Yoo, and K. Ito, “Multi-stage downscaling procedure to analyse the impact of exposure concentration in a factory on a specific worker through computational fluid dynamics modelling”, *Indoor and Built Environment*, vol. 27, no. 4, pp. 486–498, 2018. doi: 10.1177/1420326X16677331.
- [9] S. J. Cao, “Challenges of using CFD simulation for the design and online control of ventilation systems,” *Indoor and Built Environment*, vol. 28, no. 1, pp. 3–6, 2019. doi: 10.1177/1420326X18810568.
- [10] F. Chen, S. C. M. Yu, and A. C. K. Lai, “Modeling particle distribution and deposition in indoor environments with a new drift-flux model”, *Atmospheric Environment*, vol. 40, no. 2, pp. 357–367, 2006. doi: 10.1016/j.atmosenv.2005.09.044.
- [11] H. lin Liu, M. ming Liu, Y. Bai, and L. Dong, “Effects of mesh style and grid convergence on numerical simulation accuracy of centrifugal pump”, *Journal of Central South University*, vol. 22, no. 1, pp. 368–376, 2015. doi: 10.1007/s11771-015-2531-9.
- [12] P. Cardiff, “Introduction to Meshing in OpenFOAM,” *University College Dublin*, p. 70, 2017.
- [13] G. Park, C. Kim, M. Lee, and C. Choi, “Building geometry simplification for improving mesh quality of numerical analysis model”, *Applied Sciences*, vol. 10, no. 16, pp. 1-18, 2020. doi: 10.3390/APP10165425.
- [14] N. Baker, G. Kelly, and P. D. O’Sullivan, “A grid convergence index study of mesh style effect on the accuracy of the numerical results for an indoor airflow profile”, *International Journal of Ventilation*, vol. 19, no. 4, pp. 300–314, 2020. doi: 10.1080/14733315.2019.1667558.
- [15] J. Franke, A. Hellsten, H. Schlünzen, and B. Carissimo, “Best Practice Guideline for the Cfd Simulation of Flows in the Urban Environment.

- Cost 732: Quality Assurance and Improvement of Microscale Meteorological Models”, in *COST Action C14: Impact of Wind and Storm on City Life and Urban Environment*, 2007.
- [16] R. Duan et al., “Mesh type and number for the CFD simulations of air distribution in an aircraft cabin”, *Numerical Heat Transfer, Part B: Fundamentals*, vol. 67, no. 6, pp. 489–506, 2015. doi: 10.1080/10407790.2014.985991.
- [17] F. M. Sakri, M. S. M. Ali, and S. A. Z. S. Salim, “Computational investigations and grid refinement study of 3D transient flow in a cylindrical tank using OpenFOAM”, *IOP Conference Series: Materials Science and Engineering*, vol. 152, no. 1, pp. 1-13, 2016. doi: 10.1088/1757-899X/152/1/012058.
- [18] M. M. Hefny and R. Ooka, “CFD analysis of pollutant dispersion around buildings: Effect of cell geometry”, *Building and Environment*, vol. 44, no. 8, pp. 1699–1706, 2009. doi: 10.1016/j.buildenv.2008.11.010.
- [19] L. Kang and T. van Hooff, “Influence of inlet boundary conditions on 3D steady RANS simulations of non-isothermal mechanical ventilation in a generic closure”, *International Journal of Thermal Sciences*, vol. 182, p. 107792, 2022. doi: 10.1016/j.ijthermalsci.2022.107792.
- [20] H. Mohammed and A. Belkacem, “Convergence order prediction of CVFEM solutions using the richardson extrapolation method on unstructured grids”, *Journal of Advanced Research in Fluid Mechanics and Thermal Sciences*, vol. 67, no. 2, pp. 27–39, 2020.
- [21] S. Gilani, H. Montazeri, and B. Blocken, “CFD simulation of stratified indoor environment in displacement ventilation: Validation and sensitivity analysis”, *Building and Environment*, vol. 95, pp. 299–313, 2016. doi: 10.1016/j.buildenv.2015.09.010.
- [22] Y. Wu, L. Feng, M. Liu, Z. Wu, and N. Gao, “Numerical study on transient airflows and air exchange induced by door motion in thermally stratified environment”, *Building and Environment*, vol. 223, p. 109498, 2022. doi: 10.1016/j.buildenv.2022.109498.
- [23] D. Prakash and P. Ravikumar, “Analysis of thermal comfort and indoor air flow characteristics for a residential building room under generalized window opening position at the adjacent walls”, *International Journal of Sustainable Built Environment*, vol. 4, no. 1, pp. 42–57, 2015. doi: 10.1016/j.ijsbe.2015.02.003.
- [24] H. Motamedi, M. Shirzadi, Y. Tominaga, and P. A. Mirzaei, “CFD modeling of airborne pathogen transmission of COVID-19 in confined spaces under different ventilation strategies”, *Sustainable Cities and Society*, vol. 76, p. 103397, 2022. doi: 10.1016/j.scs.2021.103397.
- [25] Á. L. De Bortoli, G. S. L. Andreis, and F. N. Pereira, “Numerical Methods for Reactive Flows”, in *Modeling and Simulation of Reactive Flows*, Elsevier, 2015.
- [26] R. Viswanath, and Y. Jaluria “A Comparison of Different Solution

- Methodologies For Melting and Solidification Problems in Enclosures”, *Numerical Heat Transfer, Part B: Fundamentals*, vol. 24, no. 1, pp. 77–105, 2007.
- [27] S. Kato, “Review of airflow and transport analysis in building using CFD and network model”, *Japan Architectural Review*, vol. 1, no. 3, pp. 299–309, 2018. doi: 10.1002/2475-8876.12051.
- [28] H. Jasak, “Error analysis and estimation for finite volume method with applications to fluid flow”, PhD Thesis, 1996.
- [29] ICOP-IAQ, “Industry Code of Practice on Indoor Air Quality”, Ministry Human Resource Department Occupational Safety Health, 2010.
- [30] P. J. Roache, “Perspective: A Method for Uniform Reporting of Grid Refinement Studies”, *Journal of Fluid Engineering*, vol. 116, pp. 405–413, 1994.
- [31] T. S. Phillips, “Extrapolation-based Discretization Error and Uncertainty Estimation in Computational Fluid Dynamics Extrapolation-based Discretization Error and Uncertainty Estimation in Computational Fluid Dynamics”, M.S. thesis, Aero. Eng., Virginia Polytech. and State Univ., Virginia, Feb. 2012, [Online]. Available: <https://vtechworks.lib.vt.edu/handle/10919/31504>.
- [32] R. Castedo et al., “Application of grid convergence index to shock wave validated with LS-DYNA and ProsAir”, *Ingenieria e Investigacion*, vol. 39, no. 3, pp. 20–26, 2019. doi: 10.15446/ing.investig.v39n3.81380.
- [33] A. Alañón, E. Cerro-Prada, M. J. Vázquez-Gallo, and A. P. Santos, “Mesh size effect on finite-element modeling of blast-loaded reinforced concrete slab”, *Engineering with Computers*, vol. 34, no. 4, pp. 649–658, 2018. doi: 10.1007/s00366-017-0564-4.
- [34] S. R. Lizarose Samion, N. H. Shaharuddin, and M. S. Mat Ali, “Grid Convergence Study for Detached-Eddy Simulation of Flow over Rod-Airfoil Configuration Using OpenFOAM”, *IOP Conference Series: Materials Science and Engineering*, vol. 491, no. 1, pp. 1-7, 2019. doi: 10.1088/1757-899X/491/1/012023.
- [35] P. J. Roache, “Quantification of uncertainty in computational fluid dynamics”, *Annual Review of Fluid Mechanics*, vol. 29, pp. 123–160, 1997. doi: 10.1146/annurev.fluid.29.1.123.
- [36] V. Carrillo, J. Petrie, and E. Pacheco, “Application of the grid convergence index to a laminar axisymmetric sudden expansion flow”, *Universidad de Cuenca*, pp. 115–123, 2015.
- [37] L. E. Schwer, “Is your mesh refined enough? Estimating Discretization Error using GCI”, *7th LS-DYNA Anwenderforum*, vol. 1, no. 1, pp. 45–54, 2008.
- [38] L. Kwasniewski, “Application of grid convergence index in FE computation”, *Bulletin of the Polish Academy of Sciences: Technical Sciences*, vol. 61, no. 1, pp. 123–128, 2013. doi: 10.2478/bpasts-2013-0010.

- [39] M. Sukri and M. Ali, “Validation study on external wind noise prediction using OpenFOAM”, *Journal of Mechanical Engineering*, vol. 15, no. 1, pp. 111–126, 2018.
- [40] M. . Ibrahim, M. . Mohamad, N. Ikegaya, and A. A. Razak, “Numerical Investigation on the Effect of Building Overhang on the Flow within Idealised Two-dimensional Street Canyon”, *ESTEEM Academic Journal*, vol. 17, no. 11, pp. 67–77, 2021.
- [41] M. A. Zainol et al., “The effect of urban obstacles on the flow distribution at pedestrian area”, *IOP Conference Series: Materials Science and Engineering*, vol. 834, no. 1, pp. 1-7, 2020. doi: 10.1088/1757-899X/834/1/012023.
- [42] S. Giersch and S. Raasch, “How Do Dust Devil-Like Vortices Depend on Model Resolution? A Grid Convergence Study Using Large-Eddy Simulation”, *Boundary-Layer Meteorology*, vol. 187, no. 3, pp. 703–742, 2023. doi: 10.1007/s10546-023-00792-3.
- [43] Y. Zhao and X. Su, “IMM FSI Model Validations and Applications for Compressible Flows”, in *Computational Fluid-Structure Interaction*, Academic Press, Elsevier, pp. 355-408, 2019.

Reducing The Risk of Agglomeration and Shrinkage Ceramic Body from Al_2O_3 - ZrO_2 Composition

Norfauzi Tamin *, Ng Chuan Huat, Abdul Hamid
IM Tech Focus Group, Faculty of Technical and Vocational Education,
Universiti Tun Hussien Onn Malaysia, Parit Raja, Johor, MALAYSIA
*norfauzi@uthm.edu.my

Umar Al Amani Azlan
Faculty of Mechanical and Manufacturing Engineering Technology,
Universiti Teknikal Malaysia Melaka, Air Keroh, Melaka, MALAYSIA

ABSTRACT

This study introduces the effect of ceramic composition that consists of Alumina (Al_2O_3)-Zirconia (ZrO_2)-Chromia (Cr_2O_3) compositions on agglomerate and shrinkage for cutting tool development. Shrinkage is a problem in the development of ceramic cutting tools other than the occurrence of particle agglomerate on the body structure. Finer grain size significantly contributes to the ceramic body's shrinkage and agglomeration. This study analyzed grain size and its relationship with shrinkage and agglomerates. The powders were ball-milled with 80 wt% Al_2O_3 -20 wt% ZrO_2 -0.6 wt% Cr_2O_3 and then compacted and sintered at 1400 °C to examine their shrinkage and investigate microstructure by scanning electron microscopy (SEM) machine. The results show that ZrO_2 has a larger particle size of 6.10 μm and Cr_2O_3 has a finer measure of 1.24 μm . When blended with the ball mill, the mix of Al_2O_3 - ZrO_2 - Cr_2O_3 was obtained is 7.30 μm , showing that the ball mill can uniformly mix all the particles and reduce the risk of agglomeration. The microstructural analysis found that Cr_2O_3 covers and fills up the space between Al_2O_3 and ZrO_2 compared to without Cr_2O_3 . The combination of agglomerate and shrinkage of Al_2O_3 - ZrO_2 - Cr_2O_3 was responsible for the performance of the ceramic cutting tool fabricated.

Keywords: Agglomeration; Shrinkage; Ceramic; Cutting Tool

Introduction

Engineering or advanced ceramics are inorganic non-metallic materials widely used in high-performance engineering applications. The production of advanced ceramic gives the ideal arrangement and a practical, superior other option to conventional materials, for example, metals and plastics. Ceramics can be called oxide-based, carbides, nitrides, and borides. According to Salamon [1] and Bala et al. [2], the desired properties of advanced ceramics are wear resistance, stability against thermal resistance, thermal insulation, electrical insulation, and non-magnetic. Through these properties, ceramic cutting tools are capable of machining AISI 1045 [3]. Besides that, industrial ceramics applications include automotive components, medical, insulation materials, shielding materials army, coating materials, nuclear reactors, and artificial bone.

Nowadays, most ceramic products use Al_2O_3 and ZrO_2 materials because the nature of the two materials enables the production of a compact and sturdy structure. The use of Al_2O_3 powder in the fabrication of ceramic cutting tools is sufficient to produce a robust structure to carry out lathe machining work [4]-[5]. According to Tong et al. [6], Shafeiey et al. [7], and Tuan et al. [8], the refined grains and mechanical properties of the ZrO_2 structure can improve the strength of Al_2O_3 ceramic cutting tools. However, there is a challenging issue when using nano-sized ZrO_2 powder. A high tendency to agglomerate between grains can cause a decrease in the mechanical performance of ceramic cutting tools. As a result of the agglomeration, ZrO_2 is not dispersed uniformly in the composition of the green body [9]. Agglomerate is inevitable due to the fineness of the ceramic powder used in the composition and the need to analyze the condition and its effects on the ceramic powder mixture. The additive material should be considered and studied to strengthen the composition of the Al_2O_3 - ZrO_2 ceramic Cr_2O_3 body, such as using a powder. One of the powerful mixtures and additives used for ceramic cutting tools is Cr_2O_3 [3]. According to Manshor et al. [10] and Kunkun et al. [11], Cr_2O_3 is added to Al_2O_3 to provide fracture toughness because it can form a solid isovalent solution.

Green body shrinkage occurs when the particle size changes due to the effect of the sintering. Shrinkage refers to a reduction in the size of the compacted green body after sintering. It is caused by the closure of porosity inside the ceramic body during the sintering process [12]. The microstructure of the ceramic cutting tool is initially in the small grains form, then continues to expand during the sintering process. The sintering process affects the shrinkage rate due to the molecular and grain movement of the solid ceramic body during the sintering process [13]-[14]. There are three stages of transformation during the sintering of ceramic cutting tools. In the initial stage, there are some degrees of atomic mobility among grain particles, and sharply concave necks are formed between individual particles. The process occurs

when the grain size changes at the initial stage of sintering, where the microstructure of the ceramic cutting tool consists of porosity between the grains. As the sintering process continues, the pores between the grains continue to close as the grains expand to cover the spaces and voids. This condition causes shrinkage because the pores have been decomposed, and the grains grow to their maximum level (depending on the sintering temperature) [15].

As a result of this phenomenon, the structure of the ceramic cutting tool becomes denser, and it has better physical and mechanical properties. The shrinkage is calculated based on the diameter and thickness of the cutting tool, as the changes in diameter and thickness are more significant for the cutting tool to fit into the holder.

Experimental Procedure

The mixing process of Al₂O₃-ZrO₂-Cr₂O₃ compositions is done using the dry method. Each ceramic powder is weighed evenly with a 4 gram, then placed in a bottle/jar and mixed evenly using a ball mill machine with a 40 rpm rotation speed at 9 hours of rotation time. This ball mill machine produces a finer and uniformly powder mixture. The powder is then poured into a mould and compacted using a mechanical press and press up to 5 tons to get the determined shape of the green body. A Cold Isostatic Press (CIP) machine is used with 300 MPa for 30 seconds to further compact the green body. Then, the green body of Al₂O₃-ZrO₂-Cr₂O₃ is sintered up to 1400 °C for 9 hours to obtain a solid and compact ceramic body. Figure 1 shows the process of fabricating ceramic cutting tools.



Figure 1: Process cutting tool development

X-ray diffraction (XRD) is an analytical method used to identify the phase of the crystalline material. In this study, XRD was used to detect the presence of Al_2O_3 , ZrO_2 , and Cr_2O_3 elements inside a single ceramic body. Figure 2 shows the XRD machine used in this study.

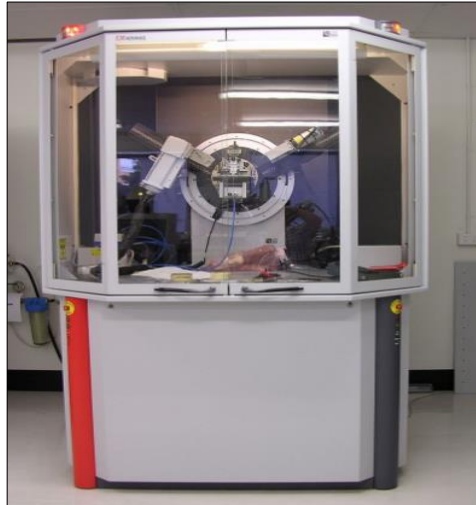


Figure 2: X-ray diffraction (XRD) brand D8 Advance model MSE 4003

Measurement

The grain size and surface contact were measured on each ceramic powder, and then the ceramic mixture was analysed using Malvern master-sizer equipment, as shown in Figure 3. Combination focused 80 wt% Al_2O_3 -20 wt% ZrO_2 -0.6 wt% Cr_2O_3 .



Figure 3: Malvern master-sizer

Specimens were measured at three places using a digital calliper for diameter and thickness before the sintering process was carried out and then averaged. The average diameter and thickness before the sintering process is

carried out are 12 mm and 6 mm, respectively. After the sintering process, the same measurement method is performed to obtain an average value to be compared before and after sintering and converted to a percentage. Figure 4 shows the specimen before and after the sintering process is carried out. While for analysis, microstructure and agglomerate identification were carried out using SEM machines, as seen in Figure 5.

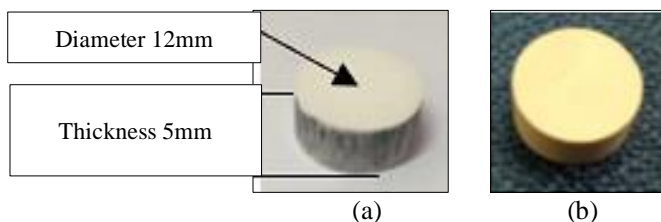


Figure 4: Ceramic cutting tool; (a) before sintering, and (b) after sintering



Figure 5: Scanning electron microscopy (SEM)

Results and Discussion

The study was conducted by identifying the grain size, shrinkage rate, agglomeration, grain contact surface, and microstructure analysis of fabricated ceramic cutting tool by comparing two compositions of Al_2O_3 - ZrO_2 and Al_2O_3 - ZrO_2 - Cr_2O_3 . Shrinkage identification was performed to identify the effect on the composition of each powder. At the same time, microstructure analysis determines the causes and consequences of the composition used against powder agglomeration. Powder identification is the first step and the subsequent study about the structure's agglomeration and the effect that causes shrinkage.

Powder characteristics

Figure 6 compares the average grain size after mixing $\text{Al}_2\text{O}_3\text{-ZrO}_2$ and $\text{Al}_2\text{O}_3\text{-ZrO}_2\text{-Cr}_2\text{O}_3$. Since the size of ZrO_2 used in this study only presented around 20% compared to Al_2O_3 (80%), it is expected that the fine ZrO_2 covers the space between the necks of Al_2O_3 grains. Al_2O_3 and ZrO_2 materials can react chemically with each other. However, they have different grain sizes and shapes to produce a compact structure when compaction and sintering. While the properties of the ceramic body from the mixture of $\text{Al}_2\text{O}_3\text{-ZrO}_2\text{-Cr}_2\text{O}_3$ powders depended on the grain distribution, which is critically influenced by the processing method. Adding Cr_2O_3 , which has a finer grain size and can react chemically to the composition, can close the space between the Al_2O_3 and ZrO_2 neck during the sintering process.

Agglomeration strongly depended on the surface contact area between particles. A bigger surface contact area increased the attraction between the particles due to stronger Van Der Waals forces [16]. As shown in Figure 7, Cr_2O_3 has the largest surface contact area of $4.84 \text{ m}^2/\text{g}$, which means this Cr_2O_3 has the strongest tendency to form an agglomerate. On the other hand, the particle size of Al_2O_3 which is dominant in the mixture, has $0.0574 \text{ m}^2/\text{g}$, the lowest tendency to form an agglomerate. When $\text{Al}_2\text{O}_3\text{-ZrO}_2$ and $\text{Al}_2\text{O}_3\text{-ZrO}_2\text{-Cr}_2\text{O}_3$ powders ball-milled together, the average surface contact area obtained is $0.61 \text{ m}^2/\text{g}$ and $0.82 \text{ m}^2/\text{g}$, respectively, and slightly lower than ZrO_2 ($0.983 \text{ m}^2/\text{g}$). This indicates a tendency for $\text{Al}_2\text{O}_3\text{-ZrO}_2$ to agglomerate almost equivalent to ZrO_2 .

Agglomeration

Agglomerate can be prevented using the grinding/ milling method [17]-[18]. Using a ball mill machine is one of the grinding methods indirectly capable of reducing agglomerated powder with a rough surface to a finer material and can mix uniformly with other ceramic powders. During the ball milling process, the ball mill machine grinds and crushes the ceramic powder and mixes it evenly [19]-[20]. The rotational impact from the $\text{Al}_2\text{O}_3\text{-ZrO}_2$ mixture makes the particles blend homogeneously in the powder bed (bottle/jar) to produce uniform grain distribution for the whole cutting tool structure [21]. The reduction of the Cr_2O_3 surface contact area from $4.84 \text{ m}^2/\text{g}$ to $0.82 \text{ m}^2/\text{g}$ after $\text{Al}_2\text{O}_3\text{-ZrO}_2\text{-Cr}_2\text{O}_3$ ball milled shows that using this technique capable of removing soft agglomerate that appears in the powder mixture and Figure 8 shows an example of agglomeration of small powder.

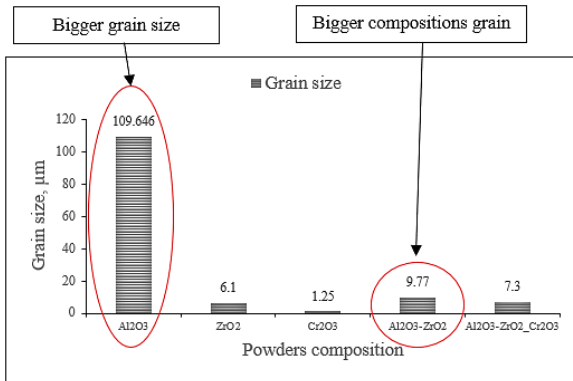


Figure 6: Comparison of average grain size

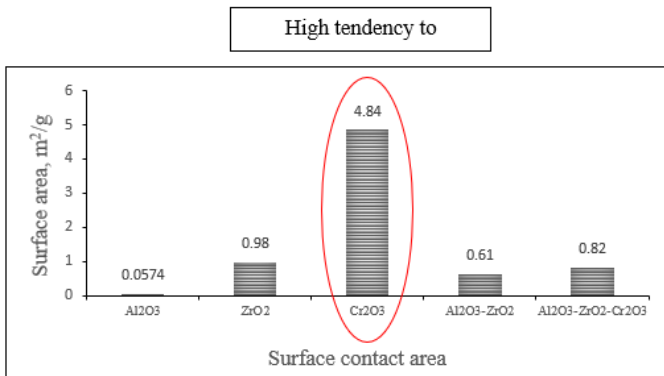


Figure 7: Comparison of surface contact area

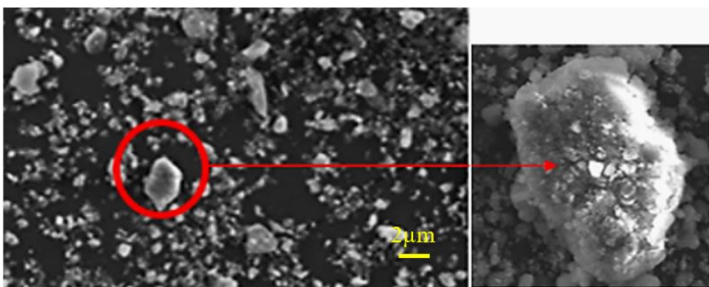


Figure 8: Agglomeration of small powder

Figure 9(a) shows an X-ray diffraction (XRD) pattern of the percentage difference between ZrO_2 against Al_2O_3 content. Analysis shows that Al_2O_3 and ZrO_2 can merge or consolidate because of chemical reactions during when sintering process. While Figure 9(b) indicates that Cr_2O_3 can react with Al_2O_3 when sintered. It's in line with the study conducted by Manshor et al. [10]; Al_2O_3 reacts with Cr_2O_3 because it can form a solid solution isovalent. However, Figure 7 generally does not show ZrO_2 and Cr_2O_3 consolidating or responding. Since Cr is hardly soluble in Zr, the ion of Cr should be dissolved and diffuse through the surface of Al_2O_3 . Cr_2O_3 is added to the Al_2O_3 - ZrO_2 composition that has been dissolved when the sintering process is carried out [22]. This vaporised Cr_2O_3 could be heterogeneously distributed to the upper surface area of Al_2O_3 - ZrO_2 , resulting in partial grain growth to the surface, and some of the Al_2O_3 grain can consolidate and merge with Cr_2O_3 .

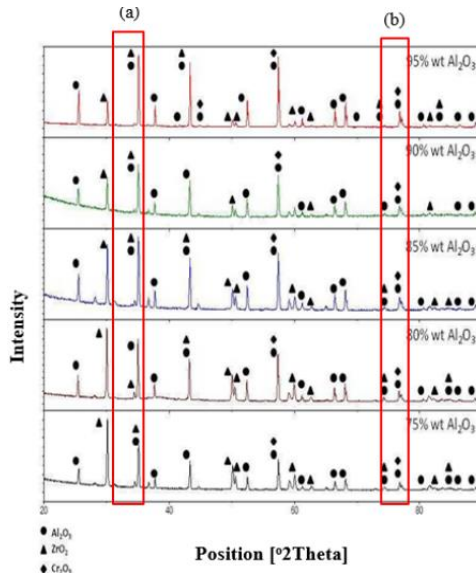


Figure 9: XRD pattern wt.% ZrO_2 on Al_2O_3

The microstructure composition in Figure 10(b) shows more compactness with a significant reduction in porosity on the surface of the ceramic cutting tool. Cr_2O_3 can help cover the spaces between ZrO_2 and Al_2O_3 grains on the necks. The diagram can be interpreted clearly that 0.6 wt% Cr_2O_3 is enough to accelerate grain growth and can help strengthen the composition of Al_2O_3 80 wt% and ZrO_2 20 wt%. Compared with Figure 10(a), there is much porosity on the surface, and proved by the cross-section in Figure 11(a), the cross-section has much porosity and is seen like patches inside the cutting tool.

However, each grain is seen to be firmly bonded to each other and is better than Figure 11(b). This phenomenon is due to the evaporation that occurs on Cr_2O_3 in the ceramic body. The sintering process causes Cr_2O_3 , in the composition of Al_2O_3 and ZrO_2 in the solid body, to evaporate and redeposit over the ceramic surface, which in turn reacts to the Al_2O_3 on the ceramic body surface [23]. The addition of Cr_2O_3 to Al_2O_3 - ZrO_2 significantly affects the quality of ceramic cutting tools; the ZrO_2 proportion is ideal for reinforcing the grain position, and the addition of Cr_2O_3 helps to strengthen the surface of the cutting tool by covering the porosity between Al_2O_3 and ZrO_2 .

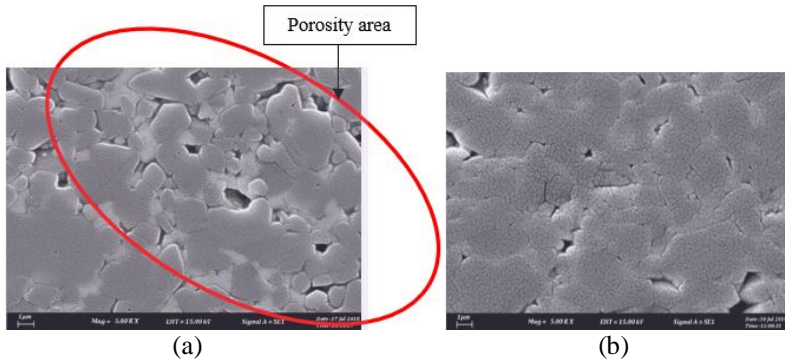


Figure 10: Surface comparison between (a) Al_2O_3 - ZrO_2 , and (b) Al_2O_3 - ZrO_2 - Cr_2O_3

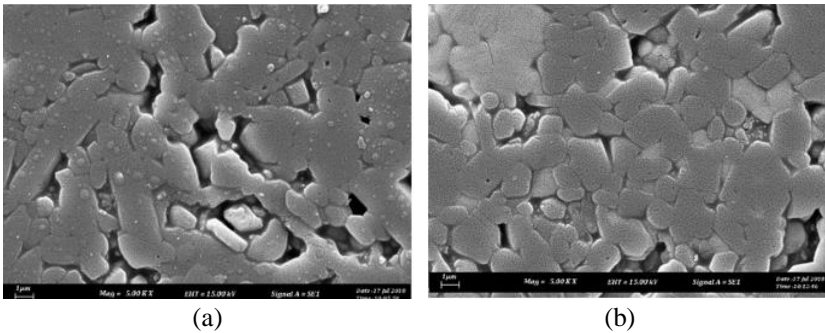


Figure 11: Cross-section comparison between (a) Al_2O_3 - ZrO_2 , and (b) Al_2O_3 - ZrO_2 - Cr_2O_3

Shrinkage

Table 1 shows a composition between Al_2O_3 and ZrO_2 , while the significant difference in diameter shrinkage between Al_2O_3 - ZrO_2 and Al_2O_3 - ZrO_2 - Cr_2O_3 can be seen in Figure 12. The shrinkage of Al_2O_3 - ZrO_2 composition is higher

than $\text{Al}_2\text{O}_3\text{-ZrO}_2\text{-Cr}_2\text{O}_3$. The apparent difference is due to the presence of Cr_2O_3 on $\text{Al}_2\text{O}_3\text{-ZrO}_2$, which reinforces the surface of the ceramic mixture. The Cr_2O_3 added to the Al_2O_3 and ZrO_2 materials evaporates during the firing process. Then the Cr_2O_3 covers the surface of the ceramic mixer, which becomes more robust and has the advantage of wear resistance and heat resistance [12]. According to Renold and Ramesh [24], the shrinking will change during the sintering process by adding additives to the ceramic mixture, and the size of the additive particles affects the order of ceramic shrinkage. Using Cr_2O_3 as an additive to Al_2O_3 and ZrO_2 is very helpful in toughening the synthesised ceramic body through the ceramic body observation, as seen in Figures 8 and 9.

Table 1: Powder composition between Al_2O_3 , ZrO_2 , and Cr_2O_3

Composition	Al_2O_3 (%)	ZrO_2 (%)	Cr_2O_3 (%)
A	95	5	
B	90	10	
C	85	15	0.6
D	80	20	
E	75	25	

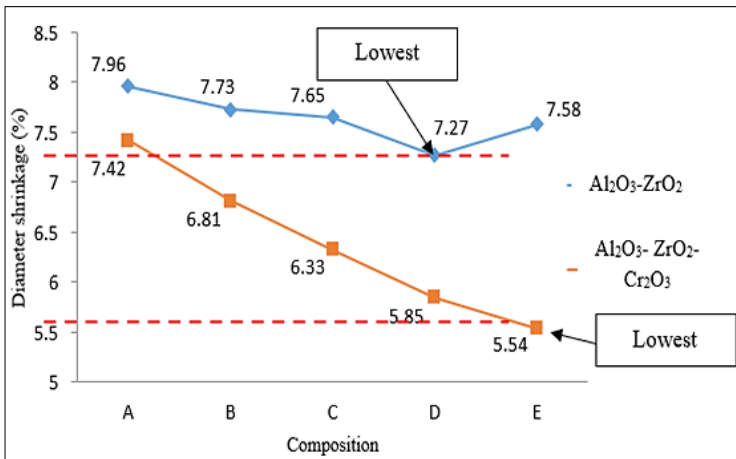


Figure 12: Comparison of diameter shrinkage

The addition of Cr_2O_3 against $\text{Al}_2\text{O}_3\text{-ZrO}_2$ is seen to have much impact on the thickness shrinkage, as seen in Figure 13. The addition of the Cr_2O_3 powder increases the strength of the surface of the ceramic cutting tools. However, the thickness difference in the cutting tool diameter does not matter very much because it depends on the tool holder used. In many instances, the

thickness of the cutting tool can be changed on the tool holder, which is adjustable in the range of 5 to 7 mm [3]. Although the percentage of thickness shrinkage increases, it does not exceed 10% and is still in the range of shrinkage percentage for Al_2O_3 - ZrO_2 . This shrinkage occurs due to adding Cr_2O_3 to Al_2O_3 and ZrO_2 powder. The addition of Cr_2O_3 is seen to help overcome excessive shrinkage; however, the use of ZrO_2 based on percentage impacts the shrinkage. Shrinkage cannot be avoided because ZrO_2 blocks vary when sintered; the higher the ZrO_2 percentage, the higher the percentage of shrinkage that will occur [25].

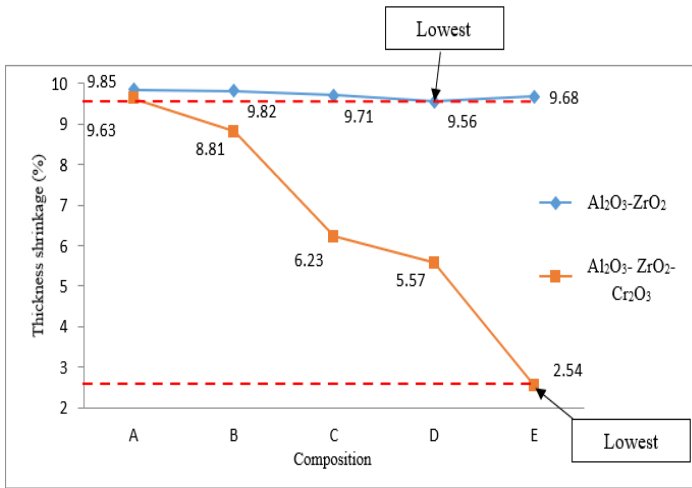


Figure 13: Comparison of thickness shrinkage in millimeters (mm)

Conclusion

The shrinkage rate comparison between two ratio compositions of Al_2O_3 - ZrO_2 and Al_2O_3 - ZrO_2 - Cr_2O_3 was studied to identify the effects of the mixture. Agglomeration occurred due to the grain size and the impact of the contact area. It was analysed in detail to determine the cause of agglomerate and shrinkage in the composition used. Further studies need to be carried out with a mixture of other materials that can reduce the shrinkage and porosity resulting from agglomerate by researching a mixture of compositions other than Cr_2O_3 , for example, a mixture of Mg, B4N against Al_2O_3 - ZrO_2 . Based on this study, it can be concluded that:

- i. Cr_2O_3 grains are the smallest at 1.25 μm , and the surface contact is the largest at 4.84 m^2/g compared to the grain size of Al_2O_3 and ZrO_2 grains.

- ii. The tendency of agglomeration in single Cr_2O_3 grain is very high because of the large surface area due to the small grain size.
- iii. The Al_2O_3 - ZrO_2 mixture increased grain size to $9.77 \mu\text{m}$ and recorded a surface area of $0.61 \text{ m}^2/\text{g}$ compared to a single ZrO_2 and Al_2O_3 that only recorded $6.10 \mu\text{m}$ and $0.98 \text{ m}^2/\text{g}$, respectively.
- iv. The Cr_2O_3 addition of as much as $0.6 \text{ wt}\%$ against Al_2O_3 - ZrO_2 can help reduce agglomerate, which is the grain size increases to $7.30 \mu\text{m}$ and surface area of $0.82 \text{ m}^2/\text{g}$.
- v. Al_2O_3 - ZrO_2 and Al_2O_3 - Cr_2O_3 can chemically react with each other through consolidation. While ZrO_2 and Cr_2O_3 cannot react chemically because Cr_2O_3 can't dissolve with ZrO_2 , there will be evaporation.
- vi. Observation on the microstructure of Al_2O_3 - ZrO_2 - Cr_2O_3 is much denser than Al_2O_3 - ZrO_2 , which features high porosity. The vaporation of Cr_2O_3 , when sintered, shows that it redeposits to the surface and chemically reacts to the Al_2O_3 on the surface of the ceramic body. While the microstructure on the cross-section or the inside of Al_2O_3 - ZrO_2 - Cr_2O_3 shows porosity, it is still better than the Al_2O_3 - ZrO_2 mixture.
- vii. The shrinkage rate of Al_2O_3 - ZrO_2 is higher than Al_2O_3 - ZrO_2 - Cr_2O_3 , where the shrinkage is very significant with each addition of $\text{wt}\%$ ZrO_2 . It's caused by the result of the evaporation processes of Cr_2O_3 that occurs and leaves an empty space in the composition of the mixture.

Contributions of Authors

The authors confirm the equal contribution in each part of this work. All authors reviewed and approved the final version of this work.

Funding

Communication of this research is made possible through monetary assistance from Universiti Tun Hussein Onn Malaysia and the UTHM Publisher's Office via Publication Fund E15216.

Conflict of Interests

All authors declare that they have no conflicts of interest

Acknowledgment

The authors would like to express their gratitude to the IM tech focus group, Faculty of Technical and Vocational Education, Universiti Tun Hussien Onn Malaysia, who has supported and enabled this work to be carried out through the grant of Tier 1 Q169.

References

- [1] T. A. Otitoju, P. U. Okoye, G. Chen, Y. Li, M. O. Okoye, and S. Li, "Advanced ceramic components: Materials, fabrication, and applications", *Journal of Industrial and Engineering Chemistry*, vol. 35, pp. 34-65, 2020.
- [2] S. G. Bala, K.R. Venkata, S. Janardhan, K. Shiprath, H. Manjunatha, M. Ramesha, P. N. V. Krishna, S. Ramesh, and B. T. Anil, "Metal and metal oxide based advanced ceramics for electrochemical biosensors-a short review", *Frontier in Material*, vol. 8, pp. 1-9, 2021.
- [3] T. Norfauzi, A. B. Hadzley, U. A. A. Umar, M. M. FAIZ, M. F. Naim, and A. A. Aziz, "Comparison Machining Performance of Al₂O₃, ZTA and ZTA Doped Cr₂O₃ cutting tools on AISI 1045", *Material Research Express*, vol. 6, no. 1, p. 016547, 2018.
- [4] H. A. Bakar, N. Fahmi, F. Mokhtar, N. F. Tamin, U. A. A. Azlan, and R. Izamshah, "Fabrication and machining performance of powder compacted alumina based cutting tool", *MATEC Web of Conferences*, vol. 150, no. 04009, pp. 1-5, 2018.
- [5] G. Edwin, R. Mirosław, P. Sergey, S. Dmitry, C. Leszek, and M. Tomasz, "Effect of SiC addition to Al₂O₃ ceramics used in cutting tools", *Materials*, vol. 13, no. 22, p. 5195, 2020.
- [6] E. Bódis, K. Molnár, J. Móczó, and Z. Károly, "preparation and characterization of fibrous alumina and zirconia toughened alumina ceramics with gradient porosity", *Nanomaterials*, vol. 12, pp. 4165, 2022.
- [7] W. Wang, J. Chen, X. Sun, G. Sun, Y. Liang, and J. Bi, "Influence of additives on microstructure and mechanical properties of alumina ceramics", *Materials*, vol. 15, p. 2956, 2022.
- [8] M. M. Coutinho, and A. C. P. Nascimento, "Four-point bending fatigue behavior of Al₂O₃-ZrO₂ ceramic biocomposites using CeO₂ as dopant", *Materials Research*, vol. 25, no. 20220199, pp. 1-10, 2022.
- [9] Rylski, and K. Siczek, "The effect of addition of nanoparticles, especially ZrO₂-based, on tribological behavior of lubricants", *Lubricants*, vol. 8, no. 3, pp. 1- 23. 2020.
- [10] A. Fiorati, F. Florit, A. Mazzei, S. Buzzaccaro, B. Rossi, R. Piazza, R. Rota, and L. D. Nardo, "Dispersions of zirconia nanoparticles close to the

- phase boundary of surfactant-free ternary mixtures”, *Langmuir*, vol. 37, no. 14, p. 4072–4081. 2021.
- [11] H. Manshor, A. Z. Azhar, R. A. Rashid, S. Sulaiman, E. C. Abdullah, and Z. A. Ahmad, “Effects of Cr_2O_3 addition on the phase, mechanical properties, and microstructure of zirconia toughened alumina added with TiO_2 (zta-TiO_2) ceramic Composite”, *International Journal of Refractory Metals and Hard Materials*, vol. 61, pp. 40–45, 2016.
- [12] C. Kunkun, Z. Yingyi, F. Tao, H. Shahid, S. A. Tahani, W. Jie, Z. Xu, and A. Shafaqat, “Effects of Cr_2O_3 content on microstructure and mechanical properties of Al_2O_3 matrix composites”, *Coatings*, vol. 11, no. 2, p. 234, 2021.
- [13] F. Thummler, and R. Oberacker, “Introduction to powder metallurgy”, *Materials Characterization*, vol. 5803, no. 95, pp. 80037-80049, 2014.
- [14] A. B. Hadzley, T. Nurfauzi, U. A. A. Umar, A. A. Afuza, M. M. Faiz, and M. F. Naim, “Effect of sintering temperature on density, hardness and tool wear for alumina-zirconia cutting tool”, *Journal of Mechanical Engineering and Sciences*, vol. 13, no. 1, pp. 4648-4660, 2019.
- [15] E. E. E. Gültekin, “The effects of heating rate and sintering temperature on the strength, firing shrinkage, and bulk density of porcelain tiles”, *Journal of the Australian Ceramic Society*, vol. 54, pp. 39–46, 2018
- [16] S. Somiya, “Handbook of advanced ceramics-materials, applications, processing, and properties”, in *Handbook of Advanced Ceramics-Materials, Applications, Processing, and Properties*, 2nd Ed. Academic Press, 2013, pp. 51–60, 2013.
- [17] N. F. Amat, A. Muchtar, S. A. Muhammad, M. J. Ghazali, and Y. Norziha, “Preparation of presintered zirconia blocks for dental restorations through colloidal dispersion and cold isostatic pressing”, *Ceramics International*, vol. 44, no. 6, pp. 6409–6416, 2018.
- [18] C. H. Haron, A. Muchtar, and N. F. Kundor, “Keutuhan permukaan bahan keluli perkakas setelah pengisaran hujung menggunakan perkakas karbida bersalut”, *Jurnal Teknologi*, vol. 41, no. 1 pp. 29–42, 2004.
- [19] S. N. Grigoriev, and M. A. Volosova, “Comprehensive analysis of internal and surface defects of ceramics”, *The International Conference on Nanomaterial, Semiconductor and Composite Materials*, vol. 65, no. 20040, pp. 1-4, 2016.
- [20] K. E. H. K. Ishak, S. Saad, S. F. S. Hashim, and H. Hussin, “Statistical analysis of dry grinding of mica in planetary mill”, *Journal of Science & Technology*, vol. 30, no. 3, pp. 2191-2204. 2022.
- [21] K. Rajaonarivony, X. Rouau, K. Lampoh, J. Y. Delenne, and C. M. Laigle, “Fine comminution of pine bark: how does mechanical loading influence particles properties and milling efficiency?”, *Bioengineering*, vol. 6, no. 4, p. 102, 2019.

- [22] P. L. Guzzo, A. A. A. Tino, and J. B. Santos, “The onset of particle agglomeration during the dry ultrafine grinding of limestone in a planetary ball mill”, *Powder Technology*, vol. 284, pp. 122–129, 2015.
- [23] W. Guo, Q. He, A. Wang, T. Tian, C. Liu, L. Hu, H. Wang, W. Wang, and Z. Fu, “Effects of ball milling on the densification behavior, microstructure, and mechanical properties of TiB₂-SiC ceramics”, *Journal of Materials Research and Technology*, vol. 15, pp. 6700-6712, 2021.
- [24] T. Norfauzi, A. B. Hadzley, U. A. A. Azlan, A. A. Afuza, M. M. Faiz and M. F. Naim, “Fabrication and machining performance of ceramic cutting tool based on the Al₂O₃-ZrO₂-Cr₂O₃ compositions”, *Journal of Materials Research and Technology*, vol. 8, no. 6, pp. 5114-5123, 2019.
- [25] E. S. Renold and T. Ramesh, “Shrinkage characteristics studies on conventional sintered zirconia toughened alumina using a computed tomography imaging technique”, *International Journal of Refractory Metals and Hard Materials*, vol. 54, pp. 383–394, 2016.
- [26] E. Salahi, “Sintering behaviour and mechanical properties of alumina/zirconia multilayers composite via nano-powder processing”, *Ceramics International*, vol. 40, no. 2, pp. 2717–2722, 2014.

The Effects of Titanium Dioxide (TiO₂) Content on the Dry Sliding Behaviour of AA2024 Aluminium Composite

Hamid M. Mahan

Samara National Research University, Samara, RUSSIA
Technical Institute of Baquba, Middle Technical University, Baghdad, IRAQ

S.V. Konovalov, Irina Panchenko

Siberian State Industrial University, Siberian, RUSSIA

Mudhar A. Al-Obaidi*

Technical Institute of Baquba, Middle Technical University, Baghdad, IRAQ
*dr.mudhar.alaubedy@mtu.edu.iq

ABSTRACT

The low density, low expansion coefficient, and strong corrosion resistance at room temperature of Aluminium alloys have made them a popular choice for engineering applications. In this study, Aluminium AA2024 alloys are prepared with different weight contents of ceramic material, titanium oxide (TiO₂) nanoparticles (0%, 2.5%, 5%, and 7.5% wt.) of a particle size of 30 nm using the metal stir casting method. The hardness property and wear resistance with the effect of heat treatment are investigated using a pin-on-disc wear device for both the base alloy and the reinforced alloys. The result shows the prosperity of 5wt.% of TiO₂ to attain the optimum hardness and wear resistance. Using the optimum content of TiO₂ and heat treatment, the hardness and wear resistance of 5wt.% TiO₂-AA2024 nanocomposite has been significantly improved after heat treatment over the unreinforced Aluminium matrix. Statistically, the hardness and wear resistance are improved by 68% and 22%, respectively. This is due to an increased number of fine precipitates besides their uniformly distributed after heat treatment. Furthermore, casting AA2024 Aluminium alloy material mainly has S (Al₂CuMg) and Al₃TiCu phases. The appearance of a large number of S phases causes a significant improvement in the properties of the alloy.

Keywords: *Metal matrix; Nanoparticles; Microstructure; Heat treatment; Wear resistance*

Introduction

Technologically advanced industries such as aerospace, automobiles, power plants, etc. have been demanding materials of high-strength, temperature-resistant with a high "strength to weight" ratio. Thus, many scholars in the area of materials science have developed materials with highly prosperous properties of strength, hardness, and toughness for a wide set of industries. This also necessitates the invention of superior cutting tool materials in order to maintain productivity. Composite materials are among the oldest and newest structural materials. The long history of composites is fascinating because it allows engineers to create completely new materials with precise combinations of properties required for specific tasks [1].

One of the most difficult aspects of producing strong, light, and low-cost engineering materials is getting a high strength-to-weight ratio suited for vehicles [2]. The global need for such products for the automobile and aerospace industries has attracted the attention of researchers in the field of composite materials [3]-[4]. Due to their excellent mechanical properties, Aluminium Matrix Composites (AMCs) are advanced materials that combine the characteristics of light and tough matrix material with hard ceramic reinforcement [5]. AMCs are able to satisfy the market need for lightweight, durable, and high-performance components. The high corrosion resistance of Aluminium and its alloys is due to the formation of an oxide layer on their surface which resists corrosion in many environments [6]-[7]. Ships, transportation, and pipes of oil, gas, or water all this structure will suffer from corrosion. Corrosion can result in structure failure and sometimes this failure is tragic. Nowadays, the prevention of corrosion becomes more important [8]. AMCs strengthened using ceramic particles have become popular for various automotive and aerospace applications because of their mechanical characteristics. The wear rate of AMCs can be improved by adding hard ceramic reinforcement. Aluminium alloy AA2024 contains Cu, Mg, Mn, and some other minor alloying elements and has good a mechanical properties ratio at elevated temperatures, high ductility, fatigue, and fracture resistance [9].

To assess Al-Si alloys, Rajaram et al. [10] examined wear related to the Al-Si alloys at different temperatures, from ambient to a temperature of 350 °C. The stir casting technique was applied to fabricate Al-Si alloys. A practically uniform distribution that is related to the silicon particles has been indicated via microstructural research. The fractography specified that the fracture behaviour regarding the Al-Si alloys has been changing from brittle to ductile modes with increasing temperature. The wear tests indicated that wear resistance regarding the Al-Si alloys has been increased with an increase in

temperature. Throughout the sliding process, oxidational wear has been predominant with developed composite materials by reinforcing Aluminium metal with added silicon carbide in different weight percent ratios, followed by stir casting fabrication [11]. The distribution of SiC was observed to be intra-granular. The results showed that the SiC particles were refined to the grain size of the alloy matrix which improved the bonding in the matrix with an increase in their microhardness. An increase in SiC content shifted the fracture mode from ductile to brittle [12]-[13].

Sevik and Kurnaz [14] utilised the pressure die-casting technique to produce metal-matrix composites related to Al-Si-based alloys, as well as Al₂O₃ particles with volume fractions of 0.05, 0.10, and 0.15, and sizes 44, 85, and 125 µm. Wear, hardness, density, and tensile strength have been studied. The addition of Al₂O₃ particles has increased the density of the composite. Additionally, the composite's hardness has also increased due to an increase in particle volume fraction and a decrease in particle size. The particle volume fractions, and the size are increased by decreasing the composite's tensile strength. There is a decrease in the composite's wear rate with an increase in particle volume fraction, also with a decrease in particle size, yet it has been proportionally increasing with applied load. The wear mechanism with regard to the unreinforced alloy's surface has been plastic deformation, while for composites, there has been a deformation of the layer on the composite's surface [15]-[16].

Moy et al. [17] used solution heat treatment to prohibit corrosion. The ideal heat treatment process involved heating samples at 400 °C for 90 min, followed by cooling the samples in water. Additionally, for 120 minutes at a temperature of 200 °C, the ideal aging condition occurs in samples. The weight loss method was used to calculate the rate of corrosion of the heat-treated samples. An electron microscope has also been used to observe the microstructures of heat-treated samples. The hardness of the samples has increased with increasing the corrosion resistance of the heat-treated samples [18].

El-Mahallawi et al. [19] evaluated the effects of adding titanium dioxide (TiO₂), zirconia (ZrO₂), alumina (Al₂O₃) nanoparticles (40 nm), 0–5wt.%, at varying stirring speeds (270, 800, 1500, and 21500 rpm) to the Aluminium cast alloy A356 as a base metal matrix. According to the findings, the castings formed in the semi-solid state (600 °C) with 2 weight percent Al₂O₃ and 3 weight percent TiO₂ or ZrO₂ at 1500 rpm stirring speed has caused an increase in the mechanical properties and hardness of nano-reinforced castings manufactured with TiO₂, Al₂O₃, and ZrO₂. Several studies to improve the wear resistance of nanocomposite materials have been conducted, which include the incorporation of intragranular nanoparticles via precipitation and stir casting, as well as the development of a microstructure. Mostly, materials scientists have recently focused their attention on the utilisation of metallic materials such as nanocomposite [20]-[21].

Rao et al. [22], used the aluminium alloy 7009 and reinforced it by silica carbide (micro-particles 20-40 mm). This alloy is primarily composed of aluminium, with zinc as the main alloying element, along with smaller amounts of other elements such as copper, magnesium, and chromium. The alloy has the chemical composition of Fe-0.29%, Cu-0.01%, Mg-1.63%, Zn-5.85%, Al-rest. The study investigated the impact of varying the applied load and sliding speed on parameters such as wear rate, temperature rise, coefficient of friction, and seizure pressure. Additionally, the aging time varied between 4 to 10 hours in 2-hour increments, and the nature of the worn surface produced after wear. The results show that the coefficient of friction rises as one increase silica carbide content but falls with increasing age treatment. Heat treatment increases hardness, and particle addition in the alloy reduces wear rate and frictional heating while raising seizure pressure and temperature. The microstructure of the alloy showed primary Al dendrites and secondary intermetallic phases around the dendrites, which become more uniform with the equiaxed grain structure after heat treatment, while intermetallic precipitates are distributed both in the grain boundary and within the grains.

After reviewing the available literature, it has been found that the impact of adding titanium to Al-Cu-Mg alloys through stir casting has not been thoroughly investigated. The AA2024 aluminium alloy belongs to the Al-Cu-Mg alloy series that relies on S (Al_2CuMg) and θ (Al_2Cu) precipitates as the primary strengthening factors. Introducing titanium to this alloy group can facilitate the formation of high-strength titanium aluminides. One issue with Al-Cu-Mg alloys is their susceptibility to thermal instability at elevated temperatures. However, creating titanium aluminides, which have high thermal stability, and their even distribution throughout the aluminium matrix can enhance the thermal stability of these alloys. This study aims to fill the gap by introducing TiO_2 nanoparticles as reinforcement for aluminium AA2024 alloys.

The goal is to concurrently improve the hardness and wear resistance properties of the synthesised TiO_2 -AA2024 nanocomposites. To systematically achieve this aim, a wide range of weight contents of TiO_2 are evaluated for their effects on wear resistance and hardness in the presence of heat treatment. In other words, the purpose of this research is to gain a deeper knowledge of the effects of TiO_2 nanoparticles and heat treatment on the hardness, wear resistance, and microstructure features of TiO_2 -AA2024 nanocomposites.

Material and Methods

The chemical composition of the AA2024 matrix is shown in Table 1. TiO_2 (Titanium oxide) particulates of particle size of 30 nm are utilised as reinforcement in the present investigation. Table 2 presents the properties of

AA2024 matrix material and reinforcing material nanoparticles (TiO₂), respectively.

Table 1: Chemical composition of AA2024 -T₃ alloy [23]

Element	Mg	Si	Cu	Mn	Ti	Cr	Zn	Fe	Al
Standard	1.2-1.8	Max 0.5	3.8-4.9	0.3-0.9	Max 0.15	Max 0.1	Max 0.25	Max 0.5	90.7-94.7
Measured	1.04	0.098	5.5	0.62	0.03	0.008	0.11	0.25	Balance

Table 2: Physical-chemical properties of nanoparticles (TiO₂) [24]

Properties	TiO ₂
Density (g/cc)	4.23
chemical composition	Titanium 59.93 and oxygen 40.07
Crystal's structure	Tetragonal
Melting temperature (°C)	1843
Size range (nm)	30-50
Boiling point (°C)	2,972

The reinforcement material nanoparticles of TiO₂ were used in this study with a purity of 99.8% and a size of 30±5 nm (spherical-shaped nanoparticles) made in China (Changsha Santech Co.). Before adding TiO₂ nanopowder with the different weight percent of 2.5 wt.%, 5 wt.%, and 7.5 wt.%, AA2024 Aluminium alloy was preheated to 750 °C in a graphite crucible using an electric furnace (Nabertherm NAB-8101) to ensure the complete melting of all its components. The stir casting technique was utilized for 4 minutes at 200 rpm. The SEM picture of the TiO₂ nanopowder is shown in Figure 1. Figure 2 depicts the pouring of the melt into a steel mould. Figure 3 depicts the heat treatment techniques used, including quenching and aging. First, the AA2024 Aluminium alloy solution was heated in an electric furnace for 3 hours to a temperature of 500 °C to 510 °C. The sample was then quenched in water to bring it down to room temperature. Second, the sample was placed in an electric furnace (Gallen Hamp hot stop BR-17M / XD-17M) for 3 hours to achieve the aging (precipitation heat treatment) stage between 180 °C to 190 °C, followed by cooling in air. Figure 3 demonstrates a schematic diagram of the sequenced heat treatment processes [25].

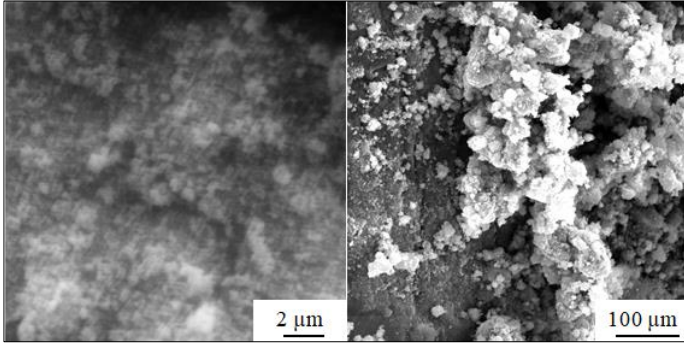


Figure 1: SEM images of spherical-shaped nanoparticles

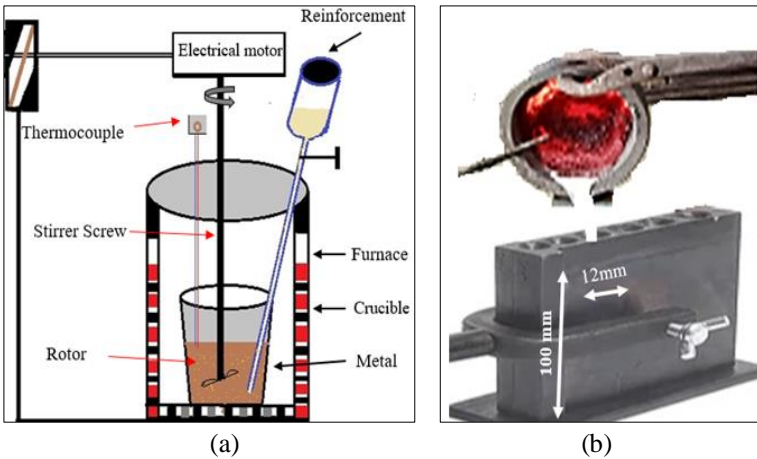


Figure 2: (a) The stir casting furnace for melting, and (b) the casting mould

The microstructural characterization of the samples was conducted by the standard metallographic procedure and etched for 15 seconds using Kroll's reagent ($\text{H}_2\text{O}:\text{HNO}_3:\text{HF}=92:6:2$). Scanning electron microscopy (SEM) (by TESCAN VEGA) and energy disperse spectroscopy (EDS) (by INCA Energy) analyses were carried out to investigate the microstructure and elemental composition distribution of materials.

The digital Vickers hardness analyser category Laryea (HBRVS-18705) was also used to determine the sample's hardness. Three samples were tested for hardness, with average readings taken for each sample. The flow chart of the experimental method and a simplified representation of the process are depicted in Figure 4.

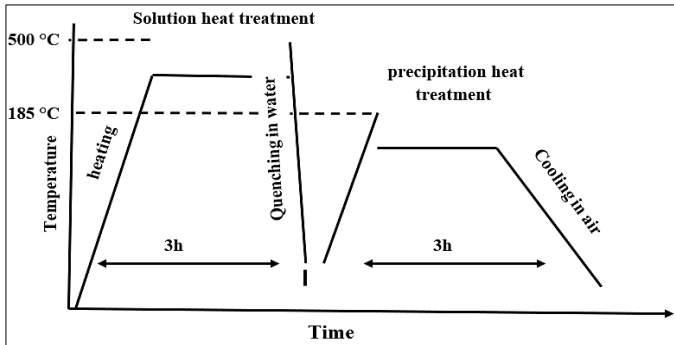


Figure 3: Heat treatment processes

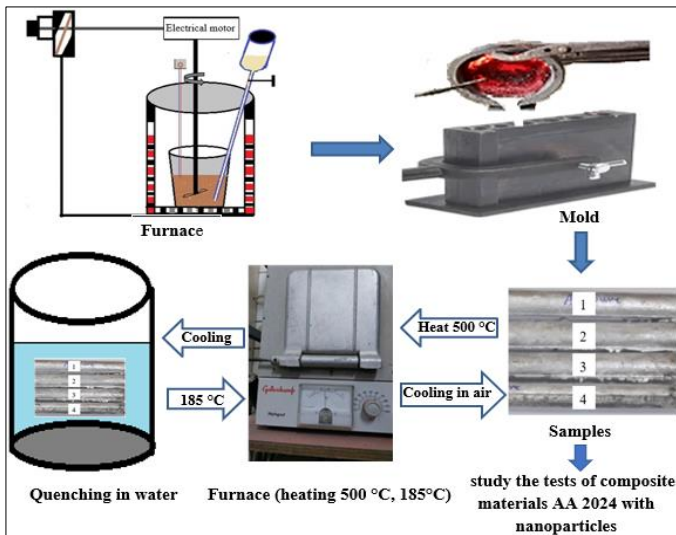


Figure 4: Diagram of the experimental method and the stir casting

A wear test was performed on the Aluminium alloy AA2024 before and after adding TiO_2 nanoparticles, per ASTM G99-95 guidelines [26]. The wear rate of the cast AA2024 alloy reinforced with nanoparticles was examined using a pin on a disc-type wear tester. The cylinder shape sample was 30 mm in length and 10 mm in diameter (note: wear specimen dimensions, according to ASTM G99-95). The disc potential speed was 277.4 rpm, while the sliding velocity was 6 cm/s and imposed loads of 5, 10, 15, and 20 N were applied for 10 minutes. The pin was made by SKD 61 (Vickers hardness=560 HV) [24] as shown in Figure 5.

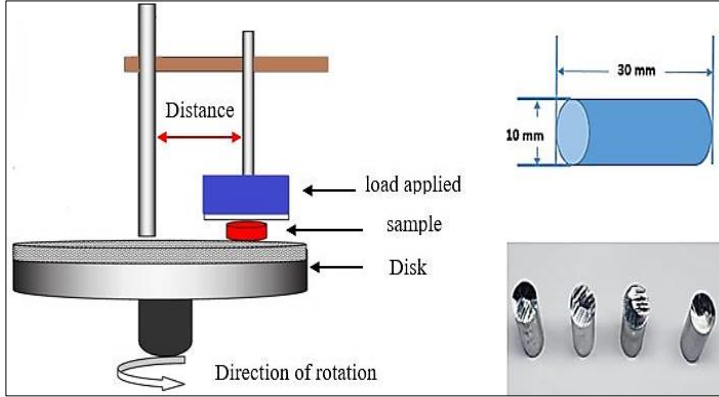


Figure 5: Diagram of pin-on-disk test (ASTM G-99)

The wear rate was determined using the weighing method by calculating the lost weight of the samples, weighing the sample before and after each test, using a sensitive digital sensor scale of 0.0001 g. Specifically, the effect of different applied loads of 5, 10, 15, and 20 N is evaluated on the wear rate while considering a fixed sliding time of 10 minutes and sliding speed of 6 m/s throughout the experiments.

The experimental procedure of determining the wear rate includes a number of steps; i) setting up the wear testing apparatus, ii) positioning the sample to be tested perpendicular to the sliding disc, iii) the cylindrical sample carrier installed by a rectangular section arm, where the radius from the centre of the sample to the centre of the disc is 5 cm, and iv) running the apparatus for a predetermined period. Equation (1) is used to calculate the wear rate.

$$\Delta W = W_1 - W_2 \quad (1)$$

ΔW : variation in mass losses (gm), W_1 : weight of the specimen before the test (gm), and W_2 : weight of specimen 2 after the test (gm).

$$W.R = \Delta w / \pi D N t \quad (2)$$

W.R: wear rate (gm/cm s)

Δw : $W_0 - W_1$

W_0 : sample weight before the test (gm)

W_1 : sample weight after the test (gm)

D : sliding distance (14 cm)

t : time (s)

N : velocity (rpm)

Results and Discussion

The mechanical properties of composite materials are directly related to the properties of the reinforcement, as well as its concentration and geometry. To a certain extent, however, both the composite's strength and its stiffness might be enhanced by increasing the volume fraction of the reinforcing material. When there is a further rise in the volume percent of the material that is being reinforced, there will not be enough matrix to contain the material that is being reinforced. Additionally, the geometry of each reinforcement and the arrangement of those reinforcements can affect the performance of the composite.

Hardness

Figure 6 shows the effects of adding TiO₂ nanoparticles at different weight percentages to Aluminium alloy on the hardness property. When compared to an initial Aluminium alloy of AA2024, the inclusions of 5 wt.% of TiO₂ without heat treatment has resulted in the maximum improvement of hardness property by 26%. Statistically, this improvement has entailed having 38 HRB compared to 30 HRB for an Aluminium alloy of AA2024.

Referring to Shahi et al. [27] and based on Hall–Petch rule, the finer intermetallic compounds can have a more effective role in the pinning of grain boundaries and enhance the hardness. However, increasing the weight percentage of TiO₂ to 7.5 wt.% causes a considerable reduction in hardness. This can be attributed to an increase in the number of fine precipitates in the sample of 7.5 wt.% of TiO₂ that might distort the microstructure of Aluminium composite. The recent results are consistent with those from a previous study by Al-Alkawi et al. [28].

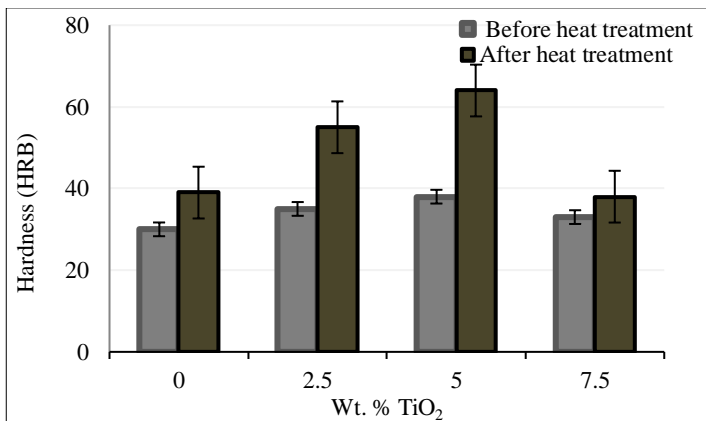


Figure 6: Effects of nanoparticles on the hardness of AA2024 composite

More importantly, the hardness values of TiO₂-AA2024 nanocomposites have significantly increased after the heat treatment as depicted in Figure 6. Statistically, the hardness property increases by 68% after the heat treatment of 5 wt.% TiO₂-AA2024 nanocomposite. Furthermore, this is an improvement of the hardness of 113% if the obtained result is compared against the hardness of AA2024 before heat treatment. This is specifically attained as a result of a uniform distribution of precipitates and particles in the microstructure, as tiny precipitates occur after heat treatment. Figure 7 introduces the optical microscopy images of different weight percentages of TiO₂.

More strain fields are created by the development of uniform and fine precipitates and IMCs, which interact with dislocations to reduce dislocation motion ability and, therefore, the hardness of samples has increased. The hardness of Al-Ti-based IMCs also grows as the weight percent of titanium oxide increases. Because of their high hardness, it is anticipated that the manufacturing of these IMCs will be the primary consideration in enhancing the hardness of alloys by adding titanium oxide. Additionally, the addition of nanoparticles up to 5 wt.% resulted in a rise of fine needle-shaped precipitates in the interdendritic regions. However, the addition of further titanium lowered their amount in this zone. As seen in Figure 7, the proportion of these intermetallic compounds rose with titanium concentration [29].

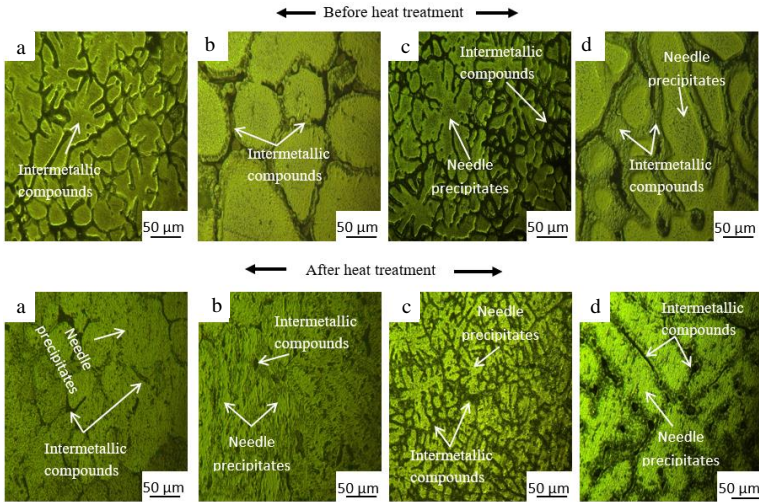


Figure 7: Optical microscopy images of; (a) sample 0 wt.% TiO₂, (b) sample 2.5 wt.% TiO₂, (c) sample 5 wt.% TiO₂, and (d) sample 7.5 wt.% TiO₂

The addition of nanoparticles resulted in the formation of a more homogeneous microstructure, leading to improved mechanical properties of the alloy. The SEM images showed that the nanoparticles were distributed uniformly throughout the matrix and played a crucial role in refining the grain size of the alloy. These findings indicate that the addition of nanoparticles is a promising approach for enhancing the properties of Aluminium alloys. To assess the microstructure and intermetallic compounds accurately, SEM images of different sample structures are presented in Figure 8. As shown in Figure 8(a), the microstructure of the titanium-free sample contained precipitates and intermetallic compounds of Al₂CuMg, Al₇Cu₂Fe, and Al (Cu, Mn, Fe, Si). Upon adding titanium and conducting heat treatment, Al₃TiCu intermetallic compound was observed to form in the microstructure, as shown in Figure 8(b). This compound can act as nucleation sites for the formation of small and uniform precipitates in the Aluminium matrix. The addition of nanoparticles can facilitate the formation of fine precipitates. Due to the high dissolving temperature of these intermetallic compounds, the inter-dendritic zone was also surrounded by Al₇Cu₂Fe and Al (Cu, Mn). By adding titanium to the sample, Al₃TiCu and Al₉TiFe intermetallic compounds were formed in the microstructure. Previous studies [25], [27] have also investigated the formation of these intermetallic compounds, copper becomes part of the titanium aluminide structure's crystal structure when present.

The content samples of 5 wt.% TiO₂ showed a more uniform distribution of the reinforcing particles within the Aluminium matrix, promoting better bonding between the matrix and reinforcement. This can be attributed to the fact that the increased concentration of TiO₂ particles promotes nucleation, leading to the formation of finer grains in the Aluminium matrix. Moreover, the high surface energy of the TiO₂ particles allows them to act as heterogeneous nucleation sites for the Aluminium during solidification, further contributing to grain refinement. Notably, increasing titanium from 2.5 to 5 wt.% of TiO₂ reduced the size of Al₂CuMg precipitates and increased the composite Al₃TiCu, as depicted in Figure 8(c). In this context, Wang et al. [30] found that when Al-Mg-Cu alloys are coupled with titanium at a weight percentage of 5 wt.%, the solubility of copper drops, and metallic compounds such as Al₃TiCu and Al₇TiCu₄ are generated following titanium addition. Figure 8 introduces the SEM images and illustrates this phenomenon. The SEM images showed that the addition of TiO₂ nanoparticles to the Aluminium alloy resulted in a refined microstructure characterised by a decrease in grain size and an increase in the density of grain boundaries. The refined microstructure led to an increase in the mechanical properties of the Aluminium alloy.

When adding 7.5 wt.% nanoparticles, the nanoparticles can agglomerate, which reduces their effectiveness as a strengthening agent. However, agglomeration and unwanted reactions between the nanoparticles and the Aluminium matrix can further reduce the effectiveness of the

nanoparticles, ultimately leading to a reduction in the mechanical properties of the material. The addition of nanoparticles changes the size and distribution of the grains in the alloy, which in turn affects its mechanical properties. The presence of nanoparticles reduces the grain size, improving the hardness and wear resistance of the alloy. Moreover, the addition of nanoparticles can also increase the thermal stability of the alloy. The nanoparticles act as barriers to the movement of dislocations in the alloy, preventing them from reaching the underlying metal. This effect helps to prevent deformation at high temperatures, leading to a reduction in the corrosion rate and an increase in the lifespan of the alloy. Specifically, the use of TiO_2 nanoparticles as a strengthening agent has been shown to upgrade the wear properties of Aluminium Matrix Composites (AMCs) [18]. However, it should be noted that the optimal weight content of TiO_2 is 5 wt.%, as it has been found to provide the best balance between hardness, wear resistance, and weight loss. The improved wear resistance is due to the formation of new phases such as AlTi_3 , which act as hard particles that prevent wear. Additionally, the nanoparticles form a barrier layer on the surface of the Aluminium matrix, preventing the penetration of corrosive agents and reducing the rate of wear.

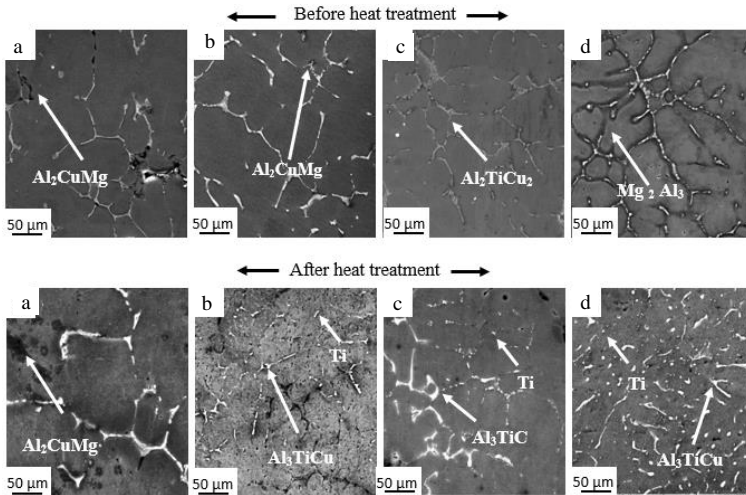


Figure 8: SEM image of AA-2024 alloy; (a) AA 2024-2.5 wt.% TiO_2 , (b) AA 2024 5 wt.% TiO_2 (c) 5 wt.% TiO_2 sample, and (d) 7.5 wt.% TiO_2

Wear resistance

Figure 9 presents the relationships between the wear resistance and applied load for a set of different nanocomposites of different weight content of TiO_2 combined with AA2024. Figure 9 depicts that utilising the optimum 5 wt.% of TiO_2 nanoparticles with Aluminium alloys would lower the wear resistance for

the whole applied loads. This is in a comparison against the other weight contents of TiO₂ and the base case of Aluminium alloy of 0 wt.% of TiO₂. Statistically, the wear resistance of AA2024 alloy has been improved by 220% after the inclusion of 5 wt.% of TiO₂. The highest increase of the hardness property for 5 wt.% TiO₂-AA2024 (Figure 6) can attribute the reason behind this. In this situation, adding 5 wt.% of TiO₂ nanoparticles allows the formation of a protective oxide layer that expands the contact area and increases the friction and wear resistance (Figures 7 and 10). It is important to mention that enhancing wear resistance is advantageous for developing a stable trilateral composite. However, the wear resistance of the reformed composite components slightly decreased when the volume fraction of TiO₂ nanoparticles was improved to 7.5% compared to those with 5% TiO₂ nanoparticles. This is due to the greater agglomeration of TiO₂ nanoparticles, making it difficult to uniformly disperse them, resulting in a decrease in their effective dispersion within the 2024 matrix. This ultimately reduces the wear resistance, as presented in Figures 9 and 10. Therefore, the deformation rate of Aluminium alloys increases as the amount of TiO₂ increases [31].

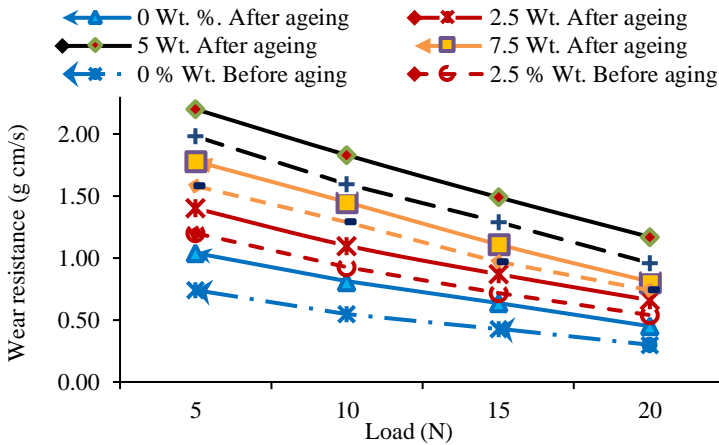


Figure 9: Wear resistance of AA2024 alloy against supplied loads before and after heat treatment

The wear resistance of the nanocomposites increased after the heat treatment for the whole applied loads (Figure 9). Statistically, the wear resistance of 5 wt.% TiO₂-AA2024 has been improved by around 22% after the heat treatment. Indeed, the utilisation of heat treatment has improved the wear resistance due to having a uniform distribution of precipitates and particles in the microstructure, as tiny precipitates occur after heat treatment. Furthermore, the reinforcing distribution has a significant impact on the composite's ductility

and fracture toughness. As a consequence, for reinforcement load-carrying capability, homogeneous reinforcement distribution is crucial [32].

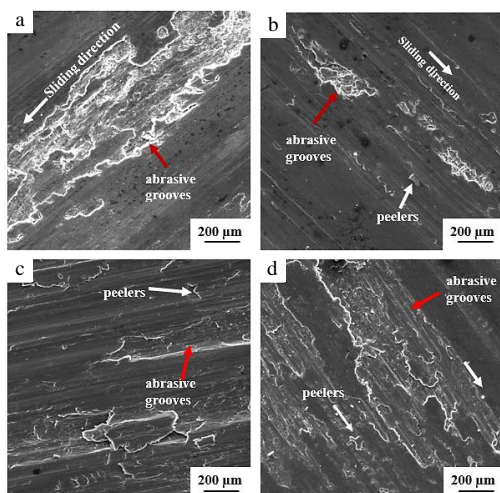


Figure 10: SEM micrographs of circular wear marks on AA2024/ TiO₂ sample after the friction test (severe deformation and plastic flow). Arrows indicate the sliding direction

Weight loss (wear rate)

Figure 11 shows that the average weight loss has significantly increased with the applied load besides considering a sliding time of 10 minutes and sliding speed of 6 m/s. Figure 11 ascertains that the load has a significant effect on weight loss, which is an indication of wear rate. At the lowest load of 5 N, the weight loss will be formed as fine particles, and it will form a protective oxide layer that would decrease the contact area between the samples and disc, one of the reasons for enhancement wear resistance of studied alloys is their ability to form protective oxide layer during wear. Therefore, the wear rate will be at its lowest value, Figure 12. At the highest applied loads, the area of the surface that makes contact between the sample and disk would be larger, increasing the friction between the two sliding surfaces and thus increasing the wear rate [30], [33].

Thus, the wear rate will have the highest value at the highest applied load. Undoubtedly, the load has a direct relationship with plastic deformation that occurs near the surface. Thus, there will be more movement of the dislocations as the load goes up and this leads to more plastic deformation.

Figure 11 also shows that the inclusion of TiO₂ into the AA2024 alloy would decrease the weight loss where the maximum reduction occurs using the 5 wt.% of TiO₂. This is specifically denoted by the maximum improvement of

hardness and wear resistance as illustrated in Figure 10. Seemingly, the oxide layer formed with 5 wt.% TiO₂-AA2024 has a harder surface than the disc substrate. Therefore, it would act as a protective third body, reducing the effect of sliding wear on the surface below. However, it should be noted that utilising TiO₂ with more than 5 wt.% would elevate the weight loss. The results are in good agreement with the findings of [30], [33].

Comparing the results of Figure 11 would introduce the advantage of heat treatment in reducing the weight loss for the whole nanocomposites compared to the ones before the heat treatment. This indicates that the sample after heat treatment was more resistant to wear than the sample before heat treatment. The wear resistance of the samples has therefore increased after annealing [18], [30] as represented in Figures 6 and 9.

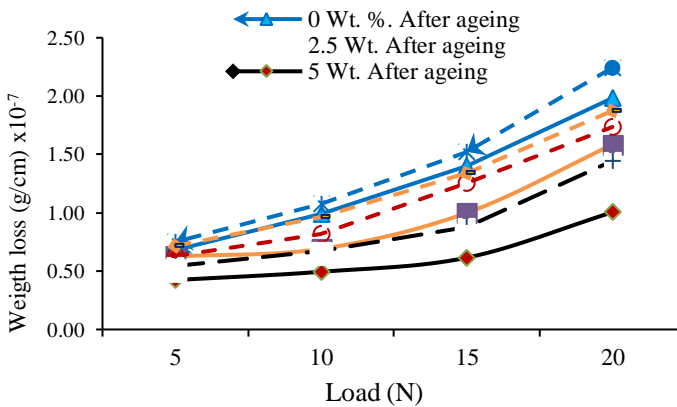


Figure 11: Variation of mass loss of specimens as a function of applied load before and after heat treatment

Optical micrograph of the contact surface

The wear surface for each sample is demonstrated in Figure 13. The wear surface had highly dimpled structures and ductile failure properties for the samples without nanoparticles. Regarding the wear of very strong Aluminium alloys, the development of microvoids surrounding coarsened precipitates causes intergranular damage. The surface displayed clear grooves that ran lengthwise, caused by the ploughing effect of harder steel particles. When more TiO₂ nanoparticles were added to the composite, the depth of these scratches reduced, indicating an improvement in wear resistance. This was because the hardness of the composite increased with an increase in the volume of TiO₂ nanoparticles. Improving the hardness of the material helped enhance its wear resistance. Furthermore, SEM images indicated irregular characteristics among wear surfaces, revealing that the wear rate was derived from various failure mechanisms. Large, clear grooves were diminished to fine

scratches along the sliding direction (Figure 13(c)) that were observed on the surface (Figure 13(a)), and abrasive wear became adhesive wear. Due to a larger number of TiO_2 nanoparticles in the matrix base, its plastic deformation was countered by a mechanically mixed layer that became a barrier to the moment of dislocation and increased wear resistance [34]-[35].

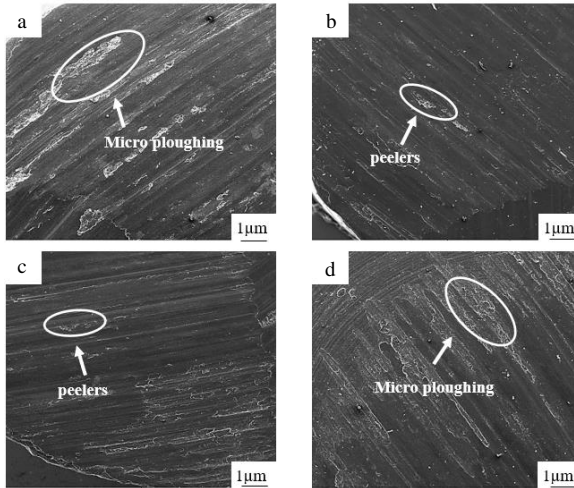


Figure 12: Worn surface morphology of AA2024 under the load 5 N; (a) AA2024 matrix material (b) AA2024-2.5 wt.% TiO_2 , (c) AA2024- 5 wt.% TiO_2 , and (d) AA2024-7.5 wt.% TiO_2

The weight loss and wear tracks of the AA2024 matrix material following heat treatment are depicted in Figure 14. It demonstrates low delamination and fracture of the transfer layer as a result of the abrasive effect of the hardened transfer particles, which results in cutting with subsequent delamination and fracture of the compacted layer [30]. Figures 14(b) and 14(c) illustrate different grooves and ridges that run parallel to one another in the sliding direction, as indicated by the red mark. Because the surface of the fixed specimens in the current experiment is in constant contact, one reason for the examined alloys' greater resistance is their capacity to produce a protective oxide layer during wear. Due to their high reactivity, Ti-based alloys exposed to an oxidative environment rapidly generate an oxide layer on the surface. Therefore, the investigated alloys have an improved wear resistance due to their ability to create a protective oxide layer while in constant contact rapidly.

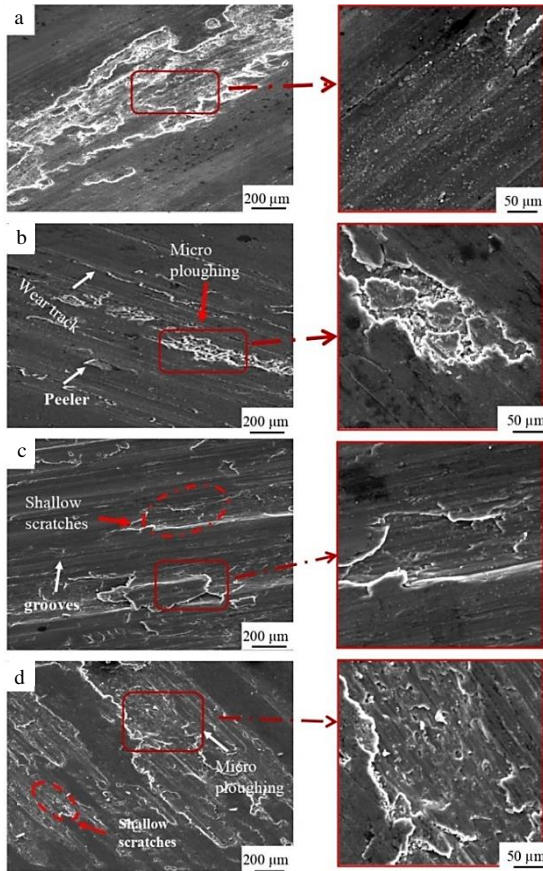


Figure 13: Morphologies of the worn surface at a load of 20 N; (a) AA2024 matrix material, (b) AA2024-2.5 wt. % TiO_2 , (c) AA2024-5 wt. % TiO_2 , and (d) AA2024-7.5 wt. % TiO_2 composite before heat treatment

The process of abrasion is linked with the creation and expansion of cracks. Any element that restricts the growth of these cracks can minimize the amount of wear. When there is a strong bond between the reinforcement and the substrate, the reinforcement particles can act as a factor to prevent the growth of cracks. Furthermore, it should be noted that when the composite surface is harder, it generates more heat during the wear process, forming oxide layers that require even higher temperatures. This ultimately enhances the wear resistance. Additionally, Figure 7 shows that the grooves are lower and wider in the matrix as compared to the composites tested under similar conditions. Figure 14(d) demonstrates the ploughing on the worn-out surface of the 7.5

wt.% of TiO₂ composite, which may be due to the sliding of oxide particles in the composite [34].

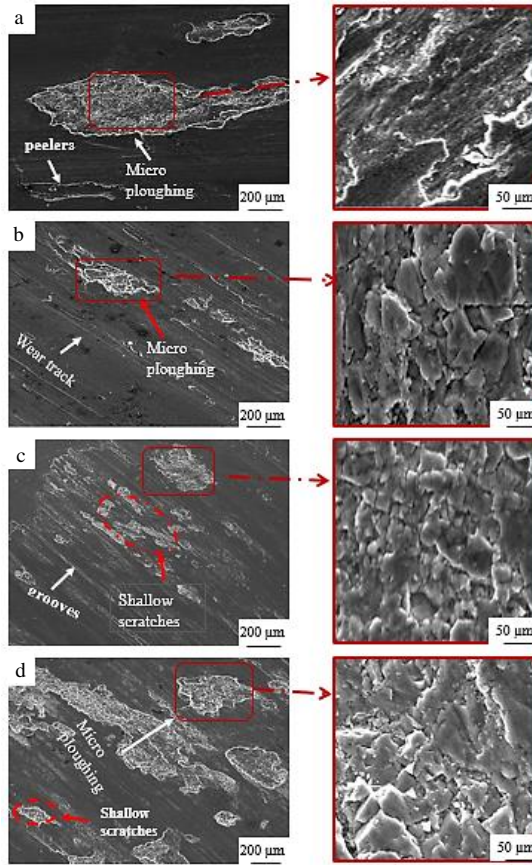


Figure 14: Morphologies of the worn surface at a load of 20 N; (a) AA2024 matrix material, (b) AA2024-2.5 wt. % TiO₂, (c) AA2024-5 wt. % TiO₂, and (d) AA2024-7.5 wt. % TiO₂ composite after heat treatment

The wear rate of the rheoformed composite components reduced insignificantly when the volume fraction of TiO₂ nanoparticles reached 7.5% compared to those with 5% TiO₂ nanoparticles. However, the increased agglomeration of TiO₂ nanoparticles made it challenging to disperse them evenly, resulting in a reduction of their effective dispersion within the 2024 matrix and ultimately decreasing the wear resistance. Both SEM tests show indications of nano-sized particle integration and entrapment inside the interdimeric interface that forms during the solidification of the dispersed

alloys. Furthermore, it is hypothesized that the homogeneous dispersion of nanoparticles provides locations for heterogeneous nucleation throughout the solidification process, leading to a more refined microstructure. The nanoparticle reinforcement in composites can be explained by the fact that particles cannot move around in the melt as it solidifies since the melt and matrix become more viscous [30].

Conclusions

TiO₂/AA2024 nanocomposites of 2.5 wt.%, 5 wt.% and 7.5 wt.% TiO₂ nanoparticles were prepared with the stir casting method, followed by heat treatment. Precipitation wear rate and hardness properties were investigated. The following conclusions can be made:

- i. Mechanical tests showed that the hardness and wear resistance have increased as the percentage of nanoparticles increases, while the wear rate has decreased as the percentage of reinforcing materials increases.
- ii. Aluminium alloy containing 5 wt.% TiO₂ nanocomposites have got the highest wear resistance and the hardest surface than the other tested nanocomposites. Thus, it can be stated that the 5 wt.% is the optimum weight content of TiO₂.
- iii. Nanoparticles have specifically enhanced the wear characteristics of the composites contributing to the development of a stable trilateral with self-lubricating features.
- iv. A bimodal microstructure has been formed in the samples as they were extruded, and it was still there after heat treatment. This is likely because the dispersed TiO₂ nanoparticles pinned the grain boundaries together.

Thus, the combination of 5 wt.% TiO₂ nanoparticles with AA2024 alloys have greatly enhanced the physical properties. In turn, this would enhance the potential of Aluminium alloys for various industrial applications.

Contributions of Authors

The authors confirm the equal contribution in each part of this work. All authors reviewed and approved the final version of this work.

Funding

This work received no specific grant from any funding agency.

Conflict of Interests

All authors declare that they have no conflicts of interest.

Acknowledgement

The researcher would like to extend their sincerest gratitude to the staff at the Samara National Research University, 443086, 34 Moskovskoye Shosse, Samara, Russia, and the Materials Engineering Department, Samara, Russia

References

- [1] S. K. Moheimani, A. Keshtgar, S. Khademzadeh, M. Tayebi, A. Rajaei, and A. Saboori “Tribological behaviour of AZ31 magnesium alloy reinforced by bimodal size B4C after precipitation hardening”, *Journal of Magnesium and Alloys*, vol. 10, pp. 3267-3280, 2021. <https://doi.org/10.1016/j.jma.2021.05.016>
- [2] D. Brough, H. Jouhara, “The aluminum industry: a review on state-of-the-art technologies, environmental impacts and possibilities for waste heat recovery”, *International Journal of Thermofluids*, vol.1–2, no. 100007, pp. 1-39, 2020. <https://doi.org/10.1016/j.ijft.2019.100007>.
- [3] P. Garg, A. Jamwal, D. Kumar, K.K. Sadasivuni, C.M. Hussain, P. Gupta, “Advance research progresses in aluminum matrix composites: manufacturing & applications”, *Journal of Materials Research and Technology*, vol. 8, no. 5, pp. 4924-4939, 2019. doi.org/10.1016/j.jmrt.2019.06.028.
- [4] R. David, V. Shrivastava, R. Dasgupta, B.K. Prasad, and I.B. Singh, “Corrosion investigation of zinc–aluminum alloy (ZA-27) matrix reinforced with in situ synthesized titanium carbide particle composite”, *Journal of Materials Engineering and Performance*, vol. 28, no. 4, pp. 2356-2364, 2019. <https://doi.org/10.1007/s11665-019-03992-6>.
- [5] H. Mahan, D. Mahjoob, K. Mahmood, "Mechanical properties of alumina nano-particles and glass fiber, kevlar fiber reinforced composites", *Journal of Engineering and Applied Sciences*, vol. 13, no. 21, pp. 9096-9100, 2018. <https://doi.org/10.3923/jeasci.2018.9096.9100>.
- [6] A. Karakaş, T.O. Fenercioğlu, T. Yalçinkaya, “The influence of flow forming on the precipitation characteristics of Al2024 alloys”, *Materials Letters*, vol. 299, pp. 218-227, 2021. doi.org/10.1016/j.matlet.2021.130066.
- [7] F. Kiarasi, M. Babaei, M. Omid Bidgoli, K. Reza Kashyzadeh, K. Asemi, K., “Mechanical characterization and creep strengthening of AZ91 magnesium alloy by addition of yttrium oxide

- nanoparticles. Proceedings of the Institution of Mechanical Engineers”, *Journal of Materials: Design and Applications*, vol. 236, no. 8, pp. 1489-1500, 2022. <https://doi.org/10.1177/14644207211073>.
- [8] X. Yu, H. Bakhtiari, J. Zhou, M.O. BidgoliK. Asemi, “Investigating the effect of reinforcing particles size and content on tensile and fatigue properties of heat-treated al7075-sic composites fabricated by the stir casting method”, *The Journal of The Minerals, Metals & Materials Society*, vol. 74, no. 5, pp. 1859-1869, 2022. <https://doi.org/10.1007/s11837-022-05248-6>.
- [9] D. Rahmatabadi, R. Hashemi, B. Mohammadi, T. Shojaee, “Experimental evaluation of the plane stress fracture toughness for ultrafine grained aluminum specimens prepared by accumulative roll bonding process”, *Materials Science and Engineering*, vol. 708, pp. 301-310, 2017. <https://doi.org/10.1016/j.msea.2017.09.085>.
- [10] S. Borji, M.K. Zanganeh, M. Ahangarkani, Z. Valefi, “The feasibility of W-Cu composite production by submicron particles addition and infiltration”, *Iranian Journal of Materials Science and Engineering*, vol. 14, no. 1, pp. 1-11, 2017. <https://doi.org/10.22068/ijmse.14.1.6>.
- [11] S. S. Ahn, S. Pathan, J. M. Koo, C. H. Baeg, C. U. Jeong, H. T. Son, S. J. Hong, “Enhancement of the mechanical properties in Al–Si–Cu–Fe–Mg alloys with various processing parameters”, *Materials*, vol. 11, no. 11, pp. 1-12, 2018. <https://doi.org/10.3390/ma11112150>.
- [12] M. Araghchi, H. Mansouri, R. Vafaei, and Y. Guo, “Novel cryogenic treatment for reduction of residual stresses in 6061 aluminum alloy”, *Materials Science and Engineering*, vol. 689, pp. 48-52, 2017. <https://doi.org/10.1016/j.msea.2017.01.095>
- [13] J. Xia, J. J. Lewandowski, M. A. Willard, “Tension and fatigue behavior of Al-2124A/SiC-particulate metal matrix composites”, *Materials Science and Engineering: A*, vol. 770, p. 138518, 2020. <https://doi.org/10.1016/j.msea.2019.138518>.
- [14] M. S. Patel, and K.S. Mukesh, “Fabrication and Investigation of mechanical properties of sic particulate reinforced AA5052 metal matrix composite”, *Journal of Modern Material*, vol. 7, no. 1, pp. 26-36, 2020. <https://doi.org/10.1016/j.matpr.2021.10.331>.
- [15] T. İsmail. “Investigation of wear behavior of particle reinforced AL/B4C composites under different sintering conditions”, *Tehnički Glasnik*, vol. 14, no. 1, pp. 7-14, 2020. <https://doi.org/10.31803/tg-20200103131032>.
- [16] J. Jiang, G. Xiao, C. Che, Y. Wang, “Microstructure, mechanical properties and wear behavior of the rheoformed 2024 aluminum matrix composite component reinforced by Al₂O₃ nanoparticles”, *Metals*, vol. 8, no. 6, p. 460, 2018. <https://doi.org/10.3390/met806460>.
- [17] M. Vaghari, R. Gholam, and S. A. Jenabali Jahromi. “Studying on the fatigue behaviour of Al- Al₂O₃ metal matrix Nanocomposites processed through powder metallurgy”, *Journal of Ultrafine Grained and*

- Nanostructured Materials*, vol. 52, no. 2, pp. 210-217, 2019. <https://doi.org/10.22059/JUFGNSM.2019.02.10>.
- [18] E. Simonetto, R. Bertolini, A. Ghiotti, S. Bruschi, S., “Mechanical and microstructural behaviour of AA7075 aluminium alloy for sub-zero temperature sheet stamping process”, *International Journal of Mechanical Sciences*, vol. 187, p. 105919, 2020. doi.org/10.1016/j.ijmecsci.2020.105919.
- [19] Y. X. Lai, W. Fan, M. J. Yin, C. L. Wu, J. H. Chen, “Structures and formation mechanisms of dislocation-induced precipitates in relation to the age-hardening responses of Al-Mg-Si alloys”, *Journal of Materials Science & Technology*, vol. 41, pp. 127-138, 2020. <https://doi.org/10.1016/j.jmst.2019.11.001>.
- [20] V. Verma, A.H.M. Sayyed, C. Sharma, D.K. Shukla “Tensile and fracture properties of epoxy alumina composite: Role of particle size and morphology”, *Journal of Polymer Research*, vol. 27, pp. 1-14, 2020. <https://doi.org/10.1007/s10965-020-02359-z>.
- [21] S. Alagarsamy, M.Ravichandran, M. Meignanamoorthy, “Multi-objective optimisation of dry sliding wear control parameters for stir casted AA7075-TiO₂ composites using Taguchi-Grey relational approach”, *Australian Journal of Mechanical Engineering*, vol. 20, no. 5, pp. 1453-1462, 2022. <https://doi.org/10.1080/14484846.2020.1815997>.
- [22] M. Singh, B. K. Prasad, D. P. Mondal, & A. K. Jha, “Dry sliding wear behaviour of an aluminium alloy–granite particle composite”, *Tribology International* vol. 34, no. 8, pp. 557-567, 2001. [https://doi.org/10.1016/S0301679X\(01\)00046-9](https://doi.org/10.1016/S0301679X(01)00046-9).
- [23] R. Farajollahi, H. J. Aval, R. Jamaati, “Effects of Ni on the microstructure, mechanical and tribological properties of AA2024-Al₃NiCu composite fabricated by stir casting process”, *Journal of Alloys and Compounds*, vol. 887, p. 161433, 2021. <https://doi.org/10.1016/j.jallcom.2021.161433>.
- [24] S. Z. A. Sakinah, W. H. Azmi, J. Alias, “Characterization of TiO₂ nanopaint for automotive application”, *IOP Conference Series: Materials Science and Engineering*, vol. 863, no. 1, p. 012053, 2021. <https://doi.org/10.1088/1757-899X/863/1/012053>.
- [25] Q. Li, X. Zhang, L.Wang, and J. Qiao, “The effect of extrusion and heat treatment on the microstructure and tensile properties of 2024 aluminum alloy”, *Materials*, vol. 15, no. 21, p. 7566, 2022. <https://doi.org/10.3390/ma15217566>.
- [26] J. Salguero, J. M. Vazquez-Martinez, I. D. Sol, M. Batista, “Application of pin-on-disc techniques for the study of tribological interferences in the dry machining of A92024-T3 (Al–Cu) alloys”, *Materials*, vol. 11, no. 7, p. 1236, 2018. <https://doi.org/10.3390/ma11071236>.
- [27] A. Shahi, M.H. Sohi, D. Ahmadkhaniha, and M. Ghambari, "In situ formation of Al–Al₃Ni composites on commercially pure aluminium by

- friction stir processing”, *The International Journal of Advanced Manufacturing Technology*, vol. 75, no. 9, pp. 1331-1337, 2014. doi.org/10.1007/s00170-014-6162-3.
- [28] H. J. M. Al-Alkawi, A.A. Al- Rasiaq, and M.A.A. Al- Jaafari. "Mechanical properties of 7075 aluminum alloy matrix /Al₂O₃ particles reinforced composites”, *Engineering and Technology Journal*, vol. 35, no. 3, Part A, pp. 239-245, 2017. doi.org/10.1016/j.matpr2020.12.747.
- [29] H. M. Mahan, S. Konovalov, I. Panchenko, “Effect of heat treatment on the mechanical properties of the aluminium alloys AA2024 with nanoparticles”, *International Journal of Applied Science and Engineering*, vol. 20, no. 2, pp. 1-6, 2023. [https://doi.org/10.6703/IJASE.202306_20\(2\).011](https://doi.org/10.6703/IJASE.202306_20(2).011).
- [30] Y. Wang, Y. Lu, S. Zhang, H. Zhang, H. Wang, and Z. Chen “Characterization and strengthening effects of different precipitates in Al–7Si–Mg alloy”, *Journal of Alloys and Compounds*, vol. 885, p. 161028, 2021. <https://doi.org/10.1016/j.jallcom.2021.161028>.
- [31] Z. Fangyuan, D. Chunzheng, S. Wei, J. Kang, “Influence of white layer and residual stress induced by hard cutting on wear resistance during sliding friction”, *Journal of Materials Engineering and Performance*, vol. 28, pp. 7649-7662, 2019. <https://doi.org/10.1007/s11665-019-04479-0>.
- [32] C. Melik “Abrasive wear behaviour of cast Al–Si–Mn alloys”, *Proceedings of the Institution of Mechanical Engineers, Part E: Journal of Process Mechanical Engineering*, vol. 233, no. 4, pp. 908-918, 2019. <https://doi.org/10.1177/0954408918818735>.
- [33] H. M. Mahan, S. Konovalov, Omran A. Shabeeb, “Enhancement of mechanical properties and microstructure of aluminium alloy AA2024 by adding TiO₂ nanoparticles”, *International Journal of Nanoelectronics and Materials*, vol. 16, no. 3, pp. 441-453, 2023.
- [34] D. Srinivasan, M. Meignanamoorthy, A. Gacem, M. Vinayagam, T. Sathish, M. Ravichandran and H.L. Allasi, “Tribological behavior of Al/ Nanomagnesium/ Aluminum nitride composite synthesized through liquid metallurgy technique”, *Journal of Nanomaterials*, vol. 2022, no. 2, pp. 1-12, 2022. <https://doi.org/10.1155/2022/7840939>.
- [35] S. Gangwar, V. Payak, V.K. Pathak, A. Jamwal and P. Gupta, “Characterization of mechanical and tribological properties of graphite and alumina reinforced zinc alloy (ZA-27) hybrid metal matrix composites”, *Journal of Composite Materials*, vol. 54. no. 30, pp. 4889-4901, 2020. <https://doi.org/10.1177/0021998320938442>.

Comparison of Different Surface Pre-Treatment on Mild Steel for Cobalt-Nickel-Iron Electroplating

Koay Mei Hyie*, Nor Azirah Mohd Fohimi, Salina Budin,
Normariah Che Maideen

Centre for Mechanical Engineering Studies, Universiti Teknologi MARA,
Cawangan Pulau Pinang, Permatang Pauh Campus, 13500 Pulau Pinang,
MALAYSIA

*koay@uitm.edu.my

Md Zin Abu

AANS Technical & Services Sdn. Bhd., Lot 27, Kawasan Perindustrian Seri
Manjung, 32040 Seri Manjung, Perak Darul Ridzuan, MALAYSIA

ABSTRACT

Electroplating is extensively practiced in the industry to fabricate corrosion-protective coatings for steel in large-scale production. Mild steel easily rusts at ambient temperature thus surface pre-treatment is mandatory to eliminate rust and superficial scale from the steel. Pre-treatment ensures that the steel surface is free from contaminants, which may interfere with the surface quality of the protective coating. This research is done to investigate the effect of different pre-treatment methods on the surface quality of mild steel rings and cobalt-nickel-iron coated mild steel rings. These surfaces were achieved by polishing the ring and subjected to alkaline degreasing, followed by immersion in sulfuric acid or sodium chloride at 10 vol % concentration and different immersion times (50 s, 55 s, and 60 s). Direct electroplating was applied to fabricate the cobalt-nickel-iron coating. The surface morphology of metal substrate and coating after electroplating were tested by scanning electron microscope (SEM), energy dispersive X-Ray (EDS), Vickers hardness, and surface roughness tests. Both types of pre-treatments provided lower surface roughness on the metal substrate and resulted in full coatings without voids formation. The results showed that pre-treatment using sulfuric acid exhibited higher hardness and a smoother coating surface. Agglomerates and cracking were observed on the surface coating treated with sodium chloride.

Keywords: *Mild steel; Surface Pre-Treatment; Coating; Sulfuric Acid; Sodium chloride*

Introduction

Preventing corrosion in ferrous metals is a major concern among engineers. Corrosion can happen at all stages in manufacturing, finishing, and maintenance. The most common forms of corrosion protection are galvanization [1], alloying [2], cathodic sacrificial protection [3], and barrier coating [4]. Recent trends in coating protection have shifted focus to nontoxic options to replace chromate and phosphate conversion coating [5]. Cobalt and its alloy coating [6] are reported to have good corrosion inhibition. Besides, green fabrication of zinc-cobalt alloy coating improved the corrosion resistance by up to 27.6% [7]. The surface hardness, wear, and corrosion resistance were enhanced with the presence of cobalt coating in nanocrystalline size [8]. However, the corrosion resistance level of the coating depends on the quality of the coating itself and the surface of the substrate to be coated. Surface quality is important as the material surface directly contacts with external loads or forces such as friction, wear, corrosion, and fatigue that may affect the performance of the materials. Surface coating is incorporated on the metal surface to improve the lifetime of the metal.

There are many methods to fabricate coating as a protection layer on ferrous metals such as hot dip galvanizing, thermal spraying, chemical vapor deposition, laser cladding, and others. Among the techniques for coating synthesis, direct electroplating is of great interest for industrial use [8]. This technique lies in its versatility, moderate costs, large-scale production, and easy control thickness. In this technique, metal substrate surface pre-treatment is recommended prior to the electroplating process. The surface pre-treatment is usually associated with sandpaper polishing, cleaning, pickling, activation, or passivation to prepare the material for plating [9]. It is reported that surface pre-treatment could improve the wettability of the surface, which allowed for a better cohesion of the coating layer and ensured a homogeneous coating [10]. Besides, the surface pre-treatment helped to remove salts, soaps, or alkaline cleaning products left on the surface to avoid staining, skip plating, or even delamination and blistering.

The most common pickling used in mild steel surface treatment is corrosive fluid such as hydrochloride acid [11]. Another corrosive acid used in pickling could be sulfuric acid [12], or a mixture of acids with toxic inhibitors [13]-[14]. Alkaline such as ammonia fluoride was also proposed in the pre-treatment of mild steel. A neutral solution such as sodium chloride was incorporated into acid, which removed the oxide layer from the substrate surface and make the surface bright without weight loss [15]. Sodium chloride has been shown to have a beneficial effect in the pickling of mild steel if mixed

with sulfuric acid instead of the addition of hydrochloric acid into sulfuric acid [16]. The addition of sodium chloride enhanced the scale removal rate. It also figures depicted that the corrosive factor of the solution decreased if the concentration of the sodium chloride was increased up to 10 vol% [17] because of the oxygen solubility in water [18].

The surface profile after surface pre-treatment of steel also showed a significant effect on coating and corrosion protection for long-term service life. A thicker coating could be adhered to by a rough metal substrate to give better corrosion protection, but there is a limit [19]. A very rough surface might contain contaminant debris and a deep valley that is difficult to be coated. It could give an impact on the pitting corrosion [17]. Thus, the surface profile investigation is essential to ensure the quality of the coating.

The above-mentioned previous study had shown that the key to having a quality final coating from the electroplating process depends on the type and concentration of the pickling solution for substrate surface pre-treatment. The objective of this study is to investigate the role of sodium chloride and sulfuric acid separately on mild steel surface pre-treatment. The surface profile of mild steel before and after electroplating with a cobalt-nickel-iron corrosion protection layer was also reported in this study.

Experimental Work

Mild steel is the most widespread form of steel in the world. Mild steel rings were used as substrates, with a total surface area of 10.79 cm². The mild steel ring specimens contained 0.15% of carbon and more than 98% of iron. The specimens were polished with silicon carbide sandpapers of 240, 400, 600, and 1000 grits using a Buehler Handimet 2 Roll Grinder. After that, the specimens were cleaned using sodium hydroxide alkaline degreaser for 10 minutes at 65 °C. The alkaline degreasing was used to remove water-insoluble contaminants. The specimens were then rinsed with distilled water and prepared for the pickling process. Pickling provides deep cleaning while also activating the metal surface by removing the oxide layer from the surface of the material. The pickling process has resulted in a pure metal surface, which is free of contaminants and oxides [14]. Subsequently, the specimens were immersed in different solutions for varying periods, as shown in Table 1.

Table 1: Pickling solution and immersion time in mild steel ring substrate

Type of pickling solution	Time of immersion (seconds)		
Sulfuric acid	50	55	60
Sodium chloride	50	55	60

A former study proposed using 12.5% of sulfuric acid and immersion time ranging from 35 s to 55 s [12]. It is recommended that 10% to 14% sulfuric acid be used for carbon steel containing less than 0.4% carbon. Therefore, in this study, 10 vol% sulfuric acid with prolonged immersion time ranging from 50 s to 60 s was applied. For comparison purposes, 10 vol% sodium chloride was also used. The specimens were then washed with distilled water and air-dried.

In the electroplating process, the plating solution was prepared in a sulfate bath electrolyte with the presence of cobalt sulfate, nickel sulfate, iron sulfate, and some additives as tabulated in Table 2. The raw materials shown in Table 2 were mixed to produce a 500 ml volume of sulphate bath electrolyte. The electrolyte was prepared at a pH level of about 3. The temperature throughout the whole electroplating process was kept around 50 °C to 54 °C. While the acidic sulphate bath and operating temperature were determined based on parameter optimization reported in a previous study [21].

Table 2: Composition of sulphate plating solution (per 500 ml solution)

Composition	Amount (gram)
Cobalt sulphate	7.03
Nickel sulphate	17.52
Iron (II) sulphate	2.78
Boric Acid (additives)	8.24
Ascorbic Acid (additives)	5.87

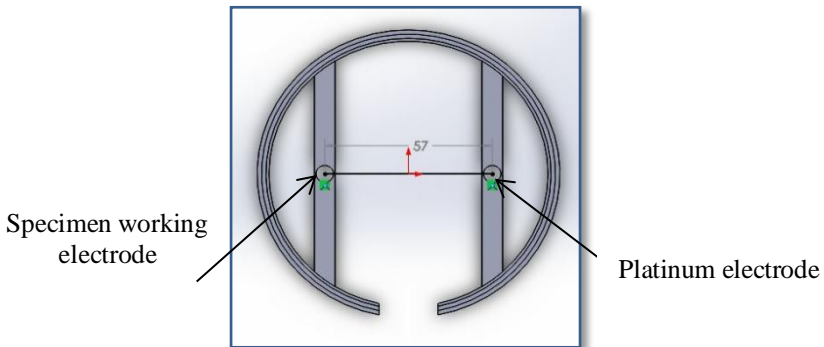


Figure 1: Schematic diagram of electrodes holder in electroplating process (top view)

The electrodes used in the electroplating process were clipped to the plastic-designed holder, as presented in Figure 1. A platinum plate was used as the auxiliary electrode (anode), whereas the mild steel ring was acting as

the working electrode (cathode). Both electrodes were placed at a distance of 57 mm to stabilize the ions' transfer during electroplating. Mild agitation was conducted throughout the electroplating process to avoid bubbles accumulating on the cathode surface, which may cause hydrogen evolution. A constant current of 1.0 A was applied for 20 minutes of electroplating time. A resultant mono-layer of cobalt-nickel-iron was produced on the mild steel specimen after electroplating.

The quality of the surface substrate and surface coating was evaluated by measuring their surface roughness and surface hardness. The surface roughness of the coating was measured using the Mitutoyo surface measuring instrument (SurfTest SJ-410) following the ISO1977 standard. Three randomly selected points on the flat side of each specimen were used to measure the surface roughness. At each point, the probe travel was set at a speed of 0.5 mm/s and a travel length of 4.8 mm. The most common expressions for surface roughness are R_a and R_q . R_a is the arithmetic mean of absolute values of the evaluation profile deviations from the mean line, as shown in Equation (1). R_q is referred to as the square root of mean roughness, as expressed in Equation (2) [19].

$$R_a = \frac{1}{n} \sum_{i=1}^n |Y_i| \quad (1)$$

$$R_q = \sqrt{\frac{1}{n} \sum_{i=1}^n (Y_i)^2} \quad (2)$$

where n is the number of segments over the evaluation length and Y_i is the deviation from the mean line.

In terms of surface hardness, the method of measurement was using the Mitutoyo Vickers hardness test. The loading (F) applied in the hardness test was 0.5 kilograms-force. Similarly to the surface roughness test, the surface hardness was tested at three different areas of specimens, while avoiding the defect area on the surface. The Vickers hardness was determined using Equation (3) [20], where diagonal lengths of the indentation (D) left on the surface of the material were measured.

$$\text{Vickers hardness, } HV \approx 1.854 \frac{F}{D^2} \quad (3)$$

where F is the load in kgf, and D is the arithmetic mean of the two diagonal lengths.

The pre-treated substrate surface and surface coating morphology were examined using a Hitachi TM3030 PLUS model scanning electron microscope

(SEM) attached with an energy dispersive X-ray (EDS) machine. The specimens were mounted on aluminium stubs, using carbon double-sided tapes for SEM and EDS analysis. Cross-sections of samples were prepared to determine the coating thickness and elemental composition.

Results and Discussion

Surface roughness

Figure 2 displays the line profiles for metal substrates before and after surface pre-treatment. It can be seen in Figure 2(a) that the metal surface without pre-treatment is rougher due to large deviations from the mean line. The average surface roughness, Ra was recorded at $1.536 \mu\text{m}$ and Rq at $2.616 \mu\text{m}$. Figure 2(b) demonstrates the surface of the metal surface after pre-treated with sulfuric acid. The surface became smoother and showed a Ra of $0.327 \mu\text{m}$ and Rq of $0.480 \mu\text{m}$. The drastic drops of Ra and Rq after pre-treatment revealed that the original mild steel had more defects such as contaminants, oxides, valleys, and grooves. A similar finding was found in contaminated Ni-Co substrate pre-treated with sulfuric acid [12]. The burrs or oxides on the substrate surface were completely removed by modified pre-treatment with sulfuric acid and further enhanced the adhesion of the coating [19]. It was believed that the oxide and contaminants interfered with the adhesion of the coating and caused corrosion creep, where the corrosion occurred under the coating interfaced with the metal surface [19]. Thus, it was essential to remove the contaminants of the metal surface to avoid corrosion failure on the coated metal.

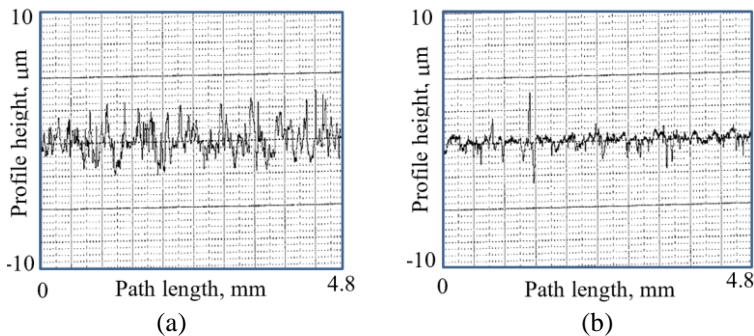


Figure 2: Roughness line profiles for mild steel surface substrate; (a) original, and (b) pre-treated with sulfuric acid at 60 seconds of immersion

Table 3 depicted the results of the surface roughness of mild steel substrate after being pre-treated with different types of solution. It is clearly

shown that the average surface roughness, Ra was significantly reduced in sulfuric acid solution as the immersion time increased. However, the surface roughness, Ra of the mild steel substrate was not affected by the time of immersion in sodium chloride. The roughness after surface pre-treatment had improved compared to the original metal surface (Ra of $1.836 \mu\text{m}$) without pre-treatment. The average Rq was lower in acid solution indicating that the deviations between peaks and valleys were smaller. When sulfuric acid (H_2SO_4) reacted with steel, the iron oxide on the mild steel (mainly iron element) surface was chemically removed and transformed into iron sulphate [12]. The reaction of cations and anions between sulfuric acid and steel is depicted in Equation (4).

Table 3: Surface roughness of mild steel substrate after surface pre-treatment

Pickling solution	Immersion time, t (s)	Average surface roughness, Ra (μm)	Average square root of the arithmetic mean, Rq (μm)
No pre-treatment (reference)	0	1.536	2.616
	50	0.927	0.502
Sulfuric acid	55	0.573	0.531
	60	0.327	0.480
	50	0.652	0.671
Sodium chloride	55	0.641	0.808
	60	0.693	0.782

The iron sulfate (FeSO_4) was believed to adhere to the steel surface and formed a protective layer [22] that covered the grooves and valleys, hence giving a lower value of Rq . However, the FeSO_4 layer was easily scaled off and poorly adherent. The FeSO_4 layer could not permanently protect the base mild steel from rusting. Thus, a permanent coating is essential to overcome the problem. Furthermore, the chloride ions in sodium chloride (neutral solution) would reduce metal loss but could initiate the formation of pits and may lead to localized corrosion, which is also known as pitting corrosion [17].



Figure 3 compared the surface roughness of cobalt-nickel-iron coated mild steel after electroplating. The surface coating of the specimen pre-treated with sodium chloride is rougher compared to the surface coating pre-treated with sulfuric acid. The surface roughness dropped when the immersion time increased. There was about 55% of reduction in surface roughness when the specimen was immersed in acidic solution from 50 seconds to 60 seconds.

However, the reduction for specimens treated with sodium chloride was smaller (24%).

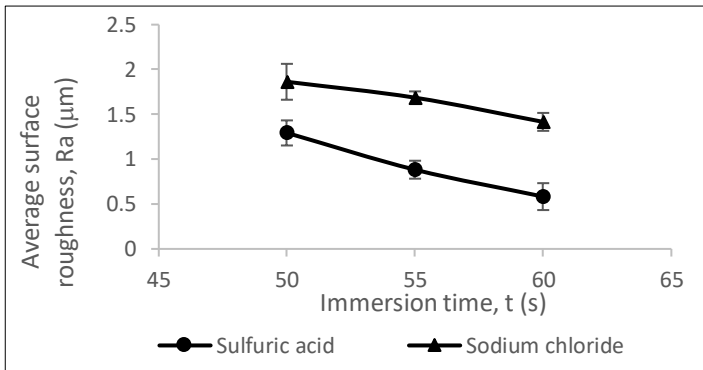


Figure 3: Surface roughness of surface coating pre-treated with different pickling solutions

Surface morphology

Figure 4 represented the surface morphology of metal substrates. The results indicated that surface pre-treatment had a significant effect on roughness and coating quality. The results show good agreement with Ra values as tabulated in Table 3. The metal substrate surface without treatment is the roughest. There are many valleys found in Figure 4(a), resulting in higher Rq values due to high deviations from mean roughness values. In contrast, Figure 4(b) showed that the metal surface pre-treated with sulfuric acid appears smoother, with only a little debris found on the surface. A similar finding had been reported [23], where static pickling produced a smoother surface than dynamic pickling.

In terms of the effect of sodium chloride pickling solution, small voids can be seen scattered throughout the surface of the specimen, as revealed in Figure 4(c). The formation of these voids could be due to corrosion activity on the surface of base metal when treated with sodium chloride [17]. It is known that chloride ions in sodium chloride promoted the hydration of iron ions from the mild steel substrate. Sodium chloride is the corrosion media that helps to remove the iron ions accumulated at the surface. It is reported that the chloride (Cl) ions are incorporated with iron (Fe) ions to form an iron oxide layer and leave cationic vacancies, which then condense at the iron interface to form small voids. These small voids are also known as pits [24]. The formation of the pits upon pre-treated with sodium chloride was illustrated in Figure 5. Figure 4(d) showed the cross-section of the specimen pre-treated with sodium chloride. It can be seen that pits are formed at the surface of the base metal. A similar SEM cross-sectional morphology of the pit was reported in the low-carbon steel treated with chloride solution [25].

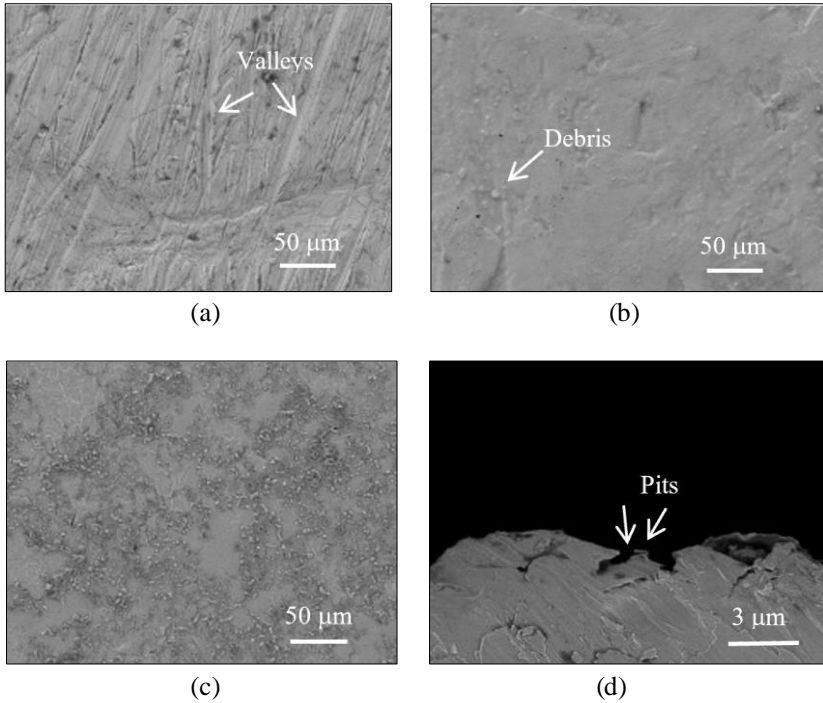


Figure 4: SEM images; (a) original mild steel, (b) mild steel pre-treated with sulfuric acid at 60 s, (c) mild steel pre-treated with sodium chloride at 60 s, and (d) cross-section of mild steel pre-treated with sodium chloride at 60 s

The surface coating with and without pre-treatment were presented in Figure 6. Figure 6(a) showed numerous agglomerates and voids appearing on the surface coating of metal specimens without surface pre-treatment. The rough surface of the coating contributed to the highest R_a values of $2.156 \mu\text{m}$ due to the large deviation of peaks and valleys from the mean line over time. The substrate surface pre-treated with sulfuric acid shows a homogeneous coating without voids and agglomerates. The coating surface morphology on the sample pre-treated with sulfuric acid was shown in Figure 6(b). The result is consistent with the surface roughness measurement, which indicated the lowest value. The uneven surface of the metal substrate is susceptible to uneven coating formation and thus results in higher surface roughness. In contrast, it can be said that the substrate surface pre-treated with sulfuric acid showed a homogeneous coating without voids and agglomerates and gave the lowest surface roughness as shown in Figure 6(b).

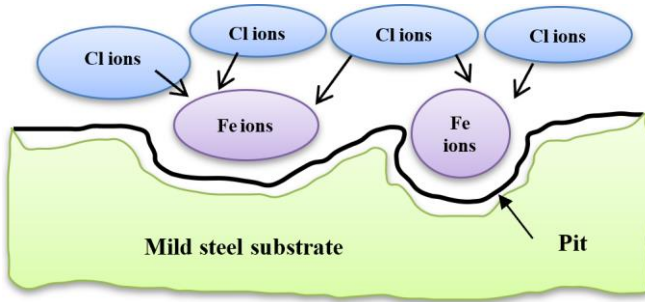


Figure 5: Illustration of sodium chloride reacted with mild steel substrate

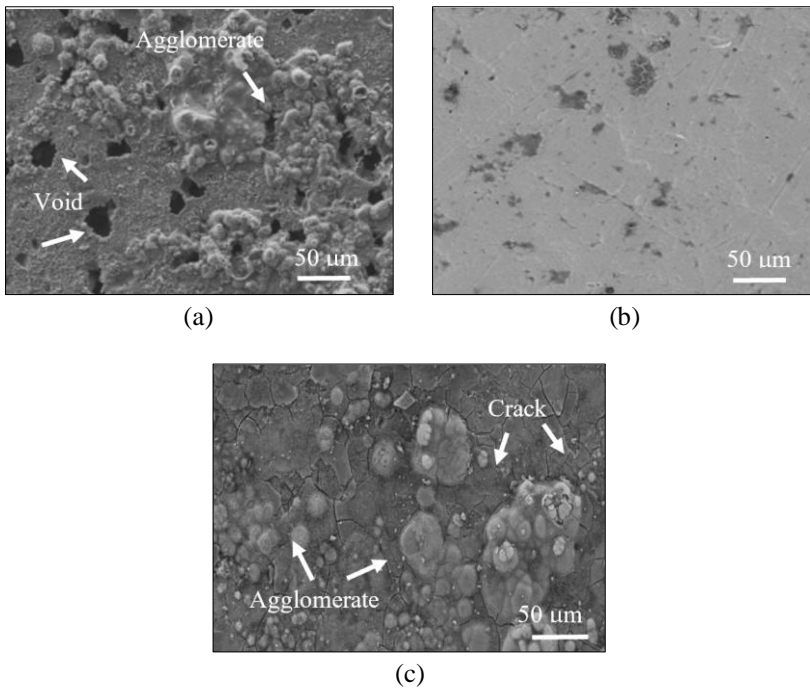


Figure 6: SEM images; (a) coating without pre-treatment, (b) coating pre-treated with sulfuric acid at 60 s, and (c) coating pre-treated with sodium chloride at 60 s

Figure 6(c) demonstrated that the coating fully covered the pits on the surface of the specimen pre-treated with sodium chloride, which led to the formation of agglomerates. This is due to surface irregularities on the pre-treated specimen as shown in Figure 4(c). Moreover, cracks were also found

throughout the entire surface. This defect was probably caused by agglomeration, which exhibited brittle rupture [26]. As a result, the surface pre-treated with sodium chloride had become rougher after being electroplated with cobalt-nickel iron.

Figure 7 showed a comparison of the thickness of the coating formed with different pre-treatment. The thickness of a mono-layer of cobalt-nickel-iron coating ranged from 10 μm to 15 μm at a constant electroplating time of 20 minutes. The thickness of the coating did not vary too much. In fact, the main factor influencing coating thickness is the electroplating process parameters [12]. The surface coating shown in Figure 7(a) is smooth on the specimen pre-treated with sulfuric acid. It is evident from Figure 7(b) that the Co-Ni-Fe coating was rougher on the specimen pre-treated with sodium chloride. Overall, the roughness of the coating surface is much lower than the thickness of the coating, which is suitable for automotive coatings that require smooth and low-profiled surfaces [19].

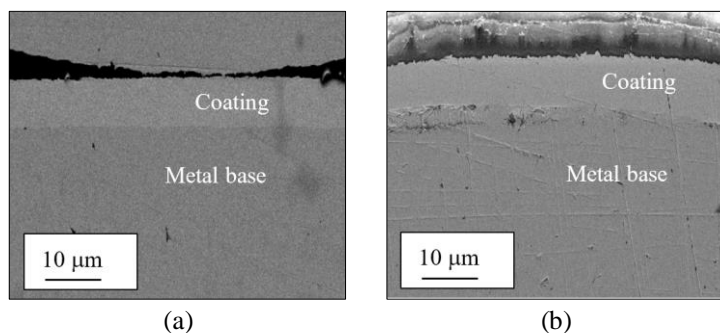


Figure 7: SEM cross-section images coated mild steel ring pre-treated with; (a) sulfuric acid, and (b) sodium chloride at 60 s time immersion

The EDS analysis was performed on the coating as well as the metal base for both pickling solutions. Both solutions presented similar results where no contaminant was visible on the coating and metal base as shown in Figure 8. It is found that the coating showed elements of cobalt (Co), iron (Fe), nickel (Ni), and carbon (C). The metal base is purely Fe and carbon (C). This result shows that all pickling solutions and contaminants were removed successfully after pre-treatment prior to Co-Ni-Fe electroplating.

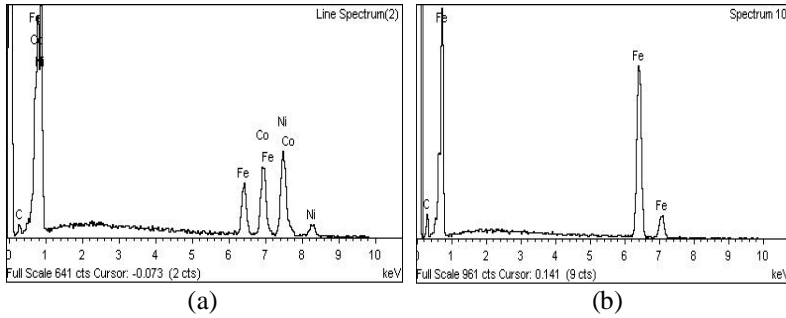


Figure 8: EDS spectrum; (a) Co-Ni-Fe coating, and (b) metal base

Surface hardness

Figure 9 showed the average surface hardness for coated specimens pre-treated with multiple pickling solutions. The sulfuric acid solution had shown to produce greater hardness compared to the sodium chloride solution. Thus, the addition of coating on the metal substrate should increase its hardness. However, it is found that the coated specimen treated with sodium chloride showed similar hardness to the mild steel substrate (114 HV). It is believed that the pits formed on the substrate surface weakened the bonding between the coating and substrate. The coating did not function well in protecting and enhancing the hardness due to the film-breaking mechanism caused by pits [24]. Cracks also occurred on the surface of the specimen pre-treated with sodium chloride, which further weakens the resistance of the specimen to external force.

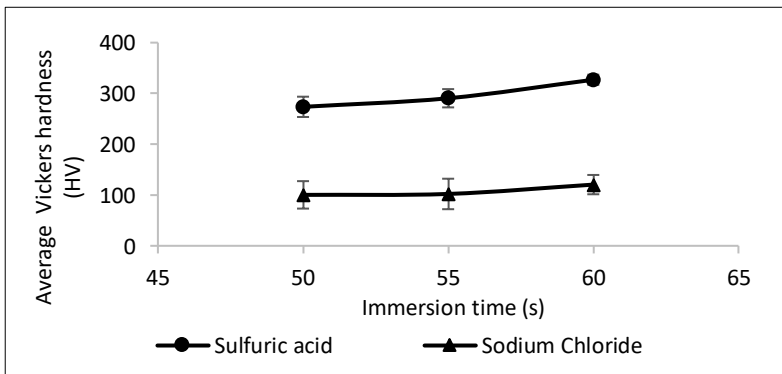


Figure 9: Surface hardness of coated mild steel pre-treated with multiple pickling solutions

The finding in Figure 9 correlated well with the surface roughness. A lower surface roughness resulted in better hardness. Hardness measured the material's resistance to plastic deformation. The acidic solution provided a smoother surface for coating and thus reduced coating defects. The smooth substrate surface enhanced the adhesion of the coating and resulted in better resistance to plastic deformation. It is reported that material with higher hardness could be more wear-resistant [27].

Conclusion

The comparison was made between the surfaces pre-treatment of mild steel using different pickling solutions after grinding and alkali degreasing. Both types of solutions were effective in removing the contaminants, rust oxide layer as well as improving the surface profile of the initial mild steel substrate. The surface pre-treatment not only reduced the roughness of the initial substrate but also minimized the voids formation problem in the coating during electroplating. However, randomly distributed pits were observed on the surface pre-treated with sodium chloride. The surface hardness of the coating was not improved after being pre-treated with sodium chloride due to agglomerates and film cracking. In comparison, the surface pre-treatment using sulfuric acid had shown promising results at a 10 vol% concentration of sulfuric acid and 60 seconds of immersion. As a uniform coating with better hardness without peeling, pitting, and cracking was obtained, it is recommended that the surface pre-treatment process must be carefully controlled when using a corrosive solution. The intention should be to clean and activate the substrate surface but not to further corrode the steel.

Contributions of Authors

The authors confirm the equal contribution in each part of this work. All authors reviewed and approved the final version of this work.

Funding

This work was supported by Ministry of Higher Education Malaysia, Grant PRGS/1/2020/TK05/UiTM/02/1. This work was also supported by AANS Technical & Services Sdn. Bhd., Grant 100-TNCPI/PRI 16/6/2 (031/2022).

Conflict of Interests

All authors declare that they have no conflicts of interest.

Acknowledgment

The authors are grateful to Ministry of Higher Education Malaysia, Research Management Institute (RMI), Universiti Teknologi MARA (UiTM) and AANS Technical & Services Sdn. Bhd., Malaysia for financial supports. The research was conducted at Centre for Mechanical Engineering Studies, UiTM Cawangan Pulau Pinang and AANS Technical & Services Sdn. Bhd. supported by Grant PRGS/1/2020/TK05/UiTM/02/1 and Grant 100-TNCPI/PRI 16/6/2 (031/2022).

References

- [1] T. Duarte, Y.A. Meyer, and W.R. Osório, “The holes of Zn phosphate and hot dip galvanizing on electrochemical behaviors of multi-coatings on steel substrates”, *Metals*, vol. 12, no. 863, pp. 1-31, 2022. <https://doi.org/10.3390/met12050863>
- [2] H. Kania, “Corrosion and anticorrosion of alloys/metals: The important global issue”, *Coatings*, vol. 13, no. 216, pp. 1-5, 2023. <https://doi.org/10.3390/coatings13020216>
- [3] D.T. Kalovelonis, D.C. Rodopoulos, T.V. Gortsas, D. Polyzos, and S.V. Tsinopoulos, “Cathodic protection of a container ship using a detailed BEM model”, *Journal of Marine Science and Engineering*, vol. 8, no. 359, pp. 1-14, 2020. <https://doi.org/10.3390/jmse8050359>
- [4] W. Chen, H. Shi, W. Liu, A. Zhao, G. Pan, A. Huang, Y. Yu, and L. Ma, “Study on the preparation and corrosion resistance properties of superhydrophobic coatings on galvanized steel”, *Metals*, vol. 13, no. 260, pp.1 -13, 2023. <https://doi.org/10.3390/met13020260Z>
- [5] M.H. Shahini, H. Eivaz Mohammadloo, and B. Ramezanzadeh, “Recent advances in steel surface treatment via novel/green conversion coatings for anti-corrosion applications: a review study”, *Journal of Coatings Technology and Research*, vol. 19, no. 1, pp. 159-199, 2022.
- [6] M. Alinezhadfar, S.N.K. Abad, and M. Mozammel, “Multifunctional cobalt coating with exceptional amphiphobic properties: self-cleaning and corrosion inhibition”, *Surfaces and Interfaces*, vol. 21, p. 100744, 2020.
- [7] S. Pandiyarajan, S.S.M. Manickaraj, A. Liao, A. Ramachandran, K. Lee, and H. Chuang, “Construction of zinc-cobalt alloy film by supercritical-CO₂ electrodeposition pathway: Evaluation of electrochemical

- robustness”, *Inorganic Chemistry Communications*, vol. 144, 2022. <https://doi.org/10.1016/j.inoche.2022.109858>
- [8] C. Ma, S.C. Wang, and F.C. Walsh, “Electrodeposition of nanocrystalline nickel–cobalt binary alloy coatings: a review”, *Transactions of the IMF*, vol. 93, no. 2 pp. 104-112, 2015.
- [9] H. Dong, Z. Luo, Y. Han, Y.M. Liu, L. Sun, and W.Y. Zhai. “The influence of pickling treatment parameters on the surface state and pre-passivation behavior of super 13Cr martensitic stainless steel”, *Coatings*, vol. 12, no. 127, pp. 1-13, 2022.
- [10] E. Uhlmann, and R. Jaczkowski, “Mechanical pretreatment before electroplating of aluminium alloy AlSi12”, *Surface and Coatings Technology*, vol. 352 pp. 483-488, 2018.
- [11] L.M.D. Andrade, C. Paternoster, P. Chevallier, S. Gambaro, P. Mengucci, and D. Mantovani, “Surface processing for iron-based degradable alloys: A preliminary study on the importance of acid pickling”, *Bioactive Materials*, vol. 11, pp. 166-180, 2022.
- [12] K. Sambasivam, and S. Begum, “Effect of pretreatment on electroplating of Ni-Co substrate contaminated with gold”, *Asian Journal of Applied Sciences*, vol. 10, no. 1, pp. 1-9, 2017.
- [13] N. Sam, S. Palanichamy, S. Chellammal, P. Kalaiselvi, and G. Subramanian, “A green pickling solution for mild steel- An alternative to ASTM Std. pickling solution (Clarke solution)”, *Journal of Materials and Environmental Science*, vol. 6, pp. 1510-1518, 2015.
- [14] A. Arkaiz, A. Francisco, and L. Felix, “Review: Acid pickling of carbon steel”, *Revista de Metalurgia*, vol. 58, no. 3, p. e226, 2022. <https://doi.org/10.3989/revmetalm.226>
- [15] B. Wang, F. Xue, Y. Sun, C. Jia, and W. Tao, “Pretreatment for electroplating of magnesium alloy”, *Journal of Chinese Society for Corrosion and Protection*, vol. 29, no. 1, pp. 24-29, 2009.
- [16] B. Gaur, T.B. Singh, and D.D.N. Singh, “Beneficial role of chloride ions during pickling of steel in sulfuric acid”, *Corrosion*, vol. 52, no. 2, pp. 154-159, 1996.
- [17] H. Fang, B. Brown, and S. Nešić, “Effects of sodium chloride concentration on mild steel corrosion in slightly sour environments”, *Corrosion*, vol. 67, no. 1, p. 015001-1, 2011.
- [18] J. Han, J.W. Carey, and J. Zhang, “Effect of sodium chloride on corrosion of mild steel in CO₂-saturated brines”, *Journal of Applied Electrochemistry*, vol. 41, no. 6, pp. 741-749, 2011.
- [19] S.G. Croll, “Surface roughness profile and its effect on coating adhesion and corrosion protection: A review”, *Progress in Organic Coatings*, vol. 148, p. 105847, 2020.
- [20] ASTM E384 – 11e1, “Standard Test Method for Knoop and Vickers Hardness of Materials”, *ASTM International*, vol. 03, no. 01, West Conshohocken, USA, 2011.

- [21] K.M. Hyie, Z. Salleh, M.C. Murad, N.R.N.M. Masdek, and N.A. Resali, “Corrosion behavior of heat treated nanocrystalline Co-Ni-Fe coating on stainless steel”, *Journal of Mechanical Engineering*, vol. SI 5, no. 2, pp. 191-203, 2018.
- [22] Z. Panossian, N.L. de Almeida, R.M.F. de Sousa, G. de Souza Pimenta, and L.B.S. Marques, “Corrosion of carbon steel pipes and tanks by concentrated sulfuric acid: a review”, *Corrosion Science*, vol. 58, pp. 1-11, 2012.
- [23] J. Peng, and M. Li, “Pickling behaviour of 2205 duplex stainless steel hot-rolled strips in sulfuric acid electrolytes”, *Advances in Materials Science and Engineering*, vol. 2020, pp. 1-10, 2020. <https://doi.org/10.1155/2020/4562418>
- [24] Z. You, Y. Lai, H. Zeng, and Y. Yang, “Influence of water and sodium chloride content on corrosion behavior of cast iron in silty clay”, *Construction and Building Materials*, vol. 238, p. 117762, 2020.
- [25] F. Xue, X. Wei, J. Dong, C.g Wang, and W. Ke, “Effect of chloride ion on corrosion behavior of low carbon steel in 0.1 M NaHCO₃ solution with different dissolved oxygen concentrations”, *Journal of Materials Science & Technology*, vol. 35, no. 4, pp. 596-603, 2019.
- [26] L.V. Giuliano, A. Buffo, M. Vanni, and G. Frungieri, “Micromechanics and strength of agglomerates produced by spray drying”, *Journal of Colloid and Interface Science Open*, vol. 9, no. 100068, pp. 1 - 12, 2023.
- [27] D.O. Dede, O. Şahin, A. Koroglu, and B. Yilmaz, “Effect of sealant agents on the color stability and surface roughness of nanohybrid composite resins”, *The Journal of Prosthetic Dentistry*, vol. 116, no. 1, pp. 119-128, 2016.

The Characterization of the Sandwich Composite Consisted of Coconut Fibre-Polyester Resin and its Variations of Wood Core

Sumarji*

Department of Mechanical Engineering, University of Jember,
Kampus Tegalboto, Jember 68121, East Java, INDONESIA
*sumarji.teknik@unej.ac.id

Wazirotus Sakinah, R. Puranggo Ganjar Widityo

Department of Naval Architecture, University of Jember, Kampus Tegalboto,
Jember 68121, East Java, INDONESIA

Mochamad Asrofi

Advanced Materials Research Group,
Center for Development of Advanced Science and Technology (CDAST),
Kampus Tegalboto, University of Jember, Jember 68121, INDONESIA

ABSTRACT

The traditional fishing vessels in Indonesia are usually made of wood material. The weakness of this vessel material is that it is easily weathered when exposed to seawater. For this reason, it is necessary to have vessel material engineering from composite sandwiches. This study aimed to prepare and investigate the flexural test, impact test, optical microscopy (OM), and scanning electron microscopy (SEM) observations of sandwich composites based on coconut fibre-polyester resin and wood core. The fabrication uses a hand lay-up method with a constant volume fraction (20% coconut coir fibre) and wood core variations type. The primary wood variations used are albizia chinensis, mahogany, shorea, and camphor. The Surface modification of fibre and wood core was conditioned without treatment and with treatment with about 5% NaOH solution for 2 hours. The study showed that the highest bending and impact strength was sandwich composite with camphor wood cores with alkali treatment for 39.75 MPa and 37.22 J/cm², respectively. The OM observations showed that the core and skin interface area failed to delaminate after flexural and impact tests. SEM observations also showed that

the bond alkalization treatment between the matrix and the fibres was quite good. In the composite skin fracture area, there is a lot of fibre brake, and a little thread pulls out. The skin matrix also shows the presence of voids. Generally, this sandwich composite is feasible for application as a material for traditional fishing vessels.

Keywords: *Sandwich Composites; Flexural Tests; Impact Tests; Coconut Fibre; Wood Core*

Introduction

Traditional fishing vessels in Indonesia are usually made of wood. This wooden vessel material is easily weathered when exposed to seawater. For this reason, it is necessary to engineer the material for waterproof fishing vessels and ensure the performance is engaging. Sandwich composites are one of the most potential ship material engineering to be developed. Sandwich composites consist of two thin skins, strong and stiff shells with a thick and light core material stacked sequentially as skin-core-shell [1]. Two layers of face sheet skin to withstand tension and compression stress, and the core material mainly bears shear emphasis [2]. Sandwich materials are often used in engineering applications because of the advantages of high bending rigidity, low structural weight and good environmental resistance [3]-[4].

Most industries try to use natural fibres as reinforcement for the manufacture of composites. The choice of natural fibres as a composite reinforcement material is because natural fibres are strong, competitive and environmentally friendly compared to synthetic fibres [5]. Types of natural fibres can be classified into several plant categories: kenaf, jute, bamboo, banana and bagasse. Fibre materials from seeds such as kapok, cotton, and coconut fibre. Fibre materials from leaves such as abaca, pineapple, and sisal. The fibre also can be obtained from grass/reeds such as wheat, rice, and corn. These natural fibre materials have been widely studied as composite reinforcement materials [6]-[7]. Natural fibre has three essential parts such as cellulose, hemicellulose and lignin. Of the three parts, cellulose is a component that affects the properties of the composite [8].

The main problem in developing natural fibre-reinforced composites is the hydrophilicity of the fibres. Hydrophilicity causes the adhesion ability to decrease and ultimately affects the mechanical properties of the composite [9]-[10]. The alkalization treatment is the most effective because it can remove wax content and impurities from the fibre surface, resulting in a rough and hydrophobic surface [11]-[12]. Alkali treatment will increase the cellulose content and remove fibre constituent components that are less effective in determining interfacial strength, namely hemicellulose, lignin or pectin [13]. Reduction of the constituents will increase the surface roughness resulting in

better mechanical interlocking. The influence of alkalis can increase tensile and flexural strength due to better interfacial bonds between the fibre and the matrix [14]-[15]. Chemical treatment increases the adhesion ability of natural fibres with the polymer matrix and improves the mechanical properties of the composites [16].

Several synthetic polymer matrices have been studied in composites such as polyester resins [17]-[20], melamine-urea-formaldehyde [21], polypropylene [22], polyethylene [23] and other synthetic polymers. Synthetic polymers are excellent composite-forming materials because they bind the reinforcement well. Synthetic polymers are potential matrix material candidates as fishing vessel composite materials because they have excellent water resistance [24]. However, combining composite sandwiches with a polyester resin matrix reinforced with natural fibres has not been explored more deeply, especially in the determination of wood species. This research is a breakthrough because of its advantages, such as good mechanical properties, lower production costs and environmental friendliness.

In this study, researchers studied the characteristics of flexural strength, impact strength, and fracture morphology of sandwich composites composed of wood core and coco fibre -polyester resin as the face skins. The mechanical properties data obtained will later be used as initial information on fishing vessel materials. This research is instrumental in designing traditional fishing vessels in Indonesia.

Materials and Methods

Materials

The polyester resin used in this study was unsaturated polyester resin with the trademark Yukalac 157 BQTN-EX produced by PT. Justus Sakti Raya, Indonesia (specific gravity 1.21 g/cm³; flexural strength 9.4 kg/mm²; flexural modulus 300 kg/mm²; young modulus 1.18 GPa; water absorption at 25 °C 0.188-0.466%). The coconut fibre (density 1.1-1.5 g/cm³), shorea wood, albizia chinensis wood, mahogany wood and camphor wood were obtained from CV Tiga Sehati, Jember, Indonesia (Google Maps Coordinate: - 8.167767164206186, 113.70906795282784). The specifications for each type of fibre are shown in Table 1. Sodium hydroxide (NaOH 99%) and MEKPO catalyst (purity 45%; molar mass 210.23; density 1.17 g/cm³) (technical grade) were purchased from UD Aneka Kimia, Jember, Indonesia.

Preparation of wood core and coir fibre

The wood as the core of the sandwich composite was shaved and smoothed with a thickness of 1 cm respectively. The wood and coconut coir fibre were washed and cleaned with water, then dried under the sun for 5-7 days. The alkalization process was done by soaking coconut coir fibre and wood in 5%

NaOH solution for 2 hours at room temperature. After that, the coconut coir fibre and wood were washed with distilled water until neutral pH. Then, it was dried under the sun for 3-5 days and continued in a drying oven for 24 hours at 60 °C.

Table 1: Chemical composition of several kinds of wood

No	Type of Woods	Chemical Compositions (%)			
		Cellulose	Hemicellulose	Lignin	Others
1	Shorea wood	44	28	23	4.5
2	Albizia chinensis	42	23	18	16
3	Mahogany wood	38	27	29	5
4	Camphor wood	52	19	26	3

Manufacturing of sandwich composite

The manufacturing of composite sandwiches was the hand lay-up method. The sandwich composite manufacturing process places a 10 mm thick core wood board into the mould, then coats it with a top composite skin with a thickness of 4 mm. Coconut fibre was arranged in a longitudinal direction with a volume fraction of 20%. The resin matrix was mixed with the hardener (1%), stirred until evenly distributed, and poured into coconut fibre with a volume fraction of 80%. After that, rolling was done on the skin's surface, followed by pressing. This process was carried out at room temperature. After drying, the specimens were disassembled from the mould and made the bottom skin. The making of bottom skin by reversing the bottom position, and it was placed on top and then put into the mould. The following process was the same as making the upper skin.

Flexural test

The flexural test used the Universal Testing Machine Hung Ta 2328 TM 113 (30 kN). The test was carried out according to ASTM C 393 standards. The test was carried out at room temperature for all specimens. In each variation, the test was carried out five repetitions. Then, the five data were averaged.

Impact test

The impact test was carried out using a Charpy 300 J impact testing machine. The test was carried out according to ASTM D5942 standards. The test was carried out at room temperature for all specimens and repeated five times for each variation.

Optical microscope observations

The microstructure observation of sandwich composites using an optical microscope model Olympus BX 41M. The observation was made with a

magnification of 100x and 500x. The fracture surface was cut to 20 x 18 mm and then observed.

Scanning Electron Microscope (SEM) observations

The fracture surface observation of sandwich composite using a Scanning Electron Microscopy (SEM) model of the Phillips XL 30 with a voltage of 10 kV. The observations were made under vacuum with a secondary electron signal for the imaging process with a magnification of 100x. The fracture surface was cut into 5 x 10 mm and observed.

Results and Discussions

Mechanical properties

Regarding mechanical properties, composite sandwich materials are influenced by core and skin materials (matrix and reinforcement). In addition, it is also influenced by the bond between the core and the skin composite and the matrix bond with the reinforcement in the skin. Figure 1 shows the flexural properties of sandwich composites with variations of core wood, without alkalization treatment and alkalization treatment 5% NaOH on core wood and coco fibre.

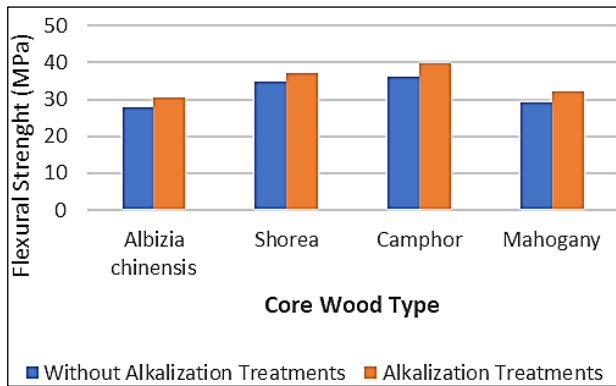


Figure 1: Flexural strength properties of all samples tested

From the flexural test data shown in Figure 1. the highest flexural strength value was obtained for the sandwich composite on camphor core wood with alkalization treatment with a value of 39.75 MPa. The lowest flexural strength was obtained from sandwich composites on albizia chinensis core wood, without alkalization treatment for 27.75 MPa. The properties of camphor wood are strong and ductile, while albizia chinensis wood is less

strong and brittle. This phenomenon shows that the core wood significantly impacts the flexural strength of sandwich composites. In the presence of 5% NaOH alkalization treatment for 2 hours on core wood and coco fibre reinforcement, the sandwich composite experienced a significant increase in flexural strength. The average increase in flexural strength was between 6.9% to 10.5%. This result proves that the alkalization treatment makes the interfacial bond between coco fibre and core wood with resin stronger [14]-[16], [24].

Impact strength properties

Figure 2 shows the impact strength properties of sandwich composites with variations of core wood, without alkali treatment and 5% NaOH alkalization treatment on core wood and coconut fibre. From the impact test data shown in Figure 2, the highest impact strength value was obtained for the sandwich composite on camphor core wood with alkalization treatment for 37.22 J/cm². The lowest impact strength was obtained from sandwich composites on albizia chinensis core wood without alkalization treatment for 27.47 J/cm².

The results of this study show that camphor wood is strong and ductile compared to albizia chinensis wood, which is more brittle. The mechanical properties of the core wood have a very significant impact on the impact strength of the sandwich composite. In the presence of 5% NaOH alkalization treatment for 2 hours on core wood and coco fibre reinforcement, the sandwich composite experienced increased impact strength.

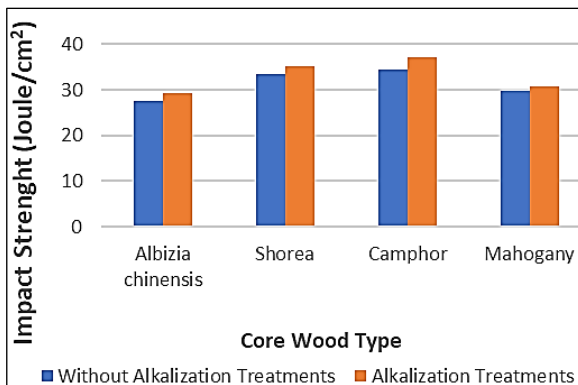


Figure 2: Impact strength properties of all samples tested

On average, there was an increase in impact strength between 3.7% to 8.4%. Fibre can distribute the stress generated evenly. The orientation of the fibre direction in this study is the longitudinal direction perpendicular to the

direction of the pendulum beating so that it can withstand the shear stress when the impact test pendulum is impacted [25].

Microstructure of sandwich composite

Figure 3 shows microscopy observations on the surface of coco fibre with and without alkalization treatment. Figure 3(a) shows the surface of the coco fibre clean from the dirt after alkalization (5% NaOH).

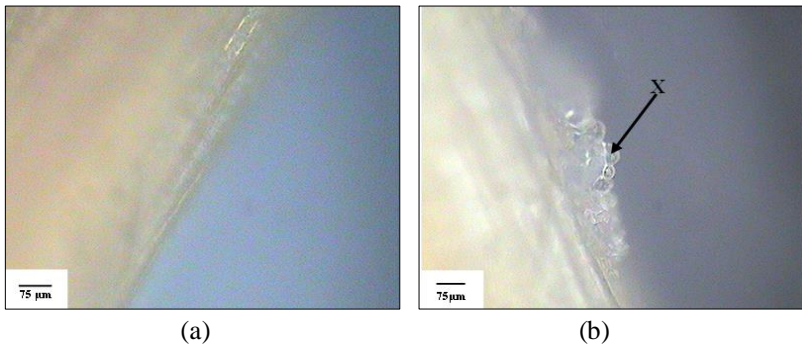


Figure 3: Micro photo of coco fibre; (a) with alkalization treatment (5% NaOH), and (b) without alkalization treatment

A clean surface and good drying will make the fibre ductile and not brittle, facilitating bonding between the fibre and the matrix [14]-[16]. Figure 3(b) shows the surface of coco fibre without alkalization treatment. The figure shows that the coco fibre's surface has a lot of dirt, which inhibits the bond between the fibre and the matrix. The increase in flexural and impact strength of sandwich composites with alkalization treatment is due to the loss of impurities attached to the fibres, which become coarse [11]-[12].

Figure 4 shows the results of microscopy observations of the sandwich composite at the core wood interface with the skin. Figure 4(a) shows the interface between the core wood and the skin, which are well bonded before the mechanical test is carried out. Figure 4(b) shows the interface between the core and skin after flexural testing, and Figure 4(c) after impact testing. From the figure, it can be seen that delamination has occurred in the skin and core interface. Bending or impact loads cause buckling in sandwich composites [1], [26].

The lower skin experiences a compressive force, while the lower skin experiences a tensile strength. The skin interface with the core cannot withstand the load perfectly due to the shifting movement of the core, resulting in delamination [27]. This case indicates that the skin and core bonds that occur are not strong enough to withstand bending or impact loads.

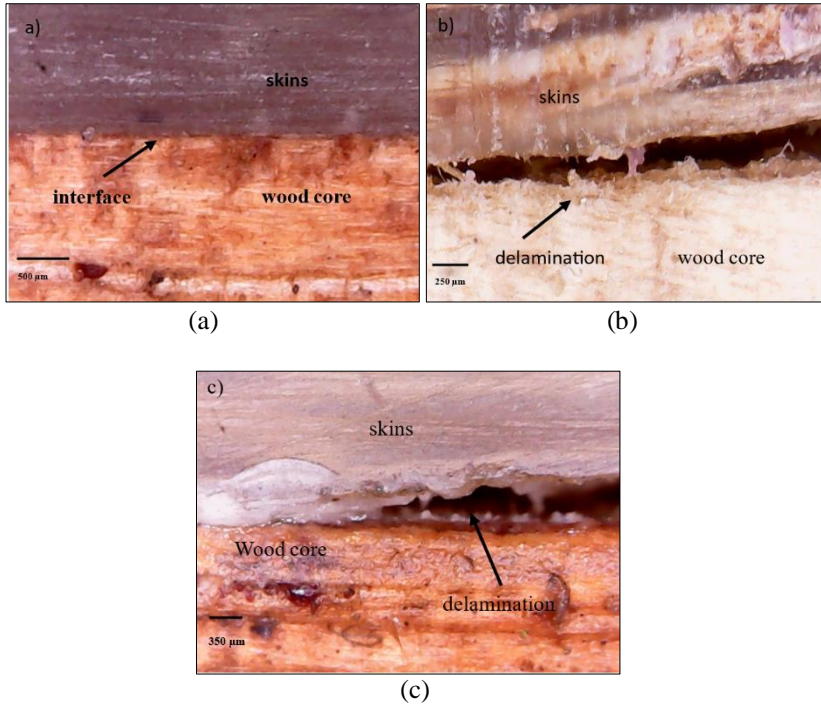


Figure 4: Micro photo of the interface of the core wood and skin of sandwich composite; (a) before the mechanical test, (b) after the flexural test, and (c) after the impact test

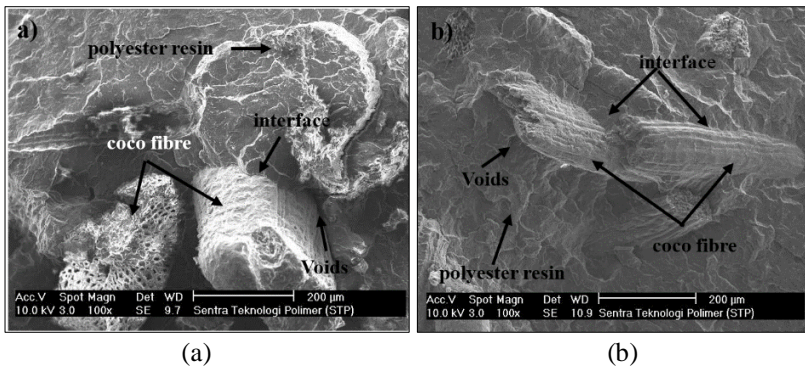


Figure 5: Fracture morphology of composite sandwich skin; (a) after flexural test, and (b) after impact test

Figure 5 shows the results of SEM observations on the fracture surface of the sandwich composite skin after mechanical testing. Figures (5a) and (5b) show the fracture morphology of the sandwich composite skin after flexural and impact tests. It can be seen that the morphology of coco fibre is rather rough and most of the matrix can bind the fibre perfectly. This phenomenon proves that the matrix effectively transfers stress to the fibre due to the excellent bond between the polyester resin matrix and the fibre. Previous researchers also reported that the alkalization treatment of the fibre produced a rough surface and good bonding interactions at the interface [12], [14]-[15].

In the sandwich composite skin fracture, there are many occurrences of brake fibres. This fibre brake can increase the flexural and impact strength of the sandwich composite due to the slight shifts between the matrix and the fibres [16]. Due to bending or impact loads, cracks will move from the polyester resin matrix through the interface to the coco fibre. If the bond at the interface is strong, then the stress that occurs is directly transmitted to the coconut fibre. This phenomenon causes fibre break [28].

In the area of the sandwich composite, skin fracture also shows a slight occurrence of pull-out fibres. The process of the fibres pulling out can reduce the flexural and impact strength of the sandwich composite due to the emergence of shear stress between the matrix and the fibres. Fibres pull-out occurs because the debonding stress of the fibre-matrix is less than the breaking stress of the fibre, so the debonding process occurs first, followed by a break in the fibre resulting in fibres pull-out [28]-[29].

Several points on the surface of the matrix indicate the presence of voids. This phenomenon is due to the poor mixing of polyester resin with coco fibre in the fabrication process. These voids occur because of air trapped in the matrix and interface. The effect of nasty gaps is the poor bonding interaction between the matrix and the fibres and also reduces the strength of the matrix [13].

Conclusion

The sandwich composite with wood core and skin from polyester resin – coconut fibre is successfully produced by hand lay-up method at room temperature. The 5% NaOH alkalization treatment increased the flexural strength and impact strength. The type of core wood in the sandwich composite significantly affects the flexural strength and impact strength. The highest flexural and impact strength was found in the sandwich composite with a camphor wood core of 39.75 MPa and 37.22 J/cm². Fracture morphology at the interface between the core and the skins indicates delamination. The morphology of the fracture on the skin shows a rough surface on the fibre, lots of fibre breaks and little fibre pull out. This result shows a good bond between

matrix and fibre. This sandwich composite may be suitable for application as a material for traditional fishing vessels.

Contributions of Authors

The authors confirm the equal contribution in each part of this work. All authors reviewed and approved the final version of this work.

Funding

This work was supported by the University of Jember with the scheme “Keris Dimas Research”

Conflict of Interests

All authors declare that they have no conflicts of interest

Acknowledgment

All authors would like to thank staff members of the Department of Mechanical Engineering and Naval Engineering, Faculty of Engineering, University of Jember for their wholehearted support and assistance during the conduction of the experiment.

References

- [1] S. Waddar, J. Pitchaimani, M. Doddamani and E. Barbero, “Buckling and vibration behaviour of syntactic foam core sandwich beam with natural fiber composite facings under axial compressive loads”, *Composites Part B: Engineering*, vol. 175, pp. 1-11, 2019. <https://doi.org/10.1016/j.compositesb.2019.107133>
- [2] J. Galos, R. Das, M. P. Sutcliffe and A. P. Mouritz, “Review of balsa core sandwich composite structures”, *Materials & Design*, vol. 221, pp. 1-24, 2022. <https://doi.org/10.1016/j.matdes.2022.111013>
- [3] H. Xie, H. Fang, W. Cai, L. Wan, R. Huo and D. Hui, “Development of an innovative composite sandwich matting with GFRP facesheets and wood core”, *Reviews on Advanced Materials Science*, vol. 60, no. 1, pp. 80-91, 2021. <https://doi.org/10.1515/rams-2021-0016>

- [4] H. Xie, L. Wan, B. Wang, H. Pei, W. Liu, K. Yue and L. Wang, “An investigation on mechanical behavior of tooth-plate-glass-fiber hybrid sandwich beams”, *Advances in Polymer Technology*, vol. 2020, pp. 1-11, 2020. <https://doi.org/10.1155/2020/6346471>
- [5] M. Arul, K. S. K. Sasikumar, M. Sambathkumar, R. Gukendran and N. Saravanan, “Mechanical and fracture study of hybrid natural fiber reinforced composite–Coir and sugarcane leaf sheath”, *Materials Today: Proceedings*, vol. 33, pp. 2795-2797, 2020. <https://doi.org/10.1016/j.matpr.2020.02.677>
- [6] A. Karimah, M. R. Ridho, S. S. Munawar, D. S. Adi, R. Damayanti, B. Subiyanto, W. Fatriasari and A. Fudholi, “A review on natural fibers for development of eco-friendly bio-composite: Characteristics, and utilizations”, *Journal of Materials Research and Technology*, vol. 13, pp. 2442-2458, 2021. <https://doi.org/10.1016/j.jmrt.2021.06.014>
- [7] S. R. Benin, S. Kannan, R. J. Bright and A. J. Moses, “A review on mechanical characterization of polymer matrix composites & its effects reinforced with various natural fibres”, *Materials Today: Proceedings*, vol. 33, pp. 798-805, 2020. <https://doi.org/10.1016/j.matpr.2020.06.259>
- [8] M. Asrofi, J. P. Saragih, S. Mulyadi, Sumarji, R. Sidartawan, S. Junus, Sujito, N. A. Shidiq, S. M. Sapuan and R. A. Ilyas, “Tensile strength and thermal resistance analysis of Polylactic Acid (PLA) and cassava starch with cellulose paper sugarcane bagasse as filler”, *Gongcheng Kexue Yu Jishu/Advanced Engineering Science*, vol. 54, no. 1, pp. 971-978, 2022.
- [9] R. Siakeng, M. Jawaid, H. Ariffin and S. M. Sapuan, “Effects of surface treatments on tensile, thermal and fibre-matrix bond strength of coir and pineapple leaf fibres with poly lactic acid”, *Journal of Bionic Engineering*, vol. 15, pp. 1035-1046, 2018. <https://doi.org/10.1007/s42235-018-0091-z>
- [10] B. S. Yew, M. Muhamad, S. B. Mohamed and F. H. Wee, “Effect of alkaline treatment on structural characterisation, thermal degradation and water absorption ability of coir fibre polymer composites”, *Sains Malaysiana*, vol. 48, no. 3, pp. 653-659, 2019. <http://dx.doi.org/10.17576/jsm-2019-4803-19>
- [11] D. Verma and K. L. Goh, “Effect of mercerization/alkali surface treatment of natural fibres and their utilization in polymer composites: Mechanical and morphological studies”, *Journal of Composites Science*, vol. 5, no. 7, p. 175, 2021. <https://doi.org/10.3390/jcs5070175>
- [12] E. Yuanita, Y. A. Husni, M. A. Mochtar, R. Lailani and M. Chalid, “The effect of alkalization treatment on fiber-matrix compatibility in natural fiber reinforced composite”, *Key Engineering Materials*, vol. 847, pp. 28-33, 2020. <https://doi.org/10.4028/www.scientific.net/KEM.847.28>
- [13] M. Asrofi, S. M. Sapuan, R. A. Ilyas and M. Ramesh, “Characteristic of composite bioplastics from tapioca starch and sugarcane bagasse fiber: Effect of time duration of ultrasonication (Bath-Type)”, *Materials*

- Today: Proceedings*, vol. 46, part 4, pp. 1626-1630, 2021. <https://doi.org/10.1016/j.matpr.2020.07.254>
- [14] L. Musyarofah, S. Sujito, E. Hidayah and E. Supriyanto, "Effect of alkalization on mechanical properties of green composites reinforced with cellulose from coir fiber", *AIP Conference Proceedings*, vol. 2242, no. 1, p. 020016, 2020. <https://doi.org/10.1063/5.0008510>
- [15] M. Boumaaza, A. Belaadi and M. Bourchak, "The effect of alkaline treatment on mechanical performance of natural fibers-reinforced plaster: Optimization using RSM", *Journal of Natural Fibers*, vol. 18, no. 12, pp. 2220-2240, 2021. <https://doi.org/10.1080/15440478.2020.1724236>
- [16] T. J. Chung, J. W. Park, H. J. Lee, H. J. Kwon, H. J. Kim, Y. K. Lee and W. Tai Yin Tze, "The improvement of mechanical properties, thermal stability, and water absorption resistance of an eco-friendly PLA/kenaf biocomposite using acetylation", *Applied Sciences*, vol. 8, no. 3, p. 376, 2018. <https://doi.org/10.3390/app8030376>
- [17] S. Sumarji, F. Ridha, D. Dwilaksana, A. Syuhri and R. Raihaan, "The effect of particle dispersion due to mixing speed on spent coffee ground composites", *Indonesian Journal of Science and Technology*, vol. 4 no. 2, pp. 188-195, 2019. <https://doi.org/10.17509/ijost.v4i2.18175>
- [18] Sumarji, I. Sholahuddin, D. Dwilaksana, A. Syuhri and A. Yanuar, "Effect of steam pre-treatment of bagasse as fiber reinforcement SCG composite", *IOP Conference Series: Materials Science and Engineering*, vol. 494, p. 012042, 2019. <https://doi.org/10.1088/1757-899X/494/1/012042>
- [19] K. Senthilkumar, N. Saba, M. Chandrasekar, M. Jawaid, N. Rajini, O. Y. Alothman and S. Siengchin, "Evaluation of mechanical and free vibration properties of the pineapple leaf fibre reinforced polyester composites", *Construction and Building Materials*, vol. 195, pp. 423-431, 2019. <https://doi.org/10.1016/j.conbuildmat.2018.11.081>
- [20] S. C. Das, D. Paul, S. A. Grammatikos, M. A. Siddiquee, S. Papatzani, P. Koralli, M. M. Jahid, M. A. Khan, S. M. Shauddin, R. A. Khan, N. Vidakis and M. Petousis, "Effect of stacking sequence on the performance of hybrid natural/synthetic fiber reinforced polymer composite laminates", *Composite Structures*, vol. 276, p. 114525, 2021. <https://doi.org/10.1016/j.compstruct.2021.114525>
- [21] K. M. Hasan, P. G. Horváth, Z. Kóczán and T. Alpár, "Thermo-mechanical properties of pretreated coir fiber and fibrous chips reinforced multilayered composites", *Scientific Reports*, vol. 11, no. 1, pp. 1-13, 2021. <https://doi.org/10.1038/s41598-021-83140-0>
- [22] A. Nugraha and A. L. Juwono, "Flexural property and water content of unidirectional polypropylene/subang pineapple leaf fiber composites", *IOP Conference Series: Materials Science and Engineering*, vol. 599, no. 1, p. 012016, 2019. <https://doi.org/10.1088/1757-899X/599/1/012016>

- [23] S. Sumarji, M. G. D. Aqsho, H. A. Basuki and M. Asrofi, "Tensile properties and fracture morphology of polyethylene ter-ephthalate mixed rice starch particle based blend composites", *Material Science Research India*, vol. 17, no. 1, pp. 47-53, 2020. <http://dx.doi.org/10.13005/msri/170107>
- [24] S. Saifuddin, M. Marzuki and D. Arifin, "Kekuatan lentur komposit sandwich kayu bakal lambung perahu sebagai core dan polyester serat gelas sebagai skin", *Jurnal Polimesin*, vol. 18, no. 1, pp. 16-22, 2020. <https://dx.doi.org/10.30811/jpl.v18i1.1579>
- [25] M.Z. Hassan, S. M. Sapuan, Z. Rasid, A. F. M. Nor, R. Dolah and M. Y. Daud, "Impact damage resistance and post-impact tolerance of optimum banana-pseudo-stem-fiber-reinforced epoxy sandwich structures", *Applied Sciences*, vol. 10, no. 2, p. 684, 2020. <https://doi.org/10.3390/app10020684>
- [26] M. J. Suriani, H. Z. Rapi, R. A. Ilyas, M. Petrù and S. M. Sapuan, "Delamination and manufacturing defects in natural fiber-reinforced hybrid composite: A review", *Polymers*, vol. 13, no. 8, p. 1323, 2021. <https://doi.org/10.3390/polym13081323>
- [27] A. S. Chermoshentseva, A. M. Pokrovskiy and L. A. Bokhoeva, "The behavior of delaminations in composite materials-experimental results", *IOP Conference Series: Materials Science and Engineering*, vol. 116, no. 1, p. 012005, 2016. <https://doi.org/10.1088/1757-899X/116/1/012005>
- [28] S. Huang, Q. Fu, L. Yan and B. Kasal, "Characterization of interfacial properties between fibre and polymer matrix in composite materials—A critical review", *Journal of Materials Research and Technology*, vol. 13, pp. 1441-1484, 2021. <https://doi.org/10.1016/j.jmrt.2021.05.076>
- [29] G. Ruano, F. Bellomo, G. Lopez, A. Bertuzzi, L. Nallim and S. Oller, "Mechanical behaviour of cementitious composites reinforced with bagasse and hemp fibers", *Construction and Building Materials*, vol. 240, pp. 1-9, 2020. <https://doi.org/10.1016/j.conbuildmat.2019.117856>

Synthesisation of Zinc Oxide Nanowires via Hybrid Microwave-Assisted Sonochemical Technique at Various Microwave Power

Maryam Mohammad

Department of Physics, Faculty of Applied Sciences,
Universiti Teknologi MARA (UiTM) Perak Branch, Tapah Campus,
Tapah Road, 35400 Perak, MALAYSIA

Mohd Firdaus Malek*, Muhammad Faizal Abd Halim,
Nurul Zulaikha Mohammad Zamri, Mohamad Dzulfiqar Bakri,
Zuraida Khusaimi

NANO-SciTech Lab (NST), Centre for Functional Materials and
Nanotechnology (FMN), Institute of Science (IOS),
Faculty of Applied Sciences, Universiti Teknologi MARA (UiTM),
40450 Shah Alam, Selangor, MALAYSIA

*mfmalek07@uitm.edu.my; mfmalek07@gmail.com

Mohamad Hafiz Mamat, Mohamad Rusop Mahmood
NANO-ElecTronic Centre (NET), School of Electrical Engineering,
College of Engineering, Universiti Teknologi MARA (UiTM),
Shah Alam 40450, Selangor, MALAYSIA

Tetsuo Soga

Department Of Electrical and Mechanical Engineering,
Nagoya Institute of Technology, Showa-Ku, Gokiso-Cho, Nagoya, 466-8555,
JAPAN

ABSTRACT

Zinc oxide nanowires (ZnO NWs) have been successfully synthesized via a hybrid microwave-assisted sonochemical technique (HMAST) using zinc acetate dehydrate as starting material. The optimized parameters were set at 12.5 mM solution concentration and a rapid deposition time of 60 minutes. The microwave power was varied from 100 to 800 Watts and the effect of microwave power on the morphological, structural, and optical properties of

the ZnO NWs has also been studied. Results showed an aligned, uniformly distributed hexagonal wurtzite structure of ZnO NWs was produced, which were augmented at 600 W microwave power, having the smallest diameter size of 29.66 nm. The XRD graph showed that the ZnO NWs produced are highly crystalline, exhibiting the sharpest and narrowest intensity of (002) peaks and a crystallite size of 18.60 nm. The transmittance spectra obtained by UV-Vis would be 89.72%, having a sharp absorption edge, implying the lower particle size of ZnO as well as exhibiting high absorbance in the ultraviolet region, indicating good crystallinity. From the findings, it can be confirmed that the microwave-assisted method helped in improving the formation of higher quality ZnO NWs that can be befittingly applied in many devices such as photocatalysts and sensors due to their excellent electrochemical properties.

Keywords: Zinc Oxide; Nanowires; Nanostructures; Microwave-Assisted; Sonochemical

Introduction

One of the many one-dimensional nanostructures and oxide-based multifunctional materials that are now being researched and studied is zinc oxide (ZnO), whose exceptional features can improve the performance of electrical devices as well as many other things [1]. Zinc oxide is categorized as a semiconductor in group II-VI, whose covalence is on the ionic-covalent bond semiconductor. It has a wide energy band (3.37 eV), high bond energy (60 meV), and good thermal and mechanical stability at ambient temperature, which makes it appealing for prospective usage in electronics, optoelectronics, and laser technologies [2]-[3]. Its distinct chemical properties are complemented by its straightforward crystal-growth process, which offers much cheaper production costs than those of other semiconductors utilized in nanotechnology. In addition, ZnO nanomaterials (ZnO NMs) have a diverse range of nanostructures with complex morphologies and applications [4]-[10], namely nanowires [11]-[12], nanorods [13], nanotubes [14], and nanobelts [15]. Numerous growth techniques have been reported for the synthesis of ZnO nanostructures (ZnO NSs) specifically ZnO NWs including chemical and physical techniques like thermal evaporation [16]-[18], Chemical Vapor Deposition (CVD) and cyclic feeding CVD [19]-[20], sol-gel deposition [21], [22], electrochemical deposition [12], [23]-[24], hydrothermal and solvothermal growth [25]-[30] as well as surfactant and capping agents-assisted growth [31]-[32]. It is also known that these nanostructures can be grown rather easily at low temperatures.

Though these prevalent growth methods for ZnO NWs currently practiced are mostly successful, they do, however, have a few drawbacks, such as low productivity or severe impurities from their employed assistant, also

known as a catalyst or precursor, which can cause complications for their actual nanodevice application. [33]. Another limitation would be that its usage requires severe conditions such as high temperature, high pressure, expensive materials, and complex procedures. Alternatively, microwave-assisted methods had been suggested to help overcome these challenges. The region of the electromagnetic spectrum that comprises microwaves has a wavelength (λ) between 1 mm and 1 m, which is equivalent to a frequency range between 300 MHz ($\lambda=1$ m) and 300 GHz ($\lambda=1$ mm) [34]-[35]. Its numerous benefits, including scalability, low energy consumption, quick growth, low cost, and simplicity of handling make it a highly acclaimed method to solve these concerns [36]-[39]. Moreover, in comparison to ZnO NSs synthesized using a more traditional method, the microwave-assisted process provides more control over the shape and dimensional dispersion of ZnO NSs [40]. This ensures a higher level of consistency for experimental results. In addition, microwave irradiation plays a crucial role in chemical reactions occurring in aqueous media [41], reducing the time [42] and cost, lowering particle size with a narrow size distribution, raising the product yield rate, and producing high-purity products in comparison to traditional techniques [43]-[46].

In addition, the traditional method of producing ZnO by solution-based approach mainly does not emphasize the solution preparation process but rather concentrated more on the effects of stabilizer instead of the reactant dispersion causing a non-homogeneous reaction during the mixing process of precursor and solvent which will contribute to the formation of a large particles size and reduce the surface area of the nanostructures. Through defects states such as grain boundaries, this behavior will lead to limited electron transport and a high recombination rate [47]. Hence, our research intends to optimize the aforementioned method by introducing the Hybrid Microwave-Assisted Sonochemical Technique (HMAST) while also investigating the impacts of microwave power on the overall properties ZnO NWs produced. This method incorporates a very effective and often employed solution-based method whereby the sonification process was incorporated during the mixing process, to significantly improve the interaction between the precursor and stabilizing agent and thus provide better overall control of the features of the nanostructure and further assisted by microwave irradiation to expedite the production process.

Methodology

The research approach is divided into three parts, which are outlined below. The initial step would be to prepare and clean the glass substrates. The zinc oxide nanoparticles (ZnO NPs) thin film is then prepared using an ultrasonic-assisted sol-gel spin coating process, yielding ZnO NPs array. It will next go through a microwave heating deposition process to produce ZnO NWs.

Preparation of ZnO nanoparticles seeded layer thin films

Zinc Oxide-Based Nanoparticles were prepared as a seed layer of thin films on a glass substrate which was deposited by an optimized ultrasonic-assisted sol-gel (sonochemical) spin-coating technique [48]-[49]. The sonicated sol-gel ZnO was prepared by dissolving 0.4 M zinc acetate dehydrates [(Zn(CH₃COO)₂·2H₂O; Merck] which acts as the precursor in the solvent of 2-methoxy ethanol [C₃H₈O₂; Merck] at room temperature. Then, at 1% of aluminum nitrate nonahydrate [Al(NO₃)₃·9H₂O; Analar] and 0.4 monoethanolamines [MEA, C₂H₇NO; R&M] were added into the solution as dopant and stabilizer, respectively. The molar ratio of MEA to zinc acetate dehydrate was maintained at 1:1, and the resultant solution was stirred at 80 °C for 40 minutes to yield a clear and homogeneous solution. Afterward, the solution was sonicated at 50 °C for 30 minutes using an ultrasonic water bath (Hwasin Technology Powersonic 405, 40 kHz) and cooled to room temperature. The solution will then be used to coat the glass substrate using the spin coating technique where 10 drops of the solution were deposited onto the substrate at a speed of 3000 rpm for 30 seconds. Lastly, the samples were preheated in an atmosphere ambient at 300 °C for 10 minutes to remove solvent and the deposition processes were repeated for the second to the fifth layer of film to achieve the required film thickness. All samples were annealed in a furnace at a temperature of 500 °C for 1 hour.

Deposition of ZnO nanowires via hybrid microwave-assisted sonochemical technique

ZnO NWs were grown via the HMAST method. An optimized 12.5 mM concentration of the solution was prepared using Zinc acetate dehydrate [(Zn(CH₃COO)₂·2H₂O; Merck] and 0.01 M hexamethylenetetramine [HMTA, C₆H₁₂N₄; Merck] as a precursor and stabilizer, respectively [50]. The reagents were dissolved and reacted in a beaker filled with 1000 mL distilled water as a solvent and stirred at 80 °C for 30 minutes to yield a clear and homogeneous solution. Next, the solution was sonicated at 50 °C for 30 minutes using an ultrasonic water bath (Hwasin Technology Powersonic 405, 40 kHz). The solution was then aged at room temperature for 1 hour and poured into a Schott bottle of 250 ml volume capacities where the optimized seed layer-coated glass substrates were placed at the bottom of the container. Afterward, the container was placed inside the 2.45 GHz microwave (SHARP 25L Microwave Oven R352ZS) which was set to a microwave power of 100 to 800 Watt for 60 minutes each. Once done, the samples were annealed at a temperature of 500 °C for 1 hour. The procedures described above are depicted in Figure 1.

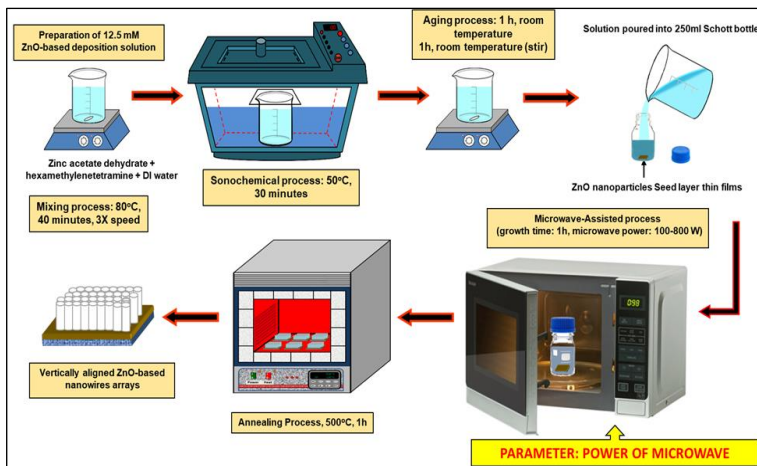


Figure 1: Deposition of ZnO NWs via a hybrid microwave-assisted sonochemical technique

Characterization method

The structural and morphological properties were characterized by X-ray diffraction (XRD, PANalytical X'Pert PRO) with Cu K-alpha radiation of a wavelength of 1.54 Å and field emission scanning electron microscope (FESEM, JEOL JSM-7600F). The optical properties were characterized by UV-visible spectroscopy (UV-Vis, Cary 5000).

Results and Discussion

Morphological and structural study

Top views of the ZnO NWs created using the HMAST approach are shown in Figure 2 which were deposited using microwave powers ranging from 100 to 800 W and an optimum solution concentration of 12.5 mM over the course of 60 minutes. It is evident that ZnO NSs were successfully produced in nanowire-type formation at the surface of the glass substrate within a very brief period of deposition time. This success may be attributed to microwave chemistry, as discussed by Abu ul Hassan et al. [51], where microwave heating provides homogeneous heat transfer to the solution mixture for chemical reactions, thereby speeding up the synthesis process.

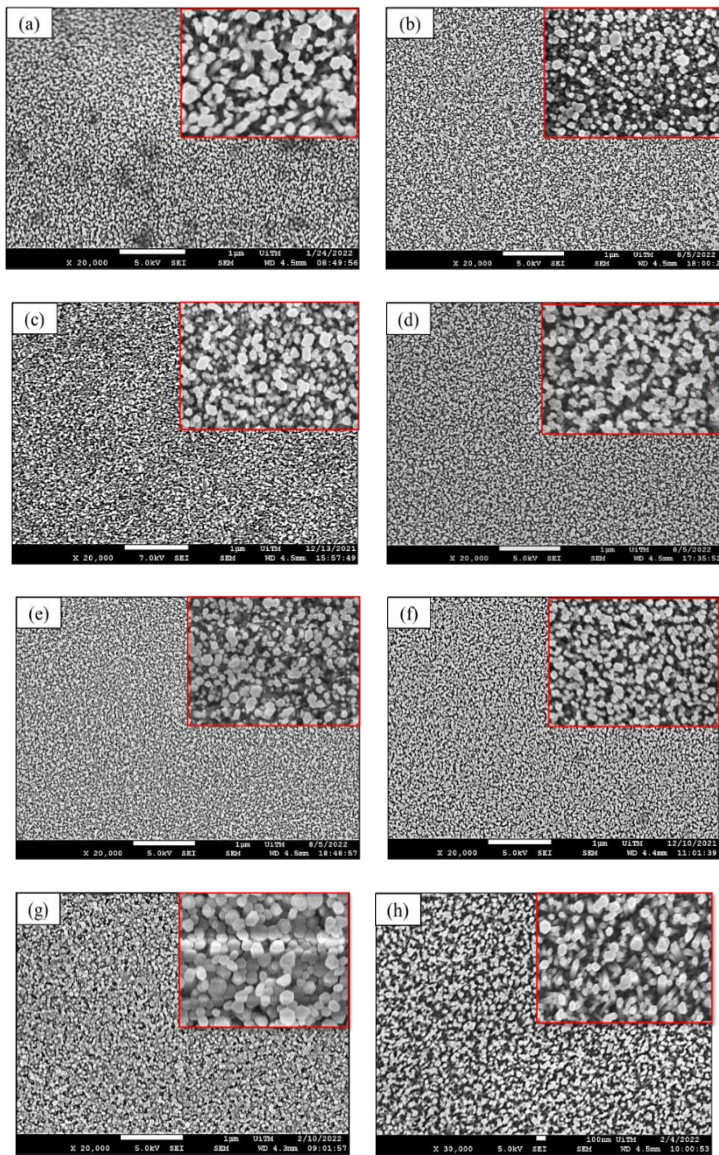


Figure 2: FESEM images of ZnO NWs by HMAST at 20000X magnification and magnified images (100000X) on the top right corner deposited at microwave power of; (a) 100 W, (b) 200 W, (c) 300 W, (d) 400 W, (e) 500 W, (f) 600 W, (g) 700 W, and (h) 800 W

In addition, compared to furnace heating, the effect of microwave growth can be seen even at relatively small microwave levels (100 W). This is explained by the reduced crystallization periods associated with the quick dissolving of precipitated hydroxides by microwave heating, as well as the rapid heating of the reaction precursors to the crystallization temperature [52]. The produced ZnO NWs have a distinct hexagonal wurtzite structure and are vertically oriented and tightly packed onto the substrate with different sizes which might be attributed to the migration rate of zinc interstitials and the vacancies are largely dependent on the change of growth temperature caused by the increase in the power of microwave [53]. Dimensions were averaged from individual nanowires according to the area distribution of nanowires from each sample where the average diameter size of the nanowires is tabulated in Table 1. It can also be observed in Figure 2(f) that the surface morphology of ZnO NWs deposited at 600 W microwave power displays the smallest diameter size and smooth uniformly distributed hexagonal NWs with a more compact structure in comparison to other samples. It is evident in Figures 2(a) to 2(f) that the nanowires' reduction in diameter size as microwave power increases from 100 to 600 W is consistent with earlier research conducted by other researchers where it was found that a higher microwave power contributes to increasing in temperature leading to the decrement in diameter size of nanostructures [54].

However, the diameter size of the nanowires starts to rise once more at power levels of 700 and 800 W as seen in Figures 2(g) and 2(h). This might be due to the microwave effect and the phenomenon of "hot spots," which is caused by the presence of zones with a higher temperature than the bulk of the aqueous solution. The maximum temperature reached in the chemical reactions during microwave heating was limited by the solution boiling temperature (105 °C for water) or higher temperature [55]. A liquid reaction mixture superheats because of these "hot spots" more than conventional heating would expect. When using a dielectric material (solid or liquid), and assuming negligible diffusion and heat losses, most of the absorbed microwave power per unit volume is converted into thermal energy within the dielectric material [56]. This is shown in the following equation where the temperature of the mixture's aqueous solution rises rapidly as the microwave power increases.

$$\frac{\Delta T}{\Delta t} = \frac{P_{abs}}{\rho C_p} = \frac{2\pi f \epsilon_0 \epsilon''_{eff} E_{rms}^2}{\rho C_p} = \frac{2\pi f \epsilon_0 \epsilon'_r \tan \delta E_{rms}^2}{\rho C_p} \quad (1)$$

where ρ is the density, C_p is the specific heat capacity, ΔT is the temperature rise or the rate of heating and t is the time.

According to Debye and Stokes' theorem, the relaxation time (τ) of dipole rotation, a spherical or nearly spherical rotating dipole with radius, r is given by the following equation [57]-[58]:

$$\tau = \frac{4\pi\eta r^3}{kT} \quad (2)$$

where η is the viscosity of the medium, k is Boltzmann's constant, and T is the temperature. Relaxation data for pure water play an important role in the study of the dielectric properties of aqueous solutions [59].

On the other hand, when the temperature rises, the water phase's viscosity decreases as shown in Equation (2), increasing the possibility that water pools would collide. Water pools become less stable as a result, which raises the likelihood that ZnO nuclei will combine. As a result, ZnO nanostructures will often expand in size [60]. The change in microstructure is also explained by the Ostwald ripening theory [61].

Table 1: Structural parameters of ZnO NWs by HMAST technique deposited at various microwave power

Sample	Microwave power (W)	Peak position (2θ)	FWHM ($^\circ$)	Crystallite size (nm)	Diameter size (nm) FESEM
(a)	100	33.86	0.190	31.98	40.51
(b)	200	33.90	0.189	29.79	37.93
(c)	300	33.82	0.186	31.63	36.90
(d)	400	33.89	0.183	33.08	35.11
(e)	500	33.86	0.173	38.01	33.60
(f)	600	33.90	0.170	32.71	29.66
(g)	700	33.91	0.202	31.98	41.53
(h)	800	33.95	0.348	18.60	45.77

The results of X-ray diffraction (XRD) for these samples further supported the FESEM results where it was found that the ZnO NWs produced are in highly crystalline form and purity. Figure 3 displays the XRD patterns of the ZnO NWs thin film generated by the HMAST technique at different microwave powers of 100 to 800 W. The indexing of the various XRD peaks was carried out in accordance with the Joint Committee on Powder Diffraction Standards (JCPDS) standard database of ZnO hexagonal wurtzite nanostructure (File no. 36-1451). The ZnO NWs formed display three distinct diffraction peaks that were observed between 20 and 60 degrees, as shown in Figures 2(a) to 2(h). The observed diffracted peaks and associated hkl values, which were positioned along the preferred c-axis orientation and were indexed

at (100), (002), and (101), are clearly visible with varying intensities. This outcome is consistent with those mentioned in previous findings [62]-[63].

The strongest (002) orientation peak, which is evident in all samples, is between 33.82° and 33.9° , showing that the particles predominantly developed in one direction, generating structures that are almost 1D or rod-like, as can be seen by observations from all the grown samples. The weak intensities of the other peaks, on the other hand, could be caused by a few distorted alignments of ZnO NWs grown on the glass substrate. Overall, the samples that were developed exhibited clear crystalline structures and no other phase formations, including amorphous structures. Additionally, it can be noted in Figure 2(f) that ZnO NWs deposited at the maximum microwave power of 600 W exhibit the sharpest and narrowest intensity of (002) peaks as compared to ZnO NWs formed at a different microwave power of 100 to 500, 700 and 800 W. This further proves that the samples synthesized using higher microwave power have higher peak intensity, in comparison to those prepared at lower powers, indicating the increase of purity of ZnO as a function of high microwave power [64].

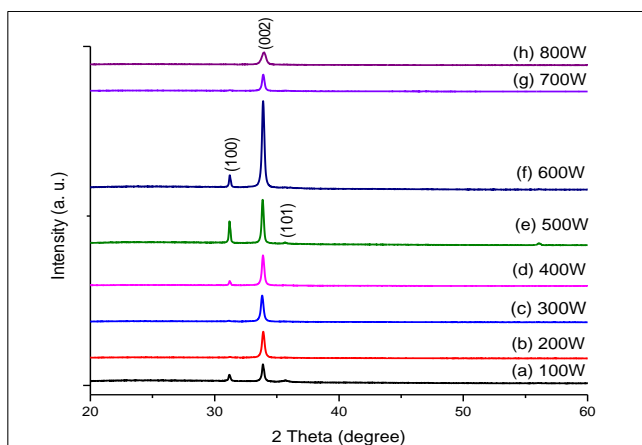


Figure 3: XRD spectra of ZnO NWs by HMAST technique deposited at various microwave power

The average crystallite sizes D (nm) of the ZnO nanowires was calculated using Scherrer's formula below.

$$D = \frac{0.9\lambda}{\beta \cos \theta} \quad (3)$$

where λ is the X-ray wavelength of Cu-K α radiation source ($=1.5418\text{\AA}$), β (in radians) is the full width at half maximum (FWHM) intensity of the diffraction peak located at 2θ and θ is the Bragg's angle.

Calculated results are shown and summarised in Table 1, where it is discovered that the average crystallite size increases from 45.62 to 51 nm with an increase in microwave power from 100 to 800W. Although ZnO nanowires can be grown as it is usually in the form of powders, our method opted for the use of substrates specifically low-cost soda lime silica glass as vertically oriented growth on a substrate offers significant benefits specifically for photocatalytic applications. The formation of nanowires is aided by the anisotropy of the ZnO crystal structure. The basal plane (001), with one end, in terminatively positive Zn lattice points and the other in partially negative oxygen lattice in various directions follow the pattern $\nu_{(0001)} > \nu_{(01\bar{1}\bar{1})} > \nu_{(01\bar{1}0)} > \nu_{(01\bar{1}1)} > \nu_{(000\bar{1})}$ [66].

Optical Properties

At room temperature, UV-Vis-NIR spectrophotometer measurements between 200 and 2200 nm are used to determine the optical characteristics of the ZnO NWs created by HMAST. The transmittance spectra of the ZnO NWs made using the HMAST approach are shown in Figure 4 at various microwave powers ranging from 100 to 800 W. Thin films' optical transmittance is known to be influenced by their surface shape. In this experiment, it was discovered that every sample developed met the criteria for transparency, which is above 80% in the visible-NIR range, and that the visible region's absorption edges are below 400 nm. This could be attributed to electron transitions from the valence band to the conduction band caused by the intrinsic ZnO band gap. It has also been widely reported in previous studies that the difference in particle size might be the reason for the variation in the absorption edges (67-69). Throughout the visible area, the transmittance spectra show an exciton peak in the 350-380 nm range and reduced absorbance above 380 nm. Sharp absorption edges suggest smaller ZnO particle sizes, while strong absorbance in the UV range suggests excellent crystallinity [70].

The highest transmittance was recorded for the sample synthesized at 100 W microwave power as can be seen in Figure 4(a) with an average transmittance of 95.11% between 400 nm and 800 nm in the visible region, whereas the lowest transmittance was obtained for the intrinsic sample at 700 W with an average transmittance of 83.43% over the same wavelength as seen in Figure 4(g).

It can also be seen in Table 2 that the transmittance decreases as the microwave power increases from 100 to 500 W. However, the transmittance increases again at a microwave power of 600 W with 89.72% transmittance which might be due to the homogeneous structure with uniformly distributed

particles and improvement in growth along the c-axis enhancing the optical scattering reduction in the ZnO thin films. The transmittance spectra started to decrease again at higher microwave power of 700-800 W which might be due to the change in structural properties as discussed previously. Overall, all the samples showed great transparency and it is also well known that strong transmittance properties may be used in electrical devices, such as the window layer in solar cells, to capture the most photons. Changes in the transmission spectrum were brought on by interferences in thin films caused by reflection at the air-ZnO and ZnO-glass interfaces [71].

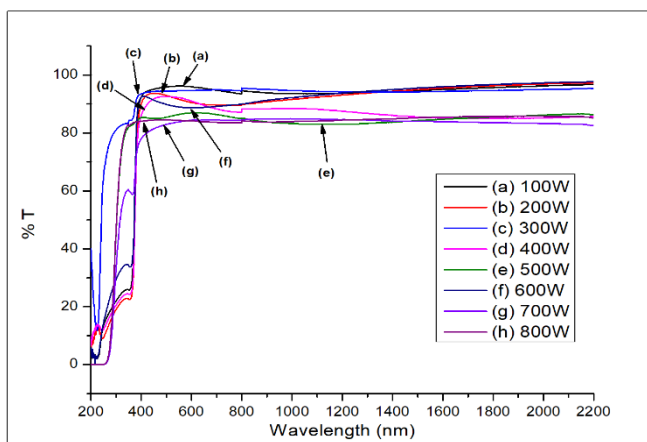


Figure 4: Transmittance spectra of ZnO NWs by HMAST technique deposited at various microwave power of (a) 100 W, (b) 200 W, (c) 300 W, (d) 400 W, (e) 500 W, (f) 600 W, (g) 700 W, and (h) 800 W as a function of wavelength

Table 2: Transmittance percentage of ZnO NWs by HMAST technique

Sample	Microwave power (W)	Average transmittance, T (%)
(a)	100	95.11
(b)	200	91.07
(c)	300	90.73
(d)	400	90.03
(e)	500	85.96
(f)	600	89.72
(g)	700	83.43
(h)	800	84.01

Conclusions

It can be concluded that highly crystalline ZnO NWs having hexagonal wurtzite structure with preferable c-axis orientation were successfully synthesized using a microwave-assisted sonochemical technique from 100 to 800 W of microwave power at 12.5 mM concentration and 60 minutes deposition time with profound improvement in its properties. It is found that the peak intensities of the ZnO NWs increase as the power increases up to 600 W indicating the high purity of ZnO NWs produced. The trend in the growth of the aligned ZnO NWs arrays produced is supported by the FESEM images of samples which indicate smaller diameter sizes of wires as the temperature rises with higher microwave power but starts getting bigger from 700 W of microwave power to 800 W. On the contrary, the XRD analysis obtained structural analysis which had shown significant phase identification according to JCPDS (File No 36-1451) highest intensity of (002) was observed to be very strong and narrow with bigger crystallite size at higher microwave power. The optical analysis of the samples also found that ZnO NWs obtained by this method have high transmittance of around 84% to 95.11% which is highly fitting to be applied in electrical devices.

Contributions of Authors

The authors confirm the equal contribution in each part of this work. All authors reviewed and approved the final version of this work.

Funding

This work was supported by Grant No. 600-RMC/YTR/5/3 (005/2021) under the Ministry of Education (MOHE) and the Universiti Teknologi MARA (UiTM), Malaysia.

Conflict of Interests

All authors declare that they have no conflicts of interest

Acknowledgment

The authors would like to thank the Research Management Centre (RMC), Universiti Teknologi MARA (UiTM), Malaysia, for their support. The authors

would also like to thank Mr. Salifairus Mohammad Jafar (UiTM Senior Science Officer) and Mr. Mohd Azlan Jaafar (UiTM Assistant Engineer) for their kind support of this research.

References

- [1] S. Baruah, R.F. Rafique, and J. Dutta, "Visible light photocatalysis by tailoring crystal defects in zinc oxide nanostructures", *Nano*, vol. 3, no. 5, pp. 399-407, 2008. <https://doi.org/10.1142/S179329200800126X>
- [2] Q. Zhou, J. Z Wen, P. Zhao, and W. A. Anderson, "Synthesis of vertically aligned zinc oxide nanowires and their application as a photocatalyst", *Nanomaterials*, vol. 7, no. 1, pp. 1-13, 2017. <https://doi.org/10.3390/nano7010009>
- [3] V. Parihar, M. Raja, and R. Paulose, "A brief review of structural, electrical and electrochemical properties of zinc oxide nanoparticles", *Reviews on Advanced Materials Science*, vol. 53, no. 2, pp. 119-130, 2018. <https://doi.org/10.1016/j.ceramint.2019.11.051>
- [4] J. Theerthagiri, S. Salla, R. A. Senthil, P. Nithyadharseni, A. Madankumar, P. Arunachalam, T. Maiyalagan, and H. S. Kim, "A review on ZnO nanostructured materials: energy, environmental and biological applications", *Nanotechnology*, vol. 30, no. 39, pp. 1-27, 2019. <https://doi.org/10.1088/1361-6528/ab268a>
- [5] B.G. Shohany, and A.K. Zak, "Doped ZnO nanostructures with selected elements-Structural, morphology and optical properties: A review", *Ceramics International*, vol. 46, no. 5, pp. 5507-5520, 2020. <https://doi.org/10.1016/j.ceramint.2019.11.051>
- [6] V.S. Bhati, M. Hojamberdiev, and M. Kumar, "Enhanced sensing performance of ZnO nanostructures-based gas sensors: A review", *Energy Reports*, vol. 6, pp. 46-62, 2020. <https://doi.org/10.1016/j.egy.2019.08.070>
- [7] P. Vishnukumar, S. Vivekanandhan, M. Misra, and A. K. Mohanty, "Recent advances and emerging opportunities in phytochemical synthesis of ZnO nanostructures", *Materials Science in Semiconductor Processing*, vol. 80, pp. 143-161, 2018. <https://doi.org/10.1016/j.mssp.2018.01.026>
- [8] M. Sheikh, M. Pazirofteh, M. Dehghani, M. Asghari, M. Rezakazemi, C. Valderrama, and J.L. Cortina, "Application of ZnO nanostructures in ceramic and polymeric membranes for water and wastewater technologies: a review", *Chemical Engineering Journal*, vol. 391, p. 123475, 2020. <https://doi.org/10.1016/j.cej.2019.123475>
- [9] A. Ramirez-Canon, M. Medina-Llamas, M. Vezzoli, and D. Mattia, "Multiscale design of ZnO nanostructured photocatalysts", *Physical*

- Chemistry Chemical Physics*, vol. 20, no. 9, pp. 6648-6656, 2018. <https://doi.org/10.1039/C7CP07984B>
- [10] H. Beitollahi, S. Tajik, F.G. Nejad, and M. Safaei, "Recent advances in ZnO nanostructure-based electrochemical sensors and biosensors", *Journal of Materials Chemistry B*, vol. 8, no. 27, pp. 5826-5844, 2020. <https://doi.org/10.1039/D0TB00569J>
- [11] A. Galdámez-Martínez, G. Santana, F. Güell, P.R. Martínez-Alanis, and A. Dutt, "Photoluminescence of ZnO nanowires: a review", *Nanomaterials*, vol. 10, no. 5, pp. 1-23, 2020. <http://dx.doi.org/10.3390/nano10050857>
- [12] C.V. Manzano, L. Philippe, and A. Serrà, "Recent progress in the electrochemical deposition of ZnO nanowires: synthesis approaches and applications", *Critical Reviews in Solid State and Materials Sciences*, vol. 47, no. 5, pp. 772-805, 2022. <https://doi.org/10.1080/10408436.2021.1989663>
- [13] A.A. Ghassan, N.A. Mijan and Y.H. Taufiq-Yap, "Nanomaterials: an overview of nanorods synthesis and optimization", *Nanorods and nanocomposites*, vol. 11, no. 11, pp. 8-33, 2019. <http://dx.doi.org/10.5772/intechopen.77453>
- [14] M.S. Lv, C. Li, Y.N. Li, X.F. Zhang, Z.P. Deng, X.L. Cheng, Y.M. Xu, L.H. Huo, and S. Gao, "Facilely controlled synthesis of porous ZnO nanotubes with rich oxygen vacancies for highly sensitive and selective detection of NO₂ at low temperature", *Sensors and Actuators B: Chemical*, vol. 375, p. 132865, 2023. <https://doi.org/10.1016/j.snb.2022.132865>
- [15] M. Hong, J. Meng, H. Yu, J. Du, Y. Ou, Q. Liao, Z. Kang, Z. Zhang, and Y. Zhang, "Ultra-stable ZnO nanobelts in electrochemical environments", *Materials Chemistry Frontiers*, vol. 5, no. 1, pp. 430-437, 2021. <https://doi.org/10.1039/D0QM00709A>
- [16] T. Van Khai, V.M. Thanh, and T. Dai Lam, "Structural, optical and gas sensing properties of vertically well-aligned ZnO nanowires grown on graphene/Si substrate by thermal evaporation method", *Materials Characterization*, vol. 141, pp. 296-317, 2018. <https://doi.org/10.1016/j.matchar.2018.04.047>
- [17] F.F. Alia Azmi, B. Sahraoui, and S.K. Muzakir, "Study of ZnO nanospheres fabricated via thermal evaporation for solar cell application", *Makara Journal of Technology*, vol. 23, no. 1, pp. 11-15, 2019. <https://doi.org/10.7454/mst.v23i1.3644>
- [18] H. Ahmoum, G. Li, S. Belakry, M. Boughrara, M.S. Su'ait, M. Kerouad, and Q. Wang, "Structural, morphological and transport properties of Ni doped ZnO thin films deposited by thermal co-evaporation method", *Materials Science in Semiconductor Processing*, vol. 123, pp. 1-5, 2021. <https://doi.org/10.1016/j.mssp.2020.105530>

- [19] P. Narin, E. Kutlu-Narin, S. Kayral, R. Tulek, S. Gokden, A. Teke, and S.B. Lisesivdin, "Morphological and optical characterizations of different ZnO nanostructures grown by mist-CVD", *Journal of Luminescence*, vol. 251, p. 119158, 2022. <https://doi.org/10.1016/j.jlumin.2022.119158>
- [20] M. Bai, M. Chen, X. Li, and Q. Wang, "One-step CVD growth of ZnO nanorod/SnO₂ film heterojunction for NO₂ gas sensor", *Sensors and Actuators B: Chemical*, vol. 373, p. 132738, 2022. <https://doi.org/10.1016/j.snb.2022.132738>
- [21] T. Amakali, L.S. Daniel, V. Uahengo, N.Y. Dzade, and N.H. De Leeuw, "Structural and optical properties of ZnO thin films prepared by molecular precursor and sol-gel methods", *Crystals*, vol. 10, no. 2, pp. 1-11, 2020. <https://doi.org/10.3390/cryst10020132>
- [22] R. Ebrahimi-fard, H. Abdizadeh, and M.R. Golobostanfard, "Controlling the extremely preferred orientation texturing of sol-gel derived ZnO thin films with sol and heat treatment parameters", *Journal of Sol-Gel Science and Technology*, vol. 93, no. 1, pp. 28-35, 2020. <https://doi.org/10.1007/s10971-019-05157-2>
- [23] F. Qiao, Q. Liang, J. Yang, Z. Chen, and Q. Xu, "A facile approach of fabricating various ZnO microstructures via electrochemical deposition", *Journal of Electronic Materials*, vol. 48, no. 4, pp. 2338-2342, 2019. <https://doi.org/10.1007/s11664-019-06988-z>
- [24] A. Pruna, Z. Wu, J.A. Zapien, Y.Y. Li, and A. Ruotolo, "Enhanced photocatalytic performance of ZnO nanostructures by electrochemical hybridization with graphene oxide", *Applied Surface Science*, vol. 441, pp. 936-944, 2018.
- [25] V. Gerbreder, M. Krasovska, E. Sledevskis, A. Gerbreder, I. Mihailova, E. Tamanis, and A. Ogurcovs, "Hydrothermal synthesis of ZnO nanostructures with controllable morphology change", *CrystEngComm*, vol. 22, no. 8, pp. 1346-1358, 2020. <https://doi.org/10.1039/C9CE01556F>
- [26] A. Katiyar, N. Kumar, R.K. Shukla, and A. Srivastava, "Substrate free ultrasonic-assisted hydrothermal growth of ZnO nanoflowers at low temperature", *SN Applied Sciences*, vol. 2, no. 8, pp. 1-7, 2020. <https://doi.org/10.1007/s42452-020-3186-1>
- [27] A.D. Faisal, R.A. Ismail, W.K. Khalef, and E.T. Salim, "Synthesis of ZnO nanorods on a silicon substrate via hydrothermal route for optoelectronic applications", *Optical and Quantum Electronics*, vol. 52, no. 4, pp. 1-12, 2020. <https://doi.org/10.1007/s11082-020-02329-1>
- [28] M. Zare, K. Namratha, K. Byrappa, D.M. Surendra, S. Yallappa, and B. Hungund, "Surfactant assisted solvothermal synthesis of ZnO nanoparticles and study of their antimicrobial and antioxidant properties", *Journal of Materials Science & Technology*, vol. 34, no. 6, pp. 1035-1043, 2018. <https://doi.org/10.1016/j.jmst.2017.09.014>

- [29] Y. Mao, Y. Li, Y. Zou, X. Shen, L. Zhu, and G. Liao, “Solvothermal synthesis and photocatalytic properties of ZnO micro/nanostructures”, *Ceramics International*, vol. 45, no. 2, pp. 1724-1729, 2019. <https://doi.org/10.1016/j.ceramint.2018.10.054>
- [30] X. Zhang, J. Chen, M. Wen, H. Pan, and S. Shen, “Solvothermal preparation of spindle hierarchical ZnO and its photocatalytic and gas sensing properties”, *Physica B: Condensed Matter*, vol. 602, pp. 1-11, 2021. <https://doi.org/10.1016/j.physb.2020.412545>
- [31] S. Zhao, Y. Shen, X. Yan, P. Zhou, Y. Yin, R. Lu, C. Han, B. Cui, and D. Wei, “Complex-surfactant-assisted hydrothermal synthesis of one-dimensional ZnO nanorods for high-performance ethanol gas sensor”, *Sensors and Actuators B: Chemical*, vol. 286, pp. 501-511, 2019. <https://doi.org/10.1016/j.snb.2019.01.127>
- [32] P. Basnet, and S. Chatterjee, “Structure-directing property and growth mechanism induced by capping agents in nanostructured ZnO during hydrothermal synthesis—A systematic review”, *Nano-Structures & Nano-Objects*, vol. 22, pp. 1-24, 2020. <https://doi.org/10.1016/j.nanoso.2020.100426>
- [33] M.N.I. Ghazali, M.A. Izmi, S.N.A. Mustaffa, S. Abubakar, M. Husham, S. Sagadevan, and S. Paiman, “A comparative approach on One-Dimensional ZnO nanowires for morphological and structural properties”, *Journal of Crystal Growth*, vol. 558, pp. 1-8, 2021. <https://doi.org/10.1016/j.jcrysgro.2020.125997>
- [34] R.T. Hitchcock, *Radio-Frequency and Microwave Radiation*, 3rd Edition, American Industrial Hygiene Association: Fairfax, VA, USA, 2004.
- [35] M. Vollmer, “Physics of the microwave oven”, *Physics Education*, vol. 39, pp. 74–80, 2004.
- [36] E. Mohammadi, M. Aliofkhaezai, M. Hasanpoor, and M. Chipara, “Hierarchical and complex ZnO nanostructures by microwave-assisted synthesis: morphologies, growth mechanism and classification”, *Critical Reviews in Solid State and Materials Sciences*, vol. 43, no. 6, pp. 475-541, 2018. <https://doi.org/10.1080/10408436.2017.1397501>
- [37] C. Mallikarjunaswamy, V. Lakshmi Ranganatha, R. Ramu, and G. Nagaraju, “Facile microwave-assisted green synthesis of ZnO nanoparticles: application to photodegradation, antibacterial and antioxidant”, *Journal of Materials Science: Materials in Electronics*, vol. 31, no. 2, pp. 1004-1021, 2020. <https://doi.org/10.1007/s10854-019-02612-2>
- [38] A. Kumar, Y. Kuang, Z. Liang, and X. Sun, “Microwave chemistry, recent advancements, and eco-friendly microwave-assisted synthesis of nanoarchitectures and their applications: a review”, *Materials Today Nano*, vol. 11, p. 100076, 2020. <https://doi.org/10.1016/j.mtnano.2020.100076>

- [39] N. Devi, S. Sahoo, R. Kumar, and R.K. Singh, "A review of the microwave-assisted synthesis of carbon nanomaterials, metal oxides/hydroxides, and their composites for energy storage applications", *Nanoscale*, vol. 13, pp. 11679-11711, 2021. <https://doi.org/10.1039/D1NR01134K>
- [40] N. Garino, T. Limongi, B. Dumontel, M. Canta, L. Racca, M., Laurenti and V. Cauda, "A microwave-assisted synthesis of zinc oxide nanocrystals finely tuned for biological applications", *Nanomaterials*, vol. 9, no. 2, pp. 1-17, 2019. <https://doi.org/10.3390/nano9020212>
- [41] K. J. Rao, B. Vaidhyanathan, M. Ganguli, and P. A. Ramakrishnan, "Synthesis of inorganic solids using microwaves", *Chemistry of Materials*, vol. 11, no. 4, pp. 882-895, 1999.
- [42] B. D. Cullity, *Elements of X-ray Diffraction*, Addison-Wesley Publishing, 1956.
- [43] P. J. Walter, S. Chalk, and H. M. Kingston, "Overview of microwave-assisted sample preparation" in *Microwave Enhanced Chemistry: Fundamentals, Sample Preparation and Applications*, HM Kingston and SJ Haswell, Ed. Am. Chem. Soc., Washington, DC, pp. 55-222, 1997.
- [44] Y. He, "Synthesis of ZnO nanoparticles with narrow size distribution under pulsed microwave heating", *China Particuology*, vol. 2, no. 4, pp. 168-170, 2004.
- [45] O. Palchik, J. Zhu, and A. Gedanken, "Microwave assisted preparation of binary oxide nanoparticles", *Journal of Materials Chemistry*, vol. 10, no. 5, pp. 1251-1254, 2000.
- [46] S. Horikoshi, R.F. Schiffmann, , J. Fukushima and N. Serpone, "Materials processing by microwave heating" in *Microwave Chemical and Materials Processing*, Springer, Singapore, pp. 321-381, pp. 2018. https://doi.org/10.1007/978-981-10-6466-1_10
- [47] M. A. Messih, M. A. Ahmed, A. Soltan, and S. S. Anis, "Synthesis and characterization of novel Ag/ZnO nanoparticles for photocatalytic degradation of methylene blue under UV and solar irradiation", *Journal of Physics and Chemistry of Solids*, vol. 135, p. 109086, 2019. <https://doi.org/10.1016/j.jpcs.2019.109086>
- [48] M. H. Mamat, M. Z. Sahdan, Z. Khusaimi, A. Z. Ahmed, S. Abdullah, and M. Rusop, "Influence of doping concentrations on the aluminum doped zinc oxide thin films properties for ultraviolet photoconductive sensor applications", *Optical Materials*, vol. 32, no. 6, pp. 696-699, 2010. <https://doi.org/10.1016/j.optmat.2009.12.005>
- [49] M. F. Malek, M. H. Mamat, M. Z. Musa, T. Soga, S. A. Rahman, S. A. Alrokayan and M. Rusop, "Metamorphosis of strain/stress on optical band gap energy of ZAO thin films via manipulation of thermal annealing process", *Journal of Luminescence*, vol. 160, pp. 165-175, 2015. <https://doi.org/10.1016/j.jlumin.2014.12.003>

- [50] X. Ge, K. Hong, J. Zhang, L. Liu, and M. Xu, "A controllable microwave-assisted hydrothermal method to synthesize ZnO nanowire arrays as recyclable photocatalyst", *Materials Letters*, vol. 139, pp. 119-121, 2015. <https://doi.org/10.1016/j.matlet.2014.10.058>
- [51] A.U.H.S. Rana, and H.S. Kim, "Growth condition-oriented defect engineering for changes in Au-ZnO contact behavior from Schottky to Ohmic and vice versa", *Nanomaterials*, vol. 8, no. 12, p. 980, 2018. <https://doi.org/10.1166/jnn.2018.14971>
- [52] H. E Unalan, P. Hiralal, N. Rupesinghe, S. Dalal, W. I. Milne, and G. A. Amaratunga, "Rapid synthesis of aligned zinc oxide nanowires", *Nanotechnology*, vol. 19, no. 25, p. 255608, 2008.
- [53] S. Rackauskas, A. G. Nasibulin, H. Jiang, Y. Tian, G. Statkute, S. D. Shandakov and E. I. Kauppinen, "Mechanistic investigation of ZnO nanowire growth", *Applied Physics Letters*, vol. 95, no. 18, p. 183114, 2009. <https://doi.org/10.1063/1.3258074>
- [54] H. R. Rajabi, R. Naghiha, M. Kheirizadeh, H. Sadatfaraji, A. Mirzaei, and Z. M. Alvand, "Microwave assisted extraction as an efficient approach for biosynthesis of zinc oxide nanoparticles: synthesis, characterization, and biological properties", *Materials Science and Engineering: C*, vol. 78, pp. 1109-1118, 2017. <https://doi.org/10.1016/j.msec.2017.03.090>
- [55] K. Bougrin, A. Loupy, and M. Soufiaoui, "Microwave-assisted solvent-free heterocyclic synthesis", *Journal of Photochemistry and Photobiology C: Photochemistry Reviews*, vol. 6, no. 2-3, pp. 139-167, 2005. <https://doi.org/10.1016/j.jphotochemrev.2005.07.001>
- [56] A. Chatterjee, T. Basak, and K. G. Ayappa, "Analysis of microwave sintering of ceramics", *AIChE Journal*, vol. 44, no. 10, pp. 2302-2311, 1998. <https://doi.org/10.1002/aic.690441019>
- [57] P. Europeïenne 1 Conseil de l'Europe, Maisonneuve S.A. Editions, Sainte Ruffine, 1996.
- [58] Y.R. Naves, Technologie et Chimie des Parfums Naturels, Masson Ed., Paris, 1974.
- [59] A. Loupy, and A. de la Hoz, "Microwaves in organic synthesis", John Wiley & Sons, Eds., 2013.
- [60] Y. He, "Synthesis of ZnO nanoparticles with narrow size distribution under pulsed microwave heating", *China Particuology*, vol. 2, no. 4, pp. 168-170, 2004. [https://doi.org/10.1016/S1672-2515\(07\)60050-5](https://doi.org/10.1016/S1672-2515(07)60050-5)
- [61] D. D. Dincov, K. A. Parrott, and K. A. Pericleous, "Heat and mass transfer in two-phase porous materials under intensive microwave heating", *Journal of Food Engineering*, vol. 65, no. 3, pp. 403-412, 2004. <https://doi.org/10.1016/j.jfoodeng.2004.02.011>
- [62] N. Salah, S. S Habib, Z. H. Khan, A. Memic, A. Azam, E. Alarfaj, and S. Al-Hamedi, "High-energy ball milling technique for ZnO nanoparticles

- as antibacterial material”, *International Journal of Nanomedicine*, vol. 6, p. 863, 2011. <https://doi.org/10.2147%2FIJN.S18267>
- [63] A. Azam, F. Ahmed, S. S. Habib, Z. H. Khan, and N. A. Salah, “Fabrication of Co-doped ZnO nanorods for spintronic devices”, *Metals and Materials International*, vol. 19, no. 4, pp. 845-850, 2013. <https://doi.org/10.1007/s12540-013-4027-1>
- [64] D. Papadaki, S. Foteinis, G. H. Mhlongo, S. S. Nkosi, D. E. Motaung, S. S. Ray, and G. Kiriakidis, “Life cycle assessment of facile microwave-assisted zinc oxide (ZnO) nanostructures”, *Science of the Total Environment*, vol. 586, pp. 566-575, 2017. <https://doi.org/10.1016/j.scitotenv.2017.02.019>
- [65] S. Baruah, M. A. Mahmood, M. T. Z. Myint, T. Bora, and J. Dutta, “Enhanced visible light photocatalysis through fast crystallization of zinc oxide nanorods”, *Beilstein Journal of Nanotechnology*, vol. 1, no. 1, pp. 14-20, 2010. <http://dx.doi.org/10.3762%2Fbjnano.1.3>
- [66] M. C. Medina, D. Rojas, P. Flores, E. Pérez-Tijerina, and M. F. Meléndrez, “Effect of ZnO nanoparticles obtained by arc discharge on thermo-mechanical properties of matrix thermoset nanocomposites”, *Journal of Applied Polymer Science*, vol. 133, no. 30, p. 43631, 2016. <https://doi.org/10.1002/app.43631>
- [67] C. V. Ramana, R. J. Smith, and O. M. Hussain, “Grain size effects on the optical characteristics of pulsed-laser deposited vanadium oxide thin films”, *Physica Status Solidi (a)*, vol. 199, no. 1, pp. R4-R6, 2003. <https://doi.org/10.1002/pssa.200309009>
- [68] H. Lin, C. P. Huang, W. Li, C. Ni, S. I. Shah, and Y. H. Tseng, “Size dependency of nanocrystalline TiO₂ on its optical property and photocatalytic reactivity exemplified by 2-chlorophenol”, *Applied Catalysis B: Environmental*, vol. 68, no. 1-2, pp. 1-11, 2006. <https://doi.org/10.1016/j.apcatb.2006.07.018>
- [69] R. S. Yadav, P. Mishra, and A. C. Pandey, “Growth mechanism and optical property of ZnO nanoparticles synthesized by sonochemical method”, *Ultrasonics Sonochemistry*, vol. 15, no. 5, pp. 863-868, 2008. <https://doi.org/10.1016/j.ultsonch.2007.11.003>
- [70] K. P. Sridevi, S. Sivakumar, and K. Saravanan, “Synthesis and characterizations of zinc oxide nanoparticles using various precursors”, *Annals of the Romanian Society for Cell Biology*, vol. 25, no. 3, pp. 8679-8689, 2021. <https://www.annalsofrscb.ro/index.php/journal/article/view/2413>
- [71] H. Li, J. Wang, H. Liu, H. Zhang, and X. Li, “Zinc oxide films prepared by sol-gel method”, *Journal of Crystal Growth*, vol. 275, no. 1-2, pp. e943-e946, 2005. <https://doi.org/10.1016/j.jcrysgro.2004.11.098>

Influence of Nano Additives on Performance, Combustion, and Emission Characteristics of Diesel Engine using Tamarind Oil Methyl Ester-Diesel Fuel Blends

Bikkavolu Joga Rao*

Department of Mechanical Engineering,
Godavari Institute of Engineering & Technology (A),
Rajahmundry-533296, INDIA
*jogarao.bikkavolu@gmail.com

Pullagura Gandhi, Vadapalli Srinivas, Chebattina Kodanda Ramarao
Department of Mechanical Engineering, GITAM Deemed to be University,
Visakhapatnam-530045, INDIA

Pathem Uma Chaithanya

Department of Mechanical Engineering,
Baba Institute of Technology and Sciences, Visakhapatnam-530041, INDIA

ABSTRACT

Hazardous emissions majorly NO_x and the poor performance of alternative fuels (biodiesel/its blends) are global concerns, as fossil fuel depletion and rising energy prices encourage researchers to rely on alternative energy sources with the addition of nano additives in the recent decade. The current experimental study investigates the performance, combustion, and emission characteristics of biodiesel-diesel mixtures dispersed with titanium dioxide (TiO₂) as a fuel additive on a 1-cylinder diesel engine. TiO₂ was dispersed in a Tamarind Oil Methyl Ester (TOME)-diesel blend (B20) in three concentrations of 40, 80, and 120 ppm via ultrasonication in the presence of QPAN80 surfactant to enhance the stability of the prepared fuel sample. A ratio of 1:4 TiO₂:QPAN80 was found to produce the highest stability and homogeneity which is evidenced by the characterization of TiO₂. The engine tests revealed that the greatest decrement in BSFC, CO, HC, and NO_x was observed as 15.2%, 15.2%, 11.10%, and 9.06%, and the maximum BTE, HRR,

and CP were improved by 9.76%, 50.32 J/degree, and 50.32 bar for the B20T80 blend correlated with B20 blend. Thus, the inclusion of TiO₂ nano additives improved overall engine performance and decreased emissions of CI engines significantly.

Keywords: Titanium Dioxide Nanoparticles; Catalytic Effect; Engine Performance; Engine Emissions; Tamarind Oil Methyl Ester

Nomenclature

AFD	Aphanizomenon Flos Biodiesel-Diesel blend	CP	Cylinder Pressure
B20	TOME 20% -80% diesel	DI	Direct Injection
B20T40	B20 with 40 mg of TiO ₂	FTIR	Fourier Transform Infrared
B20T80	B20 with 80 mg of TiO ₂	ID	Ignition Delay
B20T120	B20 with 120 mg of TiO ₂	NHRR	Net Heat Release Rate
BP	Brake Power	NOx	Nitrogen oxide
BSFC	Brake-Specific Fuel Consumption	TiO ₂	Titanium dioxide
BTE	Brake Thermal Efficiency	TOME	Tamarind Oil Methyl Ester
CI	Compression-Ignition	UHC	Unburnt Hydrocarbons
CO	Carbon monoxide	XRD	X-Ray Diffraction
CO ₂	Carbon dioxide		

Introduction

Humankind has relied on a variety of Energy sources for their need and development. In today's world, the energy problem has evolved into a worldwide concern that is threatening the security of civilizations. Fuels are crucial in the generation of large amounts of energy in different sectors like transportation, industrialization, and power generation. Fossil fuels supply 80% of the major contributors to the world's requirements [1]. Fossil fuel depletion, increasing the cost of crude oil products, and the emissions released from the prime movers using fossil fuels are the major concerns today the world is confronting and encouraging researchers to find alternative renewable sources that can perform with similar engine efficiencies less polluting emissions. Alternative source like biodiesel has been well-recognized to replace fossil fuels. Biodiesel is also expressed as mono-alkyl esters prepared from raw feedstock oils/animal fats in the presence of a catalyst and with

small-chain alcohols. The direct use of vegetable oils was restricted owing to their higher viscosity, poor atomization, carbon deposits that can clog fuel injection nozzle, and incomplete combustion [2]. Transesterification is the best and most effective method for reducing the viscosity of vegetable oil and can yield a superior quantity. The physicochemical characteristics of biodiesel are closer to the standard diesel and can run with no modifications in the engine, but biodiesel performs with less efficiency than diesel [3]-[5]. On the other side, biodiesel emits hazardous NO_x emissions which are attributed to the rich oxygen in biodiesel. Several investigations revealed various techniques like engine modifications, exhaust gas recirculation, and fuel modification techniques to decrease NO_x emissions and enhance the performance of diesel engines. The former methods enhance smoke emissions, whereas the fuel reformulation technique uses nanoparticles as a fuel additive in CI engines to address the above issue. The qualities of base fuel have been discovered to be enhanced with the addition of nanoparticles which aid in better atomization, and combustion, as a result, minimize hazardous exhaust emissions like NO_x [2], [6].

Dsilva and Bhat [5] investigated the influence of nano additives Titanium dioxide (TiO₂) dispersed in Pongamia Pinnata biodiesel-diesel fuel blends (B10, B20, and B30) on performance, combustion, and emission parameters. The test sample B20 with the inclusion of TiO₂ nano additives enhanced Brake Thermal Efficiency (BTE) by 1.47% and reduced BSFC by 7.29%. Emissions were reduced to a lower value such as Nitrogen Oxide (NO_x) (by 4.3%, 3.9%, and 4.2%), Unburnt Hydrocarbons (UHC) (by 20%, 13.6%, and 11.1%), and smoke opacity (by 9.2%, 11.04%, and 7.9%) for the nano additive B10, B20, and B30 blends respectively. Among various fuel blends, the B10T75 results in the highest Cylinder Pressure (CP), and B30T75 improves the highest Heat Release Rate (HRR). In another study, the effect of TiO₂ nanoparticles dispersed in palm oil biodiesel was studied on CI engines. Palm oil biodiesel-diesel samples were prepared in different proportions i.e., B10, B20, B30, B40, B50, and B100, and correlated to the B20 sample which was considered as a reference fuel. The fuel properties such as viscosity, flash point, cetane index, and calorific values were enhanced with the addition of 0.1% wt TiO₂ nano additive. Among all the blends, the fuel properties of the blends B20+0.1%TiO₂ and B10+0.1%TiO₂ meet the ASTM standards. Engine power and torque were improved at low speeds, and Carbon Dioxide (CO₂) and Nitrogen Oxide (NO_x) were found to be lowered by the addition of TiO₂ nanoparticles [7]. Jayabalaji and Shanmughasundaram [8] studied the performance and emission characteristics of a diesel engine using Aphanizomenon Flos (AF) biodiesel 20% and diesel 80% (B20) with TiO₂ nano additives at concentrations of 5%, 10%, and 15% which were expressed as AFD-5TiO₂, AFD-10TiO₂, and AFD-15TiO₂. Out of all the blends, the blend AFD-10TiO₂ resulted in reduced BSFC by 5% and increased BTE by 2%. Rameshbabu and Senthilkumar [9] studied the influence of TiO₂ nano

additive (with 50 and 100 ppm concentrations) with neat biodiesel (prepared from cottonseed oil) using a diesel engine. The emissions such as NO_x, Hydrocarbons (HC), Carbon Monoxide (CO), and smoke emission were reduced by 11.2%, 6.2%, 8.4%, and 5.8% respectively at full load conditions. BTE was enhanced by 0.8%, and BSFC was decreased by 1.2% with the dosage of 50 ppm TiO₂ nano additive in neat biodiesel. Whereas the addition of TiO₂ in biodiesel results in enhanced BTE by 1.1% and reduced BSFC by 1.5% regarding the neat biodiesel at each load. Karthikeyan and Viswanath [10] studied the emission characteristics of a two-cylinder diesel engine when operated with a punnai seed biodiesel-diesel sample (B30) with the inclusion of TiO₂ nanoparticles at a concentration of 25, 50, 75, and 100 ppm. The pollutants i.e., CO₂, CO, HC, NO_x, and smoke opacity were reduced when differentiated from diesel.

The previous literature survey showed that the addition of nanoparticles improves performance, combustion, and emission parameters along with the physiochemical properties. Tamarind oil is found to be the most beneficial feedstock for biodiesel preparation but has not been well recognized, and no research was found to study the performance, combustion, and emission characteristics of a CI engine with nanoparticles dispersed in TOME. Hence, this study is intended to find the overall performance of a diesel engine with the addition of TiO₂ nano additives at several dosages of 40, 80, and 120 ppm in a B20 blend.

Materials and Methodology

Materials

Biodiesel has recently gained popularity as a sustainable, environmentally friendly, and alternative fuel with the potential to significantly reduce exhaust gas emissions and thus provide a far cleaner source of energy. Tamarind trees are abundantly available everywhere in India and tamarind seed is obtained from tamarind fruit which comprises 30% of the oil yield. Along with its importance in the Indian subcontinent culinary techniques. The usage of tamarind fruit is nearly limitless since tamarind oil is unknown as a raw feedstock for biodiesel preparation and its usage in diesel engines is yet to be proposed [11]-[14]. Tamarind seeds were purchased at a low cost from Paderu, Visakhapatnam district, India. The seeds were dried under sunshine and crushed using an expeller and oil is extracted using a solvent extraction technique to find the maximum yield. Merck Laboratories, Mumbai, India, supplied the required solvents and chemicals, which were used immediately without any treatment. Methanol (99.5%), n-hexane (99%), and KOH (85%) pellets were obtained. Tamarind tree fruits and seeds are shown in Figure 1.



Figure 1: Presents tamarind tree fruits and seeds

Extraction of oil

The tamarind oil extraction was followed by a solvent extraction procedure. The pulp was separated, and the seeds were dried in the sunlight. These dried seeds were squeezed into the oil with the aid of a mechanical press. The raw oil was treated with 5% (v/v) n-Hexane at a temperature of 80 °C and then, agitated for half an hour to eliminate gel formation, sediments, and impurities. Since the n-Hexane has a low boiling point, it evaporated during the process. The treated sample was separated from impurities and the pure oil was collected in a separatory funnel after the settling particles were removed. This process was repeated until the required amount of oil was extracted. With 1 kg of seeds, 368 ml of oil was recovered.

Biodiesel synthesis

Biodiesel from tamarind oil is produced in 2 phases acid-catalyzed and base-catalyzed. In the former phase, 2 liters of tamarind oil, 330 ml of methanol, and 2% wt of H₂SO₄ were blended in a round neck bottle at a stirring speed of 600 rpm and a temperature of 50 °C for 90 mins. Following this, the solution was moved to a separating funnel and left for 2 hours [15]-[16]. Finally, the bottom layer was found to be murky and separated from the top layer. The acid content of this segregated top layer is determined to be lower which was subjected to the next phase (base-catalyzed/alkali-catalyzed treatment). 885 g of raw pretreated oil, 1.5% KOH catalyst (on a weight basis), and methanol were placed in a 2 L round-necked flask. The best molar ratio (methanol/oil) for maximum biodiesel conversion was found to be 1:6. This mixture was stirred for 1 hour at a fixed stirring speed of 500 rpm at 60 °C. After 6 hours, the bottom (glycerol) layer was drained by gravity method, and the upper layer was washed many times till the glycerol was removed [17]-[18]. Thereafter, the transesterified ester was brought to 100 °C to remove excess moisture particles. The amount of biodiesel yield was found to be 96% of the given in Equation (1).

$$\text{Biodiesel yield (wt \%)} = \left[\frac{\text{mass of biodiesel (g)}}{\text{mass of oil (g)}} \right] \times 100 \quad (1)$$

Surface modification of TiO₂ nanoparticles

The addition of TiO₂ nano additives should be consistent and safe for stability [18]. Table 1 lists the parameters of the TiO₂ nano additives employed in this investigation. For the uniform and homogeneous dispersion of nanoparticles in base fuel samples, electrostatic and steric processes were preferred. In the initial stage, the nanoparticles were coated with scattering agents, typically known as surfactants (QPAN80). The impact of surfactants on TiO₂ nanoparticles defines the stability of the base fuel. Hence, five trials were made to find the optimum ratio (TiO₂:QPAN80) i.e., 1:1, 1:2, 1:3, 1:4, and 1:5. The dispersed nano additives with QPAN80 were found to be stable, homogeneous, and consistent with a 1:4 ratio. Hence, a 1:4 optimum blend ratio was used to prepare the nano fuel blends at a concentration of 25, 50, and 75 ppm and expressed as B20T40, B20T80, and B20T120.

Table 1: Specifications of the TiO₂ nanoparticles

Manufacturer	Platonic Nanotech Private Limited- Kachwa Chowk, Dist: Godda, Jharkhand
Chemical name:	Titanium Oxide Nanoparticle (TiO ₂)
Appearance:	White powder
Purity:	>99.9%
Specific Surface area (SSA):	200-230 m ² /g
The average particle size:	30-50 nm
Bulk density (%):	0.15-0.25 g/cm ³
Atomic Weight	79.8658 g/mol
Morphology	Near spherical

Preparation of fuel samples

Nano fuels (Nanoparticles dispersed in B20 blend) were produced through two steps. The first step is to use a mechanical disseminator to disperse nanoparticles in the B20 mix and with the aid of an ultrasonic pulsing frequency approach the nano fuels were blended in the second stage, in which the TiO₂ dispersed fuel blend was placed in an ultrasonicator (Hielscher ultrasonic, 160 W, 40 kHz) for 30 minutes to avoid nanoparticle aggregation and to preserve the stable state [16], [18]. To produce a B20T40 blend, 40 ppm/0.040 g of nanoparticles were mixed into a 1 L volume of B20 blend and agitated for 30 minutes in an ultrasonicator to achieve homogeneous blending [19]. Similarly, the additional blends, B20T80 and B20T120, were produced and designated. After 30 days, these mixes were found to be stable. Table 2 shows the physicochemical parameters of diesel, B20, B20T40, B20T80, and B20T120 mixes evaluated according to ASTM standards.

Table 2: Physico-chemical characteristics of fuel blends

Fuel samples	Density at 40 °C (kg/m ³)	Viscosity (mm ² /s)	Calorific value (MJ/kg)	Flashpoint (°C)
Diesel	841	2.92	45.6	73
B20	833	3.89	41.2	75
B20T40	835	3.7	42.16	76
B20T80	841	3.74	43.21	78
B20T120	839	3.72	42.68	80
ASTM D975	850	2.0-4.5	42-46	60-80

Experimental setup

Figure 2 depicts the experimental setup. For the current investigation, a Kirloskar-made VCR, 1-cylinder, 4-s, Directe injection, CI engine was considered. The detailed engine configuration is given in Table 3. To assess tailpipe gasses, an AVL 5-Gas analyzer was utilized. Before the trials began, all of the sensors were extensively tested to ensure that experimental test errors were limited to minimal values. For 100 cycles, engine soft software was installed on the computer, and obtained the combustion data. Before the trial of the engine, it was benchmarked with standard diesel by running for 30 minutes. Then the nano-fuel samples were tested. During all the trials, the speed of the engine was maintained constant at 1500 rpm and the engine operated five times to make sure that the data was standardised at each load, and the average findings were presented. The HRR value is determined using the following Equation (2) concerning the crank angle and In-Cylinder Pressure (ICP) of Diesel, B20, B20T40, B20T80, and B20T120:

$$\frac{dQ_{net}}{d\theta} = \frac{\gamma}{\gamma-1} (P) \left(\frac{dV}{d\theta} \right) + \frac{\gamma}{\gamma-1} (V) \left(\frac{dP}{d\theta} \right) \quad (2)$$

where; $\frac{dQ_{net}}{d\theta}$ = Heat Release Rate (HRR) in (kJ/m³ CA)

V = instantaneous volume in (m³)

P = instantaneous pressure in (bar)

γ = ratio of specific heat



Figure 2: Representation of engine setup

Table 3: Specifications of engine setup

No.	Engine parameters	Specifications
1	Engine model	Kirloskar
2	No. of cylinders/ no. of strokes	¼
3	Rated power	5.7 Kw
4	Rated speed	1500 rpm
5	Bore diameter/Stroke length	100/105 mm
6	Compression ratio	18:1
7	Injection pressure	220 bar
8	Ignition timing	23° bTDC

Uncertainty analysis

Errors in engine measurements are obtained from a variety of factors. Random uncertainty refers to uncertainty related to measurement repeatability and environmental influences. It also incorporates systematic uncertainty caused by sensor faults. The uncertainties of various devices are given in Table 4. The Kragten spreadsheet technique given in Equation (3) employs to evaluate the uncertainty parameters numerically [20]. The uncertainty in calculating y for a single independent variable x_1 is represented as follows:

$$u(y, x_1) = F(x_1 + u(x_1), \dots x_n) - F(x_1, \dots x_n) \quad (3)$$

Table 4: Uncertainty about measuring devices

No	Instrument/Device	Uncertainty
1	Torque indicator, Nm	± 1% of reading
2	Fuel burette, cc	± 0.2
3	Speed sensor, rpm	± 5
4	Brake power, kW	± 0.053
5	Brake-specific fuel consumption (BSFC), g/kWh	± 5
6	Brake thermal efficiency (BTE), %	± 0.014
7	CO, ppm	± 10
8	NOx, ppm	± 5
9	Crank angle encoder, degree	± 0.5
10	A pressure transducer, bar	± 1% of reading

Because uncertainty propagation is based on the root sum of squares, the combined standard uncertainty for a dependent variable may be calculated using the individual standard uncertainties of its independent variables, as indicated in Equation (4) [21].

$$Uc(y) = \sqrt{\left\{ \left(\frac{\partial y}{\partial x_1} u_{x1} \right)^2 + \left(\frac{\partial y}{\partial x_2} u_{x2} \right)^2 \dots \dots + \left(\frac{\partial y}{\partial x_n} u_{xn} \right)^2 \right\}} \quad (4)$$

Characterization of TiO₂ nanoparticles

In the current experimental study, titanium dioxide (TiO₂) nanoparticles were combined with B20 in the form of a nanoemulsion, and their effects on CI engines were investigated. TiO₂ nanoparticles were primarily obtained from Platonic Nanotech Private Limited-Kachwa Chowk, Godda District, Jharkhand, India. The specifications of TiO₂ nanoparticles are described in Table 1. Figure 3 depicts the FT-IR (Fourier Transform Infrared) spectra of TiO₂ nanoparticles. A prominent band at 461.23 cm⁻¹ was visible in the spectra. The considerable absorption ranges from 3250 cm⁻¹ to 3700 cm⁻¹ and is accompanied by in-plane deformations at 1395.43 cm⁻¹. The exterior morphology of TiO₂ was investigated using FESEM images, as shown in Figures 4(a) and 4(b). The TiO₂ nanoparticle FESEM study was performed at the Central Analytical Laboratory of BITS- Pilani Hyderabad, India. FESEM pictures of TiO₂ nanoparticles were taken at magnifications of 65,000x and 20,000x. The HRTEM investigation was done utilizing JEOL: JEM 2100F, FEG TEM 200 kV TEM, with an ultra-thin Oxford Instruments EDS window system for a closer look. HRTEM images of TiO₂ nanoparticles are shown in Figures 4(c) and 4(d). TiO₂ nanofluid is shown clustered in these images, and the image shows TiO₂ nanoparticles to be round with a smooth surface and a mean particle size of 20 nm.

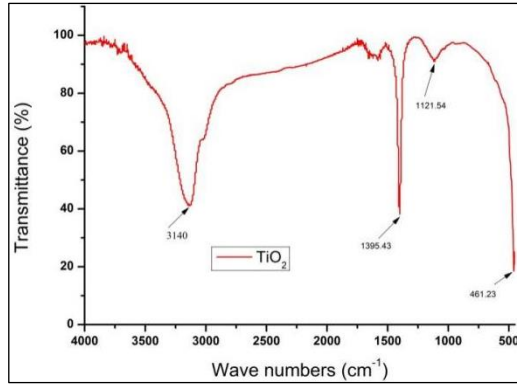


Figure 3: FTIR spectrum of TiO₂ nanoparticles

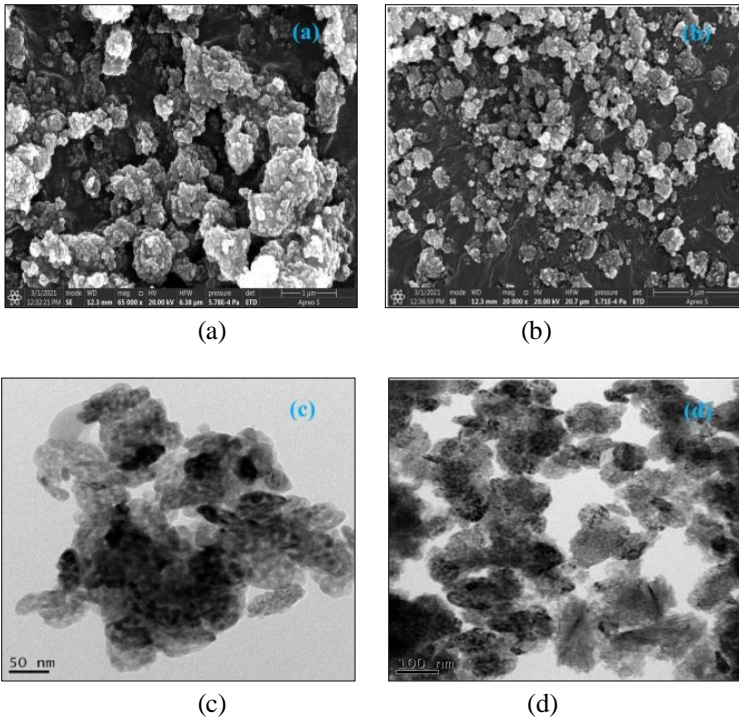


Figure 4: (a) FESEM images at; (a) 1 μm, and (b) 5 μm. HRTEM images at; (c) 50 nm, and (d) 100 nm

Results and Discussions

Combustion parameters

Cylinder pressure

The actual work output derived from the heat energy produced by the combustion fuel is represented in terms of pressure rise during a power stroke in a cycle defined by the engine combustion chamber. The CP of a CI engine is affected by fuel parameters such as viscosity, atomization and evaporation, air-fuel mixture reaction rate, ID duration, and the fuel burned during the premixed combustion stage [22]. Figure 5 displays the variations in cylinder pressure as a function of crank angle for diesel, B20, and B20 nano blends such as B20T40, B20T80, and B20T120 at maximum power output conditions.

As the surface-modified TiO₂ nano additives were scattered in the B20 blend, the CP was found to be improved much more. Because of the enhanced thermal conductivity of TiO₂ nanoparticles and the presence of oxygen in TiO₂, all of the fuel samples dispersed with TiO₂ nanoparticles demonstrated a significant increase in CP [22]-[23]. Furthermore, the TiO₂ nano additive's ability to enhance heat evenly throughout the ignition cycle is responsible for this improvement. Because the addition of nanoparticles in liquid fuels provides an enormous ability for combustion initiation, another key reason for CP improvement was increased heat transfer from TiO₂ nanoparticles to fuel owing to the surface area to volume ratio [23]. Furthermore, dispersion stability improves combustion and mass transportation characteristics, facilitating consistent and controlled combustion in the third phase of the combustion zone. Because of the presence of unburned nanoparticles, the flame lasted longer [22]-[23]. As a result, dispersion plays a vital role in retaining the nanoparticle in the liquid fuel for an extended period, hence improving combustion. The highest CP for B20T80, B20T120, and B20T40 was 50.32 bar, 49.72 bar, and 46.33 bar, respectively. According to Figure 5, B20T80 has a higher peak value of CP than B20. Similar findings were observed in various investigations [24]-[25].

Net heat release rate

Figure 6 displays the heat release rates for several fuel blends at maximum braking power vs. crank angle. Since B20 fuel has a shorter ID period, less quantity of fuel burns in the premixed zone, leading to a reduced HRR. The heat release rate was improved much further when surface-modified TiO₂ nanoparticles were introduced to the B20. The NHRR increased significantly when B20 was blended with surface-modified TiO₂ nano additives. This was attributable to the catalytic reaction activity of TiO₂ nanoparticles and increased convective heat transfer from nanoparticle to liquid fuel [23]. Increased ignition properties contribute to increased heat release [22]. Furthermore, by keeping the nanoparticle stable in the liquid, the dispersant

resulted in an increasing rate of combustion [23]. The additive-based B20 produced the most heat energy. B20T80 has the highest heat release rate of 50.32 J/degree compared to all the test fuel blends. Furthermore, the heat release rate of B20T120 and B20T40 was 49.72 J/degree and 46.33 J/degree, respectively, which were greater than diesel and B20. Similar findings were obtained in several papers [24], [26].

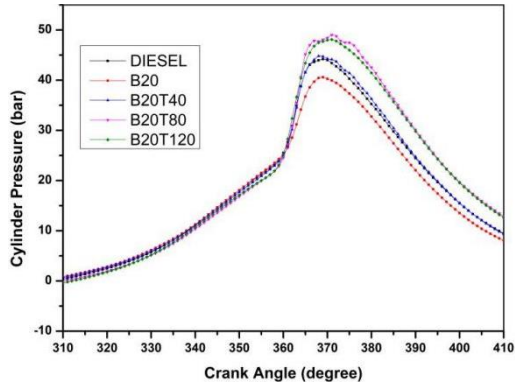


Figure 5: Cylinder pressure vs. crank angle (degree)

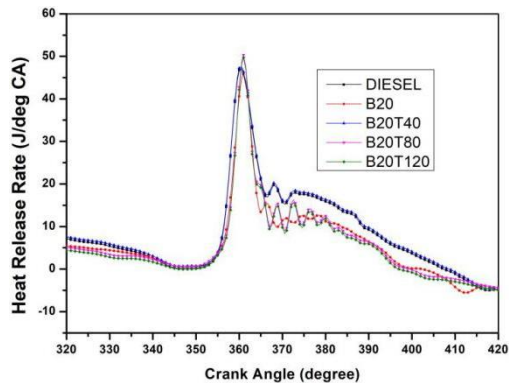


Figure 6: Heat release rate vs. crank angle (degree)

Engine performance

Brake Thermal Efficiency (BTE)

The influence of BTE concerning loads for various fuel samples is depicted in Figure 7. BTE is higher for all dispersed nano additives in B20 samples. The increase in BTE for all nano blends is due to the nanoparticle's high surface

energy and catalytic effect [8]. Furthermore, the greater surface-to-volume ratio of nano additives facilitates better evaporation and results in higher BTE [27]-[28]. Reduced BTE was obtained for B20 due to improper A/F ratio, lower calorific value, poor volatility, higher viscosity, and low combustion efficiency [29]-[30]. Maximum BTE produced was 28.45%, 29.57%, and 29.24% for B20T40, B20T80, and B20T120 blends. BTE was improved by 9.76% for the B20T80 sample. The results were correlated with previous findings [26], [31].

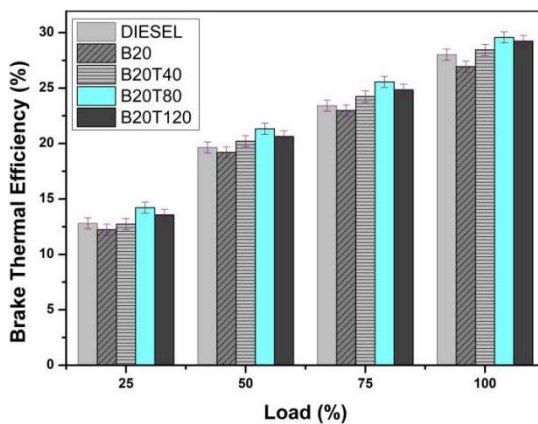


Figure 7: Variation of BTE for various samples concerning various loads

Brake-specific fuel consumption (BSFC)

The effect of BSFC for prepared samples vs. loads is illustrated in Figure 8. BSFC values represent the rate of fuel required as per the load requirements. The figure describes that the BSFC is higher for the B20 blend, which is attributed to the higher viscosity and reduced calorific value [27], [32]-[33]. BSFC was observed to be less for all nano additive blends due to the higher surface-to-volume ratio and catalytic action, thus facilitating an effective combustion process and resulting in less BSFC [30]. The reduction in BSFC was 0.43, 0.39, and 0.42 kg/kWh for B20T40, B20T80, and B20T120 samples, respectively. The maximum reduction in BSFC was 15.2% at full load for the B20T80 sample.

Emission characteristics

Carbon monoxide emissions

The variation of CO pollutants at different loads is illustrated in Figure 9. An incomplete oxidation process tends to form CO pollutants. The Highest CO emission was observed for diesel fuel, and lower values were observed for all

nano fuel samples. The reduction in CO emissions for nano additive blends was owing to the increased surface area and improved heat transfer rate with the catalytic activity of TiO₂ nanoparticles that facilitates reduced ignition delay and improved combustion process [34]-[35]. The maximum reduction of CO emissions was 15.2% for the B20T80 fuel blend at full load condition. These findings were found to be similar to the literature [28], [35].

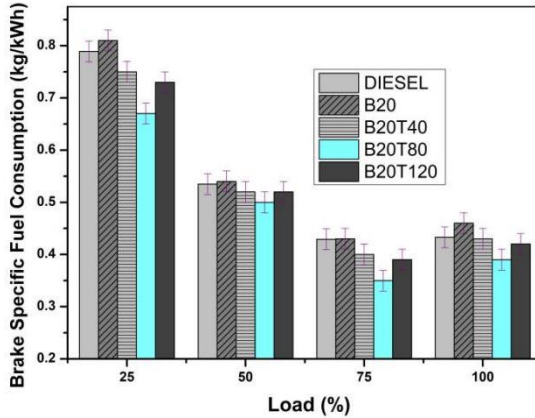


Figure 8: Variation of BTE for various samples for various loads

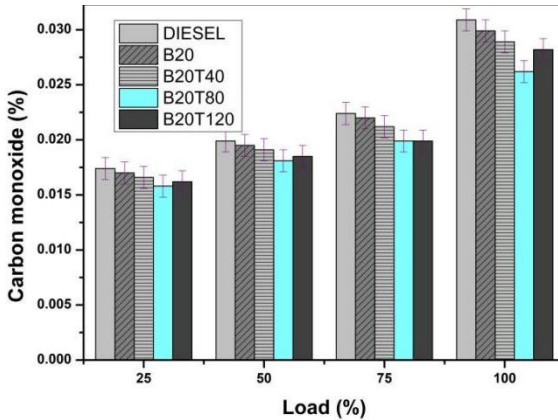


Figure 9: The variation of CO emissions vs. load (%)

Hydrocarbon emissions

The variation of HC emissions for various fuel samples is illustrated in Figure 10. It is found from the figure that sample B20 represents the highest HC emissions, which is attributed to a lower calorific value and greater value of

viscosity. HC emissions of nano fuel samples were reduced compared to diesel values. Decreased values were attributed to additional amounts of oxygen in nano additives, and improving physiochemical properties, thus improving the combustion process [36]-[37]. The HC emissions were decreased by 4.06%, 11.10%, and 5.31% for B20T40, B20T80, and B20T120 fuel blends, respectively, at full loads.

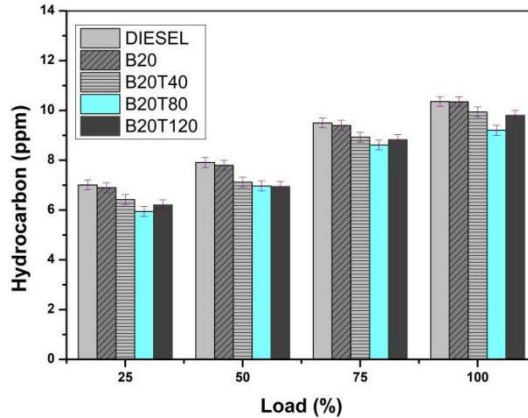


Figure 10: The variation of HC emissions vs. concerning load (%)

Nitrogen oxide emissions

The variation of NO_x emissions vs. loads is illustrated in Figure 11. NO_x emissions are formed due to the higher temperature of the engine cylinder. The oxides of nitrogen were found to be greater for the B20 blend, while the TiO₂ dispersed fuel blends reduced NO_x values at all loads due to the increased surface area to volume ratio and increased heat transfer rate of B20 [9]. The viscosity of B20 is improved by 5.13% compared to nano additive blends. Hence, the fuel blends take less time to form fuel droplets, atomize and combine with the hot surrounding air, which results in better combustion and reduced NO_x emissions [38]-[39]. Nevertheless, the addition of TiO₂ additives improves thermal conductivity and decreases the ignition lag period [40]-[41]. The maximum reduction in NO_x values were 2.07%, 9.06%, and 5% for B20T40, B20T80, and B20T120 blends, respectively

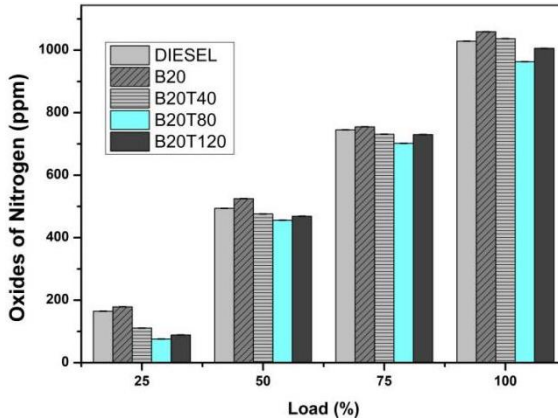


Figure 11: The variation of NO_x emissions vs. concerning load (%)

Conclusions

The biodiesel was synthesized from tamarind seed oil in the proposed investigation, and its performance, combustion, and emission characteristics were examined with the inclusion of TiO₂ nano additions at varied concentration levels of 40, 80, and 120 ppm. The dispersion of TiO₂ nanoparticles was found to be well stable at the nano additives to the surfactant ratio of 1:4. The prepared blends were tested for physicochemical properties and found the properties were within ASTM standard limits. Engine operating characteristics were found with the prepared fuel samples at a speed of 1500 rpm and under varying loads. The maximum BTE, HRR, and CP were observed by 9.76%, 50.32 J/degree, and 50.32 bar and the reduction of BSFC, CO, HC, and NO_x were observed to be 15.2%, 15.2%, 11.10%, and 9.06%, respectively for the B20T80 sample compared to the B20. According to the results and discussions, it is concluded that the inclusion of TiO₂ nanoparticles in the B20 blend (B20T80) improved overall engine characteristics and suggested use as a substitute for CI engines.

Contributions of Authors

The authors confirm the equal contribution in each part of this work. All authors reviewed and approved the final version of this work.

Funding

This work received no specific grant from any funding agency.

Conflict of Interests

All authors declare that they have no conflicts of interest

Acknowledgment

The authors sincerely thank the GITAM School of Technology, Visakhapatnam Campus, for providing laboratory facilities to conduct the research work. The authors are thankful to Sophisticate Analytical Instrument Facility (SAIF), IIT Bombay, for the analysis of the sample.

References

- [1] R. D'Silva, N. Fernandes, M. Menezes, P. D'Souza, V. Pinto, V. Kaliveer, B. K. Gopalakrishna, and T. Bhat, "Effect of TiO₂ nanoparticle concentration in Pongamia Pinnata methyl ester on performance and emission characteristics of CI engine", *AIP Conference Proceedings*, vol. 2080, no. 1, pp. 1-6, 2019. <https://doi.org/10.1063/1.5092909>
- [2] J. S. Basha and R. B. Anand, "Performance, emission, and combustion characteristics of a diesel engine using Carbon Nanotubes blended Jatropha Methyl Ester Emulsions", *Alexandria engineering journal*, Vol. 53, no. 2, pp. 259-73, 2014. <https://doi.org/10.1016/j.aej.2014.04.001>
- [3] B. Jogarao, and A. Swarna Kumari, "Biodiesel production using second-generation feedstocks: a review", *Recent Advances in Material Sciences: Select Proceedings of ICLJET 2018*, pp. 693-709, 2019. https://doi.org/10.1007/978-981-13-7643-6_57
- [4] G. R. Kannan, B. Jogarao, and R. Anand, "Improving the low-temperature properties by blending biodiesel with different liquid additives", *Petrotech-2010*, 2010.
- [5] V. V. G. Pradeep, and B. Jogarao, "Production, Performance and Emissions of Bio Diesel from Mixture of Animal Waste Fats and Degradation of Bio Diesel over Time", *International Journal of Innovative Technology and Exploring Engineering*, vol. 9, no. 4, pp. 2676–2681, 2020. <https://doi.org/10.35940/ijitee.d1838.029420>.
- [6] G. Pullagura, S. Vadapalli, P. V.V.S, J. Bikkavolu, and K. R. R. Chebattina, "Parametric study of GNPs nano addition in water diesel

- emulsified fuel on diesel engine at variable injection timings”, *Energy Sources, Part A: Recovery, Utilization, and Environmental Effects*, vol. 45, no. 3, pp. 7262-7279, 2023. <https://doi.org/10.1080/15567036.2023.2220675>
- [7] K. Fangsuwannarak, T. Fangsuwannarak, and Y. Khotbut, “Effect of Nano-TiO₂ Additives Blended in Palm Biodiesel on Compression Ignition Engine Performance”, *Journal of Clean Energy Technologies*, vol. 8, no. 3, pp. 20-23, 2020.
- [8] G. Jayabalaji, and P. Shanmugasundaram, “Effect of titanium dioxide (TiO₂) nano-fluid on performance and emission features of a diesel engine operated on aphanizomenon flos biodiesel-diesel blend”, *In Materials Science Forum*, vol. 969, pp. 421-426, 2019.
- [9] A. Rameshbabu, and G. Senthilkumar, “Emission and performance investigation on the effect of nano-additive on neat biodiesel”, *Energy Sources, Part A: Recovery, Utilization, and Environmental Effects*, vol. 43, no. 11, pp. 1315-28, 2021.
- [10] P. Karthikeyan, and G. Viswanath, “Effect of titanium oxide nanoparticles in tamanu biodiesel operated in a two cylinder diesel engine”, *Materials Today: Proceedings*, vol. 22, pp. 776-80, 2020.
- [11] V. D. Raju, P. S. Kishore, M. H. Kumar, S. R. Reddy, “Experimental investigation of alumina oxide nanoparticles effects on the performance and emission characteristics of tamarind seed biodiesel fuelled diesel engine”, *Materials Today: Proceedings*, vol. 18, pp. 1229-42, 2019.
- [12] V. D. Raju, P. S. Kishore, K. Nanthagopal, and B. Ashok, “An experimental study on the effect of nanoparticles with novel tamarind seed methyl ester for diesel engine applications”, *Energy conversion and management*, vol. 164, pp. 655-666, 2018.
- [13] V. D. Raju, H. Venu, L. Subramani, P.S. Kishore, P.L. Prasanna, and Kumar DV, “An experimental assessment of prospective oxygenated additives on the diverse characteristics of diesel engine powered with waste tamarind biodiesel”, *Energy*, vol. 203, p. 117821, 2020.
- [14] V. D. Raju, P. S. Kishore, and K. Yamini, “Experimental studies on four stroke diesel engine fuelled with tamarind seed oil as potential alternate fuel for sustainable green environment”, *European Journal of Sustainable Development Research*, vol. 2, no. 1, pp. 1-11, 2018.
- [15] M. S. Gad, B. M. Kamel, and I. A. Badruddin, “Improving the diesel engine performance, emissions and combustion characteristics using biodiesel with carbon nanomaterials”, *Fuel*, vol. 288, p. 119665, 2021.
- [16] G. Ramakrishnan, P. Krishnan, S. Rathinam, and Y. Devarajan, “Role of nano-additive blended biodiesel on emission characteristics of the research diesel engine”, *International Journal of Green Energy*, vol. 16, no. 6, pp. 435-41, 2019.
- [17] P. Tamilselvan, N. Nallusamy, and S. Rajkumar. “A comprehensive review on performance, combustion and emission characteristics of

- biodiesel fuelled diesel engines”, *Renewable and Sustainable Energy Reviews*, vol. 79, pp. 1134-59, 2017.
- [18] T. M. Ismail, K. Lu D, Ramzy, M. Abd El-Salam, and M. A. Yu G, Elkady, “Experimental and theoretical investigation on the performance of a biodiesel-powered engine from plant seeds in Egypt, *Energy*, vol. 189, p. 116197, 2019.
- [19] M. E. Soudagar, N. N. Nik-Ghazali, M. A Kalam, I. A. Badruddin, N. R. Banapurmath, and N. Akram, “The effect of nano-additives in diesel-biodiesel fuel blends: A comprehensive review on stability engine performance and emission characteristics”, *Energy Conversion and Management*, vol. 178, pp. 146-77, 2018.
- [20] P. Cremona, T. Rogaume, F. Richard, and B. Batiot, “Application of the Kragten method in order to evaluate the uncertainty of the heat release rate determination using of the cone calorimeter”, *InJournal of Physics: Conference Series*, vol. 1107, no. 3, p. 032019, 2018.
- [21] I. Leito, L. Jalukse, and I. Helm, ”Estimation of measurement uncertainty in chemical analysis (analytical chemistry) course”, *University of Tartu: Tartu, Estonia*, 2018.
- [22] S. K. Masimalai, N. Ganesan, S. Pasupathiraju, and T. Mohanraj, “Investigations on the combined effect of oxygen enrichment and water injection techniques on engine’s performance, emission and combustion of a Mahua oil based compression ignition engine”, *SAE Technical Paper*, 2018.
- [23] A. M. Kumar, M. Kannan, and G. Nataraj, “A study on performance, emission and combustion characteristics of diesel engine powered by nano-emulsion of waste orange peel oil biodiesel”, *Renewable Energy*, vol. 146, pp. 1781-1795, 2020.
- [24] B. Joga Rao, V. Srinivas, K. R. Chebattina, and P. Gandhi, “Effect of injection pressure on the performance and emission characteristics of niger-dieseethanol blends in CI engine”, *Journal of Mechanical Engineering*, vol. 18, no. 3, pp. 77-95, 2021.
- [25] G. Pullagura, S. Vadapalli, V. Varaha Siva Prasad, J. R. Bikkavolu, K. R. R. Chebattina, D. Barik, and M. S. Dennison, “Influence of Dimethyl Carbonate and Dispersant Added Graphene Nanoplatelets in Diesel-Biodiesel Blends: Combustion, Performance, and Emission Characteristics of Diesel Engine”, *International Journal of Energy Research*, vol. 2023, pp. 1-15, 2023. <https://doi.org/10.1155/2023/9989986>.
- [26] G. Pullagura, J. Bikkavolu, S. Vadapalli, K. R. Chebattina, and V. Kuchipudi, “Comparative Study of TiO₂ Nanoparticles and Alcoholic Fuel Additives-Biodiesel-Diesel Blend for Combustion, Performance, and Emission Improvements”, *International Journal of Heat and Technology*, vol. 40, no. 5, pp. 1249-57, 2022. <https://doi.org/10.18280/ijht.400517>.

- [27] L. Prabhu, S. S. Kumar, A. Anderson, and K. Rajan, "Investigation on performance and emission analysis of TiO₂ nanoparticle as an additive for biodiesel blends", *Journal of Chemical and pharmaceutical Sciences, Special*, vol. 7, pp. 408-412, 2015.
- [28] M. Annamalai, B. Dhinesh, K. Nanthagopal, P. SivaramaKrishnan, J. I. Lalvani, M. Parthasarathy, and K. Annamalai, "An assessment on performance, combustion and emission behavior of a diesel engine powered by ceria nanoparticle blended emulsified biofuel", *Energy conversion and management*, vol. 123, pp. 372-380, 2016.
- [29] M. K. Parida, P. Mohapatra, S. S. Patro, and S. Dash, "Effect of TiO₂ nano-additive on performance and emission characteristics of direct injection compression ignition engine fueled with Karanja biodiesel blend", *Energy Sources, Part A: Recovery, Utilization, and Environmental Effects*, pp. 1-10, 2020. <https://doi.org/10.1080/15567036.2020.1756991>
- [30] R. Dsilva, S. Rolvin, and B. Thirumaleshwara, "Comparative study of pongamia biodiesel blends with titanium dioxide nanoadditives on performance parameters of ci engine", *Journal of critical reviews*, vol. 10, pp. 3238-3244, 2020.
- [31] J. R. Bikkavolu, S. Vadapalli, K. R. R. Chebattina, and G. Pullagura, "Effects of stably dispersed carbon nanotube additives in yellow oleander methyl ester-diesel blend on the performance, combustion, and emission characteristics of a CI engine", *Biofuels*, pp. 1-14, 2023. <https://doi.org/10.1080/17597269.2023.2216962>
- [32] E. Buyukkaya, "Effects of biodiesel on a DI diesel engine performance, emission and combustion characteristics", *Fuel*, vol. 89, no. 10, pp. 3099-3105, 2010.
- [33] P. McCarthy, M. G. Rasul, and S. Moazzem, "Analysis and comparison of performance and emissions of an internal combustion engine fuelled with petroleum diesel and different bio-diesels", *Fuel*, vol. 90, no. 6, pp. 2147-2157, 2011.
- [34] A. K. Pandian, B. B. R. Ramesh, and D. Yuvarajan, "Emission analysis on the effect of nanoparticles on neat biodiesel in unmodified diesel engine", *Environmental Science and Pollution Research*, vol. 24, no. 29, pp. 23273-23278, 2017.
- [35] A. Praveen, R. L. Krupakaran, G. Lakshmi Narayana Rao, and B. Balakrishna, "An assessment of the TiO₂ nanoparticle concentration in the C. inophyllum biodiesel blend on the engine characteristics of a DI diesel engine", *International Journal of Ambient Energy*, vol. 43, no. 1, pp. 5464-5477, 2022.
- [36] A. Prabu, and R. B. Anand, "Emission control strategy by adding alumina and cerium oxide nano particle in biodiesel", *Journal of the energy institute*, vol. 89, no. 3, pp. 366-372, 2016.

- [37] G. Pullagura, J. Bikkavolu, S. Vadapalli, V. V. Prasad, and K. R. Chebattina, "The effect of graphene nanoplatelets on Physico-chemical properties of Sterculia foetida biodiesel-diesel fuel blends", *Materials Today: Proceedings*, pp. 1-9, 2023. <https://doi.org/10.1016/j.matpr.2023.01.173>.
- [38] R. S. Sandhi, K. R. R. Chebattina, N. R. Sambana, S. Vadapalli, G. Pullagura, and U. C. Pathem, "Evaluation of TiO₂ Nanoparticles as an Additive in Diesel-n-Butanol-Bombax Ceiba Biodiesel Blends for Enhance Performance and Emissions Control of a CI Engine", *International Journal of Heat and Technology*, vol. 39, no. 6, pp. 1930-1936, 2021.
- [39] G. Pullagura, S. Vadapalli, P. VVS, and K. R. Rao Chebattina, "Effect of dispersant added graphene nanoplatelets with diesel–Sterculia foetida seed oil biodiesel blends on diesel engine: engine combustion, performance and exhaust emissions", *Biofuels*, vol. 1, no. 12, pp. 461-472, 2022. <https://doi.org/10.1080/17597269.2022.2148876>
- [40] G. Pullagura, S. Vadapalli, V. V. S. Prasad, S. V. Datla, A. J. S. Makkena, A. S. R. Chilla, and K. R. R. Chebattina, "Aluminum Oxide as Potential Additives to N-Butanol-Diesel Blends on Emission and Performance Characteristics of the Diesel Engine", *In Recent Advances in Thermal Sciences and Engineering: Select Proceedings of ICAFFTS*, pp. 241-256, 2021. https://doi.org/10.1007/978-981-19-7214-0_20
- [41] G. Pullagura, S. Vadapalli, V. V. S. Prasad, V. Velisala, K. R. R. Chebattina, and A. R. Mohammad, "A Comprehensive Review on Nano-additives for the Enrichment of Diesel and Biodiesel Blends for Engine Applications", *Recent Advances in Thermal Sciences and Engineering: Select Proceedings of ICAFFTS 2021*, pp. 187-206, 2023. https://doi.org/10.1007/978-981-19-7214-0_16

Performance of Hybrid $\text{Al}_2\text{O}_3\text{:SiO}_2$ W:EG in PEM Fuel Cell Distributor Plate

Muhammad Syafiq Idris, Irnie Azlin Zakaria*, Putri Nur Afiqah Nazari,
Wan Ahmad Najmi Wan Mohamed

School of Mechanical Engineering, College of Engineering,
Universiti Teknologi MARA (UiTM), 41450 Shah Alam, Selangor,
MALAYSIA

*irnieazlin@uitm.edu.my

Wan Azmi Wan Hamzah

Faculty of Mechanical and Automotive Engineering Technology,
Universiti Malaysia Pahang, Pekan 26600, MALAYSIA

ABSTRACT

Efficient thermal management is essential for the optimal performance and durability of the Proton Exchange Membrane Fuel Cell (PEMFC). However, the conventional passive cooling methods require a larger heat exchanger for better heat dissipation. Alternatively, nanofluids as a coolant have gained attention recently due to their enhanced heat transfer properties. This investigation aims to evaluate the thermal performance of hybrid nanofluids in a distributor type of PEMFC cooling plate. In this investigation, 0.5% volume concentration of mono Al_2O_3 , mono SiO_2 nanofluids, and hybrid $\text{Al}_2\text{O}_3\text{:SiO}_2$ nanofluids with a mixture ratio of 10:90, 30:70, 50:50, and 70:30 in 60:40 W:EG were investigated. The cooling plate was modelled and a fixed heat flux of 6500 w/m^2 was applied to replicate the actual working parameter of PEMFC. The study shows that the heat transfer coefficient was improved by 61% in 10:90 hybrid nanofluids of $\text{Al}_2\text{O}_3\text{:SiO}_2$ in W:EG in comparison to the base fluid. Meanwhile, the accompanied pressure drops in 10:90 hybrid nanofluids of $\text{Al}_2\text{O}_3\text{:SiO}_2$ in W:EG show a reduction up to 4.38 times lower as compared to single Al_2O_3 nanofluids at Re 1800. This is advantageous since it will reduce the parasitic loss related to the PEM fuel cell.

Keywords: Hybrid Nanofluids; Heat Transfer Enhancement; Pressure Drop; PEMFC

Introduction

The urge for a reduction in dependency on fossil fuel sources has become a global direction nowadays. The depletion of fossil fuel and the carbon footprint increment has driven the direction for a renewable energy source. Hence, there is a rising trend in the adoption of alternative energy to replace current conventional internal combustion engines (ICE) with renewable energy sources as outlined by the government plan [1]. Among the potential candidates of renewable energy in the primary energy mix is hydrogen, H_2 . A fuel cell is a device that generates electrical energy from the reaction of hydrogen and oxygen via an electrochemical reaction [2]. PEM fuel cells are advantageous because of their high power density, rapid startup, and dynamic load response [3]. The lower operating temperature of PEM fuel cells which is in the range of 60 °C to 80 °C has attracted researchers in various applications including automotive, small-scale stationary power generation, and portable power applications [4]. Its higher efficiency of 60% as compared to 20% to 30% in internal combustion engines has also added value to the PEM fuel cell [5].

However, despite the advantages, the PEM fuel cell comes with one critical flaw. PEM fuel cell operates at low temperature which is at 60 °C to 80 °C provides a low driving force to remove excessive heat out of the system. This in turn will cause the accumulation of heat in the system that will affect the hydration of the most critical part of the PEM fuel cell which is the membrane electrodes assembly (MEA). An efficient heat transfer is crucially needed in PEM fuel cells to maintain the optimum condition of the membrane thus ensuring its optimal performance [3].

There are various heat removal methods for PEM fuel cells such as adaptation of larger heat exchangers and improvement in MEA material. However, these methods increase the existing cost and require a bigger package for the cooling system [6]-[8]. Yong et al. [9] reviewed cooling strategies for a large-scale PEM fuel cell while Liu et al. [10] discovered phase change cooling coupled with waste heat recovery for PEM fuel cell. In addition to that, passive cooling is also explored that enhances the coolant thermal-physical properties termed nanofluids. This passive cooling is doable for adoption in a liquid-cooled PEM fuel cell with the possibility of heat exchanger size reduction [11].

Nanofluid base fluids containing a dispersion of nano-sized particles have been shown to improve cooling liquids' thermal conductivity [12]. There are several studies done by researchers on the capability of nanofluids in increasing thermal conductivity namely Islam et al. [13] who mentioned that type and concentration of nanoparticles in nanofluids is the main factor that determines the thermal conductivity of nanofluids. An experimental work by Zakaria et al. [14]-[15] reported that there is an improvement of thermal and electrical conductivity up to 12.8% and 14.3%, respectively with the adoption

of Al_2O_3 nanofluids as compared to water as the base fluid. In addition to that, numerical work performed by Zakaria et al. [16] mentioned that Al_2O_3 nanofluids in her study have intensified the heat transfer up to 37% as compared to the base fluid. An experimental study by Khalid et al. [17] also reported an increase in thermal conductivity of up to 4.19% and 1.42% for Al_2O_3 and SiO_2 , respectively, as compared to the water. However, the implementation of nanofluids as a coolant comes with a penalty of higher pressure drop due to its high viscosity value as compared to the base fluid which eventually required higher pumping power to force the coolant around the cooling circuit [18].

The nanofluids study has progressed from mono nanofluids to hybrid and eventually ternary nanofluids, which further improve the thermo-physical properties of the base fluid [19]. The nanofluids are prepared either from single or two-step methods where two or more nanoparticles were dispersed in a base fluid. Esfe and Afrand [20] reviewed that hybrid nanofluids enhance thermal conductivity better than mono nanofluids. However, this was further investigated by Khalid et al. [21], using Al_2O_3 and SiO_2 hybrid nanofluids in PEM fuel cells. The study reported that hybrid nanofluids increase thermal conductivity up to 51.9% but only at certain mixture ratios. In the hybrid Al_2O_3 : SiO_2 water study, a lower ratio of Al_2O_3 is preferred since it enhances the heat transfer as compared to single nanofluids but not at the higher mixture ratio of Al_2O_3 . Experimental work by Sahid et al. [22] on TiO_2 : ZnO nanoparticles concluded that thermal conductivity increased as the volume concentration increased. A numerical study on hybrid nanofluids was also conducted by Idris et al. [23] for 10:90 and 50:50 ratios of hybrid Al_2O_3 : SiO_2 nanofluid in water base fluid and concluded that the most feasible fluid is hybrid 10:90 Al_2O_3 : SiO_2 nanofluids base on heat transfer and pressure drop effect.

In liquid-cooled PEM fuel cells, there are several types of cooling plates such as parallel, serpentine, and distributor type as reported by Ramos-Alvarado et al. [24]. The findings suggested that distributor type is the most recommended design for liquid-cooled because it achieved outstanding flow consistency while maintaining a remarkably low-pressure loss. In the designs of cooling plates in PEM fuel cells, mini channels were adopted as they allowed a closed-packed stack with higher heat transfer rates and lower cell temperatures. However, for the adoption of nanofluids in mini channels, there are some concerns about the additional pumping power requirement to be weighed out with the enhancement in heat transfer [25]. Apart from this, possible leakage of current produced needs to also be monitored as demonstrated by Zakaria et al. [7], [26] due to the strict limit of electrical conductivity which is $5 \mu\text{S}/\text{cm}^2$ permissible for PEM fuel cell [27].

The effect of Al_2O_3 : SiO_2 nanofluids in water has been studied previously in distributor cooling plates [28]. Al_2O_3 and SiO_2 are preferred due to the vast availability of the nanoparticles in the current market. The stability

of this hybrid combination is also proven to be excellent and suitable for a closed-loop cooling circuit application [29]. However, no study has been reported on Al₂O₃:SiO₂ hybrid nanofluids in a mixture of water:Ethylene Glycol (60:40) which is commonly used in automotive as a coolant. In this work, a distributor cooling plate was modelled and heated up by a constant heat flux of 6500 W/m² to replicate the heat generation during the reaction in actual PEM fuel cell operation [6]. The performance of the hybrid Al₂O₃:SiO₂ nanofluids in terms of heat transfer enhancement and pressure drop against base fluid, single 0.5% Al₂O₃ nanofluids, and single 0.5% SiO₂ nanofluids in distributor cooling plate of PEMFC was observed. This study is essential as it will cover a wider range of base fluids studied for hybrid Al₂O₃:SiO₂ nanofluids. The application of cooling plates is not restricted to PEM fuel cells alone, it can be adopted in any type of cooling application such as electronics heat sinks as well.

Methodology

Thermo-physical properties

The properties of nanofluids used in this study were experimentally measured using a KD2 Pro Thermal analyser for thermal conductivity and Brookfield Rheometer for dynamic viscosity. In addition to that, the density of mono nanofluids and hybrid nanofluids was calculated using Equation (1) and Equation (2) while specific heat for mono nanofluids and hybrid nanofluids was estimated from Equation (3) and Equation (4) as listed below [30]:

$$\rho_{nf} = (1 - \emptyset)\rho_f + \emptyset\rho_p \quad (1)$$

$$\rho_{hnf} = (1 - \emptyset)\rho_f + \emptyset_{p_1}\rho_{p_1} + \emptyset_{p_2}\rho_{p_2} \quad (2)$$

$$C_p = \frac{(1 - \emptyset)\rho_f C_f + \emptyset\rho_p C_p}{\rho_{nf}} \quad (3)$$

$$C_p = \frac{(1 - \emptyset)\rho_f C_f + \emptyset_{p_1}\rho_{p_1} C_{p_1} + \emptyset_{p_2}\rho_{p_2} C_{p_2}}{\rho_{hnf}} \quad (4)$$

where \emptyset refers to particle volume fraction and subscripts f , p_1 , p_2 , n_f , and h_{nf} refer to base fluid (water:EG), first nanoparticle (Al₂O₃), second nanoparticle (SiO₂), nanofluids, and hybrid nanofluids. All properties of nanoparticles and base fluid used are listed in Table 1.

The thermal conductivity of the nanofluids was measured using the KD2 Pro thermal property analyser from Decagon Devices Inc., the United

States. Meanwhile, the dynamic viscosity measurement was performed using Brookfield LVDV-III Ultra Rheometer as shown in Figure 1.

Table 1: Properties of the base fluid and nanoparticles used in the study

Fluid name	Density ρ , (kg/m^3)	Specific heat C_p , (J/kg.K)	Thermal conductivity k , (W/m.K)	Viscosity μ , (Pa.s)	Ref.
W:EG (60:40)	1056.7	3419.8	0.4096	0.002400	[31]-[32]
Al_2O_3	1071.4	3440.9	0.412	0.003500	[23]
SiO_2	1062.5	3463.1	0.411	0.003200	[30], [33]



(a)



(b)

Figure 1: (a) KD2 Pro thermal property analyser, and (b) Brookfield LVDV-III Ultra Rheometer

Modeling and simulation of PEM fuel cell cooling plate

The geometry of the cooling plate was designed using CATIA V5R20 software where the heater pad and the fluid flow model were also attached to the PEM fuel cell cooling plate. The model is an assembly of the distributor cooling plate, attached to a heater pad as shown in Figure 2 while the channel's cross-sectional detailed dimensions are shown in Figure 3 and Table 2. The cooling plate was modelled as a carbon graphite cooling plate. The bottom surface of the plate was subjected to a fixed temperature of 343 K with a constant heat flux of 6500 w/m^2 . The silicon heater pad was used to replicate the real application of the PEM fuel cell. The heat generated was conducted through the graphite cooling plate and rejected to the moving fluid that passes through the mini channel. The circulation of cooling fluid is performed through close-loop forced convection.

Several assumptions were made to simplify the simulation [28] as follows:

- i. Viscous dissipation was disregarded, and fluid properties remain constant.
- ii. The flow was in a steady state, laminar, and incompressible.
- iii. The impact of body force was disregarded.
- iv. The resulting combination can be thought of as a typical single phase, and both the fluid phase and the nanoparticles had zero relative velocities while in thermal equilibrium.
- v. Laminar flow was assumed in this mini-channel analysis as being practiced by other mini-channel researchers in their studies [34]-[35].

Based on the assumptions made beforehand, the governing equations used in this study were as follows [23]:

Continuity equation:

$$\nabla \cdot (\rho_{nf} \cdot V_m) = 0 \quad (5)$$

Momentum equation:

$$\nabla \cdot (\rho_{nf} \cdot V_m \cdot V_m) = -\nabla P + \nabla \cdot (\mu_{nf} \cdot \nabla V_m) \quad (6)$$

Cooling fluid's Energy equation:

$$\nabla \cdot (\rho_{nf} \cdot C \cdot V_m \cdot T) = \nabla \cdot (k_{nf} \cdot \nabla T) \quad (7)$$

Heat conduction through graphite cooling plate:

$$0 = \nabla \cdot (k_s \cdot \nabla T_s) \quad (8)$$

No slip boundary at the wall:

$$\vec{V} = 0(\text{at walls}) \quad (9)$$

The boundary condition at the inlet of the plate is assumed as;

$$\vec{V} = 0(\text{at walls}) \quad (10)$$

P = standard atmospheric pressure at outlet (11)

$$-k_{nf} \cdot \nabla T = q''(\text{at bottom of mini channel}) \quad (12)$$

$$-k_{nf} \cdot \nabla T = 0(\text{at top of mini channel}) \quad (13)$$

Grid independence test

The distributor-typed cooling plate was initially meshed for the simulation work as shown in Figure 4. The grid independence test was performed to optimize the selection of meshing element requirements. The optimized meshing element selected for simulation is 2731324 as shown in Figure 5. In this figure, average plate temperature was observed as it is one of the critical data gained from the simulation. It was noticed that the average plate temperature started to get constant at 2731324 meshing elements and it continued to remain constant until the value of 3061419 meshing elements.

Therefore, the optimized meshing element of 2731324 was chosen for the complete simulation work. Lower meshing elements than this will cause inaccurate results meanwhile higher meshing elements will increase the simulation lead time but still arrive at the same result accuracy [7], [36].

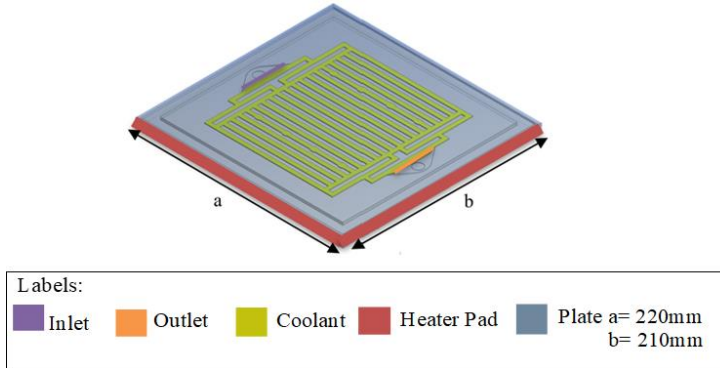


Figure 2: Distributor cooling plate of PEM fuel cell in isometric view

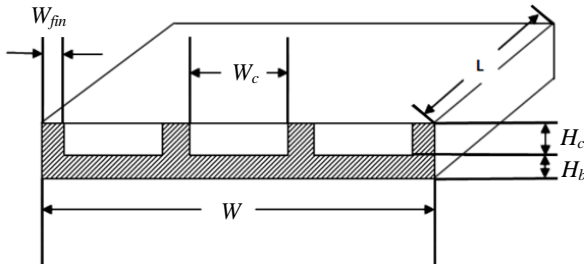


Figure 3: Cross section on the channel in the distributor cooling plate

Table 2: Detailed dimensions of the channel in the distributor cooling plate

Parameter	Diameter (mm)
W_{fin}	1
W_c	4
W	148
L	112
H_c	1
H_b	3

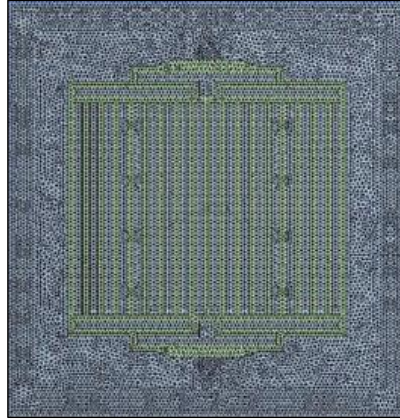


Figure 4: Meshing of distributor typed cooling plate of PEM fuel cell

Mathematical model

The heat transfer coefficient of the hybrid $\text{Al}_2\text{O}_3:\text{SiO}_2$ nanofluids and Nusselt number were calculated using Equation (14) and Equation (15), respectively. The average heat transfer coefficient, h_{ave} and Nu_{ave} calculation adopted the same mathematical equation as practiced by other researchers in this field [7], [37]-[38].

$$h_{ave} = \frac{\dot{q}}{(T_{avgplate} - T_{avgfluid})} \quad (14)$$

$$Nu_{ave} = \frac{hD_i}{k_{nf}} \quad (15)$$

The fluid flow parameter was calculated from the pressure drop and pumping power values. The pressure difference between the inlet and outlet flow was calculated using Equation (16) while the pumping power was calculated from Equation (17) [7].

$$\Delta P = P_i - P_o \quad (16)$$

$$W_{pump} = \dot{V}\Delta P \quad (17)$$

where \dot{q} , P_i , P_o , D_i , and \dot{V} was referred to as heat flux, inlet pressure, outlet pressure, inlet diameter, and volume flow rate.

Results and Discussion

Thermo-physical properties

The experimentally measured critical thermos-physical properties of hybrid $\text{Al}_2\text{O}_3:\text{SiO}_2$ nanofluids at various mixture ratios at ambient room temperature of $30\text{ }^\circ\text{C}$ are shown in Table 3. It is shown that the highest thermal conductivity of hybrid $\text{Al}_2\text{O}_3:\text{SiO}_2$ nanofluids is at 10:90 ($\text{Al}_2\text{O}_3:\text{SiO}_2$) with 0.432 W/m.K which was equivalent to 4.85% improvement as compared to its base fluid of 60:40 water:EG. This was then followed by 30:70 and 50:50 mixture ratios accordingly. It was observed that the higher value of Al_2O_3 has resulted in a lower thermal conductivity value which agrees with the findings by Khalid et al. [21].

Meanwhile, dynamic viscosity values show the highest value experienced by the 70:30 ($\text{Al}_2\text{O}_3:\text{SiO}_2$) ratio while the lowest viscosity value is at 10:90 of the mixture ratio at $30\text{ }^\circ\text{C}$. Other than thermal conductivity and dynamic viscosity, specific heat capacity and density were also determined prior to Ansys simulation analytically.

Table 3: Thermo-physical properties of hybrid nanofluids used in the simulation

Material: $\text{Al}_2\text{O}_3:\text{SiO}_2$ in 60:40 (W:EG)	Density (kg/m^3)	Specific heat capacity (J/kg.K)	Thermal conductivity (W/m.K)	Viscosity (Pa.s)
10:90	1063.422	3460.820	0.432	0.002826
30:70	1065.202	3456.368	0.428	0.002900
50:50	1066.982	3451.930	0.418	0.003039
70:30	1068.762	3447.507	0.413	0.004624

Validation of the simulation

Validation work to ensure the accuracy of the simulation data against established data published in the literature review was executed before the full simulation work. The distributor cooling plates simulation was validated against the work of Zakaria et al. [39] which used a similar base fluid of water:EG (60:40) mixture. There was a deviation range of 0.08% to 6.39% observed as compared to the established work as depicted in Figure 5. The small deviation showed that the parameters used in the simulation were accurate and fit for further analysis.

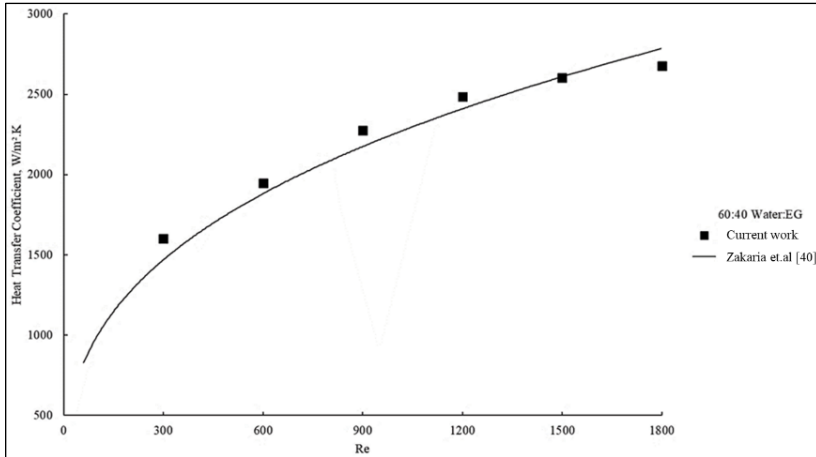


Figure 5: Validation of simulation data with published experimental work [39]

Effect on heat transfer

Average plate temperature

The initial data recorded in the effect of heat transfer is the cooling plate's temperature. Different types of cooling fluids passing through the cooling channel will result in different average temperatures as shown in Figure 6. The increment in the fluid flow rate also affected the plate temperature. As shown in Figure 6, the temperature of the plate depreciated as the Re number increased. This is a known relationship due to better cooling performance achieved at nanofluids' higher flow rate [8]. At Re 1800, 10:90 ($Al_2O_3:SiO_2$) hybrid nanofluids demonstrated the lowest plate temperature with a 1.5% reduction over water:EG mixture. This was subsequently followed by 30:70, 70:30, and 50:50 ($Al_2O_3:SiO_2$) hybrid nanofluids with 1.37%, 1.36%, and 1.20%, respectively as compared to the base fluid. Both mono nanofluids of Al_2O_3 and SiO_2 had the least reduction with 1.11% and 0.72%, respectively in comparison to the base fluid's plate temperature. The outstanding improvement in hybrid nanofluids' thermal conductivity has resulted in the improvement in the cooling plate temperature reduction in comparison to the base fluid. It was also noticed that the smaller ratio content of Al_2O_3 in a specific $Al_2O_3:SiO_2$ mixture of hybrid nanofluids has resulted in a better temperature of distributor cooling plate. The thermal conductivity value of the smaller fraction of Al_2O_3 ratio in $Al_2O_3:SiO_2$ hybrid nanofluids has shown higher values as compared to a higher fraction of Al_2O_3 as reported by Khalid et al. [22] as his novel findings.

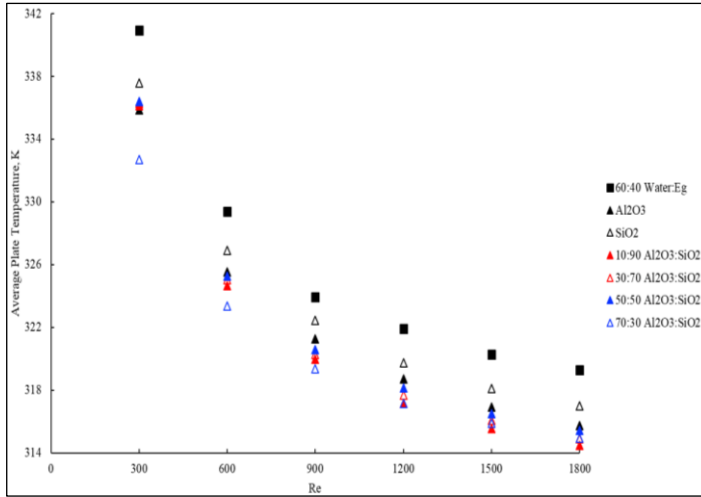


Figure 6: Effect of distributor cooling plate temperature with hybrid $\text{Al}_2\text{O}_3:\text{SiO}_2$ nanofluids, mono nanofluids, and base fluid of water:EG

Temperature contour

The effect of improvement in heat transfer was visualized graphically through the dispersion of plate temperature of base fluid W:EG, mono Al_2O_3 nanofluids, mono SiO_2 nanofluids, and four different ratios of hybrid $\text{Al}_2\text{O}_3:\text{SiO}_2$ nanofluids across the distributor typed cooling plate as depicted in Figure 7. The temperature contour was observed at the same Re 1800 for all working cooling fluids. It was observed that there was a reduction of hot spot area in cooling plates in single and hybrid $\text{Al}_2\text{O}_3:\text{SiO}_2$ nanofluids in comparison to base fluid. This might be due to lower cooling plate temperature contributed by the higher value of thermal conductivity of fluids flowing inside the plate. Higher thermal conductivity value of fluids resulting better heat transfer thus minimizing the hot spot area. The plate temperature reduction is also observed in single and hybrid $\text{Al}_2\text{O}_3:\text{SiO}_2$ nanofluids cooling plates.

Heat transfer coefficient

The cooling plate temperature reduction serves as a basis for further investigation on the improvement of heat transfer due to the hybrid $\text{Al}_2\text{O}_3:\text{SiO}_2$ nanofluids. The improvement of heat transfer coefficients for the distributor-typed cooling plate is shown in Figure 8. Overall, nanofluids' heat transfer coefficient significantly increased in hybrid nanofluids in comparison to water:EG base fluid. The linear increment of the heat transfer coefficient was also observed as the Re number was increased. The hybrid 10:90 ($\text{Al}_2\text{O}_3:\text{SiO}_2$) nanofluids gave the highest enhancement with 61.36% enhancement in comparison to the base fluid, recorded at Re 1800. The trend was subsequently

followed by 30:70 ($\text{Al}_2\text{O}_3:\text{SiO}_2$), 50:50, and 70:30 hybrid nanofluids with 50.79%, 43.46%, and 38.58% enhancement, respectively. The lower percentage concentration of Al_2O_3 nanofluids in the hybrid nanofluids ratio showed better heat transfer performance since these ratios have better thermal conductivity value than higher ratios of Al_2O_3 nanofluids which is aligned with the highlights by Khalid et. al [21]. Meanwhile, the performance of its mono Al_2O_3 nanofluids and SiO_2 nanofluids have shown slightly smaller improvement of 6.73% and 3.61% enhancement, respectively in comparison to base fluid at Re 1800. A smaller increment was noticed in mono nanofluids as compared to hybrid nanofluids due to a smaller enhancement in the thermal conductivity of mono nanofluids and base fluid as compared to hybrid nanofluids studied [21], [30]. A similar effect of Re number increment was also noticed in the heat transfer coefficient value as well. The heat transfer coefficient increased linearly as the flowrate was increased.

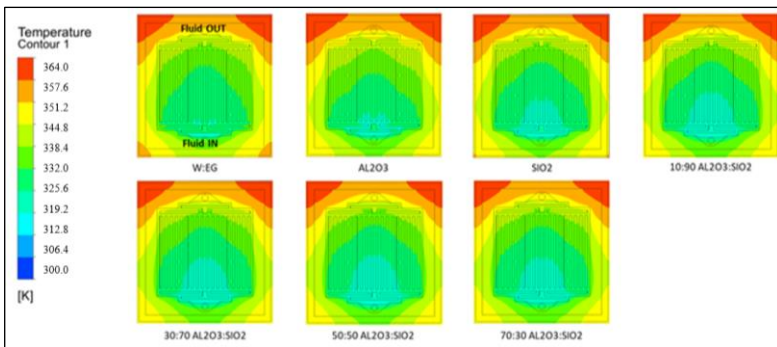


Figure 7: Distributor typed cooling plate's temperature contour

Nusselt number

The non-dimensionalized Nusselt (Nu) number was presented to show the heat transfer enhancement. The Nu number has shown a linear increment with regards to the increment in the Re number as expected. This was presented in Figure 9. The 10:90 ($\text{Al}_2\text{O}_3:\text{SiO}_2$) hybrid nanofluids showed with highest Nusselt number and subsequently followed by 30:70 ($\text{Al}_2\text{O}_3:\text{SiO}_2$), 50:50, and 70:30 hybrid nanofluids. There was also an increase in the Nu number of mono nanofluids of Al_2O_3 and SiO_2 nanofluids, but the increment was not as significant as the hybrid $\text{Al}_2\text{O}_3:\text{SiO}_2$ gave. The highest Nu number was shown by a 10:90 ratio which indicated that the 10:90 ($\text{Al}_2\text{O}_3:\text{SiO}_2$) has a greater convective heat transfer effect across the boundary as compared to the conductive heat transfer effect [40]. The 0.5 vol% concentration of hybrid $\text{Al}_2\text{O}_3:\text{SiO}_2$ in water:EG mixture enhanced the Nu number by up to 61.36% due to the increment in the convective heat transfer characteristic over conductive heat transfer.

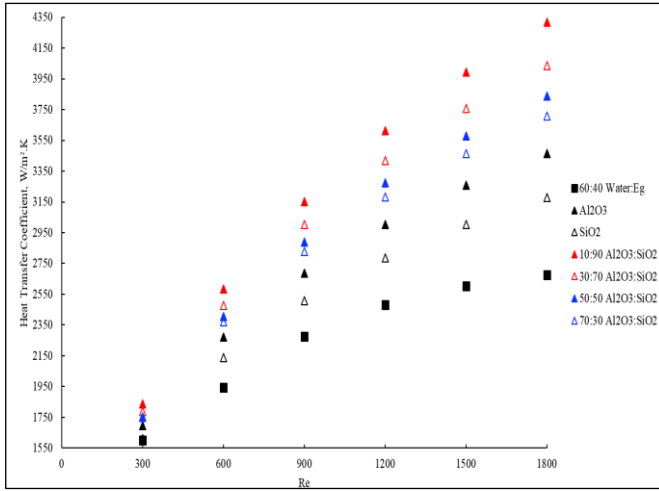


Figure 8: Performance of heat transfer coefficient in hybrid Al₂O₃:SiO₂ nanofluids, mono nanofluids, and base fluid of water:EG in distributor cooling plate

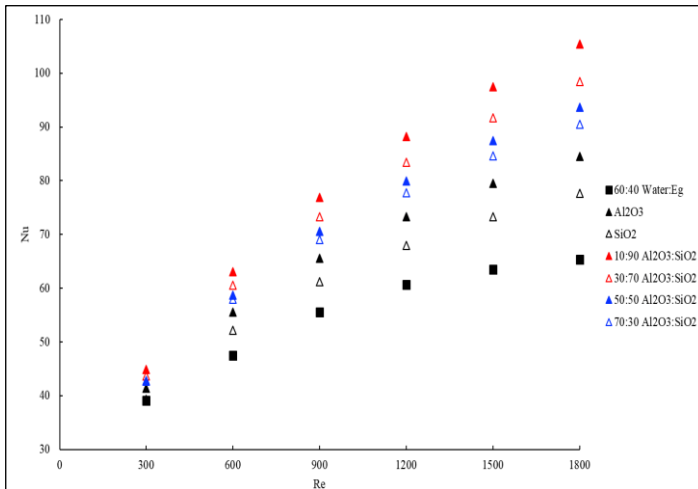


Figure 9: Distributor cooling plate Nusselt number against *Re* number

Fluid flow behaviour

As for fluid flow behaviour of hybrid Al₂O₃:SiO₂ nanofluids, mono nanofluids, and base fluid, pressure drop was recorded and translated to the pumping power effect.

Pressure drop

The pressure drop measures the difference in pressure readings between the plate's inlet and outlet. This was recorded to investigate the effect of hybrid nanofluids on the additional fluid flow required. The pressure drop readings are shown in Figure 10. Higher pressure drop was predicted as the hybrid nanofluids have higher dynamic viscosity and density in comparison to the base fluid. Moreover, the distributor plate's geometry which has sharp bends and narrow channels has made the liquid harder to circulate around the plate. The highest-pressure drop was shown by mono Al_2O_3 nanofluids which is 3 times higher followed by the mono SiO_2 nanofluids of twice higher than the base fluid respectively at Re 1800. The 70:30 (Al_2O_3 : SiO_2) was second with 128.18% and then followed by 50:50, 30:70, and 10:90 hybrid nanofluids with 115.24 %, 91.92%, and 82.13%, respectively. The result of the 10:90 mixture ratio has shown the lowest pressure drop in comparison to other mixture ratios of hybrid nanofluids which is favourable to the application. This is an interesting finding as 10:90 (Al_2O_3 : SiO_2) hybrid nanofluids showed to be the most potential candidate for PEM fuel cell cooling fluid due to its highest heat transfer enhancement but also the least impactful to the pressure drop penalty. This was due to its lower viscosity value as compared to other mixture ratios of hybrid nanofluids which has impacted such higher pressure drop [30]. This matched well with the outcomes of Khalid et al. [14] who also reported that the 10:90 ratio in water has a minimal effect on pressure drop but at a preferable heat transfer improvement in comparison to others.

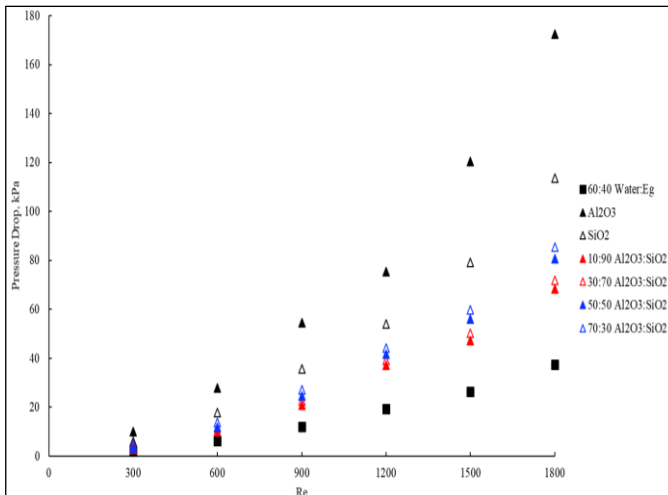


Figure 10: Comparison of pressure drop in hybrid Al_2O_3 : SiO_2 nanofluids with respect to other fluids in distributor cooling plate

Pumping power

The effect of the pressure difference between the outlet and inlet of the fluid was then translated to the increase in power needed to circulate the hybrid cooling fluids around the cooling system. Figure 11 shows the increase in pumping power with the implementation of hybrid cooling fluids. As the base fluid has lower density and viscosity values, these have resulted in lower pressure drop as compared to both hybrid nanofluids and single nanofluids. To cope with the additional pressure drop penalty, additional pumping power needs to be supplied to the hybrid nanofluid system. In the PEM fuel cell distributor cooling plate, mono Al_2O_3 nanofluids, a 70:30 ratio of hybrid nanofluids and mono SiO_2 nanofluids required among the higher pumping power which was 6.73 W, 4.01 W, and 3.61 W, respectively in comparison to water:EG base fluid of 1.23 W at Re 1800. This was followed by hybrid 50:50, 30:70, and finally 10:90 (Al_2O_3 : SiO_2) with 2.02 W, 1.55 W, and 1.34 W higher than W:EG (60:40), respectively. Nevertheless, the increase in pumping power required is considered low compared to the stack performance of at least 1 kWe.

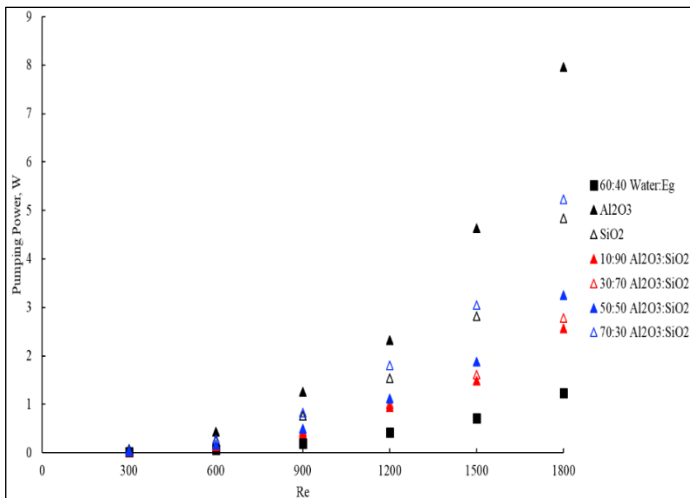


Figure 11: Effect on pumping power requirement of hybrid Al_2O_3 : SiO_2 nanofluids against single nanofluids and base fluid in distributor cooling plate

Conclusions

In this simulation work, it was concluded that there was a heat transfer enhancement experienced with the adoption of hybrid $\text{Al}_2\text{O}_3:\text{SiO}_2$ nanofluids mixture ratios of 10:90, 30:70, 50:50, and 70:30 in water: Ethylene Glycol (60:40) as a cooling fluid in PEMFC. The highest improvement was recorded with 61% enhancement in the convective heat transfer coefficient and Nusselt number with 10:90 $\text{Al}_2\text{O}_3:\text{SiO}_2$ hybrid nanofluids in W:EG (60:40) as compared to its base fluid. However, the higher pressure drop analysis was also experienced with hybrid nanofluids adoption but interestingly the 10:90 $\text{Al}_2\text{O}_3:\text{SiO}_2$ hybrid nanofluids in W:EG (60:40) was favourable due to its capability of reducing the pressure drop effect by 4.38 times lower as compared to the single Al_2O_3 nanofluids. It was shown that 10:90 ($\text{Al}_2\text{O}_3:\text{SiO}_2$) hybrid nanofluids have the most advantageous adoption compared to other candidates in terms of both heat transfer and pressure drop in the distributor cooling plate of the PEM fuel cell.

Contributions of Authors

The authors confirm the equal contribution in each part of this work. All authors reviewed and approved the final version of this work.

Funding

This work was supported by the “Geran Insentif Penyelidikan, Universiti Teknologi MARA(UiTM)” [600-RMC/GIP 5/3 (154/2021)] and College of Engineering, Universiti Teknologi MARA (UiTM) Shah Alam, Selangor, Malaysia

Conflict of Interests

All authors declare that they have no conflicts of interest

Acknowledgment

The author would like to thank Universiti Teknologi MARA (UiTM) under Geran Insentif Penyelidikan, [600-RMC/GIP 5/3 (154/2021)] and also College of Engineering, Universiti Teknologi MARA (UiTM) Shah Alam, Selangor, Malaysia on the financial supports given.

References

- [1] E. P. Unit and P. M. s. Department, "National Energy Policy, 2022-2040", 2022.
- [2] Y. Yu, M. Chen, S. Zaman, S. Xing, M. Wang, and H. Wang, "Thermal management system for liquid-cooling PEMFC stack: From primary configuration to system control strategy", *eTransportation*, vol. 12, p. 100165, 2022.
- [3] T. Wilberforce, A. G. Olabi, I. Muhammad, A. Alaswad, E. T. Sayed, A. G. Abo-Khalil, et al., "Recovery of waste heat from proton exchange membrane fuel cells – A review", *International Journal of Hydrogen Energy*, In-press, 2022. <https://doi.org/10.1016/j.ijhydene.2022.08.069>
- [4] F. Barbir, *PEM Fuel Cells : Theory and Practice*, 2005.
- [5] S. H. Yua, S. Sohna, J. H. Namb, and C.-J. Kima, "Numerical study to examine the performance of multi-pass serpentine flow-fields for cooling plates in polymer electrolyte membrane fuel cells", *Journal of Power Sources* vol. 194, pp. 697-703, 2009.
- [6] I. Zakaria, W. A. N. W. Mohamed, W. H. Azmi, A. M. I. Mamat, R. Mamat, and W. R. W. Daud, "Thermo-electrical performance of PEM fuel cell using Al₂O₃ nanofluids", *International Journal of Heat and Mass Transfer*, vol. 119, pp. 460-471, 2018.
- [7] I. A. Zakaria, W. A. N. W. Mohamed, N. H. A. Azid, M. A. Suhaimi, and W. H. Azmi, "Heat transfer and electrical discharge of hybrid nanofluid coolants in a fuel cell cooling channel application", *Applied Thermal Engineering*, vol. 210, p. 118369, 2022.
- [8] M. Saeedan, E. Afshari, and M. Ziaei-Rad, "Modeling and optimization of turbulent flow through PEM fuel cell cooling channels filled with metal foam- a comparison of water and air cooling systems", *Energy Conversion and Management*, vol. 258, p. 115486, 2022.
- [9] Z. Yong, H. Shirong, J. Xiaohui, Y. Yuntao, X. Mu, and Y. Xi, "Performance study on a large-scale proton exchange membrane fuel cell with cooling", *International Journal of Hydrogen Energy*, vol. 47, pp. 10381-10394, 2022.
- [10] G. Liu, Y. Qin, and D. Ji, "Numerical investigation of organic fluid flow boiling for proton exchange membrane fuel cell cooling and waste heat recovery", *Applied Thermal Engineering*, vol. 228, p. 120564, 2023
- [11] I. A. Zakaria, W. Mohamed, and W. A. W. Hamzah, "Numerical analysis of SiO₂ nanofluid performance in serpentine PEMFC cooling plate", *International Journal of Engineering & Technology*, vol. 7, pp. 170-174, 2018.
- [12] S. Choi, Z. Zhang, W. Yu, F. Lockwood, and E. Grulke, "Anomalous thermal conductivity enhancement in nanotube suspensions", *Applied Physics Letters*, vol. 79, pp. 2252-2254, 2001.

- [13] M. R. Islam, B. Shabani, and G. Rosengarten, "Nanofluids to improve the performance of PEM fuel cell cooling systems: a theoretical approach", *Applied Energy*, vol. 178, pp. 660-671, 2016.
- [14] I. Zakaria, W. A. Mohamed, W. H. Azmi, A. M. Mamat, R. Mamat, and W. R. Daud, "Thermo-electrical performance of PEM fuel cell using Al₂O₃ nanofluids", *International Journal of Heat and Mass Transfer*, vol. 119, pp. 460-471, 2018.
- [15] I. Zakaria, W. A. N. W. Mohamed, A. M. I. B. Mamat, R. Saidur, W. H. Azmi, R. Mamat, et al., "Experimental Investigation of Al₂O₃ - Water Ethylene Glycol Mixture Nanofluid Thermal Behaviour in a Single Cooling Plate for PEM Fuel Cell Application", *Energy Procedia*, vol. 79, pp. 252-258, 2015.
- [16] I. A. Zakaria, W. A. N. W. Mohamed, A. M. I. Mamat, K. I. Sainan, and S. F. A. Talib, "Thermal performance of Al₂O₃ in water - ethylene glycol nanofluid mixture as cooling medium in mini channel", *AIP Conference Proceedings*, vol. 1674, p. 020014, 2015.
- [17] S. Khalid, I. A. Zakaria, and W. A. N. Wan Mohamed, "Comparative analysis of thermophysical properties of Al₂O₃ and SiO₂ nanofluids", *Journal of Mechanical Engineering*, vol. SI 8, pp. 153-163, 2019.
- [18] I. A. Zakaria, Z. Michael, W. Mohamed, and W. A. Najmi, "Nanofluid as cooling medium in polymer electrolyte membrane (PEM) fuel cell: a study on potentials and possibilities", *Advanced Materials Research*, vol. 1109, pp. 319-323, 2015.
- [19] N. A. S. Muzaidi, M. A. Fikri, K. N. S. Wan Salihin Wong, A. Z. Mohammad Sofi, R. Mamat, N. Mohd Adenam, et al., "Heat absorption properties of CuO/TiO₂/SiO₂ trihybrid nanofluids and its potential future direction towards solar thermal applications", *Arabian Journal of Chemistry*, vol. 14, p. 103059, 2021.
- [20] M. H. Esfe, M. H. Hajmohammad, P. Razi, M. R. Ahangar, and A. A. Arani, "The optimization of viscosity and thermal conductivity in hybrid nanofluids prepared with magnetic nanocomposite of nanodiamond cobalt-oxide (ND-Co₃O₄) using NSGA-II and RSM", *Int Commun Heat Mass Transfer*, vol. 79, pp. 128-134, 2016.
- [21] S. Khalid, I. Zakaria, W. H. Azmi, and W. A. N. W. Mohamed, "Thermal-electrical-hydraulic properties of Al₂O₃-SiO₂ hybrid nanofluids for advanced PEM fuel cell thermal management", *Journal of Thermal Analysis and Calorimetry*, vol. 143, pp. 1555-1567, 2021.
- [22] N. Sahid, M. Rahman, K. Kadirgama, and M. Maleque, "Experimental investigation on properties of hybrid nanofluids (TiO₂ and ZnO) in water-ethylene glycol mixture", *Journal of Mechanical Engineering and Sciences*, vol. 11, pp. 3087-3094, 2017.
- [23] I. Muhammad Syafiq, Z. Irnie Azlin, and H. Wan Azmi Wan, "Heat Transfer and Pressure Drop of Water Based Hybrid Al₂O₃:SiO₂

- Nanofluids in Cooling Plate of PEMFC", *Journal of Advanced Research in Numerical Heat Transfer*, vol. 4, pp. 1-13, 04/23 2021.
- [24] B. Ramos-Alvarado, P. Li, H. Liu, and A. Hernandez-Guerrero, "CFD study of liquid-cooled heat sinks with microchannel flow field configurations for electronics, fuel cells, and concentrated solar cells", *Applied Thermal Engineering*, vol. 31, pp. 2494-2507, 2011.
- [25] I. Zakaria, Z. Michael, W. Mohamed, A. Mamat, W. Azmi, R. Mamat, *et al.*, "A review of nanofluid adoption in polymer electrolyte membrane (PEM) fuel cells as an alternative coolant", *Journal of Mechanical Engineering and Sciences*, vol. 8, pp. 1351-66, 2015.
- [26] M. A. N. Zarizi, I. A. Zakaria, M. N. I. Johari, W. A. N. Wan Mohamed, and R. M. R. Ahsan Shah, "Thermo-Electrical Behavior of Al₂O₃ and SiO₂ Nanofluids in a Proton-Exchange Membrane Fuel Cell (PEMFC) Cooling Channel", *Pertanika Journal of Science & Technology*, vol. 30, pp. 1381-1396, 2022.
- [27] I. A. Zakaria, M. R. Mustaffa, W. A. N. W. Mohamed, and A. M. I. Mamat, "Steady - State Potential Energy Recovery Modeling of an Open Cathode PEM Fuel Cell Vehicle", *Applied Mechanics and Materials*, vol. 465 - 466, pp. 114-119, 2014.
- [28] I. A. Zakaria, A. S. M. Amir Azmin, S. Khalid, W. A. Wan Hamzah, and W. A. N. Wan Mohamed, "Numerical Analysis of Aluminium Oxide and Silicon Dioxide Nanofluids in Serpentine Cooling Plate of PEMFC", *Journal of Advanced Research in Fluid Mechanics and Thermal Sciences*, vol. 72, pp. 67-79, 2021.
- [29] S. Khalid, I. Zakaria, W. Azmi, and W. Mohamed, "Thermal–electrical–hydraulic properties of Al₂O₃–SiO₂ hybrid nanofluids for advanced PEM fuel cell thermal management", *Journal Of Thermal Analysis and Calorimetry*, vol. 143, pp. 1555-1567, 2021.
- [30] M. N. I. Johari, I. A. Zakaria, W. H. Azmi, and W. A. N. W. Mohamed, "Green bio glycol Al₂O₃-SiO₂ hybrid nanofluids for PEMFC: The thermal-electrical- hydraulic perspectives", *International Communications in Heat and Mass Transfer*, vol. 131, p. 105870, 2022/02/01/ 2022.
- [31] L. S. Sundar and F. Shaik, "Heat transfer and exergy efficiency analysis of 60% water and 40% ethylene glycol mixture diamond nanofluids flow through a shell and helical coil heat exchanger", *International Journal of Thermal Sciences*, vol. 184, p. 107901, 2023.
- [32] I. A. Zakaria, W. A. N. Wan Mohamed, A. Mohd Ihsan Mamat, K. I. Sainan, M. R. Mat Nawi, and G. H. Najafi, "Numerical analysis of Al₂O₃ Nanofluids in serpentine cooling plate of PEM fuel cell", *Journal of Mechanical Engineering (JMechE)*, vol. SI (5), pp. 1-13, 2018.
- [33] M. S. Mohd Yatim, I. A. Zakaria, M. F. Roslan, and W. A. N. Wan Mohamed, "Heat transfer and pressure drop characteristics of hybrid

- $\text{Al}_2\text{O}_3\text{-SiO}_2$ ", *Journal of Mechanical Engineering*, vol. 8, pp. 145-159, 2021.
- [34] H. Ems, A. Tsubaki, B. Sukup, S. Nejati, D. Alexander, C. Zuhlke, et al., "Drag reduction in minichannel laminar flow past superhydrophobic surfaces", *Physics of Fluids*, vol. 33, p. 123608, 2021.
- [35] A. Muhammad, D. Selvakumar, and J. Wu, "Numerical investigation of laminar flow and heat transfer in a liquid metal cooled mini-channel heat sink", *International Journal of Heat and Mass Transfer*, vol. 150, p. 119265, 2020.
- [36] J. Mohamad Noor Izwan, Z. Irnie Azlin, and A. Nur Syahirah Mohammed, "Thermal Behaviour of Hybrid Nanofluids in Water: Bio Glycol Mixture in Cooling Plates of PEMFC", *CFD Letters*, vol. 14, pp. 43-55, 2022.
- [37] A. Sakanova, C. C. Keian, and J. Zhao, "Performance improvements of microchannel heat sink using wavy channel and nanofluids", *International Journal of Heat and Mass Transfer*, vol. 89, pp. 59-74, 2015.
- [38] J. Tang, C. Qi, Z. Ding, M. Afrand, and Y. Yan, "Thermo-hydraulic performance of nanofluids in a bionic heat sink", *International Communications in Heat and Mass Transfer*, vol. 127, p. 105492, 2021.
- [39] I. Zakaria, W. H. Azmi, A. M. I. Mamat, R. Mamat, R. Saidur, S. F. Abu Talib, et al., "Thermal analysis of Al_2O_3 -water ethylene glycol mixture nanofluid for single PEM fuel cell cooling plate: An experimental study", *International Journal of Hydrogen Energy*, vol. 41, pp. 5096-5112, 2016.
- [40] E. B. Agus P. Sasmito, Arun S. Mujumdar, "Numerical evaluation of various thermal management strategies for polymer electrolyte fuel cell stacks", *International Journal of Hydrogen Energy*, vol. 36, pp. 12991-13007, 2011.

Influences of Main Machining Process Parameters and Tool Wear on The Machining Damage Generated During Edge Milling CFRP Composites

Nguyen Thi-Hue, Nguyen Dinh-Ngoc*
Thai Nguyen University of Technology, VIETNAM
*ngocnd@tnut.edu.vn

ABSTRACT

Machining Carbon Fibre Reinforced Plastics (CFRPs) composites are typically accompanied by the appearance of machining damage which strongly impacts the structural integrity of composite parts during their service lives. Studying the correlation between machining damage and its affected factors has still been an open issue. Hence, it is necessary to do more research. This study focuses on investigating the influences of main process parameters and tool wear phenomenon in terms of machining length on the machining quality which was characterized by the surface roughness criterion, the ten-point max, Rz. A full factorial design of experiments was conducted including three levels of feed speed and two degrees of spindle speed. The results revealed that machining damage was mainly influenced by process parameters at a small machining distance, whereas at a longer machining distance, tool wear had a dominant effect on the machining quality than machining parameters. These findings could provide guidelines for selecting suitable machining parameters to enhance the machining quality of CFRP.

Keywords: CFRPs; Machining Quality; Edge Milling; Cutting Condition; SEM

Introduction

In recent decades, CFRP composites have been widely accepted in several

important industries such as automotive, shipping, aircraft, and sports equipment because of their advantages including dimensional stability, high specific strength, and low density. Composite parts are frequently fabricated to near-net shapes to suit certain applications [1], but excess materials in the edge of moulded CFRP parts must be removed to get the required dimensions for assembly by secondary operations like milling, drilling and trimming processes [2]-[4]. There have been the fact machining processes of CFRP composites are frequently associated with the occurrence of machining defects in the machined surfaces [5]-[6] such as matrix cracking, matrix fibre interface debonding, matrix degradation, fibre pullout [7]-[9]. The induced machining defects may harmfully impact the machined surface integrity and the mechanical properties of CFRP structures during their service lives [5], [10]. For this reason, it is necessary to clearly know and suitably select the factors which influence the generation of defects, including machining parameters, tool geometries, and the wear phenomenon of cutting tools [11]-[13].

El-Ghaoui et al. [14] showed that the combination of high cutting speed and low feed speed induces better quality of machined surface when machining composite materials generates a smaller level of theoretical chip thickness or volume of cut materials, hence machining process is easy to perform. Similar results were also observed in the studies of other researchers [15]-[16]. However, other studies [17] revealed that machining at low feed speeds and high cutting speeds can result in severe defects due to the effects of tool wear. This finding is also identically documented in the study of Haddad et al. [18]. In machining CFRP laminates, because of the low thermal conductivity of the matrix component and the highly abrasive nature of carbon fibre, the contacting areas occur friction phenomenon making the cutting edge become quickly worn out. The evaluation of tool wear can be conducted by flank wear [19]-[21], and the radius of the cutting edge [22] or by machining length [23]. Almost studies in the literature have concluded that cutting speed and feed rate have strong influences on the generation of flank wear [21]-[24]. Elgnemi et al. [25] detailed that an increase in cutting speed or an increase in feed rate leads to augmenting the average tool wear. Moreover, feed rate has more impact on tool wear than that of cutting speed. This result is consistent with those documented by [26]. However, in the study of [27], the authors showed that cutting speed has a stronger impact on tool wear compared with those feed rates because cutting speed is the major factor influencing cutting temperatures.

It is clear that there have been contradictory results on the machinability of composite materials given by researchers. Despite numerous recent studies on machining composites, it remains a challenging task due to the material behaviour depending on non-homogeneity, anisotropy, and diverse reinforcement and matrix properties. The responses between cutting tools and different workpiece materials can be completely different.

Therefore, results in an experimentally particular study are not always fully applicable to those of another specific study. In order to answer the gaps which, contain the ambiguity in the machining composite study, the impacts of machining parameters and tool wear on machining quality when carrying out edge trimming of CFRP composites were experimentally studied in this research. Average surface roughness was selected to characterize machining quality. Six new carbide-cutting tools with three-helix flutes were used for testing. A full experimental design showing the combinations between three levels of feed speed and two levels of spindle speed was used to investigate the impact of machining parameters on machining quality. The effects of tool wear on the machining quality were conducted based on the evolution of machining length.

Experimental Procedure

The specimens used in this study were fabricated by laminating P2352 prepregs according to the stacking sequence of $[90^\circ/90^\circ/-45^\circ/0^\circ/45^\circ/90^\circ/-45^\circ/90^\circ/45^\circ/90^\circ]$, where each ply has a thickness of 0.26 mm. The total theoretical dimension of each plate is 300 x 300 x 5.2 mm. Before the milling test, each plate was cut into the size of 300 x 150 x 5.2 mm with the cutting direction along 150 mm length. The CFRP properties are further described in Table 1. A Mazak vertical centre smart 530C (Yamazaki Mazak Corporation, Japan) was utilized to perform the edge milling tests. Six cutting conditions were carried out, with the combination of three feed speeds V_f , (500 mm/min, 1000 mm/min, and 1500 mm/min) and two spindle speeds N , (8000 rpm, and 10000 rpm). All tests were performed without coolant (dry machining). Each cutting condition was carried out with the machining length of 3.0 m or 3000 mm, and the feed direction parallel to the dimension of 150 mm of CFRP plate. This corresponds to twenty tool paths of the edge milling process (20 x 150 mm=3000 mm). Six new carbide tools (three-helix flutes, 6 mm shank diameter, helix angle of 45°, rake angle of 11°, and clearance angle of 9° - Figure 1) were used in edge milling. The machined surface was unfixed and quantitatively evaluated by measuring surface roughness, R_z , and its average values were calculated by three measurements. A roughness tester namely SJ-210 Mitutoyo (Mitutoyo Corporation, Japan) with a cut-off length of 0.8 mm and transverse length of 5.0 mm was employed to test the machining quality. The optical images of the cutting tool were taken by KEYENCE VHX-6000 digital microscope to state the tool wear phenomenon (Figure 2). In order to quantify the state of machining damage induced, the microstructure of machined surfaces was investigated by Scanning Electron Microscope (SEM) referenced under “JEOL-JSM 5410 LV” (Figure 3).



Figure 1: Carbide milling cutter with three-helix cutting edges

Table 1: Mechanical properties of P2352 prepreg

Density (g/cm ³)	Longitudinal shear modulus (GPa)	Longitudinal Young's modulus (GPa)	Compressive strength (MPa)	Tensile strength (MPa)	Poisson's ratio
2.63	6.21	162	1552	2844	0.34



Figure 2: Keyence VHX-6000 digital microscope



Figure 3: SEM machine referenced under JEOL-JSM 5410 LV

Results and Discussion

Analysis of induced defects observed in machined surface

After machining, the microstructures of the machined surface were analysed by using SEM observation. Three positions of machining length (L_c) were considered for each cutting condition, e.g. $L_c=15$ cm, 150 cm, and 300 cm. Figure 4 presents SEM images of the machined surface obtained at a spindle speed of 8000 rpm and feed speed of 500 mm/min. The results indicated that there was no significant difference in machining defect levels between those at machining lengths of 15 cm and 150 cm where small levels of machining defects were visualized at the fibre direction of -45° . However, at a machining length of 300 cm, a higher level of machining damage in the form of craters or valleys sited at the fibre direction of -45° was observed when using the magnification of 400 μm . The dominant type of damage observed in this case was fibre pullout. The nature of fibre pullout is due to the fact that the advance of cutting edges causes the severe out-of-plane displacement and deformation of the fibres which generate the induced defects in the forms of fibre pullout, and delamination intralaminar shear along fibre–matrix interface [28]. The machining defects dominantly observed at the position of the fibre angle of -45° as previously mentioned are attributed to the chip formation [29]. Consequently, the machined surface at fibre locations of -45° was more irregular than that at other fibre locations [30]. It was observed that the worst quality of the machining surface was obtained at a longer distance when machining with a small feed speed. This is due to the increase in contact areas between the workpiece and the cutting edge, leading to a higher level of friction, higher machining temperatures and quicker wear of the cutting edge, accordingly [18]. Wang et al. [31] suggested that materials are pushed instead of being sheared at a short cutting distance, and trimming is more difficult due to wider contact between the cutting edge and the workpiece. In this case, the springs back caused by elastic recovery after the tool passer over are experimentally observed. The bouncing back region is twice bigger than the radius of the cutting edge in the fibre locations of -45° , resulting in rougher machined surfaces at longer machining lengths. This information was confirmed by the SEM images in Figure 5 which shows the wear process of cutting edge for different distance cutting with the same machining condition previously mentioned. The wear patterns of the tool in terms of the nose radius of the cutting edge were crucially influenced by the machining distance. Indeed, from Figures 5(a) and 5(b), after a machining distance of 1.5 m, the radius of the cutting edge was importantly modified, namely worn cutting edge, and bigger compared with that before machining (sharp cutting edge). Moreover, in this case, the microchips in the form of dust stuck in the rake face of the cutting edge were visualized. When the cutting distance reached 3.0 m, the modification of the cutting edge was a higher level, and more adhered chips in the rake face were also visualized. A

similar observation was also documented in the research of Haddad et al. [18]. They explained that the machining temperatures reached the glass transition temperature (T_g) of the matrix which favours the adhesion of the broken chips on the active surface of the tools. At higher cutting distances the bigger cutting edge radius led to an increase in temperatures. This was why more adhered chips were seen in Figure 5(c).

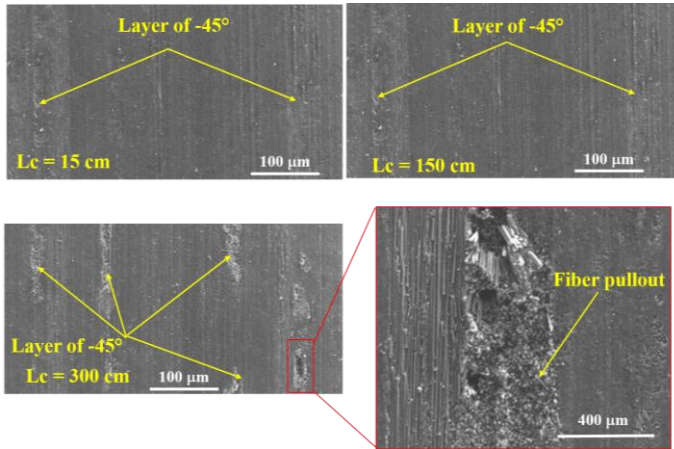


Figure 4: Machining damage observed with a feed speed of 500 mm/min and spindle speed of 8000 rpm

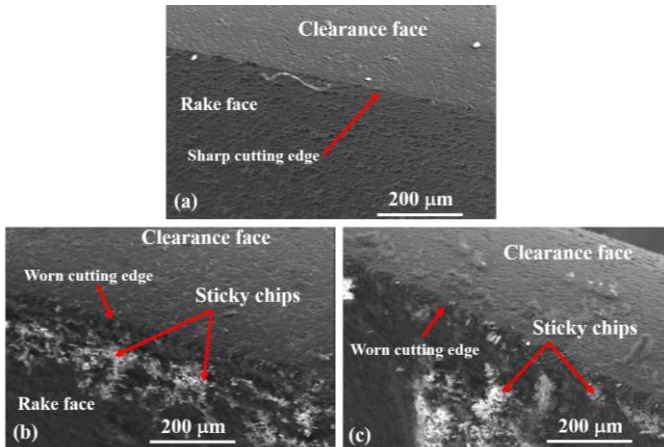


Figure 5. SEM images of cutting edges; (a) before machining and after machining distance of; (b) 1.5 m, and (c) 3.0 m for a spindle speed of 8000 rpm with a feed speed of 500 mm/min

At the cutting condition of 1000 mm/min feed speed and 8000 rpm spindle speed, the results depicted in Figure 6 showed that the machining damage level was almost identical regardless of machining length. This was explained as the cutting length is small, i.e. the cutting tool can be considered as new, and the machining damage of the surface is mainly influenced by the theoretical thickness of the chip [32]. However, as the cutting length increases, the radius of the cutting edge also increases, and the wear of the cutting edge becomes more significant, which leads to a more difficult machining process [33]. This is the wear phenomenon of cutting tools. Nevertheless, the tool wear in this cutting condition was insignificant due to the short contacting time between the workpiece and the cutting edge, in comparison with the case of a feed speed of 500 mm/min. Consequently, the degree of machining defects increases slightly as the machining length increases [11]. The variation of machining damage level with machining length at a feed speed of 1500 mm/min was similar to that given by a feed speed of 1000 mm/min. These results are consistent with those documented by Nguyen-Dinh et al. [17]. Moreover, it was observed that the machined surface exhibited similar characteristics when the spindle speed increased to 10000 rpm, regardless of the feed speed. Thus, the results obtained under this condition were not discussed in this text.

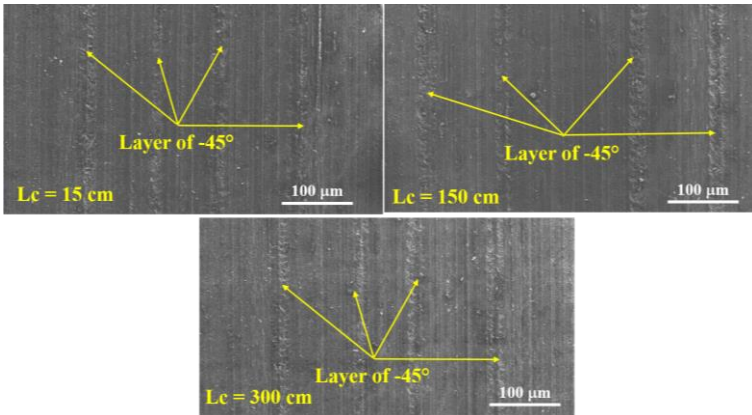


Figure 6: Machining damage observed with a feed speed of 1000 mm/min and spindle speed of 8000 rpm

Influence of process parameters on the machining quality

In this section, machining damage was quantitatively estimated to check machining quality by using ten-point mean (R_z) instead of using average surface roughness (R_a). This is according to the recommendations by the authors in the literature [11] where it was concluded that R_z is more

responsive to machining parameters than R_a and hence is more suitable for representing surface roughness of composite materials. Figure 7 shows the evolution of surface roughness as a function of machining parameters. The results showed that surface roughness decreases when feed speed varies from 500 mm/min to 1000 mm/min, but increases when feed speed changes from 1000 mm/min to 1500 mm/min. These tendencies were similarly observed in both cases of spindle speed. Regarding the first case, e.g. feed speed varies from 500 mm/min to 1000 mm/min, surface roughness (R_z) reduced from 8.46 μm to 7.56 μm corresponding to the reduction of 10.7% for a spindle speed of 8000 rpm, while the per cent reduction by 23.3% was for a spindle speed of 10000 rpm. Considering the second case, i.e. feed speed varies from 1000 mm/min to 1500 mm/min, it was noticed that surface roughness increased by 88.3% (from 7.56 μm to 14.24 μm) and by 63.9% (from 7.16 μm to 11.73 μm) for spindle speed of 8000 rpm and 10000 rpm, respectively. Moreover, it was realized that the effect of spindle speed on the surface roughness in this was less profound, likely due to the selected range of sufficient spindle speed to generate the different machining damage levels [34].

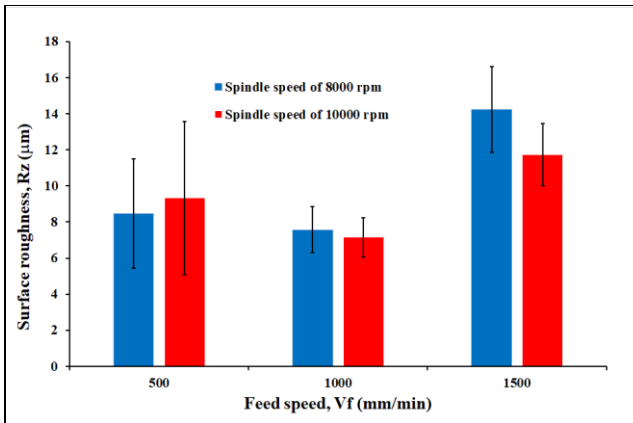


Figure 7: Influences of machining parameters on ten-point mean (R_z)

The results in Figure 7 can be interpreted that when the feed speed increases and/or the spindle speed decreases the theoretical thickness of the material to be cut also increases [2]. However, at low feed speed, tool wear increases rapidly [18], which makes the effect of cutting tool wear relatively more dominant than that of cutting condition on surface roughness [34]. This was why the surface roughness varies in opposite directions for the first and second branches of Figure 7. To be more specific, when the feed rate increased from 500 mm/min to 1000 mm/min, the surface roughness

decreased mainly due to the influence of wear. Conversely, in the remaining case, the surface roughness increases due to the important influence of the machining parameters (or chip thickness). The variations of surface roughness for the cutting condition are consistent with the variation of the degree of surface defects for the cutting mode, as presented in the previous part of this study. Notably, the results in this study differ from those reported by [2], [32] where the authors revealed that machining with low feed speed and high cutting speed can generate a good quality machining surface.

Influence of radius cutting edge on the machining quality

Figure 7 displays the average surface roughness values for each cutting condition. The values of the standard deviation were observed to be considerably high, with the highest value of $4.23 \mu\text{m}$ given by the machining condition of spindle speed of 10000 rpm and feed speed of 500 mm/min. The reason is because of the large dispersion between the measured values at the 20 tool paths of each cutting condition. In particular, it was seen that at the feed speed of 500 mm/min (in both cases of spindle speed), the standard deviation of the surface roughness was maximum. This was another clear reflection of wear on the surface quality of CFRP composite machining surfaces. The influence of wear in terms of machining length on surface roughness was able to see in Figure 8 for a spindle speed of 8000 rpm. The largest increase in roughness with the machining length was observed for a feed speed of 500 mm/min, increasing from $3.33 \mu\text{m}$ to $15.33 \mu\text{m}$ corresponding to 203.1%. Surface roughness increased with increasing in cutting distance by 62.2% and 61.7% for feed speeds of 1000 mm/min and 1500 mm/min, respectively. This increase in surface roughness is due to an increase in the radius of the cutting edge, making the cutting process more difficult as presented in Figure 5 [31]. The cutting-edge radii could be measured by Keyence VHX-6000 Digital Microscope as shown in Figure 9. The increase of cutting-edge radii at two cutting distances of 15 cm and 300 cm with a feed speed of 500 mm/min and spindle speed of 8000 rpm were shown in Figure 10. The results showed that at a cutting distance of 15 cm, the radius of the cutting edge is $9 \mu\text{m}$, while at a cutting distance of 300 cm, the one was $22 \mu\text{m}$. The dependence of surface roughness on machining length was similarly observed in the case of 10000 rpm spindle speed as shown in Figure 11. The highest augmentation of surface roughness with increasing cutting distance was observed at a feed speed of 500 mm/min. For example, surface roughness increases by 360.3% when cutting distance reaches 3.0 m at a feed speed of 500 mm/min, while the relative increases at a feed speed of 1000 mm/min and 1500 mm/min are 54.7% and 52.5%, respectively.

The machining case with a feed speed of 500 mm/min exhibits the highest increase (360.3%) in surface roughness compared to other cutting conditions. Nguyen-Dinh et al. [33] explained that when machining with a

high spindle speed, if a spiral is developed, the contact surface between the tool and the workpiece is larger than at lower spindle speed. When combined with numerous contacts per unit time at low feed speeds, this results in increased friction and heat, leading to faster tool wear [11]. The wear rate of the cutting tool directly affects the quality of the machined surface, results in many types of defects, leading to the higher value of surface roughness. The cutting edge radius given by Keyence for this machining condition was 28 μm .

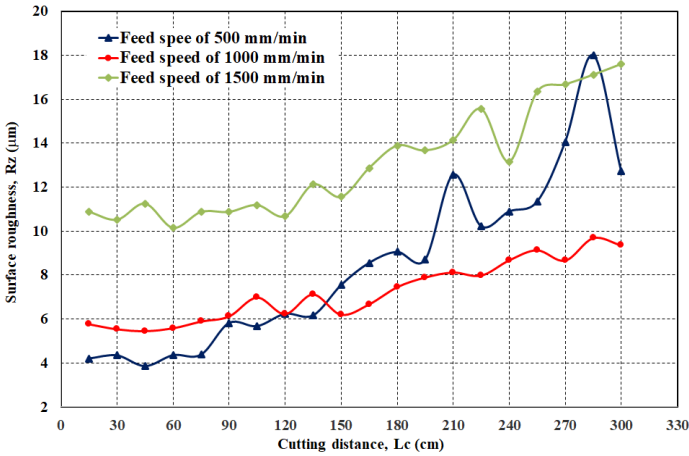


Figure 8: Evolution of Rz vs machining length for spindle speed of 8000 rpm

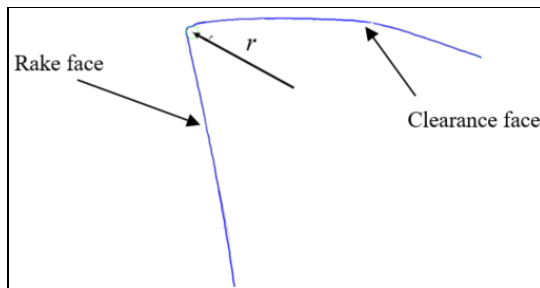


Figure 9: Profile of cutting edge radius measured from the software available in Keyence VHX-6000 digital microscope

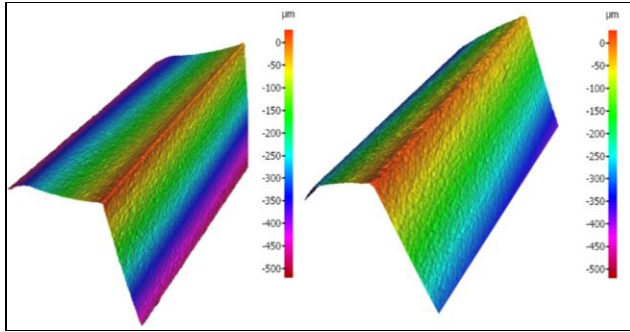


Figure 10: Cutting edge form after machining at the length of; (a) 15 cm, and (b) 300 cm with feed speed of 500 mm/min and spindle speed of 8000 rpm

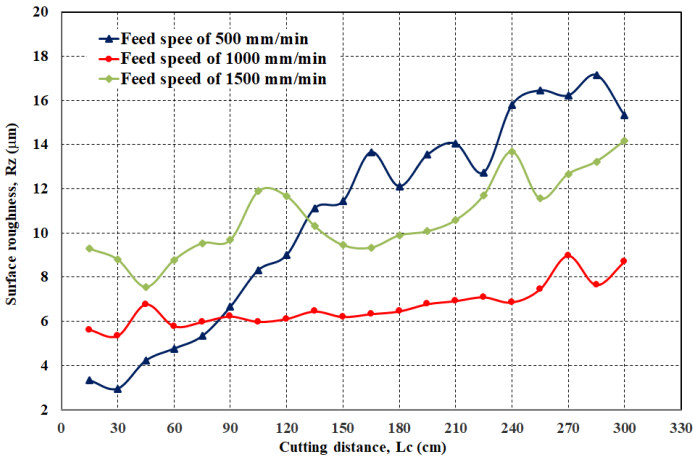


Figure 11: Evolution of R_z vs machining length for spindle speed of 10000 rpm

Conclusion

Experimental method was applied in this study to investigate the influence of machining parameters and tool wear on the quality of the machined surface when dry milling of CFRP composite plates. The quality of the machined surface was evaluated quantitatively using the surface roughness criterion. The conclusions about the research results of this study are summarized by the main results as follows:

- i. The results of qualitative assessment of the surface quality of CFRP

- composite panels were shown through SEM observations. Machining defects are found to be dependent on cutting conditions when cutting length is small. However, when the cutting length increases, wear significantly influenced the formation of machining defects (observed through SEM), especially when machining with a small feed speed.
- ii. The surface roughness measurement results accurately reflected the machining quality when correctly describing the evolutions in the occurrence of machining defects observed by SEM. That is, when the machining length increased, the machining with a small feed speed, due to the large contact between the cutting tool and the workpiece, increases the friction and cutting heat, leading to the rapid wear of the cutting edge.
 - iii. The machining length, characterized by the increase of the cutting-edge radius, had a great influence on the quality of the machined surface. Machining with a large feed speed, due to the small contact length, resulted in slower increase in the wear rate of the cutting edge, leading to little change in the quality of the machined surface in terms of evaluation. Meanwhile, machining with a small feed speed increases the contact length between the cutting edge and the workpiece, causing friction and heat to increase, leading to a rapid increase in the tip radius. As a result, the surface roughness increases rapidly by 203.1% and 360.3%, respectively when machining at the spindle rotation speed of 8000 rpm and 10000 rpm.

Contributions of Authors

All authors discussed the original idea. N.T.H carried out the experimental tests and analyzed the results, wrote the original manuscript with support from N.D.N. All authors provided critical feedback and helped shape the research, analysis, and manuscript. Finally, N.D.N supervised this work and revised the article. All authors have read and agreed to the published version of the manuscript.

Funding

This work received no specific grant from any funding agency.

Conflict of Interests

The author declares that they have no conflicts of interest.

Acknowledgment

The authors wish to thank Thai Nguyen University of Technology for funding this work.

References

- [1] R.S. Niranjana, O. Singh and J. Ramkumar, "Numerical study on thermal analysis of square micro pin fins under forced convection", *Heat and Mass Transfer*, vol. 58, pp. 263–281, 2022.
- [2] P. Ghidossi, M. El Mansori, and F. Pierron, "Edge machining effects on the failure of polymer matrix composite coupons", *Composites Part A: Applied Science and Manufacturing*, vol. 35, pp. 989-999, 2004. <https://doi.org/10.1016/j.compositesa.2004.01.015>
- [3] J. Sheikh-Ahmad, N. Urban, and H. Cheraghi, "Machining Damage in Edge Trimming of CFRP", *Materials and Manufacturing Processes*, vol. 27, pp. 802-808, 2012. <https://doi.org/10.1080/10426914.2011.648253>
- [4] Duboust, N.H Ghadbeigi, C. Pinna, S. Ayvar-Soberanis, A. Collis, R. Scaife, and K. Kerrigan, "An optical method for measuring surface roughness of machined carbon fibre-reinforced plastic composites", *Journal of Composite Materials*, vol. 51, pp. 289-302, 2016. <https://doi.org/10.1177/0021998316644849>
- [5] M. Slamani, H. Chafai, and J.F. Chatelain, "Effect of milling parameters on the surface quality of a flax fibre-reinforced polymer composite", *Proceedings of the Institution of Mechanical Engineers, Part E: Journal of Process Mechanical Engineering*, pp. 1-8, 2022. <https://doi.org/10.1177/09544089221126087>
- [6] M. Haddad, R. Zitoune, H. Bougherara, F. Eyma, B. Castanié, "Study of trimming damages of CFRP structures in function of the machining processes and their impact on the mechanical behavior", *Composites Part B: Engineering*, vol. 57, pp.136-143, 2014. <https://doi.org/10.1016/j.compositesb.2013.09.051>
- [7] A. Hejjaji, R. Zitoune, L. Crouzeix, S.L. Roux, F. Collombet, "Surface and machining induced damage characterization of abrasive water jet milled carbon/epoxy composite specimens and their impact on tensile behavior", *Wear*, vol. 376-377, pp. 1356-1364, 2017. <https://doi.org/10.1016/j.wear.2017.02.024>
- [8] W. Hintze, D. Hartmann, and C. Schütte, "Occurrence and propagation of delamination during the machining of carbon fibre reinforced plastics (CFRPs) – An experimental study", *Composites Science and Technology*, vol. 71, pp. 1719-1726, 2011. <https://doi.org/10.1016/j.compscitech.2011.08.002>

- [9] M. Slamani, J.-F. Chatelain, and H. Hamedanianpour, "Influence of machining parameters on surface quality during high speed edge trimming of carbon fibre reinforced polymers", *International Journal of Material Forming*, vol. 12, pp. 331-353, 2019. <https://doi.org/10.1007/s12289-018-1419-2>
- [10] D. N. Nguyen, P. T. M Duong, V. S. Nguyen, V. D. Luong, T. T. N. Nguyen, T. D. Hoang, D. H. Nguyen, "The Characterization of Machined Damage of CFRP Composite: Comparison of 2D and 3D Surface Roughness Performance", In *Advances in Engineering Research and Application. ICERA 2020. Lecture Notes in Networks and Systems*, vol. 178, pp. 771-779, 2021. https://doi.org/10.1007/978-3-030-64719-3_84
- [11] D.N. Nguyen, C. Bouvet, and R. Zitoune, "Influence of machining damage generated during trimming of CFRP composite on the compressive strength", *Journal of Composite Materials*, vol. 54, pp. 1413-1430, 2019. <https://doi.org/10.1177/002199831988833>
- [12] M. Haddad, R. Redouane, F. Eyma, B. Castanie, "Study of the surface defects and dust generated during trimming of CFRP: Influence of tool geometry, machining parameters and cutting speed range". *Composites Part A: Applied Science and Manufacturing*, vol. 66, pp. 142-154, 2014. <https://doi.org/10.1016/j.compositesa.2014.07.005>
- [13] R. Prakash, V. Krishnaraj, R. Zitoune, J. Sheikh-Ahmad, "High-Speed Edge Trimming of CFRP and Online Monitoring of Performance of Router Tools Using Acoustic Emission", *Materials*, vol 9, no. 10, 2016. <https://doi.org/10.3390/ma9100798>
- [14] J. Fulemova, and Z. Janda, "Influence of the Cutting Edge Radius and the Cutting Edge Preparation on Tool Life and Cutting Forces at Inserts with Wiper Geometry", *Procedia Engineering*, vol. 69, pp. 565-573, 2014. <https://doi.org/10.1016/j.proeng.2014.03.027>
- [15] K. El-Ghaoui, J.-F. Chatelain, and C. Ouellet-Plamondon, "Effect of Graphene on Machinability of Glass Fibre Reinforced Polymer (GFRP)", *Journal of Manufacturing and Materials Processing*, vol. 78, pp. 1-12, 2019. <https://doi.org/10.3390/jmmp3030078>
- [16] W. König, Ch. Wulf, P. Graß, H. Willerscheid, "Machining of Fibre Reinforced Plastics", *CIRP Annals*, vol. 34, pp. 537-548, 1985. [https://doi.org/10.1016/S0007-8506\(07\)60186-3](https://doi.org/10.1016/S0007-8506(07)60186-3)
- [17] M. Ucar, Y.W, "End-milling machinability of a carbon fibre reinforced laminated composite", *Journal of Advanced Materials*, vol. 37, pp. 46-52, 2005.
- [18] N. Nguyen-Dinh, R. Zitoune, C. Bouvet, S. Leroux, "Surface integrity while trimming of composite structures: X-ray tomography analysis", *Composite Structures*, vol. 210, pp. 735-746, 2019. <https://doi.org/10.1016/j.compstruct.2018.12.006>
- [19] M. Haddad, R Zitoune, F.Eyma, B. Castanié, "Machinability and

- surface quality during high speed trimming of multi directional CFRP”, *International Journal of Machining and Machinability of Materials*, vol. 13, pp. 289-310, 2013. [https://doi: 10.1504/ijmmm.2013.053229](https://doi.org/10.1504/ijmmm.2013.053229)
- [20] G. Caprino, I.D. Lorio, L. Nele and L. Santo, “Effect of tool wear on cutting forces in the orthogonal cutting of unidirectional glass fibre-reinforced plastics”, *Composites Part A: Applied Science and Manufacturing*, vol. 27, pp. 409-415, 1996. [https://doi.org/10.1016/1359-835X\(95\)00034-Y](https://doi.org/10.1016/1359-835X(95)00034-Y)
- [21] M.K. Nor Khairusshima, C.H. Che Hassan, A.G. Jaharah, A.K.M. Amin, A.N. Md Idriss, “Effect of chilled air on tool wear and workpiece quality during milling of carbon fibre-reinforced plastic”, *Wear*, vol. 302, pp. 1113-1123, 2013. <https://doi.org/10.1016/j.wear.2013.01.043>
- [22] D. Ozkan, M. S. Gok, H. Gokkaya, A. C. Karaoglanli, “The Effects of Cutting Parameters on Tool Wear During the Milling of CFRP Composites”, *Materials Science*, vol. 25, no. 1, pp. 42-46, 2019. <http://dx.doi.org/10.5755/j01.ms.25.1.19177>
- [23] F.-j. Wang, Jw. Yin, J.-w. Ma, Z.-y. Jia, F. Yang, B. Niu, “Effects of cutting edge radius and fibre cutting angle on the cutting-induced surface damage in machining of unidirectional CFRP composite laminates”, *The International Journal of Advanced Manufacturing Technology*, vol. 97, pp. 3107-3120, 2017. <https://doi.org/10.1007/s00170-017-0023-9>
- [24] A. Hosokawa, N. Hirose, T. Ueda, T. Furumoto, “High-quality machining of CFRP with high helix end mill”, *CIRP Annals*, vol. 63, pp. 89-92, 2014. <https://doi.org/10.1016/j.cirp.2014.03.084>
- [25] A. M. Mustafa, N.S. Shahrudin1, N.F.H. Halim1, A.N. Rozhan, M. A. Hattiar, “The Effect of Cutting Speeds on Tool Wear and Surface Roughness when Milling Carbon Fibre Reinforced Polymer”, *IOP Conference Series: Materials Science and Engineering*, vol. 1244, pp. 1-6, 2022. <https://doi.org/10.1088/1757-899X/1244/1/012018>
- [26] T. Elgnemi, V. Songmene, J. Kouam, M.B.G. Jun, A. M. Samuel, “Experimental Investigation on Dry Routing of CFRP Composite: Temperature, Forces, Tool Wear, and Fine Dust Emission”, *Materials (Basel)*, vol. 14. No. 19, p. 5697, 2021. <https://doi.org/10.3390/ma14195697>
- [27] K. Palanikumar, J.P. Davim, “Assessment of some factors influencing tool wear on the machining of glass fibre-reinforced plastics by coated cemented carbide tools”, *Journal of Materials Processing Technology*, vol. 209, pp. 511-519, 2009. <https://doi.org/10.1016/j.jmatprotec.2008.02.020>
- [28] N.F.H. Abd Halim, H. Ascroft, S. Barnes, “Analysis of Tool Wear, Cutting Force, Surface Roughness and Machining Temperature During Finishing Operation of Ultrasonic Assisted Milling (UAM) of Carbon Fibre Reinforced Plastic (CFRP)”, *Procedia Engineering*, vol. 184, pp.

- 185-191, 2017. <https://doi.org/10.1016/j.proeng.2017.04.084>
- [29] D.H. Wang, M. Ramulu, D. Arola, “Orthogonal cutting mechanism of graphite-epoxy composite. Part II Multil-directional laminate”, *International Journal of Machine Tools and Manufacture*, vol. 35, pp. 1639-1648, 1995. [https://doi.org/10.1016/0890-6955\(95\)00015-P](https://doi.org/10.1016/0890-6955(95)00015-P)
- [30] D.H. Wang, M. Ramulu, D. Arola, “Orthogonal cutting mechanism of graphite-epoxy composite. Part I: unidirectional laminate”, *International Journal of Machine Tools and Manufacture*, vol. 35, pp. 1623-1638, 1995. [https://doi.org/10.1016/0890-6955\(95\)00014-O](https://doi.org/10.1016/0890-6955(95)00014-O)
- [31] Sheikh-Ahmad, J.Y, Machining of polymer composites. Springer New York, NY, Ed. 1, 2009. <https://doi.org/10.1007/978-0-387-68619-6>
- [32] X.M. Wang, L.C. Zhang, “An experimental investigation into the orthogonal cutting of unidirectional fibre reinforced plastics”, *International Journal of Machine Tools and Manufacture*, vol. 43 no. 10, pp. 1015-1022, 2003. [https://doi.org/10.1016/S0890-6955\(03\)00090-7](https://doi.org/10.1016/S0890-6955(03)00090-7)
- [33] P. Janardhan, J. Sheikh-Ahmad, H. Cheraghi, “Edge Trimming of CFRP with Diamond Interlocking Tools”, *SAE Technical Paper 2006-01-3173*, 2006, <https://doi.org/10.4271/2006-01-3173>.
- [34] N. Nguyen-Dinh, A. Hejjaji, R. Zitoune, C. Bouvet, M. Salem, “New tool for reduction of harmful particulate dispersion and to improve machining quality when trimming carbon/epoxy composites”, *Composites Part A: Applied Science and Manufacturing*, vol. 131, pp. 1-15, 2020. 131. <https://doi.org/10.1016/j.compositesa.2020.105806>
- [35] D. N. Nguyen, V.T. Pham, T.H. Nguyen, “Effects of Machining Configurations and Process Parameters on the Machining Damage Generated During Milling CFRP Structures”, In: *Nguyen, D.C., Vu, N.P., Long, B.T., Puta, H., Sattler, KU. (eds) Advances in Engineering Research and Application. ICERA 2021. Lecture Notes in Networks and Systems*, vol. 366, pp. 400-406, 2022 https://doi.org/10.1007/978-3-030-92574-1_41

Influence of Operating Factors on Accurate Digging Depth Control of the Remote-Controlled Explosive Disposal Machine

*Dat Duy Nguyen, Dat Van Chu
Le Quy Don Technical University, Hanoi, VIETNAM*

*Sy Le Van **
PetroVietnam College, Vung Tau, VIETNAM
**sylv@pvcollege.edu.vn*

ABSTRACT

In this study, a dynamic model of the operating equipment and the hydraulic drive system of the remote-controlled explosive disposal machine were built to ensure both kinetic accuracy of digging path and the effective cutting angle. The Ruppel's control approach was applied to study the dynamics of the whole system and the influence of the arm-controlled signal, the soil digging resistance on the digging control process. In addition, a simulation model of the entire system is also performed to deeply understand the dynamic behaviour.

Keywords: *Remote Controlled Explosive Disposal Machine; Hydraulic System; Digging Depth Control; EDM*

Introduction

In the post-war period, all types of unexploded remnants such as bombs, mines and other explosive ordnances are very dangerous for the human life and society. For each war-damaged country, many national action programs have launched to deal with the consequences of bombs/mines and explosive ordnances. There are many types of explosive ordnances originating from many countries, located at different depths and terrain. The application of the remote-controlled explosive disposal machine (EDM) to clean the landmine contamination is an essential need for every country. This EDM has been

developed by some military manufacturers from developed countries (Figure 1). They were equipped with intelligent and multi-functions to serve complex operations of the bomb/mine excavation process. Although EDMs have been commercialized, there are still many challenges that need in-depth research. In the excavation process, the control operations of drivers are required to avoid any collisions with bombs/mines located under the deep ground. It is extremely difficult to take advantage of the operators' perception (remote control) while they are working in conditions of mental stress. The influence factors such as vibration and acceleration should be eliminated in the control process. In most cases, the operator does not know clearly about the position of the bucket teeth. Therefore, it is necessary to build a control system to track and follow the excavation process to maintain the set digging trajectory in the most accurate way. In the civil construction, this idea has been applied with intelligent excavators manufactured by companies such as Komatsu, Hitachi and Caterpillar [1], [2] using in digging canals, foundations or excavation of construction sites. To apply this idea to bomb/mine clearance, dynamic analysis and control approach of EDM require redesigning and recalculating for the complex operations. In addition, the commercial excavators which identify the digging depth by GPS system is extremely expensive and cannot be used in special sites. Thus, the EDM using in bomb/mine clearance must be integrated with the depth control system to position the digging depth. To build this system, it is necessary to study other methods, kinematics and dynamics of the entire mechanical, electro-hydraulic control system.

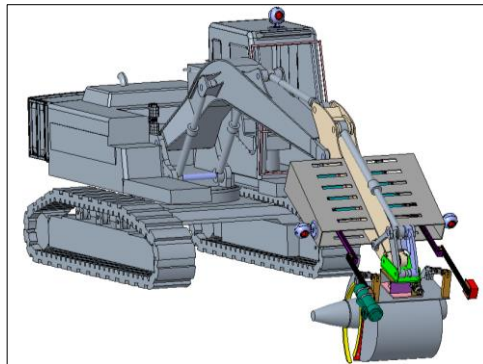


Figure 1: The EDM model

For controlling the depth of excavation, Sukharev et al. [3] introduced an automation control system for working process of a hydraulic single-bucket excavator. The author used the excavation parameters such as digging depth, length and digging direction. The working process of the excavator requires the coordination of three operations with high precision which requires a

minicomputer processor attached to the machine. This is exceedingly difficult to do by human control. Haga et al. [4] designed a control system by calculating the position of the bucket tooth head, the speed and movement direction of the bucket. The digging depth is preset from the controller. The author used three sensors for the displacement of bucket cylinder, a lifting angle of the bucket arm, and the base machine tilt. In this method, the bucket position is relatively fixed to the bucket arm, the movement of the bucket is done by the operator and the lifting and lowering operation is controlled automatically according to the speed of the bucket arm movement. As a result, soil shear angle of the bucket is constantly changing which is difficult to obtain an optimal shear angle. Ruppel et al. [5] presented a control method to ensure excavation process according to a given depth. The author uses four angle-sensors or three-cylinder displacement-sensors and one angle-sensor. These sensors are arranged for determining: the inclination of the base vehicle; the angle between the base vehicle and the boom; the angle between the boom and the arm, and the angle between the arm and the bucket. In this method, only the operation of the bucket arm is controlled by the operator while the lifting and lowering operation of the boom, the forward and backward operation of the bucket are automatically controlled by the computer to maintain both the optimal cutting angle and digging depth. This method is the most effective for operations of bomb/mine clearance. For controlling the excavation process of single- bucket hydraulic excavator, most authors focused on automatic control process and control algorithms of excavators during excavation [6]-[8]. Some authors studied the real-time visualization, monitoring of excavation trajectory, and a 3D information display system [9]-[12].

For analysing the excavator behaviours in the kinematics and dynamics aspects, the authors focused on the basic kinematic calculations of the working equipment [5], the precise control of the digging depth of hydraulic excavators [13]-[15], the orbits of points on the working equipment and a working area [2], [16] kinematic modelling and the control system of a hydraulic excavator during excavation [11], [17]. In the recent time, there has not been any study in both kinetic and dynamic aspects for a complete system including hydraulic system, working equipment, and working environment of excavation bucket.

Based on the Ruppel's controlling approach of excavation depth, this paper focuses on kinematic analysis of working structure during digging process. It is required to ensure both the accuracy of bomb/mine excavation process and optimal cutting angle of the bucket. In addition, the influence of the structural errors on the accuracy of the bucket tooth trajectory is also investigated. The established dynamic model of the hydraulic system and the operating devices will be used as an important part of the simulating model. A complete system of EDM is simulated to evaluate the kinematic and dynamic behaviours during the excavation process with a given digging depth by using LMS Amesim software. The real EDM with Ruppel's control method is also manufactured which use the results from kinematic and dynamic analysis.

Kinematics and dynamics of digging depth control

For this problem, dynamic analysis for the working equipment of a EDM was assumed as below things:

- i. The weight of arm, gripper, and boom mechanism ($m_1, m_2,$ and m_3) is located at the gravity center of each component.
- ii. The deformation of the boom, gripper and arm mechanism were neglected because their stiffness is large enough.

Figure 2 illustrates the calculating diagram of the boom mechanism, gripper and arm mechanism, where: l_1 is the length from revolute joint O_1 of the boom to the gravity center of the boom; l_2 is the length from the revolute joint O_2 of the arm to the gravity centre of the arm; l_3 is the length from the revolute joint O_3 of the gripper mechanism to the gravity center of the gripper mechanism. $F_{cy1}, F_{cy2},$ and F_{cy3} are the forces triggered off by the cylinders that drive the gripper, arm, and boom mechanism. $G_1, G_2,$ and G_3 are the weight of the gripper, arm, and boom mechanism respectively. The force due to the body weight of the operating equipment is attributed to the rod head of hydraulic cylinder. The friction is applied for hinge joints connecting hydraulic cylinders and structures of the gripper, arm, and boom mechanism as well as in hydraulic cylinders.

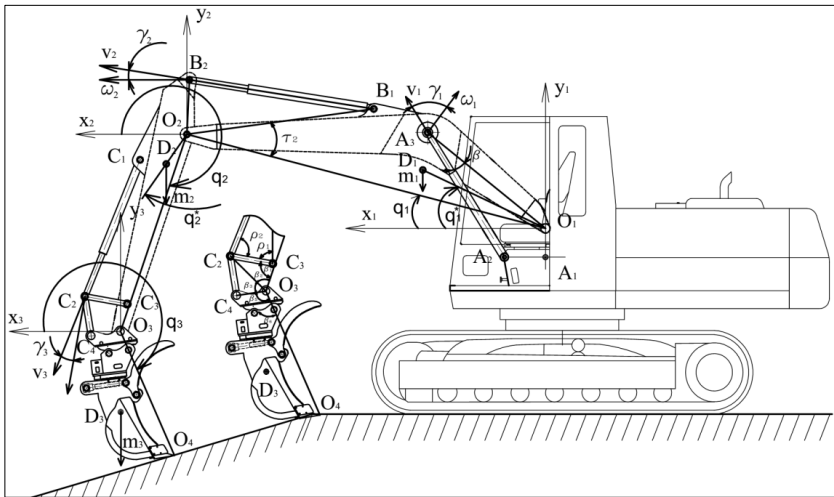


Figure 2: Calculation diagram of working equipment of EDM

The kinematic calculating diagram of the digging depth control during excavation process for the remote-controlled explosive disposal machine is shown on Figure 3.

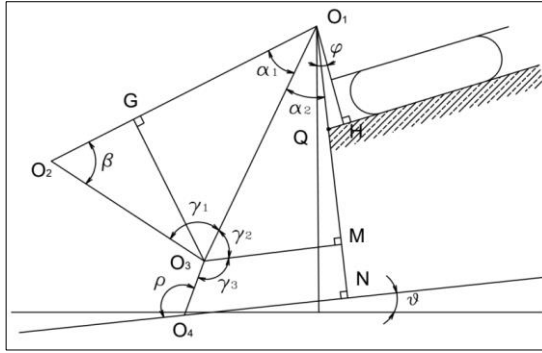


Figure 3: Calculation diagram of digging depth control

where: O_1O_2 is the boom length which is the distance between the revolute joints of the boom and the arm; O_2O_3 is the arm length which is the distance between the revolute joints of the arm and the bucket; O_3O_4 is the bucket length which is the distance from the bucket attachment to the bucket teeth; O_1H is the working height which is the distance from the boom joint to the surface of the machine base; QN is a required digging depth; ρ is a required cutting angle; ϑ is an inclination of the excavation surface; φ is the tilt angle of machine base.

At any point in the working cycle which depends on the angle value of β , the control angles $\alpha = \alpha_1 + \alpha_2 + \alpha_3$, $\alpha_3 = \varphi - \vartheta$ and $\gamma = \gamma_1 + \gamma_2 + \gamma_3$ are calculated as follows:

$$\alpha = \arcsin \frac{O_2O_3 \sin \beta}{\sqrt{O_1O_2^2 + O_2O_3^2 - 2O_1O_2O_2O_3 \cos \beta}} + \frac{\pi}{2} - \arcsin \frac{\frac{O_1H}{\cos(\varphi - \vartheta)} + QN - O_3O_4 \sin \rho}{\sqrt{O_1O_2^2 + O_2O_3^2 - 2O_1O_2O_2O_3 \cos \beta}} + \varphi - \vartheta \quad (1)$$

$$\gamma = \pi - \beta - \arcsin \frac{O_2O_3 \sin \beta}{\sqrt{O_1O_2^2 + O_2O_3^2 - 2O_1O_2O_2O_3 \cos \beta}} + \arcsin \frac{\frac{O_1H}{\cos(\varphi - \vartheta)} + QN - O_3O_4 \sin \rho}{\sqrt{O_1O_2^2 + O_2O_3^2 - 2O_1O_2O_2O_3 \cos \beta}} + \rho \quad (2)$$

The general driving calculation diagram for the working mechanisms is shown in Figure 4. The cylinder is represented by the moving mass, $m_{p.i}$, including the weight of the rod and the piston.

The load acting on the cylinders consists of two components: dynamic force which is calculated according to the referenced masses $m_{mod.i}$; static force, F_{st} , is determined by the weight of the working mechanism. The transformation from the displacement value of the cylinder to the extrapolated coordinates is determined by the transmission ratio of the mechanisms, i_{sq} .

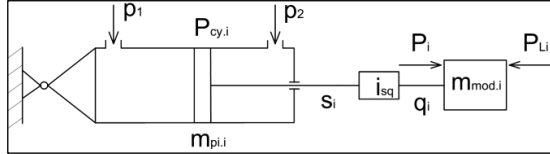


Figure 4: Calculation diagram of working cylinder

Based on the calculation diagram of the working cylinder, the system of equations representing the dynamics of the operating cylinder is as below:

$$F_{cy.i}p_{cy.i} - k_{fri-cy} \frac{ds_i}{dt} - P_{Li} = (m_{mod.i} + m_{p.i}) \frac{d^2s_i}{dt^2} \quad (3)$$

where: F_i is the force generated by the working cylinders when the mechanisms were rotated; P_{Li} is the force produced by the external loads acting on mechanisms referring to the working cylinder; $m_{mod.i}$ is the mass referring to the working cylinders; k_i is the number of working cylinders driving each mechanism.

The inertia moment, $J_{mod.i}$ is determined as a function which depends on the displacement of the rod $x_{p.i}$, the excavation resistance of the soil, and the weight of the structures during the excavation. The inertia moments of the excavation-gripper mechanism with respect to rotating axes of O_3 , O_2 , and O_1 are:

$$J_3 = m_3(l_{O_3D_3} \cos q_3)^2 \quad (4)$$

$$J_2 = m_2\left(\frac{l_{O_2O_3}}{2} \cos q_2\right)^2 + m_3(l_{O_2O_3} \cos q_2 + l_{O_3D_3} \cos q_3)^2 \quad (5)$$

$$J_1 = m_1(l_{O_1D_1} \cos q_1)^2 + m_2(l_{O_1O_2} \cos(q_1 - \tau_1) + \frac{1}{2}l_{O_2O_3} \cos q_2)^2 + m_3 \cdot (l_{O_1O_2} \cdot \cos(q_1 - \tau_1) + \frac{1}{2}l_{O_2O_3} \cdot \cos q_2 + l_{O_3D_3} \cdot \cos q_3)^2 \quad (6)$$

The modified weights of the excavation-gripper, boom, and arm mechanism referred to the driving cylinders are calculated as follows:

$$m_{mod1} = J_1 \frac{1}{(l_{O_1A_3} \cos \gamma_2)^2}; m_{mod2} = J_2 \frac{1}{(l_{O_2B_2} \cos \gamma_3)^2};$$

$$m_{mod3} = J_3 \frac{1}{(l_{C_2C_3} \cos \gamma_3)^2} \quad (7)$$

To determine the static load, Dombrowsky method is used [18], this load is applied to the working cylinders due to the mass of the working structures and the excavation resistance of the soil. The load acting on the cylinder driving the excavation-gripper mechanism is determined by the formula below:

$$P_{L_3} = \frac{m_3 g l_{O_3D_3} \cos q_3 + P_1 l_{O_3O_4} \cos(q_3 + \beta_5) - P_2 l_{O_3O_4} \sin(q_3 + \beta_5)}{l_{O_3C_2} \sin(\beta_1 + \beta_2 - \rho_2)} \quad (8)$$

The tangential component of the excavation resistance is determined by the formula below [18]:

$$P_1 = F \cdot k \quad (9)$$

where: $F = b \cdot c$ is the cross-section area of the soil chip; k is the digging resistance coefficient of the soil; b is the bucket width; and c is the thickness of the soil chip. The normal component of the excavation resistance is determined as follows:

$$P_2 = (0,1..0,2)P_1$$

When excavating with the manual method, the static moment with respect to the rotation axis passed through the point O_2 . The load acting on the cylinder driving the excavation-gripper mechanism is determined by the formulas below:

$$P_{L_2} = \frac{1}{l_{O_2B_2} \cos(\gamma_2)} \left(\frac{1}{2} m_2 g l_{O_2O_3} \cos(q_2) + m_3 g (l_{O_3D_3} \cos(q_3) + l_{O_2O_3} \cos(q_2)) + P_1 (l_{O_2O_3} \cos(q_2) + l_{O_3O_4} \cos(q_3 + \beta_5)) - P_2 (l_{O_2O_3} \sin(q_2) + l_{O_3O_4} \sin(q_3)) \right) \quad (10)$$

$$\begin{aligned}
 P_{L_1} = & \frac{1}{l_{o_1A_3} \cos(\gamma_2)} (m_1 g l_{o_1A_5} \cos(q_1^*) \\
 & + m_2 g (l_{o_1O_2} \cos(q_1^* - \tau_1) + \\
 & + \frac{1}{2} l_{o_2O_3} \cos(q_2)) + m_3 g (l_{o_1O_2} \cos(q_1^* - \tau_1) + l_{o_2O_3} \cos(q_2) \\
 & + l_{o_3D_{16}} \cos(q_3))) \quad (11)
 \end{aligned}$$

The kinematic and dynamic analyses of each component in the EDM were presented in the previous studies [19]-[21]. Consequently, a complete kinematic and dynamic behaviours for entire hydraulic system to drive the working equipment were integrated for ensuring both dynamic accurate of digging path and the effective cutting angle at the same time. A diagram of dynamic calculation for each element (main pump, main valve, and EPPR valve) and a dynamic calculation diagram of the entire hydraulic system are shown [19]. In this diagram, the displacements $s_1, s_2,$ and s_3 of the cylinders are converted into feedback signals to reduce the valve of the electric proportional pressure.

The influence of operation factors on the accuracy of digging depth.

Initial setup for dynamic simulation

The integrated dynamic behaviors of the complete system during the excavation established in the above part were utilized for evaluating the dynamic behaviors in the excavation process by using LMS Amesim software [22]-[24]. Elements in the main hydraulic system, control hydraulic system and working equipment are designed from the LMS Amesim libraries as shown in Figure 5 and Figure 6.

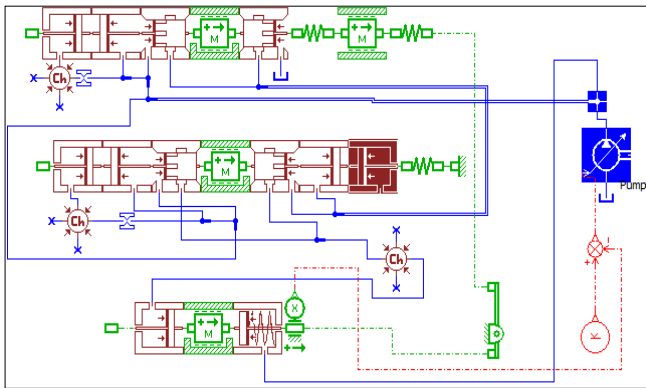


Figure 5: Simulation of the main pump with control LS-PC

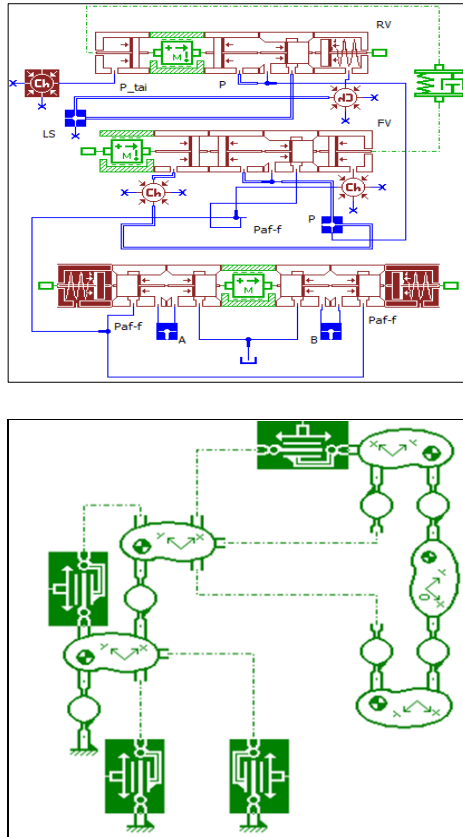


Figure 6: Simulation of the main valve and the working equipment

The input data for simulating the dynamic excavation process of EDM, the initial parameters were given as below:

- i. The base machine stands on a horizontal plane, the digging angle $\varphi = 0^\circ$ and inclination angle $\vartheta = 5^\circ$;
- ii. The pumps in the hydraulic driving system are hydraulic pump HPV 95 which has maximum operating pressure $p_{max} = 350$ bar, the specific flow of 95 cc/rev; the diameter of PC and LS valves is 10 mm with a NO mode;
- iii. The control pump uses mechanical feedback control is gear pump which has the specific flow of 36 cc/rev and maximum operating pressure at 30 bar;

- iv. Main valve has a spool diameter of 25 mm and electric proportional reducing valve has a main spool diameter of 10 mm, maximum operating pressure at 50 bar and electrical control signal $i_{max} = 800$ mA.

The operating cylinder has operating parameters such as: cylinder diameters of $D_1=105$ mm, $D_2=115$ mm, $D_3=95$ mm; rod diameter $d_1=70$ mm, $d_2=75$ mm, $d_3=65$ mm; cylinder strokes of $l_1=990$ mm, $l_2=1175$ mm, $l_3=885$ mm. Parameters of parts of operating equipment has: $O_1O_2=3.992$ m, $O_2O_3=2.214$ m, $O_3O_4=1.457$ m, $m_1=936$ kg, $m_2=410$ kg, $m_3=50$ kg.

Simulating Results and Discussion

The simulated results with The Ruppel's control approach for the complete hydraulic system are shown on Figures 7-10. The control approach must satisfy both the accurate dynamic behavior (digging path) and the optimal cutting angle during bomb/mine excavation process. The study of the excavation process is carried out in two cases:

- i. Studying the influence the control delay of the electric joystick (the degree of quick/slow open when controlling the joystick) on the accuracy of digging depth, assumed in the case of no excavation resistance of the soil;
- ii. Studying the influence the soil excavation resistance on the accuracy of digging depth for each soil layer.

The first case as shown in Figure 7, the period from 0 to 5 seconds is the control signal to move the bucket teeth into the starting position of digging operation by lowering the boom; keeping the position relative to the lifting arm of bucket hand and bucket. It is understood that current of 400 mA is supplied from the electric control hand to the pressure relief valve to control the lifting and lowering cylinder and the current of 680 mA and 560 mA are also supplied from the electric control hand to the proportional pressure relief valve to control the bucket arm and the bucket is remained the same the position. Then the absolute angular displacements (q_1 , q_2 , and q_3) of all three mechanisms of boom, arm and bucket change accordingly (Figure 8).

This control process results in moving the excavator bucket from the elevation of the coordinates (4.7 m; -0.4 m) to the starting position of the digging operation at the coordinates (3.78 m; -2.88 m) corresponding to the segment of AB (Figure 9), the excavation process is started from point B as above cases.

From the time of 5 seconds, the excavation process is operated according to the method and the kinematic relationships with the control delay of 1 second as shown on Figure 7. It is understood that the control signal from the electric control hand supplied a current from from 680 mA to 900 mA during 1 second to the EPPR valve to control the bucket arm. Then, to ensure the digging depth with the given surface inclination, the control signal is

supplied to the proportional piezoelectric relief valve to control the boom and the bucket changes respectively from 400 mA to 430 mA and from 560 mA to 390 mA with a corresponding delay of 1 second. Thus, Figure 8 showed that three driving cylinders operate with the same delay of 4 s to achieve the required value of rotation angle (q_1 , q_2 , and q_3) corresponding to BC segment of the bucket tooth displacement in the working plane (Figure 9).

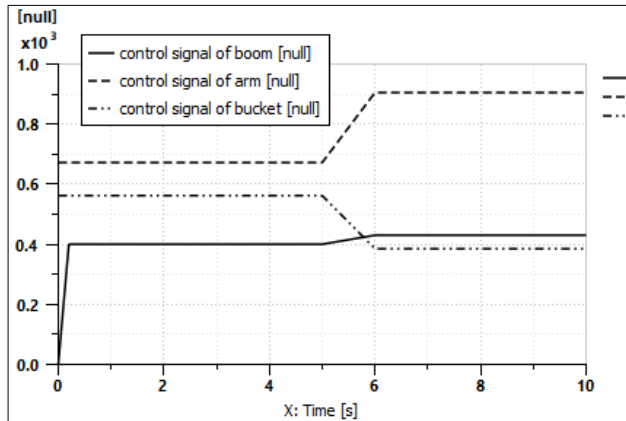


Figure 7: Control signal of the boom, arm, and bucket

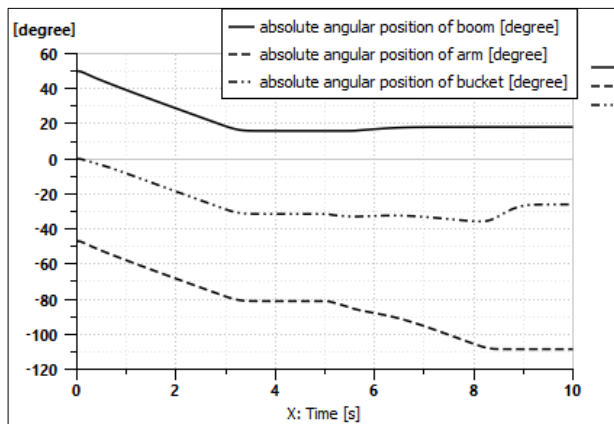


Figure 8: Angular positions of the boom, arm, and bucket

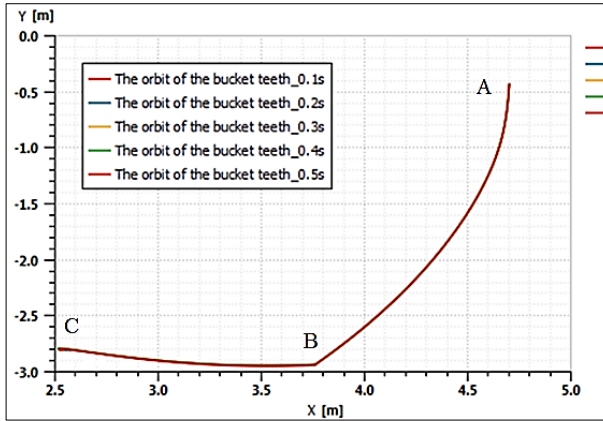


Figure 9: A orbit of bucket teeth in the working plane with different control delays

At the same time, according to this graph (Figure 9), it is found when changing the control signal from the electric control hand supplying to the proportional piezoelectric relief valve to control the bucket at different levels of delay (0.1-0.5 seconds; etc.) does not affect the displacement trajectory of the bucket teeth in the working plane (coreponding to the segments of AB and BC). It means that digging depth for each soil layer (segments of BC) completely coincides. At the same time, with an inclination angle of the digging surface of 50° , the error of the excavation depth for each soil layer is small which is in the range of ± 5 cm in accordance with the standard SNiPom4.02-91.

The bucket control process with different digging resistance is shown in Figure 10. While the digging resistance is below 2500 N, the position of the bucket teeth follows the required trajectory with the allowable error according to SNiPom4.02-91 standard. However, while the digging resistance value is above 2500 N, the position of bucket teeth follows the different trajectories with the larger digging error (over ± 10 cm), which does not meet the initial requirements. The EDM used for practical experiments is shown in Figure 11.

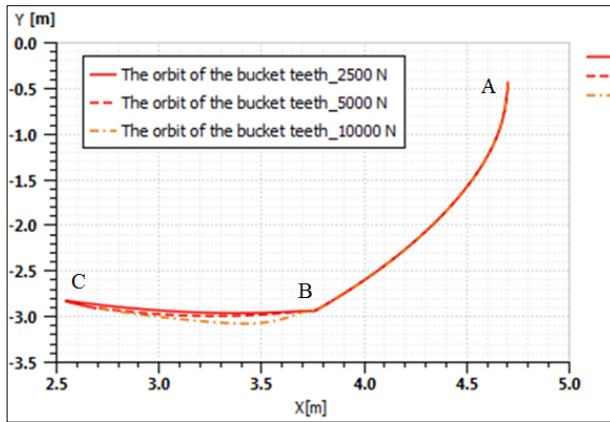


Figure 10: The orbit of the bucket teeth in the working plane at different digging resistances



Figure 11: The EDM using for practical experiments

Conclusion

The kinematic analysis for the control of digging depth by using the Ruppel's approach was presented in this study. In addition, a dynamic analysis for the entire system of the EDM including both the operating equipment system and the hydraulic driving system occurring the digging control process was also performed. This complete dynamic model is simulated on LMS Amesim environment to deeply understand the dynamic behaviour and the influence of the arm control signal, the digging resistance of the soil in the digging control process. It showed that the control of digging process has two main external influences including the operator's control and excavation resistance. The delay level of operator's control does not affect the accuracy of the digging depth, while the excavation resistance has a significant influence. Therefore,

in practice to ensure the accuracy of the excavation process, it is necessary to dig each thin layer of soil so that the digging resistance is not too great. According to the calculation with a value of 2500 N, the digging resistance will correspond to each chip thickness: for first class soil - 10 cm, for second class soil - 7 cm, for third class soil - 4 cm, for fourth class soil - 2.5 cm. For hard soils, it is very difficult to ensure the accuracy of the digging depth; therefore, the soil needs to be softened before digging.

Contributions of Authors

The authors confirm the equal contribution in each part of this work. All authors reviewed and approved the final version of this work.

Funding

This work received no specific grant from any funding agency.

Conflict of Interests

All authors declare that they have no conflicts of interest

References

- [1] Hayato Hisa, "Introduction of Products: Machine Control Hydraulic Excavator PC200i-11", *Komatsu Technical Report*, vol. 63, no. 170, 2017.
- [2] M. Kozui, T. Yamamoto, K. Koiwai, K. Yamashita and Y. Yamazaki, "Application of Digging Control based on the Center-of-Mass Velocity of the Attachment of a Hydraulic Excavator", *2019 IEEE/RSJ International Conference on Intelligent Robots and Systems (IROS)*, pp. 2314-2319, 2019. doi: 10.1109/IROS40897.2019.8968178.
- [3] R.Yu. Sukharev, A.V. Starostin. "Algorithm of an automatic control system for the working process of a hydraulic single-bucket excavator", *Vestnik SibADI*, vol. 6, no. 46, 2015.
- [4] Masakazu Haga, Watanabe Hiroshi, Kazuo Fujishima, "Digging control system for hydraulic excavator", *Mechatronics*, vol 11, no. 6, pp. 665-676, 2001.
- [5] D. A. Shekhovtsova, A. A. Ruppel, "Digging depth control device for a single-bucket excavator", *Vestnik IRGTU*, vol. 5, no. 88, 2014.

- [6] Q. Ha, M. Santos, Q. Nguyen, D. Rye, and H. Durrant-Whyte, “Robotic excavation in construction automation”, *IEEE Robotics and Automation Magazine*, vol. 9, no. 1, pp. 20–28, 2002.
- [7] Zhang Jingming, Zhang Zhen and Luo Nianning, “Kinematics Analysis and Trajectory Planning of the Working Device for Hydraulic Excavators”, *Journal of Physics Conference Series*, vol. 1601, no. 6, p. 062024, 2020. doi: 10.1088/1742-6596/1601/6/062024.
- [8] J. Gu, J. Taylor, and D. Sewar, “Proportional-integral-plus control of an intelligent excavator”, *Computer-Aided Civil and Infrastructure Engineering*, vol. 19, no. 1, pp. 16-27, 2004.
- [9] H. Yamamoto et al., “Development of the autonomous hydraulic excavator prototype using 3-D information for motion planning and control”, *IEEE/SICE International Symposium on System Integration*, pp. 49-54, 2010. doi: 10.1109/SII.2010.5708300.
- [10] M. E. Kontz, “Haptic control of hydraulic machinery using proportional valves”, PhD Dissertation. Georgia Institute of Technology, 2007.
- [11] M. Haga, W. Hiroshi, K. Fujishima, “Digging control system for hydraulic excavator”, *Mechatronics*, vol. 11, no. 6, pp. 665-676, 2001. [https://doi.org/10.1016/S0957-4158\(00\)00043-X](https://doi.org/10.1016/S0957-4158(00)00043-X)
- [12] E. Budny, M. Chłosta, W. Gutkowski, “Load-independent control of a hydraulic excavator”, *Automation in Construction*, vol. 12, no. 3, pp. 245-254, 2003. [https://doi.org/10.1016/S0926-5805\(02\)00088-2](https://doi.org/10.1016/S0926-5805(02)00088-2)
- [13] E.O. Podchasov, A.D. Terenteva, “Analysis of the accuracy of work performed by the working mechanism of a single-bucket excavator”, *MSTU im. N.E. Bauman*, Moscow, Russia, 2017.
- [14] A. D. Terenteva. “Analysis of the accuracy of displacement of the working body of a single-bucket excavator”, *Geometry of Mechanism*, Moscow, Russia, 2016.
- [15] W.Liu, X. Luo, J. Zhang, D. Niu, J. Deng, W. Sun and J. Kang, “Review on control systems and control strategies for excavators”, *Journal of Physics: Conference Series*, vol. 2301, pp. 1-16, 2022.
- [16] Bin Zhang, Shuang Wang, Yuting Liu and Huayong Yang, “Research on Trajectory Planning and Autodig of Hydraulic Excavator”, *Mathematical Problems in Engineering*, vol. 2017, pp. 1-10, 2017. <https://doi.org/10.1155/2017/7139858>.
- [17] H. Shao, H. Yamamoto, Y. Sakaida, T. Yamaguchi, Y. Yanagisawa, A. Nozue, “Automatic Excavation Planning of Hydraulic Excavator”, In: *Xiong, C., Liu, H., Huang, Y., Xiong, Y. (eds) Intelligent Robotics and Applications*, vol. 5315, pp. 1201–1211, 2008. https://doi.org/10.1007/978-3-540-88518-4_128.
- [18] B. Vladilen Ivanovich, Multipurpose road-building and technological machines (determination of parameters and selection), Russian State Library (RSL), 2006.

- [19] D. D. Nguyen, D. V. Chu, S. V. Le, “Dynamic analysis and simulation of the hydraulic control system on the remote-controlled explosive ordnance disposal machine”, *The International Journal of Manufacturing, Materials, and Mechanical Engineering*, vol. 11, no. 3, pp. 1-18, 2021. DOI: 10.4018/IJMMME.2021070103.
- [20] D. D. Nguyen, D. V. Chu, S. V. Le “Modelling and Simulation of the Hydraulic System on EODM Machine”, *In: Long, B.T., Kim, YH., Ishizaki, K., Toan, N.D., Parinov, I.A., Vu, N.P. (eds) Proceedings of the 2nd Annual International Conference on Material, Machines and Methods for Sustainable Development (MMMS2020). Lecture Notes in Mechanical Engineering*, 2021. https://doi.org/10.1007/978-3-030-69610-8_66.
- [21] Q. Ha, M. Santos, Q. Nguyen, D. Rye, and H. Durrant-Whyt, “Robotic excavation in construction automation”, *IEEE Robotics and Automation Magazine*, vol. 9, no. 1, pp. 20–28, 2002.
- [22] A.G. Gimadiev. “LMS Imagine.lab Amesim As an effective tool for modeling dynamic processes in mechatronic systems”, *Samara*, 2014. https://www.plm.automation.siemens.com/en_us/Images/Siemens-PLM-LMS-Imagine-Lab-Amesim-for-heavy-equipment-fs_tcm1023239517.pdf.
- [23] Nicolae Vasiliu, Daniela Vasiliu, Constantin Călinoiu, Radu Puhalschi, *Simulation of fluid power systems with Simcenter Amesim*, 1st Edition, CRC Press, 2018.
- [24] J. Zhang et al. “Design of Intelligent Hydraulic Excavator Control System Based on PID Method”. *In: Li, D., Zhao, C. (eds) Computer and Computing Technologies in Agriculture III. CCTA 2009. IFIP Advances in Information and Communication Technology*, vol. 317, pp 207–215, 2010. https://doi.org/10.1007/978-3-642-12220-0_31

The Influence of Repeated Heat Treatments on The Propagation of Fatigue Cracking of Medium Carburized Steel

Majid Khaleel Najem, Jamal Nayief Sultan
Northern technical university/ Tech. Eng. College-Power Mech.
Eng. Dep., - Mosul, IRAQ

Emad Toma Karash*, Adel M. Ali, Hssein A. Ibrhim
Northern Technical University - Technical Institute Mosul, IRAQ
*emadbane2007@ntu.edu.iq

ABSTRACT

The issue of metal fatigue emerged as one of the major issues in a variety of engineering designs, and the design engineers were forced to take metals' fatigue resistance into account. In this paper, multiple quenching mediums and varied heat treatments were utilized to examine the effects of various heat treatments on the development of fatigue cracking in steel. The model that was carburized, quenched in distilled water and tempered before being quenched once more in distilled water and tempered a second time had the best outcomes, the fewest cycles needed to cause the model to fail, and a correlation between the rate of fatigue crack propagation and the length of the crack, according to the results. Additionally, the analytical findings demonstrated that this model, as opposed to models with fixed stress intensity factors, has a fatigue crack growth rate. The model that was carburized, quenched in coolant, then tempered and quenched again without performing the tempered appearance failed very rapidly. The high rate of the stress intensity factor with fatigue crack propagation is shown by the data analysis. The results show a reduction in the growth amount tendency of fatigue crack in the linear region mode-III.

Keywords: Tensile Strength; Fatigue; Heat Treatment; Grain Structure; Quenching; Tempering, Carburized

Introduction

Engineering machinery and installations must fulfill the following three main requirements: to perform the required work, and function intended, have an appropriate and acceptable life service, and be able to perform production at reasonable costs. Appropriate operating period is taken into account in approximate ways at the design mode for parts subjected to repeated loads because most of the design engineers are not sufficiently familiar with the art of operation with time. Its parts after an inappropriate period of operation. The occurrence of this collapse is frequent with fatigue, so its importance increases with machines whose performance requires the presence of the property of light weight of the metal and thus the occurrence of high stresses in the metal during operation, and aircraft is one of the clear examples of this where light weight is of paramount importance.

Metal fatigue has received great attention to obtain adequate safety for machinery and engineering facilities, especially those whose collapse causes loss of life, as in the issues of aircraft parts design, where strict rules were imposed in the design so that those parts would have an appropriate resistance to fatigue. The main principles and comparisons are made based on experience to determine the acceptable fatigue resistance, as it is taken into account when designing that when a crack occurs, it does not have a destructive influence, and these rules determine the duration of operation of those different parts. In [1], they investigated the crack associated with macro-pitting in the gearbox bearing. They used the technique of accelerated bench top test to find the difference in performance between hardened AISI 52100 steel and carburized AISI 3310 steel. They found that the time of the appearance of pitting in the surface in AISI 3310 steel is twice that of hardened AISI 52100 steel.

Using the finite element method, the depth of the carburized case of SAE 8620 steel gears was predicted [2]. The martensitic growth in grain inside the carburized case, and by simulation, check the influence of carburizing and different adherent austenite contents on the large fatigue action of SAE 8620 steel catalytic gears. The model used shows that the depth of the case increases with growing heat treatment temperature and time. A large number of studies have shown that surface carburizing treatment can significantly improve the fatigue performance of steel [3]-[4]. Heat treatment techniques have been studied on stress in gears, as well as different cooling media and a mathematical and experimental model has been proposed [5]. The bending stress on carbon steel was studied and compared with the carbonization of conventional gas, and they concluded that the gas-carburized models have less resistance to all of the traditional gas-carburized models [6]. In this study [7], the relationship between the modality of how different cracks propagated and the microstructure of steel was studied. They found that decreasing the induction heat temperature from (1043-1143 K)

increases the crack propagation resistance by 30%. In [8], they investigated numerically and experimentally carburized AISI 8620 steels. They found that the results gated by numerical agreement with that got experimentally. While in [9], a mathematical model (elastic-plastic) was created using the finite element method, and this model relies on tests with the presence of a first slit to study the growth of fatigue cracking. The results showed that the hardness difference is linear from the outer surface of the model to the inside in the core of the model. In [10], the microstructure was studied on the growth of fatigue cracking of the carbonized models, and the results showed that the samples with a microstructure containing martensitic have better resistance to the growth of fatigue crack progression than those samples containing in the microstructure ferrite. Authors in [11] combined the scanning electron microscope images and Photoshop software, then the conversion rate between pixels and actual length of scale were calculated, after that the cracks parameters were known by pixel. A research in [12] provided a unified technique to evaluate changes in the amplitude of the microplasticity strain and intrinsic thermal dissipation for ASE 1045 steel. They discovered that the outcomes of this strategy are in excellent accord with those of the conventional method. In [13], they studied fatigue in the rolling contact performance of carburized steel and high-carbon steel, with the same volume fraction. The nanostructure Bainitic microstructures were obtained from the two alloy steels. They discovered that the carburized nanostructured bainitic steel's rolling contact fatigue life outperforms that of high-carbon steel. Then in [14], they studied the effect of adhesive austenite on rolling contact stress using stiffness tests, X-ray diffraction, scanning electron microscopy, and transmission electron microscopy. The rolling contact stress shows that the subsurface fragment life begins to increase as the adhesive austenite increases. The crack propagation rate of the carbon steel layer was evaluated according to SAE 4320, and it was found that as the carbon content decreased, the resistance to stress crack growth increased [15]. In [16], they used finite element modeling to find the influence of carbon allocation on residual stress in gears, then proposed a method to design the minimum case depth to obtain the lowest residual stresses. In [17], carburizing vacuum quenching and high-pressure gas were used for hollow rotational stress samples made with AISI 9310. The non-equilibrium shape has been shown to have little influence on the residual stress after quench solidification. While [18] used finite elements to thoroughly study the low-carbon steel carburization process. In [19], two allocation methods were used based on the prediction of crack characteristic size of Cr-Ni carbon steel alloy. The first is the generalized maximum and the second is the generalized Pareto allocation. The results show that the generalized maximum allocation can predict fatigue strength better than the generalized Pareto distribution allocation. In [20], a mathematical model was made to simulate a sliding gear, which is a hole for lubrication, and two models were used in that, and

the results showed that the samples with lead holes are more efficient in resisting fatigue cracking in the presence of contact stress. [21] This study focused on how austenitic grain size affected the onset and advancement of fatigue cracking for carbon steel's mode-II, and the results showed that the high leveling and finishing processes with the size of austenite grains led to an increase in the resistance to initiation and progression of fatigue cracking in the mode - II. Dynamic recrystallization was used to refine the grain size, as stated in [22]. The sliding dry wear behavior of martensite steel under various friction circumstances was taken into consideration by the authors of [23]-[24]. After being quenched and tempered twice, the microstructures and mechanical characteristics of steels with various carbon contents were examined [25]-[27]. The primary cause of this effect is the deformation of the original microstructures, which had an impact on how the microstructure changed during quenching and tempering [29]-[30]. This deformation led to the austenite grains becoming more refined and the carbides dissolving more quickly during the subsequent austenitization step [28]. With increasing initial hot rolling reduction, the results indicate an increase in Vickers hardness but a sizable drop in friction coefficient and wear rate [31].

In this article, different heat treatments, such as model quenching in different media, tempering, and repeated numerous times after carburizing on the models, are used to study the fatigue cracking propagation behavior of medium carbon steels. Selecting the most effective cooling method for usage following the quenching procedure and the kind of heat treatment. Additionally, specialized software will be employed to create equations that anticipate growth, development, and collapse under the impact of fatigue stresses.

Materials and Experimental Procedure

Materials

According to the German Standard, the medium carbon steel employed in this study is used in industry for a variety of purposes (DIN). A spectrometer was used to do a chemical analysis of the composition of medium carbon steels. Table 1 provides information on the metal used in the document's actual and typical chemical compositions.

Table 1: Results of chemical analysis for the metal used

Wt., %	C	Si	Mn	P	S	Mo	Cu	Fe
Standard value	0.42 - 0.5	0.15 - 0.35	0.5 - 0.8	≤ 0.035	≤ 0.035	-----	-----	Rem
Actual value	0.482	0.221	0.562	0.011	0.033	0.0788	0.0154	98.596

Carburization

After the extension of carburizing atoms to the surface of steel components, quenching and tempering at low temperatures is known as carburizing. The corrosion resistance, toughness, hardness, and other steel qualities can all be significantly enhanced through the carburizing process. After processing, the parts have a low-carbon martensite core that is strong and durable enough, and a hard, wear-resistant martensite surface with a small amount of soft carbide structure. We refer to steel that has been carburized as having been carburized. In this study, cylindrical carbon steel wear test samples were treated to a four-hour soaking time at 950 °C in a powder combination made up of 75% charcoal and 25% barium carbonate using pack carburizing techniques (BaCO_3). After the carburization procedure, the wear testing samples were split into three groups (A, B, and C) for heat treatment.

Heat treatments

The carburized steel specimens were split into three groups (A, B, and C) after heat treatment processes:

- i. Group (A): All carburized steel samples were cooled to room temperature using a range of quenching media including solutions (distilled water, milk, motor oil, shampoo, water, sugar, cooling fluid, and food oil) after soaking for 20 minutes at a temperature of 780 °C. The samples were then heated for 20 minutes at 230 °C.
- ii. Group (B): Each piece of carburized steel was quenched in a different quenching fluid (distilled water, milk, motor oil, shampoo, water and sugar, cooling fluid, and food oil), after soaking for 20 minutes at 780 °C. Then, to temper the samples, they were all heated to 230 °C for 20 minutes. All previously quenched steel samples were once again quenched at 770 °C in distilled water.
- iii. Group (C): All carburized steel samples were quenched in various quenching fluids (distilled water, milk, motor oil, shampoo, water and sugar, cooling fluid, and food oil), after soaking for 20 minutes at 780 °C. The samples were then heated to 230 °C and allowed to soak for 20 minutes. All previously quenched steel samples were then quenched a second time at 770 °C using distilled water as the quenching medium. Following that, each of the earlier steel samples was heated to (250 °C) for a twenty-minute soaking time.

Manufacture of fatigue test samples

The model's dimensions were as shown in Figure 1, and circular-section samples were employed with an initial incision that was 0.5 mm wide and 0.2 mm deep. The samples' ends were flattened at 90 °C to one another after being produced to the desired dimensions. To guarantee that the models' perimeters have an identical dimensional incision as shown in Figure 1. All samples that were used had their slit depth and sample diameter measured

using a coordinate measuring device. The stress ratio for all tests will be zero ($R=0$).

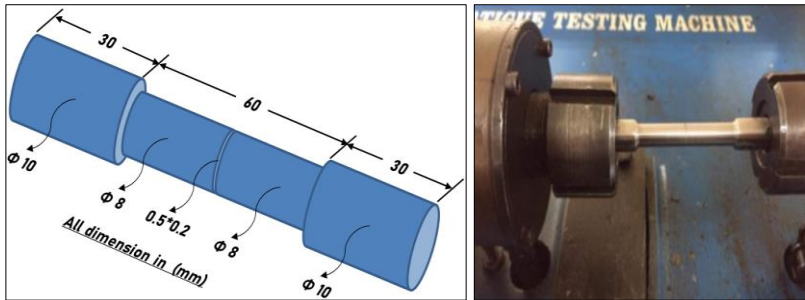


Figure 1: The machine and the dimensions of the model used in the test

Characterization of specimens from fatigue tests

To analyze the behavior of cracking propagation of the entire after executing various heat treatments, a 22 model of low-carbon steel was chosen (carburizing, quenching in different media, and tempering). They are categorized in Table 2.

Table 2: Classification of medium carbon steel samples used in fatigue tests

No.	Type of heat treatment	Group symbol - (A) (carbonation – quenching in different media, tempering)	Group symbol - (B) (carbonation – quenching in different media, tempering- quenching in distilled water)	Group symbol - (C) (carbonation – quenching in different media, tempering - quenching in distilled water, tempering)
1	As receive		AS (As Received)	
2	Carbonation and quenching in shampoo	A 1	B 1	C 1
3	Carbonation and quenching in water &	A 2	B 2	C 2
4	Carbonation and quenching in milk	A 3	B 3	C 3
5	Carbonation and quenching in food oil	A 4	B 4	C 4
6	Carbonation and quenching in motor oil	A 5	B 5	C 5
7	Carbonation and quenching in cooling	A 6	B 6	C 6
8	Carbonation and quenching in distilled	A 7	B 7	C 7

Results and Discussion

Microstructure

The produced structures were studied using a Leica DM 2500 M microscope both before and after heat treatment.

Group A: (carbonation and quenching, tempering)

The microstructure of the first group samples (group A) is shown in Figure 2. These samples were quenched at 770 °C with a range of quenching solutions (distilled water, milk, motor oil, shampoo, water, sugar, cooling fluid, and food oil), before being tempered at 230 °C.

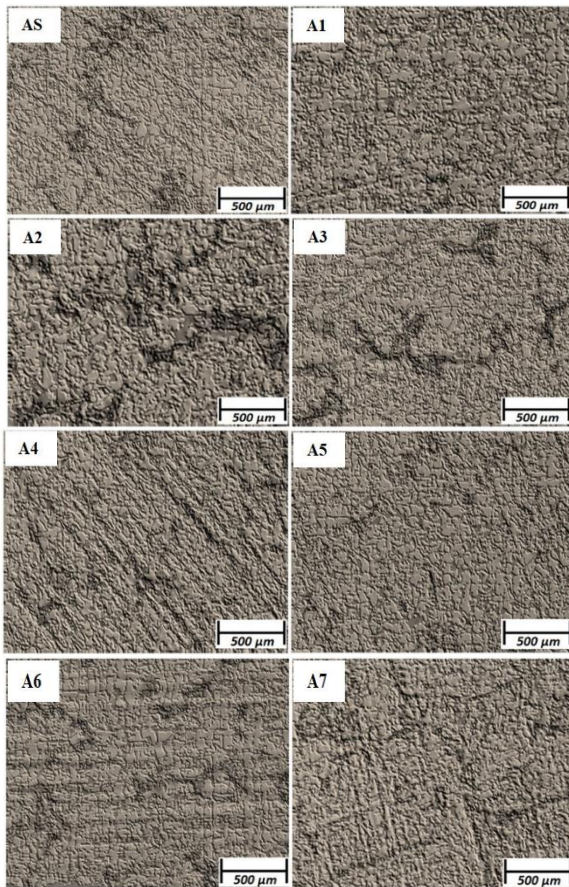


Figure 2: The microstructure of group a steel samples: carbonation – quenching, tempering

Group - B: (carbonation and quenching, tempering and quenching)

Figure 3 depicts the microstructure of the samples from the second group (group B). Carburized steel samples were quenched at 770 °C with a variety of quenching liquids (distilled water, milk, motor oil, shampoo, water, sugar, cooling fluid, and food oil), then heated to 230 °C temperature and quenched again at 770 °C using distilled water as a quenching liquid.

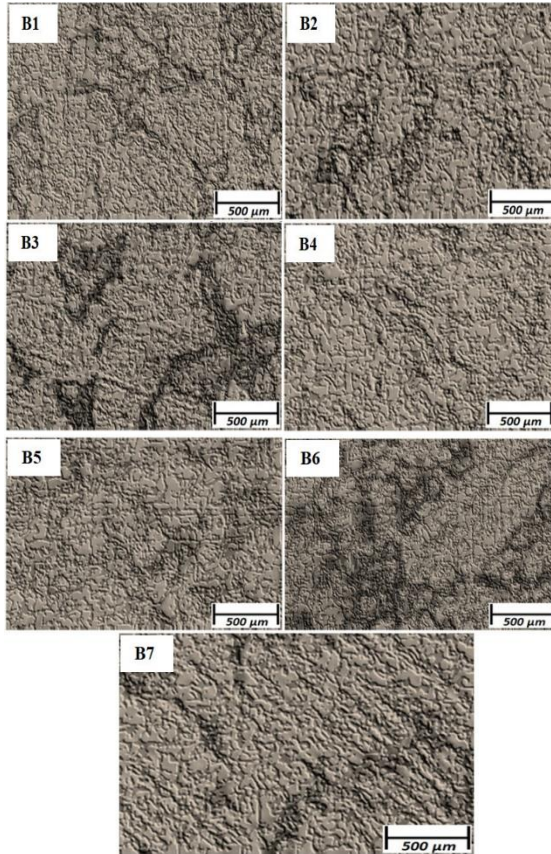


Figure 3: The microstructure of group (B) steel samples: carbonation – quenching, tempering- quenching

Group C: (carbonation, quenching, tempering and quenching, tempering)

Figure 4 depicts the microstructure of the samples from the third group (group C). In this group, several quenching liquids, such as food oil, milk, shampoo, motor oil, water with sugar, and cooling liquid, were used to

quench the carburized steel samples. They were then quenched once again with distilled water after being tempered at 230 °C. They underwent a second 250 °C tempering procedure after that.

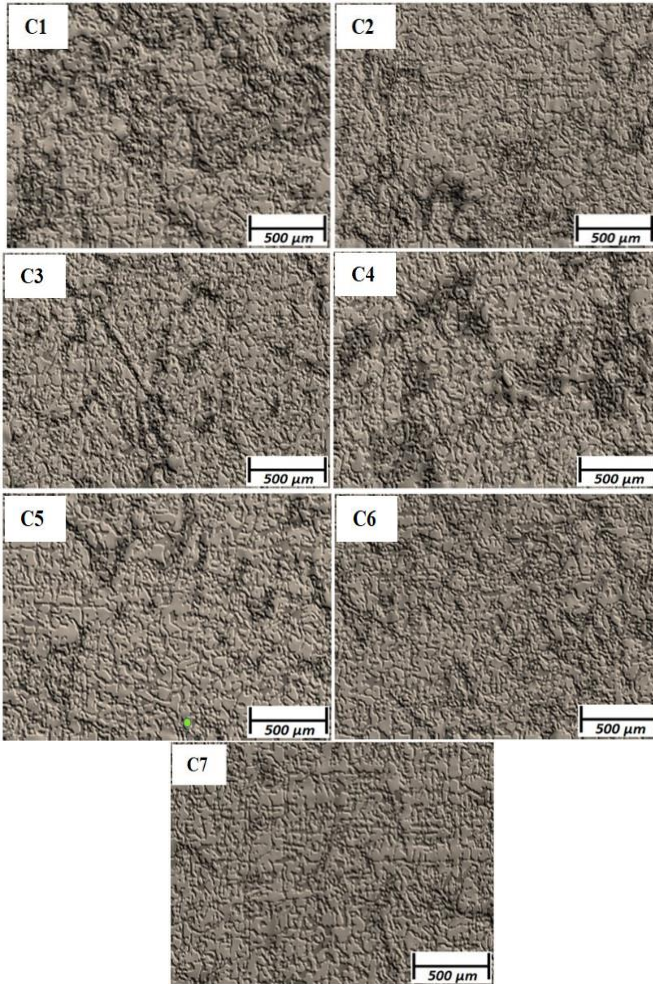


Figure 4: The microstructure of group (C) steel samples: carbonation – quenching, tempering - quenching, tempering

Figures 5-16 analyze the fatigue test results when a load of 171.073 MPa is applied to all samples that have undergone various heat treatments (distilled water, milk, motor oil, shampoo, water, sugar, cooling fluid, and food oil).

Schemes the length of the cycle number with the length of the crack

Figures 5-8 compare the findings for the three groups that were tested in terms of the association between the number of cycles and the crack length (A, B, and C). The cycle number and the crack duration for each model used in the test and in comparison to the original model are contrasted in Figure 5.

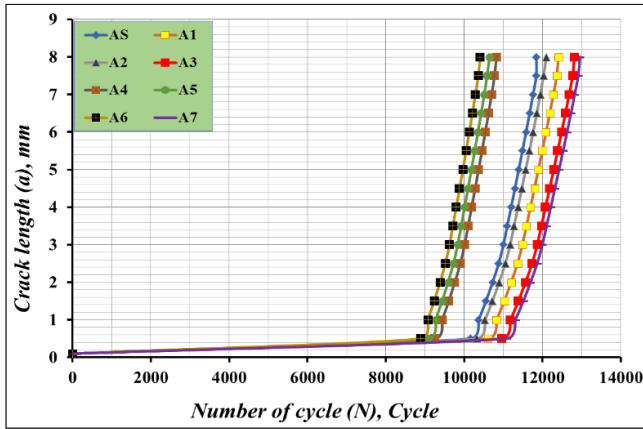


Figure 5: Appears group –A: the original specimen is compared to stress crack propagation curves

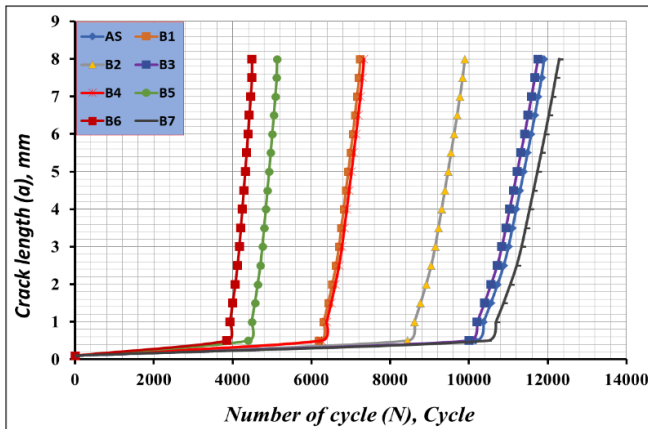


Figure 6: Appears group – B: The original specimen is compared to stress crack propagation curves

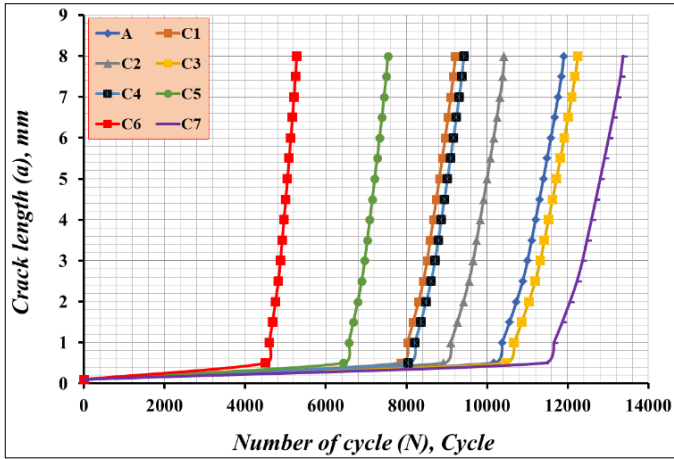


Figure 7: Appears group – C: The original specimen is compared to stress crack propagation curves

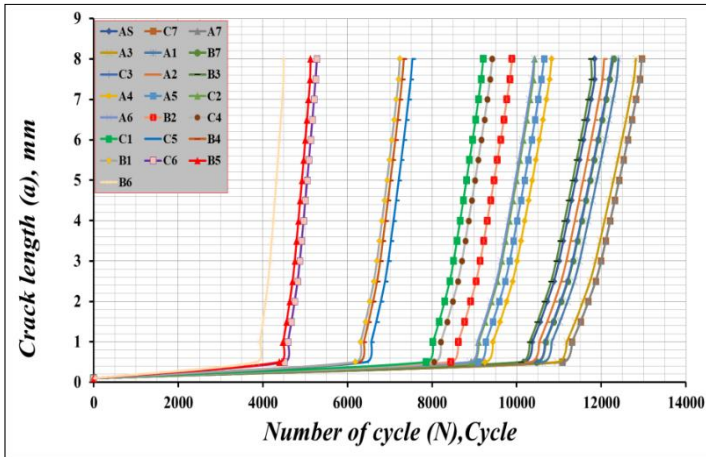


Figure 8: Appears all-groups: The original specimen is compared to stress crack propagation curves

Conclusion of the crack growth rate of fatigue

The crack growth rate (da/dN), and values of the fatigue were calculated using a finite difference (Newton forward difference, central finite difference, and Newton backward finite difference) method by entering all the values obtained from the various checks for the growth of the fatigue crack progression. For each of the analyzed models, Figures 9-12 display the

results of constructing those curves as well as the relationships between crack length (a) and crack development rate (da/dN).

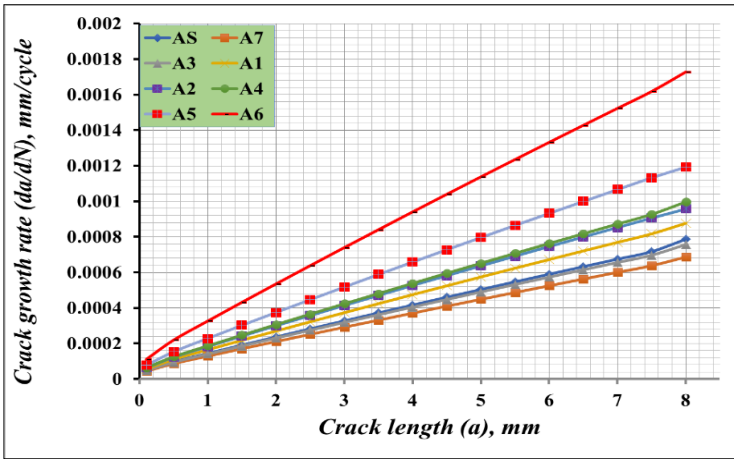


Figure 9: Shows the relation between fatigue crack growth rate and crack length for group A

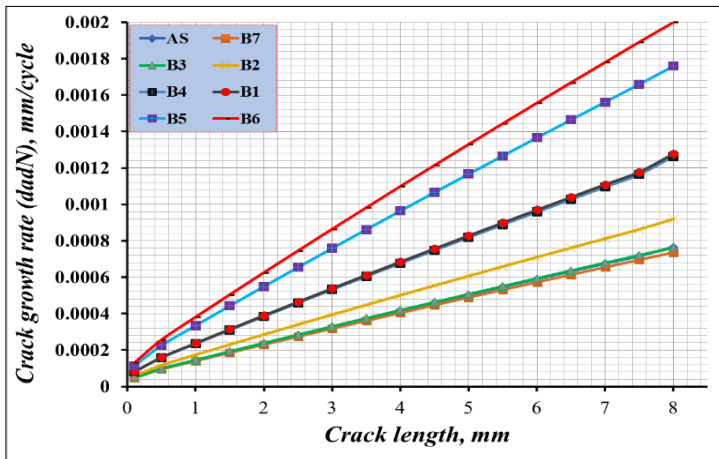


Figure 10: Demonstrates the connection between the length of group-B cracks and the rate of fatigue crack propagation.

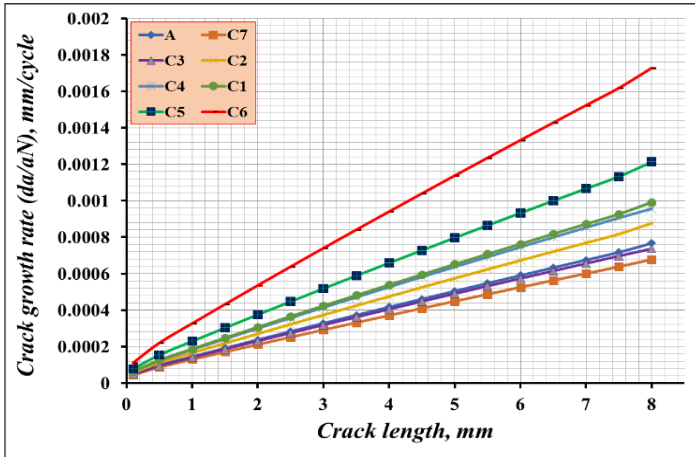


Figure 11: Demonstrates the connection between the length of the group-C crack and the rate of fatigue crack propagation

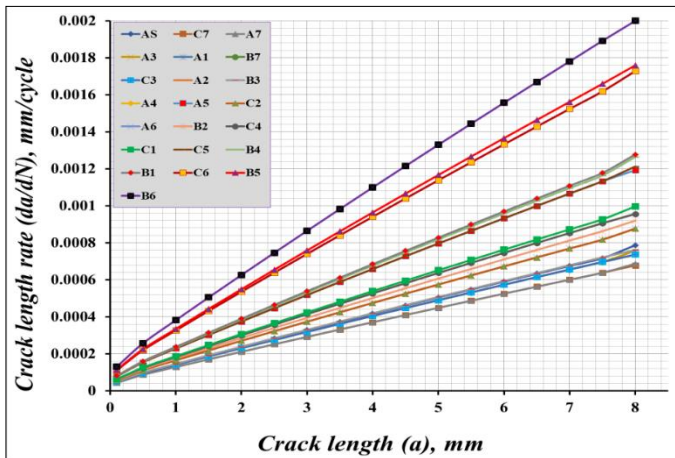


Figure 12: Demonstrates the connection between the length of cracks and the rate of fatigue crack propagation for all models

Measurement of fatigue crack propagation

For the models that had various heat treatments, 22 tests were conducted to ascertain the evolution of fatigue cracking with a first crack that had a depth of (0.2 mm), an extension of the fissure in a plane inclined at an angle of 45°, and the formation of a crack in the factory's roof. The evolution of fatigue cracking was measured using the direct current voltage drop method. By

referring to Figure 13 and using Equation (1), (2) and (3), the stress intensity factor (ΔK_{III}) was calculated [32].

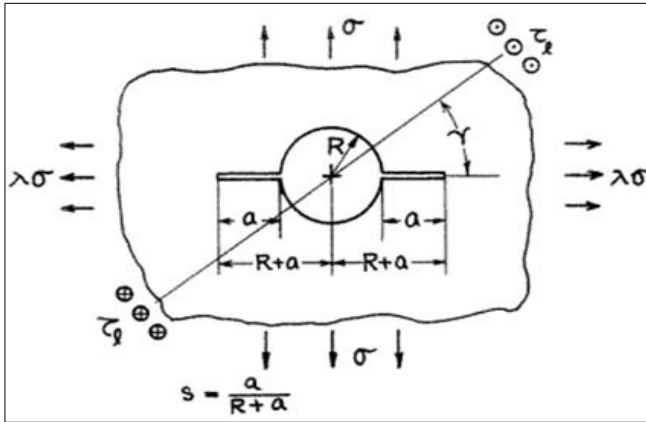


Figure 13: The model of fatigue crack propagation

$$\Delta K_{III} = \tau_N \cdot \sqrt{\pi a} \cdot F(s) \cdot \sin \gamma \quad (1)$$

where,

$$\tau_N = \frac{2T}{\pi a^3}; \quad (2)$$

$$F(s) = \sqrt{(2-s) \cdot (2-2s+s^2)} \quad (3)$$

a = Crack length, R = Radius with slit of the specimen, T = Torque
 τ_N = Net section shear stress

These criteria are given by Benthem and Koiter [33], and with accuracy is better than one percent, according to its exact method Asymptotic Approximation. A torque of $T=175 \text{ Kg.cm}=17167.5 \text{ N.mm}$ was used and a first slit of $a=0.2 \text{ mm}$ was used, and the diameter of the shaft was $d=8 \text{ mm}$. Figures 14-17 show the relation between the stress intensity factor (ΔK_{III}) and the fatigue cracking growth rate (da/dN) in the linear region mode - II, which is consistent with the Paris equation, and the mode - III which leads to the failure of the model, where the increased rate of fatigue cracking is fast in this area.

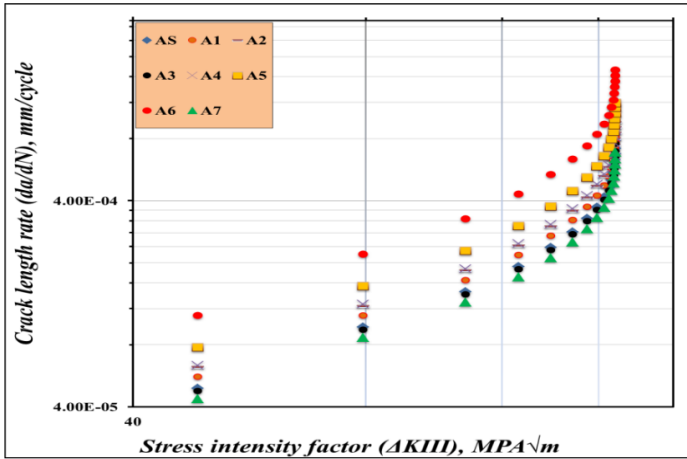


Figure 13: Relationship between the fatigue cracks growth rate (da/dN) and the factor of the stress concentration (K_{III}), at the linear region where the fatigue crack first appears, grows, and where the model breaks down for group-A

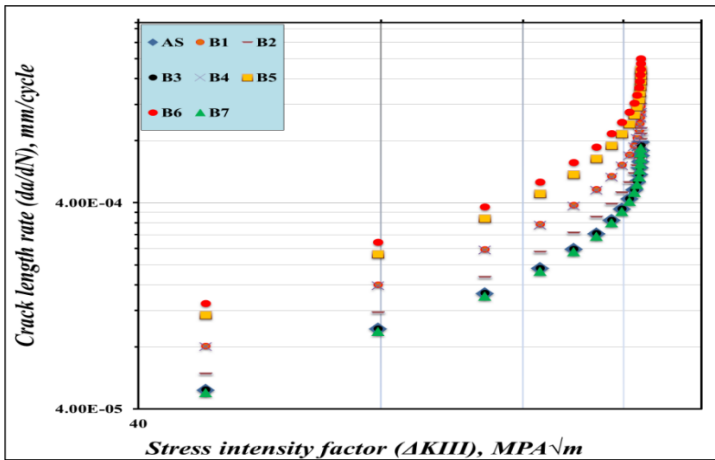


Figure 14: Relationship between the fatigue cracks growth rate (da/dN) and the factor of the stress concentration (K_{III}), at the linear region where the fatigue crack first appears, grows, and where the model breaks down for group-B

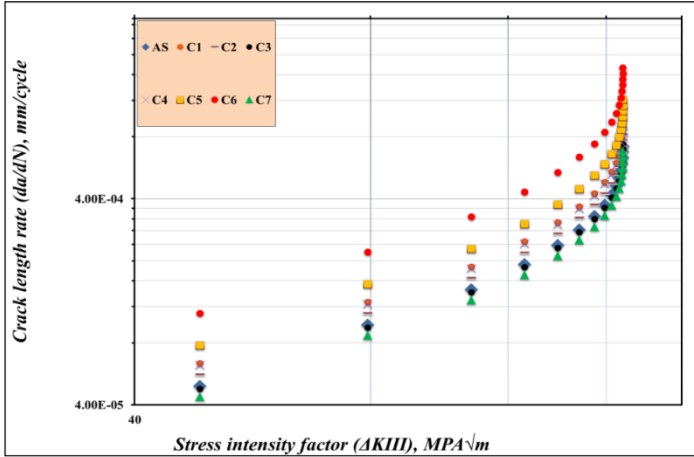


Figure 15: Relationship between the fatigue cracks growth rate (da/dN) and the factor of the stress concentration (K_{III}), at the linear region where the fatigue crack first appears, grows, and where the model breaks down for group-C

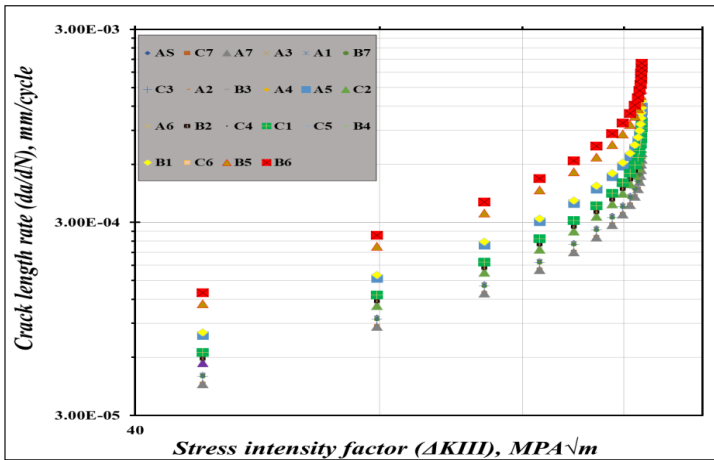


Figure 16: Relationship between the fatigue cracks growth rate (da/dN) and the factor of the stress concentration (K_{III}), at the linear region where the fatigue crack first appears, grows, and where the model breaks down for all specimens

The structure of martensitic resulting from the hardening of carbon steel in water hinders the growth of fatigue cracks. The fatigue limit rises as a

result of the interfacial barriers of the martensitic structure. The growth of these cracks is hindered by a larger microstructure consisting of martensite reviewed with a little bit of bainite, as this structure is characterized by being devoid of internal stresses that result from hardening, so the fatigue limit of the water-hardened steel increased.

Deduce crack growth behavior equations

For five models, including the original model, the best three models, and the worst model (AS, C7, A7, A3, and B6) to compare them, the Curve Expert program was used to derive the equations that describe the growth of the fatigue crack mode-III. Table 3 shows the values entered into the program, to obtain the fatigue cracks progress rate in the linear region. These equations are consistent with the Paris formula in the linear zone. The examination of those equations' findings is shown in the following Equations (4)-(8).

Table 3: It shows the values used to obtain the fatigue crack growth rate (Mode - III) in the linear region using the program Curve Expert

ΔK_{III}	AS (as received)	C7	A7	A3	B6
48.45533555	4.92028E-05	4.37833E-05	4.37833E-05	4.78285E-05	0.000129795
79.37775342	9.74173E-05	8.6687E-05	8.6687E-05	9.46962E-05	0.000256982
107.6715142	0.000144779	0.000128832	0.000128832	0.000140735	0.000381921
125.9996407	0.000191395	0.000170314	0.000170314	0.000186049	0.000504892
138.8219901	0.000237341	0.000211198	0.000211198	0.000230711	0.000626094
148.0347052	0.000282786	0.000251638	0.000251638	0.000274887	0.000745976
154.6795392	0.000327826	0.000291717	0.000291717	0.000318669	0.00086479
159.4244172	0.000372469	0.000331442	0.000331442	0.000362065	0.000982555
162.7409696	0.000416726	0.000370825	0.000370825	0.000405086	0.001099305
164.9839909	0.000460611	0.000409876	0.000409876	0.000447745	0.001215071
166.4314112	0.000504134	0.000448605	0.000448605	0.000490053	0.001329883
167.3058301	0.000547308	0.000487023	0.000487023	0.00053202	0.001443774
167.7864699	0.000590143	0.000525141	0.000525141	0.000573659	0.001556771
168.0157625	0.000632664	0.000562978	0.000562978	0.000614992	0.001668939
168.102807	0.000674885	0.000600548	0.000600548	0.000656034	0.001780315
171.2422576	0.000716884	0.000637951	0.000637951	0.00069685	0.001891599
168.1288912	0.000786884	0.000677951	0.000686884	0.000756884	0.001999654

$$\frac{da}{dN} = 2.245 * 10^{-6} \Delta K^{2.251} - 7.541 * 10^{-5}, \text{ for model (AS)} \quad (4)$$

$$\frac{da}{dN} = 1.997 * 10^{-6} \Delta K^{2.011} - 6.711 * 10^{-5}, \text{ for model (C7)} \quad (5)$$

$$\frac{da}{dN} = 1.997 * 10^{-6} \Delta K^{2.013} - 6.711 * 10^{-5}, \text{ for model (A7)} \quad (6)$$

$$\frac{da}{dN} = 2.182 * 10^{-6} \Delta K^{2.125} - 7.331 * 10^{-5}, \text{ for model (A3)} \quad (7)$$

$$\frac{da}{dN} = 5.922 * 10^{-6} \Delta K^{5.833} - 1.999 * 10^{-4}, \text{ for model (B6)} \quad (8)$$

Conclusions

The following was discovered by comparing the results of the fatigue tests before and after the various heat treatments of carbonization and quenching in various mediums, as well as a tempering after quenching of all samples, and after evaluating the data in various programs:

- i. The number of cycles required for the growth of the fatigue crack in the two models (A7, and C7) increased by 88.66% compared to the required cycles number in the original model (AS), while the number of cycles in the model (B6), which is the worst model in the tests, was less by 61.94% for the number of cycles in the original model (AS).
- ii. The figures for the crack growth rate of fatigue show a noticeable fatigue crack growth rate increase in the worst model in the test, model B2, between $0-2*10^{-3}$, in comparison to the original model, whose value was between $0-0.69*10^{-3}$, and then the crack growth rate increase was in the two models (B5, and C6), where the values of the fatigue crack growth rate were between $0-1.88*10^{-3}$.
- iii. The logarithmic figures demonstrate the relationship between the stress intensity factors and the crack length growth rate in the linear region mode - II. The model (B6) has a much higher crack length rate than the original model, but the variance in the two models' crack length rates is relatively small (A7, and C7). The figures also depict the failure zone of the model in the mode III region, where the fatigue rate values of the crack growth and the factor of stress intensity have converged. The crack development rate is rapid, and the failure process is swift in the mode III region.
- iv. The obtained equations agree with the Paris formula for fatigue crack development growth and are shown by Curve Expert software with fatigue crack growth behavior in linear zone mode-III. Since the form has superior resistance to fatigue cracking, the tendency for crack progression in this area is reduced.

Contributions of Authors

The researchers emphasize and acknowledge equal contribution to each component of our effort. The final draft of this work has been reviewed and approved by all researchers.

Funding

There was no specific grant from any funding organization for this work.

Conflict of Interests

Our authors all certify that we have no conflicts interests.

Acknowledgment

The manuscript was funded by the Research Program of the Department of Mechanical Technology at the Northern Technical University-Technical Institute in Mosul, Iraq]. (No. 2021-00533).

References

- [1] G. Benjamin, P. Mohanchand, G. D. Nicholaos, C. G. Aaron, R. S. Hyde, "The Impact of Steel Microstructure and Heat Treatment on the Formation of White Etching Cracks", *Journal of Tribology International*, vol. 134, pp. 232-239, 2019. <https://doi.org/10.1016/j.triboint.2019.02.003>.
- [2] C. Edward, C. B. Henry, K. Y Hemantha, "Multi-length scale modeling of carburization, martensitic microstructure evolution and fatigue properties of steel gears", *Journal of Materials Science & Technology*, vol. 49, pp. 157-165, 2020. <https://doi.org/10.1016/j.jmst.2019.10.044>.
- [3] N. Xiao, W. J. Hui, Y. J. Zhang, X. L. Zhao, Y. Chen, H. Dong, "High cycle fatigue behavior of a low carbon alloy steel: The influence of vacuum carburizing treatment", *Engineering Failure Analysis*, vol. 109, pp. 1-25, 2019. <https://doi.org/10.1016/j.engfailanal.2019.104215>.
- [4] X. Yanjun, Y. Yongming, Y. Wenchao, D. Mingzhen, S. Jie, W. Maoqiu, "Microstructure and fatigue properties of 17Cr2Ni2MoVNb gear steel after gas carburizing and low-pressure carburizing",

- International Journal of Fatigue*, vol. 167, part A, p. 107314, 2023. <https://doi.org/10.1016/j.ijfatigue.2022.107314>.
- [5] Y. Enesi, O. O. Salawu, A. Ajayi, A.P.I P. Inegbenebor, U.O. Uyor, “Effects of Heat Treatment Techniques on the Fatigue Behaviour of Steel Gears: A Review”, *Journal of Physics: Conference Series*, vol. 1378, no 4, pp. 1-6, 2019. <https://doi.org/10.1088/1742-6596/1378/4/042001>.
- [6] A. Osman, Ç. C. Ahmet, P. James, , B. Mohammed, “The influence of high temperature gas carburizing on bending fatigue strength of SAE 8620 steel”, *Journal Materials & Design*, vol. 30, no. 5, pp. 1792-1797, 2009. <https://doi.org/10.1016/j.surfcoat.2006.11.006>.
- [7] Kazuaki, Okada, O. Koji, T. Yoshikazu, A. Nozomu, “Crack propagation behavior of impact crack in case hardening steel subjected to combined heat treatment with excess vacuum carburizing and subsequent induction hardening”, *International journal of Transactions of the Iron and Steel institute of Japan*, vol. 60, pp. 2576-2585, 2020. <https://doi.org/10.2355/isijinternational.ISIJINT-2019-826>.
- [8] S. Yi, M. M. Sina, S. Farshid, P. Kristin, W. Trice, “Influence of engaged austenite Compressive residual stresses on rolling contact fatigue life of carburized AISI 8620 steel”, *International Journal of Fatigue*, vol. 75, pp. 135-144, 2015. <https://doi.org/10.1016/j.ijfatigue.2015.02.017>.
- [9] A. Aditya, F. S. Walvekar, Rolling contact fatigue of case carburized steels,” *International Journal of Fatigue*, vol. 95, pp. 264-281, 2017. DOI:10.1016/j.ijfatigue.2016.11.003.
- [10] H. Farivar, D. N. kshanov, S. D. L. Richter, W. Bleck, U. Prael, “Core microstructure-dependent bending fatigue behavior and crack growth of a case-hardened steel”, *Journal Materials Science and Engineering*, vol. 762, no. 5, pp. 1-24 , 2019. <https://doi.org/10.1016/j.msea.2019.138040>.
- [11] Q. Yanfei, W. Bo, L. Shudan, Xiqiang, Ren., Z. Jingyi, L. Yungang, M. Jinjun, “Improved quantitative analysis method for evaluating fatigue cracks in thermal fatigue testing”, *Journal Materials Letters*, vol. 242, pp. 115-118, 2019. <https://doi.org/10.1016/j.matlet.2019.01.113>.
- [12] T. Zhenjie, W. Haoran, B. Christian, , S. Peter, “A unified fatigue life calculation based on intrinsic thermal dissipation and microplasticity evolution”, *International Journal of Fatigue*, vol. 131, pp. 1-8, 2020. <https://doi.org/10.1016/j.ijfatigue.2019.105370>.
- [13] W. Yanhui, , Z. Fucheng, B. L. Yang, Z. Chunlei, “Rolling contact fatigue performances of carburized and high-c nanostructured bainitic steels”, *Journal of Materials*, vol. 9, no. 12, pp. 1-12 , 2016. <https://doi.org/10.3390/ma9120960>.
- [14] K. Kohei, M. Tsuyoshi, U. Kohsaku, “Influence of Engaged Austenite on Sub-surface Initiated Spalling during Rolling Contact Fatigue in

- Carburized SAE4320 Steel”, *International journal of Transactions of the Iron and Steel institute of Japan*, vol. 60, no. 8, pp. 1774-1783, 2020. <https://doi.org/10.2355/isijinternational.ISIJINT-2019-715>.
- [15] L.T. Sandor, I. Politori, C. S. Gonçalves, A. Y. C.V. Uehara, M. S. Leal, I. Ferreira, “Fatigue crack propagation in nine steels, type SAE 43XX, from 0.20 to 1.00 % C, for the simulation of the fatigue behavior in a carburized layer of the SAE 4320”, *Journal Procedia Engineering*, vol. 2, no. 1, pp. 735-742, 2010. <https://doi.org/10.1016/j.proeng.2010.03.079>.
- [16] Li Zhichao, M. Andrew, B. D. Freborg, T. S. S. Hansen, “Modeling the Influence of Carburization and Quenching on the Development of Residual Stresses and Bending Fatigue Resistance of Steel Gears”, *Journal of Materials Engineering and Performance*, vol. 22, pp. 664-672, 2013. <https://doi.org/10.1007/s11665-012-0306-0>.
- [17] L. Zhichao, “Heat treatment response of steel fatigue sample during vacuum carburization and high-pressure gas quenching process”, *ASME 2015 International Manufacturing Science and Engineering Conference*, pp. 1- 6, 2015. <https://doi.org/10.1115/MSEC2015-9395>.
- [18] I. Roslinda, A. Shahrum, T. Prakash, Z. O. Mohd, “An Experimental Investigation of Tensile Properties and Fatigue Crack Growth Behaviour for Dual Phase Steel”, *Journal of Mechanical Engineering* , vol 15, no. 2, pp. 155-167, 2018.
- [19] D. Hai Long, Bing, Liu, G. Yang, P. G. Yu, Huan, Yu., “Influence of local equivalent stress on fatigue life prediction of carburized Cr-Ni alloy steel based on evaluation of maximum crack sizes,” *Journal of Engineering Fracture Mechanics*, vol. 248, pp. 1-18, 2021, DOI: 10.1016/j.engfracmech.2021.107718.
- [20] W. Mattias, M. Arne, “Influence of material, heat treatment, grinding and shot peening on contact fatigue life of carburized steels”, *International Journal of Fatigue*, vol. 21, no. 4, pp. 309-327, 1999. [https://doi.org/10.1016/S0142-1123\(98\)00077-2](https://doi.org/10.1016/S0142-1123(98)00077-2),
- [21] R. S. Hyde, K. George, K. M. David, “The Influence of Reheat Treatments on Fatigue and Crack of Carburized Steels”, *Journal of materials & manufacturing*, SAE Transactions, vol. 103, no. 5, pp. 588-596, 1994. <https://doi.org/10.4271/940788>.
- [22] Z. Y. Zhao, R. G. Guan, Y. F. Shen, P. K. Bai, “Grain refinement mechanism of Mg-3Sn-1Mn-1La alloy during accumulative hot rolling. Journal of Mater”, *Science Technology*, vol. 91, pp. 251–261, 2021. <https://doi.org/10.1016/j.jmst.2021.02.052>.
- [23] C. H. Yin, Y. L. Liang, Y. Liang, W. Li, M. Yang, “Formation of a self-lubricating layer by oxidation and solid-state amorphization of nano-lamellar microstructures during dry sliding wear tests”, *Journal of Acta Mater*, vol. 166, pp. 208–220, 2019. <https://doi.org/10.1016/j.actamat.2018.12.049>.

- [24] Y. G. Cao, C. H. Yin, Y. L. Liang, S. H. Tang, “Lowering the coefficient of martensite steel by forming a self-lubricating layer in dry sliding wear”, *Journal of Materials Research Express*, vol. 2019, no. 6, pp. 1-15, 2019. <https://doi.org/10.1088/2053-1591/ab032a>.
- [25] Z. X. Li, B. Q. Tong, Q. L. Zhang, J. H. Yao, V. Kovalenko, “Microstructure refinement and properties of 1.0C-1.5Cr steel in a duplex treatment combining double quenching and laser surface quenching”, *Journal of Material Science Engineering*, vol. 776, p. 138994, 2020. <https://doi.org/10.1016/j.msea.2020.138994>.
- [26] J. N. Sultan, E. T. Karash, M. T. E. Kassim, A. M. Ali, H. A. Ibrhim, “The Effect of Carburization and Repeated Heat Treatment with Different Solutions on the Fatigue Resistance of Medium Carbon Steel”, *International Journal of Heat and Technology*, vol. 40, no. 6, pp. 1478-1484, 2022. <https://doi.org/10.18280/ijht.400616>.
- [27] J. N. Sultan, E. T. Karash, M. K. Najim, “Fatigue behaviour of tempered and isothermal heat treated AISI 5160 leaf spring steel”, *Jurnal Teknologithis* , vol. 85, no. 3, pp. 15-24, 2023. [Doi.org/10.11113/jurnalteknologi.v85.18640](https://doi.org/10.11113/jurnalteknologi.v85.18640)
- [28] Z. X. Li, C.S. Li, J.Y. Ren, B.Z. Li, J. Zhang, Y.Q. Ma, “Effect of cold deformation on the microstructure and impact toughness during the austenitizing process of 1.0C–1.5Cr bearing steel”, *Materials Science Engineering*, vol. 674, pp. 262-269. 2016. <https://doi.org/10.1016/j.msea.2016.07.105>.
- [29] F. Wang, D. S. Qian, L. Hua, X. H. Lu, “The effect of prior cold rolling on the carbide dissolution, precipitation and dry wear behaviors of M50 bearing steel”, *Tribology International Journal*, vol. 132, pp. 253-264, 2019. <https://doi.org/10.1016/j.triboint.2018.12.031>.
- [30] J. N. Sultan, E. T. Karash, T. K. Abdulrazzaq, M. T. Elias Kassim, “The Effect of Multi-Walled Carbon Nanotubes Additives on the Tribological Properties of Austempered AISI 4340 Steel”, *Journal Europeen des Systemes Automatises*, vol. 55, no. 3, pp. 387-396, 2022. <https://doi.org/10.18280/jesa.550311>
- [31] G. Zhou, W. Wei, Q. Liu, , “Effect of Hot Rolling on Microstructural Evolution and Wear Behaviors of G20CrNi2MoA Bearing Steel”, *Journal of Metals*, vol. 11, pp. 1-14, 2021. <https://doi.org/10.3390/met11060957>.
- [32] H. Tada, P. Paris, G. R. Irwin, “The Stress analysis of cracks handbook”, St. Louis, Paris Production Inc., 2nd Edition, 1985. <https://doi.org/10.1115/1.801535>
- [33] J. P. Benthem, W. T. Koiter, “Asymptotic approximations to crack problems. In: Methods of analysis and solutions of crack problems”, *Mechanics of fracture book series*, vol. 1, 1973. https://doi.org/10.1007/978-94-017-2260-5_3.